frontiers | Research Topics

Editors' showcase: Nanotechnology

Edited by
Jan M. Macak, Nicolae Coriolan Panoiu, John Fourkas,
Giancarlo Franzese and Wee-Jun Ong

Published in
Frontiers in Nanotechnology

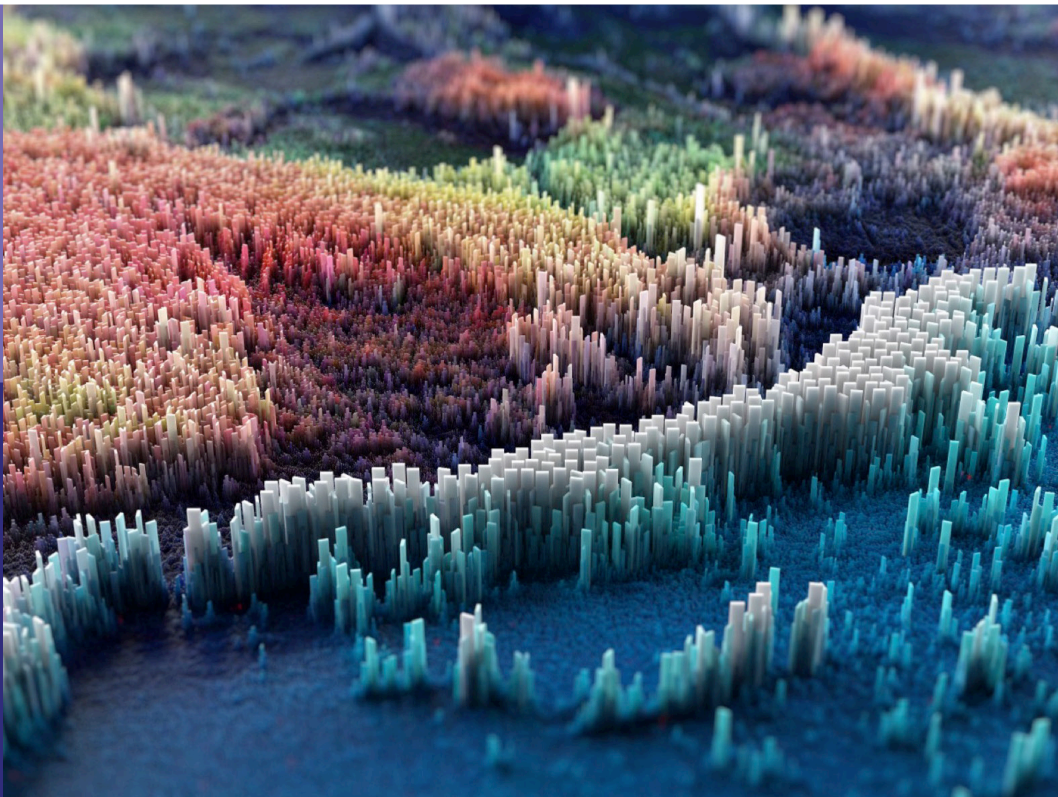

ISSN 1664-8714
ISBN 978-2-8325-5038-0
DOI 10.3389/978-2-8325-5038-0

About Frontiers

Frontiers is more than just an open access publisher of scholarly articles: it is a pioneering approach to the world of academia, radically improving the way scholarly research is managed. The grand vision of Frontiers is a world where all people have an equal opportunity to seek, share and generate knowledge. Frontiers provides immediate and permanent online open access to all its publications, but this alone is not enough to realize our grand goals.

Frontiers journal series

The Frontiers journal series is a multi-tier and interdisciplinary set of open-access, online journals, promising a paradigm shift from the current review, selection and dissemination processes in academic publishing. All Frontiers journals are driven by researchers for researchers; therefore, they constitute a service to the scholarly community. At the same time, the *Frontiers journal series* operates on a revolutionary invention, the tiered publishing system, initially addressing specific communities of scholars, and gradually climbing up to broader public understanding, thus serving the interests of the lay society, too.

Dedication to quality

Each Frontiers article is a landmark of the highest quality, thanks to genuinely collaborative interactions between authors and review editors, who include some of the world's best academicians. Research must be certified by peers before entering a stream of knowledge that may eventually reach the public - and shape society; therefore, Frontiers only applies the most rigorous and unbiased reviews. Frontiers revolutionizes research publishing by freely delivering the most outstanding research, evaluated with no bias from both the academic and social point of view. By applying the most advanced information technologies, Frontiers is catapulting scholarly publishing into a new generation.

What are Frontiers Research Topics?

Frontiers Research Topics are very popular trademarks of the *Frontiers journals series*: they are collections of at least ten articles, all centered on a particular subject. With their unique mix of varied contributions from Original Research to Review Articles, Frontiers Research Topics unify the most influential researchers, the latest key findings and historical advances in a hot research area.

Find out more on how to host your own Frontiers Research Topic or contribute to one as an author by contacting the Frontiers editorial office: frontiersin.org/about/contact

Editors' showcase: Nanotechnology

Topic editors
Jan M. Macak — University of Pardubice, Czechia
Nicolae Coriolan Panoiu — University College London, United Kingdom
John Fourkas — University of Maryland, College Park, United States
Giancarlo Franzese — University of Barcelona, Spain
Wee-Jun Ong — Xiamen University, Malaysia

Citation
Macak, J. M., Panoiu, N. C., Fourkas, J., Franzese, G., Ong, W.-J., eds. (2024).
Editors' showcase: Nanotechnology. Lausanne: Frontiers Media SA.
doi: 10.3389/978-2-8325-5038-0

Table of contents

frontiers in Nanotechnology

MINI REVIEW
published: 18 May 2021
doi: 10.3389/fnano.2021.688552

Wastewater Remediation Technologies Using Macroscopic Graphene-Based Materials: A Perspective

Rajan Arjan Kalyan Hirani[1], **Abdul Hannan Asif**[1], **Nasir Rafique**[1], **Lei Shi**[2], **Shu Zhang**[2], **Hong Wu**[1] and **Hongqi Sun**[1]*

[1]School of Engineering, Edith Cowan University, Joondalup, WA, Australia, [2]College of Materials Science and Engineering, Nanjing Forestry University, Nanjing, China

Three-dimensional (3D) graphene-based macrostructures are being developed to combat the issues associated with two-dimensional (2D) graphene materials in practical applications. The 3D macrostructures (3DMs), for example, membranes, fibres, sponges, beads, and mats, can be formed by the self-assembly of 2D graphene-based precursors with exceptional surface area and unique chemistry. With rational design, the 3D macrostructures can then possess outstanding properties and exclusive structures. Thanks to various advantages, these macrostructures are competing in a variety of applications with promising performances unlike the traditional activated carbons, biochars and hydrochars, which have less flexibilities for modifications towards versatile applications. However, despite having such a wide range of applications, 3DMs remain applicable on laboratory scale due to the associated factors like cost and extensive research. This perspective provides an overview of available graphene-based macrostructures and their diverse synthesis protocols. In the synthesis, hydrothermal route, chemical vapor deposition (CVD), wet spinning, 3D printing, vacuum filtration, spray drying and emulsion methods are highlighted. In addition, the physio-chemical properties of these macrostructures are discussed with the relationship among the porosity, surface area and the bulk density. The perspective also highlights the versatile potentials of different 3DMs in wastewater remediation by adsorption, desalination, and catalytic oxidation, etc. Following the concluding remarks, future outlooks on commercial applications of 3DMs are also provided.

Keywords: 3D macrostructures, graphene, wastewater, remediation, adsorption, advanced oxidation processes

Edited by:
Amitava Mukherjee,
VIT University, India

Reviewed by:
Sasanka Deka,
University of Delhi, India
Ivan Kozyatnyk,
Linköping University, Sweden
Wen Da Oh,
Universiti Sains Malaysia, Malaysia

***Correspondence:**
Hongqi Sun
h.sun@ecu.edu.au

Specialty section:
This article was submitted to Environmental Nanotechnology, a section of the journal Frontiers in Nanotechnology

Received: *31 March 2021*
Accepted: *03 May 2021*
Published: *18 May 2021*

Citation:
Hirani RAK, Asif AH, Rafique N, Shi L, Zhang S, Wu H and Sun H (2021) Wastewater Remediation Technologies Using Macroscopic Graphene-Based Materials: A Perspective. Front. Nanotechnol. 3:688552. doi: 10.3389/fnano.2021.688552

INTRODUCTION

Because of the exceptionally large theoretical surface area ($\approx 2600\ m^2/g$), versatile chemistry and other physicochemical properties, graphene and its derivatives of graphene oxide (GO) and reduced graphene oxide (rGO) have been employed for a vast range of applications, for example, environmental remediation, climate change mitigation, and sustainable energy application (Sun et al., 2014; Yousefi et al., 2019). Since its discovery, graphene in collaboration with various nanotechnologies has demonstrated great success in water and wastewater treatment (Sun et al., 2012; Wang et al., 2013). However, the use of these 2D nanosheets creates various challenges due to

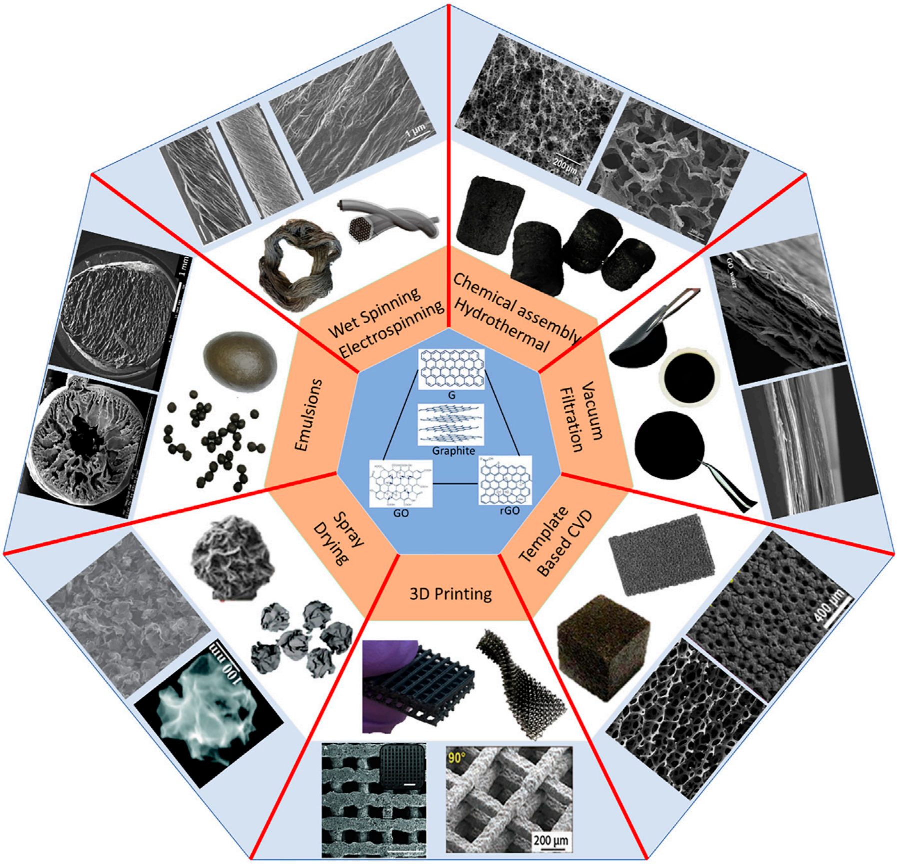

FIGURE 1 | Self-assembly of 2D graphene-based nanosheets into 3D macrostructures.

their highly hydrophilic nature (Wang et al., 2020). For instance, graphene has a very high colloidal stability in water and therefore, the challenging recovery would form major barrier in practical applications. Over the past few years, extensive efforts have been made to combat this issue. It is demonstrated that 3D graphene macrostructures can be competing alternatives to nanoscale graphene and its compounds (Chowdhury and Balasubramanian, 2017). Graphene macrostructures are a 3-dimensional form of graphene and graphene-based compounds. These macrostructures are very practical and attractive because they not only possess the efficiency of nanomaterials but the ease to manipulate and handle of bulk materials.

In the midst of this emerging research based on graphene macrostructures, we present a perspective on the applications of 3DMs in the vast area of wastewater treatment over the past decade. Rather than being exhaustive, we focus on the recent research trends with a few examples. This research topic is still emerging with very few studies presented in the past few years especially in the degradation of emerging organic contaminants.

Graphene oxide tends to easily form liquid crystal domains in water even at a very low concentration because of its high colloidal stability, high aspect ratio, and geometrical anisotropy (Xu and Gao, 2011). The major driving force of GO nanosheets into the self-assembly of 3D structure is the ordered liquid crystalline arrangement in water. The stable suspension of dispersed graphene oxide has the ability to self-assemble into the light and highly porous sponges by being spun to form fibres, cross-linked to GO beads, pressed to membranes, sprayed to form 3D particles, or even chemically deposited on templates to form foams via hydrothermal or chemical procedures such as chemical vapour deposition (CVD). These synthesis procedures are relatively easy and provide a potential to scale up for commercial applications. In addition, facile and precise control on the porosity and the surface area of the macrostructure is enabled which plays a vital role in their applications. The 3D macrostructure from self-assembly of 2D GO has been applied in various areas such as air and water purification, batteries, and sensors, among which water remediation is of particular interest. 3MDs can be used in various wastewater remediation technologies, for example, adsorption, absorption, catalysis, and desalination. **Figure 1** shows the various structures of membranes, fibres, sponges, mats, and beads with their respective synthesis for this purpose (Xu et al., 2015).

RATIONAL DESIGN OF MACROSTRUCTURE TOWARD TAILORED PHYSIOCHEMICAL PROPERTIES

The self-assembly of 2D GO nanosheets into 3D macrostructures leads to a wide range of properties and environmental performances. Most of the basic characteristics such as porosity, surface area, and bulk density are interrelated, and therefore tend to affect the efficiencies of these 3DMs in their applications. Therefore, it is very important to analyse the trends and to correlate the verse applications of 3DMs to their physiochemical properties.

Pore Structure of 3D Macrostructures

The efficiency of all materials in the removal of pollutants from wastewater highly depends on the surface area and the availability of the active sites. As such it is necessary to study the pore structure and size as they are inversely correlated to surface area and directly correlated to interconnectivity (Yousefi et al., 2019). To balance the surface area and the interconnectivity, Bai et al. suggested the synthesis of a hierarchical pore structure. The hierarchical structure has large pores which are connected with small pores. This avails a large surface area for the reaction and also provides a proper-interconnected network of pores throughout the macrostructure (Bai et al., 2015). The morphology and size of the pores are crucial parameters to consider when designing 3DMs for the removal of viscous oils and other solvents. For this application, structures with a larger pore size are desirable. Chemical vapor deposition (CVD) has been mostly used for the synthesis of sponges with the large pore. These sponges tend to have a more open structure with thin pore edges (Bong et al., 2015).

Another cost-effective method for the synthesis of sponges with large pores is the use of a template. Templates can be dipped in an aqueous dispersion of graphene oxide to coat the outer surface to form microporous graphene oxide coated sponges (Hu et al., 2014). Luo et al. fabricated the graphene sponge using polyurethane as the reinforcement. The sponge formed had a low surface energy with high adsorption capacity (Luo et al., 2017). From the above studies, it can be concluded that the porosity plays a great role since modifications and decorations on the foams affect the surface charges making the foam hydrophilic or hydrophobic. This in turn affects the capillary action of the fluids for instance in the removal of dense and more viscous contaminants than water from narrow channels (Yousefi et al., 2019).

Specific Surface Area and Bulk Density of 3D Macrostructures

Bulk density and the pore volume of 3DMs are interrelated. Generally, when the 3D macrostructure has a high bulk density, the structure is composed of more 2D nanosheets and in turn, it has fewer pores. The effect of density is one of the key considerations in the adsorption of oils and viscous solvents. Theoretically, low bulk density macrostructures should be considered for removal of oil. However, this cannot be implemented practically since contact with water could easily disintegrate these 3DMs due to their low stiffness. Hence, a balance should be considered to ensure that the structure is efficient in the removal of oils and meantime, it does not disintegrate (Yousefi et al., 2019).

TABLE 1 | Applications of 3D graphene-based macrostructures in wastewater remediation.

Removal of heavy metals

3D Macrostructure	Metal ion	Efficiency	References
TiO_2-GO hydrogel	Cr(VI)	5 mg/L in 0.5 h	Li et al. (2016)
GO microbots	Pb(II)	950 ppb in 1 h	Vilela et al. (2016)
rGO membrane	Cu(II)	149.2 mg/g	Yu Y. et al. (2021)
GO-silica hydrogel	Hg(II)	266 mg/g	Lu et al. (2019)
Fe_3O_4-GO Composite	As (III)	1,060 ppb	Guo et al. (2015)

Removal of dyes from wastewater (Adsorption)

3D Macrostructure	Dye(s)	Efficiency (g/g)	References
GO vortex ring	MB	1,004	Zhan et al. (2017)
NGO foam	Rhodamine B	900	Fang et al. (2017)
Polyethyleneimine-GO aerogel	Methyl orange	3,059	Shu et al. (2017)
Polyethyleneimine-GO aerogel	Amaranth	2,043	Shu et al. (2017)

Removal of organic solvents and oils

3D Macrostructure	Adsorbate	Adsorption capacity (g/g)	References
CNT-GO aerogel	Chloroform, acetone, and heptane	125–533	Zhan et al. (2018)
CNT-GO aerogel	Oils and solvents	100–332	Wang et al. (2017)
PVA-GO aerogel	Oils and solvents	130–274	Ye et al. (2017)

Removal of salts from water (Desalination)

3D Macrostructure	Salt	Rejection capacities	References
K-rGO membrane	NaCl	91%	Yuan et al. (2021)
GO-Nanofiltration membranes	NaCl Na_2SO_4	64.14% 93.19%	Yu H. et al. (2021)
GO-composite membranes	NaCl, $MgCl_2$ and $Pb(NO_3)_2$	Up to 92 ± 2%	Chandio et al. (2021)

Catalytic degradation of organic pollutants

Catalyst	Pollutant	Efficiency (%/min)	References
P25-GO hydrogels	MB	78%/50	Hou et al. (2012)
TiO_2-GO hydrogel	MB	100%/30	Zhang et al. (2013)
Co_3O_4/GO hydrogel	Orange II	100%/6	Duan et al. (2017)
NGA aerogel	Ibuprofen	90%/180	Wang et al. (2019)
	Phenol	100%/60	
	Naproxen	100%/45	
MnO_2/NGO	Ibuprofen	95%/120	Dong et al. (2019)

The specific surface area of 3DMs determines their efficiency in the removal of the contaminants. 2D nanosheets with a high aspect ratio provide active sites for interaction between the pollutants and catalysts. However, it should be noted that macrostructures with a higher bulk density do not necessarily lead to 3DMs with large specific surface areas (Yousefi et al., 2019). Porosity, interconnectivity and the morphology of the structure jointly determine the specific surface area of 3DMs. In a study based on the removal of methylene blue, the surface area played a great role. Liu et al. prepared a graphene hydrogel with a specific surface area of 450.3 m^2/g for the removal of dyes from wastewater. The results showed that the adsorbent was able to remove 177.3 mg/g of MB from the solution (Liu Y. et al., 2017).

From the above study, it can be concluded that specific surface area is a key that controls molecular adsorption on the surface. Among various studies conducted on 3DMs, only a few studies were able to synthesise macrostructures with surface areas larger than 1000 m^2/g. Therefore, more researches still need to be done on these macrostructures and new methods, and modifications should be proposed to advance this field. One promising solution to this problem is the rational design of pore architecture, however, this method may form larger pores and hence weaken the whole 3D structure.

APPLICATIONS IN WATER REMEDIATION

3D macrostructures have versatile applications in the removal of contaminants such as dyes, hazardous oil, organic solvents and heavy metals by adsorption, desalination and catalytic oxidation for wastewater remediation as shown in **Table 1**.

Removal of Heavy Metals From Wastewater

Heavy metals are frequently discharged to aquatic environments via mining, manufacturing industries, agriculture, automobile among others (Sulaiman et al., 2019). They pose a major hazard to both humans and ecosystems, because the high toxicity of these metals severely threat public health and may cause death in an extreme case. Graphene oxides have ion-chelating negatively charged functional groups which render their 3D macrostructures ideal for the adsorption of the heavy metals from water (Cong et al., 2012; Vilela et al., 2016). The large surface area and the highly porous structure provide ample active sites for adsorption. Yao et al. studied the removal of Cr(IV) using 3D titanium dioxide–graphene hydrogel via adsorption (Li et al., 2016), and showed that oxygen-containing functional groups on the surface of the hydrogel can enhance the adsorption of anionic metal ions by formations of hydrogen bonds. However, it is difficult to remove heavy metals from the wastewater using graphene materials alone. Therefore, external energy is required to boost this process and as such, partial electrical conductivity of graphene oxide macrostructures can be used to tackle this problem. More sophisticated techniques such as the combination of high specific surface area, porosity, introduction of photocatalytic metals oxides such as TiO_2 and partial electrical conductivity, which tend to be more advantageous than just adsorption, can be applied (Liu P. et al., 2017). Additionally, metal ions saturated with 3DMs can be separated easily from aqueous solution and can be reclaimed by acid washing to desorb the metallic phase. Further, graphene oxide-based nanocomposite materials consisting of photocatalytic nanomaterials were used to simultaneously adsorb and reduce heavy metal ions thereby quickening the reclamation process (Gao et al., 2013). Hence, it can be concluded that 3DMs are quite efficient in heavy metal removal and could be a revolution in future if this technique is applied in a commercial wastewater treatment plant.

Removal of Dyes From Wastewater

As a result of industrial growth, a wide range of dyes are being discharged to water bodies. Among all 3D macrostructures, GO sponges and beads have shown promising efficiencies in the removal of various dyes from wastewater. The adsorption of dyes on these 3D macrostructures is aided by the electrostatic forces and the π–π interaction (Sui et al., 2013; Wu et al., 2013).

The availability of the active sites on the GO structure plays a vital role in the adsorption of dyes. When GO surface comes in contact with water, the active sites are occupied by the dissolved organic matters such as humic acid which may affect the adsorption performance. However, most studies ignore this impact by the dissolved organic matters and are also limited to a few pollutants. For the commercial application, a better understanding is required on the roles of organic matters, pH of the solution, and the complexity of the multiple pollutants. Further, most of the dye adsorption is conducted in batch other than continuous tests. Also, after the adsorption, regeneration is necessary yet lacks effective methods. Further, most contaminants studied for the adsorption process in the laboratory are made of small molecules and therefore have simple chemistry. In reality, more complex and toxic organic contaminants such as pharmaceuticals and toxins present in the wastewater need to be mineralised (Yousefi et al., 2019). It can therefore be concluded that with the help of advancing technology, 3DMs could be used in commercial wastewater remediation plants to adsorb dyes, and regenerate the adsorbent for multiple uses to be viable economically.

Removal of Organic Solvents and Oils

Oil and organic solvent spills have become a major issue in terms of marine and freshwater pollution. Spills can be cleaned up by dilution, neutralisation, washing, decontamination, and absorption, most of which however are unreliable as they cause secondary pollutions. Absorption can avoid these risks and can remove the secondary contaminants (Bao et al., 2016). Various lightweight and inert traditional adsorbents have been used but the small pores limit the diffusion of more viscous fluids such as crude oil (Muhammad Shafiq et al., 2017). GO macrostructures with a large specific surface area and porosity can be used as an alternative to traditional solutions. Unlike other pollutants such as dyes and metal ions which are removed by adsorption, most hydrocarbons are eliminated from wastewater by physical absorption. This explains why sponges with high porosity are efficient in this application. Nonetheless, seawater may alter the wettability and the stability of the GO sponges upon prolonged contacts. To overcome this issue modification of GO is necessary and previous studies have shown that partial reduction of GO can be used to restore the hydrophobicity and oleophilicity of the sponge. Chemical reduction of the 3D macrostructures can favour the interactions with the target with the π–π bond (Yousefi et al., 2019).

One major advantage of using 3D macrostructures for this purpose is the easy and effective regeneration of the macrostructure. One idea of regenerating the structure is to burn off the oil without damaging the structure. Alternatively, the absorbed solvent can be squeezed out of the structure, however, the efficiency, in this case, will change. Another quite promising technique is to heat the oil-loaded macrostructure to evaporate the oil phase and simultaneously collect it by condensation for efficient recovery of oil and regeneration of the 3D macrostructure (Bi et al., 2012; Li et al., 2014).

Removal of Salts From Water as Desalination

This process is usually based on membrane technology. In recent years, graphene-based membranes have proven to be a potential candidate in the membrane synthesis for the desalination process. Graphene-based nanosheets are usually very thin and smooth which in turn ensure rapid water transportation through the defects or the channels between these sheets (Liu et al., 2016). Among various desalination techniques, two major graphene-based membrane strategies have been proposed for this purpose: highly nanoporous single sheet structures and stacked 3D macrostructures. The nanoporous single sheet membranes have etched defects which can be as a result of plasma etching or ion bombardment (Surwade et al., 2015). However, these membranes cannot be practically applied in the desalination process due to the challenges in precise control of selectivity and scaling up for commercial application (Surwade et al., 2015). As such, 3D macrostructures have been studied since they are feasible and cost-effective for the desalination process.

3D macrostructures are generally applied in the form of pressure-driven membranes. In this case, the interlayer spacing between the stacks is used to determine the selectivity of the materials for separation. Manipulation of the interlayer spacing of the stacks can be used to regulate the materials flowing through the channel of the membrane (Mi, 2014). Unlike nanoporous single-sheet membranes, 3D macrostructures can be scaled up for commercial use by the production of large-area membranes via gravure printing machine. The gravure printing machine is used in this process to align the nematic phase of graphene oxide liquid crystal suspensions for the formation of highly ordered stacks of graphene oxide. This alignment of the GO sheets enhances the stability of the membrane and also sharpens the size of the channel within the membrane to improve the permeability of water and reject the large solutes (Xu et al., 2017).

Despite putting great efforts into the fabrication of pressure-driven membranes, the current 3D macrostructures have yet exceeded the perselectivity of the state of the art thin film composite desalination membranes (Elimelech and Phillip, 2011). These membranes are allowing a higher permeability of water with a poor salt selectivity hence acting as ultrafiltration or nanofiltration processes and not reverse osmosis. Generally, the efficiency of the membrane is determined by the amount of salt it retains rather than the amount of water it permits. Hence, one major challenge with this pressure-driven membrane is to form thins and defect-free nanomaterial-based membranes for laboratory purpose. Besides, other factors such as membrane fouling and decrease in the desalination performance should also be evaluated to ensure long-term stability (Elimelech and Phillip, 2011).

3D Macrostructures for Advanced Oxidation Processes

Recently graphene-based materials have shown excellent efficiencies in advanced oxidation processes (Duan et al., 2015; Duan et al., 2016; Kang et al., 2020; Li et al., 2021). However, one major challenge is the recovery for reusability since the nanoparticles are hard to collect and recycle. One alternative method is the use of 3D macrostructures for the mineralisation of pollutants. The integrated morphology of the 3D macrostructures makes it easy to separate in the practical application. Further, hybridisation with metal oxides such as MnO_2 and Co_3O_4 can be done easily during the synthesis. This results in synergistic charge transfer and enhances mass transport which eventually increases catalytic activity. Besides, these structures also prevent the release of the catalysts in the environment (He et al., 2018).

Wang et al. synthesised N-doped 3D graphene aerogel (NGA) for catalytic oxidation of emerging contaminants like antibiotic from wastewater (Wang et al., 2019). The as-prepared catalyst was used to chemically activate peroxymonosulfate for the degradation of Ibuprofen. The results showed that about 90% of Ibuprofen was removed in 180 min. Stability and reusability were also studied by using the catalyst for three successive runs. It was seen that 90% degradation was achieved after the first-round while 51.8 and 28.4% degradations were achieved after the second and third round.

From **Table 1**, it can be concluded that graphene-based macrostructures can activate PMS for mineralisation of various pollutants. However, most studies are based on the degradation of dyes and very few studies are done on the degradation of POPs. Further research needs to be done on the degradation of various POPs. Further, stability and the reusability of the catalyst needs to be studied in detail to ensure the efficiency of the degradation not to drop significantly with each cycle. Also, more studies are required to further disclose the catalytic mechanisms of 3D graphene-based macrostructures in verse applications.

CONCLUDING REMARKS AND PERSPECTIVES

Diverse morphological forms of 3-dimensional graphene-based macrostructures can be obtained by rational synthesis and modifications according to the specific application. These macrostructures have proven to be advantageous as they are easy to manipulate and handle than nanoparticles. Furthermore, 3DM's relatively large specific surface area and porosity would play a vital role in the applications such as adsorption of heavy metals and dyes, organic solvents and oils, and catalytic oxidation thus aiding in the purification and remediation of the wastewater. Despite having such remarkable progress in the past few years, there are a few obstacles that we believe need to be overcome to capitalize on the proposed applications of graphene-based macrostructures for environmental remediation. Based on the above discussion, future outlooks can be based on below points.

1. Further studies should be conducted to investigate how these 3D graphene-based wastewater remediation technologies can be integrated into the existing wastewater treatment plants for promising outcomes. For instance, research should be done on how to integrate this treatment in the ultrafiltration process in case of a 3D graphene membrane.
2. Industrial applications require bulk production of 3DMs and therefore various environmentally friendly and economically viable processes should be developed to magnify the production on a commercial level. This also includes the preparation of the precursor (graphene oxide) as it requires a lot of costly resources hence, a breakthrough in GO synthesis is also required. This, in turn, will help to develop less expensive methods for quality wastewater treatment.
3. The applications of these 3DMs are still limited to simple separation such as oil and water separation, dye and heavy metal removals, and simple catalysis. Applications in the degradation and complete elimination of emerging contaminants such as pharmaceuticals and personal care products (PPCPs) (Asif et al., 2021) and disinfections are still quite scarce.
4. Finally, most current studies are only based on laboratory scale models to evaluate the performance of these macrostructures. With the advancement in technology and the improvement in the research sector, 3DMs applications should be driven to advanced levels such as pilot and full scale, which will be beneficial for industrial applications. This will thereby aid in developing novel wastewater remediation techniques at commercial level.

AUTHOR CONTRIBUTIONS

RH wrote the draft; AA and NR contribute to data collection and discussion; LS and SZ contribute to revision and supervision; HW contributes to review and discussion; and HS contributes to conception, supervision, and final revision. All authors contributed to manuscript revision, read, and approved the submitted version.

REFERENCES

Asif, A. H., Wang, S., and Sun, H. (2021). Hematite-based Nanomaterials for Photocatalytic Degradation of Pharmaceuticals and Personal Care Products (PPCPs): A Short Review. *Curr. Opin. Green Sustain. Chem.* 28, 100447. doi:10.1016/j.cogsc.2021.100447

Bai, J., Zhou, A., Huang, Z., Wu, J., Bai, H., and Li, L. (2015). Ultra-light and Elastic Graphene Foams with a Hierarchical Structure and a High Oil Absorption Capacity. *J. Mater. Chem. A.* 3 (45), 22687–22694. doi:10.1039/c5ta06204g

Bao, C., Bi, S., Zhang, H., Zhao, J., Wang, P., Yue, C. Y., et al. (2016). Graphene Oxide Beads for Fast Clean-Up of Hazardous Chemicals. *J. Mater. Chem. A.* 4 (24), 9437–9446. doi:10.1039/c6ta01411a

Bi, H., Xie, X., Yin, K., Zhou, Y., Wan, S., He, L., et al. (2012). Spongy Graphene as a Highly Efficient and Recyclable Sorbent for Oils and Organic Solvents. *Adv. Funct. Mater.* 22 (21), 4421–4425. doi:10.1002/adfm.201200888

Bong, J., Lim, T., Seo, K., Kwon, C.-A., Park, J. H., Kwak, S. K., et al. (2015). Dynamic Graphene Filters for Selective Gas-Water-Oil Separation. *Scientific Rep.* 5 (1), 14321. doi:10.1038/srep14321

Chandio, I., Janjhi, F. A., Memon, A. A., Memon, S., Ali, Z., Thebo, K. H., et al. (2021). Ultrafast Ionic and Molecular Sieving through Graphene Oxide Based Composite Membranes. *Desalination* 500, 114848. doi:10.1016/j.desal.2020.114848

Chowdhury, S., and Balasubramanian, R. (2017). Three-dimensional Graphene-Based Macrostructures for Sustainable Energy Applications and Climate Change Mitigation. *Prog. Mater. Sci.* 90, 224–275. doi:10.1016/j.pmatsci.2017.07.001

Cong, H.-P., Ren, X.-C., Wang, P., and Yu, S.-H. (2012). Macroscopic Multifunctional Graphene-Based Hydrogels and Aerogels by a Metal Ion Induced Self-Assembly Process. *ACS Nano* 6 (3), 2693–2703. doi:10.1021/nn300082k

Dong, Q., Wang, J., Duan, X., Tan, X., Liu, S., and Wang, S. (2019). Self-assembly of 3D MnO2/N-Doped Graphene Hybrid Aerogel for Catalytic Degradation of Water Pollutants: Structure-dependent Activity. *Chem. Eng. J.* 369, 1049–1058. doi:10.1016/j.cej.2019.03.139

Duan, L., Zhou, X., Liu, S., Shi, P., and Yao, W. (2017). 3D-hierarchically Structured Co3O4/graphene Hydrogel for Catalytic Oxidation of Orange II Solutions by Activation of Peroxymonosulfate. *J. Taiwan Inst. Chem. Eng.* 76, 101–108. doi:10.1016/j.jtice.2017.04.019

Duan, X., Ao, Z., Sun, H., Indrawirawan, S., Wang, Y., Kang, J., et al. (2015). Nitrogen-Doped Graphene for Generation and Evolution of Reactive Radicals by Metal-free Catalysis. *ACS Appl. Mater. Inter.* 7 (7), 4169–4178. doi:10.1021/am508416n

Duan, X., Sun, H., Ao, Z., Zhou, L., Wang, G., and Wang, S. (2016). Unveiling the Active Sites of Graphene-Catalyzed Peroxymonosulfate Activation. *Carbon* 107, 371–378. doi:10.1016/j.carbon.2016.06.016

Elimelech, M., and Phillip, W. A. (2011). The Future of Seawater Desalination: Energy, Technology, and the Environment. *Science* 333 (6043), 712–717. doi:10.1126/science.1200488

Fang, Q., Zhou, X., Deng, W., Liu, Y., Zheng, Z., and Liu, Z. (2017). Nitrogen-Doped Graphene Nanoscroll Foam with High Diffusion Rate and Binding Affinity for Removal of Organic Pollutants. *Small* 13 (14), 1603779. doi:10.1002/smll.201603779

Gao, H., Sun, Y., Zhou, J., Xu, R., and Duan, H. (2013). Mussel-Inspired Synthesis of Polydopamine-Functionalized Graphene Hydrogel as Reusable Adsorbents for Water Purification. *ACS Appl. Mater. Inter.* 5 (2), 425–432. doi:10.1021/am302500v

Guo, L., Ye, P., Wang, J., Fu, F., and Wu, Z. (2015). Three-dimensional Fe3O4-Graphene Macroscopic Composites for Arsenic and Arsenate Removal. *J. Hazard. Mater.* 298, 28–35. doi:10.1016/j.jhazmat.2015.05.011

He, K., Chen, G., Zeng, G., Chen, A., Huang, Z., Shi, J., et al. (2018). Three-dimensional Graphene Supported Catalysts for Organic Dyes Degradation. *Appl. Catal. B: Environ.* 228, 19–28. doi:10.1016/j.apcatb.2018.01.061

Hou, C., Zhang, Q., Li, Y., and Wang, H. (2012). P25-graphene Hydrogels: Room-Temperature Synthesis and Application for Removal of Methylene Blue from Aqueous Solution. *J. Hazard. Mater.* 205-206, 229–235. doi:10.1016/j.jhazmat.2011.12.071

Hu, H., Zhao, Z., Gogotsi, Y., and Qiu, J. (2014). Compressible Carbon Nanotube-Graphene Hybrid Aerogels with Superhydrophobicity and Superoleophilicity for Oil Sorption. *Environ. Sci. Technol. Lett.* 1 (3), 214–220. doi:10.1021/ez500021w

Kang, J., Zhou, L., Duan, X., Sun, H., and Wang, S. (2020). Catalytic Degradation of Antibiotics by Metal-free Catalysis over Nitrogen-Doped Graphene. *Catal. Today* 357, 341–349. doi:10.1016/j.cattod.2018.12.002

Li, J., Li, J., Meng, H., Xie, S., Zhang, B., Li, L., et al. (2014). Ultra-light, Compressible and Fire-Resistant Graphene Aerogel as a Highly Efficient and Recyclable Absorbent for Organic Liquids. *J. Mater. Chem. A.* 2 (9), 2934–2941. doi:10.1039/c3ta14725h

Li, J., Zhao, S., Zhang, L., Jiang, S. P., Yang, S.-Z., Wang, S., et al. (2021). Cobalt Single Atoms Embedded in Nitrogen-Doped Graphene for Selective Oxidation of Benzyl Alcohol by Activated Peroxymonosulfate. *Small* 17, 2004579. doi:10.1002/smll.202004579

Li, Y., Cui, W., Liu, L., Zong, R., Yao, W., Liang, Y., et al. (2016). Removal of Cr(VI) by 3D TiO 2 -graphene Hydrogel via Adsorption Enriched with Photocatalytic Reduction. *Appl. Catal. B: Environ.* 199, 412–423. doi:10.1016/j.apcatb.2016.06.053

Liu, G., Jin, W., and Xu, N. (2016). Two-Dimensional-Material Membranes: A New Family of High-Performance Separation Membranes. *Angew. Chem. Int. Ed.* 55 (43), 13384–13397. doi:10.1002/anie.201600438

Liu, P., Yan, T., Zhang, J., Shi, L., and Zhang, D. (2017). Separation and Recovery of Heavy Metal Ions and Salt Ions from Wastewater by 3D Graphene-Based Asymmetric Electrodes via Capacitive Deionization. *J. Mater. Chem. A.* 5 (28), 14748–14757. doi:10.1039/c7ta03515b

Liu, Y., Gao, T., Xiao, H., Guo, W., Sun, B., Pei, M., et al. (2017). One-pot Synthesis of Rice-like TiO2 /graphene Hydrogels as Advanced Electrodes for Supercapacitors and the Resulting Aerogels as High-Efficiency Dye Adsorbents. *Electrochimica Acta* 229, 239–252. doi:10.1016/j.electacta.2017.01.142

Lu, J., Wu, X., Li, Y., Liang, Y., and Cui, W. (2019). Facile Fabrication of 3D Graphene–Silica Hydrogel Composite for Enhanced Removal of Mercury Ions. *Nanomaterials* 9 (3), 314. doi:10.3390/nano9030314

Luo, Y., Jiang, S., Xiao, Q., Chen, C., and Li, B. (2017). Highly Reusable and Superhydrophobic Spongy Graphene Aerogels for Efficient Oil/water Separation. *Scientific Rep.* 7 (1), 7162. doi:10.1038/s41598-017-07583-0

Mi, B. (2014). Graphene Oxide Membranes for Ionic and Molecular Sieving. *Science* 343 (6172), 740–742. doi:10.1126/science.1250247

Muhammad Shafiq, Y., Cheong, W. K., and Lau, E. V. (2017). Graphene Aerogel - Recovery of Heavy Crude Oil from Contaminated Sand. *J. Environ. Chem. Eng.* 5 (2), 1711–1717. doi:10.1016/j.jece.2017.03.009

Shu, D., Feng, F., Han, H., and Ma, Z. (2017). Prominent Adsorption Performance of Amino-Functionalized Ultra-light Graphene Aerogel for Methyl Orange and Amaranth. *Chem. Eng. J.* 324, 1–9. doi:10.1016/j.cej.2017.04.136

Sui, Z.-Y., Cui, Y., Zhu, J.-H., and Han, B.-H. (2013). Preparation of Three-Dimensional Graphene Oxide-Polyethylenimine Porous Materials as Dye and Gas Adsorbents. *ACS Appl. Mater. Inter.* 5 (18), 9172–9179. doi:10.1021/am402661t

Sulaiman, M. B., Salawu, K., and Au, B. (2019). Assessment of Concentrations and Ecological Risk of Heavy Metals at Resident and Remediated Soils of Uncontrolled Mining Site at Dareta Village, Zamfara, Nigeria. *J. Appl. Sci. Environ. Manage.* 23 (1), 187. doi:10.4314/jasem.v23i1.28

Sun, H., Liu, S., Liu, S., and Wang, S. (2014). A Comparative Study of Reduced Graphene Oxide Modified TiO2, ZnO and Ta2O5 in Visible Light Photocatalytic/photochemical Oxidation of Methylene Blue. *Appl. Catal. B: Environ.* 146, 162–168. doi:10.1016/j.apcatb.2013.03.027

Sun, H., Liu, S., Zhou, G., Ang, H. M., Tadé, M. O., and Wang, S. (2012). Reduced Graphene Oxide for Catalytic Oxidation of Aqueous Organic Pollutants. *ACS Appl. Mater. Inter.* 4 (10), 5466–5471. doi:10.1021/am301372d

Surwade, S. P., Smirnov, S. N., Vlassiouk, I. V., Unocic, R. R., Veith, G. M., Dai, S., et al. (2015). Water Desalination Using Nanoporous Single-Layer Graphene. *Nat. Nanotech* 10 (5), 459–464. doi:10.1038/nnano.2015.37

Vilela, D., Parmar, J., Zeng, Y., Zhao, Y., and Sánchez, S. (2016). Graphene-Based Microbots for Toxic Heavy Metal Removal and Recovery from Water. *Nano Lett.* 16 (4), 2860–2866. doi:10.1021/acs.nanolett.6b00768

Wang, C., Yang, S., Ma, Q., Jia, X., and Ma, P.-C. (2017). Preparation of Carbon Nanotubes/graphene Hybrid Aerogel and its Application for the Adsorption of Organic Compounds. *Carbon* 118, 765–771. doi:10.1016/j.carbon.2017.04.001

Wang, H., Mi, X., Li, Y., and Zhan, S. (2020). 3D Graphene-Based Macrostructures for Water Treatment. *Adv. Mater.* 32 (3), 1806843. doi:10.1002/adma.201806843

Wang, J., Duan, X., Dong, Q., Meng, F., Tan, X., Liu, S., et al. (2019). Facile Synthesis of N-Doped 3D Graphene Aerogel and its Excellent Performance in Catalytic Degradation of Antibiotic Contaminants in Water. *Carbon* 144, 781–790. doi:10.1016/j.carbon.2019.01.003

Wang, S., Sun, H., Ang, H. M., and Tadé, M. O. (2013). Adsorptive Remediation of Environmental Pollutants Using Novel Graphene-Based Nanomaterials. *Chem. Eng. J.* 226, 336–347. doi:10.1016/j.cej.2013.04.070

Wu, T., Chen, M., Zhang, L., Xu, X., Liu, Y., Yan, J., et al. (2013). Three-dimensional Graphene-Based Aerogels Prepared by a Self-Assembly Process and its Excellent Catalytic and Absorbing Performance. *J. Mater. Chem. A.* 1 (26), 7612–7621. doi:10.1039/c3ta10989e

Xu, W. L., Fang, C., Zhou, F., Song, Z., Liu, Q., Qiao, R., et al. (2017). Self-Assembly: A Facile Way of Forming Ultrathin, High-Performance Graphene Oxide Membranes for Water Purification. *Nano Lett.* 17 (5), 2928–2933. doi:10.1021/acs.nanolett.7b00148

Xu, Y., Shi, G., and Duan, X. (2015). Self-Assembled Three-Dimensional Graphene Macrostructures: Synthesis and Applications in Supercapacitors. *Acc. Chem. Res.* 48 (6), 1666–1675. doi:10.1021/acs.accounts.5b00117

Xu, Z., and Gao, C. (2011). Aqueous Liquid Crystals of Graphene Oxide. *ACS Nano* 5 (4), 2908–2915. doi:10.1021/nn200069w

Ye, S., Liu, Y., and Feng, J. (2017). Low-Density, Mechanical Compressible, Water-Induced Self-Recoverable Graphene Aerogels for Water Treatment. *ACS Appl. Mater. Inter.* 9 (27), 22456–22464. doi:10.1021/acsami.7b04536

Yousefi, N., Lu, X., Elimelech, M., and Tufenkji, N. (2019). Environmental Performance of Graphene-Based 3D Macrostructures. *Nat. Nanotech* 14 (2), 107–119. doi:10.1038/s41565-018-0325-6

Yu, H., Xiao, G., He, Y., Fan, Y., Mei, X., Li, H., et al. (2021). The Intercalation of Nanoscale Lattices into Micro-sized Graphene Oxide Sheets for Enhancing Pressure-Driven Desalination Performances. *Desalination* 500, 114868. doi:10.1016/j.desal.2020.114868

Yu, Y., Wang, Z., Sun, R., Chen, Z., Liu, M., Zhou, X., et al. (2021). Self-Supported Reduced Graphene Oxide Membrane and its Cu^{2+} Adsorption Capability. *Materials* 14 (1), 146.

Yuan, S., Li, Y., Xia, Y., Selomulya, C., and Zhang, X. (2021). Stable Cation-Controlled Reduced Graphene Oxide Membranes for Improved NaCl Rejection. *J. Membr. Sci.* 621, 118995. doi:10.1016/j.memsci.2020.118995

Zhan, W., Yu, S., Gao, L., Wang, F., Fu, X., Sui, G., et al. (2018). Bioinspired Assembly of Carbon Nanotube into Graphene Aerogel with "Cabbagelike" Hierarchical Porous Structure for Highly Efficient Organic Pollutants Cleanup. *ACS Appl. Mater. Inter.* 10 (1), 1093–1103. doi:10.1021/acsami.7b15322

Zhan, Y., Yan, N., Li, Y., Meng, Y., Wang, J., Zhang, N., et al. (2017). Fabrication of Graphene Millimeter-Vortex Ring with Excellent Absorption via Solution Dripping and In-Situ Reduction Method. *Chem. Eng. J.* 327, 142–149. doi:10.1016/j.cej.2017.06.049

Zhang, Z., Xiao, F., Guo, Y., Wang, S., and Liu, Y. (2013). One-Pot Self-Assembled Three-Dimensional TiO2-Graphene Hydrogel with Improved Adsorption Capacities and Photocatalytic and Electrochemical Activities. *ACS Appl. Mater. Inter.* 5 (6), 2227–2233. doi:10.1021/am303299r

Conflict of Interest: The authors declare that the research was conducted in the absence of any commercial or financial relationships that could be construed as a potential conflict of interest.

frontiers
in Nanotechnology

ORIGINAL RESEARCH
published: 22 June 2021
doi: 10.3389/fnano.2021.698351

DFT Study on Regulating the Electronic Structure and CO_2 Reduction Reaction in BiOBr/Sulphur-Doped G-C_3N_4 S-Scheme Heterojunctions

Xingang Fei[1], *Liuyang Zhang*[1]*, *Jiaguo Yu*[1,2]* *and Bicheng Zhu*[3]

[1]State Key Laboratory of Advanced Technology for Materials Synthesis and Processing, Wuhan University of Technology, Wuhan, China, [2]School of Materials Science and Engineering, Zhengzhou University, Zhengzhou, China, [3]Laboratory of Solar Fuel, Faculty of Materials Science and Chemistry, China University of Geosciences, Wuhan, China

Edited by:
Wee-Jun Ong,
Xiamen University, Malaysia

Reviewed by:
Quanjun Xiang,
University of Electronic Science and Technology of China, China
Kai Dai,
Huaibei Normal University, China

****Correspondence:***
Liuyang Zhang
zly2017@whut.edu.cn
Jiaguo Yu
yujiaguo93@whut.edu.cn

Specialty section:
This article was submitted to Nanotechnology for Energy Applications,
a section of the journal Frontiers in Nanotechnology

Received: *21 April 2021*
Accepted: *11 May 2021*
Published: *22 June 2021*

Citation:
Fei X, Zhang L, Yu J and Zhu B (2021) DFT Study on Regulating the Electronic Structure and CO_2 Reduction Reaction in BiOBr/Sulphur-Doped G-C_3N_4 S-Scheme Heterojunctions.
Front. Nanotechnol. 3:698351.
doi: 10.3389/fnano.2021.698351

Photocatalytic CO_2 reduction is a promising method to mitigate the greenhouse effect and energy shortage problem. Development of effective photocatalysts is vital in achieving high photocatalytic activity. Herein, the S-scheme heterojunctions composed by BiOBr and g-C_3N_4 with or without S doping are thoroughly investigated for CO_2 reduction by density functional theory (DFT) calculation. Work function and charge density difference demonstrate the existence of a built-in electric field in the system, which contributes to the separation of photogenerated electron-hole pairs. Enhanced strength of a built-in electric field is revealed by analysis of Bader charge and electric field intensity. The results indicate that S doping can tailor the electronic structures and thus improve the photocatalytic activity. According to the change in absorption coefficient, system doping can also endow the heterojunction with increased visible light absorption. The in-depth investigation indicates that the superior CO_2 reduction activity is ascribed to low rate-determining energy. And both of the heterojunctions are inclined to generate CH_3OH rather than CH_4. Furthermore, S doping can further reduce the energy from 1.23 to 0.44 eV, indicating S doping is predicted to be an efficient photocatalyst for reducing CO_2 into CH_3OH. Therefore, this paper provides a theoretical basis for designing appropriate catalysts through element doping and heterojunction construction.

Keywords: graphitic carbon nitride, density functional theory, CO_2 reduction, photocatalytic, nonmetal doping, heterojunctions

INTRODUCTION

With the development of society, the greenhouse effect has posed a great threat to human life due to excessive CO_2 emission. Numerous solutions have been explored, including electrochemical Liu et al. (2016), Albo et al. (2017), thermochemical Erb and Zarzycki (2016), Gong et al. (2016), and photochemical methods (Deng et al., 2020; Deng et al., 2021; Gogoi et al., 2021; Meng et al., 2021; Zhang et al., 2021b). Among them, photocatalytic methods are promising due to the sustainability of solar light (Chen et al., 2020; Liu et al., 2020; Xu et al., 2020b; Zhen et al., 2020; Liu et al., 2021a; Wei et al., 2021a; Zhang et al., 2021c). Specifically, photocatalytic CO_2 reduction can convert CO_2 into usable hydrocarbon fuels (Huo et al., 2021; Kang et al., 2021; Ke et al., 2021; Yang et al., 2021; Yang et al., 2021b; Zhang et al., 2021d). Even though photocatalysis shows great advantages, its application in CO_2 reduction is still greatly limited because of the chemical inertness of CO_2 and low visible-light utilization. Therefore, exploration of effective photocatalysts is necessary. In the past few years, various photocatalysts have been explored for photocatalytic CO_2 reduction such as metals (Dong et al., 2020), metal sulfides (Suzuki et al., 2018; Ge et al., 2019; Wang et al., 2020; Xu et al., 2020a), metal oxides (Wang et al., 2020; Chen et al., 2021; Wang et al., 2021), and nonmetals (He et al., 2020; Fei et al., 2021). Despite the great progress, low visible-light absorption and poor catalytic activity are still common problems faced by these photocatalysts. Therefore, modification, especially element doping and heterojunction construction, have been widely implemented to improve the photocatalytic activity (Truc et al., 2019; Ren et al., 2020; Lian et al., 2021; Liu et al., 2021b). Through element doping and heterojunction construction, the electronic structure and recombination of photogenerated electron-hole pairs can be effectively regulated and inhibited.

As a promising metal-free polymeric photocatalyst, graphitic carbon nitride has features of good physicochemical stability, a narrow bandgap, and appropriate band potential (Wang et al., 2009; Li et al., 2020a; Xia et al., 2020; Xie et al., 2020; Li et al., 2021b; Zhang et al., 2021a). In addition, the CO_2 molecule exhibits a strong affinity to pyridine nitrogen in g-C_3N_4, which is beneficial for CO_2 reduction (Zhu et al., 2017). Construction of hybrids has also proven to be effective for g-C_3N_4 (Li et al., 2020b; Li et al., 2020c; Li et al., 2021a; Li et al., 2021c; Li et al., 2020d; Mei et al., 2021; Tao et al., 2021). For instance, Fu et al. designed a 2D/2D WO_3/g-C_3N_4 composite, in which atomic-level thickness of each is realized (Fu et al., 2019). The ultrathin 2D/2D WO_3/g-C_3N_4 is proven to be S-scheme heterojunction, exhibiting high redox capacity and improved photocatalytic activity. In addition, element doping can also have a great influence on the properties of g-C_3N_4 through tailoring the electronic structures (Chen et al., 2021). Tian et al. fabricated P-doped g-C_3N_4 by mixing melamine and diammonium hydrogenphosphate (Tian et al., 2020). It was found that the light absorption is redshifted with the increase of doping concentration which is due to the electronic redistribution by *P* ion doping. It can be deduced that appropriate element doping and heterojunction building is fruitful in regulating the electronic structures and improving the photocatalytic performance.

Among available photocatalysts, BiOBr is deemed to be a prominent candidate for constructing a heterojunction with g-C_3N_4. It has appropriate bandgap and layered structure where one (Bi_2O_2) slab is surrounded by the upper and lower chlorine atoms. More importantly, its unique layered structure allows the formation of 2D/2D Van der Waals heterojunction with g-C_3N_4. In addition, the BiOBr/g-C_3N_4 hybrid has already been investigated by theoretical and experimental research as photocatalysts (Jiang et al., 2018; Qu et al., 2020). It has been proven that the BiOBr/g-C_3N_4 hybrids show superior photocatalytic activities in degradation of dyes and organic pollutants. Even though theoretical and numerous experimental studies have been done on the BiOBr/g-C_3N_4, reports on CO_2 reduction are lacking, and further investigation is still needed to figure out the intrinsic photocatalytic mechanism of CO_2 reduction on BiOBr/g-C_3N_4. In addition, previous studies indicate that element doping such as S doping can promote the performance of photocatalytic CO_2 reduction (Raziq et al., 2018; Wang et al., 2018; Ojha et al., 2019). It can be inferred that the introduction of S atom into BiOBr/g-C_3N_4 (BiOBr/S-g-C_3N_4) can improve the photocatalytic CO_2 reduction performance.

Herein, the effect of sulfur doping on the BiOBr/g-C_3N_4 heterojunction is investigated by exploring electronic, optical properties, and CO_2 reduction reaction. Through the theoretical calculation, comprehensive understanding of the CO_2 reduction over BiOBr/g-C_3N_4 systems will be acquired. Furthermore, electron distribution, visible light adsorption, and CO_2 reduction will also be investigated comprehensively. It is expected that this research can provide a basis for the design of novel CO_2 reduction materials.

CALCULATION DETAILS

Vienna ab initio simulation package (VASP) was employed for calculations (Hafner, 2008). The geometry structures were optimized utilizing the generalized gradient approximation (GGA) Perdew-Burke-Ernzerhof (PBE) as exchange–correlation function (Grimme, 2006; Wu and Cohen, 2006). The DFT-D method of Grimme was selected to treat van der Waals interaction (Le et al., 2012). A 500 eV cutoff energy was adopted for the plane-wave expansion. For Brillouin-zone, a 4 × 2 × 1 Monkhorst–Pack k-point mesh was used in the geometry optimization and other properties calculation. A vacuum distance of 15 Å was used to eliminate periodic interactions between adjacent images. The convergence criteria of the geometry optimization for the energy change and maximum force were set to be 10^{-5} eV and 0.01 eV/Å, respectively.

In the process of constructing heterojunction, the lattice match is the key point. It is necessary to choose two components with similar cell parameters. Herein, a $1 \times \sqrt{3}$ single layered g-C_3N_4 is placed at the top of a 2 × 3 single-layered BiOBr for constructing 2D/2D BiOBr/g-C_3N_4 heterojunction. The 2D/2D BiOBr/S-g-C_3N_4 heterojunction is built by stacking a $1 \times \sqrt{3}$ S-g-C_3N_4 monolayer above a 2 × 3 BiOBr monolayer.

For CO_2 reduction, the reaction processes of each step were evaluated by calculating their Gibbs free energy change (ΔG) (Han and Sohn, 2005; Yan et al., 2016), which is expressed by the following equation:

$$\Delta G = \Delta H - T\Delta S + ZPE \tag{1}$$

In this formula, ΔH denotes the energy difference of each reaction step gained from DFT calculation. T represents the temperature at 298.15 K ΔS and ZPE are the change of entropy and zero-point energy, respectively.

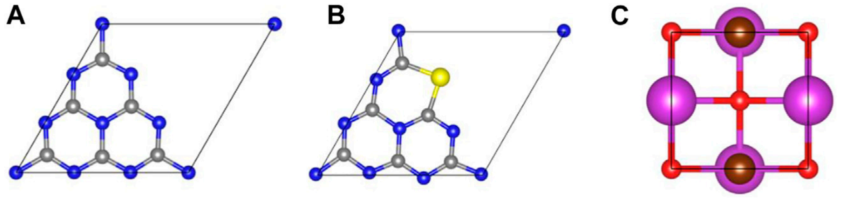

FIGURE 1 | Optimized geometric structures of monolayered g-C_3N_4, S-g-C_3N_4, and BiOBr. The C, N, S, Bi, O, and Br atoms are represented by the grey, blue, yellow, purple, orange, and brown balls, respectively.

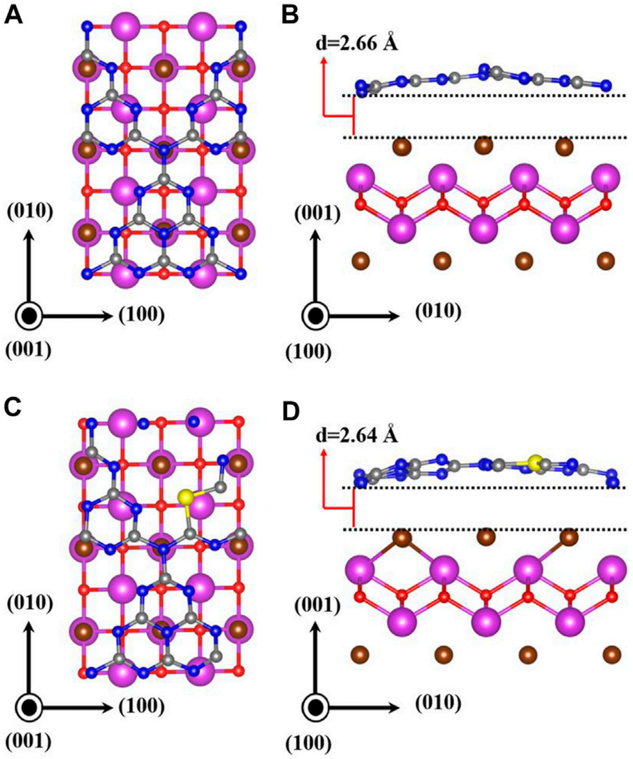

FIGURE 2 | Optimized geometric structures of BiOBr/g-C_3N_4 and BiOBr/S-g-C_3N_4 heterojunctions. **(A)** and **(C)** are the top view; **(B)** and **(D)** are the side view.

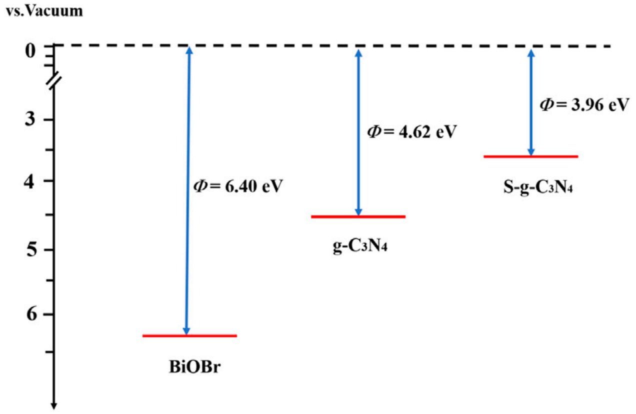

FIGURE 3 | The calculated work functions of BiOBr, g-C_3N_4, and S-g-C_3N_4. The red and black dotted lines signify the Fermi level and vacuum energy level, respectively.

RESULTS AND DISCUSSION

Geometric Structures

Prior to the investigation of heterojunctions, the geometric structures of monolayered g-C_3N_4, S-doped g-C_3N_4 (S-g-C_3N_4) and BiOBr along the (001) facet were first studied. As shown in **Figure 1**, the optimized lattice parameters are a = b = 7.13 Å for monolayered g-C_3N_4; the parameters are a = b = 3.95 Å for monolayered BiOBr. These results agree well with the experimental and theoretical results (Zhao and Dai, 2014; Bai et al., 2016; Zhu et al., 2018). According to previous research, S atom is more inclined to substitute pyridine nitrogen on g-C_3N_4 (Wang et al., 2018; Ghashghaee et al., 2020). Therefore, the doped g-C_3N_4 is constructed by replacing the 2-fold coordinated N atom with S atom (**Figure 1B**). The calculated lattice constants are a = b = 7.15 Å. Compared with the pristine g-C_3N_4, the S–C bonds in S-doped g-C_3N_4 are slightly longer than the corresponding N–C bonds because of the larger atomic radius of S atom than that of N atom. **Figures 2A,B** are the top and side view of optimized BiOBr/g-C_3N_4 heterojunction; **Figures 2C,D** depict the top and side view of optimized BiOBr/S-g-C_3N_4 heterojunction. The equilibrium distance between g-C_3N_4 and BiOBr in BiOBr/g-C_3N_4 is 2.66 Å, while it is 2.64 Å in BiOBr/S-g-C_3N_4. The equilibrium distance of these two heterojunctions exhibits the feature of van der Waals (vdW) heterojunction, indicating that a vdW interaction is established between (S-doped) g-C_3N_4 and BiOBr. Moreover, it can be seen clearly that the g-C_3N_4 in both heterojunctions changes from a planar structure to a curved structure, indicating there is an interaction between g-C_3N_4 and BiOBr.

In addition, the thermodynamic stability of BiOBr/(S-doped) g-C_3N_4 heterojunctions is evaluated by calculating the formation energy based on the following equations:

$$E_F = E_H - E_A - E_B \tag{2}$$

where E_H is the total energy of BiOBr/g-C_3N_4 or BiOBr/S-g-C_3N_4 heterojunction, E_A represents total energy of pure or S-doped g-C_3N_4, and E_B represents the total energy of BiOBr. A more negative value of binding energy suggests a more stable structure. The calculated formation energies of BiOBr/g-C_3N_4

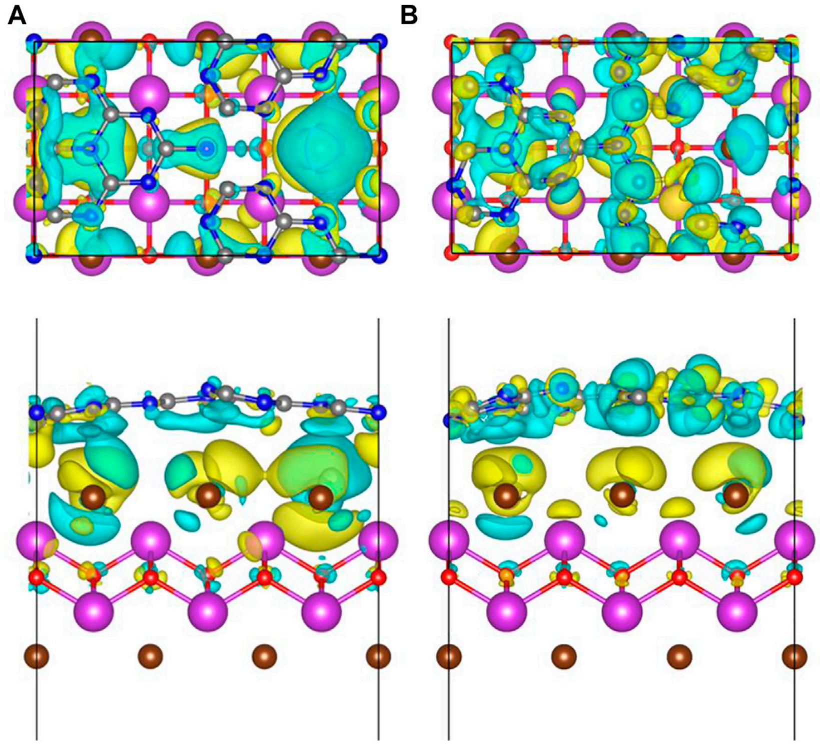

FIGURE 4 | The top and side view of charge density difference in **(A)** BiOBr/g-C_3N_4 and **(B)** BiOBr/S-g-C_3N_4. The blue and yellow areas represent charge consumption and accumulation, respectively. The isosurface value was 0.3 e·nm^{-3}.

and BiOBr/S-g-C_3N_4 are −0.52 and −0.63 eV, respectively, demonstrating that both the constructed heterojunctions are stable.

Work Function

As an important criterion to judge charge transfer, the work function is equivalent to the gap between Fermi level and vacuum level. It is expressed by the following formula:

$$\Phi = E_{\mathrm{vac}} - E_{\mathrm{F}} \tag{3}$$

where E_{vac} and E_{F} represent vacuum level and Fermi level, respectively. The work functions of g-C_3N_4, S-doped g-C_3N_4, and BiOBr are obtained and shown in **Figure 3**. The calculated Φ of g-C_3N_4 is 4.62 eV, consistent with the previous results (Mahmood et al., 2020). After the introduction of S atom, the work function is reduced to 3.96 eV. This is mainly due to the fact that S atoms own more valence electrons than N atoms, which can raise the Fermi level. In addition, it is found that the Fermi level of BiOBr (6.40 eV) is lower than those of g-C_3N_4 and S-g-C_3N_4. Therefore, it can be deduced that the electrons will flow from the pure and S-doped g-C_3N_4 to the BiOBr until reaching the uniform Fermi level.

Charge Density Difference

To intuitively reflect the charge transfer and separation between different constituents, the charge density difference is calculated by:

$$\begin{aligned}\Delta\rho = {} & \rho\left(\mathrm{BiOBr}/\left(\text{S-doped}\right) - \text{g-}C_3N_4\right) \\ & - \rho\left(\left(\mathrm{S} - \text{doped}\right)\text{-g-}C_3N_4\right) - \rho\left(\mathrm{BiOBr}\right)\end{aligned} \tag{4}$$

where ρ[BiOBr/(S-doped)-g-C_3N_4], ρ[(S-doped)-g-C_3N_4], and ρ(BiOBr) are the charge densities of S-doped or pure BiOBr/g-C_3N_4 hybrids, S-doped or pure g-C_3N_4, and BiOBr, respectively. **Figure 4** depicts the charge density difference of hybrid systems along Z axis. The charge depiction and accumulation are marked by blue and yellow regions, respectively. It is obvious that the surface of S-doped and pure g-C_3N_4 are mainly covered by the blue region, while the BiOBr surface is dominant by the yellow region. Therefore, the electrons transfer from S-doped and pure g-C_3N_4 to BiOBr in the heterojunctions, which agrees well with the analysis of aforementioned work function. Particularly, the blue and yellow coverage areas in the S-doped hybrids are broader than those in the pure hybrids, indicating that S doping brings about a stronger interface interaction. In addition, the Bader charge is calculated to quantitatively investigate the charge transfer. It is found that there are 0.08 electrons transferring from g-C_3N_4 to BiOBr. As for the S doping counterpart, the number of charge transfers from S-doped g-C_3N_4 to BiOBr increases to 0.15 e. This further confirms that the introduction of S atom to the hybrid can have a great effect on increasing interfacial electron transfer.

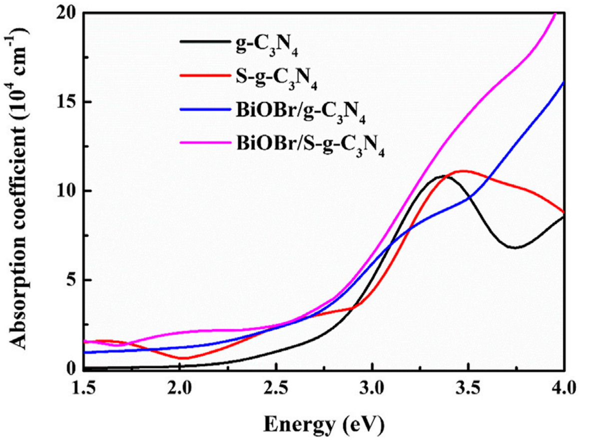

FIGURE 5 | Optical absorption coefficients of single layered g-C_3N_4, single layered S-g-C_3N_4, BiOBr/g-C_3N_4, and BiOBr/S-g-C_3N_4 heterojunction.

Strength of Built-in Electric Field

Electron transfer results in uneven charge distribution at the interface, thus forming a polarized electric field at the hybrid's interface. As an important physical quality, the electric field has a great correlation with band bending and separation of photogenic electrons and holes. The strength of the built-in field can be evaluated by the following equation:

$$E = \frac{P}{\varepsilon S d} \tag{5}$$

Herein, P is the dipole moment; ε is the dielectric constant which is equal to 8.85×10^{-12} Fm^{-1}; S represents the surface area of heterojunctions; and d represents the interfacial distance of heterojunctions. The calculated E value for doped and non-doped hybrid is 2.56×10^9 and 0.64×10^9 Vm^{-1}, respectively. Obviously, the electric field intensity of S-doped heterogeneous junction is greatly improved. This improvement is mainly attributed to the magnitude of p value, which is related to the number of electron transfers at the interface. Following the above analysis of charge transfer, the BiOBr/S-g-C_3N_4 exhibits more electron transfer at the interface, thus leading to a larger dipole moment and stronger electric field intensity.

Optical Absorption

To explore the influence of doping and heterojunction construction on light absorption, the absorption coefficient $\alpha(\omega)$ is calculated according to equation:

$$\alpha(\omega) = \sqrt{2}\omega\left[\sqrt{\varepsilon_1(\omega)^2 + \varepsilon_2(\omega)^2} - \varepsilon_1(\omega)\right]^{1/2} \tag{6}$$

where ε_1 and ε_2 denote the real and imaginary parts of dielectric function, respectively. ω is the optical frequency which determines the dielectric functions. **Figure 5** describes the calculated absorption spectra of g-C_3N_4, S-g-C_3N_4, BiOBr/g-C_3N_4, and BiOBr/S-g-C_3N_4. In the visible light range (1.5–3.1 eV), the light absorption intensity is ordered by BiOBr/S-g-C_3N_4 > BiOBr/g-C_3N_4 > S-g-C_3N_4 > g-C_3N_4. There are obvious red shift and enhanced light absorption intensity for S-g-C_3N_4, BiOBr/g-C_3N_4 relative to pure g-C_3N_4. Moreover, the strongest visible light absorption occurs in BiOBr/S-g-C_3N_4 heterojunction which further verifies the positive effect of element doping and heterojunction constructing on optical property. Therefore, both the S doping and heterojunction construction of g-C_3N_4 with BiOBr can improve the visible light absorption.

Photocatalytic Mechanism

Based on the aforesaid results, it is found that the S atom can elevate the Fermi level of g-C_3N_4, thus enhancing the strength of the built-in electric field of BiOBr/g-C_3N_4 heterojunction. To further explore the reasons for photocatalytic activity enhancement, the photocatalytic mechanism is interpreted comprehensively (**Figure 6**). According to the analysis of work function, before contact, the g-C_3N_4 possesses a higher Fermi level than the BiOBr. Upon contact, the electrons will transfer from g-C_3N_4 to the BiOBr until Fermi level is equalized. The electron flow leads to a built-in electric field pointing to BiOBr and band bending of each component. Upon light illumination, the electrons on the valance band (VB) are excited to the conduction band (CB), leaving the photogenerated holes in the VB. Under the effect of internal electric field and band bending, the holes in the g-C_3N_4 VB will combine with the electrons in the BiOBr CB at the interface. The electrons with strong reduction ability are reserved in the g-C_3N_4 CB for CO_2 reduction; holes with superior oxidation capacity in the BiOBr VB survive for oxidation reactions such as pollutant degradation. Therefore, BiOBr/g-C_3N_4 heterojunction follows the S-scheme photocatalytic mechanism. After the introduction of S atom, the doped heterojunction still follows the S-scheme photocatalytic mechanism. And the main difference between the S-doped and undoped one is their interface interaction.

Specifically, the S atom enlarges the Fermi level difference between BiOBr and g-C_3N_4 by 0.12 eV, which induces more interfacial electron transfer. Consequently, an increased interfacial field (2.56×10^{-9} V/m) is established. In general, the elevated Fermi level of S-doped heterojunction generates a stronger interfacial field, which provides a stronger force for the recombination of electrons and holes than the non-doped counterpart. Additionally, it also leads to more effective separation of electrons and holes. To sum up, the introduction of S atom can promote the photocatalytic activity by facilitating charge separation.

CO_2 Reduction

The above analysis indicates that the S atom doping can regulate electric fields and increase light absorption. In this regard, the heterojunction with S doping is expected to be a preferable photocatalyst for CO_2 reduction. Through the investigation of the reaction mechanisms, as well as identification of active sites and reduction products of BiOBr/g-C_3N_4 with or without S doping for CO_2 reduction, we will have a profound understanding of CO_2 reduction reaction.

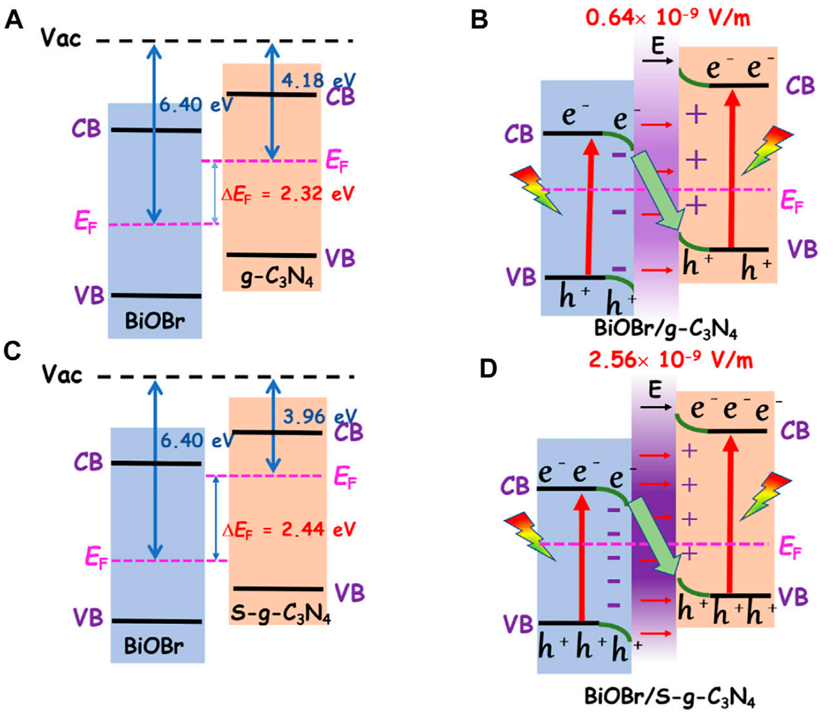

FIGURE 6 | **(A)** and **(B)** are the charge transfer mechanism in BiOBr/g-C_3N_4 before and after contact, while **(C)** and **(D)** are the charge transfer mechanism in BiOBr/S-g-C_3N_4 before and after contact.

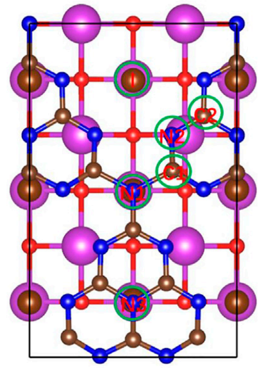

Adsorption Site	Adsorption Energy (eV)
C1	-0.170
C2	-0.194
N1	-0.168
N2	-0.184
N3	-0.169
I	-0.182

FIGURE 7 | The adsorption energy of CO_2 at different adsorption sites in BiOBr/g-C_3N_4.

As the initial step for CO_2 reduction, the absorption of CO_2 attaches importance to the further reduction processes. It is critical to find the active sites for CO_2 molecules. According to the photocatalytic mechanism of the BiOBr/(S-doped)g-C_3N_4 heterojunction, the photogenerated electrons for CO_2 reduction are mainly on the surface of g-C_3N_4. Thus, the CO_2 reaction process proceeds on the (S-doped) g-C_3N_4 side of BiOBr/g-C_3N_4. As shown in **Figure 7**, various possible adsorption sites on the g-C_3N_4 side of BiOBr/g-C_3N_4 are considered by comparing their adsorption energy. For convenience, different kinds of C and N atoms are labeled as C1, C2, C3, N1, and N2, respectively. It is found that the C2 and N2 atoms exhibit more negative adsorption energy than the rest, indicating higher affinity to CO_2. In addition, after the structure optimization, the CO_2 molecule adsorbed on the C2 site inclines to move over the N2 atom, indicating that the N2 position is the most favorable site for CO_2 adsorption. Thus, the two coordination N atoms are selected to be the active sites for the initial CO_2 adsorption, in agreement with the previous studies (Zhu et al., 2017). For the BiOBr/S-g-C_3N_4, the C2, N2, and S positions are selected as potential active sites. The calculated absorption energy for C2, N2, and S are −0.10, −0.17, and −0.14 eV, respectively. After S doping, judging from absorption energy, the two coordination N atoms still preserve the strongest affinity for CO_2 molecules. Thus, the N2 atom in the BiOBr/S-g-C_3N_4 is also treated as the initial active site. In general, both the pure and S-doped BiOBr/g-C_3N_4 exhibit strong CO_2 adsorption capacity, which is beneficial for the subsequent reduction reaction.

After the CO_2 adsorption, the following reduction processes can proceed by a hydrogenation step on the C or O atom. All the possible intermediates and reaction paths are listed in **Figure 8**. The most favorable reaction pathways of CO_2 reduction to CH_3OH or CH_4 are obtained by comparing their free energy of each step. For the pure BiOBr/g-C_3N_4, the scheme and the most stable structure of the optimal path for CO_2 reduction are depicted in **Figure 9**. The first step of the reaction is the hydrogenation of CO_2 into COOH* with a free energy of 1.23 eV. In terms of the whole barrier diagram, this step is deemed to be the rate-limiting step with the highest energy

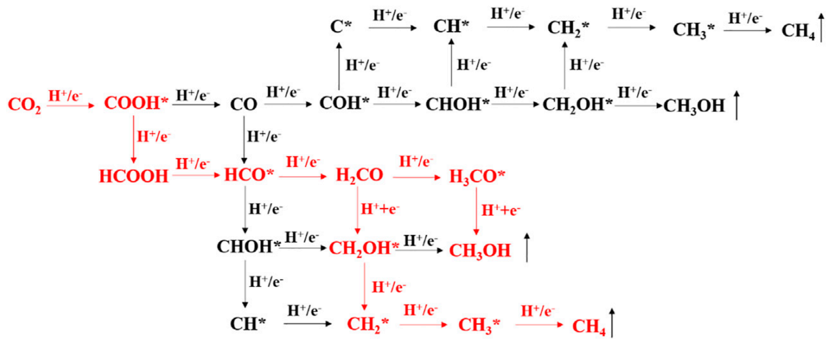

FIGURE 8 | The possible reaction paths and intermediates of CO_2 reduction by hydrogenation of C and O. The red part is the optimal reaction path on the BiOBr/g-C_3N_4 and BiOBr/S-g-C_3N_4.

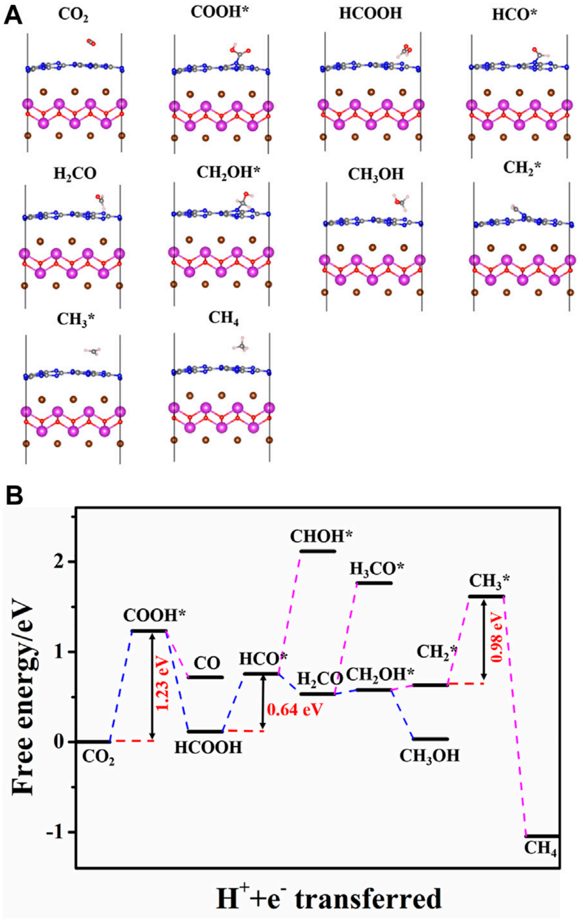

FIGURE 9 | (A) Optimized structure of reaction intermediates and **(B)** free energy diagram on the optimal path of CO_2 reduction on BiOBr/g-C_3N_4. The blue and red dotted lines indicate optimal and infeasible reaction paths, respectively. The white spheres represent H atoms.

barrier, which is due to the inertness of CO_2 molecules, and similar results have been found in other studies (Zhi et al., 2019). After the generation of COOH*, the following step is related to the acquisition of CO and HCOOH by a dehydroxylation or hydrogenation step of COOH*, respectively. The respective free energy for CO and HCOOH formation is calculated to be −0.51 and −1.12 eV, indicating that both processes are exothermic and spontaneous. Moreover, the more negative ΔG of HCOOH generation manifests that the formation of HCCOH is more competitive relative to that of CO. The desorption ability of the two intermediates is further investigated to evaluate whether they are intermediates or final products. The calculated adsorption energy for HCOOH and CO are −0.78 and −0.14 eV, respectively. The interaction between HCOOH and catalyst is strong due to the more negative adsorption energy, indicating that the HCOOH is more likely to be intermediate for the next reduction. By contrast, the CO inclines to desorb from the catalyst surface. Therefore, we focus the subsequent reaction on the hydrogenation and dehydration of HCOOH. The calculated ΔG from HCOOH to HCO* is 0.64 eV, suggesting an endothermic process. During the process of HCO* protonation, the reaction free energy of H_2CO and CHOH* differs considerably. The energy barrier for H_2CO formation is −0.22 eV, while that for CHOH* is 1.93 eV, which is apparently a non-spontaneous process. Thus, the H_2CO intermediate is more favorable for the next reaction. After comparing the free energy in generating H_3CO* (1.23 eV) and CH_2OH* (0.05 eV), the CH_2OH* is selected for the latter reaction. It is worth noting that the two products, CH_3OH and CH_4, share the same reaction path before the formation of CH_2OH*. After that, the product of CH_3OH is obtained through a hydrogenation at the C of CH_2OH*; while the CH_4 is generated by experiencing the CH_2OH*, CH_2*, CH_3*, and CH_4 reaction path. Moreover, the rate-determining step for CH_4 and CH_3OH generation on the pure and S-doped heterojuncions is the same, to explore the reaction selectivity, the free energy of each reaction step is further compared. It is obvious that the protonation of CH_2OH to CH_3OH is a spontaneous exothermic process with a free energy of −0.51 eV, while the highest energy barrier of CH_2OH to CH_4 is 0.98 eV. Thus, compared with CH_4, CH_3OH is more liable to be the final product. On the whole, among the three reduction products, i.e. CO, CH_3OH, and CH_4, the BiOBr/g-C_3N_4 heterojunction showed stronger selectivity to CO and CH_3OH than CH_4.

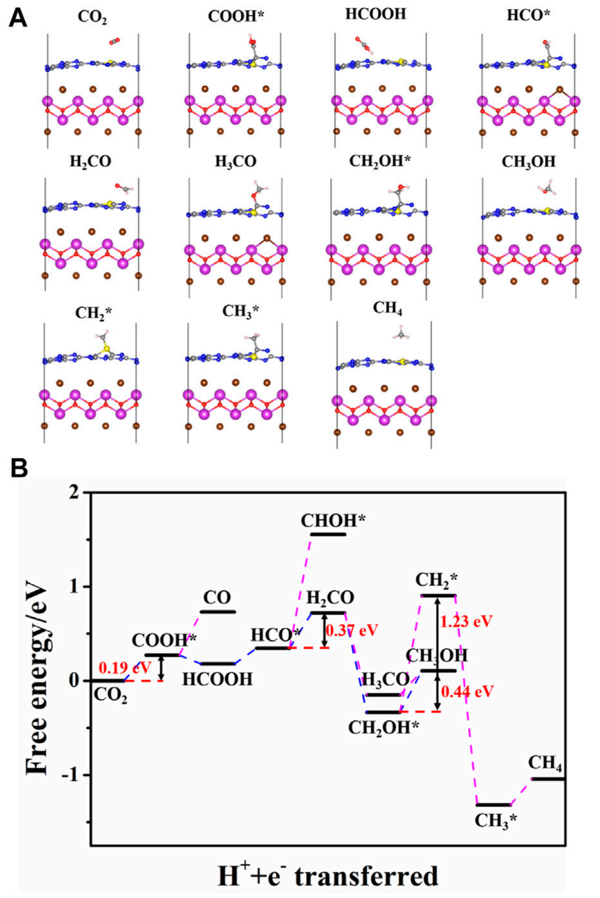

FIGURE 10 | (A) Optimized structure of reaction intermediates and **(B)** free energy diagram on the optimal path of CO_2 reduction on BiOBr/S-g-C_3N_4.

Figure 10 shows the favorable free energy scheme and the most favorable adsorption geometries of the optimal path for CO_2 reduction on BiOBr/S-g-C_3N_4. It is found that the reaction pathways for CO_2 reduction to CO, CH_3OH, and CH_4 on S-doped hybrid are the same as those on the undoped counterpart but the reaction energy of each step is quite different. The respective optimal reaction path for the CO and CH_3OH formation on the doped system still proceeds sequentially in the following order: CO_2, COOH*, CO; CO_2, COOH*, HCOOH, HCO*, H_2CO, CH_2OH*, and CH_3OH. However, the formation of CH_4 is obtained according to CO_2, COOH*, HCOOH, HCO*, H_2CO, CH_2OH*, CH_2*, CH_3*, and CH_4. For CO generation, each step of the reaction is endothermic with a rate-determining energy of 0.46 eV. It is clear that the rate-determining step for CH_3OH formation on doped hybrid is the last step, namely, conversion of CH_2OH* into CH_3OH. Unlike it, the highest energy barrier for CH_3OH on pure hybrid occurs at the first step. And the BiOBr/S-g-C_3N_4 possesses lower rate-determining energy (0.44 eV) than the undoped hybrid (1.24 eV). Thus, S-doped hybrid is more conductive to the CH_3OH formation. Moreover, in the process of CO, CH_3OH, and CH_4 generation, the energy barrier of the rate-determining step of CO and CH_4 is larger than that of CH_3OH. Therefore, the BiOBr/S-g-C_3N_4 also inclines to reduce CO_2 into CH_3OH rather than CO and CH_4.

CONCLUSION

In this work, DFT calculations are adopted to investigate the geometric structure, electronic properties, and CO_2 reduction mechanism of pristine and S-dopedBiOBr/g-C_3N_4. The charge density difference demonstrates the existence of a built-in electric field pointing to BiOBr, and the formation of S-schemeheterojunction is validated. Bader charge analysis indicates that more electrons transfer in the doped hybrids compared with the pristine one. Integrated with the calculation of the strength of thebuilt-infield, it can be inferred that S doping can enhance the interfacial electric field intensity. The improved electronic interaction is on account of the elevation of the Fermi level by S doping. Also, the computed optical absorption coefficient indicates improved visible-light absorption after S doping and construction of heterojunction. Through the investigation of CO_2 reduction, it is found that both the pure and S-doped hybrids prefer to reduce CO_2 to CH_3OH rather than CH_4. Moreover, compared with the pure heterojunction, the BiOBr/S-g-C_3N_4 exhibits a more superior CO_2 reduction activity towards CH_3OH due to the lower limiting energy. Therefore, the heterojunctions construction and nonmetal doping can lower CO_2 reduction energy barrier, which will ultimately improve the photocatalytic activity. This work will provide a theoretical basis for the design of g-C_3N_4-based photocatalysts.

DATA AVAILABILITY STATEMENT

The original contributions presented in the study are included in the article/Supplementary Material, further inquiries can be directed to the corresponding authors.

AUTHOR CONTRIBUTIONS

LZ: Conceptualization, Writing-Reviewing and Editing, Supervision. JY: Conceptualization, Methodology, Supervision. BZ: Software, Validation.

FUNDING

This work was supported by the National Key Research and Development Program of China (2018YFB1502001), the National Natural Science Foundation of China (51872220, 21905219, 51932007, U1905215, 21871217, and U1705251), the Fundamental Research Funds for Central Universities (2021IVA137), National Postdoctoral Program for Innovative Talents (BX20180231), China Postdoctoral Science Foundation (2020M672432), and the Hubei Postdoctoral Program for Innovative Research Post.

REFERENCES

Albo, J., Vallejo, D., Beobide, G., Castillo, O., Castaño, P., and Irabien, A. (2017). Copper-Based Metal-Organic Porous Materials for CO_2 Electrocatalytic Reduction to Alcohols. *ChemSusChem*, 10, 1100–1109. doi:10.1002/cssc.201600693

Bai, Y., Chen, T., Wang, P., Wang, L., Ye, L., Shi, X., et al. (2016). Size-dependent Role of Gold in G-C3N4/BiOBr/Au System for Photocatalytic CO2 Reduction and Dye Degradation. *Solar Energ. Mater. Solar Cell*. 157, 406–414. doi:10.1016/j.solmat.2016.07.001

Chen, C., Jin, J., Chen, S., Wang, T., Xiao, J., and Peng, T. (2021). *In-situ* Growth of Ultrafine ZnO on G-C3N4 Layer for Highly Active and Selective CO2 Photoreduction to CH4 under Visible Light. *Mater. Res. Bull.* 137, 111177. doi:10.1016/j.materresbull.2020.111177

Chen, Y., Su, F., Xie, H., Wang, R., Ding, C., Huang, J., et al. (2021). One-step Construction of S-Scheme Heterojunctions of N-Doped MoS2 and S-Doped G-C3N4 for Enhanced Photocatalytic Hydrogen Evolution. *Chem. Eng. J.* 404, 126498. doi:10.1016/j.cej.2020.126498

Chen, Y., Wang, F., Cao, Y., Zhang, F., Zou, Y., Huang, Z., et al. (2020). Interfacial Oxygen Vacancy Engineered Two-Dimensional G-C3N4/BiOCl Heterostructures with Boosted Photocatalytic Conversion of CO2. *ACS Appl. Energ. Mater.* 3, 4610–4618. doi:10.1021/acsaem.0c00273

Deng, H., Fei, X., Yang, Y., Fan, J., Yu, J., Cheng, B., et al. (2021). S-scheme Heterojunction Based on P-type ZnMn2O4 and N-type ZnO with Improved Photocatalytic CO2 Reduction Activity. *Chem. Eng. J.* 409, 127377. doi:10.1016/j.cej.2020.127377

Deng, H., Xu, F., Cheng, B., Yu, J., and Ho, W. (2020a). Photocatalytic CO2 Reduction of C/ZnO Nanofibers Enhanced by an Ni-NiS Cocatalyst. *Nanoscale*. 12, 7206–7213. doi:10.1039/c9nr10451h

Dong, H., Zhang, X., Lu, Y., Yang, Y., Zhang, Y.-P., Tang, H.-L., et al. (2020b). Regulation of Metal Ions in Smart Metal-Cluster Nodes of Metal-Organic Frameworks with Open Metal Sites for Improved Photocatalytic CO2 Reduction Reaction. *Appl. Catal. B: Environ.* 276, 119173. doi:10.1016/j.apcatb.2020.119173

Erb, T. J., and Zarzycki, J. (2016). Biochemical and Synthetic Biology Approaches to Improve Photosynthetic CO2-fixation. *Curr. Opin. Chem. Biol.* 34, 72–79. doi:10.1016/j.cbpa.2016.06.026

Fei, X., Tan, H., Cheng, B., Zhu, B., and Zhang, L. (2020). 2D/2D Black Phosphorus/g-C3N4 S-Scheme Heterojunction Photocatalysts for CO2 Reduction Investigated Using DFT Calculations. *Acta Phys.-Chim. Sin.* 37, 2010027. doi:10.3866/pku.Whxb202010027

Fu, J., Xu, Q., Low, J., Jiang, C., and Yu, J. (2019). Ultrathin 2D/2D WO3/g-C3N4 Step-Scheme H2-Production Photocatalyst. *Appl. Catal. B: Environ.* 243, 556–565. doi:10.1016/j.apcatb.2018.11.011

Ge, H., Xu, F., Cheng, B., Yu, J., and Ho, W. (2019). S-Scheme Heterojunction TiO 2/CdS Nanocomposite Nanofiber as H_2 -Production Photocatalyst. *ChemCatChem*. 11, 6301–6309. doi:10.1002/cctc.201901486

Ghashghaee, M., Azizi, Z., and Ghambarian, M. (2020). Conductivity Tuning of Charged Triazine and Heptazine Graphitic Carbon Nitride (G-C3N4) Quantum Dots via Nonmetal (B, O, S, P) Doping: DFT Calculations. *J. Phys. Chem. Sol.* 141, 109422. doi:10.1016/j.jpcs.2020.109422

Gogoi, D., Makkar, P., and Ghosh, N. N. (2021). Solar Light-Irradiated Photocatalytic Degradation of Model Dyes and Industrial Dyes by a Magnetic CoFe2O4/g-C3N4 S-Scheme Heterojunction Photocatalyst. *Acs Omega*. 6, 4831–4841. doi:10.1021/acsomega.0c05809

Gong, F., Cai, Z., and Li, Y. (2016). Synthetic Biology for CO2 Fixation. *Sci. China Life Sci.* 59, 1106–1114. doi:10.1007/s11427-016-0304-2

Grimme, S. (2006). Semiempirical GGA-type Density Functional Constructed with a Long-Range Dispersion Correction. *J. Comput. Chem.* 27, 1787–1799. doi:10.1002/jcc.20495

Hafner, J. (2008). Ab-initiosimulations of Materials Using VASP: Density-Functional Theory and beyond. *J. Comput. Chem.* 29, 2044–2078. doi:10.1002/jcc.21057

Han, G., and Sohn, H. Y. (2005). Kinetics of the Hydrogen Reduction of Silica Incorporating the Effect of Gas-Volume Change upon Reaction. *J. Am. Ceram. Soc.* 88, 882–888. doi:10.1111/j.1551-2916.2005.00144.x

He, F., Wang, Z., Li, Y., Peng, S., and Liu, B. (2020). The Nonmetal Modulation of Composition and Morphology of g-C3N4-Based Photocatalysts. *Appl. Catal. B: Environ.* 269, 118828. doi:10.1016/j.apcatb.2020.118828

Huo, Y., Zhang, J., Dai, K., and Liang, C. (2021). Amine-Modified S-Scheme Porous G-C3N4/CdSe-Diethylenetriamine Composite with Enhanced Photocatalytic CO2 Reduction Activity. *ACS Appl. Energ. Mater.* 4, 956–968. doi:10.1021/acsaem.0c02896

Jiang, M., Shi, Y., Huang, J., Wang, L., She, H., Tong, J., et al. (2018). Synthesis of Flowerlike G-C3N4/BiOBr with Enhanced Visible Light Photocatalytic Activity for Dye Degradation. *Eur. J. Inorg. Chem.* 2018, 1834–1841. doi:10.1002/ejic.201800110

Kang, S., Khan, H., and Lee, C. S. (2021). CO2 Selectivity of Flower-like MoS2 Grown on TiO2 Nanofibers Coated with Acetic Acid-Treated Graphitic Carbon Nitride. *Solar Energ. Mater. Solar Cell.* 221, 110890. doi:10.1016/j.solmat.2020.110890

Ke, X., Zhang, J., Dai, K., Fan, K., and Liang, C. (2021). Integrated S-Scheme Heterojunction of Amine-Functionalized 1D CdSe Nanorods Anchoring on Ultrathin 2D $SnNb_2O_6$ Nanosheets for Robust Solar-Driven CO_2 Conversion. *Sol. RRL*. 5, 2000805. doi:10.1002/solr.202000805

Le, D., Kara, A., Schröder, E., Hyldgaard, P., and Rahman, T. S. (2012). Physisorption of nucleobases on graphene: a comparative van der Waals study. *J. Phys. Condens. Matter*. 24, 424210. doi:10.1088/0953-8984/24/42/424210

Li, Q., Zhao, W., Zhai, Z., Ren, K., Wang, T., Guan, H., et al. (2020a). 2D/2D Bi2MoO6/g-C3N4 S-Scheme Heterojunction Photocatalyst with Enhanced Visible-Light Activity by Au Loading. *J. Mater. Sci. Technology* 56, 216–226. doi:10.1016/j.jmst.2020.03.038

Li, Y., Li, X., Zhang, H., Fan, J., and Xiang, Q. (2020b). Design and Application of Active Sites in G-C3N4-Based Photocatalysts. *J. Mater. Sci. Technology* 56, 69–88. doi:10.1016/j.jmst.2020.03.033

Li, Y., Zhou, M., Cheng, B., and Shao, Y. (2020c). Recent Advances in G-C3N4-Based Heterojunction Photocatalysts. *J. Mater. Sci. Technology* 56, 1–17. doi:10.1016/j.jmst.2020.04.028

Li, H., Li, F., Yu, J., and Cao, S. (2021a). 2D/2D FeNi-LDH/g-C3N4 Hybrid Photocatalyst for Enhanced CO2 Photoreduction. *Acta Phys.-Chim. Sin.* 37, 2010073. doi:10.3866/pku.Whxb202010073

Li, X., Liu, J., Huang, J., He, C., Feng, Z., Chen, Z., et al. (2021b). All Organic S-Scheme Heterojunction PDI-Ala/S-C3N4 Photocatalyst with Enhanced Photocatalytic Performance. *Acta Phys.-Chim. Sin.* 37, 2010030. doi:10.3866/pku.Whxb202010030

Li, Y., Zhang, M., Zhou, L., Yang, S., Wu, Z., and Ma, Y. (2021c). Recent Advances in Surface-Modified G-C3N4-Based Photocatalysts for H2 Production and CO2 Reduction. *Acta Phys.-Chim. Sin.* 37, 2009030. doi:10.3866/pku.Whxb202009030

Lian, X., Xue, W., Dong, S., Liu, E., Li, H., and Xu, K. (2021). Construction of S-Scheme Bi2WO6/g-C3N4 Heterostructure Nanosheets with Enhanced Visible-Light Photocatalytic Degradation for Ammonium Dinitramide. *J. Hazard. Mater.* 412, 125217. doi:10.1016/j.jhazmat.2021.125217

Liu, J., Wei, X., Sun, W., Guan, X., Zheng, X., and Li, J. (2021a). Fabrication of S-Scheme CdS-G-C3N4-Graphene Aerogel Heterojunction for Enhanced Visible Light Driven Photocatalysis. *Environ. Res.* 197, 111136. doi:10.1016/j.envres.2021.111136

Liu, L., Hu, T., Dai, K., Zhang, J., and Liang, C. (2021b). A Novel Step-Scheme BiVO4/Ag3VO4 Photocatalyst for Enhanced Photocatalytic Degradation Activity under Visible Light Irradiation. *Chin. J. Catal.* 42, 46–55. doi:10.1016/s1872-2067(20)63560-4

Liu, M., Pang, Y., Zhang, B., De Luna, P., Voznyy, O., Xu, J., et al. (2016). Enhanced Electrocatalytic CO2 Reduction via Field-Induced Reagent Concentration. *Nature*. 537, 382–386. doi:10.1038/nature19060

Liu, X., Gu, S., Zhao, Y., Zhou, G., and Li, W. (2020). BiVO4, Bi2WO6 and Bi2MoO6 Photocatalysis: A Brief Review. *J. Mater. Sci. Technology* 56, 45–68. doi:10.1016/j.jmst.2020.04.023

Mahmood, A., Shi, G., Wang, X., Xie, X., and Sun, J. (2020). Photocatalytic properties of novel two-dimensional B4C3/g-C3N4 van der Waals heterojunction with moderate bandgap and high carrier mobility: A theoretical study. *Appl. Catal. B: Environ.* 278, 119310. doi:10.1016/j.apcatb.2020.119310

Mei, F., Zhang, J., Liang, C., and Dai, K. (2021). Fabrication of Novel CoO/porous Graphitic Carbon Nitride S-Scheme Heterojunction for Efficient CO2 Photoreduction. *Mater. Lett.* 282, 128722. doi:10.1016/j.matlet.2020.128722

Meng, A., Cheng, B., Tan, H., Fan, J., Su, C., and Yu, J. (2021). TiO2/polydopamine S-Scheme Heterojunction Photocatalyst with Enhanced CO2-reduction Selectivity. *Appl. Catal. B: Environ.* 289, 120039. doi:10.1016/j.apcatb.2021.120039

Ojha, N., Bajpai, A., and Kumar, S. (2019). Visible Light-Driven Enhanced CO2 Reduction by Water over Cu Modified S-Doped G-C3N4. *Catal. Sci. Technol.* 9, 4598–4613. doi:10.1039/c9cy01185d

Raziq, F., Humayun, M., Ali, A., Wang, T., Khan, A., Fu, Q., et al. (2018). Synthesis of S-Doped Porous G-C3N4 by Using Ionic Liquids and Subsequently Coupled with Au-TiO2 for Exceptional Cocatalyst-free Visible-Light Catalytic Activities. *Appl. Catal. B: Environ.* 237, 1082–1090. doi:10.1016/j.apcatb.2018.06.009

Ren, D., Zhang, W., Ding, Y., Shen, R., Jiang, Z., Lu, X., et al. (2020). *In Situ* Fabrication of Robust Cocatalyst-Free CdS/g-C3N4 2D-2D Step-Scheme Heterojunctions for Highly Active H_2 Evolution. *Sol. RRL.* 4, 1900423. doi:10.1002/solr.201900423

Suzuki, T. M., Takayama, T., Sato, S., Iwase, A., Kudo, A., and Morikawa, T. (2018). Enhancement of CO_2 Reduction Activity under Visible Light Irradiation over Zn-Based Metal Sulfides by Combination with Ru-Complex Catalysts. *Appl. Catal. B: Environ.* 224, 572–578. doi:10.1016/j.apcatb.2017.10.053

Tao, J., Yu, X., Liu, Q., Liu, G., and Tang, H. (2021). Internal Electric Field Induced S-Scheme Heterojunction MoS2/CoAl LDH for Enhanced Photocatalytic Hydrogen Evolution. *J. Colloid Interf. Sci.* 585, 470–479. doi:10.1016/j.jcis.2020.10.028

Tian, Y., Tang, W., Xiong, H., Chen, T., Li, B., Jing, X., et al. (2020). Luminescence and Structure Regulation of Graphitic Carbon Nitride by Electron Rich P Ions Doping. *J. Lumin.* 228, 117616. doi:10.1016/j.jlumin.2020.117616

Truc, N., Bach, L., Hanh, N., Pham, T., Chi, N., Tran, D., et al. (2019). The superior Photocatalytic Activity of Nb Doped TiO_2/g-C3N4 Direct Z-Scheme System for Efficient Conversion of CO_2 into Valuable Fuels. *J. Colloid Interf. Sci.* 540, 1–8. doi:10.1016/j.jcis.2019.01.005

Wang, J., Wang, G., Cheng, B., Yu, J., and Fan, J. (2021). Sulfur-doped g-C3n4/TiO2 S-Scheme Heterojunction Photocatalyst for Congo Red Photodegradation. *Chin. J. Catal.* 42, 56–68. doi:10.1016/S1872-2067(20)63634-8

Wang, X., Maeda, K., Thomas, A., Takanabe, K., Xin, G., Carlsson, J. M., et al. (2009). A Metal-free Polymeric Photocatalyst for Hydrogen Production from Water under Visible Light. *Nat. Mater.* 8, 76–80. doi:10.1038/nmat2317

Wang, Y., Tian, Y., Yan, L., and Su, Z. (2018). DFT Study on Sulfur-Doped G-C3N4 Nanosheets as a Photocatalyst for CO2 Reduction Reaction. *J. Phys. Chem. C.* 122, 7712–7719. doi:10.1021/acs.jpcc.8b00098

Wang, Z., Chen, Y., Zhang, L., Cheng, B., Yu, J., and Fan, J. (2020). Step-scheme CdS/TiO2 Nanocomposite Hollow Microsphere with Enhanced Photocatalytic CO2 Reduction Activity. *J. Mater. Sci. Technology* 56, 143–150. doi:10.1016/j.jmst.2020.02.062

Wei, J., Chen, Y., Zhang, H., Zhuang, Z., and Yu, Y. (2021). Hierarchically Porous S-Scheme CdS/UiO-66 Photocatalyst for Efficient 4-nitroaniline Reduction. *Chin. J. Catal.* 42, 78–86. doi:10.1016/s1872-2067(20)63661-0

Wu, Z., and Cohen, R. E. (2006). More Accurate Generalized Gradient Approximation for Solids. *Phys. Rev. B.* 73, 235116. doi:10.1103/PhysRevB.73.235116

Xia, P., Cao, S., Zhu, B., Liu, M., Shi, M., Yu, J., et al. (2020). Designing a 0D/2D S-Scheme Heterojunction over Polymeric Carbon Nitride for Visible-Light Photocatalytic Inactivation of Bacteria. *Angew. Chem. Int. Ed.* 59, 5218–5225. doi:10.1002/anie.201916012

Xie, Q., He, W., Liu, S., Li, C., Zhang, J., and Wong, P. K. (2020). Bifunctional S-Scheme G-C3N4/Bi/BiVO4 Hybrid Photocatalysts toward Artificial Carbon Cycling. *Chin. J. Catal.* 41, 140–153. doi:10.1016/S1872-2067(19)63481-9

Xu, F., Meng, K., Cheng, B., Wang, S., Xu, J., and Yu, J. (2020a). Unique S-Scheme Heterojunctions in Self-Assembled TiO2/CsPbBr3 Hybrids for CO2 Photoreduction. *Nat. Commun.* 11, 4613. doi:10.1038/s41467-020-18350-7

Xu, Q., Zhang, L., Cheng, B., Fan, J., and Yu, J. (2020b). S-scheme Heterojunction Photocatalyst. *Chem.* 6, 1543–1559. doi:10.1016/j.chempr.2020.06.010

Yan, L., Lu, Y., and Li, X. (2016). A Density Functional Theory Protocol for the Calculation of Redox Potentials of Copper Complexes. *Phys. Chem. Chem. Phys.* 18, 5529–5536. doi:10.1039/c5cp06638g

Yang, Y., Zhang, D., Fan, J., Liao, Y., and Xiang, Q. (2021). Construction of an Ultrathin S-Scheme Heterojunction Based on Few-Layer g-C3N4 and Monolayer Ti3C2TX MXene for Photocatalytic CO 2 Reduction. *Sol. RRL.* 5, 2000351. doi:10.1002/solr.202000351

Zhang, B., Shi, H., Yan, Y., Liu, C., Hu, X., Liu, E., et al. (2021a). A Novel S-Scheme 1D/2D Bi2S3/g-C3N4 Heterojunctions with Enhanced H2 Evolution Activity. *Colloids Surf. A: Physicochemical Eng. Aspects.* 608, 125598. doi:10.1016/j.colsurfa.2020.125598

Zhang, X., Kim, D., Yan, J., and Lee, L. Y. S. (2021b). Photocatalytic CO2 Reduction Enabled by Interfacial S-Scheme Heterojunction between Ultrasmall Copper Phosphosulfide and G-C3N4. *ACS Appl. Mater. Inter.* 13, 9762–9770. doi:10.1021/acsami.0c17926

Zhang, X., Yang, P., and Jiang, S. P. (2021c). Pt Nanoparticles Embedded Spine-like G-C3N4 Nanostructures with superior Photocatalytic Activity for H2 Generation and CO2 Reduction. *Nanotechnology* 32, 175401. doi:10.1088/1361-6528/abdcee

Zhang, X., Yan, J., Zheng, F., Zhao, J., and Lee, L. Y. S. (2021d). Designing Charge Transfer Route at the Interface between WP Nanoparticle and G-C3N4 for Highly Enhanced Photocatalytic CO2 Reduction Reaction. *Appl. Catal. B: Environ.* 286, 119879. doi:10.1016/j.apcatb.2021.119879

Zhao, Z.-Y., and Dai, W.-W. (2014). Structural, Electronic, and Optical Properties of Eu-Doped BiOX (X = F, Cl, Br, I): A DFT+U Study. *Inorg. Chem.* 53, 13001–13011. doi:10.1021/ic5021059

Zhen, Y., Yang, C., Shen, H., Xue, W., Gu, C., Feng, J., et al. (2020). Photocatalytic Performance and Mechanism Insights of a S-Scheme G-C3N4/Bi2MoO6 Heterostructure in Phenol Degradation and Hydrogen Evolution Reactions under Visible Light. *Phys. Chem. Chem. Phys.* 22, 26278–26288. doi:10.1039/D0CP02199G

Zhi, X., Jiao, Y., Zheng, Y., and Qiao, S. Z. (2019). Impact of Interfacial Electron Transfer on Electrochemical CO_2 Reduction on Graphitic Carbon Nitride/Doped Graphene. *Small.* 15, 1804224. doi:10.1002/smll.201804224

Zhu, B., Zhang, L., Cheng, B., and Yu, J. (2018). First-principle Calculation Study of Tri-s-triazine-based G-C3N4: A Review. *Appl. Catal. B: Environ.* 224, 983–999. doi:10.1016/j.apcatb.2017.11.025

Zhu, B., Zhang, L., Xu, D., Cheng, B., and Yu, J. (2017). Adsorption Investigation of CO2 on G-C3N4 Surface by DFT Calculation. *J. CO2 Utilization*. 21, 327–335. doi:10.1016/j.jcou.2017.07.021

Conflict of Interest: The authors declare that the research was conducted in the absence of any commercial or financial relationships that could be construed as a potential conflict of interest.

frontiers in Nanotechnology

MINI REVIEW
published: 12 July 2021
doi: 10.3389/fnano.2021.723120

Recent Advancements in Photocatalytic Valorization of Plastic Waste to Chemicals and Fuels

Aizhu Chen[1], *Min-Quan Yang*[1]*, *Sibo Wang*[2]* *and Qingrong Qian*[1]*

[1] *College of Environmental Science and Engineering, Fujian Key Laboratory of Pollution Control and Resource Reuse, Fujian Normal University, Fuzhou, China,* [2] *State Key Laboratory of Photocatalysis on Energy and Environment, College of Chemistry, Fuzhou University, Fuzhou, China*

The continuous rise in plastic waste raises serious concerns about the ensuing effects on the pollution of global environment and loss of valuable resources. Developing efficient approach to recycle the plastic has been an urgent demand for realizing a sustainable circular economy. Photocatalytic valorization directly utilizes solar energy to transform plastic pollutant into chemicals and fuels, which is hardly implemented by traditional mechanical recycling and incineration strategies, thus offering a promising approach to address the contemporary waste and energy challenges. Here, we focus on the recent advances in the high-value utilization of plastic waste through photocatalysis. The basic principle and different reaction pathways for the photocatalytic valorization of plastic waste are presented. Then, the developed representative photocatalyst systems and converted products are elaborately discussed. At last, the review closes with critical thoughts on research challenges along with some perspectives for further development of this emerging and fascinating filed.

Keywords: photocatalysis, valorization, plastic waste, solar energy, chemical fuels

Edited by:
Wee-Jun Ong,
Xiamen University, Malaysia

Reviewed by:
Xin-Yao Yu,
Zhejiang University, China
Ting Zhu,
Central South University, China
Tianpeng Ding,
National University of Singapore, Singapore

Correspondence:
Min-Quan Yang
yangmq@fjnu.edu.cn
Sibo Wang
sibowang@fzu.edu.cn
Qingrong Qian
qrqian@fjnu.edu.cn

Specialty section:
This article was submitted to Nanotechnology for Energy Applications, a section of the journal Frontiers in Nanotechnology

Received: *10 June 2021*
Accepted: *28 June 2021*
Published: *12 July 2021*

Citation:
Chen A, Yang M-Q, Wang S and Qian Q (2021) Recent Advancements in Photocatalytic Valorization of Plastic Waste to Chemicals and Fuels. Front. Nanotechnol. 3:723120. doi: 10.3389/fnano.2021.723120

INTRODUCTION

Plastic as one of the most influential inventions of 20th century has been widely applied in our daily life (Andrady and Neal, 2009; Bai et al., 2019; Jie et al., 2020; Gausas et al., 2021; Zhang F et al., 2021). Currently, about 360 million tonnes (Mt) of plastic are produced each year (Martín et al., 2021), and the number is expected to double over the next 2 decades (MacArthur 2017). However, only a small portion of the produced plastic is recycled after use. Around 80% of all plastic is directly incinerated or discarded as waste annually due to the durability, which exists in landfills or in the environment (**Figure 1**), and is hard to be degraded by ambient onslaughts such as light, water, heat, and so on (MacArthur, 2017; Jehanno and Sardon, 2019; Geyer 2020; PlasticEurope, 2020). The rapid accumulation of plastic waste has resulted in a worldwide "white pollution." For example, it has been estimated that if the current trend continues, more than 8 Mt of plastic will enter the ocean each year, and the overall weight of the waste plastic will higher than that of fish in 2050 (Thompson et al., 2004; MacArthur, 2017; Uekert et al., 2018; Martín et al., 2021). Moreover, the huge production of plastic also exacerbates the global energy crisis, due to that almost all of the plastics are produced from petrochemicals derived from fossil fuel production, such as light (C_1–C_4) fractions of oil and natural gas, which accounts for ~ 6% consumption of the fossil fuel (Vollmer et al., 2020; Martín et al., 2021). The ever-increasing demand accompanying with the continuously rised discarding of plastic causes serious environmental and energy challenges, which call for reducing, increasing reuse

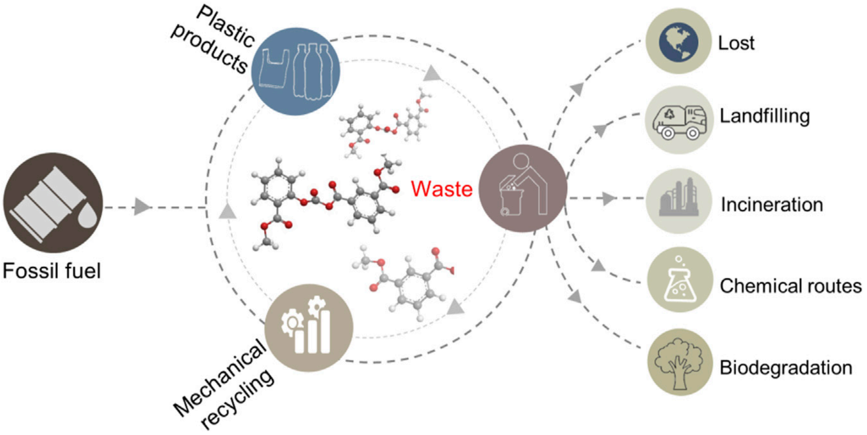

FIGURE 1 | Schematic illustration of the life cycle of plastic.

and recycling of the plastic to tackle the dilemma and moves toward circular economy (Lopez et al., 2017; Ru et al., 2020; Tennakoon et al., 2020).

In fact, the plastic waste is a misplaced resource. The vast majority of the plastics are polymer, which enables them to be valorized as new chemical feedstock *via* correct treatment (Keane, 2007). If all of the global plastic solid waste could be recycled, it would save an estimated 3.5 billion barrels of oil a year, valued at $176 billion dollars, implying a high economic benefit (Garcia and Robertson, 2017; Rahimi and García, 2017). At present, the most widely adopted strategy for the plastic waste valorization is based on mechanical recycling (Martín et al., 2021). The approach collects and reprocesses the plastic polymer as raw material for new plastic manufacturing by sorting, shredding, melting, and re-extrusion (Al-Salem et al., 2009; Kumar et al., 2011; Mark et al., 2020; Schyns and Shaver, 2021; Zhang K et al., 2021). It is favored by environmental friendliness, but commonly suffers from property deterioration of the products due to the chain scission, branching, and oxidation of the plastic polymer caused by the reprocess treatment (Mark et al., 2020; Worch and Dove, 2020). In addition, the application of the approach is limited by the type of the plastic. Only two types of polyethylene terephthalate (PET) and polyethylenes (PE) plastics are mechanically processed (Garcia and Robertson, 2017). Plastic with high temperature sensitivity or high melt viscosity not flow at elevated temperatures cannot be recycled by this approach. More importantly, the mechanical processing is incapable in handling microplastics due to their small size ($\leq$ 5 mm) and dilution (Eerkes-Medrano et al., 2015; Tofa et al., 2019; Uekert et al., 2019; Zhang F et al., 2021).

In contrast, chemical recycling is a more promising plastic valorization strategy that now sparkle in both academic and industrial arenas. The process focuses on transformation of plastic waste into small molecules, ranging from starting monomers to constituent hydrocarbons (Worch and Dove, 2020). The products not only can be re-polymerized into virgin plastic, but also can be upcycled into alternative chemicals and fuels, thus enabling the materials reusing in a closed loop. Especially, the approach is applicable to all kinds of plastic waste (Martín et al., 2021). Nevertheless, the chemical recycling is generally an energy-intensive process, requiring high temperature and/or pressure (Worch and Dove, 2020). To endorse the circular economy framework, the development of low energy input catalytic processes to efficiently transform the plastic waste into original monomer sources and targeted products is crucial.

In this context, photocatalytic recycling directly driven by solar energy provides an advanced solution to address the key challenges associated with the traditional chemical recycling efforts. Actually, the photocatalytic treatment of plastic has been a long theme, but previous research endeavors are devoted to the degradation of plastic to CO_2 (Shang et al., 2003; Zhao et al., 2007; Zhao et al., 2008; Liang et al., 2013). Until recently, the photocatalytic conversion of plastic into chemicals and fuels has been reinvigorated. It can be achieved through the selection of appropriate photocatalysts and control of the reaction conditions, thus providing an alternative method to conventional recycling process for valorization of the plastic waste. In this mini review, we focus on the up-to-date progresses of photocatalytic valorization of plastic waste to produce chemicals and fuels. The different photocatalytic conversion pathways, developed catalysts, and end products of waste plastic recycling are discussed. Also, some key issues alongside with perspectives in this field are highlighted.

BASIC PRINCIPLE FOR PHOTOCATALYTIC VALORIZATION OF PLASTIC WASTE

Photocatalysis is a mimic technology of nature photosynthesis. It typically involves three distinct steps: 1) light absorption of photocatalysts to excite charge carriers, 2) separation and transportation of the photogenerated charge carriers, and 3) redox reaction on the surface of the catalyst, as illustrated in **Figure 2** (Liu et al., 2015; Yang et al., 2015; Lu et al., 2019; Shang

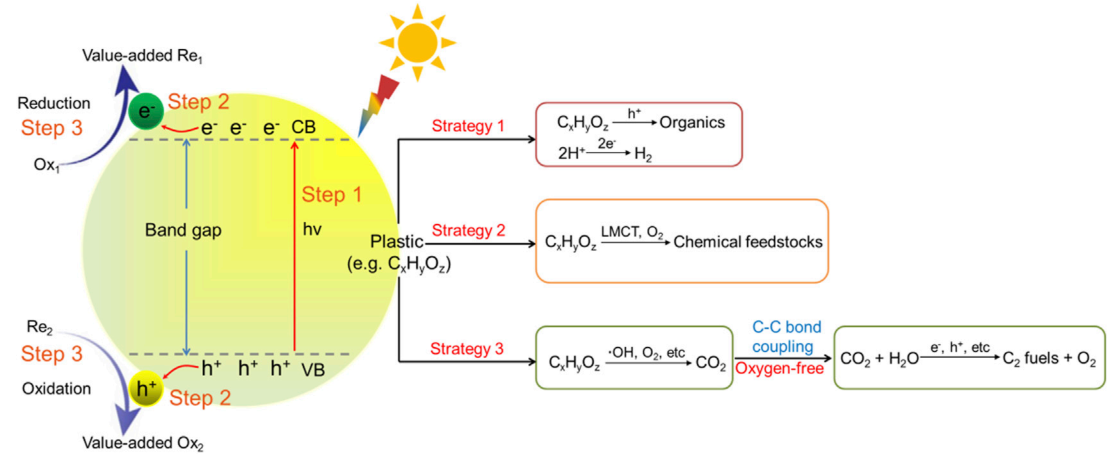

FIGURE 2 | Basic principle and three typical conversion pathways for photocatalytic valorization of plastic waste (LMCT refers to ligand to metal charge transfer).

et al., 2021). In order for photocatalysis to proceed, the energy of incident photons should be equal or higher than the band gap of photocatalysts. Meantime, the reduction potential of photoelectrons in the photocatalyst conduction band (CB) should be more negative than the value of the reactant to be reduced, while the oxidation potential of holes in the valence band (VB) should be more positive than that of the substrate to be oxidized (Habisreutinger et al., 2013; Xiao et al., 2015; Yang and Xu, 2016; Clarizia et al., 2017; Yang et al., 2018; Uekert et al., 2020a). Specifically, for photocatalytic valorization of plastic waste, the holes in the VB of photocatalyst after photoexcitation are commonly utilized for the oxidation of the plastic to generate organic products, or degrade it to CO_2, while the electrons in the photocatalyst CB can be employed to reduce the protons in H_2O to H_2, CO_2 to carbon fuels, or be captured by O_2 to involve in the subsequent oxidation of the plastic.

Depending on the different consumption pathways of the photogenerated charge carriers, the current reports for photocatalytic valorization of plastic waste can be classified into three conversion mechanisms (**Figure 2**): (i) photocatalytic plastic upgrading to fine chemicals integrated with H_2 production. The process is similar to the traditional half reaction for photocatalytic H_2 production. The plastic substrate acts as an electron donor and is oxidized by the holes of the excited photocatalyst to generate organic products, while the photogenerated electrons are transferred to the surface of the photocatalyst and reduce water to H_2; (ii) photocatalytic valorization of waste plastic to oxygenated chemical feedstocks. In this process, the C-C bond of plastic substrate is firstly cleaved to produce primary products and radical fragment, which then be further oxidized by dissolved O_2 in air or hydrolyzed under aerobic reaction conditions to give oxygenated derivatives, such as carboxylic acids; (iii) photocatalytic plastic degradation coupled with sequential CO_2 reduction to produce C_2 fuels. This strategy includes two processes, where the first step is the degradation of plastic into CO_2 through photooxidative C-C bond cleavage over photocatalyst. Then, the produced CO_2 is captured as raw material and further reduced by the same photocatalyst into C_2 fuels by photoinduced C-C coupling process. To elaborately present the three different reaction pathways, some typical examples are discussed in the below section.

PHOTOCATALYTIC PLASTIC UPGRADING TO FINE CHEMICALS INTEGRATED WITH H_2 PRODUCTION

The initial study of photocatalytic H_2 production form plastic waste can be dated back to 1981. Sakata and co-workers reported that a range of plastic [PE, polyvinyl chloride (PVC) and Teflon] could be photodecomposed to produce H_2 (Kawai and Sakata, 1981). It finds that improving the alkalinity of the reaction solution results in higher H_2 production rate. However, CO_2 is produced as a by-product in this study and the conversion efficiency is low. After that, although there are some reports about the photocatalytic treatment of plastic, nearly all of them are focused on degradation (Feng et al., 2011; de Assis et al., 2018; Das and Mahalingam, 2019). No typical study about the photocatalytic H_2 production from plastic waste has been reported. In recent years, with the urgent demand for green conversion of the continuously accumulated plastic waste and the advancement of photocatalysis, the solar-driven photocatalytic valorization re-emerges. In 2018, Reisner's group have reported a high photocatalytic H_2 evolution from a variety of plastic polymers such as polylactic acid (PLA), PET, polyurethane (PUR), and a real PET water bottle under alkaline condition (10 M NaOH), accompanying with the conversion of the polymer into organic products such as formate, acetate and pyruvate (**Supplementary Figures 1A–G**) (Uekert et al., 2018). Typical CdS semiconductor with suitable band gap and appropriate conduction band and valence band positions (CB-0.5V vs. NHE, VB + 1.9V vs. NHE) is employed in this work. Owing to the strong alkalinity, a thin layer of Cd oxide/

hydroxide shell (CdO_x) is formed on the surface of the CdS quantum dots (QDs), which can prevent the photocorrosion of the CdS. The as-prepared CdS/CdO_x QDs displays high H_2 evolution performance that is comparable to the activity of CdS-based composites for photoconverting of traditional organic substrates, such as furfural and glucose (**Supplementary Figures 1A,B**). The external quantum yields reach around 15% for PLA, 3.7 for PET, and 0.14 for PUR at $\lambda = 430$ nm.

In order to further improve the photoactivity, a simple pretreatment of the plastic substrates in 10 M NaOH solution for 24 h under dark condition of 40°C is developed. The supernatant is used for the photocatalytic reaction. As shown in **Supplementary Figure 1A**, it is obvious that the simple pre-treatment results in markedly enhanced H_2 evolution rates, four times for both PET, and PUR. This is because that the pre-treatment initiates hydrolysis, releasing monomers into solution which can be more rapidly photocatalytic converted. The negligible pre-treatment influence on PLA is due to its easy dissolvability in NaOH. Mass spectra analysis in deuterated and nondeuterated solvent confirms that the generated H_2 originates from H_2O rather than the substrate (**Supplementary Figure 1F**). Also, no gaseous CO_2 and CO_3^{2-} is detected in the solutions after reaction (**Supplementary Figure 1G**). These results verify that the polymers are partially oxidized to organic molecules. Although the overall conversion remains below 40% for all polymers, the research shows a fascinating potential for energy-saving treatment of the plastic waste without greenhouse gas discharge.

Owing to that the bare semiconductor photocatalysts generally suffers from lack of surface active sites, and rapid recombination of photogenerated charge carriers, thus limiting the overall photocatalytic performance (Majeed et al., 2016; Shi et al., 2018). To resolve the problems, Liu et al. have synthesized a CdS/MoS_2 nanoctahedral heterostructures by loading MoS_2 as cocatalyst. The composite is synthesized using $CdMoO_4$ nanoctahedron as template and precursor by *in situ* vulcanization with H_2S (**Supplementary Figures 2A,B**) (Zhao et al., 2020). This *in-situ* synthesis method forms a close and sufficient S atomic contact interface between CdS and MoS_2, which is conductive to the transfer of electrons from CdS to MoS_2. When applied to photocatalytic conversion of plastic, the hybrid CdS/MoS_2 shows significantly enhanced photocatalytic H_2 evolution rates than pure CdS and pure MoS_2 using PLA as reaction substrate under alkaline conditions (10 M NaOH) (**Supplementary Figure 2C**). Also, a high photocatalytic H_2 evolution (60.8 mmol h^{-1} g^{-1}) is observed for photocatalytic conversion of PET, demonstrating the universality of the CdS/MoS_2 composite for integrated photocatalytic H_2 production and plastic upgrading (**Supplementary Figure 2D**). ^1H NMR analysis spectra of the PLA-NaOD solution shows a new peak after photocatalytic reforming reaction, which is ascribed to the oxidation product of alkali-induced pyruvate compounds. This was consistent with the reported results of Reisner et al. (Uekert et al., 2018). However, the addition of excess $Ba(OH)_2$ solution into the supernate obtained after reaction forms white precipitate (**Supplementary Figure 2E**), indicating the generation of a certain amount of CO_2 during the photoconversion of plastic. The study confirms the crucial role of loading cocatalyst to promote the photocatalytic valorization performance.

Moreover, Li et al. have constructed a 2D/2D $MoS_2/Cd_xZn_{1\text{-}x}S$ ($0.2 \leq x \leq 0.8$, $M_t/C_xZ_{1-x}S$) heterostructure for PET photoconversion coupled with H_2 production (**Supplementary Figure 3A**) (Li et al., 2021). As shown in **Supplementary Figure 3B**, in the presence of light and photocatalyst, the H_2 evolution rates of $MoS_2/C_xZ_{1\text{-}x}S$ firstly increase with the increment of x until x = 0.5. ^1H-NMR analysis shows that in NaOH aqueous solution, the PET is mainly hydrolyzed into ethylene glycol, terephthalic acid, and glycolate before reaction (**Supplementary Figure 3C**). After 5 h illumination, some small molecular organic compounds such as formate and methanol appear in the ^1H-NMR spectrum, confirming the photocatalytic conversion of PET. Moreover, $M_{4.3}/C_{0.5}Z_{0.5}S$ shows high photocatalytic H_2 evolution stability during 5 h continuous illumination in either PET or PET-bottle-based aqueous solution (**Supplementary Figure 3D**). This work extends the catalyst for the photocatalytic plastic upgrading.

Considering the toxicity of Cd in CdS/CdO_x, in another work of Reisner, et al., they have further developed a new Cd-free catalyst, namely cyanamide-functionalized carbon nitride (CN_X) coupled with a nickel phosphide (CN_x/Ni_2P) for photocatalytic valorization of plastic (**Supplementary Figure 4A**) (Uekert et al., 2019). Carbon nitride (CN_x) has been studied widely in photocatalysis because of its non-toxic, cheap and visible light absorption. Particularly, the CN_x has strong alkali resistance, thus endowing it to be a promising competitive alternative to CdS for photocatalytic conversion of plastic. As presented in **Supplementary Figure 4B**, under low pH conditions (1 M KOH), the $CN_x|Ni_2P$ shows moderate photoactivity. The external quantum yields at $\lambda = 430$ nm is ca. 0.035 for PET and 0.101 for PLA. Increasing the alkalinity of the reaction solution can significantly improve the H_2 evolution activity, as exemplified in **Supplementary Figure 4C**. Isotopic labeling experiments with D_2O verify that H_2 originates from water rather than the substrate. ^1H NMR spectroscopy analysis of the reaction mixtures shows that the photoconversion of PET produces complex products, including terephthalate, formate, glyoxal, glycolate, acetate, and other intermediates yet without CO_3^{2-} (**Supplementary Figures 4D,G**). On the contrary, the PLA offers a much simpler system. It is oxidized primarily to small quantities of formate (i) and acetate (iv) with a small amount of CO_3^{2-} (**Supplementary Figures 4E–G**). The results are similar to those reported for photoreforming of PET with CdS/CdO_x (Uekert et al., 2018). Moreover, the photoconversion of real-world plastic wastes with low concentration of plastic, including polyester microfibers, PET bottles, and oil-coated PET bottles, over the $CN_x|Ni_2P$ has been evaluated, which also reveal noticeable H_2 evolution activity (**Supplementary Figure 4H**). The result directly proves the transformation of real-world plastic waste into both H_2 and valuable organics.

Furthermore, to overcome practical scaling challenges of traditional powder photocatalyst systems, such as sedimentation, difficult to recycle, and competing light absorption with waste solution, Reisner and co-workers have immobilized the $CN_x|Ni_2P$ photocatalyst on textured glass (**Supplementary Figure 4I**) (Uekert et al., 2020b). It has been found that the 1 cm^2 square $CN_x|Ni_2P$ panel can photoconvert waste plastic into H_2 and organic molecules with rates comparable to those of photocatalyst slurries, while enable facile photocatalyst recycling. Moreover, as shown in **Supplementary Figure 4J**, an up-scaled 25 cm^2 panel is fabricated to photoreform municipal solid waste (MSW) in seawater under lower sunlight (0.2 Sun) for 5 days, which still keeps 50% of the activity tested under ideal conditions (0% seawater, 100 mW cm^{-2}), thus further verifying the versatility and real-world applicability of the $CN_x|Ni_2P$ panel system.

PHOTOCATALYTIC VALORIZATION OF WASTE PLASTIC TO OXYGENATED CHEMICAL FEEDSTOCKS

In the above cases, the plastic is primarily hydrolyzed in alkaline solution to break the stubborn C-C chemical bonds, thereby hastening the photocatalytic process. In spite of the advantage, the alkaline pretreatment is detrimental to the natural environment. Given this aspect, it is imperative to find alternative ways to convert the plastic under mild conditions. In a study of Soo et al. (Gazi et al., 2019), they have demonstrated a vanadium (V) photocatalyst system **(Supplementary Figure 5A)** that can controllably cleave the C-C bond for organic transformations and plastic recycling in the natural environment without alkaline pretrement. The study is started by examining the performance of the V catalysts for breaking down carbon-carbon bonds in over 30 different types of chemicals. Quantitative conversions and moderate-to-high yields of aldehyde and alcohol products are obtained for all the substrates, demonstrating a broad functional group tolerance, and high catalytic applicability of the photocatalytic system.

Encouraged by the promising result, the authors further test the photocatalytic performance of the catalysts for conversion of PE **(Supplementary Figure 5B)**. Notably, the reaction has to be conducted with white LEDs at 85°C in a mixture of acetonitrile and toluene to fully dissolve the substrate. The result reveals a full conversion of the PE after 6 days. Formic acid and methyl formate are identified as some of the products. However, CO_2 is also detected, which is ascribed to the over-oxidation of formic acid. The reaction is suggested to proceed *via* LMCT mechanism. A depicted in **Supplementary Figure 5C**, the C-C bond of the hydroxyl-terminated polymer would cleave with the assistance of V catalyst to produce a carbonyl group as one of the primary products, while the other radical fragment would react with dissolved O_2 in air to eventually give another oxygenated compound. This work highlights the practicability of the photocatalytic C-C activation for transformation of plastic wastes into chemical raw materials under alkali-free condition.

PHOTOCATALYTIC PLASTIC DEGRADATION COUPLED WITH SEQUENTIAL CO_2 REDUCTION TO PRODUCE C_2 FUELS

Besides one-step conversion, Xie, and co-workers (Jiao et al., 2020) recently have reported a sequential photoinduced C-C cleavage under atmosphere and C-C bond coupling in the absence of oxygen, which for the first time realizes highly selective conversion of various waste plastic into C_2 fuels under simulated natural environment (room temperature, pure water, and simulated one-sun irradiation; **Supplementary Figure 6A**). In the research, single-unit-cell thick Nb_2O_5 layers (2.96 nm) is prepared from niobic acid atomic layer precursor as catalyst **(Supplementary Figure 6B)**, due to its high redox potentials, valence band maximum at + 2.5 V vs. NHE and the conduction band minimum at 0.9 V vs. NHE at pH 7, which is conducive for maximal exposure of active site and thus promoting the light conversion performance. The photocatalytic conversion of real-world PE, polypropylene (PP) and PVC plastics over the ultrathin Nb_2O_5 shows that the catalyst can completely degrade these plastics to CO_2 within 40, 60, and 90 h, respectively **(Supplementary Figure 6C)**. Meanwhile, CH_3COOH yields progressively increased during the photoconversion processes **(Supplementary Figure 6D)**. Through a series of control experiments, isotope labeling and synchrotron radiation vacuum ultraviolet photoionization mass spectrometry, the CH_3COOH products is verified to be generated by the photoreduction of the CO_2 generated from degradation of plastic.

Correspondingly, a specific mechanism is proposed **(Supplementary Figure 6E)**. The photoconversion of the plastic is suggested to undergo two continuous processes: initially, the plastic is oxidized by the O_2 and •OH radical to cleave C-C bond and form CO_2. Meantime, the O_2 is reduced to $O_2•^-$, H_2O_2, and H_2O. Subsequently, the resulting CO_2 is further reduced to CH_3COOH and the water was oxidized to O_2 through the photoinduced C-C coupling reaction occurring between COOH intermediates. This is significantly different with the above discussed one-step strategy, providing a fascinating alternative strategy to valorize the real-word plastic without any pretrement. However, due to the poor CO_2 reduction activity of the existing photocatalysts, the production of C_2 fuel is relatively low at present.

CONCLUSION AND OUTLOOK

In summary, the latest advances in photocatalytic valorization of plastic for fuels and chemicals production are highlighted in this mini review. Three typical conversion pathways have been classified, including (i) photocatalytic plastic upgrading to fine chemicals integrated with H_2 production; (ii) photocatalytic valorization of waste plastic to oxygenated chemical feedstocks and (iii) photocatalytic plastic degradation coupled with sequential CO_2 reduction to produce C_2 fuels. Correspondingly, the developed catalyst systems that fall into these reaction pathways, and products generated from the photocatalytic conversion of plastic are elaborately discussed. The key progresses made in this area present a fascinating alternative strategy to alleviate the white pollution crisis. Nevertheless, the investigation of photocatalytic valorization of plastic is still at an early stage of discovery, especially in comparison with the traditional photocatalytic applications, such as water splitting, CO_2 reduction, and selective organic transformations. Some great challenges including the limitations of the overall reaction efficiency, selectivity, and durability lie between the laboratory study and practical application. In order to promote the deployment of the technique, more research effort is deserved.

For example, in spite of the charming future of the research field, the developed photocatalyst system for the plastic valorization is very limited at present. Over the past 40 years, a huge amount photocatalyst systems have been developed. Only for overall all water splitting-the challenging task in photocatalysis, more than 100 metal oxides-based photocatalytic systems have been reported. In this context, the exploration of new types of photocatalysts is highly desired, which would be the most direct way to advance the photocatalytic plastic valorization.

In addition, the loading of cocatalyst is essential for achieving highly efficient, selective, and steady photocatalytic plastic conversion. The cocatalyst can play multifunctional roles including (i) boosting the separation and transfer of photogenerated charge carriers, (ii) inhibiting the photocorrosion of catalysts and (iii) promoting adsorption and activation of target molecules. Till now, great progresses are achieved in the design and synthesis of noble metal-based, transition metal-based such as metal sulfide, phosphide, nitride, and oxides cocatalysts. Thus, the tailoring of active cocatalyst would greatly contribute to achieving high-efficiency photocatalytic plastic conversion system.

Furthermore, at present, alkaline pretreatment of plastic is the most commonly utilized reaction media, which would harm the environment. Moreover, the alkaline treatment generally induces non-selective cleavage of the C-C bond to mixed short-chain organic molecules, which leads to poor selectivity of the photogenerated products. Also, the alkaline reaction media may corrode some metal oxides photocatalysts and results in deactivation. As such, developing more universal and mild solvent and pretreatment method, such as mixed organic solvent, is indispensable.

Finally, to implement the photocatalytic plastic valorization from laboratory study to "practical" application, the construction of fixed photocatalyst device must be taken into account. Particularly, the fix of photocatalyst on flexibly porous substrate should be a preferred option. This would not only prevent sedimentation and promote catalyst recycling, but also alleviate the cost of reduced mass transfer between the catalyst and reactant. In the long run, only through the collective optimization of the catalyst, reaction media and reactor, the practical application of photocatlytic plastic valorization can be reliable.

AUTHOR CONTRIBUTIONS

AC and MY conceived the idea, collected data, prepared and revised the manuscript. SW and QQ given scientific suggestions and commented on the manuscript.

FUNDING

This work was financially supported by the National Natural Science Foundation of China (21905049 and 21875037), the Award Program for Minjiang Scholar Professorship, and the Natural Science Foundation of Fujian Province (2020J01201).

SUPPLEMENTARY MATERIAL

The Supplementary Material for this article can be found online at: https://www.frontiersin.org/articles/10.3389/fnano.2021.723120/full#supplementary-material

Supplementary Figure 1 | **(A)** Photocatalytic conversion of plastics over CdS/CdO_x QDs under simulated solar light; **(B)** produced H_2 amount of the photoreforming of PET bottles under simulated solar irradiation over several days; ^{1}H-NMR spectra of PLA **(C)**, PET **(D)**, and PUR **(E)**; mass spectra of the gas evolved after photoreforming of PLA (24 h) over CdS/CdO_x QDs in **(F)** 10 M NaOH, 10 M NaOD in D_2O, or **(G)** 10 M NaOH. Conditions: AM 1.5G, 100 mW cm^{-2}, 25°C. The figure is reprinted with permission from Uekert et al. (2018), copyright 2018, Royal Society of Chemistry.

Supplementary Figure 2 | **(A)** Schematic transformation from $CdMoO_4$ to CdS/MoS_2 nanooctahedron heterostructure; **(B)** SEM image of CdS/MoS_2; **(C)** photocatalytic H_2 evolution activity of the different samples using pretreated PLA solution (stirring in 10 M KOH at 40°C for 24 h in the dark); **(D)** integrated photocatalytic H_2 production and organics upgrading of furfural alcohol (FA), bacterial cellulose membrane (BC), pretreated PLA solution and PET solution over CdS/MoS_2 in 10 M KOH; **(E)** photograph of the obtained white precipitate after adding excess $Ba(OH)_2$ solution into the supernate taken immediately after photocatalysis. Conditions: $\lambda \geq 420$ nm, 110.3 mW cm^{-2}. The figure is reprinted with permission from Zhao et al. (2020), copyright 2020, Wiley.

Supplementary Figure 3 | **(A)** The mechanism of H_2 evolution coupled with the conversion of PET plastic over $M_t/C_xZ_{1-x}S$; **(B)** the control experiment and photocatalytic H_2 evolution from pretreated PET solution (stirring in 10 M NaOH at 40°C for 24 h) of $M_{4.3}/C_xZ_{1-x}S$ ($0.2 \leq x \leq 0.8$) under simulated sunlight; **(C)** ^{1}H-NMR spectra of an aqueous solution of pretreated PET plastic before and after photocatalytic H_2 generation of 5 h; **(D)** photocatalytic H_2 evolution stability of $M_{4.3}/C_{0.5}Z_{0.5}S$ under simulated sunlight and anaerobic environment. Condition: AM 1.5 G. The figure is reprinted with permission from Li et al. (2021), copyright 2021, Wiley.

Supplementary Figure 4 | **(A)** Schematic diagram of the photocatalytic plastic valorization using a $CN_x|Ni_2P$ photocatalyst; **(B)** long-term photoreforming of pretreated PET and PLA (stirring in 2 M KOH at 40°C for 24 h in the dark); **(C)** the influence of KOH concentration for photoreforming of pretreated PET (20 h irradiation); black circles in **(C)** mark H_2 evolution per gram of substrate over $CN_x|Pt$ (2 wt%) under the same conditions; ^{1}H NMR spectra of pretreated PET **(D)** and PLA **(E, F)** after photoreforming (insets show zoomed-out views of the spectra); **(G)** chemical structures and peak assignments; **(H)** long-term photoreforming of different plastics under simulated solar light. Conditions: AM 1.5 G, 100 mW cm^{-2}, 25°C. The figure is reprinted with permission from Uekert et al. (2019), copyright 2019, American Chemical Society. **(I)** Photograph of a 25 cm^2 $CNx|Ni_2P$ panel with a schematic diagram of the photoreforming process; **(J)** up-scaled long-term H_2 evolution under ideal (100 mW cm^{-2}, pure deionized water) and worst (20 mW cm^{-2}, seawater) cases. Conditions: 100 mW cm^{-2} or 20 mW cm^{-2}, 25°C, MSW (stirring in 0.5 M KOH at 80°C for overnight). The figure is reprinted with permission from Uekert et al. (2020a), copyright 2020, Wiley.

Supplementary Figure 5 | **(A)** Structure of the V-based photocatalyst; **(B)** the conversion scheme of PE over the V catalysts; **(C)** proposed reaction mechanism for the cascade C-C bond cleavage in polyethylene-monoalcohol. The bonds that undergo cleavage are highlighted in bold and red. Conditions: white LEDs, 85°C. The figure is reprinted with permission from Gazi et al. (2019), copyright 2019, Wiley.

Supplementary Figure 6 | **(A)** Schematic illustration for converting various waste plastic into C_2 fuels by a designed sequential pathway under simulated natural environment conditions; **(B)** atomic force microscopy image of Nb_2O_5; **(C)** the yield of CO_2 during the photoconversion of pure PE, PP, and PVC over the Nb_2O_5 atomic layers; **(D)** the yield of CH_3COOH under the simulated solar light; **(E)** schematic representations for the band-edge positions of Nb_2O_5 atomic layers along with the potentials of CO_2, H_2O, H_2O_2, and O_2 redox couples at pH 7 and the proposed two-step C-C bond cleavage and coupling mechanism from pure PE into CH_3COOH. Conditions: AM 1.5G, 100 mW cm^{-2}, 298 ± 0.2 K. The figure is reprinted with permission from Jiao et al. (2020), copyright 2020, Wiley.

REFERENCES

Al-Salem, S. M., Lettieri, P., and Baeyens, J. (2009). Recycling and Recovery Routes of Plastic Solid Waste (PSW): A Review. *Waste Manage.* 29 (10), 2625–2643. doi:10.1016/j.wasman.2009.06.004

Andrady, A. L., and Neal, M. A. (2009). Applications and Societal Benefits of Plastics. *Phil. Trans. R. Soc. B* 364 (1526), 1977–1984. doi:10.1098/rstb.2008.0304

Bai, B., Jin, H., Fan, C., Cao, C., Wei, W., and Cao, W. (2019). Experimental Investigation on Liquefaction of Plastic Waste to Oil in Supercritical Water. *Waste Manage.* 89, 247–253. doi:10.1016/j.wasman.2019.04.017

Clarizia, L., Russo, D., Di Somma, I., Andreozzi, R., and Marotta, R. (2017). Hydrogen Generation through Solar Photocatalytic Processes: A Review of the Configuration and the Properties of Effective Metal-Based Semiconductor Nanomaterials. *Energies* 10 (10), 1624. doi:10.3390/en10101624

Das, S., and Mahalingam, H. (2019). Dye Degradation Studies Using Immobilized Pristine and Waste Polystyrene-TiO_2/rGO/g-C_3N_4 Nanocomposite Photocatalytic Film in a Novel Airlift Reactor under Solar Light. *J. Environ. Chem. Eng.* 7 (5), 103289. doi:10.1016/j.jece.2019.103289

de Assis, G. C., Skovroinski, E., Leite, V. D., Rodrigues, M. O., Galembeck, A., Alves, M. C. F., et al. (2018). Conversion of "Waste Plastic" into Photocatalytic Nanofoams for Environmental Remediation. *ACS Appl. Mater. Inter.* 10 (9), 8077–8085. doi:10.1021/acsami.7b19834

Eerkes-Medrano, D., Thompson, R. C., and Aldridge, D. C. (2015). Microplastics in Freshwater Systems: A Review of the Emerging Threats, Identification of Knowledge Gaps and Prioritisation of Research Needs. *Water Res.* 75, 63–82. doi:10.1016/j.watres.2015.02.012

Feng, H.-M., Zheng, J.-C., Lei, N.-Y., Yu, L., Kong, K. H.-K., Yu, H.-Q., et al. (2011). Photoassisted Fenton Degradation of Polystyrene. *Environ. Sci. Technol.* 45 (2), 744–750. doi:10.1021/es102182g

Garcia, J. M., and Robertson, M. L. (2017). The Future of Plastics Recycling. *Science* 358 (6365), 870–872. doi:10.1126/science.aaq0324

Gausas, L., Kristensen, S. K., Sun, H., Ahrens, A., Donslund, B. S., Lindhardt, A. T., et al. (2021). Catalytic Hydrogenation of Polyurethanes to Base Chemicals: From Model Systems to Commercial and End-of-Life Polyurethane Materials. *JACS Au* 1 (4), 517–524. doi:10.1021/jacsau.1c00050

Gazi, S., Đokić, M., Chin, K. F., Ng, P. R., and Soo, H. S. (2019). Visible Light-Driven Cascade Carbon-Carbon Bond Scission for Organic Transformations and Plastics Recycling. *Adv. Sci.* 6 (24), 1902020. doi:10.1002/advs.201902020

Geyer, R. (2020). "Production, Use, and Fate of Synthetic Polymers," in *Plastic Waste and Recycling*, 13–32. doi:10.1016/B978-0-12-817880-5.00002-5

Habisreutinger, S. N., Schmidt-Mende, L., and Stolarczyk, J. K. (2013). Photocatalytic Reduction of CO_2 on TiO_2 and Other Semiconductors. *Angew. Chem. Int. Ed.* 52 (29), 7372–7408. doi:10.1002/anie.201207199

Jehanno, C., and Sardon, H. (2019). Dynamic Polymer Network Points the Way to Truly Recyclable Plastics. *Nature* 568 (7753), 467–468. doi:10.1038/d41586-019-01209-3

Jiao, X., Zheng, K., Chen, Q., Li, X., Li, Y., Shao, W., et al. (2020). Photocatalytic Conversion of Waste Plastics into C_2 Fuels under Simulated Natural Environment Conditions. *Angew. Chem. Int. Ed.* 59 (36), 15497–15501. doi:10.1002/anie.201915766

Jie, X., Li, W., Slocombe, D., Gao, Y., Banerjee, I., Gonzalez-Cortes, S., et al. (2020). Microwave-Initiated Catalytic Deconstruction of Plastic Waste into Hydrogen and High-Value Carbons. *Nat. Catal.* 3 (11), 902–912. doi:10.1038/s41929-020-00518-5

Kawai, T., and Sakata, T. (1981). Photocatalytic Hydrogen Production from Water by the Decomposition of Poly-Vinylchloride, Protein, Algae, Dead Insects, and Excrement. *Chem. Lett.* 10 (1), 81–84. doi:10.1246/cl.1981.81

Keane, M. A. (2007). Catalytic Conversion of Waste Plastics: Focus on Waste PVC. *J. Chem. Technol. Biotechnol.* 82 (9), 787–795. doi:10.1002/jctb.1757

Kumar, S., Panda, A. K., and Singh, R. K. (2011). A Review on Tertiary Recycling of High-Density Polyethylene to Fuel. *Resour. Conservation Recycling* 55 (11), 893–910. doi:10.1016/j.resconrec.2011.05.005

Li, Y., Wan, S., Lin, C., Gao, Y., Lu, Y., Wang, L., et al. (2021). Engineering of 2D/2D $MoS_2/Cd_XZn_{1-X}S$ Photocatalyst for Solar H_2 Evolution Coupled with Degradation of Plastic in Alkaline Solution. *Sol. RRL* 5 (6), 2000427. doi:10.1002/solr.202000427

Liang, W., Luo, Y., Song, S., Dong, X., and Yu, X. (2013). High Photocatalytic Degradation Activity of Polyethylene Containing Polyacrylamide Grafted TiO_2. *Polym. Degrad. Stab.* 98 (9), 1754–1761. doi:10.1016/j.polymdegradstab.2013.05.027

Liu, S., Tang, Z.-R., Sun, Y., Colmenares, J. C., and Xu, Y.-J. (2015). One-Dimension-Based Spatially Ordered Architectures for Solar Energy Conversion. *Chem. Soc. Rev.* 44 (15), 5053–5075. doi:10.1039/c4cs00408f

Lopez, G., Artetxe, M., Amutio, M., Bilbao, J., and Olazar, M. (2017). Thermochemical Routes for the Valorization of Waste Polyolefinic Plastics to Produce Fuels and Chemicals. A Review. *Renew. Sustain. Energ. Rev.* 73, 346–368. doi:10.1016/j.rser.2017.01.142

Lu, K.-Q., Qi, M.-Y., Tang, Z.-R., and Xu, Y.-J. (2019). Earth-Abundant MoS_2 and Cobalt Phosphate Dual Cocatalysts on 1D CdS Nanowires for Boosting Photocatalytic Hydrogen Production. *Langmuir* 35 (34), 11056–11065. doi:10.1021/acs.langmuir.9b01409

MacArthur, E. (2017). Beyond Plastic Waste. *Science* 358 (6365), 843. doi:10.1126/science.aao6749

Majeed, I., Nadeem, M. A., Al-Oufi, M., Nadeem, M. A., Waterhouse, G. I. N., Badshah, A., et al. (2016). On the Role of Metal Particle Size and Surface Coverage for Photo-Catalytic Hydrogen Production: A Case Study of the Au/CdS System. *Appl. Catal. B: Environ.* 182, 266–276. doi:10.1016/j.apcatb.2015.09.039

Mark, L. O., Cendejas, M. C., and Hermans, I. (2020). The Use of Heterogeneous Catalysis in the Chemical Valorization of Plastic Waste. *ChemSusChem* 13 (22), 5808–5836. doi:10.1002/cssc.202001905

Martín, A. J., Mondelli, C., Jaydev, S. D., and Pérez-Ramírez, J. (2021). Catalytic Processing of Plastic Waste on the Rise. *Chem* 7, 1487–1533. doi:10.1016/j.chempr.2020.12.006

PlasticEurope (2020). Plastic-the Facts 2020. Available at: https://www.plasticseurope.org/en/ resources/publications/4312-plastics-facts-2020.

Rahimi, A., and García, J. M. (2017). Chemical Recycling of Waste Plastics for New Materials Production. *Nat. Rev. Chem.* 1 (6). doi:10.1038/s41570-017-0046

Ru, J., Huo, Y., and Yang, Y. (2020). Microbial Degradation and Valorization of Plastic Wastes. *Front. Microbiol.* 11, 442. doi:10.3389/fmicb.2020.00442

Schyns, Z. O. G., and Shaver, M. P. (2021). Mechanical Recycling of Packaging Plastics: A Review. *Macromol. Rapid Commun.* 42 (3), 2000415. doi:10.1002/marc.202000415

Shang, J., Chai, M., and Zhu, Y. (2003). Photocatalytic Degradation of Polystyrene Plastic under Fluorescent Light. *Environ. Sci. Technol.* 37 (19), 4494–4499. doi:10.1021/es0209464

Shang, W., Li, Y., Huang, H., Lai, F., Roeffaers, M. B. J., and Weng, B. (2021). Synergistic Redox Reaction for Value-Added Organic Transformation via Dual-Functional Photocatalytic Systems. *ACS Catal.* 11 (8), 4613–4632. doi:10.1021/acscatal.0c04815

Shi, R., Ye, H.-F., Liang, F., Wang, Z., Li, K., Weng, Y., et al. (2018). Interstitial P-Doped CdS with Long-Lived Photogenerated Electrons for Photocatalytic Water Splitting without Sacrificial Agents. *Adv. Mater.* 30 (6), 1705941. doi:10.1002/adma.201705941

Tennakoon, A., Wu, X., Paterson, A. L., Patnaik, S., Pei, Y., LaPointe, A. M., et al. (2020). Catalytic Upcycling of High-Density Polyethylene via a Processive Mechanism. *Nat. Catal.* 3 (11), 893–901. doi:10.1038/s41929-020-00519-4

Thompson, R. C., Olsen, Y., Mitchell, R. P., Davis, A., Rowland, S. J., John, A. W., et al. (2004). Lost at Sea: Where Is All the Plastic? *Science* 304 (5672), 838. doi:10.1126/science.1094559

Tofa, T. S., Kunjali, K. L., Paul, S., and Dutta, J. (2019). Visible Light Photocatalytic Degradation of Microplastic Residues with Zinc Oxide Nanorods. *Environ. Chem. Lett.* 17 (3), 1341–1346. doi:10.1007/s10311-019-00859-z

Uekert, T., Bajada, M. A., Schubert, T., Pichler, C. M., and Reisner, E. (2020b). Scalable Photocatalyst Panels for Photoreforming of Plastic, Biomass and Mixed Waste in Flow. *ChemSusChem*. doi:10.1002/cssc.202002580

Uekert, T., Kasap, H., and Reisner, E. (2019). Photoreforming of Nonrecyclable Plastic Waste over a Carbon Nitride/Nickel Phosphide Catalyst. *J. Am. Chem. Soc.* 141 (38), 15201–15210. doi:10.1021/jacs.9b06872

Uekert, T., Kuehnel, M. F., Wakerley, D. W., and Reisner, E. (2018). Plastic Waste as a Feedstock for Solar-Driven H_2 Generation. *Energy Environ. Sci.* 11 (10), 2853–2857. doi:10.1039/c8ee01408f

Uekert, T., Pichler, C. M., Schubert, T., and Reisner, E. (2020a). Solar-Driven Reforming of Solid Waste for a Sustainable Future. *Nat. Sustain.* 4 (5), 383–391. doi:10.1038/s41893-020-00650-x

Vollmer, I., Jenks, M. J. F., Roelands, M. C. P., White, R. J., Harmelen, T., Wild, P., et al. (2020). Beyond Mechanical Recycling: Giving New Life to Plastic Waste. *Angew. Chem. Int. Ed.* 59 (36), 15402–15423. doi:10.1002/anie.201915651

Worch, J. C., and Dove, A. P. (2020). 100th Anniversary of Macromolecular Science Viewpoint: Toward Catalytic Chemical Recycling of Waste (And Future) Plastics. *ACS Macro Lett.* 9 (11), 1494–1506. doi:10.1021/acsmacrolett.0c00582

Xiao, F.-X., Miao, J., Tao, H. B., Hung, S.-F., Wang, H.-Y., Yang, H. B., et al. (2015). One-Dimensional Hybrid Nanostructures for Heterogeneous Photocatalysis and Photoelectrocatalysis. *Small* 11 (18), 2115–2131. doi:10.1002/smll.201402420

Yang, M.-Q., Gao, M., Hong, M., and Ho, G. W. (2018). Visible-to-NiR Photon Harvesting: Progressive Engineering of Catalysts for Solar-Powered Environmental Purification and Fuel Production. *Adv. Mater.* 30 (47), 1802894. doi:10.1002/adma.201802894

Yang, M.-Q., Han, C., Zhang, N., and Xu, Y.-J. (2015). Precursor Chemistry Matters in Boosting Photoredox Activity of Graphene/Semiconductor Composites. *Nanoscale* 7 (43), 18062–18070. doi:10.1039/c5nr05143f

Yang, M.-Q., and Xu, Y.-J. (2016). Photocatalytic Conversion of CO_2 over Graphene-Based Composites: Current Status and Future Perspective. *Nanoscale Horiz.* 1 (3), 185–200. doi:10.1039/c5nh00113g

Zhang, F., Zhao, Y., Wang, D., Yan, M., Zhang, J., Zhang, P., et al. (2021). Current Technologies for Plastic Waste Treatment: A Review. *J. Clean. Prod.* 282, 124523. doi:10.1016/j.jclepro.2020.124523

Zhang, K., Hamidian, A. H., Tubić, A., Zhang, Y., Fang, J. K. H., Wu, C., et al. (2021). Understanding Plastic Degradation and Microplastic Formation in the Environment: A Review. *Environ. Pollut.* 274, 116554. doi:10.1016/j.envpol.2021.116554

Zhao, L., Dong, T., Du, J., Liu, H., Yuan, H., Wang, Y., et al. (2020). Synthesis of CdS/MoS_2 Nanooctahedrons Heterostructure with a Tight Interface for Enhanced Photocatalytic H_2 Evolution and Biomass Upgrading. *Sol. RRL* 5, 2000415. doi:10.1002/solr.202000415

Zhao, X., Li, Z., Chen, Y., Shi, L., and Zhu, Y. (2008). Enhancement of Photocatalytic Degradation of Polyethylene Plastic with CuPc Modified TiO_2 Photocatalyst under Solar Light Irradiation. *Appl. Surf. Sci.* 254 (6), 1825–1829. doi:10.1016/j.apsusc.2007.07.154

Zhao, X. u., Li, Z., Chen, Y., Shi, L., and Zhu, Y. (2007). Solid-Phase Photocatalytic Degradation of Polyethylene Plastic under UV and Solar Light Irradiation. *J. Mol. Catal. A: Chem.* 268 (1), 101–106. doi:10.1016/j.molcata.2006.12.012

Conflict of Interest: The handling Editor declared a past co-authorship with one of the authors (SW).

The remaining authors declare that the research was conducted in the absence of any commercial or financial relationships that could be construed as a potential conflict of interest.

frontiers in Nanotechnology

MINI REVIEW
published: 17 December 2021
doi: 10.3389/fnano.2021.809329

Recent Advances on Lignocellulosic-Based Nanopesticides for Agricultural Applications

Pedro Henrique Correia de Lima[1], *Débora Ribeiro Antunes*[1], *Mariana Monteiro de Lima Forini*[1], *Montcharles da Silva Pontes*[2], *Bruno Dufau Mattos*[3] and *Renato Grillo*[1]*

[1]Department of Physics and Chemistry, School of Engineering, São Paulo State University (UNESP), Ilha Solteira, Brazil, [2]Natural Resources Program, Center for Natural Resources Studies (CERNA), Mato Grosso do Sul State University (UEMS), Dourados, Brazil, [3]Department of Bioproducts and Biosystems, School of Chemical Engineering, Aalto University, Espoo, Finland

Controlled release systems of agrochemicals have been developed in recent years. However, the design of intelligent nanocarriers that can be manufactured with renewable and low-cost materials is still a challenge for agricultural applications. Lignocellulosic building blocks (cellulose, lignin, and hemicellulose) are ideal candidates to manufacture ecofriendly nanocarriers given their low-cost, abundancy and sustainability. Complexity and heterogeneity of biopolymers have posed challenges in the development of nanocarriers; however, the current engineering toolbox for biopolymer modification has increased remarkably, which enables better control over their properties and tuned interactions with cargoes and plant tissues. In this mini-review, we explore recent advances on lignocellulosic-based nanocarriers for the controlled release of agrochemicals. We also offer a critical discussion regarding the future challenges of potential bio-based nanocarrier for sustainable agricultural development.

Keywords: nanopesticides, biopolymers, lignocellulosic materials, nanotechnology, nano-enabled agriculture, sustainable agriculture, circular bioeconomy

Edited by:
Amitava Mukherjee,
VIT University, India

Reviewed by:
Suresh Kaushik,
Indian Agricultural Research Institute
(ICAR), India

***Correspondence:**
Renato Grillo
renato.grillo@unesp.br
renato.grillo@ymail.com

Specialty section:
This article was submitted to
Environmental Nanotechnology,
a section of the journal
Frontiers in Nanotechnology

Received: 04 November 2021
Accepted: 22 November 2021
Published: 17 December 2021

Citation:
Lima PHC, Antunes DR, Forini MML, Pontes MS, Mattos BD and Grillo R (2021) Recent Advances on Lignocellulosic-Based Nanopesticides for Agricultural Applications. Front. Nanotechnol. 3:809329. doi: 10.3389/fnano.2021.809329

INTRODUCTION

The development of environmentally friendly tools that can produce crops or livestock without negative impact on humans and the environment is central to the Sustainable Development Goals. Nowadays, with the development of nanotechnology, researchers are obtaining good outcomes using nanomaterials (NMs) (Mattos et al., 2017; Guo et al., 2021; Sikder et al., 2021). For instance, engineered nanoparticles (ENPs) are capable of improving the efficiency of pesticides and fertilizers through the controlled release of agrochemicals, as well as by providing enhanced plant performance or by enabling plants to act as real-time sensors, actuators, or electronic devices (Baker et al., 2017; Saleem and Zaidi, 2020; Agathokleous et al., 2020; Acharya and Pal, 2020; Usman et al., 2020; Singh et al., 2021; Grillo et al., 2021a). The increased surface area to volume ratio of the ENPs enables a greater control of interfacial interactions with a given cargo to act on demand or specific stimuli as well as many other features. Besides, several factors such as surface charge, particle size, composition, solubility, and manufacturing methods can be exploited to control the interaction of ENPs with specific plants and organisms (Jogaiah et al., 2021), with the goal of developing targeted systems. Although most of the current nanopesticides or nanocarriers

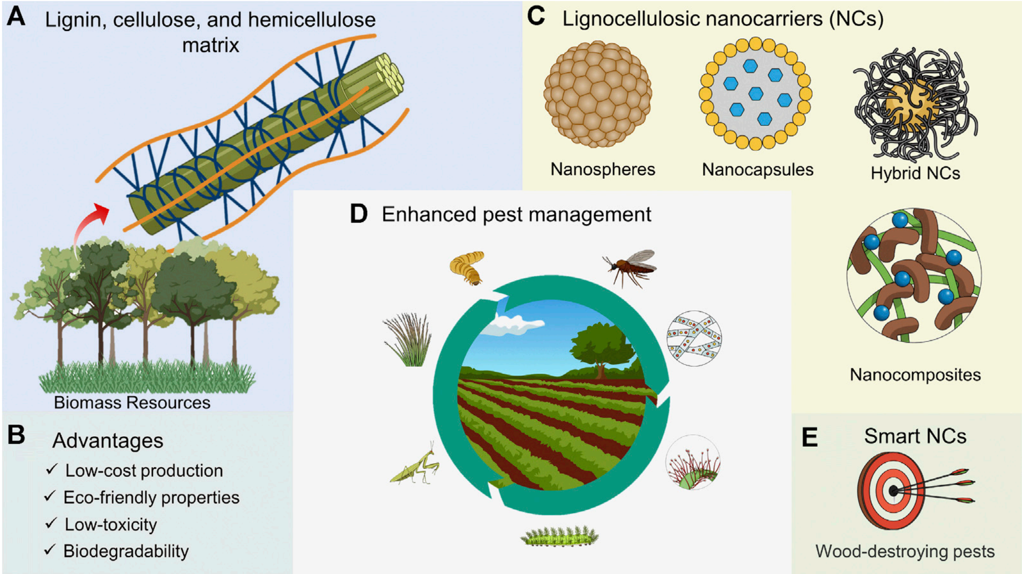

FIGURE 1 | Schematic representation of a **(A)** lignocellulosic building blocks matrix, **(B)** advantages to produce, and **(C)** different types of nanopesticides that can **(D)** enhance pest management (e.g., weeds, viruses, bacteria, fungi, and insects) as well as display unique properties such as **(E)** targeting wood-destroying pests.

are developed from synthetic (e.g., polymers) building blocks, several systems have been developed using biopolymers as tools for the controlled release system of agrochemicals (Mattos et al., 2017). Lignocellulosic-based nanopesticides are biodegradable and offer an interesting platform to produce safe-by-design nanopesticides as they can be non-toxic (Chamundeeswari et al., 2019; Zhang et al., 2019; Bhattacharyya et al., 2020; Shrestha et al., 2021; Ur Rahim et al., 2021) (**Figure 1**). Moreover, lignocellulosic material can be obtained from agriculture side streams, which is ideal to reduce costs during the production of nanopesticides, which are intended to be applied in large scale agricultural operations. This strategy also indicates a *from plant-to-plant* effort, ideal for a circular bioeconomy landscape.

There are mainly three non-edible lignocellulosic biopolymers that have been used in the development of materials: cellulose, lignin, and hemicellulose, along with pectin, tannins, acids, and proteins (Okolie et al., 2021). Even though the manipulation of its feedstock is challenging to engineer, lignocellulosic materials have low-cost production and eco-friendly properties (Li et al., 2021a). Although lignocellulosic-based nanocarriers are still under development for the agricultural sector, several advances have been achieved thus making this technology useful for nano-enabled agriculture. The increased use of lignocellulosics in nano-enabled agriculture is expected to take place because there are new technologies that can 1) increase the extraction efficiency of lignocellulosic materials; 2) modify lignocellulosic structures for desired properties; and 3) design hybrid nanostructures with controllable shape and size. Nonetheless, the application of lignocellulosics in nano-enabled agriculture is currently related to the controlled delivery and release of pesticides and nutrients (Worrall et al., 2018; Papadopoulos et al., 2019; Chen et al., 2020a; Teo and Wahab., 2020). However, lignocellulosic nanomaterials could potentially stabilize emulsions (such as those used in oil borne pesticides) instead conventional surfactants in multiphase systems (Tardy et al., 2021). In this review we summarize and discuss the recent advances in lignocellulosic nanocarriers for agricultural applications; in addition, we offer a critical discussion regarding the future challenges of lignocellulosic nano-enabled materials for sustainable agricultural development.

TYPES OF LIGNOCELLULOSIC-BASED NANOPESTICIDES FOR AGRICULTURE

Cellulose-Based Nanopesticides

Cellulose is a linear polymer composed of several hundreds of glucose units linked by β-1,4-glycosidic bonds (**Figure 2A**). Cellulose is highly abundant, being sourced from agro-industrial biomass (from 1st generation to wastes and residues), marine biomasses, and microorganisms. (Kaya and Tabak., 2020; Siqueira et al., 2020; Teo and Wahab., 2020; Bahloul et al., 2021). Cellulose nanomaterials have been marketed in several sectors of the economy, including agriculture. However, cellulose intra- and intermolecular hydrogen bonding interactions hinder its dissolution in water although being highly hydrophilic (Credou and Berthelot, 2014; Shatkin and Kim, 2015). Therefore, several studies have focused on the chemical modification of cellulose using a variety of routes to modify its physicochemical properties, enable dissolution, and therefore to facilitate the conception of nanocarriers that can be applied for improving agrochemical efficacy (Rop et al., 2020; Machado et al., 2021). For instance, dialdehyde carboxymethyl cellulose (DCMC) and carboxymethyl cellulose (CMC) were conjugated with zein (a protein from corn) to develop nanocarriers for avermectin (Chen et al., 2020b; Hao et al., 2020). In both cases, the resulting nanopesticides showed high

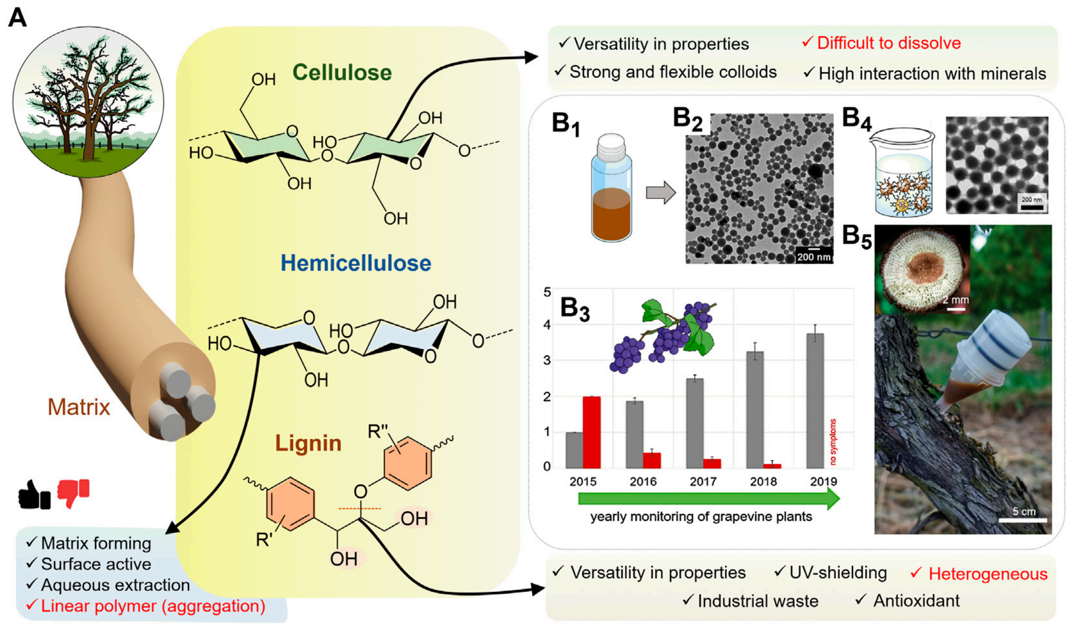

FIGURE 2 | (A) Types of lignocellulosic materials (cellulose, hemicellulose (e.g., xylan) and lignin) pointing out their main advantages (black) and disadvantages (red). **(B1)** Representation of a formulation containing lignin nanoparticles. **(B2)** Transmission electron microscopy image of pyraclostrobin-loaded lignin nanoparticles in the range of 100—300 nm. **(B3)** Effect of empty lignin (gray bars) and fungicide-loaded lignin (red bars) NPs on Esca leaf symptoms in four Portugieser grapevine plants monitored yearly from 2015 to 2019. **(B4)** Transmission electron microscopy image of fungicide-loaded lignin NPs. **(B5)** Lignin-based fungicide-loaded NPs being applied in a grapevine plant to target Esca. **(B2,B3)** were reproduced with permission from Machado, 2020, Copyright (2020) American Chemical Society, and **(B4,B5)** were reproduced with permission from Machado, 2020, Copyright (2019) John Wiley and Sons. Further permissions related to the material excerpted should be directed to the ACS and John Wiley and Sons.

leaf adhesion as well as efficient protection of the active ingredient against ultraviolet light (UV) when compared to its conventional form. Avermectin has been also encapsulated in CMC-grafted polyethyleneglycol (PEG) nanoparticles (Zhu et al., 2020) and in CMC grafted poly 2,2,3,4,4,4-hexafluorobutyl methacrylate (PHFBA) (Su et al., 2021a); both showed enhanced insecticidal activity against fall webworm (*Hyphantria cunea*) and an improved of the release profile of the active ingredient for 95 h, respectively. Additionally, glycine methyl ester (GLY) and glycidyl methacrylate (GMA) were used as intermediate and organic nitrogen sources, respectively, to modify CMC during the synthesis of a nanopesticide containing emamectin benzoate. Such nanopesticide and nanofertilizer increased the insecticidal activity against the diamondback moth insect (*Plutella xylostella*) and showed a potential system to be used as organic nitrogen fertilizer without toxic effect on seed germination (Zhao et al., 2021a).

On the other hand, nanoparticles crosslinked by cellulose have received an increased attention in the agricultural sector due to their good stability under environmental conditions (Sun et al., 2020). For instance, stimuli-responsive nanocapsules based on cellulose modified with fatty acid (undec-10-enoic) loaded captan and pyraclostrobin were developed against apple canker (*Neonectria ditissima*), and the results showed that the active ingredients were released when triggered by the presence of cellulolytic fungi (Machado et al., 2021). Another study showed the fabrication of carboxymethylcellulose sodium salt and hydroxyethyl cellulose-based biodegradable hydrogels using citric acid (CA) as a crosslinker; good water uptake and a sustainable release profile were observed (Das et al., 2021).

A mixture of (nano)cellulose with inorganic (nano)materials (for example clays) opens up strategies for the design of nanopesticides with a widened pallet of biological, thermal, and structural properties. For instance, carboxymethyl cellulose hydrogels filled with nanocellulose and nanoclays (Bauli et al., 2021) or cellulose-g-poly (ammonium acrylate-co-acrylic acid)/nano-hydroxyapatite (Rop et al., 2020) showed good efficiency on hydrogel nutrient release and improved the moisture retention around the plant in the soil. Furthermore, a hybrid nanopesticide composed of hollow mesoporous silica/hydroxypropyl cellulose was reported to control rice blast fungus (*Magnaporthe oryzae*), and a dual-responsive release profile of the active ingredient was observed when in presence of cellulase (enzyme) or under acid conditions (Gao et al., 2021a). Moreover, layered double hydroxides (LDH) were mixed with CMC to fabricate polymeric nanocomposite able to mitigate the downside effect of herbicides in paddy cultivation (Sharif et al., 2021). In addition, they observed high adhesion of nanocellulose towards hydrophilic surfaces has led to the development of biogenic nanohybrids containing biogenic silica and cellulose nanofibers for the encapsulation of various molecules including a biopesticide (thymol) (Mattos and Magalhães, 2016; Mattos et al., 2018).

TABLE 1 | Examples of lignocellulosic-based nanopesticides.

Lignocellulosic-based materials	Composition	Size (nm)	Agrochemical	Findings	References
Cellulose	Sodium carboxymethyl cellulose grafted by styrene/methyl methacrylate and butyl acrylate	180–280	Avermectin	Anti-ultraviolet photolysis ability of the active ingredient was improved and the release time was prolonged	Chen et al. (2018)
Cellulose	Myrtenal-based nanocellulose/diacylhydrazine	—	Boscalid and chlorothalonil	Complexes exhibited comparable or better antifungal activity than the commercial one against several fungi	Li et al. (2021c)
Lignin	Sodium lignosulfonate/poly (vinyl alcohol)-valine	~10	Emamectin benzoate	Higher bioactivity of nanogels compared to non-nanoformulations	Zhang et al. (2021b)
Lignin	Sodium lignosulfonate	162	Pyraclostrobin cyclohexanone	Nanocapsules improved control efficacy on tomato crown and root rot compared to micro- and other nanoformulations	Luo et al. (2020)
Lignin	Sodium lignosulfonate/epoxy resin	150	Abamectin	Higher efficiency to control root-knot nematodes (*Meloidogyne incognita*) compared to conventional agrochemicals	Zhang et al. (2020b)
Lignin	Sodium lignosulfonate	150–250	Emamectin benzoate	Nanopesticide improved the photostability of the active ingredient, as well enhanced the insecticidal activity against *Prodenia. Litura* (leafworm) when compared to the commercial formulation. Nanopesticide also exhibited pH-mediated release property	Cui et al. (2019)
Xylan	Lignin/xylan	166–210	Avermectin	Lignin–xylan hybrid nanospheres showed well-defined core-shell structures with encapsulation efficiency above 57%. Nanopesticide also showed enzyme-mediated release property	Jiang et al. (2020)
Tannic Acid	Fe^{3+}/tannic acid	141–160	Tebuconazole	Nanocapsules showed high fungicidal activities against rice sheath blight (*Rhizoctonia solani*) and wheat head blight (*Fusarium graminearum*) pathogenic fungi	Dong et al. (2021)
Tannic Acid	Mesoporous silica nanoparticles/copper/tannic acid	137	Pyraclostrobin	The complexes coating could improve the photostability of the active ingredient, as well enhanced deposition efficiency on rice leaves with good antifungal activity against Rhizoctonia solani	Liang et al. (2021)
Abietic acid	Carboxymethyl celulose/glycidyl methacrylate/rosin	167	Avermectin	Nanopesticide displays enhanced dispersibility and stability of the active ingredient, and improves the affinity and light stability on cucumber leaf, maintaining good insecticidal activity against *Plutella xylostella*	Zhao et al. (2021b)
Salicylic acid	p-amino salicylic acid-modified polysuccinimide	155–290	Avermectin	Aqueous nanopesticides showed a cumulative release rate of 70% with a pH-responsive profile. It was also reported to have good insecticide activity against *Plutella xylostella*	Su et al. (2021c)

The difficulty of promoting dissolution of cellulose, in parallel with the current regulation on bioplastics that defines cellulose derivatives as plastics, will accelerate the development of nanocarriers from cellulose colloids, such as cellulose nanofibers, which have unique physicochemical properties such as higher surface area, nanodimension, high-temperature resistance, and biocompatibility (Shahi et al., 2021; Tardy et al., 2021). Cellulose nanofibers (CNFs) have been reported as potential high performers in nanoformulations of fertilization (do Nascimento et al., 2021), as well as cellulose nanocrystals (CNC) with chitosan to control tomato bacterial speck disease (Schiavi et al., 2021), among others (**Table 1**). For its diversity and abundance, cellulose is an outstanding material with a list of properties yet to be explored as a nanopesticide thus, understanding better its composition and potential interactions with agrochemicals and non- target and target organisms is essential to the future design of sustainable nano-enabled agriculture.

Lignin-Based Nanopesticides

Lignin is a three-dimensional and complex aromatic biopolymer that is bound to cellulose and hemicellulose within the plant cell wall microstructure (**Figure 2A**). Furthermore, it has attracted great attention due to its availability at large scales (Lizundia et al., 2021). In the last years, lignin-based nanoparticles (LNPs) have been used in agriculture against fungus, and insects due to their eco-friendly properties, low cost, and good encapsulating properties; however, this formulation is insoluble in the aqueous environment, which raises some technical difficulties when producing nanocarriers or promoting cargo delivery. Nevertheless, production of LNPs has been demonstrated to be possible for upscaling at reasonable cost (Abbati de Assis et al., 2018; Bangalore Ashok et al., 2018). For instance, stem lignin nanoparticles have been used as matrix in the controlled release of the herbicide diuron (Yearla and Padmasree, 2016). Chemical modifications in lignin to control their interactions with water and solubility (Balakshin and Capanema, 2015; Agustin et al., 2019; Falsini et al., 2019; Ma et al., 2020; Machado et al., 2020), also facilitate their use in nano-enabled strategies for agriculture. For instance, sodium lignosulfonate can electrostatically interact with other polymers [e.g., chitosan (Li et al., 2019)], and cationic surfactant [e.g., dodecyl dimethyl benzyl ammonium chloride (Zhang et al., 2021a), cetyltrimethylammonium bromide (Peng et al., 2020)] by self-assembly to form stimuli-responsive nanopesticides (**Table 1**). Kraft lignin (KL) has a tunable amphiphilic nature due to the abundant phenolic hydroxyl groups capable of forming a stable double-layered nanomaterial with ionic surfactants (Ela et al., 2020), nanocapsules with olive oil (Falsini et al., 2020), and is also able to chelate cationic metals (Sipponen et al., 2017). Other nanopesticides have also been synthesized with alkali lignin (AL) (Yin et al., 2020), organosolv lignin (Zhang et al., 2020a), and methacrylate lignin (Yiamsawas et al., 2021).

In this regard, some interesting studies have been using lignin nanoparticles for the controlled release of fungicide to target Esca (a type of grapevine trunk disease that negatively impacts grape yields and the wine industry around the world). For instance, Machado et al. (2020) developed several fungicide-loaded lignin nanocarriers (**Figure 2B$_{1,2}$**) to be applied in a single injection into *Vitis vinifera* ("Portugieser") plants, and the results showed successfully inhibition of lignase-producing fungi (e.g., *Phaeomoniella chlamydospora* and *Phaeoacremonium minimum*) as well as fungicide efficiency for at least 4 years against Esca (**Figure 2B$_3$**). Furthermore, two other stimuli-responsive lignin-based nanocarriers were developed for the treatment of Esca (Fischer et al., 2019; Peil et al., 2020). In both studies, the fungi associated with Esca degraded lignin through secretion of ligninolytic enzymes (e.g., laccases and peroxidases) and, thus, released fungal spores (*Trichoderma reesei*) (Peil et al., 2020) and the hydrophobic fungicide pyraclostrobin (Fischer et al., 2019) loaded in lignin nanocarriers (**Figure 2B$_{4,5}$**). Moreover, another triggered strategy is based on the controlled release of micronutrients , such as copper and iron, to fertilize and protect plants against various pathogens (Gazzurelli et al., 2020; Li et al., 2021b).

Despite the development of numerous lignin-based nanocarriers for agriculture, the great challenge of these nanoformulations is still the complexity and variability of chemical structure of this resource given the batch-to-batch variations in the extraction process. In this context, studies such as those by Beckers et al. (2021) have been important as it is possible to synthesize lignin-like monomers (e.g., phenylcoumaran and β-O-4-aryl ether) able to comprise linkages found in native lignin with promising results. Nevertheless, lignin-first biorefining approaches have recently been proposed to produce well-defined lignin structures that can be further utilized in a more systematic way (Lourencon et al., 2019).

Hemicellulose-Based Nanopesticides

Hemicellulose is a biopolymer with a degree of polymerization of ca. 50–200 and molecular weight below 90 kDa, thus a much smaller building block when compared to cellulose or lignin (Ye et al., 2021). Hemicelluloses represent 15–25% of the wood cell-wall but can reach up to 45% in annual, seasonal plants. Such biopolymers include xyloglucans, xylans (**Figure 2A**), mannans and glucomannans, and beta-glucans. A wide range of applications has been associated with hemicellulose, such as the generation of chemical products, packaging materials, drug delivery systems, and more recently as pesticide delivery systems (Naidu et al., 2018; Wijaya et al., 2021). The extraction of hemicellulose comes from lignocellulosic biomass, wood, foliage, grass, and agricultural residues and can be carried out using organic solvent but more commonly with hydrothermal extractions (Naidu et al., 2018).

Due to the low water solubility of hemicelluloses, there are still some challenges to produce stable hemicellulose-based nanocarriers for the controlled release of agrochemicals. However, several examples have been demonstrated in recent years. Beckers et al. (2020a) described the first synthesis of nanocarriers built from xylan extracted from corn cobs to contain the fungicide pyraclostrobin, by interfacial polymerization method of diisocyanate of toluene (TDI) in an inverse emulsion. Hence, such nanopesticide was colloidally stable in water and cyclohexane for several weeks as well as it was efficient against phytopathogenic fungi (*Botrytis cinerea*) as the biocide release from the xylan nanocarriers was stimulated by the fungi. In another study, xylan-based nanoparticles (without active ingredients) were fabricated and their antifungal effect was studied on corn husk fiber and on the high-density polyethylene (HDPE) composite. Such nanoparticles prevented the formation of hyphae in wood as well as increased the strength of the composite (Gao et al., 2021b). Additionally, lignin sulfonate-based nanocarriers containing hemicellulose residues showed potential for controlled delivery of agrochemicals such as the fungicides pyraclostrobin or prothioconazole (Beckers et al., 2020b). In addition, xylan-based nanoparticles are advantageous for their biocompatibility, biodegradability, and low-cost biological material (Beckers et al., 2020b). Recently, lignin-xylan and arabinoxylan nanoparticles were also reported as an enzymatic-responsive for pesticides release (Jiang et al., 2020) (**Table 1**) as well as a gene delivery system for CRISR-Cas9 DNA (Sarker et al., 2020), respectively.

β-Glucan is a homopolymer, an abundant class of polysaccharides in plants, fungi, and bacteria. Most recently, ß-Glucan-based nanocarriers have been extensively studied as drug delivery systems (Su et al., 2021b). For instance, Kaziem et al. (2022) developed a smart-delivery formulation based on carboxymethylated-β-glucans on the mesoporous silica nanoparticles (MSNs) surfaces after loading chlorothalonil (CHT) fungicide, with bioactivity against phytopathogens better than commercial formulation and lower toxicity to manure worm (*Eisenia fetida*) and zebra fish (*Danio rerio*). In another study with the same formulation, the authors observed that CHT@MSNs-β-glucans showed 2.6 times lower toxicity to the planktonic crustacean (*Daphnia magna*) and also exhibited lower effects on soil microbial abundance than commercial chlorothalonil (Kaziem et al., 2021), which improves its use as a nano-enabled agrochemical.

Other Lignocellulosic Materials-Based Nanopesticides

Other lignocellulosic materials, even in minor quantities, are rising in agriculture as compounds of nanocarriers. Pectin (Pec), a structural compound present in the primary cell walls of higher plants has been applied for the development of nano-enabled delivery systems for agrochemicals. Pectin has been used to configure an intelligent stimuli-responsive carrier triggered by pectinase, an enzymes produced by plants, filamentous fungi, bacteria, and yeasts. Moreover, a hybrid system comprising mesoporous silica nanoparticles and pectin (MSN-Pec) could delivery prochloraz (a fungicide) slowly, showing potential to be used in rice crops (Abdelrahman et al., 2021). Pectin-based nanocarriers showed promising behavior to mitigate drought stress in plants of arid and semi-arid environments (Sharma et al., 2017). Carbendazim-loaded chitosan-pectin nanoparticles showed a good response against pathogenic fungi *Fusarium pxysporum* and *Aspergillus parasiticus* (Kumar et al., 2017). Composite systems, such as chitosan/tripolyphosphate/pectin nanoparticles, were reported as a delivery system for paraquat herbicide to reduce the toxic behavior to alveolar and mouth cell lines, as well as to enhance the herbicidal activity against maize and mustard plants (Rashidipour et al., 2019). Thus, the nanoencapsulation of paraquat improves its herbicidal activity and reduces its toxic and mutagenic effects (Grillo et al., 2015; Pontes et al., 2021; Rashidipour et al., 2021).

Tannins, especially tannic acid, have been used in nanopesticide formulations (**Table 1**) as an additive to promote better foliage adhesion of particulates (Yu et al., 2019; Zhi et al., 2020). The ability of tannins to promote multiple and diverse secondary interactions towards virtually any surface has warranted their utilization to modify nanocarriers surfaces while adding UV protection and antioxidant properties (both useful to increase the lifetime of the active ingredient) (Guo et al., 2016). Finally, acids such as rosin (abietic acid) and salicylic acid are used in the attempt to create efficient nanocarriers (**Table 1**) (Zhao et al., 2021b; Su et al., 2021c).

CONCLUDING REMARKS AND CHALLENGES AHEAD

Current research on the smart nano-enabled delivery systems for pesticides has opened a new way to view the stimuli-responsive controlled release of crop protectants and to the development of novel agro-technological products. Despite the complexity of biomolecules and the challenges on generating stable nanoformulations, lignocellulosic-based nanocarriers have shown promising features that can be further explored in advanced, and renewable nanocarriers for agriculture. These carriers display unique properties (e.g., targeting wood-destroying pests), low cost, and good biodegradability rate. However, the number of studies on the mechanism of action of these nanopesticides as well as their toxicity impacts in the environment is still very limited (Grillo et al., 2021b). Moreover, little is known about the biodegradation of biopolymers after their modification or compositing, which still restricts their wider utilization in large-scale platforms such as crop protection. Therefore, further research on lignocellulosic nanomaterials is necessary in order to improve the efficient use of biomass resources as well as achieving environmental sustainability in agriculture.

AUTHOR CONTRIBUTIONS

PL, DA, and MF writing, review and editing the manuscript, MP and BM review and editing the manuscript, and RG conceptualization, writing, review, editing and supervision the manuscript. All authors contributed to manuscript revision, read, and approved the submitted version.

FUNDING

The authors acknowledge funding from National Council for Scientific and Technological Development, CNPq (Grant no. #427498/2018-0), São Paulo Research Foundation, FAPESP (#2020/12769-0), and Coordenação de Aperfeiçoamento de Pessoal de Nível Superior—Brasil, CAPES—Finance Code 001.

ACKNOWLEDGMENTS

MF thanks FAPESP for scholarship (#2020/12769-0).

REFERENCES

Abbati de Assis, C., Greca, L. G., Ago, M., Balakshin, M. Y., Jameel, H., Gonzalez, R., et al. (2018). Techno-Economic Assessment, Scalability, and Applications of Aerosol Lignin Micro- and Nanoparticles. *ACS Sust. Chem. Eng.* 6 (9), 11853–11868. doi:10.1021/acssuschemeng.8b02151

Abdelrahman, T. M., Qin, X., Li, D., Senosy, I. A., Mmby, M., Wan, H., et al. (2021). Pectinase-responsive Carriers Based on Mesoporous Silica Nanoparticles for Improving the Translocation and Fungicidal Activity of Prochloraz in rice Plants. *Chem. Eng. J.* 404, 126440. doi:10.1016/j.cej.2020.126440

Acharya, A., and Pal, P. K. (2020). Agriculture Nanotechnology: Translating Research Outcome to Field Applications by Influencing Environmental Sustainability. *NanoImpact* 19, 100232. doi:10.1016/j.impact.2020.100232

Agathokleous, E., Feng, Z., Iavicoli, I., and Calabrese, E. J. (2020). Nano-pesticides: A Great challenge for Biodiversity? the Need for a Broader Perspective. *Nano Today* 30, 100808. doi:10.1016/j.nantod.2019.100808

Agustin, M. B., Penttilä, P. A., Lahtinen, M., and Mikkonen, K. S. (2019). Rapid and Direct Preparation of Lignin Nanoparticles from Alkaline Pulping Liquor by Mild Ultrasonication. *ACS Sust. Chem. Eng.* 7 (24), 19925–19934. doi:10.1021/acssuschemeng.9b05445

Bahloul, A., Kassab, Z., El Bouchti, M., Hannache, H., Qaiss, A. E. K., Oumam, M., et al. (2021). Micro- and Nano-Structures of Cellulose from Eggplant Plant (Solanum Melongena L) Agricultural Residue. *Carbohydr. Polym.* 253, 117311. doi:10.1016/j.carbpol.2020.117311

Baker, S., Volova, T., Prudnikova, S. V., Satish, S., and Prasad M.N., N. (2017). Nanoagroparticles Emerging Trends and Future prospect in Modern Agriculture System. *Environ. Toxicol. Pharmacol.* 53, 10–17. doi:10.1016/j.etap.2017.04.012

Balakshin, M., and Capanema, E. (2015). On the Quantification of Lignin Hydroxyl Groups With31P and13C NMR Spectroscopy. *J. Wood Chem. Techn.* 35 (3), 220–237. doi:10.1080/02773813.2014.928328

Bangalore Ashok, R. P., Oinas, P., Lintinen, K., Sarwar, G., Kostiainen, M. A., and Österberg, M. (2018). Techno-economic Assessment for the Large-Scale Production of Colloidal Lignin Particles. *Green. Chem.* 20 (21), 4911–4919. doi:10.1039/c8gc02805b

Bauli, C. R., Lima, G. F., de Souza, A. G., Ferreira, R. R., and Rosa, D. S. (2021). Eco-friendly Carboxymethyl Cellulose Hydrogels Filled with Nanocellulose or Nanoclays for Agriculture Applications as Soil Conditioning and Nutrient Carrier and Their Impact on Cucumber Growing. *Colloids Surf. A: Physicochemical Eng. Aspects* 623, 126771. doi:10.1016/j.colsurfa.2021.126771

Beckers, S. J., Fischer, J., and Wurm, F. R. (2021). Synthetic Lignin-like and Degradable Nanocarriers. *Polym. Chem.* 12 (32), 4661–4667. doi:10.1039/d1py00818h

Beckers, S. J., Wetherbee, L., Fischer, J., and Wurm, F. R. (2020a). Fungicide-loaded and Biodegradable Xylan-based Nanocarriers. *Biopolymers* 111 (12), e23413. doi:10.1002/bip.23413

Beckers, S., Peil, S., and Wurm, F. R. (2020b). Pesticide-Loaded Nanocarriers from Lignin Sulfonates-A Promising Tool for Sustainable Plant Protection. *ACS Sust. Chem. Eng.* 8 (50), 18468–18475. doi:10.1021/acssuschemeng.0c05897

Bhattacharyya, C., Roy, R., Tribedi, P., Ghosh, A., and Ghosh, A. (2020). “Biofertilizers as Substitute to Commercial Agrochemicals,” in *Agrochemicals Detection, Treatment and Remediation* (Kolkata, India: Butterworth-Heinemann), 263–290. doi:10.1016/B978-0-08-103017-2.00011-8

Chamundeeswari, M., Jeslin, J., and Verma, M. L. (2019). Nanocarriers for Drug Delivery Applications. *Environ. Chem. Lett.* 17 (2), 849–865. doi:10.1007/s10311-018-00841-1

Chen, H., Lin, G., Zhou, H., Zhou, X., Xu, H., and Huang, S. (2018). Preparation of Avermectin/grafted CMC Nanoparticles and Their Sustained Release Performance. *J. Polym. Environ.* 26, 2945–2953. doi:10.1007/s10924-018-1182-y

Chen, L., Zhou, H., Hao, L., Li, Z., Xu, H., Chen, H., et al. (2020b). Dialdehyde Carboxymethyl Cellulose-Zein Conjugate as Water-Based Nanocarrier for Improving the Efficacy of Pesticides. *Ind. Crops Prod.* 150, 112358. doi:10.1016/j.indcrop.2020.112358

Chen, Z., Ragauskas, A., and Wan, C. (2020a). Lignin Extraction and Upgrading Using Deep Eutectic Solvents. *Ind. Crops Prod.* 147, 112241. doi:10.1016/j.indcrop.2020.112241

Credou, J., and Berthelot, T. (2014). Cellulose: from Biocompatible to Bioactive Material. *J. Mater. Chem. B* 2 (30), 4767–4788. doi:10.1039/c4tb00431k

Cui, J., Mo, D., Jiang, Y., Gan, C., Li, W., Wu, A., et al. (20192019). Fabrication, Characterization, and Insecticidal Activity Evaluation of Emamectin Benzoate–Sodium Lignosulfonate Nanoformulation with pH-Responsivity. *Ind. Eng. Chem. Res.* 58, 19741–19751. doi:10.1021/acs.iecr.9b03171

Das, D., Prakash, P., Rout, P. K., and Bhaladhare, S. (2021). Synthesis and Characterization of Superabsorbent Cellulose-Based Hydrogel for Agriculture Application. *Starch-Stärke* 73 (1-2), 1900284. doi:10.1002/star.201900284

do Nascimento, D. M., Nunes, Y. L., de Almeida, J. S., Leitão, R. C., Feitosa, J., Dufresne, A., et al. (2021). Development of an Integrated Process to Produce CNFs and Lignin and its Potential Applications for Agrochemical Delivery. *Cellulose* 28, 1–14. doi:10.1007/s10570-021-04200-2

Dong, J., Chen, W., Feng, J., Liu, X., Xu, Y., Wang, C., et al. (2021). Facile, Smart, and Degradable Metal–Organic Framework Nanopesticides Gated with FeIII-Tannic Acid Networks in Response to Seven Biological and Environmental Stimuli. *ACS Appl. Mater. Inter.* 13 (16), 19507–19520. doi:10.1021/acsami.1c04118

Ela, R. C. A., Tajiri, M., Newberry, N. K., Heiden, P. A., and Ong, R. G. (2020). Double-shell Lignin Nanocapsules Are a Stable Vehicle for Fungicide Encapsulation and Release. *ACS Sust. Chem. Eng.* 8 (46), 17299–17306. doi:10.1021/acssuschemeng.0c06686

Falsini, S., Tani, C., Schiff, S., Gonnelli, C., Clemente, I., Ristori, S., et al. (2020). A New Method for the Direct Tracking of *In Vivo* Lignin Nanocapsules in Eragrostis Tef (Poaceae) Tissues. *Eur. J. Histochem.* 64 (2). doi:10.4081/ejh.2020.3112

Falsini, S., Clemente, I., Papini, A., Tani, C., Schiff, S., Salvatici, M. C., et al. (2019). When Sustainable Nanochemistry Meets Agriculture: Lignin Nanocapsules for Bioactive Compound Delivery to Plantlets. *ACS Sust. Chem. Eng.* 7 (24), 19935–19942. doi:10.1021/acssuschemeng.9b05462

Fischer, J., Beckers, S. J., Yiamsawas, D., Thines, E., Landfester, K., and Wurm, F. R. (2019). Targeted Drug Delivery in Plants: Enzyme-Responsive Lignin Nanocarriers for the Curative Treatment of the Worldwide Grapevine Trunk Disease Esca. *Adv. Sci. (Weinh)* 6, 1802315. doi:10.1002/advs.201802315

Gao, X., Fan, S., Pang, J., Rahman, M. Z., Zhu, D., Guo, S., et al. (2021b). Preparation of Nano-Xylan and its Influences on the Anti-fungi Performance of Straw Fiber/HDPE Composite. *Ind. Crops Prod.* 171, 113954. doi:10.1016/j.indcrop.2021.113954

Gao, Y., Liu, Y., Qin, X., Guo, Z., Li, D., Li, C., et al. (2021a). Dual Stimuli-Responsive Fungicide Carrier Based on Hollow Mesoporous Silica/hydroxypropyl Cellulose Hybrid Nanoparticles. *J. Hazard. Mater.* 414, 125513. doi:10.1016/j.jhazmat.2021.125513

Gazzurelli, C., Migliori, A., Mazzeo, P. P., Carcelli, M., Pietarinen, S., Leonardi, G., et al. (2020). Making Agriculture More Sustainable: an Environmentally Friendly Approach to the Synthesis of Lignin@ Cu Pesticides. *ACS Sust. Chem. Eng.* 8 (39), 14886–14895. doi:10.1021/acssuschemeng.0c04645

Grillo, R., Clemente, Z., de Oliveira, J. L., Campos, E. V., Chalupe, V. C., Jonsson, C. M., et al. (2015). Chitosan Nanoparticles Loaded the Herbicide Paraquat: the Influence of the Aquatic Humic Substances on the Colloidal Stability and Toxicity. *J. Hazard. Mater.* 286, 562–572. doi:10.1016/j.jhazmat.2014.12.021

Grillo, R., Mattos, B. D., Antunes, D. R., Forini, M. M., Monikh, F. A., and Rojas, O. J. (2021a). Foliage Adhesion and Interactions with Particulate Delivery Systems for Plant Nanobionics and Intelligent Agriculture. *Nano Today* 37, 101078. doi:10.1016/j.nantod.2021.101078

Grillo, R., Fraceto, L. F., Amorim, M. J. B., Scott-Fordsmand, J. J., Schoonjans, R., and Chaudhry, Q. (2021b). Ecotoxicological and Regulatory Aspects of Environmental Sustainability of Nanopesticides. *J. Hazard. Mater.* 404, 124148. doi:10.1016/j.jhazmat.2020.124148

Guo, J., Tardy, B. L., Christofferson, A. J., Dai, Y., Richardson, J. J., Zhu, W., et al. (2016). Modular Assembly of Superstructures from Polyphenol-Functionalized Building Blocks. *Nat. Nanotechnol* 11 (12), 1105–1111. doi:10.1038/nnano.2016.172

Guo, S., He, F., Song, B., and Wu, J. (2021). Future Direction of Agrochemical Development for Plant Disease in China. *Food and Energy Security* 10(4), e293. doi:10.1002/fes3.293

Hao, L., Lin, G., Lian, J., Chen, L., Zhou, H., Chen, H., et al. (2020). Carboxymethyl Cellulose Capsulated Zein as Pesticide Nano-Delivery System for Improving Adhesion and Anti-UV Properties. *Carbohydr. Polym.* 231, 115725. doi:10.1016/j.carbpol.2019.115725

Jiang, Y., Chen, Y., Tian, D., Shen, F., Wan, X., Xu, L., et al. (2020). Fabrication and Characterization of Lignin-Xylan Hybrid Nanospheres as Pesticide Carriers with Enzyme-Mediated Release Property. *Soft Matter* 16 (39), 9083–9093. doi:10.1039/d0sm01402h

Jogaiah, S., Paidi, M. K., Venugopal, K., Geetha, N., Mujtaba, M., Udikeri, S. S., et al. (2021). Phytotoxicological Effects of Engineered Nanoparticles: An Emerging Nanotoxicology. *Sci. Total Environ.* 801, 149809. doi:10.1016/j.scitotenv.2021.149809

Kaya, M., and Tabak, A. (2020). Recycling of an Agricultural Bio-Waste as a Novel Cellulose Aerogel: A green Chemistry Study. *J. Polym. Environ.* 28 (1), 323–330. doi:10.1007/s10924-019-01609-6

Kaziem, A. E., Yang, L., Lin, Y., Kazem, A. E., Xu, H., and Zhang, Z. X. (2021). Pathogenic Invasion-Responsive Carrier Based on Mesoporous Silica/β-Glucan Nanoparticles for Smart Delivery of Fungicides. *ACS Sust. Chem. Eng.* 9 (27), 9126–9138. doi:10.1021/acssuschemeng.1c02962

Kaziem, A. E., Yang, L., Lin, Y., Song, Z., Xu, H., and Zhang, Z. (2022). Efficiency of Mesoporous Silica/carboxymethyl β-glucan as a Fungicide Nano-Delivery System for Improving Chlorothalonil Bioactivity and Reduce Biotoxicity. *Chemosphere* 287, 131902. doi:10.1016/j.chemosphere.2021.131902

Kumar, S., Kumar, D., and Dilbaghi, N. (2017). Preparation, Characterization, and Bio-Efficacy Evaluation of Controlled Release Carbendazim-Loaded Polymeric Nanoparticles. *Environ. Sci. Pollut. Res.* 24 (1), 926–937. doi:10.1007/s11356-016-7774-y

Li, B., Lin, G., Duan, W., Wang, X., and Cen, B. (2021c). Synthesis of Myrtenal-Based Nanocellulose/Diacylhydrazine Complexes with Antifungal Activity for Plant Protection. *J. Agric. Food Chem.* 69 (44), 12956–12965. doi:10.1021/acs.jafc.1c02694

Li, P., Huang, Y., Fu, C., Jiang, S. X., Peng, W., Jia, Y., et al. (2021a). Eco-friendly Biomolecule-nanomaterial Hybrids as Next-generation Agrochemicals for Topical Delivery. *EcoMat* 3, e12132. doi:10.1002/eom2.12132

Li, T., Lü, S., Yan, J., Bai, X., Gao, C., and Liu, M. (2019). An Environment-Friendly Fertilizer Prepared by Layer-By-Layer Self-Assembly for pH-Responsive Nutrient Release. *ACS Appl. Mater. Inter.* 11 (11), 10941–10950. doi:10.1021/acsami.9b01425

Li, T., Lü, S., Wang, Z., Huang, M., Yan, J., and Liu, M. (2021b). Lignin-based Nanoparticles for Recovery and Separation of Phosphate and Reused as Renewable Magnetic Fertilizers. *Sci. Total Environ.* 765, 142745. doi:10.1016/j.scitotenv.2020.142745

Liang, Y., Song, J., Dong, H., Huo, Z., Gao, Y., Zhou, Z., et al. (2021). Fabrication of pH-Responsive Nanoparticles for High Efficiency Pyraclostrobin Delivery and Reducing Environmental Impact. *Sci. Total Environ.* 787, 147422. doi:10.1016/j.scitotenv.2021.147422

Lizundia, E., Sipponen, M. H., Greca, L. G., Balakshin, M., Tardy, B. L., Rojas, O. J., et al. (2021). Multifunctional Lignin-Based Nanocomposites and Nanohybrids. *Green. Chem.* 23, 6698–6760. doi:10.1039/d1gc01684a

Lourencon, T. V., Greca, L. G., Tarasov, D., Borrega, M., Tamminen, T., Rojas, O. J., et al. (2019). Lignin-first Integrated Hydrothermal Treatment (HTT) and Synthesis of Low-Cost Biorefinery Particles. *ACS Sust. Chem. Eng.* 8 (2), 1230–1239. doi:10.1021/acssuschemeng.9b06511

Luo, J., Zhang, D. X., Jing, T., Liu, G., Cao, H., Li, B. X., et al. (2020). Pyraclostrobin Loaded Lignin-Modified Nanocapsules: Delivery Efficiency Enhancement in Soil Improved Control Efficacy on *Tomato Fusarium* crown and Root Rot. *Chem. Eng. J.* 394, 124854. doi:10.1016/j.cej.2020.124854

Ma, M., Dai, L., Xu, J., Liu, Z., and Ni, Y. (2020). A Simple and Effective Approach to Fabricate Lignin Nanoparticles with Tunable Sizes Based on Lignin Fractionation. *Green. Chem.* 22, 2011–2017. doi:10.1039/d0gc00377h

Machado, T. O., Beckers, S. J., Fischer, J., Müller, B., Sayer, C., de Araújo, P. H. H., et al. (2020). Bio-Based Lignin Nanocarriers Loaded with Fungicides as a Versatile Platform for Drug Delivery in Plants. *Biomacromolecules* 21, 2755–2763. doi:10.1021/acs.biomac.0c00487

Machado, T. O., Beckers, S. J., Fischer, J., Sayer, C., de Araújo, P. H. H., Landfester, K., et al. (2021). Cellulose Nanocarriers via Miniemulsion Allow Pathogen-specific Agrochemical Delivery. *J. Colloid Interf. Sci.* 601, 678–688. doi:10.1016/j.jcis.2021.05.030

Mattos, B. D., Greca, L. G., Tardy, B. L., Magalhães, W. L. E., and Rojas, O. J. (2018). Green Formation of Robust Supraparticles for Cargo Protection and Hazards Control in Natural Environments. *Small* 14 (29), e1801256. doi:10.1002/smll.201801256

Mattos, B. D., Tardy, B. L., Magalhães, W. L. E., and Rojas, O. J. (2017). Controlled Release for Crop and wood protection: Recent Progress toward Sustainable and Safe Nanostructured Biocidal Systems. *J. Control. Release* 262, 139–150. doi:10.1016/j.jconrel.2017.07.025

Mattos, B. D., and Magalhães, W. L. (2016). Biogenic Nanosilica Blended by Nanofibrillated Cellulose as Support for Slow-Release of Tebuconazole. *J. Nanoparticle Res.* 18 (9), 1–10. doi:10.1007/s11051-016-3586-8

Naidu, D. S., Hlangothi, S. P., and John, M. J. (2018). Bio-based Products from Xylan: A Review. *Carbohydr. Polym.* 179, 28–41. doi:10.1016/j.carbpol.2017.09.064

Okolie, J. A., Nanda, S., Dalai, A. K., and Kozinski, J. A. (2021). Chemistry and Specialty Industrial Applications of Lignocellulosic Biomass. *Waste Biomass Valor.* 12 (5), 2145–2169. doi:10.1007/s12649-020-01123-0

Papadopoulos, A. N., Bikiaris, D. N., Mitropoulos, A. C., and Kyzas, G. Z. (2019). Nanomaterials and Chemical Modifications for Enhanced Key Wood Properties: A Review. *Nanomaterials (Basel)* 9 (4), 607. doi:10.3390/nano9040607

Peil, S., Beckers, S. J., Fischer, J., and Wurm, F. R. (2020). Biodegradable, Lignin-Based Encapsulation Enables Delivery of Trichoderma Reesei with Programmed Enzymatic Release against grapevine Trunk Diseases. *Mater. Today Bio* 7, 100061. doi:10.1016/j.mtbio.2020.100061

Peng, R., Yang, D., Qiu, X., Qin, Y., and Zhou, M. (2020). Preparation of Self-Dispersed Lignin-Based Drug-Loaded Material and its Application in Avermectin Nano-Formulation. *Int. J. Biol. Macromol* 151, 421–427. doi:10.1016/j.ijbiomac.2020.02.114

Pontes, M. S., Antunes, D. R., Oliveira, I. P., Forini, M. M., Santos, J. S., Arruda, G. J., et al. (2021). Chitosan/tripolyphosphate Nanoformulation Carrying Paraquat: Insights on its Enhanced Herbicidal Activity. *Environ. Sci. Nano* 8 (5), 1336–1351. doi:10.1039/d0en01128b

Rashidipour, M., Maleki, A., Kordi, S., Birjandi, M., Pajouhi, N., Mohammadi, E., et al. (2019). Pectin/Chitosan/Tripolyphosphate Nanoparticles: Efficient Carriers for Reducing Soil Sorption, Cytotoxicity, and Mutagenicity of Paraquat and Enhancing its Herbicide Activity. *J. Agric. Food Chem.* 67 (20), 5736–5745. doi:10.1021/acs.jafc.9b01106

Rashidipour, M., Rasoulian, B., Maleki, A., Davari, B., Pajouhi, N., and Mohammadi, E. (2021). Pectin/chitosan/tripolyphosphate Encapsulation Protects the Rat Lung from Fibrosis and Apoptosis Induced by Paraquat Inhalation. *Pestic. Biochem. Physiol.* 178, 104919. doi:10.1016/j.pestbp.2021.104919

Rop, K., Mbui, D., Karuku, G. N., Michira, I., and Njomo, N. (2020). Characterization of Water Hyacinth Cellulose-G-Poly (Ammonium Acrylate-Co-Acrylic Acid)/nano-Hydroxyapatite Polymer Hydrogel Composite for Potential Agricultural Application. *Results Chem.* 2, 100020. doi:10.1016/j.rechem.2019.100020

Saleem, H., and Zaidi, S. J. (2020). Recent Developments in the Application of Nanomaterials in Agroecosystems. *Nanomaterials (Basel)* 10 (12), 2411. doi:10.3390/nano10122411

Sarker, N. C., Ray, P., Pfau, C., Kalavacharla, V., Hossain, K., and Quadir, M. (2020). Development of Functional Nanomaterials from Wheat Bran Derived Arabinoxylan for Nucleic Acid Delivery. *J. Agric. Food Chem.* 68 (15), 4367–4373. doi:10.1021/acs.jafc.0c00029

Schiavi, D., Balbi, R., Giovagnoli, S., Camaioni, E., Botticella, E., Sestili, F., et al. (2021). A Green Nanostructured Pesticide to Control Tomato Bacterial Speck Disease. *Nanomaterials* 11 (7), 1852. doi:10.3390/nano11071852

Shahi, N., Wang, P., Adhikari, S., Min, B., and Rangari, V. K. (2021). Biopolymers Fractionation and Synthesis of Nanocellulose/Silica Nanoparticles from Agricultural Byproducts. ACS Sustainable. *Chem. Eng.* 9 (18), 6284–6295. doi:10.1021/acssuschemeng.0c09342

Sharif, S. N. M., Hashim, N., Isa, I. M., Bakar, S. A., Saidin, M. I., Ahmad, M. S., et al. (2021). Polymeric Nanocomposite-Based Herbicide of Carboxymethyl Cellulose Coated-Zinc/Aluminium Layered Double Hydroxide-Quinclorac: A Controlled Release Purpose for Agrochemicals. *J. Polym. Environ.* 29 (6), 1817–1834. doi:10.1007/s10924-020-01997-0

Sharma, R., Bajpai, J., Bajpai, A. K., Acharya, S., Kumar, B., and Singh, R. K. (2017). Assessment of Water Retention Performance of Pectin-Based Nanocarriers for Controlled Irrigation in Agriculture. *Agric. Res.* 6 (2), 139–149. doi:10.1007/s40003-017-0257-7

Shatkin, J. A., and Kim, B. (2015). Cellulose Nanomaterials: Life Cycle Risk Assessment, and Environmental Health and Safety Roadmap. *Environ. Sci. Nano* 2 (5), 477–499. doi:10.1039/c5en00059a

Shrestha, S., Kognou, A. L. M., Zhang, J., and Qin, W. (2021). Different Facets of Lignocellulosic Biomass Including Pectin and its Perspectives. *Waste Biomass Valor.* 12 (9), 4805–4823. doi:10.1007/s12649-020-01305-w

Sikder, A., Pearce, A. K., Parkinson, S. J., Napier, R., and O'Reilly, R. K. (2021). Recent Trends in Advanced Polymer Materials in Agriculture Related Applications. *ACS Appl. Polym. Mater.* 3 (3), 1203–1217. doi:10.1021/acsapm.0c00982

Singh, H., Sharma, A., Bhardwaj, S. K., Arya, S. K., Bhardwaj, N., and Khatri, M. (2021). Recent Advances in the Applications of Nano-Agrochemicals for Sustainable Agricultural Development. *Environ. Sci. Process. Impacts* 23 (2), 213–239. doi:10.1039/d0em00404a

Sipponen, M. H., Rojas, O. J., Pihlajaniemi, V., Lintinen, K., and Österberg, M. (2017). Calcium Chelation of Lignin from Pulping Spent Liquor for Water-Resistant Slow-Release Urea Fertilizer Systems. *ACS Sust. Chem. Eng.* 5 (1), 1054–1061. doi:10.1021/acssuschemeng.6b02348

Siqueira, J. G. W., Rodrigues, C., de Souza Vandenberghe, L. P., Woiciechowski, A. L., and Soccol, C. R. (2020). Current Advances in On-Site Cellulase Production and Application on Lignocellulosic Biomass Conversion to Biofuels: a Review. *Biomass and Bioenergy* 132, 105419. doi:10.1016/j.biombioe.2019.105419

Su, S., Chen, L., Hao, L., Chen, H., Zhou, X., and Zhou, H. (2021a). Fluorinated Sodium Carboxymethyl Cellulose Nanoparticles as Carrier for Improving Adhesion and Sustaining Release of AVM. *J. Macromolecular Sci. A* 58 (4), 219–231. doi:10.1080/10601325.2020.1840922

Su, S., Chen, L., Hao, L., Chen, H., Zhou, X., and Zhou, H. (2021c). Preparation of P-Amino Salicylic Acid-Modified Polysuccinimide as Water-Based Nanocarriers for Enhancing Pesticide Stability and Insecticidal Activity. *Colloids Surf. B: Biointerfaces* 207, 111990. doi:10.1016/j.colsurfb.2021.111990

Su, Y., Chen, L., Yang, F., and Cheung, P. C. K. (2021). Beta-d-glucan-based Drug Delivery System and its Potential Application in Targeting Tumor Associated Macrophages. *Carbohydr. Polym.* 253, 117258. doi:10.1016/j.carbpol.2020.117258

Sun, H., Erdman, W., III, Yuan, Y., Mohamed, M. A., Xie, R., Wang, Y., et al. (2020). Crosslinked Polymer Nanocapsules for Therapeutic, Diagnostic, and Theranostic Applications. *Wiley Interdiscip. Rev. Nanomed Nanobiotechnol* 12 (6), e1653. doi:10.1002/wnan.1653

Tardy, B. L., Mattos, B. D., Otoni, C. G., Beaumont, M., Majoinen, J., Kämäräinen, T., et al. (2021). Deconstruction and Reassembly of Renewable Polymers and Biocolloids into Next Generation Structured Materials. *Chem. Rev.* 121 (22), 14088–14188. doi:10.1021/acs.chemrev.0c01333

Teo, H. L., and Wahab, R. A. (2020). Towards an Eco-Friendly Deconstruction of Agro-Industrial Biomass and Preparation of Renewable Cellulose Nanomaterials: A Review. *Int. J. Biol. macromolecules* 161, 1414–1430. doi:10.1016/j.ijbiomac.2020.08.076

Ur Rahim, H., Qaswar, M., Uddin, M., Giannini, C., Herrera, M. L., and Rea, G. (2021). Nano-Enable Materials Promoting Sustainability and Resilience in Modern Agriculture. *Nanomaterials* 11 (8), 2068. doi:10.3390/nano11082068

Usman, M., Farooq, M., Wakeel, A., Nawaz, A., Cheema, S. A., Rehman, H. U., et al. (2020). Nanotechnology in Agriculture: Current Status, Challenges and Future Opportunities. *Sci. Total Environ.* 721, 137778. doi:10.1016/j.scitotenv.2020.137778

Wijaya, C. J., Ismadji, S., and Gunawan, S. (2021). A Review of Lignocellulosic-Derived Nanoparticles for Drug Delivery Applications: Lignin Nanoparticles, Xylan Nanoparticles, and Cellulose Nanocrystals. *Molecules* 26 (3), 676. doi:10.3390/molecules26030676

Worrall, E. A., Hamid, A., Mody, K. T., Mitter, N., and Pappu, H. R. (2018). Nanotechnology for Plant Disease Management. *Agronomy* 8 (12), 285. doi:10.3390/agronomy8120285

Ye, L., Han, Y., Wang, X., Lu, X., Qi, X., and Yu, H. (2021). Recent Progress in Furfural Production from Hemicellulose and its Derivatives: Conversion Mechanism, Catalytic System, Solvent Selection. *Mol. Catal.* 515, 111899. doi:10.1016/j.mcat.2021.11189

Yearla, S. R., and Padmasree, K. (2016). Exploitation of Subabul Stem Lignin as a Matrix in Controlled Release Agrochemical Nanoformulations: a Case Study with Herbicide Diuron. *Environ. Sci. Pollut. Res. Int.* 23 (18), 18085–18098. doi:10.1007/s11356-016-6983-8

Yiamsawas, D., Kangwansupamonkon, W., and Kiatkamjornwong, S. (2021). Lignin-based Nanogels for the Release of Payloads in Alkaline Conditions. *Eur. Polym. J.* 145, 110241. doi:10.1016/j.eurpolymj.2020.110241

Yin, J. M., Wang, H. L., Yang, Z. K., Wang, J., Wang, Z., Duan, L. S., et al. (2020). Engineering Lignin Nanomicroparticles for the Antiphotolysis and Controlled Release of the Plant Growth Regulator Abscisic Acid. *J. Agric. Food Chem.* 68 (28), 7360–7368. doi:10.1021/acs.jafc.0c02835

Yu, M., Sun, C., Xue, Y., Liu, C., Qiu, D., Cui, B., et al. (2019). Tannic Acid-Based Nanopesticides Coating with Highly Improved Foliage Adhesion to Enhance Foliar Retention. *RSC Adv.* 9 (46), 27096–27104. doi:10.1021/10.1039/c9ra05843e

Zhang, D. X., Liu, G., Jing, T. F., Luo, J., Wei, G., Mu, W., et al. (2020). Lignin-Modified Electronegative Epoxy Resin Nanocarriers Effectively Deliver Pesticides against Plant Root-Knot Nematodes (Meloidogyne incognita). *J. Agric. Food Chem.* 68 (47), 13562–13572. doi:10.1021/acs.jafc.0c01736

Zhang, D. X., Du, J., Wang, R., Luo, J., Jing, T. F., Li, B. X., et al. (2021a). Core/Shell Dual-Responsive Nanocarriers via Iron-Mineralized Electrostatic Self-Assembly for Precise Pesticide Delivery. *Adv. Funct. Mater.* 31, 2102027. doi:10.1002/adfm.202102027

Zhang, D. X., Wang, R., Cao, H., Luo, J., Jing, T. F., Li, B. X., et al. (2021b). Emamectin Benzoate Nanogel Suspension Constructed from Poly (Vinyl Alcohol)-Valine Derivatives and Lignosulfonate Enhanced Insecticidal Efficacy. *Colloids Surf. B: Biointerfaces* 209, 112166. doi:10.1016/j.colsurfb.2021.112166

Zhang, L., Peng, X., Zhong, L., Chua, W., Xiang, Z., and Sun, R. (2019). Lignocellulosic Biomass Derived Functional Materials: Synthesis and Applications in Biomedical Engineering. *Curr. Med. Chem.* 26 (14), 2456–2474. doi:10.2174/0929867324666170918122125

Zhang, S., Fu, X., Tong, Z., Liu, G., Meng, S., Yang, Y., et al. (2020a). Lignin–Clay Nanohybrid Biocomposite-Based Double-Layer Coating Materials for Controllable-Release Fertilizer. *ACS Sust. Chem. Eng.* 8 (51), 18957–18965. doi:10.1021/acssuschemeng.0c06472

Zhao, M., Zhou, H., Hao, L., Chen, H., and Zhou, X. (2021a). A High-efficient Nano Pesticide-fertilizer Combination Fabricated by Amino Acid-modified Cellulose Based Carriers. *Pest Manag. Sci.* doi:10.1002/ps.6655

Zhao, M., Zhou, H., Hao, L., Chen, H., and Zhou, X. (2021b). Natural Rosin Modified Carboxymethyl Cellulose Delivery System with Lowered Toxicity for Long-Term Pest Control. *Carbohydr. Polym.* 259, 117749. doi:10.1016/j.carbpol.2021.117749

Zhi, H., Yu, M., Yao, J., Sun, C., Cui, B., Zhao, X., et al. (2020). A Facile Approach to Increasing the Foliage Retention of Pesticides Based on Coating with a Tannic acid/Fe3+ Complex. *Coatings* 10 (4), 359. doi:10.3390/coatings10040359

Zhu, H., Shen, Y., Cui, J., Li, N., Wang, C., Cui, B., et al. (2020). Avermectin Loaded Carboxymethyl Cellulose Nanoparticles with Stimuli-Responsive and Controlled Release Properties. Industrial. *Crops Prod.* 152, 112497. doi:10.1016/j.indcrop.2020.112497

Conflict of Interest: The authors declare that the research was conducted in the absence of any commercial or financial relationships that could be construed as a potential conflict of interest.

frontiers | Frontiers in Nanotechnology

TYPE Original Research
PUBLISHED 04 August 2022
DOI 10.3389/fnano.2022.948337

OPEN ACCESS

EDITED BY
John Fourkas,
University of Maryland, College Park,
United States

REVIEWED BY
Alexandra Joshi-Imre,
The University of Texas at Dallas,
United States
Arun K. Singh,
PEC University of Technology, India

*CORRESPONDENCE
M. J. Naughton,
naughton@bc.edu

SPECIALTY SECTION
This article was submitted to
Nanofabrication,
a section of the journal
Frontiers in Nanotechnology

RECEIVED 19 May 2022
ACCEPTED 11 July 2022
PUBLISHED 04 August 2022

CITATION
Naughton JR, Varela JA, Connolly TJ,
Shepard S, Dodge TE, Kempa K,
Burns MJ, Christianson JP and
Naughton MJ (2022), Suppression of
crosstalk in multielectrode arrays with
local shielding.
Front. Nanotechnol. 4:948337.
doi: 10.3389/fnano.2022.948337

Suppression of crosstalk in multielectrode arrays with local shielding

J. R. Naughton[1], J. A. Varela[2], T. J. Connolly[3], S. Shepard[4], T. E. Dodge[1], K. Kempa[1], M. J. Burns[1], J. P. Christianson[2] and M. J. Naughton[1]*

[1]Department of Physics, Boston College, Chestnut Hill, MA, United States, [2]Department of Psychology and Neuroscience, Boston College, Chestnut Hill, MA, United States, [3]Department of Biology, Boston College, Chestnut Hill, MA, United States, [4]Integrated Sciences Nanofabrication Clean Room Facility, Boston College, Chestnut Hill, MA, United States

Electrical crosstalk can constrain the performance of multielectrode arrays in electro- and neurophysiology, in terms of both stimulation and recording. This is especially so at high electrode density, desirable for spatiotemporal mapping of bioelectrical signals from multiple cells. Channel interference due to crosstalk is currently only partially addressed, *via* continuous interleaved sampling or post-data acquisition spike sorting. Here, we show that a locally-shielded electrode architecture significantly suppresses crosstalk, and enables multi-site recording at high electrode density without the need for spike sorting. Arrays of shielded electrodes, prepared by micro- and nanofabrication techniques in a vertically-oriented coaxial geometry, demonstrate at least a 400 times improvement in spatial density over the unshielded case.

KEYWORDS

multielectrode array, extracellular, optogenetics, nanofabrication, crosstalk

Introduction

The brain contains both large- and small-scale spatiotemporal organization, with different functions taking place on multiple spatial and temporal scales. To gain insight into the rules that underlie brain function, it is generally accepted that networks of neurons need to be studied (Nadasdy et al., 1998), as opposed to individual neurons in isolation. The extracellular multielectrode array (MEA) is an appropriate device for stimulation of and recording from large numbers of neurons (as well as other electrogenic cells), as it is capable of simultaneously recording both the slow activity associated with changes in the local field potential (an aggregate of the surrounding synaptic inputs) and the fast activity associated with multi-unit neuronal discharges nearby. In order to gain a mechanistic description of the biophysical contributors to neuronal network processes, it is necessary to isolate single-unit activity. Given the size and spacing of neurons within networks [on the 1–10 µm scale (Heathcote and Sargent, 1987)], this requires a device capable of high spatial resolution. While MEAs can be fabricated at high densities [down to 10's of μm pitch (Multichannel Systems, 2021; Miccoli et al., 2019)], a limiting factor in achieving higher spatial resolution is isolating the activity of individual neurons within the larger array (Ventura and Gerkin, 2012).

Due the spread of the extracellular current into surrounding ionic medium originating from action potentials, the number of effective recording channels in a device will be reduced below their actual number if they are of a critical spacing or smaller. The extent to which an electric field originating from a neuron is recorded by multiple electrodes, rather than by/at a single recording site, may be defined as electrical crosstalk (Wilke et al., 2011). The reciprocal of this situation, coinciding fields from multiple neurons at a single recording site (which then aggregate as a single input instead of multiple distinct inputs) is equally problematic. Overlapping electric potentials and fields are undesirable for both recording and stimulation, the latter being identified as an issue in, for example, MEA technology used for visual prostheses (Nelson et al., 2017). One definition of the degree to which a single pixel of an electrode array dominates all neighboring pixels was given by Wilke, et al. (2011) as the crosstalk coefficient $CT = E_{N-1(x,y,z)}/E_{\mathrm{N}(\mathrm{x,y,z})}$, where $|E|_{N(x,y,z)}$ is the electric field magnitude at a point (x, y, z) with all electrodes in the array active, and $|E|_{N-1(x,y,z)}$ is the field at that point with a chosen electrode inactive. This ratio will be the same for electric potential (voltage). CT ranges from 0 to 1, with the low end being minimal crosstalk (measured electric field dominated by the measuring electrode of interest) and the upper end being high crosstalk (multiple electrodes contributing to the measured electric field).

If the overlap between neuronal events (spikes) is relatively small, a common tool used by neuroscientists to isolate individual neurons in multi-unit recordings is the post-data acquisition process of spike sorting. This involves grouping recorded spikes into clusters based on the similarity of their waveforms (Rey et al., 2015) (i.e., voltage dynamics over time). Spike sorting extracts individual spike waveforms out of a temporal window of collected spikes and is highly dependent on the sampling rate. Each datum point of a spike is a possible "feature" to be used for differentiation from other spikes and therefore the problem starts off being an N-dimensional one, where N is the number of data points per spike. Here, the complexity increases exponentially as a function of recorded events and can quickly becomes computationally intensive (Prentice et al., 2011; Hilgen et al., 2017).

The duration of an action potential is on the order of a few milliseconds and so a typical 40 kHz sampling rate will yield 50–100 points per spike. If the sampling rate is too low, it risks becoming insufficient, as cutting out data points can cause an unintentional shift in the maximum point used for alignment. A higher sampling rate corresponds to more data points and a higher accuracy in representing the signal, but requires more computational power. To lower this burden, methods have been developed in order to lower the dimensionality of the problem. One simple method for feature extraction is to take the basic characteristics of a waveform (amplitude, duration/width, rise time, square of the signal, etc.) and use them to differentiate signals. However, it has been shown that this is not always reliable (Lewicki, 1998). Another simple approach called template matching relies on choosing template spike shapes for each unit (Gerstein and Clark, 1964). The shape is then used as a metric in assigning and matching waveforms. However, in addition to manual intervention being problematic, sparsely-firing neurons could be missed with this approach (Quiroga et al., 2007), and action potentials in many types of neurons exhibit intrinsic plasticity evident as experience-dependent changes in membrane ionic conductances and corresponding changes to the dynamics of the action potential (Debanne et al., 2019). The most common feature-extraction and dimensionality-reduction method is principal component analysis (PCA) (Harris et al., 2000; Shoham et al., 2003). While the details of this method are beyond the scope of this paper, the idea is to find an ordered set of orthogonal basis vectors that captures the directions of largest variance in the data and represents any waveform as a linear combination of those principal components (Person, 1901; Quiroga, 2013). Despite these challenges, spike sorting algorithms currently remain a standard process in analysis of neurological data and new methods or refinements are continually being made (Ekanadham et al., 2014; Kadir et al., 2014; Swindale and Spacek, 2014). However, establishing metrics for evaluating spike sorters is an on-going process, with some research showing there is no one-size-fits-all algorithm (Buccino et al., 2020; Magland et al., 2020; Hall et al., 2021).

The most challenging issue to the spike sorting method is the subject of focus for this paper: overlapping spikes or, as defined above, crosstalk. Two or more neurons in close proximity firing synchronously or with a small enough delay will have overlapping extracellular action potentials. This could be interpreted as a signal from a single neuron, rather than from distinguishable neurons. Furthermore, the extracellular waveform originating from an action potential changes shape as it travels through space. Given that field potentials can travel hundreds of microns in ionic solution, the waveform picked up at one location could be drastically different at another and therefore incorrectly interpreted as two unique signals (Einevoll et al., 2012). Outside of spike sorting, various techniques have been utilized to try to minimize the effect of crosstalk by designing devices that constrain the generated electric fields (Chai et al., 2008; Wong et al., 2009; Moghaddam et al., 2011; Kaur et al., 2021).

In this paper, we show that local electrical shielding through a coaxial structure (Naughton et al., 2016) greatly reduces crosstalk when compared to the conventional bare, unshielded electrode. Two stimulation methods, electrical and optical, are employed to demonstrate the utility of local shielding versus the unshielded case, *via* electrode recordings of stimulated voltage transients. In the optical stimulation experiment, optogenetically-transfected

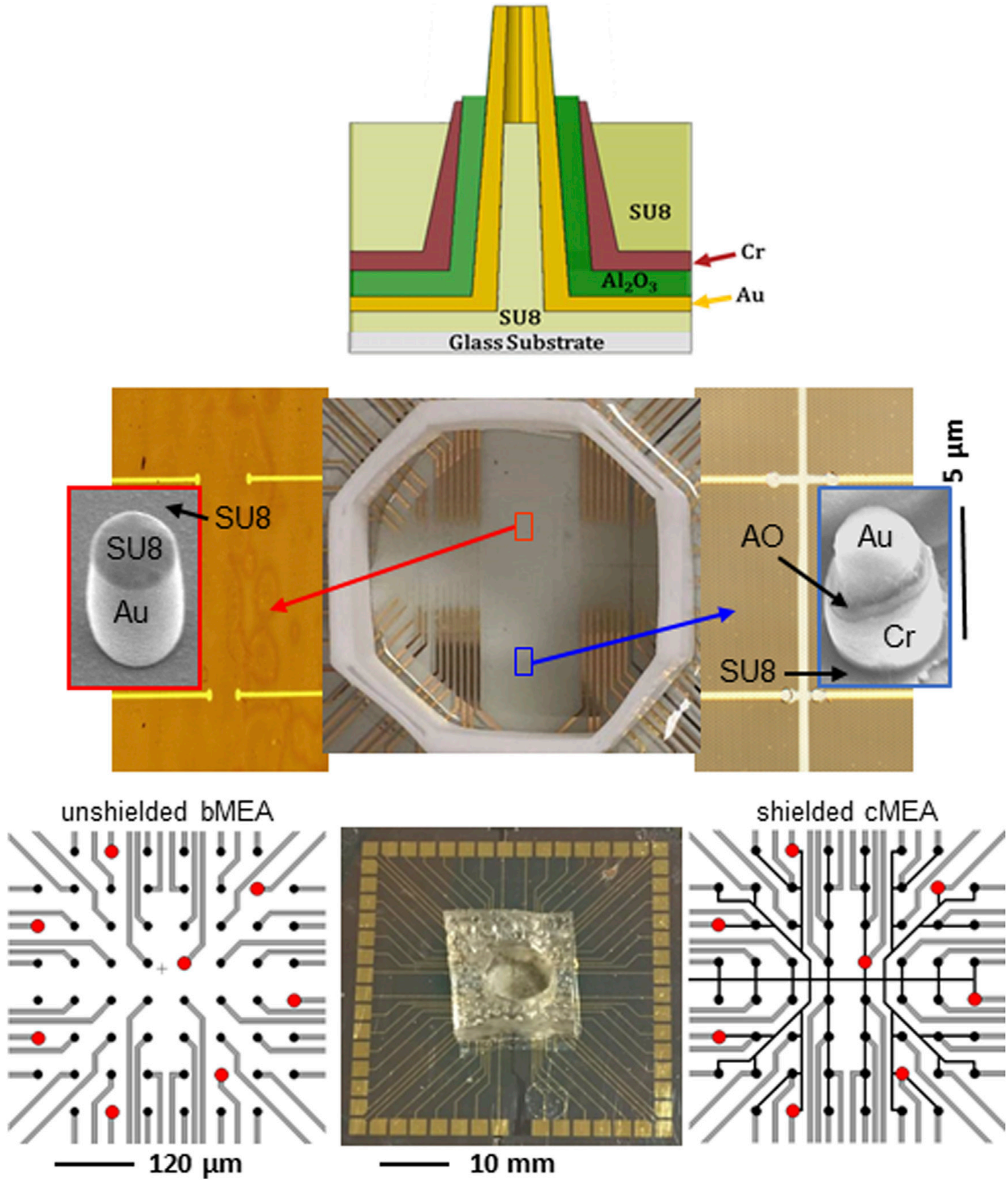

FIGURE 1
Multielectrode array devices used for electrical and optical stimulation. Upper: Schematic of coaxial electrode comprising the cMEA device. Middle: Electrical stimulation device (center) with unshielded, bare electrode/bMEA (left) and shielded, coaxial electrode/cMEA (right) regions. Left and right are magnified views of the respective regions, each containing rows of sensing areas with varying separation. The sensing areas are the 10 µm in diameter circles at the ends of gold address lines. All areas outside of sensing areas have been passivated (insulated). Zoomed insets show SEM images of respective individual, ~2 µm diameter, vertically-oriented electrodes. Constituent material labeled (AO = Al_2O_3). Lower: Optical stimulation device with cMEA chip with well (center), and wiring schematics for bMEA (left) and cMEA (right), both with 10 mm diameter sensing regions (black dots) at 60 mm pitch. Red dots indicate 20 mm-diameter transparent areas on the substrate and under the sensors, facilitating optical illumination up through the electrode cores.

human embryonic kidney cells (HEK 293-ChR2) were employed, as proxies for electrogenic cells such as neurons. Two types of devices were fabricated for each stimulation method: bare multielectrode arrays (bMEA) and coaxial multielectrode arrays (cMEA). Figure 1 upper shows a schematic of an individual coaxial electrode, with its constituent materials. In Figure 1

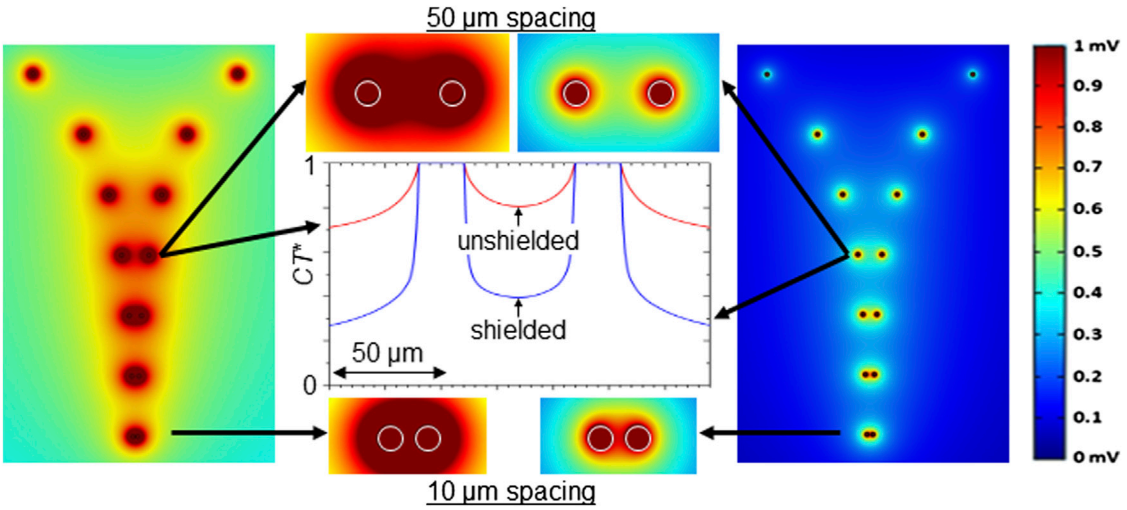

FIGURE 2
Finite element modeling. Top view of simulated equipotential contours for (left) bare and (right) shielded electrodes (5 μm height, 20 μm-diameter), biased at 1 mV, with electrode spacings, from the top of 1,000, 500, 250, 100, 50, 25, and 10 μm. Color bar at far right indicates strength of signal from a source (e.g., action potential/neuron spike) sensed by an electrode. Middle panel shows magnified view of 50 and 10 μm spacing rows, as well as calculated *CT** values versus distance for the 50 μm spacing. The coaxial, shielded electrodes include simulated radially coatings of 200 nm Al_2O_3 and 120 nm Cr, the latter with height 3 μm.

middle, we show optical images of the wiring layout for the electrical device (bare = red arrow, coax = blue arrow), and electron microscope images of an individual electrode for each type. In Figure 1 lower, we show the wiring layouts for the optical devices, and a photograph of an actual chip. We indicate representative locations of clear holes (red dots) in an otherwise optically-opaque metal film on the glass substrates onto which the MEAs (pixels = black dots) were fabricated. These holes enabled localized optical illumination and excitation *via* from below. In each cMEA stimulation device, the outer conductors/shields of the coaxes were common, with the cores individually electrically-addressed.

Results

Simulations

We also modeled/simulated the performance of unshielded and shielded MEA configurations. Using the finite element method (FEM) simulation software COMSOL Multiphysics (RRID: SCR_014767), a computational model of the device was made employing realistic material parameters, intending to examine the overlap of electric potential of a pair of electrode sensing areas as a function of electrode separation. A pattern of seven rows of electrode pairs, arranged with each row having a specific separation distance (from 5 μm to 1,000 μm), was placed in a simulated electrolyte solution (having nominally the same electrical properties as the medium used in the electrical experiment, i.e., static dielectric constant $\varepsilon \sim 80$, dc electrical conductivity $\sigma \sim 1.5$ S/m). Although crosstalk and the detection of field potentials *in situ* are influenced by a myriad of factors including cell type, distance from electrode and the nature of the contact with electrodes, the purpose of this simulation was to find the amplitude of the potential at the recording electrode surface generated by a source (e.g., neuron spike) as a function of separation distance. Green-Lorentz reciprocity reduces this problem to solving Poisson's equation for the scalar potential generated from the recording electrode as a voltage source (Lorentz, 1896).

Simulations were performed for bare, unshielded and coaxial, shielded electrodes for a range of electrode diameters and heights, as well as, for the shielded case, with an outer shield of various heights relative to that of the core electrode. Shown in Figure 2 are results for 20 μm-diameter, 5 μm-tall electrode pairs, with the shields in the coaxial case 60% the height of the core (i.e., 3 μm). Experiments were later performed with bare electrodes and coaxial electrodes having such 60% shielding. For clarification, the simulations of pairs were performed separately for each separation distance, all with 1 mV excitation. The 10 and 50 μm separation results are expanded in the middle panel of Figure 2. Throughout, dark red (blue) represents regions where an electrode strongly (weakly) senses the source signal, as indicated by the color scale at right. It is clear from the images that unshielded electrodes (left images) experience overlap in the sensing regions of adjacent electrodes at separation distances far greater than do the shielded electrodes (right images). For distances of 50–100 μm and less,

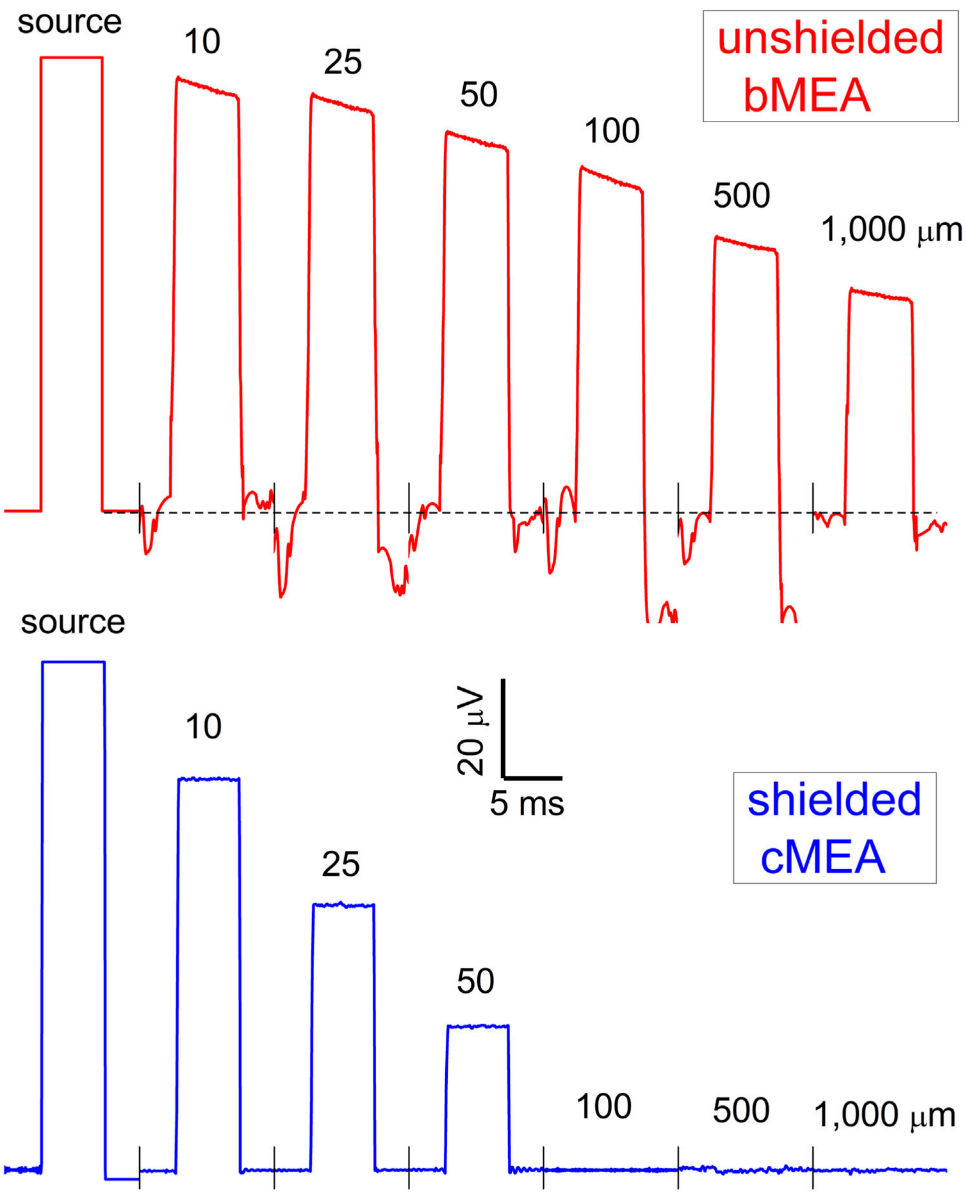

FIGURE 3
Recording with bMEA and cMEA under electrical excitation. Voltage pulse of (100 μV, 5 ms) as applied to one electrode in the arrays of Figure 1-upper indicated as source, with recorded waveforms of the bMEA (upper) and cMEA (lower) at distances from source as shown.

the sensing regions of the unshielded electrodes appreciably overlap. This effectively renders two individual electrodes as a single electrode of larger size, representing a loss in pixelation density and thus an emergence of crosstalk. Conversely, even at separation distance as small as 10 μm (bottom of middle panel in Figure 2), the shielded electrodes continue to show a separation of signal with $CT^* \leq 0.8$. Here, $CT^* = |V(d)|/|V(0)|$. CT*is an effective crosstalk coefficient and $|V(d)|$ is the signal of a particular sensing region a distance d from the excitation source. Simulation results for CT^*, from linear cuts through neighboring electrodes at 50 μm spacing, are shown in the center panel of the figure.

It is important to note that these simulations are largely scale invariant. That is, if the bare electrodes were of smaller or larger diameter than those simulated in Figure 2, the sensing regions would overlap and still be dominated by crosstalk at separation distances of a few times the electrode diameter. Multiple 2D and 3D geometries have been simulated and the results are qualitatively the same. Since the goal of this work is to move to higher density arrays eventuating in a sensing region comprised of a single coax, we made the geometry of the simulation as to compare a single coaxial structure with conventional MEA technology (a single, flat, cylindrical pad). While our experimental arrays feature multiple coaxial structures within a single sensor region, the simulations represent a conservative estimate of field overlap since the experimental arrays have more shielding surface area. For comparison, in conventional MEA architectures, the field distribution will likely be larger because of the lack of local shielding and greater surface area found in a capped cylinder (as opposed to the coaxial structure which has the cap removed). Therefore, the results of this simulation can give one a sense of the maximum pixelation allowed, given an electrode size, in order to avoid a large amount of crosstalk.

Electrical and optical stimulation

For electrical stimulation experiments, the well of the device in Figure 1 (middle), containing independent bMEA and cMEA regions, was filled with an electrolyte buffer solution using a pipette. Starting with the bMEA device and the 1 mm separation row, and moving incrementally to the 5 μm separation row, a voltage pulse was sent to one left electrode (using a Ag/Cl pellet in the electrolyte buffer solution as a ground), with voltage signals at all remaining electrodes recorded simultaneously. The experiment was repeated using the right electrode of a particular row as the stimulating electrode, to ensure mirror symmetry. Raw data traces for distances from excitation source d = 10, 25, 50, 100, 500, and 1,000 μm are shown in Figure 3 (upper, in red). For tests on the cMEA, one coax location's shield (rather than a distant wire) was set to ground. The same procedure as above was performed (signal injected on the left, followed by the right, to confirm symmetry). Raw cMEA data traces are shown in Figure 3 (lower, in black), again for d = 10–1,000 μm. Data from five-sweep trials were averaged and the mean values plotted with error bars showing the dispersion in the steady-state value. It was observed from experiments that signals recorded during the first sweep were highest, while subsequent sweeps moved towards a steady state value.

For optical stimulation, optically-evoked field potentials were detected in HEK-293 cells transfected with the blue-light sensitive channelrhodopsin protein ChR2(H134R) (Zhang et al., 2007). Transfection and culture processes on the arrays, described in previous work (Naughton et al., 2016), were used. Devices were aligned in the measuring apparatus amplifier (Multichannel Systems MEA-2100) and one of the 60 channels was set to ground. To ensure one had live, working cells throughout the array (i.e., capable of optical actuation), a 473 nm wavelength laser was aligned above an array and illuminated the sample. Once cell viability was confirmed *via* captured deflections, the laser was moved to backside alignment, sequentially positioned to several sites below the array, and five-sweep trials were performed. Representative raw data plots of voltages at the source (i.e., a cell excited at the illuminated coax) and at multiple channel distances from that source are shown in Figure 4, for both the bMEA (upper) and cMEA (lower) devices. It can be seen there that, for each light-excitation site, the deflections in the local field were confined to only a few proximate (i.e., illuminated) sensing regions for the cMEA, as opposed to nearly full signal at least 180 μm away in the bMEA. We note that the waveforms of the optically-induced deflections in HEK cells seen by the cMEA appear somewhat different from those seen by the bMEA. Both the bare electrodes and the cores of the shielded array are capacitively coupled to the signal from the cells, but the shielding in the latter serve to significantly reduce this coupling. Assuming the same liquid medium impedance R for both structures, this serves to correspondingly reduce the time constant $\tau = RC$ of the cMEA measuring circuit. Specifically, the data in Figure 4 yield $\tau \sim 475$ and 120 ms for the bMEA and cMEA, respectively. We have simulated the capacitance C of these circuits using electromagnetic finite element modeling routines (CST Studio Suite), and calculate a capacitance ratio of $C_{\mathrm{bMEA}}/C_{\mathrm{cMEA}} = 5 \pm 2$, consistent with the measured ratio of ~4. As such, the cMEA structure better represents the extracellular true response.

For both electrical and optical stimulation, the recorded electrical response was confined to sensing areas in close proximity to the stimulation location for the cMEA device. On the other hand, this response persisted to significantly larger distances for the bMEA device. In Figure 3, electrical stimulation, it can be seen that the response is ~75% suppressed a distance of 50 μm from the source for the cMEA, but only ~15% suppressed for the bMEA case. Beyond that distance, cMEA electrodes detect no residual signal, while almost half the stimulation signals persist out to 1 mm distance in the bMEA. Both electrical and optical stimulation results reflect the suppression of channel crosstalk in the shielded environment provided the cMEA.

Discussion

In order to quantitatively compare the two devices, data were collected and trials for each experiment averaged. The electrode voltage at the point of excitation was named $V(0)$. The distances to the surrounded electrodes were calculated and the crosstalk coefficient CT^*, introduced above, was extracted for each electrode. Like the CT discussed in the introduction, a large CT^* corresponds to high crosstalk, since the sensing region is capturing a large portion of the source. We show in Figure 5 the voltage response, plotted as effective crosstalk $CT^* = V(d)/V(0)$, versus distance d from excitation for the electrical and optical stimulation experiments, from data in Figures 3, 4 as well from as additional like experiments (averaged data ± standard deviation

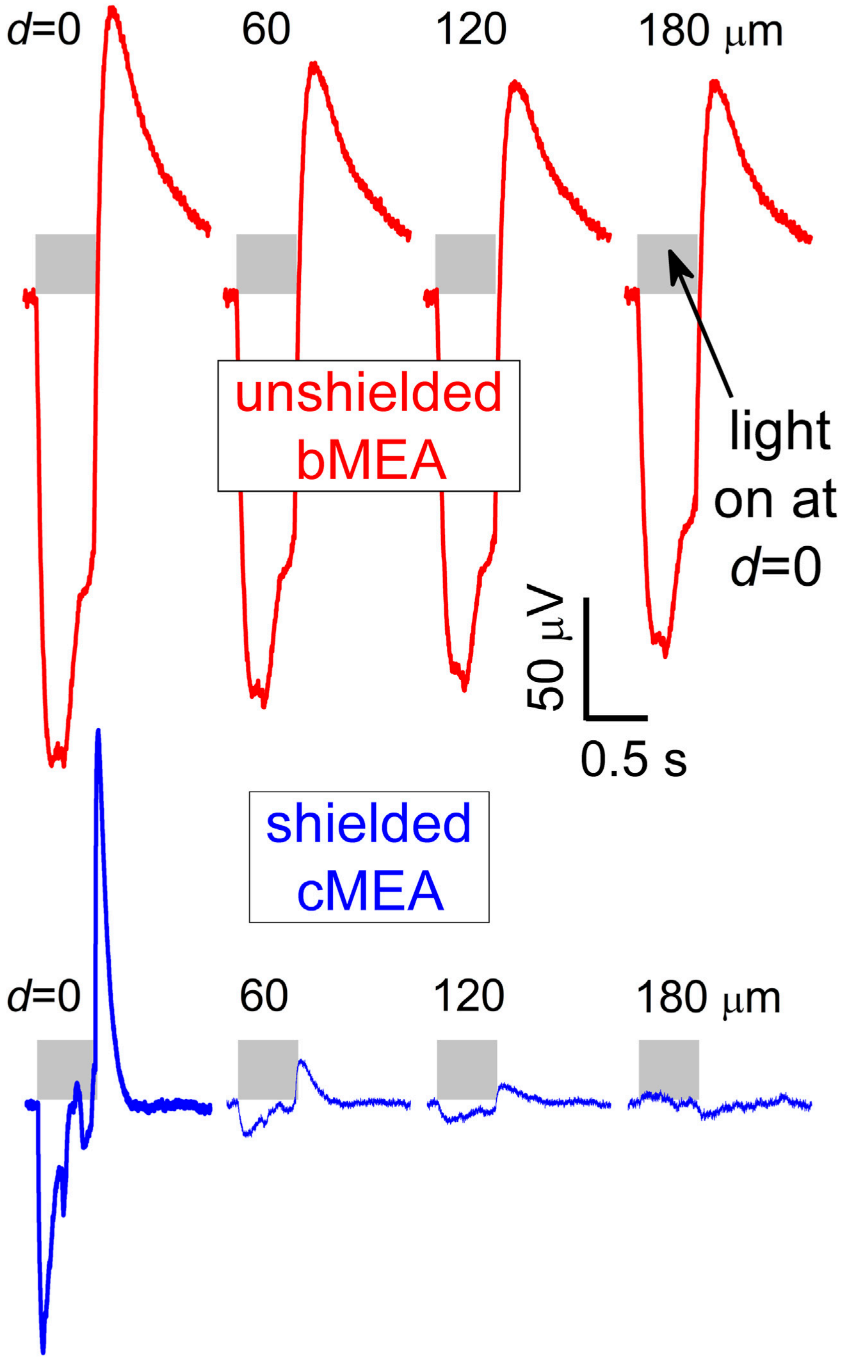

FIGURE 4
Recording with bMEA and cMEA under optical excitation. Voltage response vs. time of optogenetically-transfected HEK-293 cells for the bMEA (upper) and cMEA (lower) devices in sensing regions at indicated distances *d* from backside-illuminated (0.5 s duration, shaded regions) stimulation location (*d* = 0). Large extracellular potentials were evident at the site of stimulation and nearby electrodes in the bMEA but only at the site of stimulation on the cMEA. All windows correspond to 1.5 s recordings.

shown). Red (blue) symbols are data from unshielded bMEA (shielded cMEA) samples, open (solid) symbols are from optical (electrical) experiments. The dashed lines represent the computer simulated response using the same formalism as employed for Figure 2. Data sets from two of each type of MEA device are shown (thus the two symbol types for each). By combining the optical and electrical stimulation data sets, one sees a common trend, in that for both experiments, the coax outperforms bare

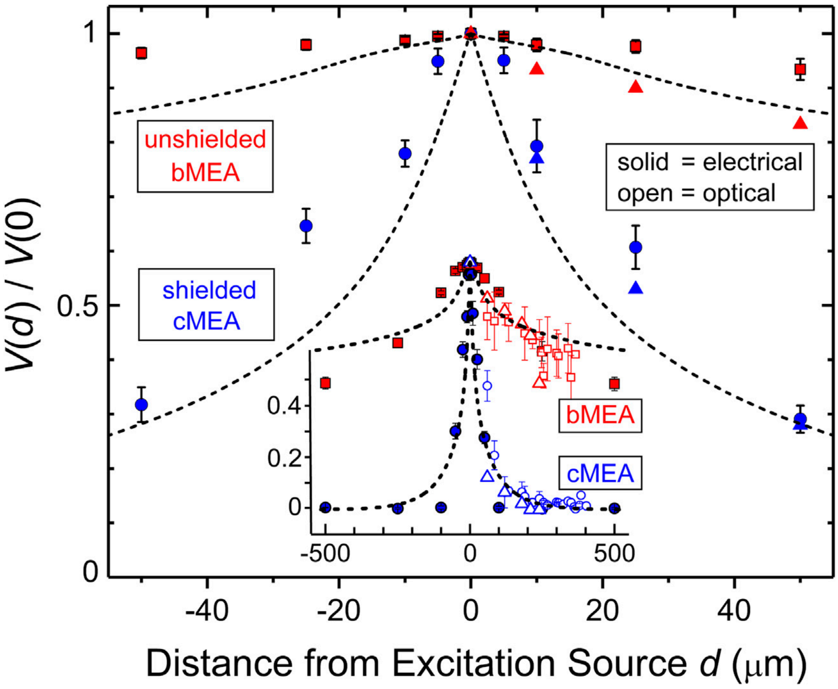

FIGURE 5
Comparison of excitation and device types. Main panel: Effective crosstalk coefficient $V(d)/V_o$ vs. distance *d* from excitation source for electrical excitation experiments, for both unshielded bMEA (red symbols) and shielded cMEA (blue symbols) devices. Inset: Wider range of data, out to d = 500 μm, for both electrical (solid symbols) and optical (open symbols) stimulation. Standard deviations are indicated. Lines are results from simulations of electrical response versus *d*, for both types of devices. Different symbols for same conditions refer to results on different identical devices. Data from five-sweep trials were averaged and mean values plotted with error bars showing ± standard deviation.

electrodes in reducing crosstalk. These results are summarized in Figure 5, where one can see that the effective crosstalk coefficient for the shielded electrodes is significantly lower than that for the bare electrodes for all distances greater than a few micrometers from the source. This corresponds to significantly better suppression or filtering of stray electric fields from sources far from the recording device. In the bare electrode devices, sensing regions within 100 μm of the signal still show a *CT** more than 0.9, which corresponds to very large crosstalk. Such signal overlap might become problematic from the perspective of establishing ground-truth data. One can get a quantitative sense of the effect of local shielding in MEA technology from Figure 5. That is, using 50% crosstalk as a representative gauge, the shielded, coaxial case yields a ~20× improvement in linear spatial resolution (~25 vs. 500 μm for unshielded, Figure 5). This corresponds to a 20^2 ~ 400× improvement for an areal device, e.g., versus a typical MEA.

The main limitation of this study is the selected cell culture used in the optical stimulation experiment. The technical ease in achieving transfection for optogenetic applications, high density to ensure electrode coverage, electrical characteristics, and high survivability of HEK cells make them a suitable choice in a proof-of-concept study. However, there is an obvious difference between HEK cells and neurons such as those typically cited in neural studies. An appropriate next step would be to culture transfected neurons or hippocampal slices. This would further develop the proof-of-concept on two dimensions: 1) showing crosstalk reduction in cells with well-known electrical characteristics and thus able to verify ground-truth measurements, and 2) testing the morphology dynamics of the cell-coaxial electrode interface. Moving from a quasi-2D system, as that found in conventional MEA technology, to a 3D architecture could help prevent cell drift, while at the same time, promote cell engulfment of the inner electrode, which has shown the ability to record subthreshold signals and, coupled with electroporation, intracellular activity by penetrating the cell membrane. We do not, however, anticipate that different cell lines will have a profound effect on the results.

Summary and conclusion

The experiments and simulations presented herein demonstrate the suppression of crosstalk enabled by local shielding through the use of a coaxial electrode architecture. They suggest that, in order to avoid signal overlap in high density multielectrode arrays, a coaxial or similarly locally-shielded architecture could be utilized. While current state-of-the-art electrode arrays (e.g., HD MEAs, CMOS-based multiplexing sensor arrays, neuropixels) achieve high density, crosstalk represents a rate-limiting effect on spatial resolution. Conversely, the present coaxial architecture, in addition to achieving even higher pixel density than presented here (nothing in the fabrication process prevents us from pushing the pixel density into the nanoscale), is able to reduce electrical crosstalk and thus maintain high spatial resolution. Theoretically, the shielded architecture can improve until the thermal noise floor becomes dominant. For nanoscale coaxial arrays, using the Johnson-Nyquist noise equation as a first order approximation, one should still have a practical S/N ratio with a noise floor of tens of microvolts. The device characteristics could be further improved by the changing the impedance through increasing the inner electrode surface area (lowering the shield) or changing the inter-electrode (inner—outer metal annulus) gap.

In the reciprocal paradigm, where electrodes are utilized for evoking cell behavior through electrical stimulation, we have shown the coaxial architecture is advantageous in achieving localized cell engagement. This advantage also extends to isolated optical stimulation. Instead of achieving targeted optical stimulation through beam steering or scanning-based approaches, the shielded electrode facilitates *in situ* optical integration. Future work in device development could also move to an entirely on-device optical component, thus allowing high speed, individually addressable optoelectronic recording and modulation. In addition to alleviating the burden of advanced optical methods, such adoption could reduce dependence on spike sorting, elaborate as algorithms for such have been developed, in analysis of multicell recordings using multielectrode/microelectrode arrays. The locally-shielded array configuration can thus find future utility in connectomic studies of neuronal and other electrogenic cell configurations.

Materials and methods

For devices for optical stimulation experiments, a 10/300 nm Ti/Au layer, thick enough to be optically opaque in the 400–700 nm wavelength range, was sputter deposited onto glass substrates, followed by standard photolithography and wet etching to yield eight 20 μm-diameter openings (in the metal) spaced 300 μm apart. These openings were necessary to facilitate light (from a 472 nm laser), later used to evoke ion currents in HEK cells, to transmit through the glass and up through the cores of the pillars, then onto a specified region, rather than macro-illuminating the sample (to the full diameter of the light cone and thus covering multiple sensing regions). The light cone of the laser was measured to be ~300 μm in diameter in the geometry employed, such that only one region would be illuminated at a time. Nanoimprint lithography (NIL) was then used on 5 μm-thick SU8 photoresist to create a 10 mm^2 area pillar array (containing 2 μm diameter, 5 μm tall pillars at 10 μm hcp pitch) (Rizal et al., 2013) atop this metal film. After depositing a 10/120 nm Ti/Au layer (to serve as the bMEA electrode metal or the cMEA core electrode metal), an 8 × 8 square array of 10 μm diameter sensing areas (each encompassing on average three pillar electrodes to be wired in parallel) at 60 μm pitch was patterned using photolithography, and a subsequent wet chemical etch left 60 individually addressed sensing areas (i.e., excluding the four corners). These sensing areas were aligned with the aforementioned openings in the light-confining metal layer. Atomic layer deposition (ALD) was used to deposit a 225 nm thick aluminum oxide layer covering the entire sample (thus passivating the address lines), and photolithography plus wet etching was used to open up holes over the macroscale pad (pin-out) regions.

For the coaxial structures, an outer metal layer of 120 nm thickness Cr was further deposited (to serve as the coax shield electrode) and photolithography + wet etching was used to pattern the Cr. To expose the inner coax metal as well as to decapitate the pillars to facilitate the transmission of light through the 2 μm core of each pillar in the sensing area, and thus allow for optical stimulation, two processes were used. An SU8 layer was spun on and baked to form a mechanical stabilization layer. Next, a chemical mechanical polisher was used to decapitate the pillars and standard wet chemical etching was used to lower the heights of the Cr and alumina layers around the coax pillar core. A plasma etch process was then used to lower the height (thickness) of the SU8 filler. In order for the HEK cells to be grown and contained within the electrode region, a PDMS liquid-confining well (5 mm diameter, 10 mm height) was attached to the substrate, also using PDMS.

For the electrical stimulation experiments, devices were also fabricated on glass substrates. A NIL process similar to that described above was used to create two SU8 pillar array regions (10 mm^2 areas containing similar 2 μm diameter, 5 μm tall pillars at 10 μm pitch), with the regions separated by 50 mm. Each region comprised a 20 μm diameter sensing area, which contained on average seven individual pillars. The sensing areas were arranged as seven rows of pairs, each row having a different separation distance, from 1,000 to 10 μm. One region contained a bMEA, and the other a cMEA. A metal layer (10/110 nm Ti/Au) was deposited *via* physical vapor deposition and photolithography + wet etching was used to define the 28 individually addressed sensing areas in each of the two pillar regions (56 total areas). Next, a 200 nm thick aluminum oxide layer was deposited on the entire sample using ALD. Holes were etched in the alumina in order to access the Au layer macro pads (where the address lines originating from the sensing areas terminated) corresponding the pin locations on the pre-amplifier board. Finally, a 120 nm Cr layer was deposited using physical vapor deposition. Photolithography was used to pattern the cMEA region, so as to leave Cr covering 28 sensing areas and to have subsequent address lines coming from each area. To expose the cMEA inner metal, an anisotropic lithographic process was combined with subsequent wet etching in order to lower the heights of the Cr and alumina layers. The resulting outer metal to inner metal height ratio was ~0.6. Two plastic wells fabricated using a 3D printer were attached with PDMS to contain an electrolyte buffer solution (aCSF) within the bare and coaxial electrode regions.

In preparation for experiments, the bMEA and cMEA regions were characterized by measuring DC resistance (in air) between the individual electrodes for the bare electrode region and between all terminals (inner and outer electrode as well as inter-electrode) for the coaxial region. Typical resistances were in the GΩ range, indicating no shorts in the circuit. Capacitance of the coaxial samples was also measured and those results checked against the calculated values according to the equation for a coaxial capacitor: $c = 2\pi l\varepsilon \ln(r_{outer}/r_{inner})$. Measured values were within 10% of the calculated values, with differences attributed, in part, to stray capacitance originating from the unshielded portions of the coaxes. Additionally, the devices needed to be sterilized prior to cell culture. This was done by placing them in a sterilization packet: a bag which contains a scaffold that expands to let steam pass to its inner contents during the sterilizing process and then contracts during a cooling phase to insulate the inside from any foreign contaminates. The packet was placed inside a steam autoclave and a standard dry process was run at 100°C for 30 min with a 30 min cool down phase). After the devices were autoclaved, they were placed inside a sterile hood until the HEK cells were ready to be plated (placed on the devices).

As mentioned earlier, optically-evoked field potentials were detected using HEK-293 transfected with the blue-light sensitive channelrhodopsin protein ChR2(H134R) (Lorentz, 1896). Transfection and culture processes, described in previous work (Naughton et al., 2016), were used. To ensure cell adherence to the bare electrode and coaxial structures contained in two separate PDMS wells, the two devices were incubated in a sterile solution of 0.01% poly-l-lysine overnight at 37°C 5% CO_2. HEK-ChR2 cells were trypsinized from cell culture dishes and recovered by centrifugation at 595 g for 6 min at 4°C. The cells were resuspended in DMEM 10% FBS media containing 250 μg/ml G418 at a density of ~ 10^6 cells/ml. A 0.1 ml aliquot of cells was added to one well of a coaxial device and cultured overnight at 37°C 5% CO_2. The seeding density of cells almost completely covered both the bare electrode and coaxial structures within 24–48 h of subsequent cell culture and adherence. The color of the medium was carefully monitored to ensure cell health. From previous experiments, we noticed that dark yellow meant the medium needed to be changed and that there was cell overgrowth. Since we selected for cells of successful transfection, we wanted the entire pillar region to be covered in HEK293-ChR2 cells to ensure every sensing region was covered and therefore was a potential stimulation zone. Once it was evident there was cell overgrowth (yellow colored medium), the medium was aspirated and replaced with fresh medium. Immediately after this, the devices were covered in aluminum foil (to avoid exposure to stimulating light) and the devices were brought to the Multichannel Systems amplifier for measurement. A 473 nm DPSS laser (Model BL473-100FC ADR-700A, Shanghai Laser and Optics Century Co., Ltd.) coupled to a multimode 200 μm diameter optical fiber (0.39 NA, Thor Labs) with a spot size of ~350 μm was used for photo stimulation. Prior to placing the devices in the amplifier system, the laser light was characterized using the same process described in previous work (Naughton et al., 2016). The maximum intensity was found to be 20 mW/cm^2 and this level was used throughout the experiment.

The bMEA was uncovered, placed in the amplifier system, and the macropads were aligned with the pins. A Ag/Cl pellet was placed into the electrolyte buffer solution to act as a ground, since no other ground was present in the area. All 60 channels were monitored simultaneously to ensure the baseline voltage reached a steady state for each sensing region. Initially, the data acquisition program was run continuously and the laser was aligned for topside illumination. The laser was manually actuated and the illumination area was moved throughout the entire sensing region. This was done to ensure a positive response from the cells. Once cell response due to optical stimulation was visually confirmed, the laser was adjusted and attached to a micromanipulator for backside illumination. The data acquisition program was changed to a trigger capture program using a TTL signal (Stimulus Generator STG4002, Multichannel Systems) with a 0.5 s square wave pulse. The laser was then moved to several sites below the area containing the individual sensing regions and a five sweep trial was performed at each spot (with averages displayed in Figure 4 and peak averages ± standard deviations in Figure 5). All 60 channels were monitored throughout each trial and the approximate laser location was noted prior to stimulation. Throughout the experiment, deflections could be seen in all illuminated working channels. For the bMEA region, a Ag/Cl pellet was again placed into the electrolyte buffer solution to act as a ground, since no other ground was present in the area. A pulse generator program was used to send in a train of 100 μV, 500 ms square-wave pulses spaced 1 s apart.

Data availability statement

The original contributions presented in the study are included in the article. Further inquiries can be directed to the corresponding author.

Author contributions

MN conceived of the project. JN, JC, MB, and MN designed the experiments. JN and SS fabricated the arrays. TC and JN prepared the HEK-293 cells. JN performed the device simulations. JN, JV, JC, and MN performed the experiments. TD and KK did analysis and simulation of the capacitive response. All authors contributed to the theoretical and experimental analysis of the results. JN, MB, JC, and MN wrote the paper. Correspondence and requests for materials should be addressed to MN (Email: naughton@bc.edu).

Funding

Funding for these studies included NIH Grants MH110907 and MH109545 to JC.

Conflict of interest

Publisher's note

References

Buccino, A. P., Hurwitz, C. L., Garcia, S., Magland, J., Siegle, J. H., Hurwitz, R., et al. (2020). SpikeInterface, a unified framework for spike sorting. *Elife* 9, e61834. doi:10.7554/eLife.61834

Chai, X., Li, L., Wu, K., Zhou, C., Cao, P., and Ren, Q. (2008). C-sight visual prostheses for the blind. *IEEE Eng. Med. Biol. Mag.* 27, 20–28. doi:10.1109/MEMB.2008.923959

Debanne, D., Inglebert, Y., and Russier, M. (2019). Plasticity of intrinsic neuronal excitability. *Curr. Opin. Neurobiol.* 54, 73–82. doi:10.1016/j.conb.2018.09.001

Einevoll, G. T., Franke, F., Hagen, E., Pouzat, C., and Harris, K. D. (2012). Towards reliable spike-train recordings from thousands of neurons with multielectrodes. *Curr. Opin. Neurobiol.* 22, 11–17. doi:10.1016/j.conb.2011.10.001

Ekanadham, C., Tranchina, D., and Simoncelli, E. P. (2014). A unified framework and method for automatic neural spike identification. *J. Neurosci. Methods* 222, 47–55. doi:10.1016/j.jneumeth.2013.10.001

Gerstein, G. L., and Clark, W. A. (1964). Simultaneous studies of firing patterns in several neurons. *Science* 143, 1325–1327. doi:10.1126/science.143.3612.1325

Hall, N. J., Herzfeld, D. J., and Lisberger, S. G. (2021). Evaluation and resolution of many challenges of neural spike sorting: A new sorter. *J. Neurophysiology* 126, 2065–2090. doi:10.1152/jn.00047.2021

Harris, K. D., Henze, D. A., Csicsvari, J., Hirase, H., and Buzsáki, G. (2000). Accuracy of tetrode spike separation as determined by simultaneous intracellular and extracellular measurements. *J. Neurophysiol.* 84, 401–414. doi:10.1152/jn.2000.84.1.401

Heathcote, R. D., and Sargent, P. B. (1987). Growth and morphogenesis of an autonomic ganglion. I. Matching neurons with target. *J. Neurosci.* 7, 2493–2501.

Hilgen, G., Sorbaro, M., Pirmoradian, S., Muthmann, J. O., Kepiro, I. E., Ullo, S., et al. (2017). Unsupervised spike sorting for large-scale, high-density multielectrode arrays. *Cell Rep.* 18, 2521–2532. doi:10.1016/j.celrep.2017.02.038

Kadir, S. N., Goodman, D. F., and Harris, K. D. (2014). High-dimensional cluster analysis with the masked EM algorithm. *Neural Comput.* 26, 2379–2394. doi:10.1162/NECO_a_00661

Kaur, M., Gupta, N., Kumar, S., Raj, B., and Singh, A. K. (2021). Comparative radio-frequency and crosstalk analysis of carbon-based nano-interconnects. *IET Circuits Devices &amp. Syst.* 15, 493–503. doi:10.1049/cds2.12044

Lewicki, M. S. (1998). A review of methods for spike sorting: The detection and classification of neural action potentials. *Netw. Comput. Neural Syst.* 9, R53–R78. doi:10.1088/0954-898x_9_4_001

Lorentz, H. A. (1896). Het theorema van Poynting over energie in het elektromagnetisch veld en een paar algemeene stellingen over de voorplanting van het licht. *Vers. Konig. Akad. Wetensch.* 4, 176–187.

Magland, J., Jun, J. J., Lovero, E., Morley, A. J., Hurwitz, C. L., Buccino, A. P., et al. (2020). SpikeForest, reproducible web-facing ground-truth validation of automated neural spike sorters. *Elife* 9, e55167. doi:10.7554/eLife.55167

Miccoli, B., Mora Lopez, C., Goikoetxea, E., Putzeys, J., Sekeri, M., Krylychkina, O., et al. (2019). High-density electrical recording and impedance imaging with a multi-modal CMOS multielectrode array chip. *Front. Neurosci.* 13, 641. doi:10.3389/fnins.2019.00641

Moghaddam, G. K., Wilke, R. G., Dokos, S., Suaning, G. J., and Lovell, N. H. (2011). "Electrode design to optimize ganglion cell activation in a retinal neuroprosthesis: A modeling study," in 2011 5th International IEEE/EMBS Conference on Neural Engineering, Cancun, Mexico, 27 April 2011 - 01 May, 542–545. doi:10.1109/NER.2011.5910605

Multichannel Systems (2021). *Multichannel systems MCS GmbH*. Reutlingen, Germany: Harvard Bioscience, Inc. Available at: http://www.multichannelsystems.com.

Nadasdy, Z., Csicsvari, J., Penttonen, M., Hetke, J., Wise, K., and Buzsaki, G. (1998). "Extracellular recording and analysis of neuronal activity: From single cells to ensembles," in *Neuronal ensembles: Strategies for recording and decoding*. Editors H. B. Eichenbaum and J. L. Davis (New York: Wiley-Liss), 17–55.

Naughton, J. R., Connolly, T., Varela, J. A., Lundberg, J., Burns, M. J., Chiles, T. C., et al. (2016). Shielded coaxial optrode arrays for neurophysiology. *Front. Neurosci.* 10, 252. doi:10.3389/fnins.2016.00252

Nelson, M. J., Valtcheva, S., and Venance, L. (2017). Magnitude and behavior of cross-talk effects in multichannel electrophysiology experiments. *J. Neurophysiol.* 118, 574–594. doi:10.1152/jn.00877.2016

Person, K. (1901). On lines and planes of closest fit to system of points in space. *Phil. Mag.* 2, 559–572.

Prentice, J. S., Homann, J., Simmons, K. D., Tkacik, G., Balasubramanian, V., and Nelson, P. C. (2011). Fast, scalable, Bayesian spike identification for multielectrode arrays. *PloS One* 6, e19884. doi:10.1371/journal.pone.0019884

Quiroga, R. Q., Reddy, L., Koch, C., and Fried, I. (2007). Decoding visual inputs from multiple neurons in the human temporal lobe. *J. Neurophysiol.* 98, 1997–2007. doi:10.1152/jn.00125.2007

Quiroga, R. Q. (2013). Spike sorting. *Scholarpedia* 2, 3583. doi:10.4249/scholarpedia.3583

Rey, H. G., Pedreira, C., and Quiroga, R. Q. (2015). Past, present and future of spike sorting techniques. *Brain Res. Bull.* 119, 106–117. doi:10.1016/j.brainresbull.2015.04.007

Rizal, B., Archibald, M. M., Connolly, T., Shepard, S., Burns, M. J., Chiles, T. C., et al. (2013). Nanocoax-based electrochemical sensor. *Anal. Chem.* 85, 10040–10044. doi:10.1021/ac402441x

Shoham, S., Fellows, M. R., and Normann, R. A. (2003). Robust, automatic spike sorting using mixtures of multivariate t-distributions. *J. Neurosci. Methods* 127, 111–122. doi:10.1016/s0165-0270(03)00120-1

Swindale, N. V., and Spacek, M. A. (2014). Spike sorting for polytrodes: A divide and conquer approach. *Front. Syst. Neurosci.* 8, 6. doi:10.3389/fnsys.2014.00006

Ventura, V., and Gerkin, R. C. (2012). Accurately estimating neuronal correlation requires a new spike-sorting paradigm. *Proc. Natl. Acad. Sci. U. S. A.* 10919, 7230–7235. doi:10.1073/pnas.1115236109

Wilke, R. G. H., Moghadam, G. K., Lovell, N. H., Suaning, G. J., and Dokos, S. (2011). Electric crosstalk impairs spatial resolution of multielectrode arrays in retinal implants. *J. Neural Eng.* 8, 046016–046027. doi:10.1088/1741-2560/8/4/046016

Wong, Y. T., Chen, S. C., Seo, J. M., Morley, J. W., Lovell, N. H., and Suaning, G. J. (2009). Focal activation of the feline retina via a suprachoroidal electrode array. *Vis. Res.* 49, 825–833. doi:10.1016/j.visres.2009.02.018

Zhang, F., Wang, L. P., Brauner, M., Liewald, J. F., Kay, K., Watzke, N., et al. (2007). Multimodal fast optical interrogation of neural circuitry. *Nature* 446, 633–639. doi:10.1038/nature05744

frontiers | Frontiers in Nanotechnology

TYPE Perspective
PUBLISHED 04 October 2022
DOI 10.3389/fnano.2022.999923

OPEN ACCESS

EDITED BY
Jan M. Macak,
University of Pardubice, Czechia

REVIEWED BY
Nathan Ryan Bruce Boase,
Queensland University of Technology,
Australia

*CORRESPONDENCE
Jonathan M. Zuidema,
jonathan.zuidema@marionegri.it

SPECIALTY SECTION
This article was submitted to
Nanomaterials,
a section of the journal
Frontiers in Nanotechnology

RECEIVED 21 July 2022
ACCEPTED 15 September 2022
PUBLISHED 04 October 2022

CITATION
Morillas-Becerill L, De Cola L and
Zuidema JM (2022), Inorganic
nanoparticle empowered biomaterial
hybrids: Engineered payload release.
Front. Nanotechnol. 4:999923.
doi: 10.3389/fnano.2022.999923

Inorganic nanoparticle empowered biomaterial hybrids: Engineered payload release

Lucía Morillas-Becerill[1], Luisa De Cola[1,2] and
Jonathan M. Zuidema[1,2]*

[1]Dipartimento di Scienze Farmaceutiche, Universitá Degli Studi di Milano, Milan, Italy, [2]Department of Molecular Chemistry and Pharmacology, Istituto di Ricerche Farmacologiche Mario Negri IRCCS, Milan, Italy

There are many challenges in delivering active pharmaceutical ingredients from biomaterials, including retention of payload activity, accurate temporal release, and precise spatial administration, to name only a few. With our constantly increasing knowledge of biology and physiology, pathologies that require therapeutic interventions are becoming more understood. While the desired temporal and spatial administration of a therapy might be theorized, the ability to deliver an active therapeutic in a precise location during a specific time frame is often challenging. This has led researchers to develop hybrid biomaterials containing inorganic nanoparticles in order to combine the advantages of both inorganics and organics in payload delivery applications. Organic materials have many beneficial properties, including the ability to form networks and matrices to create three-dimensional structures from the nanometer to centimeter scale, biodegradability, the versatility to use both synthetic and natural precursors, and ease of chemical modifications, while inorganic materials offer highly controllable nanoscale features, can entrap and protect therapeutics, and have degradation properties that can be tightly regulated. Here in, we discuss the current state-of-the-art in active pharmaceutical ingredient delivery from biomaterial hybrids, demonstrate the added levels of control that these hybrid biomaterials offer, and give our perspective on future innovations in the field.

KEYWORDS

hybrid biomaterials, inorganic nanoparticles, drug delivery, hydrogels, polymer scaffolds, silica nanoparticles, tissue engineering

Introduction

Innovations in biomaterial design have accelerated greatly over the last decades, expanding from materials that have limited interactions with the body to current designs where natural, synthetic, composite, living, stimuli responsive and/or actuable biomaterials not only interact with cells and tissues but can also instruct specific outcomes post implantation (Dos Santos et al., 2020; Lavrador et al., 2021). Implanted organic biomaterials are most commonly in the form of hydrogels or polymer scaffolds, and can either be injected into tissues or preformed structures can be surgically placed into an exposed area (Pawelec et al., 2018; Babu et al., 2021). One important property engineered into biomaterials is the capability to release active pharmaceutical ingredients (APIs) for applications ranging from cancer therapeutics to nervous system repair (Fadia et al., 2020; Yang et al., 2020; Ciciriello et al., 2021). Releasing APIs from implantable biomaterials has several advantages, including on site release with tunable kinetics, administration of multiple APIs from the same biomaterial, and actuable payload release (Dumont et al., 2015; Rambhia and Ma, 2015; Gayet et al., 2020). As a way to more precisely regulate API release kinetics from biomaterials, inorganic nanoparticles have begun to be incorporated into their structure to form nanoparticle-laden composites. These composites allow for the advantages of organic biomaterials, formation of 3D architectures, biodegradability, cellular adhesion, and diverse material selections, to be combined with the advantages of inorganic nanoparticles, including designed degradability, tunable nanoscale sizes, the capability to include mesopores into the nanoparticles, and, importantly, entrapment and protection of APIs.

Inorganic nanoparticles used in biomedical applications are derived from many different materials, including gold, silver, iron oxide, clay, silicon, and silica (Park et al., 2009; Mousa et al., 2018; Dutz et al., 2020; Kankala et al., 2020; Mitchell et al., 2021; Morillas-Becerril et al., 2021). Gold nanoparticles are inert and nontoxic, can be synthesized with diameters ranging from 1–150 nm, and offer photophysical properties as well as the ability for drugs to be incorporated onto their surface (Ghosh et al., 2008). Silver nanoparticles are readily fabricated below 100 nm, and show the most promise in biomedical applications as anti-bacterial and anti-fungals (Nene et al., 2021). Super paramagnetic iron oxide nanoparticles can be fabricated in a range of sizes from >10 nm to more than 200 nm and their magnetic properties allow them to be contrasting agents in biomedical imaging (Dadfar et al., 2019). It is difficult to make these three classes of nanoparticles porous, limiting the potential to trap APIs within these particles. Clay nanoparticles are layered silicate structures that crystalize into nanoparticles, and their interactions with biologics make them intriguing carriers for drug delivery, but their variability and solubility may be problematic (Dawson and Oreffo, 2013). Silicon nanoparticles, especially porous silicon nanoparticles (pSiNPs), are most commonly created through electrochemical etching of crystalline silicon in sizes ranging from ~70 nm to multiple micrometers, and their large pore volume, biodegradability, and ease of surface functionalization make them excellent API carriers (Canham, 1995; Li et al., 2018). Fabrication of these particles predominately requires hydrofluoric acid and there is variability in their size distribution. Mesoporous silica nanoparticles (MSNs) are most commonly synthesized through the surfactant templating approach, and their large pore volume, tunable sizes and shapes, and ease of surface functionalization give them exceptional properties for API delivery (Manzano and Vallet-Regi, 2020). However, controlling their biodegradation properties can be difficult. While the main research thrust in particle development for applications in health has been towards nanomedicine, the unique properties of inorganic nanoparticles have begun to lead researchers to incorporate them into biomaterials to create multifunctional hybrid materials with a greater level of control of API release.

Inorganic nanoparticles incorporated into three-dimensional biomaterials

There are many different strategies that have been used to incorporate inorganic nanoparticles into biomaterials, and these procedures are selected based on several factors, including the desired material properties, the fabrication processes of both the inorganic nanoparticles and the biomaterial, and the desired application. Hydrogels, polymer networks that have the ability to retain water and form a swollen gel, are used extensively as biomaterials due to their biocompatibility, resemblance to native tissues in mechanical properties and water content, ease of fabrication, injectability, and their versatility to be readily modified to induce cell adhesion and growth (Kim et al., 1992; Mandal et al., 2020). Inorganic nanoparticles have been incorporated into hydrogels through three general design principles: 1) micro or nano-gels that stabilize nanoparticles, 2) nanoparticles non-covalently incorporated into the hydrogel network, and 3) nanoparticles covalently crosslinked in a hydrogel matrix (Thoniyot et al., 2015). One straightforward fabrication approach is the formation of a hydrogel in a nanoparticle suspension that non-covalently incorporates nanoparticles into the hydrogel structure (Sershen et al., 2002). Nanoparticles have also been incorporated into hydrogels after gelation, either through addition of nanoparticles during hydrogel swelling or through various centrifugation steps with a preformed hydrogel (Pardo-Yissar et al., 2001; Jones and Lyon, 2003). Another approach loads nanoparticle precursors into crosslinked hydrogels with the addition of reducing agents forming nanoparticles throughout the hydrogel network (Wang et al., 2004). Nanoparticles themselves have been used as crosslinkers for hydrogels, incorporating them directly into the hydrogel network to impact the hydrogel mechanical properties and gelation rate (Skelton et al., 2013; Rose et al., 2014; Fiorini et al., 2016). By applying these techniques, inorganic nanoparticles can be incorporated into hydrogels in order to capitalize on the advantages of both material types. This has allowed researchers to create hydrogels with unique characteristics, including self-healing (Wu et al., 2020), photothermal activity (Sershen et al., 2005), magnetically induced hydrogel disruption (Qin et al., 2009), anti-bacterial effects (Urzedo et al., 2020), and

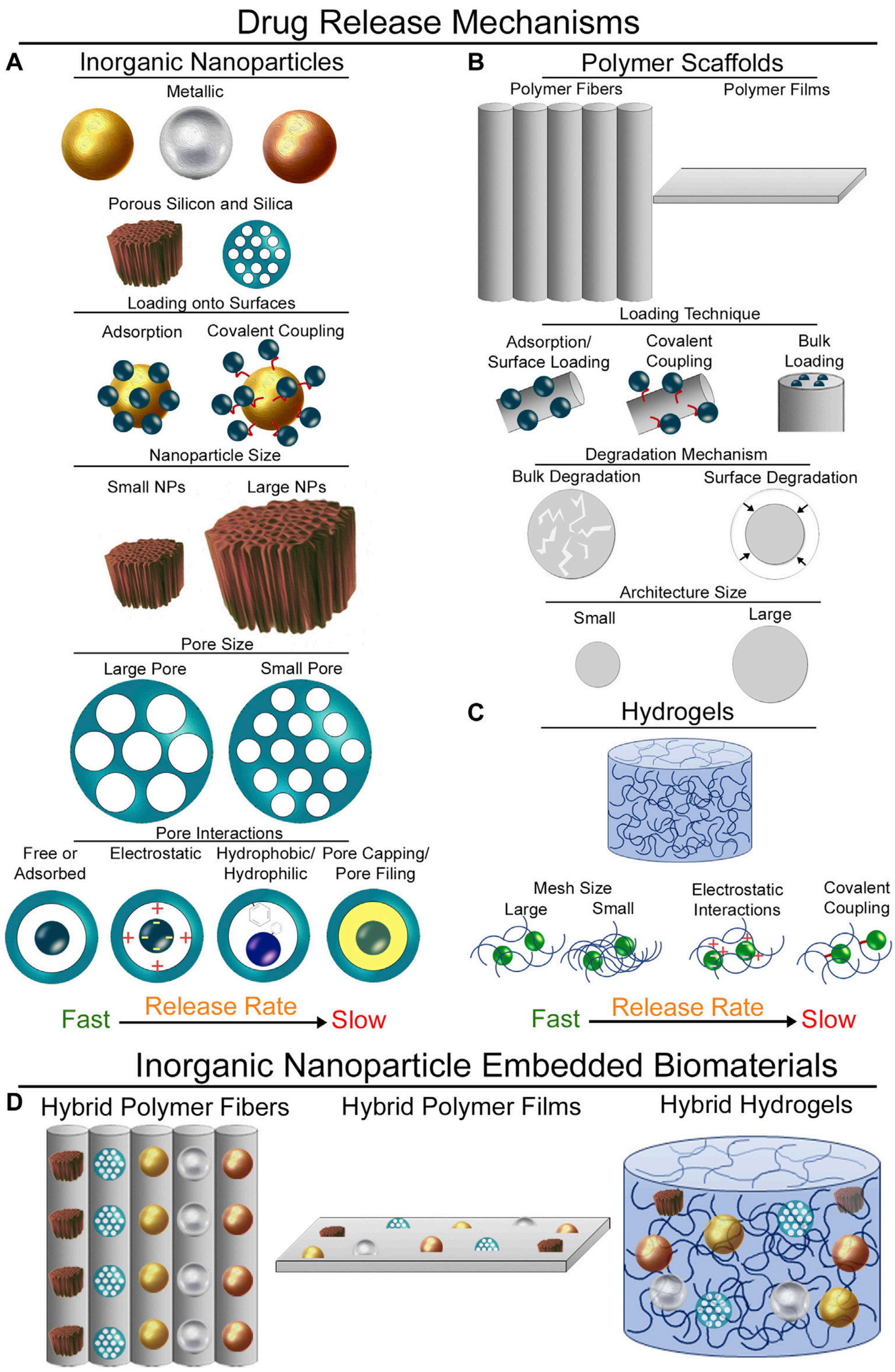

FIGURE 1
Mechanisms of payload release. **(A)** Mechanisms of drug release from different inorganic nanoparticles. Surface loading techniques, nanoparticle size, pore size, and pore interactions all impact the release rate of APIs from inorganic nanoparticles. **(B)** API release from polymer scaffolds. Loading techniques, degradation mechanisms of the polymer, and architecture size of the polymer structures impact payload release rate. **(C)** Release of APIs from hydrogels is impacted by hydrogel mesh size, electrostatic and other affinity-based interactions, or the ability to covalently couple APIs into the hydrogel network. **(D)** Inorganic nanoparticles incorporated into biomaterials. These drug release mechanisms can all be combined by incorporating inorganic nanoparticles into biomaterial scaffolds.

electrical conductivity (Koppes A.N et al., 2016), demonstrating the various functions that these materials may possess.

Biodegradable polymers represent a class of biomaterial scaffolds that are used extensively in tissue engineering (Zhang and King, 2020). They can be fabricated into a variety of structures, including films (Lyu et al., 2019), tissue engineering scaffolds (Daly et al., 2012; Shahriari et al., 2017; Pawelec et al., 2018), microneedles (Sullivan et al., 2010), and micro- and nano-fibers (Venugopal and Ramakrishna, 2005). Polymer films are readily fabricated via casting or spin coating, and porosity can be incorporated into scaffolds through particulate leaching from the polymer films (Suntornnond et al., 2015). Microneedles are commonly fabricated through creation of a master mold followed by filling molds with polymers of interest (Park et al., 2005). Micro- and nano-fibers are made predominately *via* electrospinning, but other techniques, including blow spinning, centrifugal or force spinning, or thermal drawing, have also been applied to make these structures (Coffer et al., 2005; Padron et al., 2013; Behrens et al., 2014; Canales et al., 2015; Koppes R.A et al., 2016; Dos Santos et al., 2020; Rihova et al., 2021). Because most of these polymer structures are made from a polymer melt or from polymers dissolved in an organic solvent, inorganic nanoparticles can be readily mixed into the melt or polymer solution prior to creation of the 3D structure and incorporated throughout the formed architectures (Fan et al., 2009; Kashanian et al., 2010; Kim et al., 2010; Johnson et al., 2019; Yadid et al., 2019). Inorganic nanoparticles can also be coupled onto the surface of these materials, creating polymer structures that have surfaces composed of inorganic nanoparticles (Demir et al., 2018; Funnell et al., 2021). One other approach is pressing inorganic particles into polymer structures via heating of the polymers near their melt temperatures, pressing dried particles onto the structures, and then cooling the polymers back below their melt temperature (Irani et al., 2015; Bodiford et al., 2018). 3D printing of polymer solutions and melts containing inorganic nanoparticles is another more recent advance in this field, allowing for tightly controlled three-dimensional architectures with nanoparticles embedded throughout (dos Santos et al., 2021). Using these approaches, inorganic nanoparticles are incorporated into biomaterials to capitalize on the advantageous properties of both materials.

Drug delivery from inorganic nanoparticles

Inorganic nanoparticles are being extensively explored in nanomedicine due to their capability to load APIs and target them to tissues of interest. There are several strategies that can be used to incorporate payloads within metal nanoparticles, including covalent attachment of the API to the surface of the nanoparticles (Gibson et al., 2007) (Figure 1A). There are also non-covalent interactions that have been applied by modifying the surface of gold nanoparticles to create electrostatic affinity towards nucleic acids and anionic proteins (Sandhu et al., 2002). Modifying iron oxide NP surfaces (Hola et al., 2015) allows drugs to be loaded into the interspace of nanoparticle clusters (Bakandritsos et al., 2012) or linked to an activated nanoparticle surface (Magro et al., 2014). Porous inorganic nanoparticles are especially attractive for applications in API delivery because of the large pore volume they offer to load APIs inside the structure of the nanoparticle. Pores allow for an added control of drug release kinetics, where pore size, surface chemistry, and pore capping or filling strategies can be used to tailor API release from these structures (Figure 1A). pSiNPs and MSNs have been studied extensively as API carriers because of these properties (Anglin et al., 2008; Slowing et al., 2008). APIs can be loaded using a variety of techniques, including covalent attachment to the surface (Secret et al., 2013; Zhang et al., 2019), affinity adsorption (Liu et al., 2013; Kaasalainen et al., 2015; Kwon et al., 2017; Zilony et al., 2017), oxidation trapping (Fry et al., 2014; Kim et al., 2016), calcium and magnesium silicate trapping (Kang et al., 2016; Wang et al., 2018), during synthesis (Prasetyanto et al., 2016), post-synthesis adsorption (Wang et al., 2014), adsorption and subsequent rapid solvent evaporation (Mellaerts et al., 2008), and pore-capping following drug incorporation (Lai et al., 2003; Giri et al., 2005; Aznar et al., 2009; Zhao et al., 2009).

Polymer scaffolds in drug delivery

Polymer scaffolds, especially those composed of polycaprolactone, polylactic acid, polyglycolide, and copolymers such as poly (lactic-*co*-glycolic acid), have been used extensively in tissue engineering due to their biocompatibility, biodegradability, and ease of manufacturing (Liu and Ma, 2004; Place et al., 2009). These advantageous properties have led researchers to develop techniques to release APIs from polymers. The most commonly employed strategy is to blend the polymer and drug together either in solution or in a polymer melt prior to formation of the scaffold. Drug release is governed by several factors, including polymer degradation (bulk vs. surface) and the scale of the polymer architecture (Figure 1B) (Xu et al., 2017). While this method works well for hydrophobic APIs with commonly employed synthetic polymers, blending does not work well for hydrophilic APIs. Soak loading is one technique that can be used to overcome this limitation (Cho et al., 2015), but this technique can lead to burst release of the drug from the surface. In order to extend the release timeframe, APIs have been covalently linked to the polymer surface (Seifu and Nath, 2019). Fabrication specific techniques have also been employed to incorporate APIs into polymer scaffolds. Specifically, electrospinning allows for the formation of core-

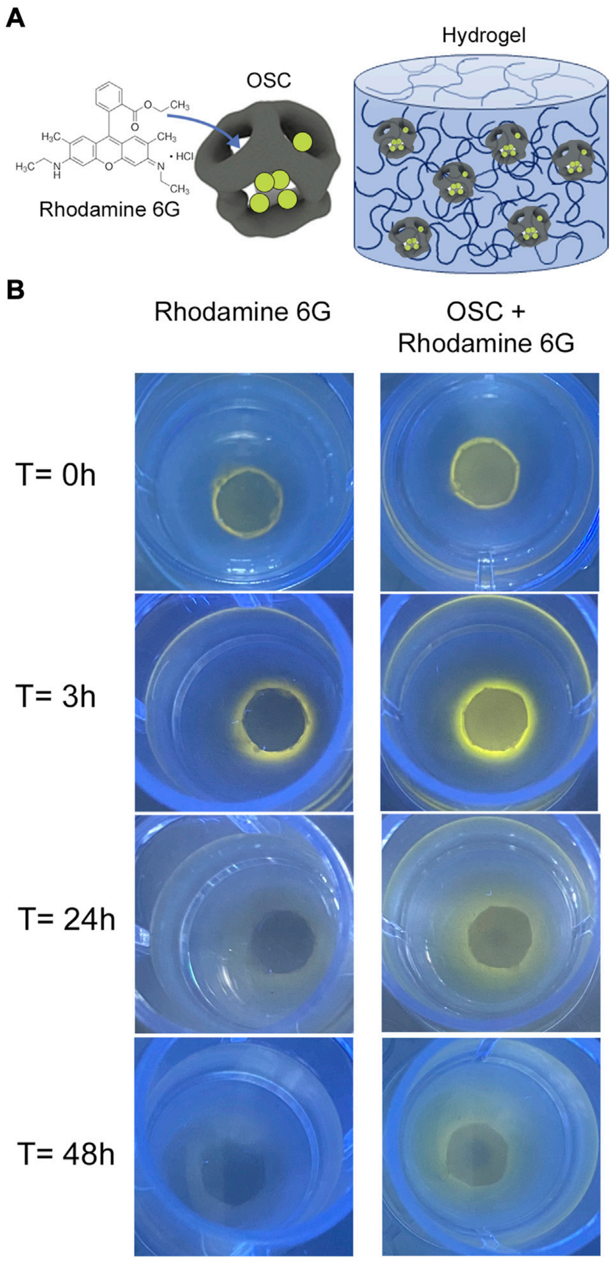

FIGURE 2
Rhodamine 6G release from OSC incorporated polyacrylamide hydrogels. **(A)** Schematic depicting hydrogel design. Rhodamine 6G was loaded into OSCs, following by physical entrapment in UV crosslinked polyacrylamide hydrogels. **(B)** Release of rhodamine 6G from hydrogels. Rhodamine 6G control hydrogels are compared to rhodamine 6G-loaded OSC incorporated hydrogels. At t = 0, rhodamine 6G control and OSC hydrogels are crosslinked into the center of the molds. At t = 3 h, the release of rhodamine 6G from control hydrogels is obvious as the dye can diffuse out of the gel through the network mesh and as the gel swells. In the OSC-rhodamine hydrogels, very little diffusion is evident. 24 h after crosslinking control hydrogels have very low amounts of rhodamine visible, while the OSC-rhodamine hydrogels still have rhodamine in the center and around the crosslinked hydrogel. At 48 h, there is nearly no rhodamine visible in the control hydrogels, while rhodamine 6G is still visible in the center the OSC-rhodamine crosslinked hydrogels and throughout the hydrogel mold.

sheath fibers, where the inner core can be hydrophilic and the outer polymer sheath can be formed to be hydrophobic (Sill and von Recum, 2008; Hu et al., 2014), and centrifugal spinning has been used to incorporate water soluble vitamins into fibers (Rihova et al., 2022). However, hydrophilic APIs may not be homogenously distributed throughout the polymer structures and fabrication techniques need to be optimized for each API type.

Hydrogels in drug delivery

Hydrogels offer many beneficial properties in API delivery, providing spatial control of API release in their site of implantation, temporal control through polymer network interactions, and protection of APIs from the native tissue environment (Li and Mooney, 2016). The most straightforward approach for incorporation of APIs is through mixing the payload with the hydrogel precursors prior to gel formation (Leach and Schmidt, 2005). The mesh size plays an important role in API release rates with this technique (Figure 1C) (Amsden, 1998). Hydrogels have also been designed to electrostatically interact with charged APIs to modulate their release (Tabata and Ikada, 1998). Other affinity-based mechanisms have been exploited to control API release (Delplace et al., 2016) including covalent attachment of aptamers into hydrogel networks (Soontornworajit et al., 2010), extracellular matrix-protein interactions (Sakiyama-Elbert and Hubbell, 2000), protein-protein interactions (Pakulska et al., 2013), and co-polymers containing hydrophobic domains (Thatiparti et al., 2010). Covalently binding of desired payloads to the hydrogel backbone represents a highly stable incorporation strategy that can greatly extend API release (Mann et al., 2001). The difficulty in loading hydrophobic drugs, the relatively quick release of hydrophilic APIs, and the problems associated with covalently crosslinking APIs into hydrogel networks leave areas for further innovation in the design of drug eluting hydrogels.

Payload delivery from hybrid biomaterials

Hybrid biomaterials offer diverse mechanisms to control API release kinetics. These biomaterials create complex drug interactions with the implanted scaffolds, first through the API loading strategy employed, then the choice of material and architecture, and finally through affinities to the biomaterial network. Polymeric nano-and micro-fibers have been created with drug loaded inorganic nanoparticles embedded throughout (Figure 1D) (Elsherbini and Sabra, 2022). API loaded MSNs have been used extensively to create these hybrid materials using electrospinning techniques (Qiu et al., 2013; Zhou et al., 2015; Lim et al., 2016; Yuan et al., 2016; Chen et al., 2019; Lian et al., 2019; Wang et al., 2019; Sun et al., 2020; Mohebian et al., 2021; Xu et al., 2021; Batista et al., 2022). This approach can be used to extend release of loaded APIs since the nanoparticles act to protect their payloads. They also provide a versatile platform, where different classes of APIs can be loaded into the MSNs while the fabrication procedure of the hybrid fibers remains largely unchanged. Importantly, APIs can be incorporated both throughout the polymer network and within loaded nanoparticles to have two different drug release profiles (Yuan et al., 2016; Samadzadeh et al., 2021; Xu et al., 2021). This allows for quick release of the incorporated API followed by a long-term sustained release due to loading into the nanoparticles. Other nanoparticles have also been used in these strategies, including amorphous calcium phosphate (Fu et al., 2016), graphene oxide (Rezaei et al., 2021), and zinc oxide (Fazli et al., 2016). Further control of drug release from these scaffolds can be added by incorporating magnetic nanoparticles into scaffolds (Kim et al., 2013). Through application of an alternating magnetic field, magnetic nanoparticles in the scaffolds generate heat to induce swelling of the polymers and release incorporated payloads. Similar strategies can be used to incorporate pSiNPs into fibrous scaffolds. Spray nebulization techniques have been used to create nanofibrous scaffolds containing API loaded porous silicon nanoparticles (Zuidema et al., 2018; Zuidema et al., 2020a; Zuidema et al., 2020b). These platforms are highly versatile, and by simply changing the approach to load APIs into nanoparticles, the same fabrication technique was used for prolonged release of active proteins, nucleic acid-based devices and aptamers, and hydrophilic APIs. API loaded porous silicon particles have also been incorporated into poly (ε-caprolactone) films to slow release kinetics (Irani et al., 2015; Bodiford et al., 2018).

There are several mechanisms with which to control drug release from hybrid hydrogels, and the most elementary is through passive diffusion out of the nanoparticle and through the hydrogel matrix. Silica nanoparticles loaded with ibuprofen (Zhao et al., 2014), antibiotics (Alvarez et al., 2014), and proteins (Lee et al., 2013; Fiorini et al., 2016) have been embedded into hydrogels to prolong their release compared to loading the APIs directly into a hydrogel. We demonstrate this concept here to provide an obvious visual to show the power of these hybrid materials. Rhodamine 6G was loaded into poly (ethylene glycol) conjugated, cage-like organosilica nanoparticles (OSCs) following a previously reported two-step bottom-up protocol (Supplementary Material) (Talamini et al., 2021). The OSCs have a relatively small diameter (44 ± 4 nm, Supplementary Figure S1A), that allows them to be uniformly distributed throughout the precursor solution without forming aggregates. Their cage-like structure provides space for API loading while protecting the payload inside the cage. While these properties are beneficial for applications in nanomedicine, they can also be employed to control payload release from hybrid materials. OSCs were then non-covalently incorporated into a polyacrylamide hydrogel (Figure 2A). As a control, free rhodamine 6G was dispersed in the hydrogel precursor solution prior to gelation. Qualitative release of rhodamine 6G was then visualized over time from the hydrogels (Figure 2B). Rhodamine 6G hydrogels were placed in the center of a hydrogel mold so visualization of the release could be monitored. After only 3 h of incubation in PBS, it is apparent that the control hydrogels have begun to release rhodamine 6G from the hydrogel network, while only a small amount of the rhodamine can be seen outside the original area of gelation in the OSC hydrogels. The rhodamine could freely diffuse into the solution when no nanoparticles were present. Even after 48 h, rhodamine 6G can be visualized in the nanoparticle containing gels where there is only a small amount of rhodamine 6G in the surrounding hydrogel from the controls at this time frame. This experiment demonstrates how inorganic nanoparticles can be used to control the release of small molecules out of hydrogel networks. While this model system provides a visual of the advantages of these hybrids, more advanced designs are easily envisioned. Engineering the particle degradation timeline can be used to precisely release payloads instead of the elementary release kinetics demonstrated here, while incorporation of API-loaded nanoparticles into hydrogels that biodegrade on-demand may provide a means to release a nanoparticle from hours, to days, to even weeks after a hydrogel is implanted. Beyond nanoparticle loading, there are several other mechanisms with which to control drug release from hybrid hydrogels which include electro-responsive, magnetically responsive, and light responsive mechanisms (Liu et al., 2006; Giri et al., 2011; Yan et al., 2012; Merino et al., 2015). As an example, pSiNPs combined with gold nanorods have been incorporated into alginate hydrogels, and near infrared light can be used to trigger release from these materials (Zhang et al., 2018).

Discussion

There are many unexplored research avenues that may elicit even further control of API release from inorganic nanoparticle biomaterial hybrids. In hybrid hydrogels, many different drug interactions can be foreseen that will improve control of API release timelines. API release first can be governed by loading into inorganic nanoparticles, and the rate can be controlled through applying adsorption loading, adding electrostatic interactions, adjusting the pore size, covalent attachment, or capping/filling the pores after loading. Once an API leaves the nanoparticle, release can be further controlled by interactions with the hydrogel network. This may be through affinity with the hydrogel itself, either through controlling the mesh size of the hydrogel or electrostatic interactions. More advanced affinities can be envisioned, such as releasing an API from an inorganic nanoparticle with affinity to an aptamer coupled to the hydrogel, as previous studies have demonstrated the ability of aptamers to sequester chemokines inside a hydrogel (Enam et al., 2017). Recent advances in hydrogel design explore injectable microparticle hydrogels that can assemble to form granular hydrogels (Daly et al., 2020; Darling et al., 2020; Muir et al., 2022). Incorporating API-loaded inorganic nanoparticles into hydrogel microparticles could be used to further control the release characteristics from these biomaterials. 3D printing strategies can also be used, where API-loaded inorganic nanoparticles are printed into hydrogels during fabrication. Within polymeric scaffolds, new pathways to control API release can also be envisioned. The ability to load and protect different categories of APIs into pSiNPS and fabricate nanofibers from solutions of polymers in organic solvents can be exploited in many different ways. One clear advancement would be to incorporate multiple therapeutics into the same scaffold. This could be done by loading different APIs into inorganic nanoparticles, and incorporating all the nanoparticles together into polymer solutions prior to fabrication. Through this process, there are possibilities to release proteins, nucleic acids, and small molecule drugs all from the same scaffold. Release rates can be controlled by selection of the polymer used to create the scaffolds and the API loading technique (Zuidema et al., 2020a).

The field of API delivery from inorganic nanoparticle incorporated biomaterials is still relatively young, and as advances to both inorganic nanoparticles and biomaterial scaffolds are realized, further complexities can be engineered into these hybrids. Currently, one of the major limitations in the field is incorporating nanoparticles only into specific regions of biomaterials. Nanoparticle location impacts API release over time, and can be important at tissue interfaces and for creating API gradients. If a pathology can be improved by releasing two APIs, location of the nanoparticles also plays a key role in their release profiles. 3D printing will play a role in selective placement of different NPs throughout biomaterial regions, however, this becomes more complicated for applications that require injectable materials. Other limitations are in optimizing biomaterial mechanical properties, since most inorganic nanoparticles will create stiff nanoregions throughout biomaterials that may impact cellular growth. Nonetheless, as nanotechnology fabrication techniques become more ubiquitous and costs decrease, combining nanoparticles with biomaterials will be a common research thrust for control of API release from biomaterials. It can be envisioned that precise API release paradigms can be achieved using biomaterial hybrids that traditional biomaterials cannot realize. With applications foreseen in diverse areas- ranging from cancer therapy, wound healing, bone repair, and nervous system regeneration- research into biomaterials that exploit the advantages of nanotechnology will continue to evolve towards applications in the clinic.

Data availability statement

The raw data supporting the conclusions of this article will be made available by the authors, without undue reservation.

Author contributions

LM-B and JZ conceived the experiments. LD provided laboratory support. LM-B synthesized nanoparticles, performed the experiments, and collected the data. JZ and LM-B wrote the manuscript. LM-B, LD, and JZ discussed the results and commented on the manuscript. This project was coordinated by JZ.

Funding

This project received funding through the European Union's Horizon 2021 research and innovation program under the Marie Skłodowska-Curie grant agreement No. 1016770 ("PACMAN"). JZ is a Marie Skłodowska-Curie fellow.

Acknowledgments

The authors acknowledge the support of the APC central fund of the University of Milan.

Conflict of interest

The authors declare that the research was conducted in the absence of any commercial or financial relationships that could be construed as a potential conflict of interest.

Publisher's note

Supplementary material

The Supplementary Material for this article can be found online at: https://www.frontiersin.org/articles/10.3389/fnano.2022.999923/full#supplementary-material

References

Alvarez, G. S., Helary, C., Mebert, A. M., Wang, X. L., Coradin, T., and Desimone, M. F. (2014). Antibiotic-loaded silica nanoparticle-collagen composite hydrogels with prolonged antimicrobial activity for wound infection prevention. *J. Mat. Chem. B* 2 (29), 4660–4670. doi:10.1039/c4tb00327f

Amsden, B. (1998). Solute diffusion within hydrogels. Mechanisms and models. *Macromolecules* 31 (23), 8382–8395. doi:10.1021/ma980765f

Anglin, E. J., Cheng, L., Freeman, W. R., and Sailor, M. J. (2008). Porous silicon in drug delivery devices and materials. *Adv. Drug Deliv. Rev.* 60 (11), 1266–1277. doi:10.1016/j.addr.2008.03.017

Aznar, E., Marcos, M. D., Martinez-Manez, R., Sancenon, F., Soto, J., Amoros, P., et al. (2009). pH- and photo-switched release of guest molecules from mesoporous silica supports. *J. Am. Chem. Soc.* 131 (19), 6833–6843. doi:10.1021/ja810011p

Babu, S., Albertino, F., Omidinia Anarkoli, A., and De Laporte, L. (2021). Controlling structure with injectable biomaterials to better mimic tissue heterogeneity and anisotropy. *Adv. Healthc. Mat.* 10 (11), e2002221. doi:10.1002/adhm.202002221

Bakandritsos, A., Papagiannopoulos, A., Anagnostou, E. N., Avgoustakis, K., Zboril, R., Pispas, S., et al. (2012). Merging high doxorubicin loading with pronounced magnetic response and bio-repellent properties in hybrid drug nanocarriers. *Small* 8 (15), 2381–2393. doi:10.1002/smll.201102525

Batista, H., Freitas, J. P., Abrunheiro, A., Goncalves, T., Gil, M. H., Figueiredo, M., et al. (2022). Electrospun composite fibers of PLA/PLGA blends and mesoporous silica nanoparticles for the controlled release of gentamicin sulfate. *Int. J. Polym. Mater. Polym. Biomaterials* 71 (9), 635–646. doi:10.1080/00914037.2021.1876053

Behrens, A. M., Casey, B. J., Sikorski, M. J., Wu, K. L., Tutak, W., Sandler, A. D., et al. (2014). *In situ* deposition of PLGA nanofibers via solution blow spinning. *ACS Macro Lett.* 3 (3), 249–254. doi:10.1021/mz500049x

Bodiford, N. K., McInnes, S. J. P., Voelcker, N. H., and Coffer, J. L. (2018). Porous silicon-poly(ε-caprolactone) film composites: evaluation of drug release and degradation behavior. *Biomed. Microdevices* 20 (3), 71. doi:10.1007/s10544-018-0313-5

Canales, A., Jia, X. T., Froriep, U. P., Koppes, R. A., Tringides, C. M., Selvidge, J., et al. (2015). Multifunctional fibers for simultaneous optical, electrical and chemical interrogation of neural circuits *in vivo*. *Nat. Biotechnol.* 33 (3), 277–284. doi:10.1038/nbt.3093

Canham, L. T. (1995). Bioactive silicon structure fabrication through nanoetching techniques. *Adv. Mat.* 7 (12), 1033–1037. doi:10.1002/adma.19950071215

Chen, X. B., Xu, C., and He, H. (2019). Electrospinning of silica nanoparticles-entrapped nanofibers for sustained gentamicin release. *Biochem. Biophysical Res. Commun.* 516 (4), 1085–1089. doi:10.1016/j.bbrc.2019.06.163

Cho, S. J., Jung, S. M., Kang, M., Shin, H. S., and Youk, J. H. (2015). Preparation of hydrophilic PCL nanofiber scaffolds via electrospinning of PCL/PVP-b-PCL block copolymers for enhanced cell biocompatibility. *Polymer* 69, 95–102. doi:10.1016/j.polymer.2015.05.037

Ciciriello, A. J., Smith, D. R., Munsell, M. K., Boyd, S. J., Shea, L. D., and Dumont, C. M. (2021). IL-10 lentivirus-laden hydrogel tubes increase spinal progenitor survival and neuronal differentiation after spinal cord injury. *Biotechnol. Bioeng.* 118 (7), 2609–2625. doi:10.1002/bit.27781

Coffer, J. L., Whitehead, M. A., Nagesha, D. K., Mukherjee, P., Akkaraju, G., Totolici, M., et al. (2005). Porous silicon-based scaffolds for tissue engineering and other biomedical applications. *Phys. Stat. Sol.* 202 (8), 1451–1455. doi:10.1002/pssa.200461134

Dadfar, S. M., Roemhild, K., Drude, N. I., von Stillfried, S., Knuchel, R., Kiessling, F., et al. (2019). Iron oxide nanoparticles: Diagnostic, therapeutic and theranostic applications. *Adv. Drug Deliv. Rev.* 138, 302–325. doi:10.1016/j.addr.2019.01.005

Daly, A. C., Riley, L., Segura, T., and Burdick, J. A. (2020). Hydrogel microparticles for biomedical applications. *Nat. Rev. Mat.* 5 (1), 20–43. doi:10.1038/s41578-019-0148-6

Daly, W., Yao, L., Zeugolis, D., Windebank, A., and Pandit, A. (2012). A biomaterials approach to peripheral nerve regeneration: bridging the peripheral nerve gap and enhancing functional recovery. *J. R. Soc. Interface* 9 (67), 202–221. doi:10.1098/rsif.2011.0438

Darling, N. J., Xi, W. X., Sideris, E., Anderson, A. R., Pong, C., Carmichael, S. T., et al. (2020). Click by click microporous annealed particle (MAP) scaffolds. *Adv. Healthc. Mat.* 9 (10), 1901391. doi:10.1002/adhm.201901391

Dawson, J. I., and Oreffo, R. O. C. (2013). Clay: New opportunities for tissue regeneration and biomaterial design. *Adv. Mat.* 25 (30), 4069–4086. doi:10.1002/adma.201301034

Delplace, V., Obermeyer, J., and Shoichet, M. S. (2016). Local affinity release. *Acs Nano* 10 (7), 6433–6436. doi:10.1021/acsnano.6b04308

Demir, U. S., Shahbazi, R., Calamak, S., Ozturk, S., Gultekinoglu, M., and Ulubayram, K. (2018). Gold nano-decorated aligned polyurethane nanofibers for enhancement of neurite outgrowth and elongation. *J. Biomed. Mat. Res. A* 106 (6), 1604–1613. doi:10.1002/jbm.a.36365

Dos Santos, D. M., Correa, D. S., Medeiros, E. S., Oliveira, J. E., and Mattoso, L. H. C. (2020). Advances in functional polymer nanofibers: From spinning fabrication techniques to recent biomedical applications. *ACS Appl. Mat. Interfaces* 12 (41), 45673–45701. doi:10.1021/acsami.0c12410

dos Santos, J., de Oliveira, R. S., de Oliveira, T. V., Velho, M. C., Konrad, M. V., da Silva, G. S., et al. (2021). 3D printing and nanotechnology: A multiscale Alliance in personalized medicine. *Adv. Funct. Mat.* 31 (16), 2009691. doi:10.1002/adfm.202009691

Dumont, C. M., Park, J., and Shea, L. D. (2015). Controlled release strategies for modulating immune responses to promote tissue regeneration. *J. Control. Release* 219, 155–166. doi:10.1016/j.jconrel.2015.08.014

Dutz, S., Buske, N., Landers, J., Grafe, C., Wende, H., and Clement, J. H. (2020). Biocompatible magnetic fluids of Co-doped iron oxide nanoparticles with tunable magnetic properties. *Nanomaterials* 10 (6), 1019. doi:10.3390/nano10061019

Elsherbini, A. M., and Sabra, S. A. (2022). Nanoparticles-in-nanofibers composites: Emphasis on some recent biomedical applications. *J. Control. Release* 348, 57–83. doi:10.1016/j.jconrel.2022.05.037

Enam, S. F., Krieger, J. R., Saxena, T., Watts, B. E., Olingy, C. E., Botchwey, E. A., et al. (2017). Enrichment of endogenous fractalkine and anti-inflammatory cells via aptamer-functionalized hydrogels. *Biomaterials* 142, 52–61. doi:10.1016/j.biomaterials.2017.07.013

Fadia, N. B., Bliley, J. M., DiBernardo, G. A., Crammond, D. J., Schilling, B. K., Sivak, W. N., et al. (2020). Long-gap peripheral nerve repair through sustained release of a neurotrophic factor in nonhuman primates. *Sci. Transl. Med.* 12 (527), eaav7753. doi:10.1126/scitranslmed.aav7753

Fan, D. M., Loni, A., Canham, L. T., and Coffer, J. L. (2009). Location-dependent controlled release kinetics of model hydrophobic compounds from mesoporous silicon/biopolymer composite fibers. *Phys. Status Solidi* 206 (6), 1322–1325. doi:10.1002/pssa.200881118

Fazli, Y., Shariatinia, Z., Kohsari, I., Azadmehr, A., and Pourmortazavi, S. M. (2016). A novel chitosan-polyethylene oxide nanofibrous mat designed for controlled co-release of hydrocortisone and imipenem/cilastatin drugs. *Int. J. Pharm.* 513 (1-2), 636–647. doi:10.1016/j.ijpharm.2016.09.078

Fiorini, F., Prasetyanto, E. A., Taraballi, F., Pandolfi, L., Monroy, F., Lopez-Montero, I., et al. (2016). Nanocomposite hydrogels as platform for cells growth, proliferation, and chemotaxis. *Small* 12 (35), 4881–4893. doi:10.1002/smll.201601017

Fry, N. L., Boss, G. R., and Sailor, M. J. (2014). Oxidation-induced trapping of drugs in porous silicon microparticles. *Chem. Mat.* 26, 2758–2764. doi:10.1021/cm500797b

Fu, Q. W., Zi, Y. P., Xu, W., Zhou, R., Cai, Z. Y., Zheng, W. J., et al. (2016). Electrospinning of calcium phosphate-poly(D, L-lactic acid) nanofibers for sustained release of water-soluble drug and fast mineralization. *Int. J. Nanomedicine* 11, 5087–5097. doi:10.2147/Ijn.S114224

Funnell, J. L., Ziemba, A. M., Nowak, J. F., Awada, H., Prokopiou, N., Samuel, J., et al. (2021). Assessing the combination of magnetic field stimulation, iron oxide nanoparticles, and aligned electrospun fibers for promoting neurite outgrowth from dorsal root ganglia *in vitro*. *Acta Biomater.* 131, 302–313. doi:10.1016/j.actbio.2021.06.049

Gayet, R. V., de Puig, H., English, M. A., Soenksen, L. R., Nguyen, P. Q., Mao, A. S., et al. (2020). Creating CRISPR-responsive smart materials for diagnostics and programmable cargo release. *Nat. Protoc.* 15 (9), 3030–3063. doi:10.1038/s41596-020-0367-8

Ghosh, P., Han, G., De, M., Kim, C. K., and Rotello, V. M. (2008). Gold nanoparticles in delivery applications. *Adv. Drug Deliv. Rev.* 60 (11), 1307–1315. doi:10.1016/j.addr.2008.03.016

Gibson, J. D., Khanal, B. P., and Zubarev, E. R. (2007). Paclitaxel-functionalized gold nanoparticles. *J. Am. Chem. Soc.* 129 (37), 11653–11661. doi:10.1021/ja075181k

Giri, A., Bhowmick, M., Pal, S., and Bandyopadhyaya, A. (2011). Polymer hydrogel from carboxymethyl guar gum and carbon nanotube for sustained trans-dermal release of diclofenac sodium. *Int. J. Biol. Macromol.* 49 (5), 885–893. doi:10.1016/j.ijbiomac.2011.08.003

Giri, S., Trewyn, B. G., Stellmaker, M. P., and Lin, V. S. Y. (2005). Stimuli-responsive controlled-release delivery system based on mesoporous silica nanorods capped with magnetic nanoparticles. *Angew. Chem. Int. Ed.* 44 (32), 5038–5044. doi:10.1002/anie.200501819

Hola, K., Markova, Z., Zoppellaro, G., Tucek, J., and Zboril, R. (2015). Tailored functionalization of iron oxide nanoparticles for MRI, drug delivery, magnetic separation and immobilization of biosubstances. *Biotechnol. Adv.* 33 (6), 1162–1176. doi:10.1016/j.biotechadv.2015.02.003

Hu, X. L., Liu, S., Zhou, G. Y., Huang, Y. B., Xie, Z. G., and Jing, X. B. (2014). Electrospinning of polymeric nanofibers for drug delivery applications. *J. Control. Release* 185, 12–21. doi:10.1016/j.jconrel.2014.04.018

Irani, Y. D., Tian, Y., Wang, M. J., Klebe, S., McInnes, S. J., Voelcker, N. H., et al. (2015). A novel pressed porous silicon-polycaprolactone composite as a dual-purpose implant for the delivery of cells and drugs to the eye. *Exp. Eye Res.* 139, 123–131. doi:10.1016/j.exer.2015.08.007

Johnson, C. D. L., Ganguly, D., Zuidema, J. M., Cardina, T. J., Ziemba, A. M., Kearns, K. R., et al. (2019). Injectable, magnetically orienting electrospun fiber conduits for neuron guidance. *ACS Appl. Mat. Interfaces* 11 (1), 356–372. doi:10.1021/acsami.8b18344

Jones, C. D., and Lyon, L. A. (2003). Photothermal patterning of microgel/gold nanoparticle composite colloidal crystals. *J. Am. Chem. Soc.* 125 (2), 460–465. doi:10.1021/ja027431x

Kaasalainen, M., Rytkonen, J., Makila, E., Narvanen, A., and Salonen, J. (2015). Electrostatic interaction on loading of therapeutic peptide GLP-1 into porous silicon nanoparticles. *Langmuir* 31 (5), 1722–1729. doi:10.1021/la5047047

Kang, J., Joo, J., Kwon, E. J., Skalak, M., Hussain, S., She, Z. G., et al. (2016). Self-sealing porous silicon-calcium silicate core-shell nanoparticles for targeted siRNA delivery to the injured brain. *Adv. Mat.* 28, 7962–7969. doi:10.1002/adma.201600634

Kankala, R. K., Han, Y. H., Na, J., Lee, C. H., Sun, Z. Q., Wang, S. B., et al. (2020). Nanoarchitectured structure and surface biofunctionality of mesoporous silica nanoparticles. *Adv. Mat.* 32 (23), 1907035. doi:10.1002/adma.201907035

Kashanian, S., Harding, F., Irani, Y., Klebe, S., Marshall, K., Loni, A., et al. (2010). Evaluation of mesoporous silicon/polycaprolactone composites as ophthalmic implants. *Acta Biomater.* 6 (9), 3566–3572. doi:10.1016/j.actbio.2010.03.031

Kim, D., Zuidema, J. M., Kang, J., Pan, Y., Wu, L., Warther, D., et al. (2016). Facile surface modification of hydroxylated silicon nanostructures using heterocyclic silanes. *J. Am. Chem. Soc.* 138 (46), 15106–15109. doi:10.1021/jacs.6b08614

Kim, E. S., Kim, S. H., and Lee, C. H. (2010). Electrospinning of polylactide fibers containing silver nanoparticles. *Macromol. Res.* 18 (3), 215–221. doi:10.1007/s13233-010-0316-4

Kim, S. W., Bae, Y. H., and Okano, T. (1992). Hydrogels - swelling, drug loading, and release. *Pharm. Res.* 9 (3), 283–290. doi:10.1023/A:1015887213431

Kim, Y. J., Ebara, M., and Aoyagi, T. (2013). A smart hyperthermia nanofiber with switchable drug release for inducing cancer apoptosis. *Adv. Funct. Mat.* 23 (46), 5753–5761. doi:10.1002/adfm.201300746

Koppes, A. N., Keating, K. W., McGregor, A. L., Koppes, R. A., Kearns, K. R., Ziemba, A. M., et al. (2016). Robust neurite extension following exogenous electrical stimulation within single walled carbon nanotube-composite hydrogels. *Acta Biomater.* 39, 34–43. doi:10.1016/j.actbio.2016.05.014

Koppes, R. A., Park, S., Hood, T., Jia, X. T., Poorheravi, N. A., Achyuta, A. H., et al. (2016). Thermally drawn fibers as nerve guidance scaffolds. *Biomaterials* 81, 27–35. doi:10.1016/j.biomaterials.2015.11.063

Kwon, E. J., Skalak, M., Bertucci, A., Braun, G., Ricci, F., Ruoslahti, E., et al. (2017). Porous silicon nanoparticle delivery of tandem peptide anti-infectives for the treatment of *Pseudomonas aeruginosa* lung infections. *Adv. Mater.* 29 (35), 1701527. doi:10.1002/adma.201701527

Lai, C. Y., Trewyn, B. G., Jeftinija, D. M., Jeftinija, K., Xu, S., Jeftinija, S., et al. (2003). A mesoporous silica nanosphere-based carrier system with chemically removable CdS nanoparticle caps for stimuli-responsive controlled release of neurotransmitters and drug molecules. *J. Am. Chem. Soc.* 125 (15), 4451–4459. doi:10.1021/ja028650l

Lavrador, P., Esteves, M. R., Gaspar, V. M., and Mano, J. F. (2021). Stimuli-responsive nanocomposite hydrogels for biomedical applications. *Adv. Funct. Mat.* 31 (8), 2005941. doi:10.1002/adfm.202005941

Leach, J. B., and Schmidt, C. E. (2005). Characterization of protein release from photocrosslinkable hyaluronic acid-polyethylene glycol hydrogel tissue engineering scaffolds. *Biomaterials* 26 (2), 125–135. doi:10.1016/j.biomaterials.2004.02.018

Lee, J. H., Park, J. H., Eltohamy, M., Perez, R., Lee, E. J., and Kim, H. W. (2013). Collagen gel combined with mesoporous nanoparticles loading nerve growth factor as a feasible therapeutic three-dimensional depot for neural tissue engineering. *RSC Adv.* 3 (46), 24202–24214. doi:10.1039/c3ra43534b

Li, J., and Mooney, D. J. (2016). Designing hydrogels for controlled drug delivery. *Nat. Rev. Mat.* 1 (12), 16071. doi:10.1038/natrevmats.2016.71

Li, W., Liu, Z. H., Fontana, F., Ding, Y. P., Liu, D. F., Hirvonen, J. T., et al. (2018). Tailoring porous silicon for biomedical applications: From drug delivery to cancer immunotherapy. *Adv. Mater.* 30 (24), 1703740. doi:10.1002/adma.201703740

Lian, M. F., Sun, B. B., Qiao, Z. G., Zhao, K., Zhou, X. J., Zhang, Q. Q., et al. (2019). Bi-layered electrospun nanofibrous membrane with osteogenic and antibacterial properties for guided bone regeneration. *Colloids Surfaces B Biointerfaces* 176, 219–229. doi:10.1016/j.colsurfb.2018.12.071

Lim, H. C., Nam, O. H., Kim, M. J., El-Fiqi, A., Yun, H. M., Lee, Y. M., et al. (2016). Delivery of dexamethasone from bioactive nanofiber matrices stimulates odontogenesis of human dental pulp cells through integrin/BMP/mTOR signaling pathways. *Int. J. Nanomedicine* 11, 2557–2567. doi:10.2147/Ijn.S97846

Liu, D. F., Bimbo, L. M., Makila, E., Villanova, F., Kaasalainen, M., Herranz-Blanco, B., et al. (2013). Co-delivery of a hydrophobic small molecule and a hydrophilic peptide by porous silicon nanoparticles. *J. Control. Release* 170 (2), 268–278. doi:10.1016/j.jconrel.2013.05.036

Liu, T. Y., Hu, S. H., Liu, T. Y., Liu, D. M., and Chen, S. Y. (2006). Magnetic-sensitive behavior of intelligent ferrogels for controlled release of drug. *Langmuir* 22 (14), 5974–5978. doi:10.1021/la060371e

Liu, X. H., and Ma, P. X. (2004). Polymeric scaffolds for bone tissue engineering. *Ann. Biomed. Eng.* 32 (3), 477–486. doi:10.1023/B:ABME.0000017544.36001.8e

Lyu, J. S., Lee, J. S., and Han, J. (2019). Development of a biodegradable polycaprolactone film incorporated with an antimicrobial agent via an extrusion process. *Sci. Rep.* 9, 20236. doi:10.1038/s41598-019-56757-5

Magro, M., Campos, R., Baratella, D., Lima, G., Hola, K., Divoky, C., et al. (2014). A magnetically drivable nanovehicle for curcumin with antioxidant capacity and MRI relaxation properties. *Chem. Eur. J.* 20 (37), 11913–11920. doi:10.1002/chem.201402820

Mandal, A., Clegg, J. R., Anselmo, A. C., and Mitragotri, S. (2020). Hydrogels in the clinic. *Bioeng. Transl. Med.* 5 (2), e10158. doi:10.1002/btm2.10158

Mann, B. K., Schmedlen, R. H., and West, J. L. (2001). Tethered-TGF-beta increases extracellular matrix production of vascular smooth muscle cells. *Biomaterials* 22 (5), 439–444. doi:10.1016/S0142-9612(00)00196-4

Manzano, M., and Vallet-Regi, M. (2020). Mesoporous silica nanoparticles for drug delivery. *Adv. Funct. Mat.* 30 (2), 1902634. doi:10.1002/adfm.201902634

Mellaerts, R., Mols, R., Jammaer, J. A. G., Aerts, C. A., Annaert, P., Van Humbeeck, J., et al. (2008). Increasing the oral bioavailability of the poorly water soluble drug itraconazole with ordered mesoporous silica. *Eur. J. Pharm. Biopharm.* 69 (1), 223–230. doi:10.1016/j.ejpb.2007.11.006

Merino, S., Martin, C., Kostarelos, K., Prato, M., and Vazquez, E. (2015). Nanocomposite hydrogels: 3D polymer-nanoparticle synergies for on-demand drug delivery. *Acs Nano* 9 (5), 4686–4697. doi:10.1021/acsnano.5b01433

Mitchell, M. J., Billingsley, M. M., Haley, R. M., Wechsler, M. E., Peppas, N. A., and Langer, R. (2021). Engineering precision nanoparticles for drug delivery. *Nat. Rev. Drug Discov.* 20 (2), 101–124. doi:10.1038/s41573-020-0090-8

Mohebian, Z., Babazadeh, M., Zarghami, N., and Mousazadeh, H. (2021). Anticancer efficiency of curcumin-loaded mesoporous silica nanoparticles/nanofiber composites for potential postsurgical breast cancer treatment. *J. Drug Deliv. Sci. Technol.* 61, 102170. doi:10.1016/j.jddst.2020.102170

Morillas-Becerril, L., Franco-Ulloa, S., Fortunati, I., Marotta, R., Sun, X. H., Zanoni, G., et al. (2021). Specific and nondisruptive interaction of guanidium-functionalized gold nanoparticles with neutral phospholipid bilayers. *Commun. Chem.* 4 (1), 93. doi:10.1038/s42004-021-00526-x

Mousa, M., Evans, N. D., Oreffo, R. O. C., and Dawson, J. I. (2018). Clay nanoparticles for regenerative medicine and biomaterial design: A review of clay bioactivity. *Biomaterials* 159, 204–214. doi:10.1016/j.biomaterials.2017.12.024

Muir, V. G., Qazi, T. H., Weintraub, S., Maldonado, B. O. T., Arratia, P. E., and Burdick, J. A. (2022). Sticking together: Injectable granular hydrogels with increased functionality via dynamic covalent inter-particle crosslinking. *Small* 18, 2201115. doi:10.1002/smll.202201115

Nene, A., Galluzzi, M., Hongrong, L., Somani, P., Ramakrishna, S., and Yu, X. F. (2021). Synthetic preparations and atomic scale engineering of silver nanoparticles for biomedical applications. *Nanoscale* 13 (33), 13923–13942. doi:10.1039/d1nr01851e

Padron, S., Fuentes, A., Caruntu, D., and Lozano, K. (2013). Experimental study of nanofiber production through forcespinning. *J. Appl. Phys.* 113 (2), 024318. doi:10.1063/1.4769886

Pakulska, M. M., Vulic, K., and Shoichet, M. S. (2013). Affinity-based release of chondroitinase ABC from a modified methylcellulose hydrogel. *J. Control. Release* 171 (1), 11–16. doi:10.1016/j.jconrel.2013.06.029

Pardo-Yissar, V., Gabai, R., Shipway, A. N., Bourenko, T., and Willner, I. (2001). Gold nanoparticle/hydrogel composites with solvent-switchable electronic properties. *Adv. Mat.* 13 (17), 1320–1323. doi:10.1002/1521-4095(200109)13:17<1320::aid-adma1320>3.0.co;2-8

Park, J.-H., Gu, L., Maltzahn, G. v., Ruoslahti, E., Bhatia, S. N., and Sailor, M. J. (2009). Biodegradable luminescent porous silicon nanoparticles for *in vivo* applications. *Nat. Mat.* 8, 331–336. doi:10.1038/NMAT2398

Park, J. H., Allen, M. G., and Prausnitz, M. R. (2005). Biodegradable polymer microneedles: Fabrication, mechanics and transdermal drug delivery. *J. Control. Release* 104 (1), 51–66. doi:10.1016/j.jconrel.2005.02.002

Pawelec, K. M., Koffler, J., Shahriari, D., Galvan, A., Tuszynski, M. H., and Sakamoto, J. (2018). Microstructure and *in vivo* characterization of multi-channel nerve guidance scaffolds. *Biomed. Mat.* 13 (4), 044104. doi:10.1088/1748-605X/aaad85

Place, E. S., George, J. H., Williams, C. K., and Stevens, M. M. (2009). Synthetic polymer scaffolds for tissue engineering. *Chem. Soc. Rev.* 38 (4), 1139–1151. doi:10.1039/b811392k

Prasetyanto, E. A., Bertucci, A., Septiadi, D., Corradini, R., Castro-Hartmann, P., and De Cola, L. (2016). Breakable hybrid organosilica nanocapsules for protein delivery. *Angew. Chem. Int. Ed.* 55 (10), 3323–3327. doi:10.1002/anie.201508288

Qin, J., Asempah, I., Laurent, S., Fornara, A., Muller, R. N., and Muhammed, M. (2009). Injectable superparamagnetic ferrogels for controlled release of hydrophobic drugs. *Adv. Mat.* 21 (13), 1354–1357. doi:10.1002/adma.200800764

Qiu, K. X., He, C. L., Feng, W., Wang, W. Z., Zhou, X. J., Yin, Z. Q., et al. (2013). Doxorubicin-loaded electrospun poly(L-lactic acid)/mesoporous silica nanoparticles composite nanofibers for potential postsurgical cancer treatment. *J. Mat. Chem. B* 1 (36), 4601–4611. doi:10.1039/c3tb20636j

Rambhia, K. J., and Ma, P. X. (2015). Controlled drug release for tissue engineering. *J. Control. Release* 219, 119–128. doi:10.1016/j.jconrel.2015.08.049

Rezaei, H., Shahrezaee, M., Monfared, M. J., Karkan, S. F., and Ghafelehbashi, R. (2021). Simvastatin-loaded graphene oxide embedded in polycaprolactone-polyurethane nanofibers for bone tissue engineering applications. *J. Polym. Eng.* 41 (5), 375–386. doi:10.1515/polyeng-2020-0301

Rihova, M., Ince, A. E., Cicmancova, V., Hromadko, L., Castkova, K., Pavlinak, D., et al. (2021). Water-born 3D nanofiber mats using cost-effective centrifugal spinning: comparison with electrospinning process: A complex study. *J. Appl. Polym. Sci.* 138 (5), 49975. doi:10.1002/app.49975

Rihova, M., Lepcio, P., Cicmancova, V., Frumarova, B., Hromadko, L., Bures, F., et al. (2022). The centrifugal spinning of vitamin doped natural gum fibers for skin regeneration. *Carbohydr. Polym.* 294, 119792. doi:10.1016/j.carbpol.2022.119792

Rose, S., Prevoteau, A., Elziere, P., Hourdet, D., Marcellan, A., and Leibler, L. (2014). Nanoparticle solutions as adhesives for gels and biological tissues. *Nature* 505 (7483), 382–385. doi:10.1038/nature12806

Sakiyama-Elbert, S. E., and Hubbell, J. A. (2000). Development of fibrin derivatives for controlled release of heparin-binding growth factors. *J. Control. Release* 65 (3), 389–402. doi:10.1016/S0168-3659(99)00221-7

Samadzadeh, S., Babazadeh, M., Zarghami, N., Pilehvar-Soltanahmadi, Y., and Mousazadeh, H. (2021). An implantable smart hyperthermia nanofiber with switchable, controlled and sustained drug release: Possible application in prevention of cancer local recurrence. *Mater. Sci. Eng. C* 118, 111384. doi:10.1016/j.msec.2020.111384

Sandhu, K. K., McIntosh, C. M., Simard, J. M., Smith, S. W., and Rotello, V. M. (2002). Gold nanoparticle-mediated Transfection of mammalian cells. *Bioconjug. Chem.* 13 (1), 3–6. doi:10.1021/bc015545c

Secret, E., Maynadier, M., Gallud, A., Gary-Bobo, M., Chaix, A., Maillard, P., et al. (2013). Anionic porphyrin-grafted porous silicon nanoparticles for photodynamic therapy. *Chem. Commun.* 49, 4202–4204. doi:10.1039/C3CC38837A

Seifu, M. F., and Nath, L. K. (2019). Polymer-drug conjugates: Novel carriers for cancer chemotherapy. *Polymer-Plastics Technol. Mater.* 58 (2), 158–171. doi:10.1080/03602559.2018.1466172

Sershen, S. R., Mensing, G. A., Ng, M., Halas, N. J., Beebe, D. J., and West, J. L. (2005). Independent optical control of microfluidic valves formed from optomechanically responsive nanocomposite hydrogels. *Adv. Mat.* 17 (11), 1366–1368. doi:10.1002/adma.200401239

Sershen, S. R., Westcott, S. L., Halas, N. J., and West, J. L. (2002). Independent optically addressable nanoparticle-polymer optomechanical composites. *Appl. Phys. Lett.* 80 (24), 4609–4611. doi:10.1063/1.1481536

Shahriari, D., Koffler, J. Y., Tuszynski, M. H., Campana, W. M., and Sakamoto, J. S. (2017). Hierarchically ordered porous and high-volume polycaprolactone microchannel scaffolds enhanced axon growth in transected spinal cords. *Tissue Eng. Part A* 23 (9-10), 415–425. doi:10.1089/ten.TEA.2016.0378

Sill, T. J., and von Recum, H. A. (2008). Electro spinning: Applications in drug delivery and tissue engineering. *Biomaterials* 29 (13), 1989–2006. doi:10.1016/j.biomaterials.2008.01.011

Skelton, S., Bostwick, M., O'Connor, K., Konst, S., Casey, S., and Lee, B. P. (2013). Biomimetic adhesive containing nanocomposite hydrogel with enhanced materials properties. *Soft Matter* 9 (14), 3825–3833. doi:10.1039/c3sm27352k

Slowing, I. I., Vivero-Escoto, J. L., Wu, C. W., and Lin, V. S. Y. (2008). Mesoporous silica nanoparticles as controlled release drug delivery and gene transfection carriers. *Adv. Drug Deliv. Rev.* 60 (11), 1278–1288. doi:10.1016/j.addr.2008.03.012

Soontornworajit, B., Zhou, J., Zhang, Z. Y., and Wang, Y. (2010). Aptamer-Functionalized *in situ* injectable hydrogel for controlled protein release. *Biomacromolecules* 11 (10), 2724–2730. doi:10.1021/bm100774t

Sullivan, S. P., Koutsonanos, D. G., Martin, M. D., Lee, J. W., Zarnitsyn, V., Choi, S. O., et al. (2010). Dissolving polymer microneedle patches for influenza vaccination. *Nat. Med.* 16 (8), 915–920. doi:10.1038/nm.2182

Sun, J., Fan, Y., Zhang, P., Zhang, X., Zhou, Q., Zhao, J., et al. (2020). Self-enriched mesoporous silica nanoparticle composite membrane with remarkable photodynamic antimicrobial performances. *J. Colloid Interface Sci.* 559, 197–205. doi:10.1016/j.jcis.2019.10.021

Suntornnond, R., An, J., Yeong, W. Y., and Chua, C. K. (2015). Biodegradable polymeric films and membranes processing and forming for tissue engineering. *Macromol. Mat. Eng.* 300 (9), 858–877. doi:10.1002/mame.201500028

Tabata, Y., and Ikada, Y. (1998). Protein release from gelatin matrices. *Adv. Drug Deliv. Rev.* 31 (3), 287–301. doi:10.1016/S0169-409x(97)00125-7

Talamini, L., Picchetti, P., Ferreira, L. M., Sitia, G., Russo, L., Violatto, M. B., et al. (2021). Organosilica cages target hepatic sinusoidal endothelial cells avoiding macrophage filtering. *Acs Nano* 15 (6), 9701–9716. doi:10.1021/acsnano.1c00316

Thatiparti, T. R., Shoffstall, A. J., and von Recum, H. A. (2010). Cyclodextrin-based device coatings for affinity-based release of antibiotics. *Biomaterials* 31 (8), 2335–2347. doi:10.1016/j.biomaterials.2009.11.087

Thoniyot, P., Tan, M. J., Karim, A. A., Young, D. J., and Loh, X. J. (2015). Nanoparticle-hydrogel composites: Concept, design, and applications of these promising, multi-functional materials. *Adv. Sci. (Weinh).* 2 (1-2), 1400010. doi:10.1002/advs.201400010

Urzedo, A. L., Goncalves, M. C., Nascimento, M. H. M., Lombello, C. B., Nakazato, G., and Seabra, A. B. (2020). Cytotoxicity and antibacterial activity of alginate hydrogel containing nitric oxide donor and silver nanoparticles for topical applications. *ACS Biomater. Sci. Eng.* 6 (4), 2117–2134. doi:10.1021/acsbiomaterials.9b01685

Venugopal, J., and Ramakrishna, S. (2005). Applications of polymer nanofibers in biomedicine and biotechnology. *Appl. Biochem. Biotechnol.* 125 (3), 147–158. doi:10.1385/Abab:125:3:147

Wang, C., Flynn, N. T., and Langer, R. (2004). Controlled structure and properties of thermoresponsive nanoparticle-hydrogel composites. *Adv. Mat.* 16 (13), 1074–1079. doi:10.1002/adma.200306516

Wang, J., Kumeria, T., Bezem, M. T., Wang, J., and Sailor, M. J. (2018). Self-reporting photoluminescent porous silicon microparticles for drug delivery. *ACS Appl. Mat. Interfaces* 10 (4), 3200–3209. doi:10.1021/acsami.7b09071

Wang, Y., Cui, W. G., Zhao, X., Wen, S. Z., Sun, Y. L., Han, J. M., et al. (2019). Bone remodeling-inspired dual delivery electrospun nanofibers for promoting bone regeneration. *Nanoscale* 11 (1), 60–71. doi:10.1039/c8nr07329e

Wang, Y. Z., Sun, L. Z., Jiang, T. Y., Zhang, J. H., Zhang, C., Sun, C. S., et al. (2014). The investigation of MCM-48-type and MCM-41-type mesoporous silica as oral solid dispersion carriers for water insoluble cilostazol. *Drug Dev. Industrial Pharm.* 40 (6), 819–828. doi:10.3109/03639045.2013.788013

Wu, M., Chen, J. S., Huang, W. J., Yan, B., Peng, Q. Y., Liu, J. F., et al. (2020). Injectable and self-healing nanocomposite hydrogels with ultrasensitive pH-responsiveness and tunable mechanical properties: Implications for controlled drug delivery. *Biomacromolecules* 21 (6), 2409–2420. doi:10.1021/acs.biomac.0c00347

Xu, L. G., Li, W., Sadeghi-Soureh, S., Amirsaadat, S., Pourpirali, R., and Alijani, S. (2021). Dual drug release mechanisms through mesoporous silica nanoparticle/electrospun nanofiber for enhanced anticancer efficiency of curcumin. *J. Biomed. Mat. Res. A* 110, 316–330. doi:10.1002/jbm.a.37288

Xu, Y. H., Kim, C. S., Saylor, D. M., and Koo, D. (2017). Polymer degradation and drug delivery in PLGA-based drug-polymer applications: A review of experiments and theories. *J. Biomed. Mat. Res.* 105 (6), 1692–1716. doi:10.1002/jbm.b.33648

Yadid, M., Feiner, R., and Dvir, T. (2019). Gold nanoparticle-integrated scaffolds for tissue engineering and regenerative medicine. *Nano Lett.* 19 (4), 2198–2206. doi:10.1021/acs.nanolett.9b00472

Yan, B., Boyer, J. C., Habault, D., Branda, N. R., and Zhao, Y. (2012). Near infrared light triggered release of biomacromolecules from hydrogels loaded with upconversion nanoparticles. *J. Am. Chem. Soc.* 134 (40), 16558–16561. doi:10.1021/ja308876j

Yang, M., Lee, S. Y., Kim, S., Koo, J. S., Seo, J. H., Jeong, D. I., et al. (2020). Selenium and dopamine-crosslinked hyaluronic acid hydrogel for chemophotothermal cancer therapy. *J. Control. Release* 324, 750–764. doi:10.1016/j.jconrel.2020.04.024

Yuan, Z. M., Pan, Y., Cheng, R. Y., Sheng, L. L., Wu, W., Pan, G. Q., et al. (2016). Doxorubicin-loaded mesoporous silica nanoparticle composite nanofibers for long-term adjustments of tumor apoptosis. *Nanotechnology* 27 (24), 245101. doi:10.1088/0957-4484/27/24/245101

Zhang, D. X., Yoshikawa, C., Welch, N. G., Pasic, P., Thissen, H., and Voelcker, N. H. (2019). Spatially controlled surface modification of porous silicon for sustained drug delivery applications. *Sci. Rep.* 9, 1367. doi:10.1038/s41598-018-37750-w

Zhang, F., and King, M. W. (2020). Biodegradable polymers as the pivotal player in the design of tissue engineering scaffolds. *Adv. Healthc. Mat.* 9 (13), 1901358. doi:10.1002/adhm.201901358

Zhang, H. B., Zhu, Y. Q., Qu, L. L., Wu, H. Y., Kong, H. X., Yang, Z., et al. (2018). Gold nanorods conjugated porous silicon nanoparticles encapsulated in calcium alginate nano hydrogels using microemulsion templates. *Nano Lett.* 18 (2), 1448–1453. doi:10.1021/acs.nanolett.7b05210

Zhao, P. K., Liu, H. Y., Deng, H. B., Xiao, L., Qin, C. Q., Du, Y. M., et al. (2014). A study of chitosan hydrogel with embedded mesoporous silica nanoparticles loaded by ibuprofen as a dual stimuli-responsive drug release system for surface coating of titanium implants. *Colloids Surfaces B Biointerfaces* 123, 657–663. doi:10.1016/j.colsurfb.2014.10.013

Zhao, Y. N., Trewyn, B. G., Slowing, I. I., and Lin, V. S. Y. (2009). Mesoporous silica nanoparticle-based double drug delivery system for glucose-responsive controlled release of insulin and cyclic AMP. *J. Am. Chem. Soc.* 131 (24), 8398–8400. doi:10.1021/ja901831u

Zhou, X. J., Chen, L., Wang, W. Z., Jia, Y. T., Chang, A. N., Mo, X. M., et al. (2015). Electrospun nanofibers incorporating self-decomposable silica nanoparticles as carriers for controlled delivery of anticancer drug. *RSC Adv.* 5 (81), 65897–65904. doi:10.1039/c5ra11830a

Zilony, N., Rosenberg, M., Holtzman, L., Schori, H., Shefi, O., and Segal, E. (2017). Prolonged controlled delivery of nerve growth factor using porous silicon nanostructures. *J. Control. Release* 257, 51–59. doi:10.1016/j.jconrel.2016.12.008

Zuidema, J. M., Bertucci, A., Kang, J., Sailor, M. J., and Ricci, F. (2020a). Hybrid polymer/porous silicon nanofibers for loading and sustained release of synthetic DNA-based responsive devices. *Nanoscale* 12 (4), 2333–2339. doi:10.1039/c9nr08474f

Zuidema, J. M., Dumont, C. M., Wang, J., Batchelor, W. M., Lu, Y. S., Kang, J., et al. (2020b). Porous silicon nanoparticles embedded in poly(lactic-co-glycolic acid) nanofiber scaffolds deliver neurotrophic payloads to enhance neuronal growth. *Adv. Funct. Mat.* 30 (25), 2002560. doi:10.1002/adfm.202002560

Zuidema, J. M., Kumeria, T., Kim, D., Kang, J. Y., Wang, J. A. N., Hollett, G., et al. (2018). Oriented nanofibrous polymer scaffolds containing protein-loaded porous silicon generated by spray nebulization. *Adv. Mat.* 30 (12), 1706785. doi:10.1002/adma.201706785

frontiers | Frontiers in Nanotechnology

TYPE Original Research
PUBLISHED 04 October 2022
DOI 10.3389/fnano.2022.982644

Processing helix–coil transition data: Account of chain length and solvent effects

Knarik Yeritsyan, Matjaz Valant and Artem Badasyan*

Materials Research Laboratory, University of Nova Gorica, Nova Gorica, Slovenia

OPEN ACCESS

EDITED BY
Giancarlo Franzese,
University of Barcelona, Spain

REVIEWED BY
Rudolf Podgornik,
University of Chinese Academy of Sciences, China
Tomaz Urbic,
University of Ljubljana, Slovenia

*CORRESPONDENCE
Artem Badasyan,
artem.badasyan@ung.si,
abadasyan@gmail.com

SPECIALTY SECTION
This article was submitted to Computational Nanotechnology, a section of the journal Frontiers in Nanotechnology

RECEIVED 30 June 2022
ACCEPTED 14 September 2022
PUBLISHED 04 October 2022

CITATION
Yeritsyan K, Valant M and Badasyan A (2022), Processing helix–coil transition data: Account of chain length and solvent effects.
Front. Nanotechnol. 4:982644.
doi: 10.3389/fnano.2022.982644

Numerous nanobiotechnologies include manipulations of short polypeptide chains. The conformational properties of these polypeptides are studied *in vitro* by circular dichroism and time-resolved infrared spectroscopy. To find out the interaction parameters, the measured temperature dependence of normalized helicity degree needs to be further processed by fitting to a model. Using recent advances in the Hamiltonian formulation of the classical Zimm and Bragg model, we explicitly include chain length and solvent effects in the theoretical description. The expression for the helicity degree we suggest successfully fits the experimental data and provides hydrogen bonding energies and nucleation parameter values within the standards in the field.

KEYWORDS

short polypeptide chains, helix-coil, degree of helicity, water model, Zimm and Bragg model

1 Introduction

A variety of short polypeptide chains are widely used in bionanotechnological applications, in particular for self-assembling nanomaterials which have well-ordered structures (Loo et al., 2011; Hwa Chan et al., 2017; Tong et al., 2022). Understanding the conformational stability of short polypeptides in various solvents is thus crucial for tuning the technological processes. These facts make obvious the necessity for a simple and tractable model that would simultaneously account for the finite size and solvent effects.

Helix–coil transition models are thermodynamic theories describing the conformations of linear polymers in solution. One of the most common transition models is the Zimm–Bragg (ZB) (Zimm and Bragg, 1959) model with its extensions and variations. Although Zimm and Bragg formulated their model in the 1950s, it appeared to be very successful and is still widely used for fitting experimental data (Schreck and Yuan, 2011; Wood et al., 2011; Neelamraju et al., 2015). Together with its strength, the original model formulation is phenomenological and lacks a microscopic Hamiltonian. When attempting to incorporate the influence of solvent into the approach, the lack of model Hamiltonian makes it unclear how the ZB model parameters should be adjusted to describe solvent effects, especially when it comes to solvents with directional interactions, such as water. Recently, a spin Hamiltonian formulation of the ZB model was suggested (Badasyan et al., 2010). Thus, the thermodynamics of the ZB model was reconstructed from statistical mechanics. Coupled with the spin description of water–biopolymer interactions from Goldstein (1984), Ananikyan et al. (1990), Badasyan et al. (2011), and Badasyan et al. (2014), the approach resulted in an algorithm to process the helix–coil experimental data (Badasyan et al., 2021) for longer polypeptides. Separately, the effects of finite chain length within the ZB model have been thoroughly studied (Badasyan, 2021).

In addition to obvious biotechnological relevance, there are not so many studies of short polypeptide chains in water. The seminal study of Scholtz et al. (1991) has set the standards in the field. The authors used a single-helical sequence approximation of the Zimm and Bragg model of α-helix to coil transition in order to process the experimental data for short polypeptides of lengths from 14 to 50 residues. Unfortunately, the fits reported in their Figure 3 are not convincing, and the coefficient of determination R^2 ranges from 0.3 to 0.91, as reported in Table 1 (Scholtz et al., 1991).

Recently, Ren et al. (2017) and Wang et al. (2004) considered different aspects of polypeptide unfolding in shorter chains and also suffered from poor fit. It is unclear whether the poor fit is a consequence of the inapplicability of the single-sequence approximation for the chain lengths studied, or whether the Zimm–Bragg model fails, *per se*. Last but not least, solvent effects undoubtedly play an important role and need to be taken into account on the same grounds as the effects of finite size.

There are other important effects, for instance, related to the differences in sequence and charge. Although they are relevant in principle, we will limit our study to the consideration of finite size and water-like solvent effects.

In this article, based on our recent amendments to the seminal Zimm and Bragg model, we suggest and approve the validity of an algorithm to treat the experimental data on the helix–coil transition of short polypeptides in water.

2 Model and methods

2.1 The classical definition of the ZB model

The Zimm and Bragg model (Zimm and Bragg, 1959) of helix–coil transition in a polypeptide chain is most of the time discussed in its simplest, nearest neighbor version. Two model parameters are taken into account: stability parameter s and nucleation parameter σ. Assigning 0 to coil state and 1 to helical state, constructing the transfer-matrix of statistical weights, and solving the determinant, we arrive at an explicit expression for the characteristic equation in the form of a second order polynomial in λ (Zimm and Bragg, 1959; Badasyan et al., 2010):

$$\lambda^2 - (s+1)\lambda + s(1-\sigma) = 0; \qquad \lambda_{1,2} = \frac{1}{2}\left[1 + s \pm \sqrt{(1-s)^2 + 4\sigma s}\right], \tag{1}$$

where σ is the nucleation parameter which has an entropic contribution and describes the difficulty of initiating the helix, and s is the stability parameter which has both enthalpic and entropic contributions and has a meaning of a statistical weight, usually represented in terms of a (Gibbs or Helmholtz) free energy change between the helix and coil states:

$$s = e^{-\beta(G_{helix} - G_{coil})} = e^{-\Delta G/T}. \tag{2}$$

Herein, $\beta = 1/T$, and we measure temperature T in energy units. The Zimm–Bragg model describes the state of a peptide unit, which comprised many atoms with a single spin variable and is, therefore, a coarse-grained model. The free energies in Eq. 2 are thus thermodynamic quantities averaged at the level of a repeated unit and should not be confused with the statistical quantities, referring to the whole polypeptide chain. When we take into account that the two ends of a chain are free from H-bonds for the partition function of the Zimm–Bragg model, we will have

$$Z(\sigma, s, N) = C_1\lambda_1^N(\sigma, s) + C_2\lambda_2^N(\sigma, s) = \lambda_1^N\left[C_1 + C_2 e^{-N/\xi}\right], \tag{3}$$

where N is the number of repeat units in the entire chain, $C_1 = \frac{1-\lambda_2}{\lambda_1-\lambda_2}$, $C_2 = \frac{\lambda_1-1}{\lambda_1-\lambda_2}$, and

$$\xi(\sigma, s) = \ln^{-1}\left(\frac{\lambda_1}{\lambda_2}\right) \tag{4}$$

is the spatial correlation length.

One of the most important measurable and theoretical quantities to describe the helix to coil transition in biopolymers is the degree of helicity, which is defined as an average relative number of H-bonds between repeated units. The degree of helicity in the ZB model is defined through the partition function and eigenvalues, and in terms of model parameters s and σ, it reads as

$$\theta_{ZB}(\sigma, s, N) = \frac{1}{N}\frac{\partial \ln Z}{\partial \ln s}. \tag{5}$$

To find the transition temperature T_m, we should search for an inflection point on the transition curve. To find it, we need to take the second derivative of helicity degree θ to be 0 (Badasyan, 2021):

$$\theta''(\sigma, s, N) = 0. \tag{6}$$

The transition interval is found in the following way:

$$\Delta T(\sigma, s, N) = -\left(\left.\frac{d\theta}{dT}\right|_{T_m}\right)^{-1} = -\Delta s\left(\left.\frac{ds}{dT}\right|_{T_m}\right)^{-1}, \tag{7}$$

where $\Delta s = 1/(d\theta/ds)$. For greater details, an interested reader is referred to Badasyan (2021).

2.2 Hamiltonian definition of the ZB model

As discussed earlier, to include the solvent effects into account, we need a Hamiltonian formulation of the ZB model. But even before introducing the solvent part of the Hamiltonian, we need to step back and review the Hamiltonian formulation of the ZB model itself, as presented in Badasyan et al. (2010). The model is a version of an earlier one (Ananikyan et al., 1990) and is based on two parameters: the energy parameter $W = V + 1 = e^{U/T}$, where U is the energy of the H-bond and T is the temperature; the parameter Q of entropic origin, which is the ratio between the number of all accessible states *versus* the number of states in the helical conformation. Assume that a Q-valued spin variable γ_i describes the state of the ith repeated unit and $\gamma_i = 1$ value corresponds to the repeated unit in the ordered, helical state, while other $Q - 1$ identical values are for the coil state. $Q \geq 2$ condition describes the degeneracy of the coil state. The Hamiltonian of such a model reads

$$-\beta H_{ZB}(\{\gamma_i\}) = J\sum_{i=1}^{N}\delta_i^{(2)} = J\sum_{i=1}^{N}\delta(\gamma_i,1)\delta(\gamma_{i+1},1), \tag{8}$$

where N is the number of repeat units, and $J = U/T$ is the temperature-reduced energy of H-bonding between polymeric units. $\delta_k^{(2)} = \delta(\gamma_k,1)\delta(\gamma_{k+1},1)$, where $\delta(\gamma_k, 1)$ stands for the Kronecker symbol, which is different from zero only when $\gamma_k = 1$, $k = \overline{1,N}$.

The partition function Z can be obtained as

$$Z(V,Q) = \sum_{\{\gamma_i=1\}}^{Q} e^{-\beta H_{ZB}(\{\gamma_i\})} = \sum_{\{\gamma_i=1\}}^{Q}\prod_{i=1}^{N}\left[1 + V\delta(\gamma_i,1)\delta(\gamma_{i+1},1)\right]$$
$$= \sum_{\{\gamma_i=1\}}^{Q}\prod_{i=1}^{N}\left(\hat{M}\right)_{\gamma_i,\gamma_{i+1}}, \tag{9}$$

where $(\hat{M})_{\gamma_i,\gamma_{i+1}}$ are elements of the $Q \times Q$ matrix of statistical weights.

The characteristic equation for the Hamiltonian Eq. 8.

$$\Lambda^2 - (W - 1 + Q)\Lambda + (W - 1)(Q - 1) = 0 \tag{10}$$

converts into the classical Zimm–Bragg expression Eq. 1 after a simple change of variables $\lambda = \frac{\Lambda}{Q}$; $\sigma = \frac{1}{Q}$; $s = \frac{W-1}{Q}$:

$$\lambda^2 - (s + 1)\lambda + s(1 - \sigma) = 0. \tag{11}$$

Therefore, the Hamiltonian in Eq. 8 provides exactly the same thermodynamics as the ZB model, hence, can be considered equivalent to it (Badasyan et al., 2010).

The degree of helicity is defined as the average relative number of H-bonds. In the previous model, an H-bond is formed between two repeat units when both are in the same helical conformation state ($\gamma = 1$). So, we can write the degree of helicity as

$$\theta(\sigma,s,N) = <\delta(\gamma_i,1)\delta(\gamma_{i+1},1)> = \frac{1}{N}\frac{\partial\ln Z}{\partial\ln s}\frac{s+\sigma}{s}. \tag{12}$$

As we see the degree of helicity of the ZB model in the Hamiltonian representation in Eq. 12, it differs from the classical representation in Eq. 5 by the term of $\frac{s+\sigma}{s}$, which is very close to 1 only when the parameter $\sigma \rightarrow 0$.

2.3 Solvent effects and finite size effects within the ZB model

We assume that H-bond formation with solvent is possible only for those repeat units of the polymer that do not participate in intramolecular H-bonding and two vacancies appear after one intramolecular H-bond is broken. To each solvent molecule near repeat unit i, a spin variable μ_i, with values from 1 to q, is assigned. One broken $N - H...O = C$ H-bond originates two binding vacancies for solvent; therefore, for each γ_i, there are two μ_is. Orientation 1 of spin μ is the bonded one, with energy U_{ps}; all other $q - 1$ orientations correspond to coil configuration and zero energy (Badasyan et al., 2014).

The Hamiltonian of such a solvent model is

$$-\beta H_{CS}\left(\{\gamma_i\},\{\mu_i^j\}\right) = I\sum_{i=1}^{N}\left(1 - \delta_i^{(2)}\right)\cdot\sum_{j=1}^{2}\delta\left(\mu_i^j,1\right)$$
$$= I\sum_{i=1}^{N}\left[1 - \delta(\gamma_i,1)\delta(\gamma_{i+1},1)\right]$$
$$\cdot\left[\delta\left(\mu_i^1,1\right) + \delta\left(\mu_i^2,1\right)\right], \tag{13}$$

where $I = \frac{U_{ps}}{T}$ is the reduced energy of a polymer–solvent H-bond, resulting in the total partition function of the ZB model as

$$Z_{total} = \sum_{\{\gamma_i\}}\sum_{\{\mu_i^j\}}\exp\left(-\beta H_{total}\left(\{\gamma_i\},\{\mu_i^j\}\right)\right)$$
$$= \sum_{\{\gamma_i\}}\exp\left(-\beta H_{ZB}(\{\gamma_i\})\right)\sum_{\{\mu_i^j\}}\exp\left(-\beta H_{CS}\left(\{\gamma_i,\mu_i^j\}\right)\right)$$
$$= \sum_{\{\gamma_i\}}\prod_{i=1}^{N}\left[1 + V\delta_i^{(2)}\right]\sum_{\{\mu_i^j\}}\exp\left(-\beta H_{CS}\left(\{\gamma_i,\mu_i^j\}\right)\right). \tag{14}$$

This expression includes both *in vacuo* form of the partition function and the term due to solvent. Solvent degrees of freedom μ_i^j can be summed out in Eq. 14, resulting in (see Badasyan et al. (2014))

$$Z_{total}(W,Q,K,q) = (q + K - 1)^{2N}\sum_{\{\gamma_i\}}\prod_{i=1}^{N}\left[1 + \tilde{V}\delta_i^{(2)}\right] = (q + K - 1)^{2N} Z\left(\tilde{W},Q\right), \tag{15}$$

where $K = e^I$, $\tilde{V} = \tilde{W} - 1$, and

$$\tilde{W}(W,K,q) = \frac{q^2 e^J}{\left(q + e^I - 1\right)^2} = \frac{q^2 W}{(q + K - 1)^2}. \tag{16}$$

According to the relationship between W and s for the renormalized energetic parameter $\tilde{s}$, using the change of variables, we will have the following equation (Badasyan et al., 2021):

$$\tilde{s}\left(t,t_0,h,h_{ps},Q,q\right)=\frac{\tilde{W}-1}{Q}=\frac{1}{Q}\left[\left(e^{-\frac{h}{R(t-t_0)}}+\frac{e^{\frac{h_{ps}-h}{R(t-t_0)}}-e^{-\frac{h}{R(t-t_0)}}}{q}\right)^{-2}-1\right], \tag{17}$$

where $Q = 1/\sigma$, h is the single H-bond energy within the polypeptide, and h_{ps} is a single polypeptide–solvent H-bond energy; $R = k_B N_A$ is the ideal gas constant. To make the fit results tractable, from Eq. 17 on, we measure the temperature t in Kelvin and energy in Joule/mole. The entropic cost value of q is chosen to be 16 according to the specifications of H-bonding angles of a water molecule (see Eq. 16 of Badasyan et al. (2021) for the justification of the value chosen). Recent studies of hydrated proteins report the appearance of $t - t_0$ temperature shift as a result of the presence of partially glassy states reflecting the non-Arrhenius relaxation in experiments (Adam and Gibbs, 1965). t_0 is a fitting parameter standing for the glass transition temperature in supercooled liquid (see Badasyan et al. (2021) for details). The final expression for helicity degree with the account of solvent effects and the final lengths is as follows:

$$\theta(\tilde{s},\sigma,N)=\frac{\tilde{s}+\sigma}{N}\frac{\partial \ln Z_{total}}{\partial \tilde{s}}, \tag{18}$$

where $\tilde{s}$ is given by Eq. 17 and Z_{total} is given by Eq. 15.

The eigenvalues and the correlation length do not depend on chain length N, but the partition function does. The partition function in Eq. 15 has three size-dependent limits (Badasyan, 2021): 1) infinite chain limit ($N \to \infty$); 2) long-chain limit ($N \gg \xi$); and 3) short-chain limit, also known as a single sequence approximation ($N < \xi$). Interestingly, there is a gap in the validity of approximations for the practically most relevant chain lengths between two and five correlation lengths. The last fact makes it relevant to use the most general expression for the partition function, valid for any N:

$$Z(\tilde{s},\sigma,N)=\frac{1-\lambda_2}{\lambda_1-\lambda_2}\lambda_1^N+\frac{\lambda_1-1}{\lambda_1-\lambda_2}\lambda_2^N. \tag{19}$$

3 Results and discussion

3.1 Fitting model to experimental data

Using the analytic form of the degree of helicity, we have obtained Eq. 18. We are ready to fit the experimental data and find inter- and intra-molecular H-bonding energies, nucleation parameter σ, and glass transition temperature t_0.

TABLE 1 Results obtained from fitting for experimental data taken from Scholtz et al. (1991). The first column shows chain length (in repeated units), and the next four columns show fitting parameters, described in the text; numbers in brackets show errors in percentages. Nucleation parameter σ is recalculated as 1/Q. For all fits, the coefficient of determination is $R^2 = 0.999$. Energies are measured in Joules per mole and temperature in Kelvins.

N, r.u.	t_0, *K*	*h*, $Jmol^{-1}$	h_{ps}, $Jmol^{-1}$	*Q*	σ
14	219.5(2.3)	4691.4(5.1)	4596.3(4.9)	295.4(1.8)	0.00339
20	212.9(0.9)	6288.9(2.1)	6126.7(2.0)	342.4(1.1)	0.00292
26	236.7(0.4)	5662.3(1.6)	5550.9(1.5)	332.9(0.7)	0.00300
32	232.7(0.4)	6161.1(1.3)	6034.3(1.3)	345.1(0.6)	0.00290
38	231.2(0.4)	6416.4(1.4)	6284.0(1.4)	350.8(0.6)	0.00285
50	245.6(0.3)	5743.0(1.4)	5646.2(1.4)	336.2(0.5)	0.00297

We start with the data from Scholtz et al. (1991). Scholtz et al. (1991) measured thermal unfolding curves for a series of alanine-based peptides with repeating sequences and varying chain lengths. We digitized their results presented in Figure 3 and fitted them into our model. Results of the fit are presented in Table 1 and Figure 1.

As one can see from Table 1, the overall quality of fit is very good, the value of the coefficient of determination is $R^2 = 0.999$, and errors of fitted quantities are small. Not surprisingly, from Figure 1, an excellent fit to experimental data is seen much better than in the original article (Scholtz et al., 1991). All the energies, obtained from the fit, fall within the range of values expected for hydrogen bonding in polypeptides. They cannot be compared to the fit results of Scholtz et al. (1991), since the theory they used did not contain any quantities of solvent and reports only one energy. Instead, our approach, in addition to the intramolecular (inside polypeptide) hydrogen bonding energy h, accounts for the intermolecular (polypeptide-solvent) energy h_{ps}. Since for all chain lengths considered, $h > h_{ps}$, no cold denaturation can take place in the system, although the suggested approach is applicable for the case of cold denaturation as well (Badasyan et al., 2021). The only quantity, which can be directly compared, is the nucleation parameter, for which we got an averaged value of $\sigma = 0.003$, practically equal to the value 0.0029 reported in Table 1 of Scholtz et al. (1991).

Another study of helix–coil transitions in Ala-based polypeptides of different lengths was performed by Wang et al. (2004). The mean residue ellipticity $[\theta]_{222}$ at 222 nm as a function of temperature can be converted to helicity degree using the following convention (Wang et al., 2004):

$$\begin{gathered}\theta_H=-44000\cdot(1-x/n)+100T\\ \theta_C=+640-45\cdot T\\ \theta=\frac{[\theta]_{222}-\theta_C}{\theta_H-\theta_C}.\end{gathered} \tag{20}$$

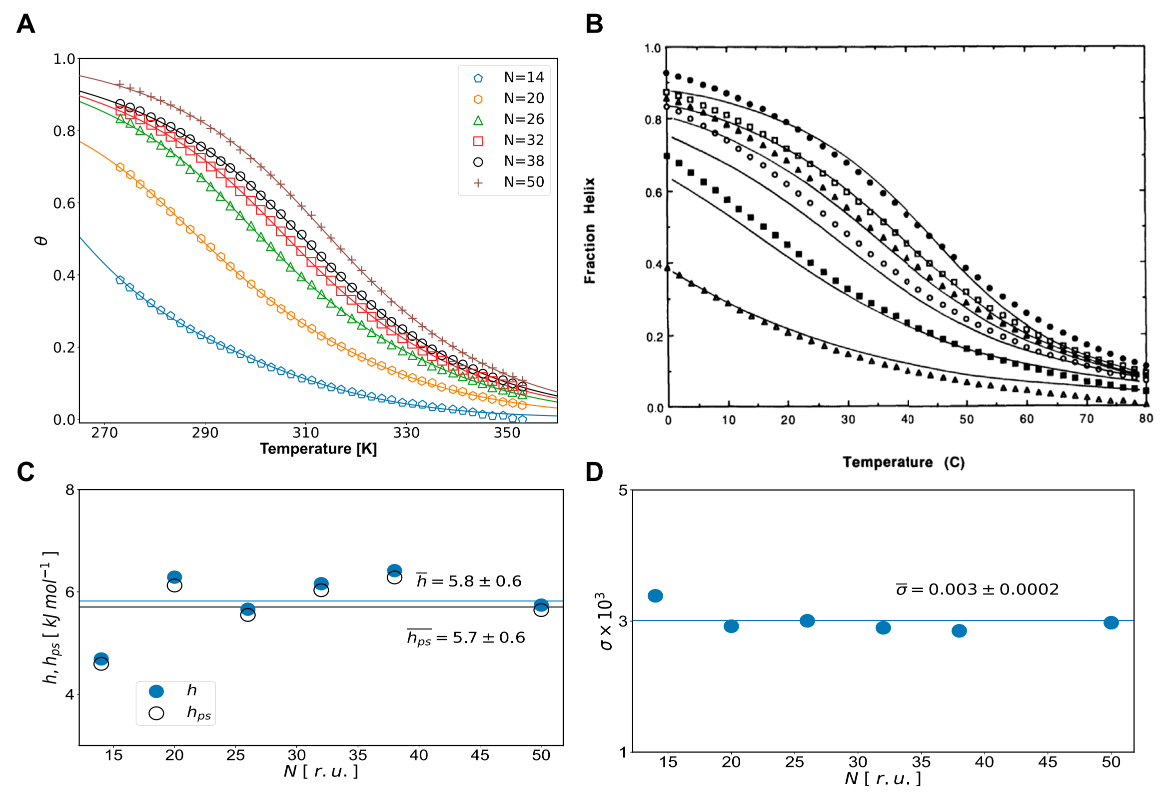

FIGURE 1
(A) Helicity degrees for different chain lengths (*N*, *r.u.*). The data points (symbols) are taken from Scholtz et al. (1991). Solid lines are fits of Eq. 18 to experimental data. Fitting values are reported in Table 1: **(B)** fraction helix (helicity degree) data with original fits reproduced from Figure 3 of Scholtz et al. (1991) (with permission from Biopolymers journal), **(C)** inter- (h_{ps}) and intramolecular (h) H-bonding energies, and **(D)** nucleation parameter σ vs. *N*. Averages and standard deviations are shown in the graph.

n is the number of repeat units in the chain; *x* is a constant equal to 2.5, used for correction of non-hydrogen bonded carbonyls not contributing to θ_H (Wang et al., 2004).

Here again, we fit our Eq. 18 (Wang et al., 2004) to data points. Results of the fit are presented in Table 2 and Figure 2.

We again see a very good overall quality of fit with $R^2 = 0.999$ and small errors of fitted quantities. The energies, obtained from the fit, fall within the range of values, expected for hydrogen bonding in polypeptides. However, these energies are certainly higher for polyAla sequences of Ting Wang et al. (2004), as compared to Glu, Lys, and Ala mixtures of Scholtz et al. (1991). In both Figures 1B and 2B, *h* and h_{ps} values are close to each other. On the one hand, this is as expected: both are H-bonding energies. On the other hand, it is surprising how close these energies are; a small alteration of the balance can bring global changes. As to the nucleation parameter, it shows a wider span of values around σ = 0.003. Ting Wang et al. (2004) reported the value of $\sigma = 0.002$, resulting from fitting the kinetic data. We see it reasonably close to our value, considering that the models used are different.

TABLE 2 Results obtained from fitting for experimental data taken from Wang et al. (2004). Quantities and units same as in Table 1. For all fits, the coefficient of determination is R^2 = 0.999.

N, r.u.	t_0, *K*	*h*, *Jmol*$^{-1}$	h_{ps}, *Jmol*$^{-1}$	*Q*	*σ*
14	196.7(3.1)	6498.1(3.9)	6391.8(3.8)	277.7(0.8)	0.00360
19	126.6(10.1)	10334.7(5.2)	10022.6(5.0)	329.0(1.5)	0.00304
24	171.3(2.6)	11349.3(4.6)	10965.5(4.1)	425.2(2.1)	0.00235
29	210.2(0.7)	8181.3(1.5)	7949.3(1.5)	385.4(0.8)	0.00259
34	186.9(1.3)	9248.0(2.1)	8939.4(2.0)	409.4(1.2)	0.00244

The same approach, as we have shown in our recent publication (Badasyan et al., 2021), can also fit cold denaturation data, but since $h > h_{ps}$ for the data considered, cold denaturation is not observed.

Ren et al. (2017) performed helix–coil experiments with synthetic homopolypeptide samples of different lengths. The results were compared with the Schellman and ZB models. For short chains, the ZB model was reported to fit well, while for longer chains, the authors reported that fit was not achieved. When trying to

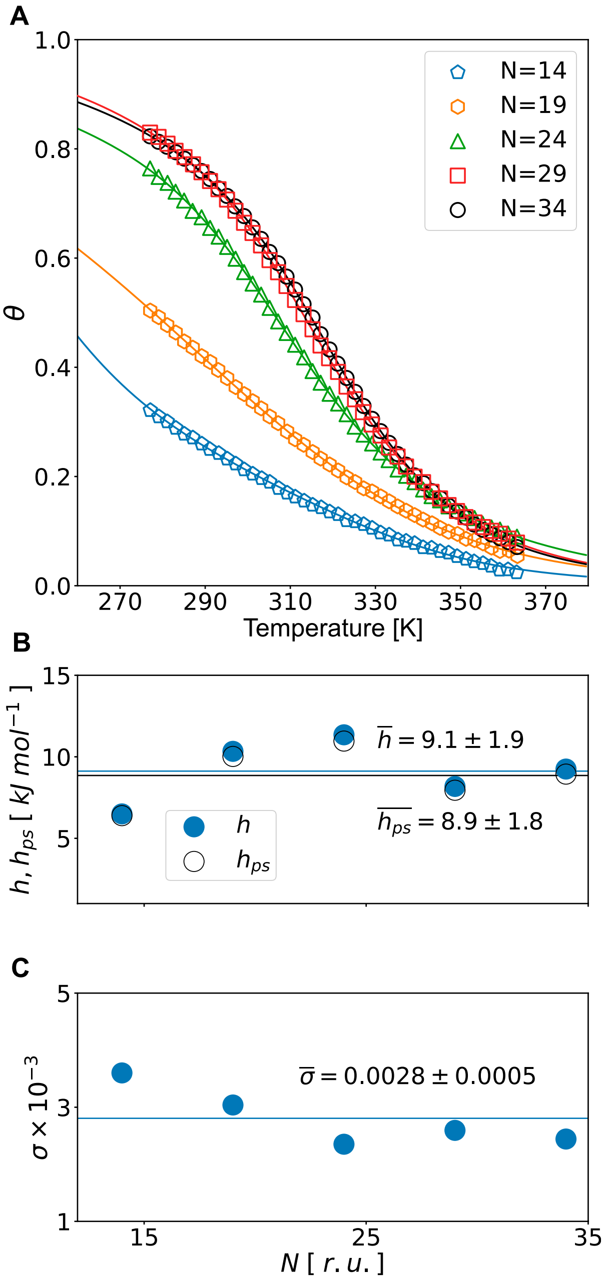

FIGURE 2
(A) Helicity degrees for different chain lengths (*N*, *r.u.*). The data points were taken from Ting Wang et al. (2004). Solid lines are fits of experimental data using Eq. 18. Fitted values from Table 2: **(B)** inter- (h_{ps}) and intramolecular (h) H-bonding energies and **(C)** nucleation parameter σ vs. N. Averages and standard deviations are shown in the graph.

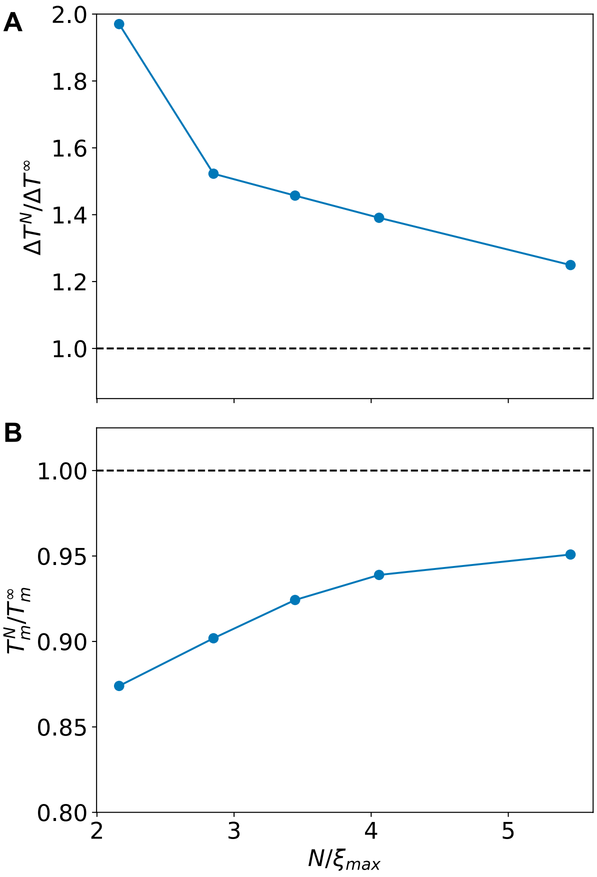

FIGURE 3
Transition interval and temperature in relative units over a range of reduced chain lengths for the transition data obtained from Scholtz et al. (1991). As we see, there are five correlation lengths and the finite size effects are still strong.

reproduce their results, we noted certain inconsistencies with the experimental data reported in Ren et al. (2017). For instance, it is not clear whether refer to the helicity degrees or fractions of denaturation. When comparing Zimm and Bragg (1959), Scholtz et al. (1991), and Wang et al. (2004), the transition curves have opposite behaviors. Anyway, even corrected, the fit is not converging or is very poor for the Ren et al. (2017) data, with either their formulas or our expression Eq. 18 (Wang et al., 2004). For the abovementioned reasons, we have excluded their data from consideration.

3.2 Transition temperature and interval analysis

The fitted curves of helicity degree we have obtained can be used to calculate transition temperatures and transition intervals from Eq. 6 to Eq. 7 for every chain. This way we can obtain the size scaling of these relevant quantities.

Transition temperature T_m^N for finite chains of length N can be found using the Eq. 6 (Neelamraju et al., 2015) condition. For infinite chains, the transition temperature T_m^∞ can be estimated by inserting $\tilde{s} = 1 - 2\sigma$ in Eq. 17 (Ren et al., 2017).

Transition interval ΔT^N for finite chains is found in Eq. 7 (Schreck and Yuan, 2011). Its infinite chain limit expression ΔT^∞ can be estimated analytically as $4\sqrt{\sigma}$.

As shown in Figure 3, fitted experimental curves follow the size-scaling trends in both transition interval and temperature, as reported of Badasyan (2021) recently. Moreover, at all chain lengths considered in Scholtz et al. (1991), systems are beyond the single-sequence approximation but below the limit of long chains for the Zimm–Bragg model.

4 Conclusion

We have extended the application of the Zimm–Bragg model to the simultaneous account of chain length and solvent effects. Using derived formulas, we successfully analyze the experimental data for the set of two polypeptides and show a better fit as compared to the originally reported one. As a result, it became clear that the poor fit reported in Scholtz et al. (1991) and Wang et al. (2004) can be overcome by a detailed analysis of the size and solvent effects. Last but not least, we confirm once more the statement made in Badasyan (2021) that in many real-world applications and nanobiotechnologies, the characteristic chain lengths fall between those of a single-sequence approximation and a long-chain limit. It means special care should be taken when estimating the stabilities of short polypeptides.

Although we have neglected the effects arising from the difference in amino acid sequences and related charges, our approach represents an improvement over previous approaches and allows us to achieve better fitting of the experimental data, suggesting that our fitting parameters account in an implicit way for the average effect of sequence and charges for small polypeptides (Schiro and Weik, 2019; Mallamace et al., 2016).

Data availability statement

The data analyzed in this study is subject to the following licenses/restrictions: data were digitized from the published manuscripts and properly cited in the body of manuscript. Requests to access these datasets should be directed to abadasyan@gmail.com.

Author contributions

AB and KY designed and developed the overall method and approach. AB and MV supervised the research. KY and AB wrote the code and analyzed the data. KY and AB wrote the article. All authors read and commented on the article.

Acknowledgments

Authors acknowledge financial support from the Slovenian Research Agency through program P2-0412.

Conflict of interest

The authors declare that the research was conducted in the absence of any commercial or financial relationships that could be construed as a potential conflict of interest.

Publisher's note

References

Adam, G., and Gibbs, J. H. (1965). On the temperature dependence of cooperative relaxation properties in glass-forming liquids. *J. Chem. Phys.* 43, 139–146. doi:10.1063/1.1696442

Ananikyan, N. S., Hajryan, S. A., Mamasakhlisov, E. S., and Morozov, V. F. (1990). Helix-coil transition in polypeptides: A microscopical approach. *Biopolymers* 30, 357–367. doi:10.1002/bip.360300313

Badasyan, A. (2021). System size dependence in the zimm–bragg model: Partition function limits, transition temperature and interval. *Polymers* 13 (12), 1985. doi:10.3390/polym13121985

Badasyan, A. V., Giacometti, A., Mamasakhlisov, Y. Sh., Morozov, V. F., and Benight, A. S. (2010). Microscopic formulation of the Zimm-Bragg model for the helix-coil transition. *Phys. Rev. E* 81, 021921. doi:10.1103/physreve.81.021921

Badasyan, A. V., Tonoyan, Sh. A., Mamasakhlisov, Y. Sh., Giacometti, A., Benight, A. S., and Morozov, V. F. (2011). Competition for hydrogen-bond formation in the helix-coil transition and protein folding. *Phys. Rev. E* 83, 051903. doi:10.1103/physreve.83.051903

Badasyan, A. V., Tonoyan, Sh. A., Giacometti, A., Podgornik, R., Parsegian, V. A., Mamasakhlisov, Y. Sh., et al. (2014). Unified description of solvent effects in the helix-coil transition. *Phys. Rev. E* 89, 022723. doi:10.1103/physreve.89.022723

Badasyan, A., Tonoyan, S., Valant, M., and Grdadolnik, J. (2021). Implicit water model within the Zimm-Bragg approach to analyze experimental data for heat and cold denaturation of proteins. *Commun. Chem.* 4, 57. doi:10.1038/s42004-021-00499-x

Goldstein, R. E. (1984). Potts model for solvent effects on polymer conformation. *Phys. Lett. A* 104, 285–289. doi:10.1016/0375-9601(84)90072-0

Hwa Chan, K., Lee, W. H., Zhuo, S., and Ni, M. (2017). Harnessing supramolecular peptide nanotechnology in biomedical applications. *Int. J. Nanomedicine* 12, 1171–1182. doi:10.2147/ijn.s126154

Loo, Y., Zhang, S., and Hauser, C. A. E. (2011). From short peptides to nanofibers to macromolecular assemblies in biomedicine. *Biotechnol. Adv.* 30 (3), 593–603. doi:10.1016/j.biotechadv.2011.10.004

Mallamace, F., Corsaro, C., Mallamace, D., Vasi, S., Vasi, C., Baglioni, P., et al. (2016). Energy landscape in protein folding and unfolding. *PNAS* 113, 3159–3163. doi:10.1073/pnas.1524864113

Neelamraju, S., Oakley, M. T., and Johnston, R. L. (2015). Chiral effects on helicity studied via the energy landscape of short (D, L)-alanine peptides. *J. Chem. Phys.* 143, 165103. doi:10.1063/1.4933428

Ren, Y., Baumgartner, R., Fu, H., Schoot, van der P., Cheng, J., and Lin, Y. (2017). Revisiting the helical cooperativity of synthetic polypeptides in solution. *Biomacromolecules* 18 (8), 2324–2332. doi:10.1021/acs.biomac.7b00534

Schiro, G., and Weik, M. (2019). Role of hydration water in the onset of protein structural dynamics. *J. Phys. Cond. Mat.* 31, 463002. doi:10.1088/1361-648X/ab388a

Scholtz, J. M., Qian, H., York, E. J., Stewart, J. M., and Baldwin, R. L. (1991). Parameters of helix-coil transition theory for alanine-based peptides of varying chain lengths in water. *Biopolymers* 31 (13), 1463–1470. doi:10.1002/bip.360311304

Schreck, J. S., and Yuan, J. M. (2011). A statistical mechanical approach to protein aggregation. *J. Chem. Phys.* 135, 235102. doi:10.1063/1.3666837

Tong, L., Lu, X. M., Zhang, M. R., Hu, K., and Li, Z. (2022). Peptide-based nanomaterials: Self-assembly, properties and applications. *Bioact. Mater.* 11, 268–282. doi:10.1016/j.bioactmat.2021.09.029

Wang, T., Zhu, Y., Getahun, Z., Du, D., Huang, C. Y., DeGrado, W. F., et al. (2004). Length dependent helix–coil transition kinetics of nine alanine-based peptides. *J. Phys. Chem. B* 108 (39), 15301–15310. doi:10.1021/jp037272j

Wood, G. G., Clinkenbeard, D. A., and Jacobs, D. J. (2011). Nonadditivity in the alpha-helix to coil transition. *Biopolymers* 954, 240–253. doi:10.1002/bip.21572

Zimm, B. H., and Bragg, J. K. (1959). Theory of the phase transition between helix and random coil in polypeptide chains. *J. Chem. Phys.* 31, 526–535. doi:10.1063/1.1730390

frontiers | Frontiers in Nanotechnology

TYPE Original Research
PUBLISHED 11 October 2022
DOI 10.3389/fnano.2022.988997

Thermal feature-size enhancement in multiphoton photoresists

Nikolaos Liaros[1†], Zuleykhan Tomova[1†],
Sandra A. Gutierrez Razo[1†], John S. Bender[1], Amanda J. Souna[1],
Robert J. Devoe[2], David A. Ender[2], Brian J. Gates[2] and
John T. Fourkas[1,3,4,5]*

[1]Department of Chemistry and Biochemistry, University of Maryland, College Park, MD, United States,
[2]Corporate Research Process Laboratory, 3M Co, 208-1-1 3M Center, St. Paul, MN, United States,
[3]Institute for Physical Science and Technology, University of Maryland, College Park, MD, United States,
[4]Maryland Quantum Materials Center, University of Maryland, College Park, MD, United States,
[5]Maryland NanoCenter, University of Maryland, College Park, MD, United States

We demonstrate a new approach for decreasing the feature size in multiphoton absorption polymerization (MAP). Acrylic photoresists containing the photoinitiator KL68 (bis-[4-(diphenylamino) stryl]-1-(2-ethylhexyloxy), 4-(methoxy)benzene) exhibit a proportional velocity (PROVE) dependence, yielding smaller feature sizes at lower fabrication speeds. The feature size in this photoresist decreases substantially with a temperature increase of less than 10°C when all other fabrication parameters are kept constant, suggesting that the PROVE behavior results from local heating. Although higher temperatures have previously been associated with decreased feature sizes in MAP, the effect observed here is considerably stronger than in previous work, and is shown to be a property of the photoinitiator. This discovery opens the door to exploiting thermal gradients to improve resolution in MAP lithography.

KEYWORDS

multiphoton absorption polymerization, photopolymerization, resolution enhancement, thermal effects, proportional velocity dependence

OPEN ACCESS

EDITED BY
Virginie Ponsinet,
UPR8641 Centre de Recherche Paul Pascal (CRPP), France

REVIEWED BY
Carole Ecoffet,
UMR7361 Institut de Sciences des Matériaux de Mulhouse, France
Shih-Hsin Hsu,
Purdue University, United States

*CORRESPONDENCE
John T. Fourkas,
fourkas@umd.edu

†These authors have contributed equally to this work

SPECIALTY SECTION
This article was submitted to Nanofabrication, a section of the journal Frontiers in Nanotechnology

RECEIVED 07 July 2022
ACCEPTED 16 September 2022
PUBLISHED 11 October 2022

CITATION
Liaros N, Tomova Z, Gutierrez Razo SA, Bender JS, Souna AJ, Devoe RJ, Ender DA, Gates BJ and Fourkas JT (2022), Thermal feature-size enhancement in multiphoton photoresists. *Front. Nanotechnol.* 4:988997. doi: 10.3389/fnano.2022.988997

Introduction

There is currently a tremendous demand for the rapid prototyping and manufacture of three-dimensional (3D) parts with feature sizes as small as a few tens of nanometers (Fourkas et al., 2021), for use in application spaces such as microelectronics (Camposeo et al., 2019), photonics (Campbell et al., 2000), biomedicine (Pan and Wang, 2011), the automotive industry (Finkbeiner, 2013), and telecommunications (Wu et al., 2015). The ability to fabricate geometrically complex structures using a broad range of materials has made additive manufacturing techniques attractive means for microfabrication (Ngo et al., 2018). Multiphoton absorption polymerization (MAP) is a unique approach to additive manufacturing, given this technique's high resolution and its inherent 3D fabrication capability for structures with complex geometries (Lafratta et al., 2007).

MAP is most often performed using negative-tone photoresists, which are materials that become cross-linked, and therefore insoluble, upon sufficient exposure to light. Typical acrylic photoresists consist of a mixture of multifunctional monomers and a radical photoinitiator. Upon photoexcitation, the photoinitiators generate radicals, leading to a cross-linking chain reaction that, with sufficient exposure, renders the material insoluble.

Due to the nonlinear nature of multiphoton excitation, the polymerization reaction is contained within the focal volume of a tightly focused laser beam, where the crosslinking induced exceeds the solubility threshold. The shape and size of the laser focus determine the geometry and size of individual volume elements (voxels). Voxels can have a transverse dimension as small as 100 nm when excitation is performed using an 800 nm, ultrafast laser (Lafratta et al., 2007; Sugioka and Cheng, 2014). MAP has fostered a revolution in the rapid prototyping and on-demand creation of parts with sub-micron resolution. For instance, MAP has been used for the fabrication of micromachines (Farrer et al., 2006), 3D photonic crystals (Rybin et al., 2015), microring resonators (Li et al., 2008), waveguides (Klein et al., 2005), microlasers (Yokoyama et al., 2003), and scaffolds for cell growth (Allen et al., 2005; Basu et al., 2005).

Typical photoinitiators in multiphoton photoresists exhibit positive contrast, meaning that the size of the fabricated features increases with decreasing fabrication velocity, or, equivalently, with increasing exposure. However, recently a number of photoinitiators have been shown to exhibit apparent "negative contrast" (Stocker et al., 2011). Photoresists formulated with such photoinitiators exhibit proportional velocity (PROVE) behavior (Stocker et al., 2011), i.e., the size of fabricated features increases with increasing fabrication velocity. PROVE materials open the door to new applications that demand higher precision in nanofabrication.

Here we present a study of MAP lithography in acrylic photoresists with the photoinitiator bis-[4-(diphenylamino) stryl]-1-(2-ethylhexyloxy), 4-(methoxy)benzene (KL68) (Devoe et al., 2011). We demonstrate that these photoresists exhibit PROVE behavior resulting from a novel mechanism, local heating. We show that the feature size in photoresists containing KL68 decreases substantially with an increase in temperature of less than 10°C. In contrast, in MAP photoresists based on conventional photoinitiators, the feature size decrease over this temperature range is minimal or non-existent, as observed previously by Kawata and co-workers (Takada et al., 2008). Our findings open the door to using thermal effects to achieve improved resolution in MAP.

Materials and methods

Sample preparation

The photoinitiators we examined included bis-[4-(diphenylamino) stryl]-1-(2-ethylhexyloxy), 4-(methoxy) benzene (KL68), Lucirin TPO-L, malachite green carbinol base (MGCB), and malachite green carbinol hydrochloride (MCB•HCl). KL68 (Figure 1A) was synthesized as reported previously (Leatherdale et al., 2007). Lucirin TPO-L, MGCB and MCB•HCl were purchased from Sigma Aldrich, and were used as received. Photoresist samples were prepared by mixing two monomers, which, unless otherwise noted, were tris (2-hydroxy ethyl) isocyanurate triacrylate (Sartomer 368) and ethoxylated trimethylolpropanetriacrylate (Sartomer 499), in a 1:1 weight ratio (SR368/499). This formulation was chosen for its low shrinkage and high adhesion (Baldacchini et al., 2004). Photoinitiators were dissolved in the monomer mix at the weight percentages discussed below. Because the 2-photon-absorption cross section of KL68 is substantially greater than that of the other photoinitiators used, the weight percent of KL68 used was considerably smaller so that the laser power used for exposure was similar for all photoresists. After preparation, each photoresist was placed in a sample vial and left on a rotator overnight. No attempt was made to remove oxygen or radical inhibitors from the photoresists, as our goal was to study the polymerization behavior under the conditions most often used in the laboratory.

#1 glass coverslips (Corning) were used as substrates for our experiments. The coverslips were first cleaned in an oxygen plasma for 4 min. The coverslips were then immersed in a solution of 93% ethanol, 5% distilled water, and 2% (3-acryloxypropyl) trimethoxysilane by volume for 14 h, following by rinsing in ethanol for 1 h and drying at 95°C for 1 h. This acrylation procedure promotes adhesion of polymerized structures.

A photoresist sample was mixed and filtered through a 0.2-μm-pore-diameter filter, after which one drop was placed on an acrylated cover slip. A coverslip was taped to a microscope slide, covered with another coverslip, and then mounted on a sample holder for MAP experiments. The piece of cellophane tape between the two coverslips set the thickness of the photoresist film at ~60 μm. After exposure, the unpolymerized resin was removed by rinsing twice in ethanol for 2 min each, and once in water for 2 min. After development, the samples were left to dry at room temperature. For examination with a scanning electron microscope (SEM), the coverslips were attached to a mount with carbon tape and covered with a ~20 nm platinum/palladium layer using a sputter coater.

Optical setup

MAP was performed with a tunable, mode-locked, Ti: sapphire oscillator (Coherent Mira 900-F) with a center wavelength of 800 nm, a pulse duration of ~150 fs, and a repetition rate of 76 MHz. For photodeactivation studies, a second, identical oscillator was used at 800 nm in continuous-

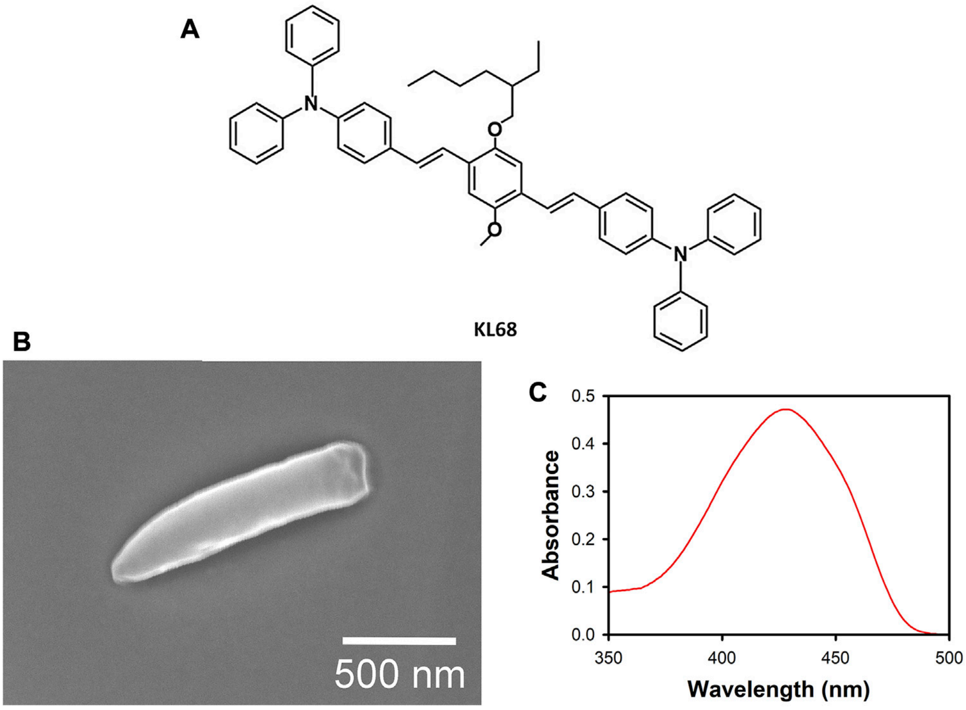

FIGURE 1
(A) The chemical structure of KL68. **(B)** A scanning electron micrograph of a representative fallen voxel from a KL68 photoresist at 24°C (see Figure 3A). **(C)** The UV/visible absorption spectrum of KL-68 in toluene (0.02 mM).

wave (CW) mode for inhibition of polymerization. The two beams were combined in a polarizing beam cube and directed to the sample through a 100 ×, 1.45 NA oil-immersion objective (Zeiss α Plan-FLUAR) mounted on an inverted microscope (Zeiss Axiovert 100). Cover slips with photoresist samples were mounted on a 3-axis piezoelectric stage (Physik Instrumente) for fine sample positioning in all dimensions. The piezo stage was attached to a motor-driven stage (Ludl Electronic Products, Ltd.) for coarse sample positioning. The movement of the piezo stage was controlled using a LabVIEW program, and fabrication was followed in real time using a CCD camera and a monitor. For reciprocity measurements, the minimum average power at which fabricated lines were observed was determined visually (Tomova et al., 2016) on the display screen. During all measurements, the axial position of the focal plane was kept fixed to ensure that a constant distance was maintained above the coverslip surface. For accurate measurement of the polymerization threshold powers, a reflected portion of the 800 nm beam (~5%) was chopped at a fixed frequency and was sent to a calibrated Si photodiode, the output of which was sent to a lock-in amplifier (Stanford Research Systems, SR810) referenced to the chopping frequency.

Temperature studies

The effect of temperature on polymerization efficiency was studied in photoresist samples containing KL68, MGCB, and Lucirin TPO-L. The temperature of each sample was controlled by an objective heater (Bioptechs Inc.). The sample was allowed to come to thermal equilibrium at each temperature before measurements were made.

For estimation of the voxel size through SEM analysis, we used the ascending scan method (Sun et al., 2002; Sun et al., 2003). Rows of voxels were fabricated for each photoresist and temperature. Every row contained 20 voxels, each of which was exposed for 0.5 s at a fixed laser power. This exposure time was chosen because in a typical radical photoresist the voxel dimensions (Sun et al., 2003) and the exposure threshold (Yang et al., 2019; Liaros and Fourkas, 2020) become relatively insensitive to small changes in exposure time, allowing for the creation of more reproducible voxels. The focal height above the substrate was increased by 100 nm for each consecutive voxel in the row. At some focal height, the voxel is attached only weakly to the surface, and so falls over upon development. An SEM of a representative fallen voxel that was used in the analysis below is shown in Figure 1B.

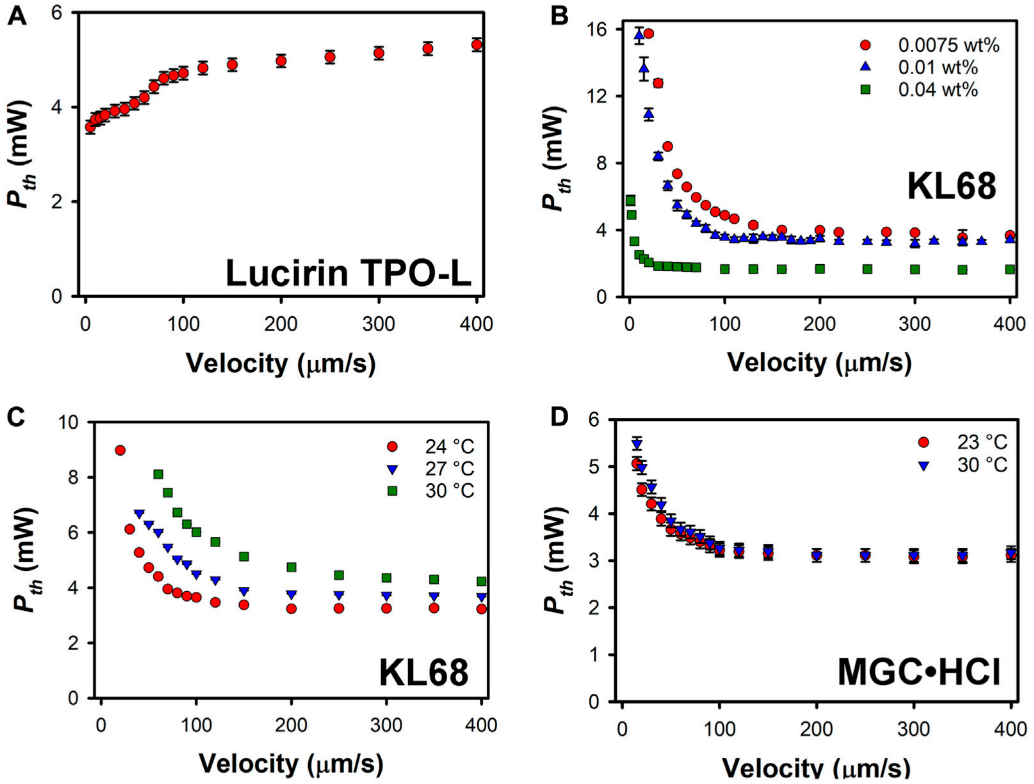

FIGURE 2
Threshold power as a function of velocity for **(A)** 1 wt% Lucirin TPO-L in 1:1 S368/499 at 24°C, **(B)** KL-68 at 0.0075 wt%, 0.01 wt%, and 0.04 wt% in 1:1 S368/499, **(C)** 0.01 wt% KL68 in 1:1 SR368/499 at 24°C, 27°C, and 30°C, and **(D)** 0.01 wt% MGC•HCl in 1:1 SR368/499 at 23°C and 30°C. In all experiments the excitation wavelength was 800 nm. The error bars represent the standard deviation in the exposure threshold based on multiple measurements. In some cases the error bars are smaller than the symbols.

Results

KL68 characterization

The UV/visible absorption spectrum of KL68 in toluene shows an absorption band centered at ~430 nm (Figure 1C). Based on this spectrum, we expect that 800 nm excitation should fall within the 2-photon absorption band for this material.

In the simplest model of exposure, the same exposure dose leads to the same degree of crosslinking, regardless of the exposure duration. Such behavior is known as reciprocity. In the case of 2-photon excitation, reciprocity implies that so long as the integral of the square of the irradiance over the exposure time is the same, then the degree of crosslinking should be the same. Reciprocity is only observed in radical photoresists in limited circumstances (Yang et al., 2019; Liaros and Fourkas, 2020). Nevertheless, the threshold power for polymerization in radical photoresists typically increases as the fabrication velocity increases (and thereby the exposure time decreases). Such behavior is observed, for instance, in a 1:1 SR368/499 photoresist containing the conventional, Norrish Type I radical photoinitiator, Lucirin TPO-L (Figure 2A). The threshold power depends strongly on fabrication velocity up to ~100 μm/s, after which the dependence becomes weaker. At even higher fabrication velocities the threshold power becomes nearly independent of velocity (Supplementary Figure S1A). The structure in the data at velocities below 100 μm/s hints at the existence of complex photopolymerization dynamics. Given our estimated beam diameter of 0.5 μm, the exposure time at a given point is approximately half of the inverse velocity in μm/s. A logarithmic plot of the threshold power as a function of the exposure time (Supplementary Figure S1B) is flat at exposure times between 0.1 and 1 ms. This behavior has been shown in similar systems to be due to oxygen diffusion occurring on a shorter time scale than exposure (Yang et al., 2019). At longer exposure times the power threshold decreases, which in similar systems has been attributed to diffusion of the initiator being faster than the exposure time (Yang et al., 2019). Interestingly, our data show two distinct periods of decreasing threshold within this time range; the source of this bimodal decrease is unclear. These results for Lucirin TPO-L can be viewed as baseline data for the typical polymerization dynamics of 1:1 SR368/499 photoresists.

Figure 2B shows the threshold power for polymerization as a function of fabrication velocity for three different concentrations of KL68 in a 1:1 SR368/499 photoresist. The polymerization threshold power decreases significantly as the fabrication velocity is increased, before levelling off at higher fabrication velocities. The higher the photoinitiator concentration, the lower the velocity at which the threshold power becomes insensitive to velocity. Corresponding logarithmic plots of the threshold power as a function of exposure time (Supplementary Figure S2) are flat at short times and grow linearly at longer times. The slopes in this latter region are similar for the two lower concentrations, and smaller for the highest concentration. The same behavior has been observed in photoresists with KL68 concentrations up to 0.1 wt%. Photoresists with even higher KL68 concentrations were not examined in detail due to their high photosensitivity, but the same PROVE behavior was still observed.

The data in Figure 2B; Supplementary Figure S2 indicate that in KL68 photoresists, longer exposure times result in less crosslinking than do shorter exposure times. In other words, KL68 endows PROVE behavior in these photoresists, implying that the light that drives the exposure also inhibits the exposure in some manner. As in other PROVE photoresists, the crosslinking must occur relatively slowly, such that at higher velocities the focal point moves away from an exposed region before crosslinking is complete, removing the source of inhibition and decreasing the exposure threshold (Stocker et al., 2011). In the PROVE materials explored previously, this behavior was attributed to the existence of a long-lived, photodeactivatable state in the photoinitiation pathway. In such a case, deactivation is driven by linear absorption of the same laser that drives multiphoton excitation in the photoinitiator (Stocker et al., 2011).

To check for the presence of this phenomenon, a CW beam of the same wavelength as the mode-locked excitation beam can be employed simultaneously (Li et al., 2009). In the case of KL68 photoresists, addition of a CW, 800 nm beam with a power of up to 120 mW during the 800 nm, 2-photon excitation of the KL68 photoresists at an average laser power of 12 mW did not have any impact on the exposure threshold. This finding indicates that photodeactivation of electronic states is not the mechanism underlying the PROVE behavior in this system, and that ultrafast pulses are essential to deactivation.

Temperature studies

As an alternative hypothesis, we explored whether local heating by the excitation beam is responsible for the observed PROVE behavior. Such heating arises primarily from effects precipitated by absorption to an excited electronic state, such as intramolecular vibrational relaxation and solvation. Therefore, when there is no linear absorption at the excitation wavelength, heating is only significant upon ultrafast pulsed excitation, which can drive multiphoton absorption. Heating during exposure has been demonstrated to be modest in a representative multiphoton photoresist, on the order of a few °C (Mueller et al., 2013). Such a small temperature increase would not typically be expected to have a significant effect on the polymerization threshold or the feature size (Takada et al., 2008). To determine whether thermal effects play a role in the KL-68 photoresists studied here, an objective heater was used to control the sample temperature. The threshold power for polymerization was measured as a function of fabrication velocity in a sample containing 0.01 wt% KL 68 in 1:1 SR368/499 at 24°C, 27°C, and 30°C. The data in Figure 2C demonstrate that the polymerization threshold increases significantly between 24°C and 30°C at all velocities examined. At all temperatures, the polymerization threshold decreases as the fabrication velocity increases from 20 μm/s to 300 μm/s, and then remains independent of velocity for fabrication velocities up to the highest measured here, 1 cm/s (see also Supplementary Figure S3A). Corresponding logarithmic plots of the threshold power as a function of exposure time are shown in Supplementary Figure S3B.

As a control, we performed temperature-dependent experiments in photoresists containing either Lucirin TPO-L or MGC•HCl as the photoinitiator in 1:1 SR368/499. Lucirin TPO-L is a conventional radical photoinitiator, and at 1 wt% in the photoresist we observed no statistically significant difference in the polymerization threshold between 23°C and 30°C. As shown in Figures 2A,D, a photoresist containing 0.25 wt% MGC•HCl exhibits PROVE behavior at both 23°C and 30°C, and there is no statistically significant difference between the data at the two temperatures. The corresponding logarithmic plots of the threshold power as a function of exposure time are shown in Supplementary Figure S4.

The above results indicate that thermal effects have a strong impact on the photopolymerization dynamics of KL68 photoresists as compared to conventional photoinitiators, and even to PROVE photoinitiators studied previously. To investigate whether temperature influences the feature size, we studied the voxel dimensions as a function of temperature in a 0.01 wt% KL68 photoresist. To create the voxels, we chose a laser power that was above the polymerization threshold at 24°C, and that did not cause any sample damage for an exposure time of 0.5 s, which is comparable to the longest exposure times used in Figure 3. With increasing temperature, reference lines and voxels became less visible, indicating a lower polymerization rate.

Figure 3A shows the voxel height and width as a function of temperature for this photoresist. Both the average voxel height and width decrease with increasing temperature. A temperature increase of 3 °C causes the average voxel height to go from ~1,150 nm to ~980 nm, a decrease of ~17%. The average voxel width goes from ~310 to ~270 nm, a decrease of ~15%. Above 27°C, no polymerization was observed at the laser power used.

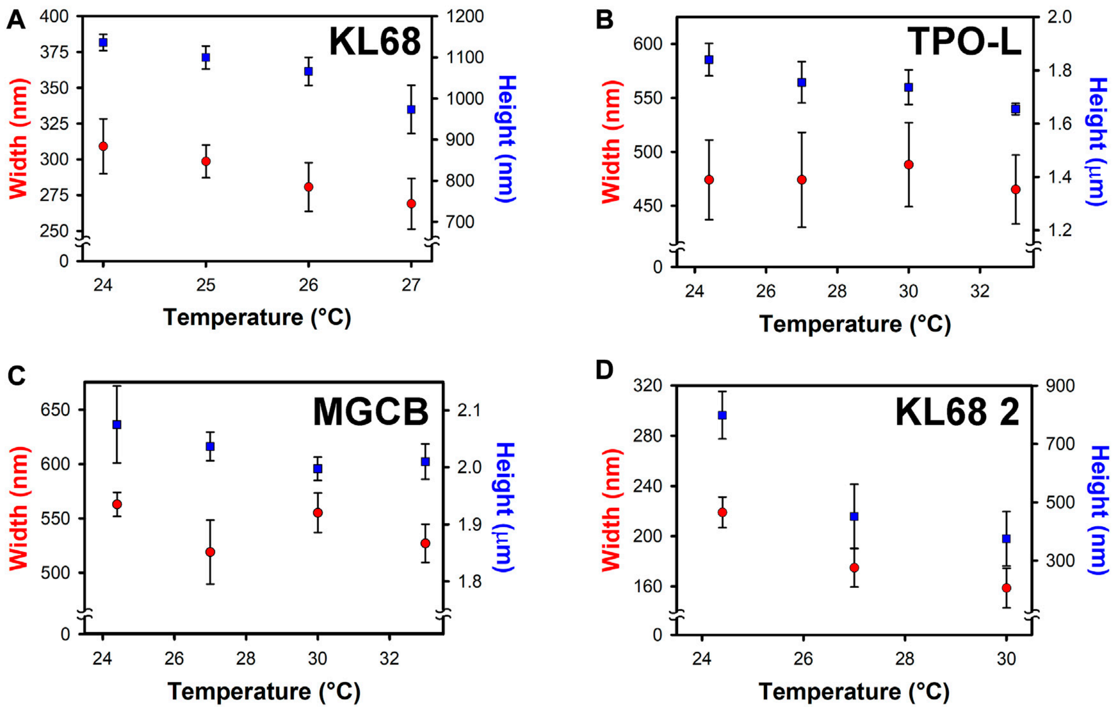

FIGURE 3
Temperature dependence of the voxel height (squares) and width (circles) in a photoresist composed of **(A)** 0.05 wt% KL68 in 1:1 SR368/499 at a fixed irradiance and exposure time. **(B)** Voxel size temperature dependence for 3 wt% Lucirin TPO-L in 1:1 SR368/499. **(C)** Voxel size temperature dependence for 1.5 wt% MGCB in 1:1 SR368/499. **(D)** Voxel size temperature dependence for 0.05 wt% KL68 in a 3:1 mixture of SR351/285. The error bars represent ±1 standard deviation as determined by measuring at least 10 voxels in each case.

To determine whether the observed temperature dependence arises from the photoresist or from the photoinitiator, we performed control experiments with the same monomer mixture using either Lucirin TPO-L or MGCB as the photoinitiator. As shown in Figure 3B, for a 3 wt% Lucirin TPO-L photoresist the average voxel width was nearly constant throughout this temperature range. Some of the voxels were deformed, resulting in a larger deviation in the mean voxel dimensions than in the case of the KL68 photoresist. The results for a 1.5 wt% MGCB photoresist are shown in Figure 3C. The average widths of the voxels ranged between ~560 nm at the lowest temperature to ~520 nm at the highest temperature, a decrease of ~8%. The average voxel height ranged from 2.08 μm at the lowest temperature to 2.00 μm at the highest temperature, a decrease of ~4%. The fact that the two control photoresists exhibit considerably smaller, and likely statistically insignificant, changes in voxel dimensions over a temperature range that is twice as large as the one accessible for the KL68 photoresist indicates that although the photoresist composition might play a minor role in the temperature-dependent behavior of the KL68 photoresists, the photoinitiator itself is the most important contributor. To explore this effect further, we studied KL68 photoresists formulated with different monomers. In Figure 3D we present the voxel dimensions from photoresists that contained 0.05 wt% KL68 in a 3:1 by weight mixture of trimethylolpropane triacrylate (SR351) and tetrahydrofurfuryl acrylate (SR285). Increasing the temperature from 24°C to 30°C causes the average voxel height to decrease by approximately 50%, from ~800 to ~400 nm, and the average width to decrease by ~38%, from ~220 to ~160 nm.

Discussion

The data presented here indicate that the PROVE behavior observed in radical photoresists that incorporate KL68 as the photoinitiator is thermal in origin, in contrast to previously reported photoinitiators in which PROVE behavior arises from photodeactivation of a long-lived intermediate. Furthermore, our experiments demonstrate that this thermal effect can be harnessed to enhance resolution in MAP.

For the same monomer mixture, the results of temperature-dependent exposure-threshold and voxel-size experiments with KL68 as the photoinitiator differ substantially from those for the control photoinitiators, Lucirin TPO-L, MGCB, and MGC•HCl. The magnitude of the thermal effect with KL68 is also dependent on the monomer mixture. These results all support the conclusion that the initiation mechanism for KL68 differs from that of the other photoinitiators studied here. Lucirin TPO-L is a classic, Norrish Type I photoinitiator that undergoes photolysis to create reactive radicals upon electronic excitation (Roffey, 1982). MGCB and MGC•HCl are both believed to eject electrons upon photoexcitation (Stocker et al., 2011). These electrons are solvated in the photoresist, eventually leading to the initiation of radical photopolymerization. Deactivation for these photoinitiators is photoinduced, and is believed to result from back transfer of the solvated electrons (Li et al., 2009).

Photoinitiators such as KL68 are believed to induce radical polymerization *via* the transfer of an electron to a monomer (Cumpston et al., 1999). When an electron is transferred to another molecule, as opposed to being solvated within the photoresist, photoinduced back transfer with near-infrared light may not be able to occur. Furthermore, if polymerization were initiated immediately upon electron transfer, then a reduced rate of polymerization at an increased temperature would be indicative of a decreased electron-transfer rate. Although such a scenario is not impossible, the magnitude of the decrease in polymerization rate in the second photoresist studied here renders this possibility unlikely given that the electron transfer is photoinduced, and therefore would not be expected to have a high barrier (Marcus, 1993).

The most likely explanation for our results is that photoinduced electron transfer from the photoinitiator to a monomer creates a weakly reactive species that can eventually lead to a crosslinking reaction. In this scheme, the mechanism of deactivation would be thermally-induced electron back transfer. Regenerating the neutral photoinitiator in its ground state is an exergonic process, but a barrier must be overcome for this back transfer to occur. The strong temperature dependence of the thermal deactivation rate further suggests that the Gibbs free energy of activation for the back-transfer process is high, a situation that is not uncommon (Marcus, 1993).

The two KL68 photoresist compositions investigated here exhibit substantially different temperature sensitivities. The viscosity of the SR499/SR368 photoresist is orders of magnitude greater than that of the SR351/SR285 photoresist, although both photoresists are more viscous than typical solvents. It is therefore somewhat surprising that the SR351/SR285 photoresist exhibits the stronger temperature dependence in the polymerization rate. A lower viscosity should lead to a greater rate of cage escape for the geminate ion pair created by photoinduced electron transfer (Olmsted and Meyer, 1987). If anything, this rate should increase modestly at higher temperature. Because cage escape prevents back transfer, a higher temperature should increase the efficiency of photoinitiation. We estimate the viscosity of the SR351/SR285 photoresist to be 80 cP, which may be high enough to minimize the importance of cage escape.

The energetics of the electron-transfer process depends upon the species involved. Because the electron must be transferred from an excited KL68 molecule to a monomer, changing the monomers will change the energetics. The SR351/SR285 photoresist may therefore have a higher Gibbs free energy of activation for back transfer, which would lead to a stronger temperature dependence for the voxel size.

We should also consider the fact that the SR351/SR285 photoresist forms a polymer with a considerably lower degree of crosslinking than that created by the SR499/SR368 photoresist, given that the SR285 monomer contains only a single acrylate group. Thus, the gelation point of the SR351/SR285 photoresist occurs at a higher degree of conversion than is the case for the SR499/SR368 photoresist. This difference may also lead to a higher degree of sensitivity to the kinetics of the photoinitiation process in the SR351/SR285 photoresist.

Conclusion

We have studied MAP in acrylic photoresists incorporating the photoinitiator KL68. We find that photoresists containing KL68 exhibit PROVE behavior, which means that the size of fabricated features increases with increasing fabrication velocity. The mechanism for PROVE behavior with KL68 is different from that of previously studied PROVE photoinitiators. In particular, the polymerization efficiency in KL68-based photoresists exhibits a strong temperature dependence.

KL68 is one of many push-pull molecules with high 2-photon absorption cross sections that have been developed as photoinitiators for MAP (Cumpston et al., 1999; Malval et al., 2009; Nazir et al., 2013). Such molecules typically initiate polymerization *via* photoinduced electron transfer, and so may also exhibit the type of temperature-dependent behavior observed here. It would be interesting to explore thermal PROVE behavior in other such systems. The energetics of back transfer, and therefore the temperature dependence of the process, can be tuned by varying both the photoinitiator and the monomers. Still, further work is required to ascertain the exact mechanism of resolution enhancement so that the potential of this phenomenon can be harnessed to full advantage. It will also be of interest to explore whether species such as oxygen and radical inhibitors influence the thermal effects described here. This new mechanism for PROVE behavior presents an intriguing new path towards controlling and improving resolution in MAP.

Data availability statement

The raw data supporting the conclusion of this article will be made available by the authors, without undue reservation.

Author contributions

NL, ZT, SG, RD, BG, DE, and JF contributed to conception and design of the study. NL, ZT, SG, JB, and AS performed the investigation and analyzed the data. NL, ZT, and JF wrote the original draft, and NL, ZT, SG, RD, BG, DE, and JF reviewed and edited the manuscript. JF supervised the project.

Funding

NL acknowledges support by the Research Corporation for Science Advancement (RCSA) and the National Science Foundation (NSF) through a Cottrell Fellowship. The Cottrell Fellowship Initiative is partially funded by a National Science Foundation award to RCSA (CHE-2039044).

Conflict of interest

RD, BG, and DE were employed by 3M Co.

The remaining authors declare that the research was conducted in the absence of any commercial or financial relationships that could be construed as a potential conflict of interest.

Publisher's note

Supplementary material

The Supplementary Material for this article can be found online at: https://www.frontiersin.org/articles/10.3389/fnano.2022.988997/full#supplementary-material

References

Allen, R., Nielson, R., Wise, D. D., and Shear, J. B. (2005). Catalytic three-dimensional protein architectures. *Anal. Chem.* 77, 5089–5095. doi:10.1021/ac0507892

Baldacchini, T., Lafratta, C. N., Farrer, R. A., Teich, M. C., Saleh, B. E. A., Naughton, M. J., et al. (2004). Acrylic-based resin with favorable properties for three-dimensional two-photon polymerization. *J. Appl. Phys.* 95, 6072–6076. doi:10.1063/1.1728296

Basu, S., Cunningham, L. P., Pins, G. D., Bush, K. A., Taboada, R., Howell, A. R., et al. (2005). Multiphoton excited fabrication of collagen matrixes cross-linked by a modified benzophenone dimer: Bioactivity and enzymatic degradation. *Biomacromolecules* 6, 1465–1474. doi:10.1021/bm049258y

Campbell, M., Sharp, D. N., Harrison, M. T., Denning, R. G., and Turberfield, A. J. (2000). Fabrication of photonic crystals for the visible spectrum by holographic lithography. *Nature* 404, 53–56. doi:10.1038/35003523

Camposeo, A., Persano, L., Farsari, M., and Pisignano, D. (2019). Additive manufacturing: Applications and directions in photonics and optoelectronics. *Adv. Opt. Mat.* 7, 1800419. doi:10.1002/adom.201800419

Cumpston, B. H., Ananthavel, S. P., Barlow, S., Dyer, D. L., Ehrlich, J. E., Erskine, L. L., et al. (1999). Two-photon polymerization initiators for three-dimensional optical data storage and microfabrication. *Nature* 398, 51–54. doi:10.1038/17989

Devoe, R. J., Lee, T.-C., Larsen, J. K., Ender, D. A., Sahlin, J. J., Sykora, C. R., et al. (2011). "High photosensitivity two-photon photoresists for large area surface microstructuring," in *MRS Proceedings*. Cambridge, UK: Cambridge University Press, 1365, pp. mrss11–1365-tt09–14

Farrer, R. A., Lafratta, C. N., Li, L., Praino, J., Naughton, M. J., Saleh, B. E., et al. (2006). Selective functionalization of 3-D polymer microstructures. *J. Am. Chem. Soc.* 128, 1796–1797. doi:10.1021/ja0583620

Finkbeiner, S. (2013). "Mems for automotive and consumer electronics," *MRS Proceedings*. Cambridge, UK: Cambridge University Press, 1365, pp. mrss11–1365-tt09–14

Fourkas, J. T., Gao, J., Han, Z., Liu, H., Marmiroli, B., Naughton, M. J., et al. (2021). Grand challenges in nanofabrication: There remains plenty of room at the bottom. *Front. Nanotechnol.* 3, 700849. doi:10.3389/fnano.2021.700849

Klein, S., Barsella, A., Leblond, H., Bulou, H., Fort, A., Andraud, C., et al. (2005). One-step waveguide and optical circuit writing in photopolymerizable materials processed by two-photon absorption. *Appl. Phys. Lett.* 86, 211118. doi:10.1063/1.1915525

Lafratta, C. N., Fourkas, J. T., Baldacchini, T., and Farrer, R. A. (2007). Multiphoton fabrication. *Angew. Chem. Int. Ed.* 46, 6238–6258. doi:10.1002/anie.200603995

Leatherdale, C. A., Schardt, C. R., Thompson, D. S., and Thompson, W. L. (2007). *Multi-photon reactive Compositions with inorganic Particles and Method for fabricating structures*. US 2007/0264501 A1. United States patent application.

Li, L., Gattass, R. R., Gershgoren, E., Hwang, H., and Fourkas, J. T. (2009). Achieving λ/20 resolution by one-color initiation and deactivation of polymerization. *Science* 324, 910–913. doi:10.1126/science.1168996

Li, L., Gershgoren, E., Kumi, G., Chen, W.-Y., Ho, P. T., Herman, W. N., et al. (2008). High-performance microring resonators fabricated with multiphoton absorption polymerization. *Adv. Mat.* 20, 3668–3671. doi:10.1002/adma.200800032

Liaros, N., and Fourkas, J. T. (2020). Methods for determining the effective order of absorption in radical multiphoton photoresists: A critical analysis. *Laser Phot. Rev.* 15, 2000203. doi:10.1002/lpor.202000203

Malval, J.-P., Morlet-Savary, F., Chaumeil, H., Balan, L., Versace, D.-L., Jin, M., et al. (2009). Photophysical properties and two-photon polymerization ability of a nitroalkoxystilbene derivative. *J. Phys. Chem. C* 113, 20812–20821. doi:10.1021/jp9075977

Marcus, R. A. (1993). Electron transfer reactions in chemistry: Theory and experiment (nobel lecture). *Angew. Chem. Int. Ed. Engl.* 32, 1111–1121. doi:10.1002/anie.199311113

Mueller, J. B., Fischer, J., Mange, Y. J., Nann, T., and Wegener, M. (2013). *In-situ* local temperature measurement during three-dimensional direct laser writing. *Appl. Phys. Lett.* 103, 123107. doi:10.1063/1.4821556

Nazir, R., Danilevicius, P., Gray, D., Farsari, M., and Gryko, D. T. (2013). Push–pull acylo-phosphine oxides for two-photon-induced polymerization. *Macromolecules* 46, 7239–7244. doi:10.1021/ma4010988

Ngo, T. D., Kashani, A., Imbalzano, G., Nguyen, K. T. Q., and Hui, D. (2018). Additive manufacturing (3d printing): A review of materials, methods, applications and challenges. *Compos. Part B Eng.* 143, 172–196. doi:10.1016/j.compositesb.2018.02.012

Olmsted, J., and Meyer, T. J. (1987). Factors affecting cage escape yields following electron-transfer quenching. *J. Phys. Chem.* 91, 1649–1655. doi:10.1021/j100290a071

Pan, T., and Wang, W. (2011). From cleanroom to desktop: Emerging micro-nanofabrication technology for biomedical applications. *Ann. Biomed. Eng.* 39, 600–620. doi:10.1007/s10439-010-0218-9

Roffey, C. G. (1982). *Photopolymerization of surface coatings*. New York: Wiley-Interscience.

Rybin, M., Shishkin, I., Samusev, K., Belov, P., Kivshar, Y., Kiyan, R., et al. (2015). Band structure of photonic crystals fabricated by two-photon polymerization. *Crystals* 5, 61–73. doi:10.3390/cryst5010061

Stocker, M. P., Li, L., Gattass, R. R., and Fourkas, J. T. (2011). Multiphoton photoresists giving nanoscale resolution that is inversely dependent on exposure time. *Nat. Chem.* 3, 223–227. doi:10.1038/nchem.965

Sugioka, K., and Cheng, Y. (2014). Femtosecond laser three-dimensional micro- and nanofabrication. *Appl. Phys. Rev.* 1, 041303. doi:10.1063/1.4904320

Sun, H.-B., Takada, K., Kim, M.-S., Lee, K.-S., and Kawata, S. (2003). Scaling laws of voxels in two-photon photopolymerization nanofabrication. *Appl. Phys. Lett.* 83, 1104–1106. doi:10.1063/1.1599968

Sun, H.-B., Tanaka, T., and Kawata, S. (2002). Three-dimensional focal spots related to two-photon excitation. *Appl. Phys. Lett.* 80, 3673–3675. doi:10.1063/1.1478128

Takada, K., Kaneko, K., Li, Y.-D., Kawata, S., Chen, Q.-D., and Sun, H.-B. (2008). Temperature effects on pinpoint photopolymerization and polymerized micronanostructures. *Appl. Phys. Lett.* 92, 041902. doi:10.1063/1.2834365

Tomova, Z., Liaros, N., Gutierrez Razo, S. A., Wolf, S. M., and Fourkas, J. T. (2016). *In situ* measurement of the effective nonlinear absorption order in multiphoton photoresists. *Laser Phot. Rev.* 10, 849–854. doi:10.1002/lpor.201600079

Wu, S.-Y., Yang, C., Hsu, W., and Lin, L. (2015). 3d-Printed microelectronics for integrated circuitry and passive wireless sensors. *Microsyst. Nanoeng.* 1, 15013. doi:10.1038/micronano.2015.13

Yang, L., Münchinger, A., Kadic, M., Hahn, V., Mayer, F., Blasco, E., et al. (2019). On the schwarzschild effect in 3d two-photon laser lithography. *Adv. Opt. Mat.* 7, 1901040. doi:10.1002/adom.201901040

Yokoyama, S., Nakahama, T., Miki, H., and Mashiko, S. (2003). Two-photon-induced polymerization in a laser gain medium for optical microstructure. *Appl. Phys. Lett.* 82, 3221–3223. doi:10.1063/1.1573350

frontiers | Frontiers in Nanotechnology

TYPE Mini Review
PUBLISHED 01 December 2022
DOI 10.3389/fnano.2022.1047055

Label-free designed nanomaterials enrichment and separation techniques for phosphoproteomics based on mass spectrometry

Chandrababu Rejeeth[1,2]* and Alok Sharma[3]

[1]School of Biomedical Engineering, Med-X Research Institute, Shanghai Jiao Tong University, Shanghai, China, [2]Department of Biochemistry, Periyar University, Salem, India, [3]Department of Pharmacognosy, ISF College of Pharmacy, Moga Punjab, India

OPEN ACCESS

EDITED BY
Jan M. Macak,
University of Pardubice, Czechia

REVIEWED BY
Vadivalagan Chithravel,
China Medical University, Taiwan
Nipun Babu,
University of Nebraska-Lincoln,
United States

*CORRESPONDENCE
Chandrababu Rejeeth,
crejee@gmail.com

SPECIALTY SECTION
This article was submitted to Nanomaterials, a section of the journal Frontiers in Nanotechnology

RECEIVED 17 September 2022
ACCEPTED 21 November 2022
PUBLISHED 01 December 2022

CITATION
Rejeeth C and Sharma A (2022), Label-free designed nanomaterials enrichment and separation techniques for phosphoproteomics based on mass spectrometry.
Front. Nanotechnol. 4:1047055.
doi: 10.3389/fnano.2022.1047055

The surface chemical characteristics of nanomaterials have a substantial impact on the affinity probe used to enrich proteins and peptides for MALDI-MS analysis of a real human sample. Detecting phosphoproteins involved in signalling is always difficult, even with recent developments in mass spectrometry, because protein phosphorylation is often temporary from complicated mixtures. This review summarizes current research on the successful enrichment of various intriguing glycoproteins and glycol peptides using surface affinity materials with distinctive qualities such as low cost, excellent structural stability, diversity, and multifunction. As a consequence, this review will provide a quick overview of the scholars from various backgrounds who are working in this intriguing interdisciplinary field. Label-free cancer biomarkers and other diseases will benefit from future challenges.

KEYWORDS

label-free, nanometerials, MALDI-MS, proteins, peptides

Introduction

Phosphorylation is the main post-translational protein adjustment, influencing signal transduction, quality articulation, cell cycle, cytoskeletal guideline, and apoptosis, among other cell flagging pathways (Wang et al., 2014; Müller, 2018; Ramazi and Zahiri, 2021). Phosphoproteomics has been a prominent study issue since it is critical for interpreting biological changes and discovering new techniques to identify and treat sickness (Arrington et al., 2017; Farooq et al., 2022). Enrichment of objective biomolecules is usually required in today's biological examinations because direct detection of target biomolecules is often difficult due to numerous typical constraints (e.g., low abundance of objective biomolecules, the presence of contaminants) (Angel et al., 2012; Rejeeth et al., 2018). Affinity materials with unique benefits such as reasonable price range, amazing physical consistency, diversity, and functionality have been widely used for enriching objective biomolecules from complicated biological samples based on the peculiar affinity communication systems between the affinity materials and the objective biomolecules (Limo et al., 2018; Zhou and Pang, 2018). In response of the fast development in material science, particularly the development of nanotechnologies, a variety of excellent affinity materials have been developed to enrich different biological molecules (Ray et al., 2010; Tiambeng et al., 2020). Interestingly, in the field of phosphoproteomics, affinity materials for increasing phosphorylated proteins/ peptides are getting a lot of attention (Wang et al., 2015) (Riley and Coon, 2016).

Mass spectrometry (MS) with great specificity and faster data processing has been the most dynamic and crucial tool for phosphoproteomics research in recent years (Iwamoto and Shimada, 2018; Macklin et al., 2020). Regardless, due to significant issues such as the low abundance of phosphorylated proteins/peptides resulting from high heterogeneity and low stoichiometry of protein phosphorylation, the sign victory impact of high-overflow parts (e.g., nonphosphorylated atoms, lipids, and salts), and the low ionisation productivity of phosphorylated proteins/ peptides in MS examination, direct MS-based phosphoproteomics investigation is not recommended (Goel et al., 2018; Bekker-Jensen et al., 2020). As a result, performing preliminary analysis before MS has become a crucial step in efficiently reducing the complexity of proteome preliminaries and concentrating phosphorylated proteins/ peptides to improve MS investigation outcomes (Angel et al., 2012). Enrichment analysis prior to MS has become a vital step in successfully lowering the complexity of proteome trials and concentrating phosphorylated proteins/peptides in order to improve MS analysis outcomes up to this point (Nakayasu et al., 2021). The employment of a linker molecule to render metal ions impotent on a porosity bead, polymer bead, or nanomaterial is one of the most extensively used technologies, and great effort has gone into constructing the IMAC material (Colón and Furukawa, 2020). Linkers like iminodiacetic acid and nitrilotriacetic acid are commonly used to chelate metal ions. The attached metal ions were easily washed away during the sample loading and washing procedure due to the comparatively anaemic interaction, dramatically lowering the enrichment efficiency (Rodzik et al., 2020) (Fang et al., 2017).

Unfortunately, intrinsic difficulties such as high-cost antibodies, limited universal applicability, and biological sample decay hamper these approaches (Morofuji et al., 2016; Zhou and Rossi, 2017). Affinity material-based enrichment approaches, on the other hand, have a number of advantages, including universality, low cost, and minimal impact on the structural integrity of phosphorylated proteins/peptides (Wang et al., 2015; Rejeeth et al., 2018; Zhang et al., 2019; Rejeeth et al., 2022). However, affinity material-based approaches still face nonspecific binding of nonphosphorylated proteins/peptides, which can significantly hamper the selective enrichment of phosphorylated proteins/peptides (Delom and Chevet, 2006; Rainer and Bonn, 2015). Developing high-performance affinity materials remains the most important and broadly used way to improve the enrichment performance of affinity material-based strategies, despite the addition of some auxiliary measures (e.g., chemical treatment of the biological sample, pH directive of loading buffers, and additive addition) (Gabriel et al., 2019; Keeble Anthony et al., 2019).

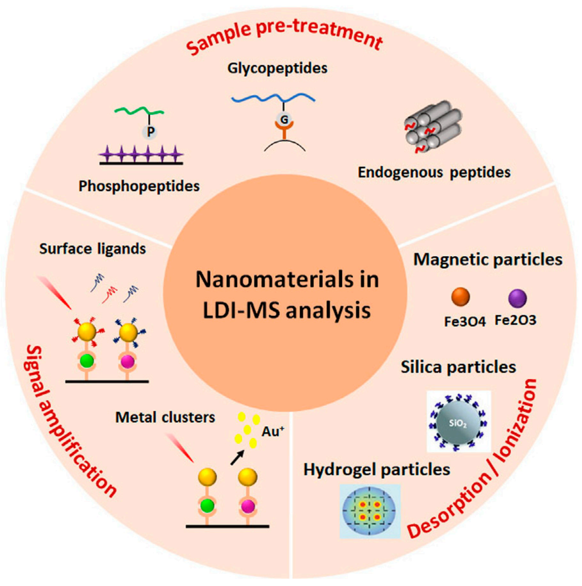

SCHEME 1
Schematic illustration of phosphopeptide enrichment for MS detection using diverse affinity materials.

The present state of affinity materials for the enrichment of phosphorylated proteins and peptides is discussed in this review. The focus will be on the design and creation of affinity materials, as well as the presentation and discussion of relevant enrichment methods. The difficulties and future directions of this discipline will also be highlighted. Because several assessments on specific topics, such as MS technology, enrichment conditions, and enrichment protocols, have already been completed, the details of some related issues, such as MS technology, enrichment conditions, and enrichment protocols, are not presented here.

Affinity-bound nanoparticles: Manufacturing and properties

Biomolecule-conjugated nanoparticles (NPs) have been shown to have promising uses in bioanalysis. The reviewed affinity materials are grouped into three types depending on the species of the affinity site: magnetic-based affinity materials, silica-based affinity matrials and hydrogel-based affinity materials (Scheme 1). In the meantime, the enrichment

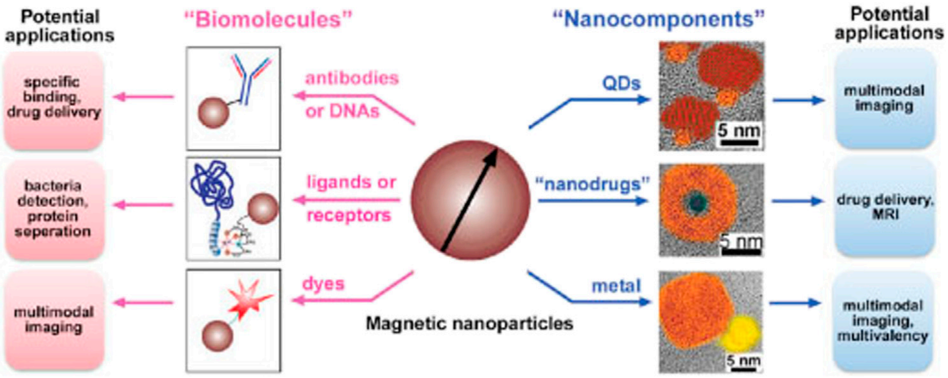

FIGURE 1
The scheme illustrates two strategies to fabricate multifunctional magnetic nanoparticles and their potential applications. Reproduced from ref 30. Copyright 2003 American Chemical Society.

processes utilised by these affinity materials will be described. In general, the three particles involve the use of various reducing agents, formation management, size preparation, and the discovery of some interesting previous literature reports for medication and gene delivery against various cancers and other ailments.

Magnetic nanoparticles

Magnetic nanoparticles are made up of an inorganic core containing paramagnetic/superparamagnetic structures like magnetite (Fe3O4) or maghemite (Fe2O3), as well as a shielding layer, which is often made up of polymers and gives colloidal stability and solubility (Gao et al., 2009; Wu et al., 2015). Magnetic nanoparticles (MNPs) have been studied for a variety of uses. In order to provide imaging, treatments, and targeting modalities, MNPs must be encased in biocompatible materials, primarily polymeric ligands containing chemical functional groups to conjugate biomolecules and ligands (See Figure 1).

Due to their unique properties and modalities in fields such as imaging, drug administration, magnetic separation, and purification, magnetic particles, particularly superparamagnetic MNPs, have increased in prominence in biomedical research in recent decades (Ali et al., 2021). Superparamagnetic iron oxide nanoparticles (SPIONs) have been used in tumour imaging, stem cell detection, metastatic breast cancer imaging, Alzheimer's disease detection, lymph node imaging, and many more imaging applications as an intrinsic T2 magnetic resonance imaging (MRI) contrast agent (Cheng et al., 2014; Fatima et al., 2021). Readers can be enticed to look into extensive evaluations in this sector. SPIONs have been used in a variety of applications, including chemotherapeutics, gene transfer, and hyperthermia (Musielak et al., 2019; Suciu et al., 2020).

Magnetic separation has significant potential in biological research because it allows for targeted capture that is selective, sensitive, and regulated (Yildiz, 2016). Magnetic separation, which employs an external magnetic field to trap target molecules with MNPs *via* affinity interaction, may be more time, labour, and yield efficient than complex and time-consuming chromatographic separations and purifications (Zborowski and Chalmers, 2011; Musielak et al., 2019). To create a design a superparamagnetic-magnetically responsive only in the presence of an external magnetic field-adsorbent or catcher with high magnetization must be used with proper features such as stability, biocompatibility, and having binding units affinity ligands to capture the target of interest with high specificity and selectivity, and a superparamagnetic-magnetically responsive only in the presence of an external magnetic field-adsorbent or catcher with high magnetization must be used with proper features such as stability (Suciu et al., 2020).

The immobilisation of affinity ligands on the surface of particles toward the target proteins is the basis for magnetic particle-based separation of proteins such as antibodies, biomarkers, and enzymes, and a comprehensive list of applications, including homemade and commercial magnetic particles, has been reviewed elsewhere (Mani et al., 2011; Yildiz, 2016). On the other hand, the goal of this article is to discuss recent research in this field. Immobilized metal affinity chromatography (IMAC) has long been a favoured enrichment method in phosphoproteomics (Ndassa et al., 2006). Apart from electronic attraction, IMAC is prepared using metal cations with unoccupied organisation orbitals, and chelation between the immobilised metal cations and the phosphoryl oxygen in phosphorylated proteins/peptides is the primary enrichment mechanism (Balmant et al., 2016). The matrix supports carrying chelating ligands are normally synthesised first, and then the metal cations are immobilised onto the chelating ligands to form IMAC affinity materials. Cu2+, Zn2+, Fe3+, Ga3+, Al3+,

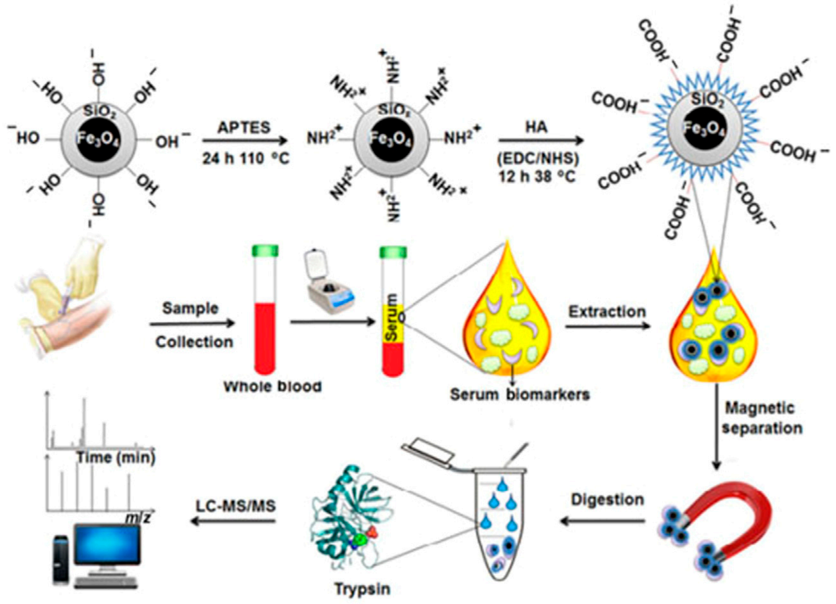

FIGURE 2
Schematic illustration for the preparation of Fe3O4@SiO2@HA particles and their application in the extraction and detection of biomarkers from human serum samples by MS. Reproduced from ref 7. Copyright 2018 Springer.

Ti4+, and Zr4+ are some of the metal cations that have been employed in IMAC thus far. In traditional IMAC materials, the most frequent metal cations are Fe3+ and Ga3+ (Ruprecht et al., 2015). Antibody-free approaches are promising and need to be developed for real-case applications in serum to address the limitations of antibody-based techniques in terms of robustness, expense, and throughput. In this work, we demonstrated a novel approach using hyaluronic acid (HA)-modified materials/devices for the extraction, detection, and profiling of serum biomarkers *via* ligand-protein interactions. Figure 2 shown using hyaluronic acid (HA)-modified materials/devices (e.g., Fe_3O^4@SiO^2@HA) (Rejeeth et al., 2018).

Due to the unusual coordination specificity of metal (IV)-phosphate chemistry, Zr4+-IMAC and Ti4+-IMAC with phosphate group as chelating ligands displayed greater selectivity for phosphopeptides than regular Fe3+-IMAC beads (Ruprecht et al., 2015). Iminodicitic acid (IDA) and nitrilotriacetic acid (NTA) are two chelating ligands that are frequently employed to immobilise metal cations (e.g., Fe3+ and Ga3+) (Blankespoor et al., 2005). Sample loading and washing could impair the immobilised metal cations since each metal cation can only bind to one NTA or IDA ligand. Figure 3 discusses, scientists are on the lookout for new chelating ligands with greater chelating ability. As a result, novel, extremely effective chelating ligands such as arsenate (AsO32), phosphate (PO32), adenosine triphosphate (ATP), and dopamine have proved successful in immobilising metal cations, particularly Ti4+ and Zr4+ (Yan et al., 2013).

As affinity probes, magnetic nanoparticles (Fe3O4@Al2O3) efficiently concentrate polyhistidine (His)-tagged proteins/peptides from complicated materials (Zhang et al., 2013). This method can be used to quickly determine whether or not a sample contains His6-tagged organisms. Cell lysates containing recombinant Shiga-like toxins labelled with His6 were used as samples to demonstrate that this technology may be used to examine exceedingly complex samples (Schmit et al., 2019). The entire analysis procedure takes around 10 min, including on-plate enrichment and enzymatic digestion, followed by MALDI-MS analysis (Rühl et al., 2017). For similar reasons, magnetic nanoparticles (MNP) with amine functionalization are roughly four times smaller than those previously utilised. Researchers compared the enrichment performance of the magnetic nanoparticle approach to a commercially available glycopeptide enrichment kit offered by EMD Millipore using tandem mass tags from Thermo Scientific (Bodnar and Perreault, 2013). The MNP approach is easy to apply and takes less than 10 min, and it enriches sialylatedglycopeptides quantitatively and qualitatively more than a commercially available kit (Bodnar and Perreault, 2013). Another study used magnetic nanoparticles modified with polyethyleneimine (PEI) as a highly selective affinity probe. The particles collected phosphopeptides from a tryptic digest of a protein mixture that contained 0.07% (mole/mole) phosphoproteins, which is the highest selectivity ever observed. In matrix-assisted laser desorption/ionization mass spectrometry analysis, the detection limits of phosphopeptides generated from bovine casein and casein were 5 fmol (Chen et al.,

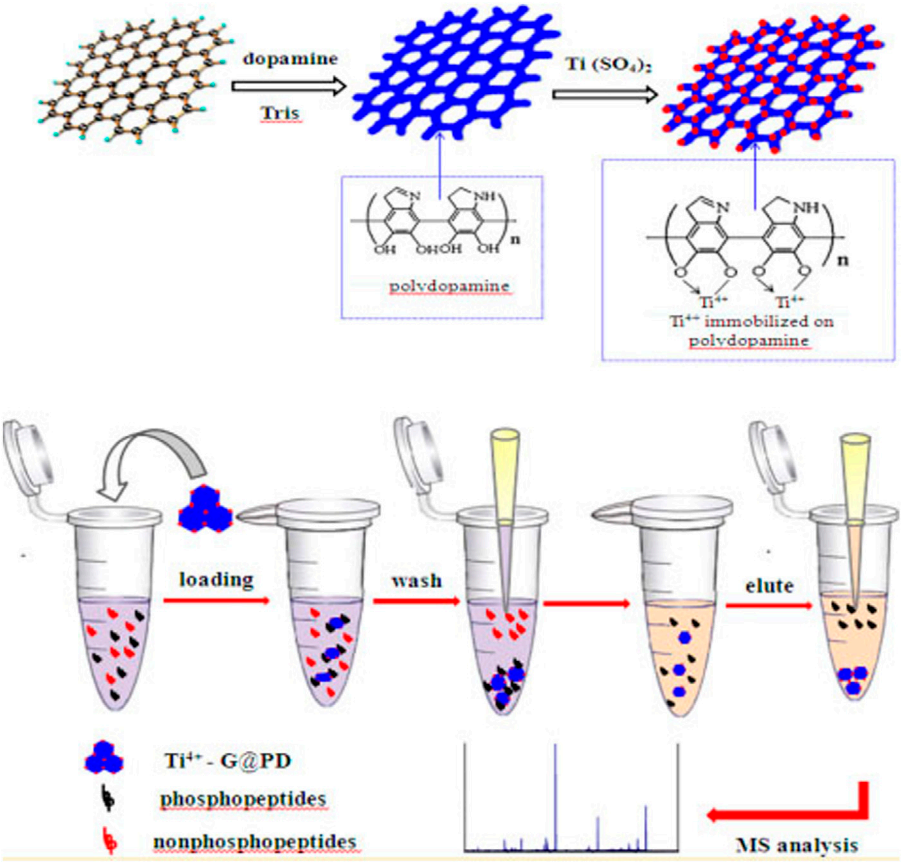

FIGURE 3
The Ti4+-G@PD with the above unique properties was anticipated to have excellent performance for the selective enrichment of phosphopeptides, which would be highly beneficial for mass spectrometric analysis. Reproduced from ref 45. Copyright 2003 American Chemical Society.

2011). This method was also utilised to boost the amount of phosphopeptides in a non-fat milk protein digest. Using antibodies against target peptides, MNPs could concentrate serum biomarker peptide fragments. MNPs were conjugated to polyclonal antibodies against the tumour necrosis factor (TNF) peptide and utilised to collect TNF from a TNF-spiked blood sample, followed by MS analysis (Dunning and Lame, 2018). These effective applications to single glycoproteins and complete proteome combinations collected from physiological fluids revealed magnetic practical flexibility that is unrivalled.

Silica particles

Two synthesis methods for silica nanoparticles include the Stober process and reverse micro emulsion (Koźlecki et al., 2016). A water in oil (w/o) micro emulsion is formed up of a homogeneous mixture of water, oil, and surfactant molecules (Koźlecki et al., 2016). The Stober method involves hydrolysis and condensation of siloxane precursors (such as tetraethylorthosilicate TEOS) with ethanol and ammonia to produce silica particles (Kim and Kim, 2002). This method has been used to incorporate a variety of organic colour chemicals. They are classified as spherical, mesoporous, or macrospores in biomedical applications (Borzęcka et al., 2022). Spherical silica NPs, on the other hand, carry cargo through encapsulation or conjugation. Mesopores (pore sizes ranging from 2 to 30 nm) and macrospores are the two types of pores found in mesoporous silica NPs (50–100 nm pore size) (Narayan et al., 2018). Physical and chemical adsorption are frequently utilised to disperse active payloads. The release profile of payloads delivered by porous silica NPs is controlled by chemical linkers or silica matrix degradation, whereas the "gatekeeper" strategy of modifying the inner surface of the pores to control the binding affinity with drugs controls the release profile of payloads delivered by porous silica NPs (Jafari et al., 2019).

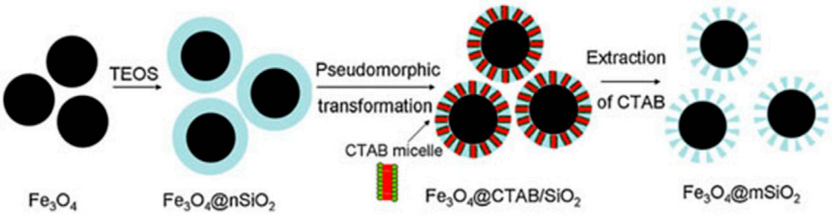

FIGURE 4
Schematic diagram for the preparation of monodisperse Fe3O4@mSiO2 microspheres. Reproduced from ref 63. Copyright 2012 Elsevier.

MO modified mesoporous silica composites with various affinity sites were made using simple techniques that took into account the unique qualities of mesoporous silica (e.g., size exclusion effect, high surface area, easy modifiability, and stable skeleton) as well as MO affinity ability (e.g., solgel) (Mamaeva et al., 2013). These compounds can extract phosphopeptides from complicated biosamples quickly and selectively (e.g., human serum). Using mesoporous silica particles, titanium phosphonate was employed to selectively extract phosphopeptides from complicated peptide and protein combinations (Kim et al., 2010). Using MALDI-TOFMS detection, the limit of detection for phosphopeptides from -casein and standard phosphopeptide spikes in human serum was as low as 1.25 fmol (Karayel et al., 2020). The modified mesoporous silica particles were then utilised to enrich phosphopeptides from the serum of patients with hepatocellular carcinoma and healthy persons, which were subsequently evaluated using MALDI-TOFMS. MALDI-TOF MS/MS results for blood phosphopeptide profiling were also confirmed utilising a combination of isobaric tagging for relative and absolute quantitative labelling (Rauniyar and Yates, 2014). The substantial disparities in serum phosphopeptide profiling between cancer patients and healthy people emphasise the technique's utility in cancer detection and biomarker development. This approach could be applied to a wide range of biological samples and disorders. Microspheres with a Fe3O4@nSiO2 core and a perpendicularly oriented mesoporous SiO2 shell (Fe3O4@nSiO2@mSiO2) were used to develop a novel peptide enrichment approach (Chen et al., 2010). The magnetic receptivity of the Fe3O4@nSiO2@mSiO2 microspheres is advantageous, as it speeds up and simplifies the enrichment process. The microspheres' highly organised nanoscale pores (2 nm) and high surface areas were shown to have a good size-exclusion effect for peptide adsorption. A Fe3O4@nSiO2@mSiO2 microsphere was also investigated. The microspheres were used to concentrate endogenous peptides in rat brain extract on a large scale. After enrichment, the sample was examined with an Automated nano-LC-ESI-MS/MS, revealing a total of 60 distinct peptides (Bian et al., 2020). Figure 4 shown the Fe3O4@nSiO2@mSiO2 microspheres are a viable contender for selectively separating and enriching endogenous peptides from difficult biological samples due to their simple and low-cost production as well as the convenient and efficient enrichment procedure (Zhu et al., 2012).

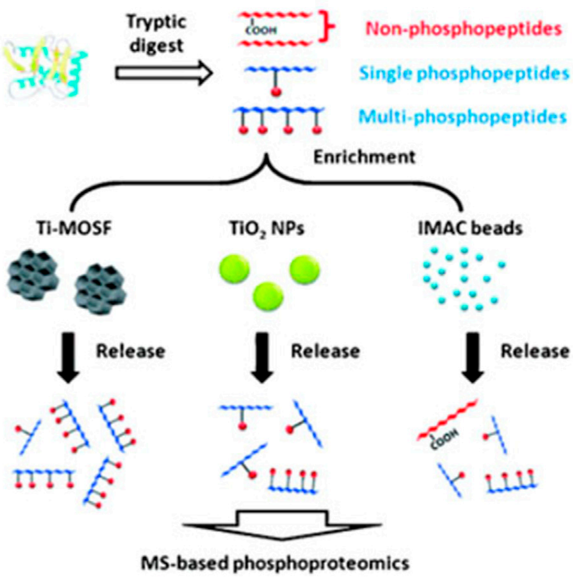

FIGURE 5
Schematic illustration of strategies employed for enriching phosphopeptides. Reproduced from ref 66. Copyright 2009 Wiley.

Phosphate-imprinted mesoporous silica nanoparticles (MSNs) as a sorbent for phosphopeptide selective enrichment and an offline combination with matrix-assisted laser desorption ionization-time-of-flight mass spectrometry (MALDI-TOF MS) for very efficient protein phosphorylation analysis (Rahi et al., 2016). To make the molecule, a new technology called dual-template docking guided molecular imprinting was applied (DTD-OMI). High phosphopeptide selectivity, interference tolerance, rapid binding equilibrium, and substantial binding capacity were among the attributes of the molecularly imprinted

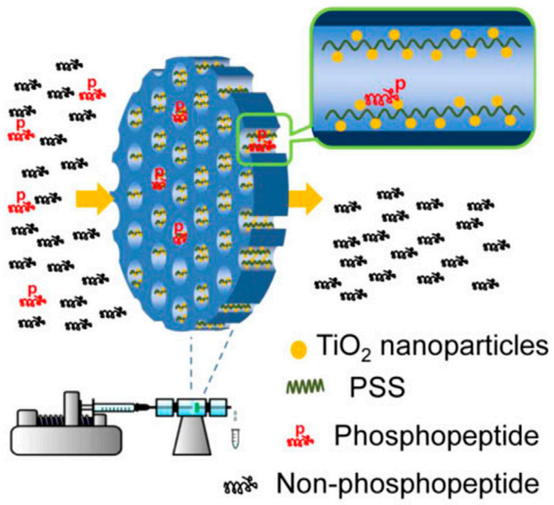

FIGURE 6
Schematic illustration of strategies employed for enriching phosphopeptides. Reproduced from ref 69. Copyright 2013 American Chemical Society.

mesoporous material produced, making it an ideal sorbent for selective phosphopeptide enrichment.

Macroporous silica with open big pores outperforms mesoporous silica in terms of MOs loading and subsequent phosphorylated protein/peptide binding to affinity composites. For chromatography, a mechanically stable silica microparticle with macrosized interior pores (1.6 m particles with 100 nm pores) was developed (Mann et al., 2013). Concanavalin A (Con A) and Aleuriaaurantia lectin (AAL) were used to derivatize the material, and the binding capabilities were examined using conventional glycoproteins. Con A was able to bind 75 g of a common glycoprotein in a 50 1 mm column, demonstrating good binding capacity for microaffinity enrichment. In a 50 1 mm column, Con A was able to bind 75 g of a common glycoprotein, exhibiting good binding capacity for microaffinity enrichment (Mann et al., 2013). Importantly, in some mesoporous materials with lengthy channels, the open macroporous structure can allow effective mass transmission while avoiding the so-called "shadow effect." Figure 5 shown to make Al-MOSF and Ti-MOSF, Al2O3 and TiO2 were placed onto macroporous ordered silica foam, respectively (MOSF) (Wan et al., 2009).

Hydrogel particles

Using cellulose as a matrix, a new simple synthetic technique for producing magneticcellulose or nanocomposite microspheres was successfully developed. The cellulose matrix's micro-nano porous architectures were critical in *in situ* synthesising TiO2 nanoparticles while preserving TiO2's basic structure and character, enabling for enrichment in a hostile environment (Montoya et al., 2011). Due to their strong capture capability, the novel magnetic cellulose/ TiO2 nanocomposite microspheres (MCTiMs) showed high effectiveness for selective extraction of trace phosphopeptides from tryptic digest of alp-casein and human serum samples. With a molar ratio of 1:1000, MCTiMs were used to preferentially concentrate phosphopeptides from alpha-casein and BSA mixtures, which was significantly better than commercial TiO2 nanoparticles (Kupcik et al., 2019). The Figure 6 shown TiO2 nanoparticles implanted in the magnetic cellulose microspheres had high specific surface areas and a high adsorbing nature, resulting in a strong Lewis acid-base interaction, according to our findings. As a result, MCTiMs will

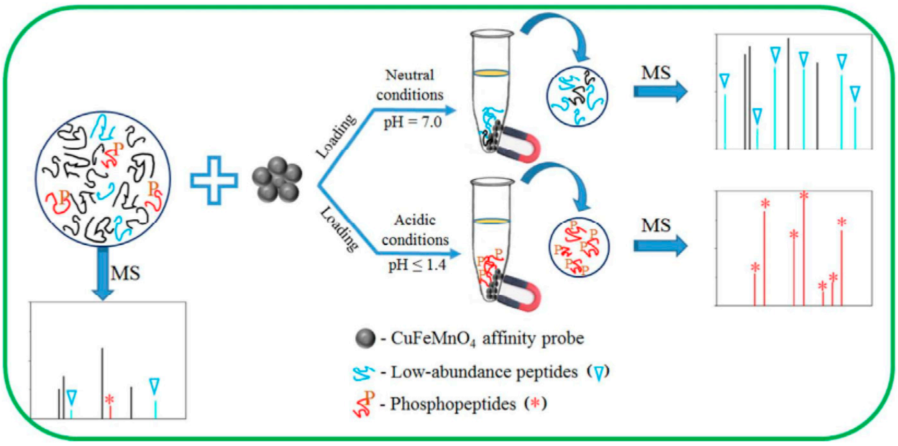

FIGURE 7
Schematic illustration of strategies employed for enriching phosphopeptides. Reproduced from ref 72. Copyright 2017 American Chemical Society.

be a great choice for phosphopeptide enrichment in complex systems using MS (Tan et al., 2013).

For the first time, magnetic cellulose/TiO2 nanocomposite microspheres (MCTiMs) were made using a two-step process. In the first stage, magnetic cellulose microspheres (MCMs) were created by microwave heating cellulose/Fe3O4 colloidal micro-droplets efficiently to induce the sol-gel transition (Luo et al., 2009). MCTiMs were generated in the second step by dispersing MCMs in TiO2 precursor solution and then generating TiO2 nanoparticles *in situ* in MCMs' micro-nano pores. Meanwhile, the amount of TiO2 in MCTiMs may be controlled by changing the precursor solution feeding volume to make MCTiMs-1, MCTiMs-2, MCTiMs-3, and MCTiMs-5, a series of MCTiMs (Duan et al., 2015). Meanwhile, the amount of TiO2 in MCTiMs may be controlled by changing the precursor solution feeding volume to make MCTiMs-1, MCTiMs-2, MCTiMs-3, and MCTiMs-5, a series of MCTiMs. The growth of a more compact shell layer at a higher level of TBOT resulted in an impediment for TBOT diffusing into the microspheres due to the uncontrolled creation of TiO2 nanoparticles on the surface of microspheres. The successful application of phosphopeptide enrichment necessitates the use of microspheres with excellent magnetic response qualities. Using an external magnetic field, MCTiMs with a sensitive magnetic response can be swiftly removed from peptide solutions, allowing for convenient recycling. A tryptic digest of alpha-casein, a combination of alpha casein and BSA, and fresh human blood samples were used to demonstrate the selectivity of MCTiMs for phosphopeptides. The process and procedure for phosphopeptide enrichment utilising MCTiMs are proposed. The TiO2 nanoparticles were firmly attached in the pores of MCTiMs, and the magnetic cellulose matrix's pore wall safeguarded their structure and reaction activity. During the incubation process, phosphopeptides diffused rapidly into the magnetic cellulose microspheres, colliding with TiO2 nanoparticles and quickly anchoring on the TiO2 surface *via* Lewis reaction. Enrichment was successful and effective. Based on Lewis acid-base interaction, TiO2 with a positively charged surface can selectively adsorb phosphorylated species at acidic pH, and TiO2 with a large surface area has a stronger binding ability on phosphopeptides (Tan et al., 2013).

Magnetic celluloseTiO2 was developed by Duan's research team for selective phosphopeptide enrichment. Magnetic cellulose microspheres were created using Solgel (MCMs). The transition of cellulose Fe3O4 colloidal microdroplets is caused by microwave heating. Then MCMs were distributed in TiO2 precursor solution and *in situ* manufactured TiO2 nanoparticles within the porous structure of MCMs to make magnetic celluloseTiO2nanocomposite microspheres (MCTiMs) (Long et al., 2017). MCTiMs had their magnetic hysteresis curve reduced, but they still allowed for efficient separation under external magnetic fields. Using the Lewis acid-base method, the phosphopeptides could be efficiently bonded to the nanosphere and separated, as shown in Figure 7.

Conclusion

A wide range of affinity materials for enrichment of phosphorylated proteins/peptides based on diverse enrichment processes have been developed during the last few decades. Despite significant progress, the majority of these materials' applications are still in their infancy. The bulk of these affinity materials were tested utilising similar or even rigid assessment systems (e.g., digest mixes of standard pure phosphorylated and nonphosphorylated proteins, human serum, and nonfat milk), demanding more extensive and precise testing. It is important to note that proper enrichment conditions, such as pH and solvent composition, are also necessary for effective phosphoproteomics uses of these materials. Furthermore, because different affinity materials might have complementary enrichment capability, a mixture of affinity materials can be used when a comprehensive analysis of exceedingly complicated biosamples is required. Furthermore, the interaction mechanisms and concepts between affinity materials and target phosphorylated molecules are critical for the design of desired efficient affinity materials, though the bulk of these are unknown and require further research.

A substantial amount of research will be committed to the enhancement and production of affinity materials to meet the needs of phosphoproteomics analysis, in tandem with the development of phosphoproteomics analysis. More powerful multifunctional affinity materials are projected to come from the combination of established preparation methods and emerging technologies (e.g., nanotechnology). Understanding the basic microscopic enrichment methods and principles could be another challenge, thus further research will be done in this area to provide theoretical guidance for the design and fabrication of powerful affinity materials.

Author contributions

All authors listed have made a substantial, direct, and intellectual contribution to the work and approved it for publication.

Acknowledgments

The authors are gratefully acknowledged by Dr. D. S. Kothari Postdoctoral Fellowship, No. F.4-2/2006 (BSR)/BL/19-20/0217 from the University Grants Commission (UGC) of India and Periyar University, Salem, India for providing the necessary facilities in this study.

Conflict of interest

The authors declare that the research was conducted in the absence of any commercial or financial relationships that could be construed as a potential conflict of interest.

Publisher's note

References

Ali, A., Shah, T., Ullah, R., Zhou, P., Guo, M., Ovais, M., et al. (2021). Review on recent progress in magnetic nanoparticles: Synthesis, characterization, and diverse applications. *Front. Chem.* 9, 629054. doi:10.3389/fchem.2021.629054

Angel, T. E., Aryal, U. K., Hengel, S. M., Baker, E. S., Kelly, R. T., Robinson, E. W., et al. (2012). Mass spectrometry-based proteomics: Existing capabilities and future directions. *Chem. Soc. Rev.* 41 (10), 3912–3928. doi:10.1039/c2cs15331a

Arrington, J. V., Hsu, C.-C., Elder, S. G., and Andy Tao, W. (2017). Recent advances in phosphoproteomics and application to neurological diseases. *Analyst* 142 (23), 4373–4387. doi:10.1039/c7an00985b

Balmant, K. M., Zhang, T., and Chen, S. (2016). Protein phosphorylation and redox modification in stomatal guard cells. *Front. Physiol.* 7, 26. doi:10.3389/fphys.2016.00026

Bekker-Jensen, D. B., Bernhardt, O. M., Hogrebe, A., Martinez-Val, A., Verbeke, L., Gandhi, T., et al. (2020). Rapid and site-specific deep phosphoproteome profiling by data-independent acquisition without the need for spectral libraries. *Nat. Commun.* 11 (1), 787. doi:10.1038/s41467-020-14609-1

Bian, Y., Zheng, R., Bayer, F. P., Wong, C., Chang, Y.-C., Meng, C., et al. (2020). Robust, reproducible and quantitative analysis of thousands of proteomes by micro-flow LC–MS/MS. *Nat. Commun.* 11 (1), 157. doi:10.1038/s41467-019-13973-x

Blankespoor, R., Limoges, B., Schöllhorn, B., Syssa-Magalé, J.-L., and Yazidi, D. (2005). Dense monolayers of metal-chelating ligands covalently attached to carbon electrodes electrochemically and their useful application in affinity binding of histidine-tagged proteins. *Langmuir* 21 (8), 3362–3375. doi:10.1021/la047139y

Bodnar, E. D., and Perreault, H. (2013). Qualitative and quantitative assessment on the use of magnetic nanoparticles for glycopeptide enrichment. *Anal. Chem.* 85 (22), 10895–10903. doi:10.1021/ac402332z

Borzęcka, W., Pereira, P. M. R., Fernandes, R., Trindade, T., Torres, T., and Tomé, J. P. C. (2022). Spherical and rod shaped mesoporous silica nanoparticles for cancer-targeted and photosensitizer delivery in photodynamic therapy. *J. Mat. Chem. B* 10, 3248–3259. doi:10.1039/d1tb02299g

Chen, C.-T., Wang, L.-Y., and Ho, Y.-P. (2011). Use of polyethylenimine-modified magnetic nanoparticles for highly specific enrichment of phosphopeptides for mass spectrometric analysis. *Anal. Bioanal. Chem.* 399 (8), 2795–2806. doi:10.1007/s00216-010-4623-6

Chen, H., Liu, S., Yang, H., Mao, Y., Deng, C., Zhang, X., et al. (2010). Selective separation and enrichment of peptides for MS analysis using the microspheres composed of Fe3O4@nSiO2 core and perpendicularly aligned mesoporous SiO2 shell. *Proteomics* 10 (5), 930–939. doi:10.1002/pmic.200900553

Cheng, K., Yang, M., Zhang, R., Qin, C., Su, X., and Cheng, Z. (2014). Hybrid nanotrimers for dual T1 and T2-weighted magnetic resonance imaging. *ACS Nano* 8 (10), 9884–9896. doi:10.1021/nn500188y

Colón, Y. J., and Furukawa, S. (2020). Understanding the role of linker flexibility in soft porous coordination polymers. *Mol. Syst. Des. Eng.* 5 (1), 284–293. doi:10.1039/c9me00117d

Delom, F., and Chevet, E. (2006). Phosphoprotein analysis: From proteins to proteomes. *Proteome Sci.* 4 (1), 15. doi:10.1186/1477-5956-4-15

Duan, J., He, X., and Zhang, L. (2015). Magnetic cellulose–TiO2 nanocomposite microspheres for highly selective enrichment of phosphopeptides. *Chem. Commun.* 51 (2), 338–341. doi:10.1039/c4cc08442j

Dunning, C. M., and Lame, M. E. (2018). *Development of a hybrid immunoaffinity-LC-MS/MS method for the quantification of active biotherapeutics targeting TNF-α in serum.* 720006317. Waters Corporation.

Fang, X., Liu, Y., Jimenez, L., Duan, Y., Adkins, G. B., Qiao, L., et al. (2017). Rapid enrichment and sensitive detection of multiple metal ions enabled by macroporous graphene foam. *Anal. Chem.* 89 (21), 11758–11764. doi:10.1021/acs.analchem.7b03336

Farooq, A., Bhat, K. A., Mir, R. A., Mahajan, R., Nazir, M., Sharma, V., et al. (2022). Emerging trends in developing biosensor techniques to undertake plant phosphoproteomic analysis. *J. Proteomics* 253, 104458. doi:10.1016/j.jprot.2021.104458

Fatima, A., Ahmad, M. W., Al Saidi, A. K. A., Choudhury, A., Chang, Y., and Lee, G. H. (2021). Recent advances in gadolinium based contrast agents for bioimaging applications. *Nanomater. (Basel)* 11 (9), 2449. doi:10.3390/nano11092449

Gabriel, J., Höfner, G., and Wanner, K. T. (2019). A library screening strategy combining the concepts of MS binding assays and affinity selection mass spectrometry. *Front. Chem.* 7, 665. doi:10.3389/fchem.2019.00665

Gao, J., Gu, H., and Xu, B. (2009). Multifunctional magnetic nanoparticles: Design, synthesis, and biomedical applications. *Acc. Chem. Res.* 42 (8), 1097–1107. doi:10.1021/ar9000026

Goel, R. K., Paczkowska, M., Reimand, J., Napper, S., and Lukong, K. E. (2018). Phosphoproteomics analysis identifies novel candidate substrates of the nonreceptor tyrosine kinase, src-related kinase lacking C-terminal regulatory tyrosine and N-terminal myristoylation sites (SRMS). *Mol. Cell. Proteomics* 17 (5), 925–947. doi:10.1074/mcp.ra118.000643

Iwamoto, N., and Shimada, T. (2018). Recent advances in mass spectrometry-based approaches for proteomics and biologics: Great contribution for developing therapeutic antibodies. *Pharmacol. Ther.* 185, 147–154. doi:10.1016/j.pharmthera.2017.12.007

Jafari, S., Derakhshankhah, H., Alaei, L., Fattahi, A., Varnamkhasti, B. S., and Saboury, A. A. (2019). Mesoporous silica nanoparticles for therapeutic/diagnostic applications. *Biomed. Pharmacother.* 109, 1100–1111. doi:10.1016/j.biopha.2018.10.167

Karayel, Ö., Tonelli, F., Virreira Winter, S., Geyer, P. E., Fan, Y., Sammler, E. M., et al. (2020). Accurate MS-based Rab10 phosphorylation stoichiometry determination as readout for LRRK2 activity in Parkinson's disease. *Mol. Cell. Proteomics* 19 (9), 1546–1560. doi:10.1074/mcp.ra120.002055

Keeble Anthony, H., Turkki, P., Stokes, S., Khairil Anuar Irsyad, N. A., Rahikainen, R., Hytönen Vesa, P., et al. (2019). Approaching infinite affinity through engineering of peptide–protein interaction. *Proc. Natl. Acad. Sci. U. S. A.* 116 (52), 26523–26533. doi:10.1073/pnas.1909653116

Kim, J., Kim, B. C., Lopez-Ferrer, D., Petritis, K., and Smith, R. D. (2010). Nanobiocatalysis for protein digestion in proteomic analysis. *Proteomics* 10 (4), 687–699. doi:10.1002/pmic.200900519

Kim, K. D., and Kim, H. T. (2002). Formation of silica nanoparticles by hydrolysis of TEOS using a mixed semi-batch/batch method. *J. Sol-Gel Sci. Technol.* 25 (3), 183–189. doi:10.1023/a:1020217105290

Koźlecki, T., Polowczyk, I., Bastrzyk, A., and Sawiński, W. (2016). Improved synthesis of nanosized silica in water-in-oil microemulsions. *J. Nanoparticles* 2016, 1–9. doi:10.1155/2016/8203260

Kupcik, R., Macak, J. M., Rehulkova, H., Sopha, H., Fabrik, I., Anitha, V. C., et al. (2019). Amorphous TiO(2) nanotubes as a platform for highly selective phosphopeptide enrichment. *ACS Omega* 4 (7), 12156–12166. doi:10.1021/acsomega.9b00571

Limo, M. J., Sola-Rabada, A., Boix, E., Thota, V., Westcott, Z. C., Puddu, V., et al. (2018). Interactions between metal oxides and biomolecules: From fundamental understanding to applications. *Chem. Rev.* 118 (22), 11118–11193. doi:10.1021/acs.chemrev.7b00660

Long, X.-Y., Zhang, Z.-J., Li, J.-Y., Sheng, D., and Lian, H.-Z. (2017). Controllable preparation of CuFeMnO4 nanospheres as a novel multifunctional affinity probe for efficient adsorption and selective enrichment of low-abundance peptides and phosphopeptides. *Anal. Chem.* 89 (19), 10446–10453. doi:10.1021/acs.analchem.7b02476

Luo, X., Liu, S., Zhou, J., and Zhang, L. (2009). *In situ* synthesis of Fe3O4/cellulose microspheres with magnetic-induced protein delivery. *J. Mat. Chem.* 19 (21), 3538–3545. doi:10.1039/b900103d

Macklin, A., Khan, S., and Kislinger, T. (2020). Recent advances in mass spectrometry based clinical proteomics: Applications to cancer research. *Clin. Proteomics* 17 (1), 17. doi:10.1186/s12014-020-09283-w

Mamaeva, V., Sahlgren, C., and Lindén, M. (2013). Mesoporous silica nanoparticles in medicine—recent advances. *Adv. Drug Deliv. Rev.* 65 (5), 689–702. doi:10.1016/j.addr.2012.07.018

Mani, V., Chikkaveeraiah, B. V., and Rusling, J. F. (2011). Magnetic particles in ultrasensitive biomarker protein measurements for cancer detection and monitoring. *Expert Opin. Med. diagn.* 5 (5), 381–391. doi:10.1517/17530059.2011.607161

Mann, B. F., Mann, A. K. P., Skrabalak, S. E., and Novotny, M. V. (2013). Sub 2-μm macroporous silica particles derivatized for enhanced lectin affinity enrichment of glycoproteins. *Anal. Chem.* 85 (3), 1905–1912. doi:10.1021/ac303274w

Montoya, A., Beltran, L., Casado, P., Rodríguez-Prados, J.-C., and Cutillas, P. R. (2011). Characterization of a TiO2 enrichment method for label-free quantitative phosphoproteomics. *Methods* 54 (4), 370–378. doi:10.1016/j.ymeth.2011.02.004

Morofuji, N., Ojima, H., Hiraoka, N., Okusaka, T., Esaki, M., Nara, S., et al. (2016). Antibody-based proteomics to identify an apoptosis signature for early recurrence of hepatocellular carcinoma. *Clin. Proteomics* 13 (1), 28. doi:10.1186/s12014-016-9130-0

Müller, M. M. (2018). Post-translational modifications of protein backbones: Unique functions, mechanisms, and challenges. *Biochemistry* 57 (2), 177–185. doi:10.1021/acs.biochem.7b00861

Musielak, M., Piotrowski, I., and Suchorska, W. M. (2019). Superparamagnetic iron oxide nanoparticles (SPIONs) as a multifunctional tool in various cancer therapies. *Rep. Pract. Oncol. Radiother.* 24 (4), 307–314. doi:10.1016/j.rpor.2019.04.002

Nakayasu, E. S., Gritsenko, M., Piehowski, P. D., Gao, Y., Orton, D. J., Schepmoes, A. A., et al. (2021). Tutorial: Best practices and considerations for mass-spectrometry-based protein biomarker discovery and validation. *Nat. Protoc.* 16 (8), 3737–3760. doi:10.1038/s41596-021-00566-6

Narayan, R., Nayak, U. Y., Raichur, A. M., and Garg, S. (2018). Mesoporous silica nanoparticles: A comprehensive review on synthesis and recent advances. *Pharmaceutics* 10 (3), 118. doi:10.3390/pharmaceutics10030118

Ndassa, Y. M., Orsi, C., Marto, J. A., Chen, S., and Ross, M. M. (2006). Improved immobilized metal affinity chromatography for large-scale phosphoproteomics applications. *J. Proteome Res.* 5 (10), 2789–2799. doi:10.1021/pr0602803

Rahi, P., Prakash, O., and Shouche, Y. S. (2016). Matrix-assisted laser desorption/ionization time-of-flight mass-spectrometry (MALDI-TOF MS) based microbial identifications: Challenges and scopes for microbial ecologists. *Front. Microbiol.* 7, 1359. doi:10.3389/fmicb.2016.01359

Rainer, M., and Bonn, G. K. (2015). Enrichment of phosphorylated peptides and proteins by selective precipitation methods. *Bioanalysis* 7 (2), 243–252. doi:10.4155/bio.14.281

Ramazi, S., and Zahiri, J. (2021). Post-translational modifications in proteins: Resources, tools and prediction methods. *Database.* 2021, baab012. doi:10.1093/database/baab012

Rauniyar, N., and Yates, J. R. (2014). Isobaric labeling-based relative quantification in shotgun proteomics. *J. Proteome Res.* 13 (12), 5293–5309. doi:10.1021/pr500880b

Ray, S., Chandra, H., and Srivastava, S. (2010). Nanotechniques in proteomics: Current status, promises and challenges. *Biosens. Bioelectron.* 25 (11), 2389–2401. doi:10.1016/j.bios.2010.04.010

Rejeeth, C., Pang, X., Zhang, R., Xu, W., Sun, X., Liu, B., et al. (2018). Extraction, detection, and profiling of serum biomarkers using designed Fe3O4@SiO2@HA core–shell particles. *Nano Res.* 11 (1), 68–79. doi:10.1007/s12274-017-1591-6

Rejeeth, C., Sharma, A., Kannan, S., Kumar, R. S., Almansour, A. I., Arumugam, N., et al. (2022). Label-free electrochemical detection of the cancer biomarker platelet-derived growth factor receptor in human serum and cancer cells. *ACS Biomater. Sci. Eng.* 8 (2), 826–833. doi:10.1021/acsbiomaterials.1c01135

Riley, N. M., and Coon, J. J. (2016). Phosphoproteomics in the age of rapid and deep proteome profiling. *Anal. Chem.* 88 (1), 74–94. doi:10.1021/acs.analchem.5b04123

Rodzik, A., Pomastowski, P., Sagandykova, G. N., and Buszewski, B. (2020). Interactions of whey proteins with metal ions. *Int. J. Mol. Sci.* 21 (6), 2156. doi:10.3390/ijms21062156

Rühl, M., Golghalyani, V., Barka, G., Bahr, U., and Karas, M. (2017). Enhanced on-plate digestion of proteins using a MALDI-digestion chamber. *Int. J. Mass Spectrom.* 416, 37–45. doi:10.1016/j.ijms.2016.11.011

Ruprecht, B., Koch, H., Medard, G., Mundt, M., Kuster, B., and Lemeer, S. (2015). Comprehensive and reproducible phosphopeptide enrichment using iron immobilized metal ion affinity chromatography (Fe-IMAC) columns. *Mol. Cell. Proteomics* 14 (1), 205–215. doi:10.1074/mcp.m114.043109

Schmit, N. E., Neopane, K., and Hantschel, O. (2019). Targeted protein degradation through cytosolic delivery of monobody binders using bacterial toxins. *ACS Chem. Biol.* 14 (5), 916–924. doi:10.1021/acschembio.9b00113

Suciu, M., Ionescu, C. M., Ciorita, A., Tripon, S. C., Nica, D., Al-Salami, H., et al. (2020). Applications of superparamagnetic iron oxide nanoparticles in drug and therapeutic delivery, and biotechnological advancements. *Beilstein J. Nanotechnol.* 11, 1092–1109. doi:10.3762/bjnano.11.94

Tan, Y.-J., Sui, D., Wang, W.-H., Kuo, M.-H., Reid, G. E., and Bruening, M. L. (2013). Phosphopeptide enrichment with TiO2-modified membranes and investigation of tau protein phosphorylation. *Anal. Chem.* 85 (12), 5699–5706. doi:10.1021/ac400198n

Tiambeng, T. N., Roberts, D. S., Brown, K. A., Zhu, Y., Chen, B., Wu, Z., et al. (2020). Nanoproteomics enables proteoform-resolved analysis of low-abundance proteins in human serum. *Nat. Commun.* 11 (1), 3903. doi:10.1038/s41467-020-17643-1

Wan, J., Qian, K., Qiao, L., Wang, Y., Kong, J., Yang, P., et al. (2009). TiO2-Modified macroporous silica foams for advanced enrichment of multi-phosphorylated peptides. *Chem. Eur. J.* 15 (11), 2504–2508. doi:10.1002/chem.200802079

Wang, Y.-C., Peterson, S. E., and Loring, J. F. (2014). Protein post-translational modifications and regulation of pluripotency in human stem cells. *Cell Res.* 24 (2), 143–160. doi:10.1038/cr.2013.151

Wang, Z.-G., Lv, N., Bi, W.-Z., Zhang, J.-L., and Ni, J.-Z. (2015). Development of the affinity materials for phosphorylated proteins/peptides enrichment in phosphoproteomics analysis. *ACS Appl. Mat. Interfaces* 7 (16), 8377–8392. doi:10.1021/acsami.5b01254

Wu, W., Wu, Z., Yu, T., Jiang, C., and Kim, W.-S. (2015). Recent progress on magnetic iron oxide nanoparticles: Synthesis, surface functional strategies and biomedical applications. *Sci. Technol. Adv. Mat.* 16 (2), 023501. doi:10.1088/1468-6996/16/2/023501

Yan, Y., Zheng, Z., Deng, C., Li, Y., Zhang, X., and Yang, P. (2013). Hydrophilic polydopamine-coated graphene for metal ion immobilization as a novel immobilized metal ion affinity chromatography platform for phosphoproteome analysis. *Anal. Chem.* 85 (18), 8483–8487. doi:10.1021/ac401668e

Yildiz, I. (2016). Applications of magnetic nanoparticles in biomedical separation and purification. *Nanotechnol. Rev.* 5 (3), 331–340. doi:10.1515/ntrev-2015-0012

Zborowski, M., and Chalmers, J. J. (2011). Rare cell separation and analysis by magnetic sorting. *Anal. Chem.* 83 (21), 8050–8056. doi:10.1021/ac200550d

Zhang, L., Zhu, X., Jiao, D., Sun, Y., and Sun, H. (2013). Efficient purification of His-tagged protein by superparamagnetic Fe3O4/Au–ANTA–Co2+ nanoparticles. *Mater. Sci. Eng. C* 33 (4), 1989–1992. doi:10.1016/j.msec.2013.01.011

Zhang, R., Rejeeth, C., Xu, W., Zhu, C., Liu, X., Wan, J., et al. (2019). Label-free electrochemical sensor for CD44 by ligand-protein interaction. *Anal. Chem.* 91 (11), 7078–7085. doi:10.1021/acs.analchem.8b05966

Zhou, H.-X., and Pang, X. (2018). Electrostatic interactions in protein structure, folding, binding, and condensation. *Chem. Rev.* 118 (4), 1691–1741. doi:10.1021/acs.chemrev.7b00305

Zhou, J., and Rossi, J. (2017). Aptamers as targeted therapeutics: Current potential and challenges. *Nat. Rev. Drug Discov.* 16 (3), 181–202. doi:10.1038/nrd.2016.199

Zhu, G.-T., Li, X.-S., Gao, Q., Zhao, N.-W., Yuan, B.-F., and Feng, Y.-Q. (2012). Pseudomorphic synthesis of monodisperse magnetic mesoporous silica microspheres for selective enrichment of endogenous peptides. *J. Chromatogr. A* 1224, 11–18. doi:10.1016/j.chroma.2011.12.045

frontiers | Frontiers in Nanotechnology

TYPE Original Research
PUBLISHED 10 March 2023
DOI 10.3389/fnano.2023.1112100

OPEN ACCESS

EDITED BY
Fangwei Ye,
Shanghai Jiao Tong University, China

REVIEWED BY
Ce Shang,
King Abdullah University of Science and Technology, Saudi Arabia
Ming Fang,
Anhui University, China

*CORRESPONDENCE
Qun Ren,
renqun@tju.edu.cn
Jianwei You,
jvyou@seu.edu.cn
Wei E. I. Sha,
weisha@zju.edu.cn

SPECIALTY SECTION
This article was submitted to Nanophotonics,
a section of the journal
Frontiers in Nanotechnology

RECEIVED 30 November 2022
ACCEPTED 28 February 2023
PUBLISHED 10 March 2023

CITATION
Wang X, Wang X, Ren Q, Cai H, Xin J, Lang Y, Xiao X, Lan Z, You J and Sha WEI (2023), Temperature-controlled optical switch metasurface with large local field enhancement based on FW-BIC.
Front. Nanotechnol. 5:1112100.
doi: 10.3389/fnano.2023.1112100

Temperature-controlled optical switch metasurface with large local field enhancement based on FW-BIC

Xiuyu Wang[1], Xiaoman Wang[1], Qun Ren[2,3]*, Haocheng Cai[2], Jihong Xin[1], Yuxin Lang[2], Xiaofei Xiao[4], Zhihao Lan[5], Jianwei You[3]* and Wei E. I. Sha[6]*

[1]Tianjin Key Laboratory of Imaging and Sensing Microelectronic Technology, School of Microelectronics, Tianjin University, Tianjin, China, [2]School of Electrical and Information Engineering, Tianjin University, Tianjin, China, [3]State Key Laboratory of Millimeter Waves, School of Information Science and Engineering, Southeast University, Nanjing, China, [4]Department of Physics, Imperial College London, London, United Kingdom, [5]Department of Electronic and Electrical Engineering, University College London, London, United Kingdom, [6]Key Laboratory of Micro-Nano Electronic Devices and Smart Systems of Zhejiang Province, College of Information Science and Electronic Engineering, Zhejiang University, Hangzhou, China

Introduction: Many researchers have explored the bound states in the continuum (BIC_S) as a particular bound wave state which can be used to achieve a very high Q-factor. High-Q factor devices, typically based on the bound states in the continuum (BIC_S), are well used in the fields of hypersensitive biochemical sensors, non-linear effects enhancement, plasmon lasers, and hi-performance filtering. However, symmetrical-protected BIC is difficult to achieve experimentally high-Q factor because it strongly depends on the geometry and can be destroyed by any slight disturbance in the potential well.

Methods: Therefore, we proposed a parameter-adjusted Friedrich-Wintergen BIC based on the analysis model of time-coupled model theory, where the target system parameters can be tuned to achieve high-Q excitation.

Results: Moreover, considering the tunability and flexibility of the components in various practical applications, we integrate active materials into metasurface arrays with the help of external stimuli to achieve modulation of high-Q resonances. Our results demonstrate that an optical resonator based on FW-BIC can modulate the BIC state by changing the intermediate gap.

Discussion: The BIC state and the high-Q factor Fano resonance can be dynamically tuned by adding temperature-sensitive VO_2 material.

KEYWORDS

FW-BIC, terahertz, metasurfaces, optical switch, high-Q

1 Introduction

With the bound states lying inside the continuum spectrum and coexisting with extended waves, bound state in the continuum (BIC) was initially proposed in quantum mechanics and widely used in diverse scientific fields as a particular bound state located in the radiation region (Lu et al., 2021b; Bogdanov et al., 2019; Hsu et al., 2016). The bound states lie inside the continuum spectrum and coexist with extended waves (Wang et al., 2022a; Kang et al., 2022). Bound states in the continuums (BICs) differ from conventional wave-binding mechanisms because they are perfectly bound by the system without any radiation. BIC mode can be achieved in two methods (Huang et al., 2021). One is to construct a symmetry-protected BIC, wherein the capture mode with a certain symmetry is embedded into an apparent-symmetric continuum, preventing the capture mode from leaking (Cong and Singh, 2019). Because even the smallest disturbance may destroy the potential well, this kind of BIC may be difficult to obtain experimentally (Sadreev, 2021). Another is to create a Friedrich-Wintergen BIC (FW-BIC), where the target system parameters are tuned to achieve high-Q excitation *via* continuous cancellation (Zhao et al., 2020; Friedrich and Wintgen, 1985).

Textcolorred with a broad application in highly sensitive refractive sensors (Meng et al., 2022; Bogdanov et al., 2019; Chen et al., 2022), electric field enhancement (Ren et al., 2018; electromagnetic induced transparency (Azzam et al., 2018) and non-linear effects enhancement (Mittleman, 2017; Lu et al., 2021a; Fang et al., 2018) as well as a significant demand in photonic systems. High-Q resonators greatly enhance the interaction between light and matter, reduce the radiation loss of devices. Be capable of capturing the energy in the resonator in the BIC mode with little leakage into the continuum, an extremely high-Q factor could be achieved in the BIC (Lee et al., 2020). Due to the infinite lifetime and the absence of leakage in an ideal BIC, external excitations cannot couple to the BIC, and the ideal BIC is unobservable in the electromagnetic spectrum (Doeleman et al., 2018). However, by introducing structural perturbations in the metasurfaces supporting the BIC, the high-Q resonance mode induced by the two low-Q mode couplings identifies the emergence of a quasi-BIC in the far-field response (Ren et al., 2021).

When considering the diverse practical applications of the optical medium's components in optical switching, optical sensors, and hyperactivity spetroscopy, their tunability and flexibility are noteworthy (Ren et al., 2019; Han et al., 2021; Fang et al., 2021). It can be observed that passively adjusting the geometrical parameters of the resonance structure allows for a finite extent of tuning of the resonance frequency, modulation depth, and linewidth of the Fano resonance. The results have initially demonstrated that accurate active control of the Fano resonance can be achieved at additional levels in bringing active materials into the meta surface arrays, such as semiconductors, graphene (Xiao et al., 2018; Ren et al., 2020; Lan et al., 2021; Wang et al., 2022a), and VO_2 (Yang et al., 2022). VO_2, as an active material, has temperature-sensitive insulator-metal transition (IMT) characteristics, and its conductivity can rapidly increase by 4-5 orders of magnitude under external thermal excitation (Fan et al., 2013; Zhu et al., 2012; Mandal et al., 2011; Liu et al., 2012; Zhao et al., 2018).

In this paper, we propose a split-ring resonator based on Friedrich-Wintergen BIC (FW-BIC). We tune the high-Q factor Fano resonance of the split-ring resonator by adding temperature sensitive vanadium dioxide material (VO_2). High-Q factor Fano resonances coupled with significant near-field enhancement in optical cavities are essential for a wide range of applications in filtering and sensing, lasers, and non-linear effects enhancement. A metasurface array with an integrated active material enables active control of the components, which is beneficial for various practical applications such as optical switches, optical sensors, and transitivity spectroscopy. The proposed metasurface provides a platform for trapping and manipulating electromagnetic waves provided by free-space radiation. The employed theoretical model can be generalized to help design quasi-BIC in other frequency regions.

2 Materials and methods

To experimentally realize the FW-BIC response of the coupled resonance, we designed a device consisting of a split-ring resonator. The period P of the metasurface is 200 μm, and the other parameters are shown in Figure 1. The metamaterial structure consists of an aluminum device and a silicon substrate. The aluminum thickness is 1 μm, and electrical conductivity is $3.74 \times 10^7 S/m$. The silicon substrate is 20 μm thick, $\epsilon = 11.7$, and 100 μm thick glass below. Our structure is resonant at a terahertz frequency, with both an inductor-capacitance (LC) mode and a dipole mode. In our structure, the resonance frequency of the LC mode can be tuned by changing the intermediate gap (g_2) to produce the FW-BIC state with little effect on the resonance frequency of the dipole mode. The two-sided gap can affect the resonance frequency of the dipole mode. The function of regulating the BIC position or quasi-BIC to BIC conversion is achieved by adding sensitive materials at different sites, such as temperature-sensitive vanadium oxides. With such a plateau, we can control the frequency detuning between the two modes near the ideal BIC. We performed simulations using the finite element method (FEM) with COMSOL Inc (2020) to obtain the response.

Here, a two-mode system coupled by two ports is described using a time-coupled mode theory model to better explain the principle of Friedrich-Wintergen (Zhao et al., 2019; Suh et al., 2004):

$$\frac{\mathrm{d}}{\mathrm{d}t}\begin{bmatrix} r_1 \\ r_2 \end{bmatrix} = \begin{bmatrix} d_{11} & d_{12} \\ d_{21} & d_{22} \end{bmatrix}\begin{bmatrix} p_{1+} \\ p_{2+} \end{bmatrix} + j\begin{bmatrix} \omega_1 + j\tau_1 & d + j\tau_{12} \\ d + j\tau_{21} & \omega_2 + j\tau_2 \end{bmatrix}\begin{bmatrix} r_1 \\ r_2 \end{bmatrix}$$

As given by the formula, the coupling coefficient between mode i and port j is expressed by $d_{ij}\,(i, j \in 1, 2)$; the input amplitudes of ports 1 and 2 are p_{1+} and p_{2+}; ω_1 and ω_2, τ_1 and τ_2 indicate the resonant frequency and attenuation rate of the two modes, respectively; d is the direct coupling rate between the two modes; τ_{12} and τ_{21} are the coupling coefficients generated by damping, and finally, the resonance amplitude of the mode supported by the system could be expressed by r_1 and r_2. Due to the symmetry of the system, $\tau_{12} = \tau_{21} = \sqrt{\tau_1 \tau_2}$.

In this system, the output wave that excites the resonant mode is represented as follows:

$$\begin{bmatrix} p_{1-} \\ p_{2-} \end{bmatrix} = \begin{bmatrix} r & t \\ t & r \end{bmatrix}\begin{bmatrix} p_{1+} \\ p_{2+} \end{bmatrix} + \begin{bmatrix} c_{11} & c_{12} \\ c_{21} & c_{22} \end{bmatrix}\begin{bmatrix} r_1 \\ r_2 \end{bmatrix}$$

where p_{1-} and p_{2-} are the outgoing wave amplitudes at ports 1 and 2; r and t are the direct reflection and transmission coefficient between the ports in the absence of the resonant modes; c_{ij} is the coupling coefficient between the port j and the mode i; r_1 and r_2 are the resonance amplitude of modes supported by the system.

Under the above framework, the transmission coefficients of uncoupled single mode and coupling mode can be calculated. The transmission valley in the transmission occurs at the resonant

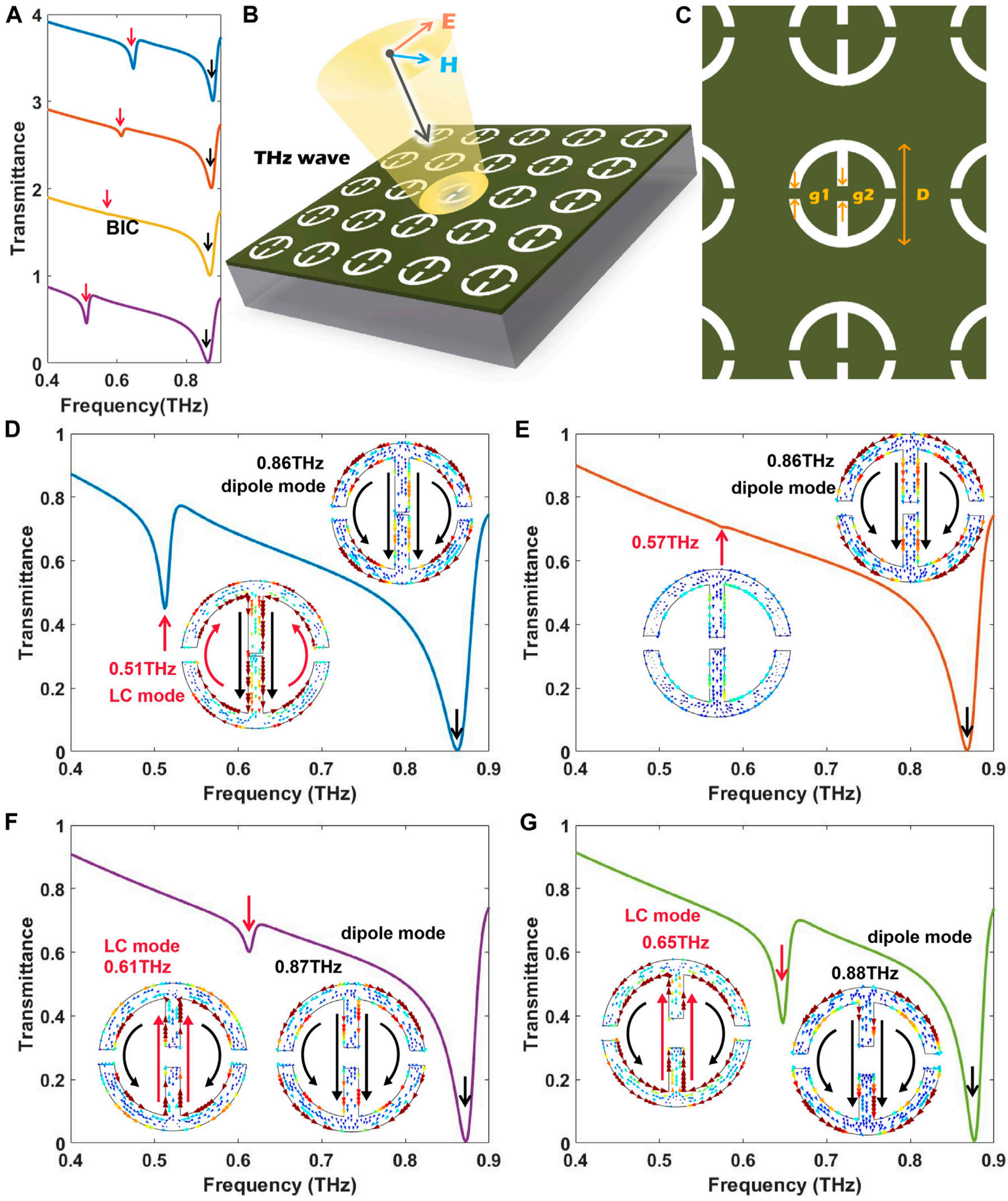

FIGURE 1
Illustration of the generation of BIC *via* coupled resonant modes, model design and measurement of transmission spectra. **(A)** The transmission coefficient for different frequency settings. The Q-factor is infinite in the BIC mode. (The red arrows label ω_1 and the black arrows label ω_2.). **(B)** 3D schematic diagram of the metasurfaces. **(C)** Schematic of the metasurface design. The design dimensions are as follows: period p = 100 μm, the ring outer diameter D = 120 μm, width W = 10 μm, double seam width g_1 = 10 μm, control the shift of g_2. **(D)** The amplitude transmission spectrum of the metasurface at g_2 = 2 μm under the Y polarization and the current distribution corresponding to the transmission valley. **(E)** The amplitude transmission spectrum of the metasurface of g_2 = 8 μm, and the current distribution corresponds to the transmission valley. **(F)** The amplitude transmission spectrum of the metasurface of g_2 = 14 μm, and the current distribution corresponds to the transmission valley. **(G)** The amplitude transmission spectrum of the metasurface at g_2 = 20 μm and the current distribution correspond to the transmission valley.

frequencies (ω_1 and ω_2) for each individual mode. The transmission spectrum is represented by a Fano response with two transmission valleys and a peak. Once the two modes are coupled to each other, the resonant frequencies of the two resonance modes correspond to the transmission valleys, and the coupling between the two modes forms a transmission peak. $\omega_1 + j\tau_1$ and $\omega_2 + j\tau_2$ demonstrate two complex eigenvalues exhibited by the coupled resonator, where the imaginary and real parts are the resonant frequency and attenuation rate of the hybrid eigenmode, respectively. $Q = \omega/(2\tau)$ is expressed as a quality factor for the eigenmode. The peak transmission coefficient corresponds to one eigenmode with a high-Q factor, while the other eigenmode suppressed by the high attenuation rate has a Q value less than 1. The Fano resonance may shift with the frequency detuning between the resonant modes ($\delta\omega = \omega_1 - \omega_2$) as shown in Figure 1. One of the eigenmodes is promoted to the BIC state, and the eigenvalue radiation becomes a pure imaginary number due to a loss of zero when the Friedrich-Wintgen condition ($\delta\omega\sqrt{\tau_1\tau_2} = n(\tau_1 - \tau_2)$) is satisfied.

3 Results

As shown in Figure 1, when the two-sided gap g_1 is 10 μm unchanged, the peak of quasi-BIC appears when the intermediate gap g_2 size is 2 μm. The current distribution indicates that 0.51 *THz* corresponds to the LC mode and 0.86 *THz* corresponds to the dipole mode. The transport peak at 0.55 *THz* results from the coupling of the LC and dipole mode and act as a quasi-BIC mode. It has been reported that the Fano resonances can be excited by a set of antiparallel magnetic dipoles that are weakly coupled to the free space and emerge as high-Q resonances. Since the LC mode and the dipole mode are coupled to each other through resonant and leaky channels, the quasi-BIC mode has been theoretically and computationally predicted to have Fano line shapes. As the gap g_2 increases, the LC mode moves towards a higher frequency, closing to the dipole resonance frequency. A decrease in the frequency detuning leads to a decrease in the transmission peak and an increase in the Q-factor. When the gap size is 14 μm, the BIC can be identified by the vanishing of the Fano transmission peak. As for the FW-BIC, on the one hand, the surface current is weak, suggesting that it is barely coupled to free-space radiation and is entirely confined by bound states in the absence of leaky channels.

On the other hand, the faint in-phase collective current on the upper and lower arms of the resonator with the same incident THz wave direction comes from the dipole resonance of the symmetric structure. When the BIC condition is broken by increasing the gap size of g_2, the transmission peak appears again. At this time, the surface current is considerably excited, and the current direction on the resonator surface is rearranged, indicating that the bound state is coupled with the incident radiation, thus generating quasi-BIC resonance. Note that unlike symmetry-protected BIC, quasi-BIC of FW-BIC in this structure is realized by changing the gap size without destroying the symmetry.

Recently, a few studies have tentatively demonstrated that Fano resonances enable precise active control at an additional level if specific active materials are integrated into metasurface arrays, such as semiconductors, graphene, and vanadium dioxide. As an active material, VO_2 has temperature-sensitive insulator-metal transition (IMT) characteristics. Its conductivity can be rapidly increased by 4-5 orders of magnitude under external thermal excitation, and it is only one order of magnitude lower than gold. VO_2 can be expressed as a material with dielectric $\epsilon_r = 9$ in the terahertz band, and its conductivity can shift from $10S/m$ to $100000S/m$ with the increase of temperature.

Since the gap on both sides can affect the resonance frequency of the dipole mode, in order to realize the function of regulating the BIC position, we designed the Al-VO_2 hybrid metasurface, as shown in Figure 2. Interactions between electrons, orbitals, and crystal structures can cause abrupt changes in the electromagnetic and thermal properties of VO_2 near the phase transition temperature. During the phase transition, VO_2 dramatically changes the properties of electromagnetic waves at all wavelengths, especially in the terahertz band. At temperatures lower than the phase transition temperature, VO_2 is in the insulating phase, and the band gap of VO_2 is $6eV$, which allows THz wave to fully penetrate the equivalent transparent state. At temperatures higher than the phase transition temperature, VO_2 is a metallic phase and its Fermi level coincides with the 3D band of the V atom, such that the band gap of VO_2 becomes 0. At this point, VO_2 can approximately replace the metal, which leads to a reduction of the equivalent gap width and thus affects the position of the FW-BIC. As can be seen from the simulation results, for the designed Al-VO_2 hybrid metasurface, we can easily shift the frequency corresponding to the BIC from 0.64 *THz* to 0.69 *THz* by using external thermal excitation to shift the temperature.

4 Discussion

Based on the above analysis of the time-domain coupled model, for an ideal FW-BIC, the decay rate of this mode (τ) should be close to 0, and hence the theoretical Q-factor ($Q = \omega/(2\tau)$) should be approximately infinite. For the lossy BIC in the experiment, although the energy leakage from the element surface to the port is 0, the ohmic loss in the metal and the dielectric loss in the substrate will still lead to a large decal rate, thus leading to a finite Q-factor. Therefore, we used COMSOL to reduce the imaginary part of the ϵ to 10^{-5} to calculate the Q-factor of BIC with a near-loss-free metal (the first Brillouin zone of the square lattice is plotted on the top left in Figure 3). Figure 3 shows the Q factors of eigenmodes close to 0.56 *THz* calculated by this method. Figure 3 shows the Q factors of eigenmodes close to 0.56 *THz* calculated by this method, and the Q factor of BIC rises rapidly to a maximum value at the point of Γ. The insertion diagram below shows the possible eigenmodes near 0.56 *THz* in the M-Γ direction.

In the BIC state, the energy transfer of electromagnetic waves is mainly in the *z*-axis direction, so that the magnetic field is confined in the x-o-y plane. However, in the case of a quasi-BIC, a part of the magnetic field arises out of the x-o-y plane due to energy leakage. Therefore, the energy leakage in the case of a quasi-BIC can be easily verified by monitoring the magnetic field component in the *z*-axis direction. We monitored the z-directional magnetic field strength of the metal split-ring resonator pair at the Fano resonance, as shown in Figure 4. Split-ring resonator has nearly no *Z*-direction magnetic field in the BIC state, indicating no energy leakage in the split-ring resonator and an extremely strong *Z*-direction magnetic field around the split-ring resonator in the quasi-BIC state. It can be seen that the magnetic field in the quasi-BIC state is enhanced more than that in the BIC state, indicating a significant magnetic field leakage.

By varying the intermediate gap (g_2), we can tune the resonant frequency of the LC mode to switch between the BIC state and the

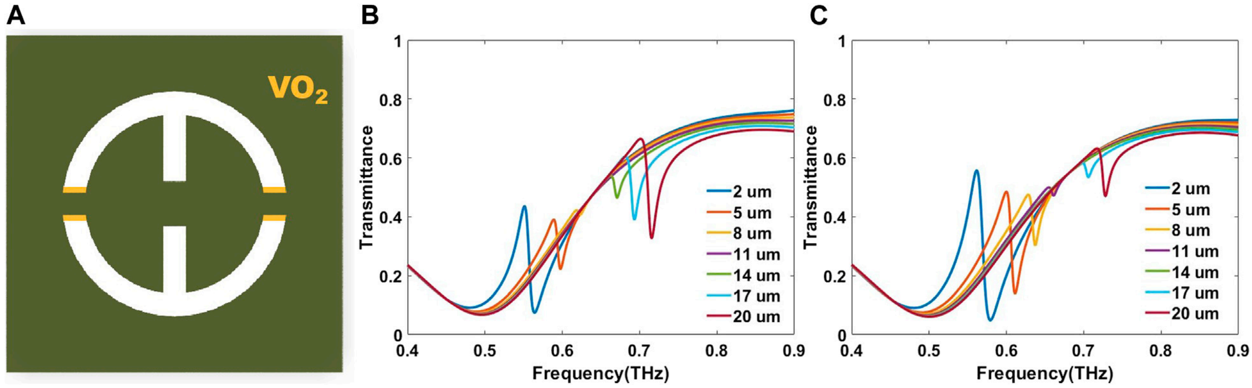

FIGURE 2
(A) Schematic diagram of the $Al - VO_2$ metasurface. The metal design dimensions are as follows: period p = 100 μm, the ring outer diameter D = 120 μm, width W = 10 μm, double seam width g_1 = 15 μm, control the change of g_2. Vanadium oxide filling both sides seam width to 10 μm. **(B)** The low-temperature regime and the amplitude transmission spectrum of the metasurfaces of different g_2. **(C)** High-temperature state, the amplitude transmission spectrum of the metasurfaces of different g_2.

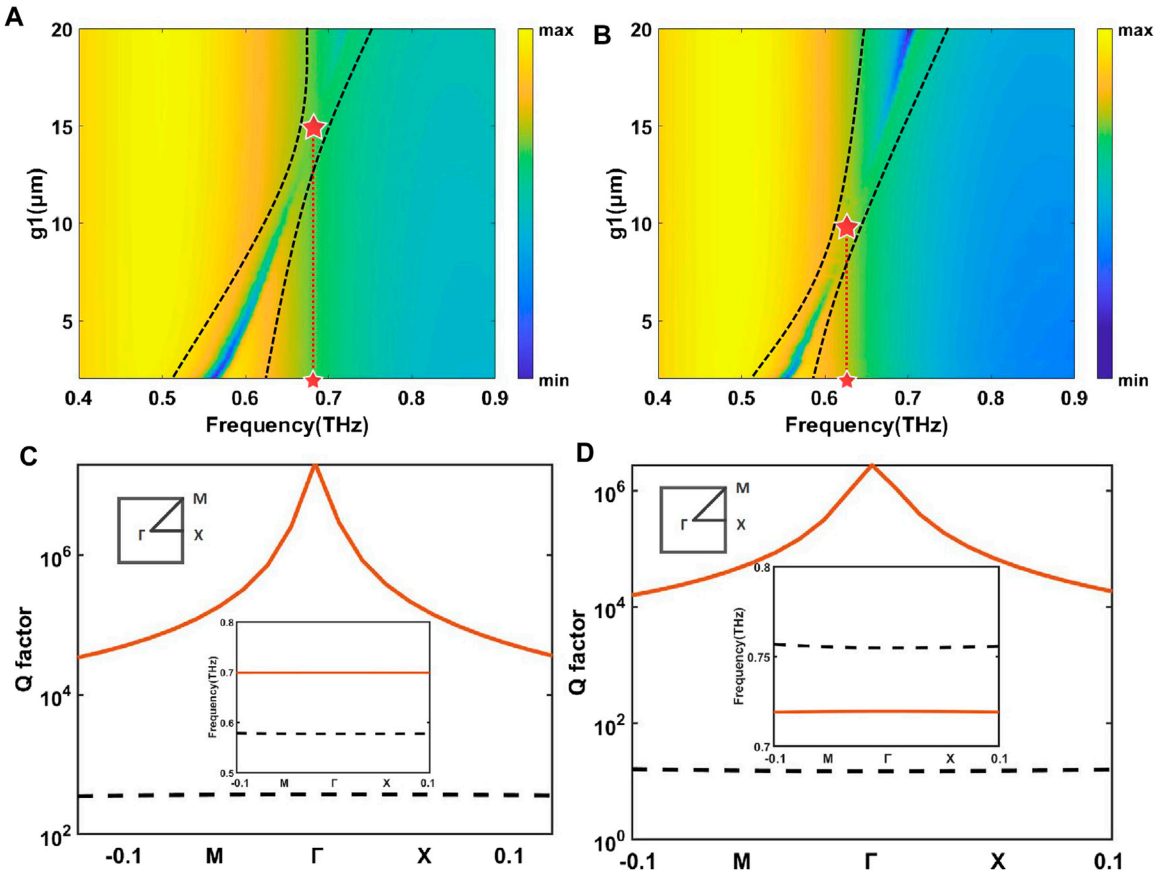

FIGURE 3
(A) The colour plot of the simulated transmission spectra of the BIC at low temperatures by scanning g_2 from 2 μm to 20 μm. **(B)** The colour plot of the simulated transmission spectra of the BIC at the high-temperature state by sweeping g_2 from 2 μm–20 μm. **(C)** The Q factor and band structure correspond to the low-temperature BIC (inset) state. **(D)** The Q factor and band structure correspond to the high-temperature BIC (inset) state. The metal loss is reduced, and the imaginary part ϵ of the dielectric constant is reduced to $10^{-5}S/m$. The quasi-BIC we study appears at the Γ point in the first red Brillouin zone with an extremely high Q factor.

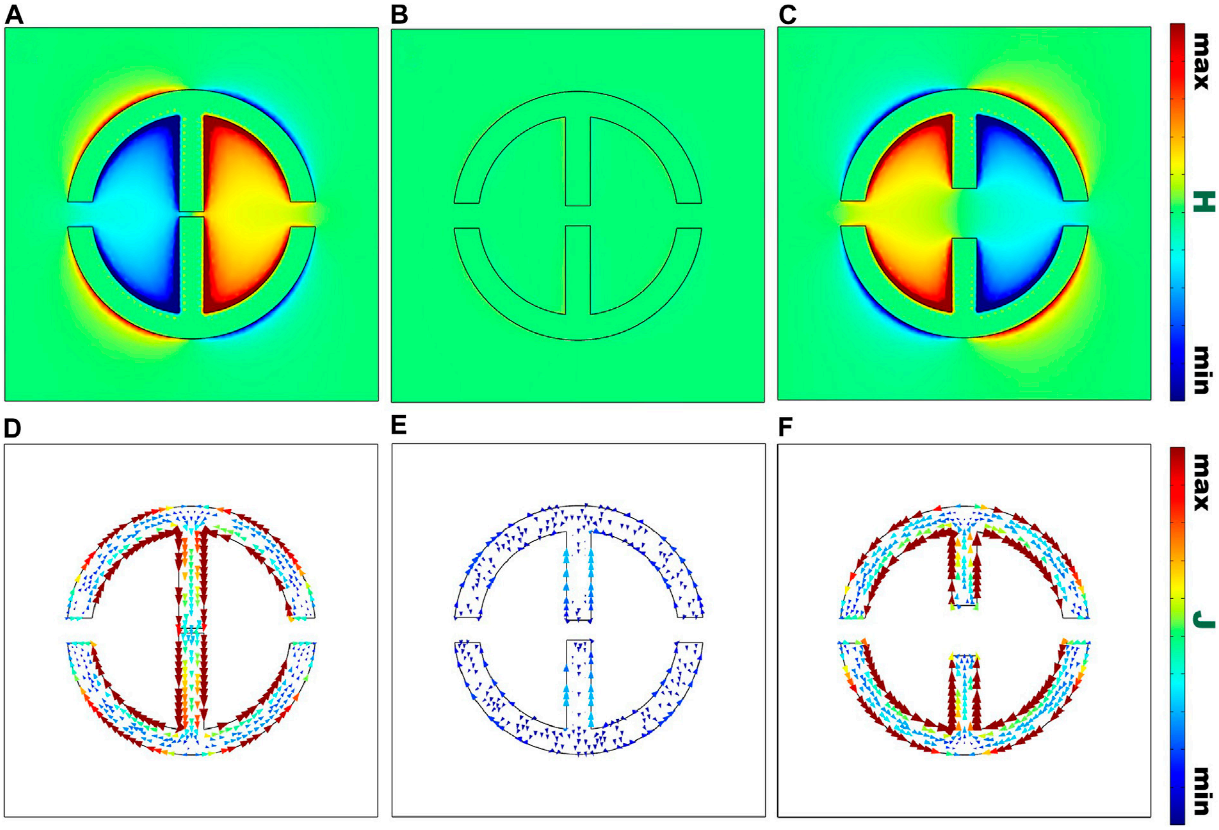

FIGURE 4
(A) *Z* direction magnetic field strength corresponds to the quasi-BIC mode of g_2 = 2 μm. **(B)** *Z* direction magnetic field strength corresponds to the BIC mode of g_2 = 8 μm. **(C)** The *Z*-direction magnetic field strength corresponds to the quasi-BIC mode of g_2 = 20 μm. **(D)** The x-o-y plane current corresponds to the quasi-BIC mode of g_2 = 2 μm. **(E)** The x-o-y plane current corresponds to the BIC mode of g_2 = 8 μm. **(F)** The x-o-y plane current corresponds to the quasi-BIC mode of g_2 = 20 μm.

quasi-BIC state, which slightly affects the resonant frequency of the dipole mode. Therefore, in order to achieve adjustable BIC resonance and active switch of Fano resonance, we embed VO_2 in the middle gap to present the dielectric state and mental state at different temperatures as well as realize the control by employing external thermal excitation.

The conductivity of VO_2 can be expressed by the effective medium theory (EMT) formula: (Lu et al., 2021a).

$$(1-g)\sigma_{eff}^2 + [g\sigma_i + g\sigma_m - \sigma_i + f_v(\sigma_i - \sigma_m)]\sigma_{eff} - g\sigma_i\sigma_m = 0$$

where g is the shape-related parameter controlling the seepage threshold. σ_i, σ_m and σ_{eff} is the conductivity of insulating phase, metal phase and effective frequency, respectively, f_v is the volume fraction of the metal domain. Wherein, the volume fraction of metal phase f_v can be expressed as: (Ma et al., 2020).

$$f_v = f_{max}\left(1 - \frac{1}{1 + e^{\frac{T-T_0}{\Delta T}}}\right)$$

where $f_{\max}$ = 0.95 is the maximum volume fraction of metal composition at the highest temperature in vanadium dioxide, T is the regulated VO_2 temperature, T_0 is the phase transition temperature, the heating point and cooling point are 68 °C and 64 °C respectively, $\Delta T = 2$ °C is the transition width. From the above equations, it is clear that tuning the temperature can alter the volume fraction of the metallic phase and thus the conductivity of VO_2. As the temperature increases from room temperature to above the phase transition temperature, the VO_2 embedded in the intermediate gap will gradually decrease the equivalent intermediate gap width. The transmission peak at 0.63 *THz* is the result of coupling between the LC and dipole mode. As the equivalent gap approaches the gap corresponding to the BIC mode, the frequency detuning $(|\delta\omega|)$ almost satisfies the Friedrich-Wintgen condition $(\delta\omega\sqrt{\tau_1\tau_2} = n(\tau_1 - \tau_2))$, which will reduce the transmission peak.

The metasurfaces supporting quasi-BIC modes can provide significant local field enhancement due to high Q resonances. The electric field is confined to the gap region for metal split-ring resonator, leading to a substantial electric field enhancement. The simulation results in Figure 5 show that when g_2 = 2 μm, the quasi-BIC mode achieves a maximum electric field enhancement of 163 at the resonant frequency of the coupled mode compared to the BIC mode when g_2 = 9 μm. For a metasurface with BIC modes, the electric field enhancement disappears because the incident wave does not couple to the coupled modes of the metasurface. For the *Al*-VO_2 hybrid metasurface in Figure 5, as the temperature increases, the equivalent intermediate gap decreases and the electric field

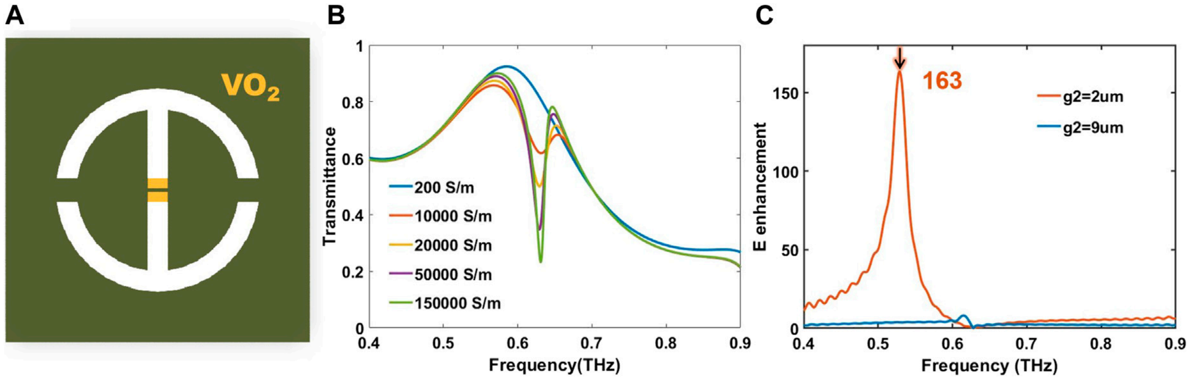

FIGURE 5
(A) Schematic diagram of the $VO_2 - Al$ metasurface. The metal design dimensions are as follows: period p = 100 μm, the ring outer diameter D = 120 μm, width W = 10 μm, both side seam width g_1 = 10 μm, g_2 = 8 μm. After vanadium oxide filling, the intermediate seam width changes to 2 μm. **(B)** The amplitude transmission spectrum of the metasurfaces at the corresponding conductivity to different temperatures. High-temperature state, the amplitude transmission spectrum of the metasurfaces of different g_2. **(C)**Simulated field enhancement of the metasurface center. Electric field enhancement to quasi-BIC responses distant from the BIC point (red) and close to the BIC point (blue). Field enhancement away from the BIC point (red) can reach 163.

enhancement gradually increases. It is shown that the closer the quasi-BIC state is to the BIC state, the higher the quality factor and the lower the electric field enhancement rate.

In this paper, we propose a split-ring resonator based on the Friedrich-Wintergen BIC. By changing the parameters and using magnetic field leakage to confirm the split-ring resonator's BIC mode, we are able to generate high-Q resonances. Additionally, we tune the frequency positions of the temperature-sensitive vanadium dioxide material at various points in the BIC and high-Q factor Fano resonance switches. The metasurface supporting the quasi-BIC mode has been shown to be capable of generating a local electric field increase of 163 approximately, which is critical for a variety of applications in filtering, sensing, and enhancing non-linear effects. Metasurface arrays integrated with novel active materials enable active control of components as a function of optical switches. It provides a platform for capturing and manipulating electromagnetic waves *via* free-space radiation.

Data availability statement

The original contributions presented in the study are included in the article/supplementary material, further inquiries can be directed to the corresponding authors.

Author contributions

XYW, XMW, and QR contributed to conception and design of the study. HC, JX, and YL performed the statistical analysis. XMW wrote the first draft of the manuscript. XX, ZL, JY, and WS wrote sections of the manuscript. All authors contributed to manuscript revision, read, and approved the submitted version.

Funding

This work was financially sponsored by National Natural Science Foundation of China (12104339), Open Fund of State Key Laboratory of Millimeter Wave, Southeast University (K202216) and China Postdoctoral Science Foundation funded project (258023).

Conflict of interest

The authors declare that the research was conducted in the absence of any commercial or financial relationships that could be construed as a potential conflict of interest.

Publisher's note

References

Azzam, S. I., Shalaev, V. M., Boltasseva, A., and Kildishev, A. V. (2018). Formation of bound states in the continuum in hybrid plasmonic-photonic systems. *Phys. Rev. Lett.* 121, 253901. doi:10.1103/PhysRevLett.121.253901

Bogdanov, A. A., Koshelev, K. L., Kapitanova, P. V., Rybin, M. V., Gladyshev, S. A., Sadrieva, Z. F., et al. (2019). Bound states in the continuum and Fano resonances in the strong mode coupling regime. *Adv. Photonics* 1, 016001. doi:10.1117/1.AP.1.1.016001

Chen, S., Ren, Q., Zhang, K., Wei, E., Hao, T., Xu, H., et al. (2022). A highly sensitive and flexible photonic crystal oxygen sensor. *Sensors Actuators B Chem.* 355, 131326. doi:10.1016/j.snb.2021.131326

COMSOL Inc (2020). *Simulate real-world designs, devices, and processes with multiphysics software*. Stockholm, Sweden: COMSOL Inc. https://www.comsol.com/

Cong, L., and Singh, R. (2019). Symmetry-protected dual bound states in the continuum in metamaterials. *Adv. Opt. Mater.* 7, 1900383. doi:10.1002/adom.201900383

Doeleman, H. M., Monticone, F., den Hollander, W., Alù, A., and Koenderink, A. F. (2018). Experimental observation of a polarization vortex at an optical bound state in the continuum. *Nat. Photonics* 12, 397–401. doi:10.1038/s41566-018-0177-5

Fan, F., Gu, W. H., Chen, S., Wang, X. H., and Chang, S. J. (2013). State conversion based on terahertz plasmonics with vanadium dioxide coating controlled by optical pumping. *Opt. Lett.* 38, 1582–1584. doi:10.1364/ol.38.001582

Fang, M., Huang, Z., Wei, E., and Soukoulis, C. M. (2021). Modelling of the fluctuation and coherent dynamics in active metamaterial devices. *IEEE Trans. Nanotechnol.* 20, 543–551. doi:10.1109/tnano.2021.3092059

Fang, M., Niu, K., Huang, Z., Wei, E., Wu, X., Koschny, T., et al. (2018). Investigation of broadband terahertz generation from metasurface. *Opt. Express* 26, 14241–14250. doi:10.1364/oe.26.014241

Friedrich, H., and Wintgen, D. (1985). Interfering resonances and bound states in the continuum. *Phys. Rev. A* 32, 3231–3242. doi:10.1103/PhysRevA.32.3231

Han, S., Pitchappa, P., Wang, W., Srivastava, Y. K., Rybin, M. V., and Singh, R. (2021). Extended bound states in the continuum with symmetry-broken terahertz dielectric metasurfaces. *Adv. Opt. Mater.* 9, 2002001. doi:10.1002/adom.202002001

Hsu, C. W., Zhen, B., Stone, A., Joannopoulos, J., and Soljačić, M. (2016). Bound states in the continuum. *Nat. Rev. Mater.* 1, 16048. doi:10.1038/natrevmats.2016.48

Huang, L., Chiang, Y. K., Huang, S., Shen, C., Deng, F., Cheng, Y., et al. (2021). Sound trapping in an open resonator. *Nat. Commun.* 12, 4819–4827. doi:10.1038/s41467-021-25130-4

Kang, M., Zhang, Z., Wu, T., Zhang, X., Xu, Q., Krasnok, A., et al. (2022). Coherent full polarization control based on bound states in the continuum. *Nat. Commun.* 13, 4536. doi:10.1038/s41467-022-31726-1

Lan, Z., You, J. W., Ren, Q., Sha, W. E. I., and Panoiu, N. C. (2021). Second-harmonic generation via double topological valley-hall kink modes in all-dielectric photonic crystals. *Phys. Rev. A* 103, L041502. doi:10.1103/PhysRevA.103.L041502

Lee, S. G., Kim, S. H., and Kee, C. S. (2020). Bound states in the continuum (bic) accompanied by avoided crossings in leaky-mode photonic lattices. *Nanophotonics* 9, 4373–4380. doi:10.1515/nanoph-2020-0346

Liu, M., Hwang, H. Y., Tao, H., Strikwerda, A. C., Fan, K., Keiser, G. R., et al. (2012). Terahertz-field-induced insulator-to-metal transition in vanadium dioxide metamaterial. *Nature* 487, 345–348. doi:10.1038/nature11231

Lu, C., Lu, Q., Gao, M., and Lin, Y. (2021a). Dynamic manipulation of thz waves enabled by phase-transition vo2 thin film. *Nanomaterials* 11, 114. doi:10.3390/nano11010114

Lu, C., Wang, C., Xiao, M., Zhang, Z. Q., and Chan, C. T. (2021b). Topological rainbow concentrator based on synthetic dimension. *Phys. Rev. Lett.* 126, 113902. doi:10.1103/PhysRevLett.126.113902

Lu, Y., Feng, X., Wang, Q., Zhang, X., Fang, M., Sha, W. E., et al. (2021c). Integrated terahertz generator-manipulators using epsilon-near-zero-hybrid nonlinear metasurfaces. *Nano Lett.* 21, 7699–7707. doi:10.1021/acs.nanolett.1c02372

Ma, J., Wang, Z. H., Liu, H., Fan, Y. X., and Tao, Z. Y. (2020). Active switching of extremely high-q fano resonances using vanadium oxide-implanted terahertz metamaterials. *Appl. Sci.* 10, 330. doi:10.3390/app10010330

Mandal, P., Speck, A., Ko, C., and Ramanathan, S. (2011). Terahertz spectroscopy studies on epitaxial vanadium dioxide thin films across the metal-insulator transition. *Opt. Lett.* 36, 1927–1929. doi:10.1364/ol.36.001927

Meng, B., Wang, J., Zhou, C., and Huang, L. (2022). Bound states in the continuum supported by silicon oligomer metasurfaces. *Opt. Lett.* 47, 1549–1552. doi:10.1364/OL.453076

Mittleman, D. M. (2017). Perspective: Terahertz science and technology. *J. Appl. Phys.* 122, 230901. doi:10.1063/1.5007683

Ren, Q., Feng, F., Yao, X., Xu, Q., Xin, M., Lan, Z., et al. (2021). Multiplexing-oriented plasmon-mos2 hybrid metasurfaces driven by nonlinear quasi bound states in the continuum. *Opt. Express* 29, 5384–5396. doi:10.1364/OE.414730

Ren, Q., You, J., and Panoiu, N. (2019). Large enhancement of the effective second-order nonlinearity in graphene metasurfaces. *Phys. Rev. B* 99, 205404. doi:10.1103/physrevb.99.205404

Ren, Q., You, J. W., and Panoiu, N. C. (2020). Comparison between the linear and nonlinear homogenization of graphene and silicon metasurfaces. *IEEE Access* 8, 175753–175764. doi:10.1109/ACCESS.2020.3026313

Ren, Q., You, J. W., and Panoiu, N. C. (2018). Giant enhancement of the effective Raman susceptibility in metasurfaces made of silicon photonic crystal nanocavities. *Opt. Express* 26, 30383–30392. doi:10.1364/OE.26.030383

Sadreev, A. F. (2021). Interference traps waves in an open system: Bound states in the continuum. *Rep. Prog. Phys.* 84, 055901. doi:10.1088/1361-6633/abefb9

Suh, W., Wang, Z., and Fan, S. (2004). Temporal coupled-mode theory and the presence of non-orthogonal modes in lossless multimode cavities. *IEEE J. Quantum Electron.* 40, 1511–1518. doi:10.1109/jqe.2004.834773

Wang, L., Zhao, Z., Du, M., Qin, H., Ako, R. T., and Sriram, S. (2022a). Tuning symmetry-protected quasi bound state in the continuum using terahertz meta-atoms of rotational and reflectional symmetry. *Opt. Express* 30, 23631–23639. doi:10.1364/OE.454739

Wang, X., Xin, J., Ren, Q., Cai, H., Han, J., Tian, C., et al. (2022b). Plasmon hybridization induced by quasi bound state in the continuum of graphene metasurfaces oriented for high-accuracy polarization-insensitive two-dimensional sensors. *Chin. Opt. Lett.* 20, 042201. doi:10.3788/col202220.042201

Xiao, S., Wang, T., Liu, T., Yan, X., Li, Z., and Xu, C. (2018). Active modulation of electromagnetically induced transparency analogue in terahertz hybrid metal-graphene metamaterials. *Carbon* 126, 271–278. doi:10.1016/j.carbon.2017.10.035

Yang, D., Wang, W., Lv, E., Wang, H., Liu, B., Hou, Y., et al. (2022). Programmable vo2 metasurface for terahertz wave beam steering. *iScience* 25, 104824. doi:10.1016/j.isci.2022.104824

Zhao, X., Chen, C., Kaj, K., Hammock, I., Huang, Y., Averitt, R. D., et al. (2020). Terahertz investigation of bound states in the continuum of metallic metasurfaces. *Optica* 7, 1548–1554. doi:10.1364/OPTICA.404754

Zhao, X., Zhang, J., Fan, K., Duan, G., Schalch, J., Keiser, G. R., et al. (2019). Real-time tunable phase response and group delay in broadside coupled split-ring resonators. *Phys. Rev. B* 99, V. doi:10.1103/physrevb.99.245111

Zhao, Y., Huang, Q., Cai, H., Lin, X., and Lu, Y. (2018). A broadband and switchable vo2-based perfect absorber at the thz frequency. *Opt. Commun.* 426, 443–449. doi:10.1016/j.optcom.2018.05.085

Zhu, Y., Zhao, Y., Holtz, M., Fan, Z., and Bernussi, A. A. (2012). Effect of substrate orientation on terahertz optical transmission through vo 2 thin films and application to functional antireflection coatings. *JOSA B* 29, 2373–2378.

frontiers | Frontiers in Nanotechnology

TYPE Original Research
PUBLISHED 18 May 2023
DOI 10.3389/fnano.2023.1181362

Check for updates

OPEN ACCESS

EDITED BY
Giancarlo Franzese,
University of Barcelona, Spain

REVIEWED BY
Gionni Marchetti,
University of Barcelona, Spain
Hender Lopez,
Technological University Dublin, Ireland

*CORRESPONDENCE
Christoffer Åberg,
✉ christoffer.aberg@rug.nl

RECEIVED 07 March 2023
ACCEPTED 26 April 2023
PUBLISHED 18 May 2023

CITATION
Yang B, Richards CJ, Gandek TB, de Boer I, Aguirre-Zuazo I, Niemeijer E and Åberg C (2023), Following nanoparticle uptake by cells using high-throughput microscopy and the deep-learning based cell identification algorithm Cellpose.
Front. Nanotechnol. 5:1181362.
doi: 10.3389/fnano.2023.1181362

Following nanoparticle uptake by cells using high-throughput microscopy and the deep-learning based cell identification algorithm Cellpose

Boxuan Yang, Ceri J. Richards, Timea B. Gandek, Isa de Boer, Itxaso Aguirre-Zuazo, Else Niemeijer and Christoffer Åberg*

Pharmaceutical Analysis, Groningen Research Institute of Pharmacy, University of Groningen, Groningen, Netherlands

How many nanoparticles are taken up by human cells is a key question for many applications, both within medicine and safety. While many methods have been developed and applied to this question, microscopy-based methods present some unique advantages. However, the laborious nature of microscopy, in particular the consequent image analysis, remains a bottleneck. Automated image analysis has been pursued to remedy this situation, but offers its own challenges. Here we tested the recently developed deep-learning based cell identification algorithm Cellpose on fluorescence microscopy images of HeLa cells. We found that the algorithm performed very well, and hence developed a workflow that allowed us to acquire, and analyse, thousands of cells in a relatively modest amount of time, without sacrificing cell identification accuracy. We subsequently tested the workflow on images of cells exposed to fluorescently-labelled polystyrene nanoparticles. This dataset was then used to study the relationship between cell size and nanoparticle uptake, a subject where high-throughput microscopy is of particular utility.

KEYWORDS

nanoparticles, cell uptake, fluorescence microscopy, high-throughput, machine learning, image segmentation, modelling, Cellpose

1 Introduction

The interaction between nanoparticles and cells is studied for a number of applications; within medicine for drug delivery (Shi et al., 2017; Akinc et al., 2019; Wolfram and Ferrari, 2019; Kulkarni et al., 2021; Mitchell et al., 2021), imaging (Bogart et al., 2014; Yu and Zheng, 2015; Kim et al., 2018; Han et al., 2019), vaccination (Friedrichs and Bowman, 2021; Fries et al., 2021; Kisby et al., 2021), and cell therapies (Chakravarty et al., 2010; Stewart et al., 2016; Xiong et al., 2021) and within toxicology to ensure the safe implementation of nanotechnology (Oberdörster et al., 2005; Rivera-Gil et al., 2013; Valsami-Jones and Lynch, 2015; Park et al., 2017; Kah et al., 2021). The ultimate effect of the nanoparticle, whether it is a therapeutic or an adverse one, ultimately depends on the number of particles that may exert said effect. While nanoparticles have been shown to cause effects on cells indirectly over a barrier (Bhabra et al., 2009; Sood et al., 2011; Dugershaw et al., 2020), in most cases their effects occur within the cell, and consequently the number of nanoparticles that enter a cell remains a key question (Åberg, 2021).

To investigate the uptake of nanoparticles by cells, a range of techniques have been used and developed, including Inductively Coupled Plasma Mass Spectrometry (ICP-MS) for metal-containing particles (Chithrani et al., 2006; Cho et al., 2009), magnetophoresis for magnetic particles (Wilhelm et al., 2002), and flow cytometry for fluorescently labelled particles (Salvati et al., 2018), just to name a few [see previous literature for a more comprehensive list; (Salvati et al., 2018; Åberg, 2021)].

Optical microscopy is also a useful technique, in particular for fluorescently labelled particles (Jiang et al., 2010a; Schübbe et al., 2010; Åberg et al., 2021), but also for particles that intrinsically exhibit fluorescence [*e.g.*, quantum dots (Jiang et al., 2010b; Summers et al., 2011)] as well as particles that scatter light strongly (Gibbs-Flournoy et al., 2011). In fact, microscopy has a range of advantages (in particular for adherent cells) that sets it apart from many other techniques to measure nanoparticle cell uptake. Perhaps the most obvious one is that it is possible to directly observe the cell, and thereby relate its accumulated amount of nanoparticles to its phenotypic traits (*e.g.*, cell area) (Panet et al., 2017; Rees et al., 2019), or other characteristics (Caicedo et al. (2017) [*e.g.*, cell cycle state, (Kim et al., 2012; Åberg et al., 2017), as well as its local environment (Snijder et al., 2009)]. Another advantage is that in principle it is possible to explicitly count the number of particles inside a cell, as opposed to relying on more indirect measures such as fluorescence intensity. Admittedly nanoparticles often accumulate within the same organelles inside cells (Sandin et al., 2012; Åberg et al., 2016), and the resulting clusters are often below the diffraction limit, so counting individual objects is not sufficient to gain knowledge of the total number of particles. However, to resolve such clusters one may use super-resolution approaches (Schermelleh et al., 2019), such as stimulated emission depletion microscopy (Schübbe et al., 2010; Müller et al., 2012), or estimate the number of particles within a cluster based on the total fluorescence intensity of the cluster (Wang et al., 2009; Åberg et al., 2016; Rees et al., 2019).

A major disadvantage of microscopy, however, is that the resulting image analysis is labour-intensive and consequently it is typically only applied to a handful of cells. Imaging cytometry can certainly offset the low-throughput character of microscopy (Summers et al., 2011), and may be useful for many applications, but some of the advantages of microscopy are also lost (*e.g.*, the possibility of observing the cell in its native state). Various approaches to make microscopy more high-throughput have consequently been pursued, including within the nanoparticle-cell interactions field (Brayden et al., 2015; Collins et al., 2017). One such approach is the usage of automatic cell identification algorithms, both using commercial (Panarella et al., 2016; Kelly et al., 2021) and free (Panarella et al., 2016; Rees et al., 2019) software. In particular, the free software CellProfiler (Carpenter et al., 2006; Kamentsky et al., 2011; McQuin et al., 2018; Stirling et al., 2021) is quite popular for this purpose, within biological imaging in general and for nanoparticle-cell studies in particular. A quite different approach is the physical separation of the cells, by seeding the cells on specifically prepared arrays where cells only adhere within predefined and well-separated areas (Murschhauser et al., 2019), thereby completely avoiding the difficulty of identifying where one cell ends and the other begins.

More recently, deep-learning (LeCun et al., 2015) based algorithms have been developed to improve automatic cell identification. This is the approach we took in the work reported here; specifically, we used the deep-learning based algorithm Cellpose (Stringer et al., 2021; Pachitariu and Stringer, 2022), and developed a workflow that couples high-throughput microscopy of cells to a semi-automatic identification of the cells based on Cellpose. This workflow was set up because by necessity only limited fields of view of the full sample can be captured, and these views have to subsequently be united post-acquisition into a full(er) view of the sample. Our workflow ensures that all cells are identified, that no cells are identified twice, and that all cells are complete (as opposed to two halves of a cell being identified separately in two images). While the automatic cell identification by Cellpose worked very well, we also included a manual inspection step in the workflow to review the automatic cell identification. We tested the workflow by applying it to microscopy images of cells exposed to polystyrene nanoparticles. Subsequently this dataset was used to investigate the relationship between cell size and nanoparticle uptake (Panet et al., 2017; Rees et al., 2019; Åberg et al., 2021), a topic where microscopy has several advantages over other techniques and where high-throughput is very much desired.

2 Materials and methods

2.1 Materials

HeLa cervical adenocarcinoma cells were acquired from American Type Culture Collection (ATTC; CCL-2TM, lot no. 61647128). Minimal Essential Medium (MEM) containing Earle's salts and l-glutamine, Foetal Bovine Serum (FBS), Dulbecco's Modified Eagle Medium (DMEM), Dulbecco's Phosphate Buffered Saline (PBS) without $CaCl_2$ and $MgCl_2$, and 0.05% trypsin–EDTA were purchased from ThermoFisher (Gibco, Life Technologies).

Yellow/green carboxylated polystyrene nanoparticles of 100 and 500 nm diameter (excitation 505 nm; emission 515 nm) and Wheat Germ Agglutinin (WGA) conjugated with Alexa Fluor 555 were obtained from ThermoFisher (Gibco, Life Technologies) and used without further modifications. DAPI was purchased from AppliChem. and Mowiol 4-88 was acquired from Merck Millipore. Glycerol was obtained from ThermoFisher.

2.2 Cell culture

HeLa cells were cultured under standard conditions (37°C, humidified atmosphere and 5% CO_2) in MEM supplemented with 10% (v/v) FBS (cMEM) or DMEM supplemented with 10% (v/v) FBS (cDMEM). Mycoplasma tests were performed regularly and showed no contamination.

2.3 High-throughput fluorescence microscopy

Microscopy coverslips of 12 mm diameter were placed in each well of a 24-well plate. HeLa cells cultured in cMEM were seeded at a density of 50,000 cells per well and left to adhere to the substrate by incubation overnight at 37°C under a humidified atmosphere and 5% CO_2. Nanoparticle dispersions were prepared by diluting the nanoparticle stock in cMEM to obtain the appropriate concentrations. The cells were exposed to the particles by replacing the medium with the nanoparticle dispersion, after which the cells were further incubated for 4 h at 37°C under a humidified atmosphere and 5% CO_2. Subsequently, the nanoparticle-containing medium was removed and the cells were washed with PBS, followed by fixation using 4% formaldehyde following the protocol provided by the manufacturer. The fixing solution was removed and cells were washed with PBS. Subsequently, the cells were stained using WGA diluted in PBS (1:200 dilution) by incubation at 37°C for 10 min, followed by washing with PBS. Nuclei were stained by incubation with DAPI diluted in PBS (1:5,000) for 5–10 min at room temperature and subsequent rinsing. Finally, the coverslips were mounted on microscope slides (ThermoScientific) using 200 mg/mL Mowiol dissolved in glycerol and left at room temperature for 24 h. The cells were observed with a 40× oil objective using a Zeiss AxioObserver Z1 microscope equipped with a CMOS-colour camera PL-B623 Pixelink 3.1 Megapixels and using TissueFAXS acquisition software.

2.4 Image analysis using CellProfiler

The images were analysed using Cellprofiler (McQuin et al., 2018) (version 3.1.8). To account for a non-uniform intensity of the nuclear (DAPI) signal, however, ilastik (Berg et al., 2019) (version 1.3.3) was first used to identify the nuclei. The IdentifyPrimaryObject module in CellProfiler was then used to identify the nuclei in the binary image output by ilastik. Subsequently, the IdentifySecondaryObjects module in CellProfiler was used to identify the cells from the cytoplasm (WGA) signal, working with the “Propagation” method of the IdentifySecondaryObjects module. The “Propagation” method starts from each nucleus and stops when hitting another cell or when the intensity is below a threshold (McQuin et al., 2018). The threshold was set after measuring the background intensity in a region without cells.

2.5 Image analysis using Cellpose

The workflow is described in the main text. Briefly, Cellpose (Stringer et al., 2021) was run on all images, using the same cell diameter (100 pixels) throughout. The identified cells were manually checked. In a few images, air bubbles were present, in which case the cells within the bubble were removed. Identified cells touching the border were removed from each image and subsequently identified cells that were part of two neighbouring images were removed from the right and/or bottom of the two images. Measurements were then performed on the resulting identified cells: Cell area was evaluated as the number of pixels within and including each outline from Cellpose, multiplied by the size of a pixel (0.228151 μm) squared. Nanoparticle fluorescence was evaluated as the sum of the fluorescence intensity within each outline from Cellpose. Unless otherwise stated, an estimate of the background fluorescence was subtracted from the nanoparticle fluorescence of each cell. The estimate of the background fluorescence was calculated from an empirical linear relationship between the background fluorescence and cell area, evaluated from cells not exposed to nanoparticles as described in Supplementary Figure S3. To show that the conclusions do not depend upon this background subtraction we also show results without it (see main text). When fitting mathematical models to the distribution of experimental data, we fitted to the empirical cumulative distribution function derived from the experimental data (rather than the histogram of experimental values), thereby making the fitting procedure independent of the bins chosen for the histograms.

2.6 Simulations

In order to compare the relationship between cell area and nanoparticle uptake within the model, simple numerical simulations were performed. These simulations were based on the same assumptions as the model, and the results obtained from the simulations were analysed in the same way as the experimental data. In total, 50,000 cells were simulated. Their areas were sampled from a gamma distribution (Eq. 1 below) with a certain shape parameter, k, and scale parameter, θ. The shape and scale parameters were taken from experimental data (Figure 3 below), unless otherwise noted. To evaluate nanoparticle uptake into the simulated cells, for each cell i, the number of nanoparticles it took up was sampled from a Poisson distribution with rate parameter $\lambda A_i C t$, where λ is the rate of uptake per unit area and concentration, A_i the area of the cell, C nanoparticle concentration, and t time. The nanoparticle concentration, C, and time, t, was set according to the experimental conditions the simulations were supposed to describe, while the rate of uptake, λ, was evaluated from fits to the experimental data (*e.g.*, Figure 4B below). Nanoparticle/cell area histograms were determined in the same way as from the experimental data, aside from that the total number of cells were scaled down to the experimentally sampled number of cells for ease of comparison.

2.7 Flow cytometry

HeLa cells cultured in cDMEM were seeded in 24-well plates 2 days or 1 day prior to the nanoparticle exposure at a density of approximately 150,000 cells per well. The well plates were left to incubate at 37°C under a humidified atmosphere and 5% CO_2 until the day of the experiment.

A 500 nm particle dispersion at a concentration of 100 or 150 μg/mL was freshly prepared on the day of the experiment under minimal light and under sterile conditions. The nanoparticle stock was vortexed, after which a small amount was diluted in cDMEM to the right concentration. The resulting dispersion was vortexed before incubation in a warm bead bath for at least 30 min to allow for the formation of a biomolecular corona.

Prior to nanoparticle exposure to cells, the nanoparticle dispersion was briefly vortexed again to ensure a homogenous suspension of the nanoparticles. Then the medium was removed from the wells and replaced with nanoparticle dispersion. The cells were further incubated for various times at 37°C under a humidified atmosphere and 5% CO_2. After nanoparticle exposure, the nanoparticle dispersions were removed and the cells were washed once with cDMEM and twice with PBS. Subsequently, the cells were detached with the addition of trypsin and incubation for 5 min at 37°C under a humidified atmosphere and 5% CO_2. The detached cell suspensions were diluted in cDMEM and centrifuged for 5 min at 250 relative centrifugal force, after which the supernatant was removed by inversion. The cells were resuspended in PBS before flow cytometry measurement.

Measurements were performed using a Novocyte Quanteon (Agilent) flow cytometer. The yellow-green nanoparticles were excited at 488 nm and emission was collected at 530/30 nm. Forward scattering area (FSC-A) and side scattering area (SSC-A) were used to separate living cells from debris and dead cells. These living cells were further separated from doublets using FSC-A against forward scattering height (FSC-H). Cells with no particles and cells with one particle were analysed separately as described in the main text. As a control, a dispersion of 500 nm particles at a concentration of 20 μg/mL was also run through the flow cytometer.

2.8 Particle dispersion characterisation

The 100 nm particle dispersions were characterised using Nanoparticle Tracking Analysis (NTA). The particles were dispersed at a concentration of 10^9 particles/mL in PBS and cMEM respectively. The cMEM dispersions were left for at least an hour to allow for biomolecular corona formation. The dispersions were measured at room temperature using a NanoSight LM14, measuring at 5 sections of each sample. The results were analysed using NTA 3.0 software (Malvern) and are presented as the average ± standard deviation over the five sections (Supplementary Table S1) or as the full distribution (Supplementary Figure S1).

The 500 nm particle dispersions were characterised using dynamic light scattering by dispersing the particles in PBS and cDMEM, respectively, at a concentration of 150 μg/mL, the highest concentration used when exposing the particles to cells. The cDMEM dispersions were left for at least an hour to allow for biomolecular corona formation. The dispersions were measured at room temperature using a Malvern ZetaSizer Nano ZS (Malvern Instruments, Malvern, United Kingdom). Three measurements of at least 10 runs were recorded for each condition. The measurements were analysed using ZetaSizer Software version 7.13 (Malvern Instruments, Malvern, United Kingdom). The results are presented as the average ± standard deviation over three replicate samples of the z average and polydispersity index evaluated by cumulant analysis (Supplementary Table S1) or the distributions from CONTIN analysis (Supplementary Figure S2).

3 Results

As a nanoparticle model system, we used commercially available yellow/green fluorescently labelled carboxylated polystyrene nanoparticles of 100 nm diameter, because we have previous data on the uptake of these particles to compare to and to support our conclusions (Kim et al., 2012; Varela et al., 2012; Varela et al., 2015; Åberg et al., 2016; Vtyurina et al., 2021; Åberg et al., 2021; de Boer et al., 2022). As a cell model, we used HeLa (human adenocarcinomic cervical epithelial) cells, a well-characterised and well-used cell line (Collinet et al., 2010; Simpson et al., 2012). We also used 500 nm diameter sized yellow/green fluorescently labelled carboxylated polystyrene nanoparticles, because their strong fluorescence proved crucial for further support of our conclusions, as will transpire below. In line with previous studies (dos Santos et al., 2011; Kim et al., 2012; Åberg et al., 2016; Vtyurina et al., 2021; de Boer et al., 2022), dynamic light scattering showed that these nanoparticles are fairly monodisperse and remain well-dispersed in cell culture medium supplemented with serum (Supplementary Table S1 and Supplementary Figures S1, S2).

For measuring cellular nanoparticle uptake using microscopy with high-throughput it is necessary to automatically identify (segment) the cells in the microscopy images. To test the possibility of doing so, HeLa cells were fixed and incubated with DAPI (4′,6-diamidino-2-phenylindole), to stain the cell nuclei, and fluorescently-labelled WGA (Alexa Fluor 555-labelled Wheat Germ Agglutinin) to stain the cytoplasm (Figure 1A).

In a preliminary investigation, we used the open-source software CellProfiler (Carpenter et al., 2006; McQuin et al., 2018) to identify the cells in the images. More specifically, we first used the machine-learning based program ilastik (Berg et al., 2019) to identify the nuclei, as their intensity sometimes varied between cells. Subsequently, we used the "propagation" method in CellProfiler to find the cell borders (Figure 1B; see Materials and Methods for details). Unfortunately, we noticed some issues with the cell identification, typically when two cells bordered each other, where sometimes the borders identified by the algorithm did not match the borders that are quite clear from the original image (*cf.* Figures 1D, F; Figures 1E, G). While the identification can probably be optimised to some degree by changing parameters and, if all else fails, be corrected manually, we found the identification to be less than optimal.

As an alternative, we thus turned to Cellpose (Stringer et al., 2021). We had to optimise the choice of one parameter, cell size, since Cellpose has been trained on microscopy images of a different resolution compared to ours. However, once we had found a reasonable value for the cell size parameter, we found that cell identification worked very well (Figure 1C). In particular, we found that Cellpose identified the cell borders close to what the original image would suggest (*cf.* Figures 1D, H; Figures 1E, I). It is beyond the scope of the present work to fully compare the CellProfiler- and Cellpose-based approaches; however, see Chen and Murphy (2022) for a study along these lines. Suffice to say here that Cellpose clearly performed better than our usage of CellProfiler (*cf.* Figures 1D, F; Figures 1E, G). Nevertheless, some misidentification did occur (*e.g.*, Figure 1C; arrow), which could potentially be remedied by optimisation of the staining procedure and/or changing the cell

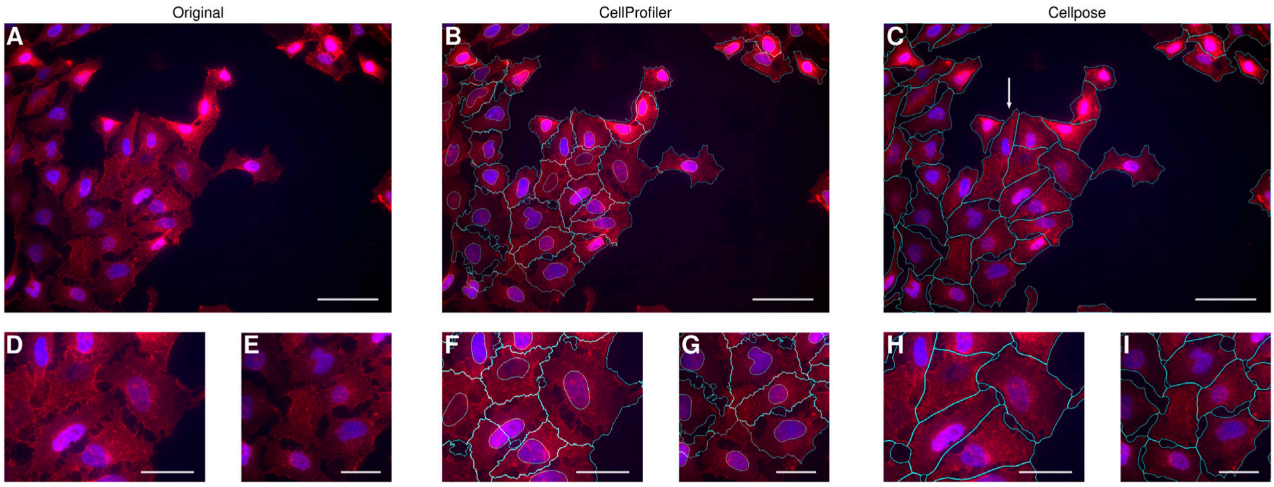

FIGURE 1
Comparison of automatic cell identification using different software. HeLa cells were labelled with WGA to distinguish the cytoplasm (red) and with DAPI to distinguish the nuclei (blue). **(A–C)** One field of view of the cell culture. Scale bars 50 µm. **(D–I)** Zoom-in at two different locations within the field of view. Scale bars 25 µm. **(A,D–E)** Original image from which it is easy to discern individual cells by eye. **(B,F–G)** Cells (cyan) and their nuclei (also cyan) identified using CellProfiler (in combination with ilastik). The outline of many of the cells correspond to what one may discern by eye, but in some cases the outlines clearly do not capture the actual cell borders (*cf.* panels **D,F**; and **E,G**, respectively). **(C, H–I)** Cells (cyan) identified using Cellpose. The outline of the majority of the cells correspond to what one may discern by eye, including those examples where our usage of CellProfiler did not result in a sufficiently accurate identification (*cf.* panels **D, F, H**; and **E, G, I**, respectively). Nevertheless, there were some cells that were not correctly identified, for example, the cell indicated by a white arrow in panel **C**, which is actually 2 cells (*cf.* panel **A**) though the DAPI staining of the second cell is somewhat faint.

identification parameters (other than cell size). Despite these misidentifications, we reasoned that there were so few misidentifications that correcting these manually would be quick, especially given the rather efficient graphical user interface available for Cellpose (where shortcuts and mouse gestures make correction swift).

Having convinced ourselves that the cells could be identified well and fast, we proceeded by acquiring microscopy images. We employed an automatic imaging system (TissueFAXS) that allowed us to acquire many fields of view of cells in widefield mode, for a total of up to 1,900 cells per sample (more is possible, but was not necessary here). Each field of view was composed of 1,392 × 1,040 pixels, corresponding to 318 × 237 μm^2. The images were acquired in a 7 × 9 grid (Figure 2A), where there was substantial overlap between images to ensure that all cells would be fully included in (at least) one image (Figure 2B) and thereby avoid eventual issues from identified cells having to be stitched together from two different images (Figure 2C).

To analyse these images, after a bit of trial-and-error we arrived at the workflow depicted by Figure 2E, which we found to be quite efficient: First, we ran Cellpose on all microscopy images with a fixed (optimised) cell size. Depending upon the specifics of the computer hardware (especially the presence or absence of graphical processing units, GPUs) and the number of images, this step can take some time. As an admittedly informal guide, it took 25 min to analyse 63 images of 1,392 × 1,040 pixels and in total 1,900 cells with a cell size of 100 pixels on a computer without GPU support. This analysis can, however, be executed without any human intervention. As a next step, we subsequently went through each image and corrected any misidentified cells. This becomes quite efficient after learning all software shortcuts, but nevertheless is somewhat labour intensive. Again as an informal guide, it took us around 90 min to do this for 63 images containing in total some 1,900 identified cells. The (local) density of cells is a major factor here, as cells are typically well-identified when fairly isolated, while the majority of errors occur in dense areas.

At this point we thus had only cells that were considered to be well-identified, but had many cells that were identified in several images. Next, for each image we removed all identified cells touching any of the borders of that image. This discards all identified cells at the overall grid border (Figure 2D), the size and other characteristics of which we cannot know for sure, since they were not fully captured in any image. However, it also discards a large number of identified cells within the overlap regions (Figure 2F). A prerequisite for this step to make sense is thus that each cell is captured fully in at least one image (ensured by choosing a large overlap distance) because then removing the identified cells touching the border will not matter as the cell will also have been identified in a neighbouring image. We carried out this step as follows: For each image, we considered each pixel along each of the four borders (left, top, right, and bottom). If a pixel had been identified to belong to a certain cell, then that cell was removed (from the whole image). This step was performed in a fully automated fashion, something that can be done without expending any substantial computing power. This is advantageous as it decreases the amount of human effort, as well as time.

After this step, we removed all remaining identified cells that were included in two neighbouring images, always keeping the identified cell that was identified either in the left or upper neighbouring image (Figure 2G). The choice of left and upper is,

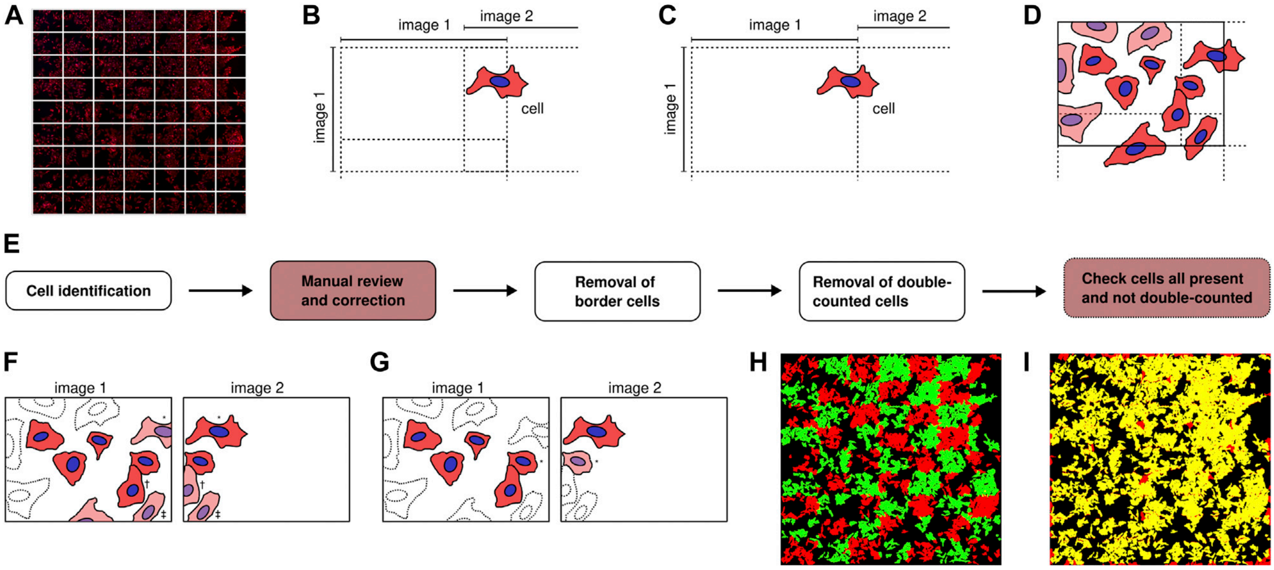

FIGURE 2
Illustration of high-throughput microscopy and image analysis. **(A)** Microscopy images were acquired in a grid to cover a large area. **(B)** Schematic of the situation (which we employed) when the microscopy images are acquired in such a way that they overlap. The indicated cell is here in both image 1 and 2, but only part of the cell is in image 1, while the whole cell is in image 2. Analysis of this cell is consequently easiest if performed in image 2. **(C)** Schematic of the situation when the microscopy images are acquired in such a way that they do not overlap (contrary to our set up). In this case, the indicated cell is in both image 1 and 2, but is not complete in either. Analysis of this cell consequently needs to be stitched together from two different images. **(D–G)** Algorithm to ensure each identified cell is included in the dataset only once. The cells that are discarded in each step are shaded, while cells that were previously discarded are shown with dotted outlines. **(D)** All cells on the overall outer border are removed, thereby keeping only cells that were fully captured in (at least) one image. **(E)** Depiction of the different steps of the workflow. The steps that can be fully automated have a white background, while the steps that involves manual operation have a red background. The final step is not strictly necessary. **(F)** All identified cells on the border of each image (not just the border of the overall area) are removed. Potentially this could lead to removal of some correctly identified cells, but if the overlap between images is large enough, then each cell will be captured in at least one image and there will be no cells lost. For example, the cell indicated by an asterisk (*) is removed from image 1, but is fully included in image 2. Similarly, the cell indicated by a dagger (†) is removed from image 2, but is fully included in image 1. The cell indicated by a double dagger (‡) is removed from both image 1 and 2; it should therefore be included in the image below image 1 or 2, if the overlap is large enough. **(G)** Finally, all remaining identified cells within the overlap region that are in two images are removed from one image, always keeping such an identified cell in the uppermost or leftmost of the two images. For example, the cell indicated by an asterisk (*) is included in both image 1 and 2. This cell is kept in the identification related to image 1, since image 1 is to the left of image 2. **(H)** To ensure that there is no double counting of identified cells, a useful quick check is to overlay the images of all the identified cells, alternating the colour (here between red and green) between each image. A cell that is included in two images then easily stands out as it will be in both colours (here yellow). **(I)** Similarly, a quick check to see if all the cells that were originally identified (before the algorithm illustrated by panel **D,F–G** potentially removed them) is to overlay the originally identified cells (here red) with the final dataset (here green). Cells that have been removed are then readily visible as they are only in one colour (here red).

of course, arbitrary, but has to be performed consistently throughout the grid. We carried out this step in the following way: For each overlap region, we considered the identified cells that were identified in the left (upper) image. For each such identified cell, we found the identified cells, if any, that were identified in the right (bottom) image and which overlapped with the cell identified in the left (upper) image. The overlapping cells identified in the right (bottom) image were then removed, if the overlap was large enough (to allow a slightly different identification in the two overlapping images). Again this step was fully automated and does not require a substantial amount of computing power; consequently it can be performed quickly and without human intervention.

Finally we checked that all cells that were originally identified were still included in the dataset and included only once. This can be done quite efficiently by displaying the full grid of images (in reduced resolution) in such a way that the images are overlapped by the amount they were overlapped upon acquisition and alternating the colour between each image (Figure 2H). An identified cell that is present in two images will then exhibit both colours and easily stand out by eye. Similarly to ensure that all cells that were originally identified are still present in the dataset, one can overlap both sets of identified cells, again in two colours. A cell that has been removed during the overall procedure will then have only one colour (Figure 2I). In our dataset this occurred for cells along the outer borders (by design), but also some other cells were removed in this way (Figure 2I). This can be corrected manually, but since they are clearly a minority one can also proceed without them.

Having thus created a dataset containing ~1,900 cells we then quantified the cell area distribution, since cell area is a parameter where a microscopy-based method exhibits clear advantages over other high-throughput methods. For example, flow cytometry is certainly high-throughput, but does not give an accurate estimate of cell size (Shapiro, 2003). Furthermore, cell-to-cell variability in nanoparticle uptake has been suggested to be driven by cell area Rees et al. (2019). We thus evaluated the area, A, of each identified cell and from that the cell area distribution (Figure 3). We may observe that the distribution is not a normal distribution, but rather exhibits a wider tail towards larger cell sizes. Previous reports have

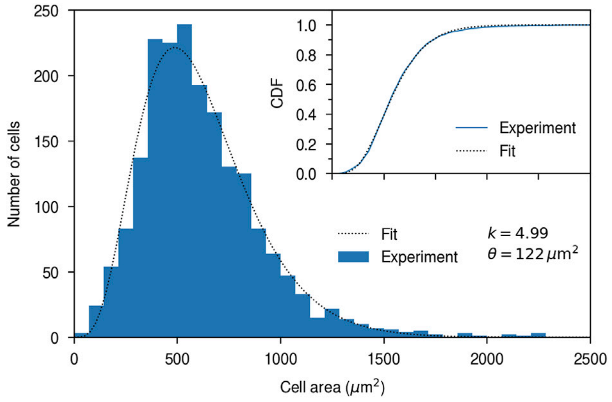

FIGURE 3
HeLa cell area quantified using high-throughput microscopy. HeLa cells were stained with DAPI (cell nuclei) and WGA (cytoplasm) and observed using fluorescence microscopy (as in Figure 1). The histogram shows experimental data, while the dotted line is a fit of a gamma distribution (Eq. 1) to the data. *k* and θ are the resulting fitting parameters. Note that the fit was performed on the cumulative distribution function, so as to be independent of the bins chosen for the histogram. (Inset) Cumulative distribution function showing the goodness of fit. (Blue) Empirical cumulative distribution. (Dotted line) Fit. Same *x*-axis as the main figure.

described the cell area distribution, *f*(*A*), in terms of a gamma distribution (Rees et al., 2019)

$$f(A) = \frac{1}{\Gamma(k)\theta^k} A^{k-1} e^{-A/\theta} \tag{1}$$

where Γ is the gamma function, k is a shape parameter and θ a scale parameter. Consistent with this description, we find that a gamma distribution provides an excellent fit to the data (Figure 3; inset), and from such a fit we can evaluate the parameters to be $k = 4.99$ and $\theta = 122\ \mu m^2$. It should be noted that [like previous work (Rees et al., 2019)] the cell area here is quantified using two-dimensional microscopy, so the area is perhaps best interpreted as the projected cell area, rather than the full cell surface area embedded in three-dimensional space. Nevertheless, if we assume that the latter is proportional to the projected cell area, then the two areas will have the same shape of the distribution.

Having set up the workflow to identify the HeLa cells using high-throughput microscopy, we then exposed the cells to 100 nm nanoparticles (Figure 4A). Nanoparticle uptake was quantified in terms of the total nanoparticle fluorescence per cell. Part of the measured fluorescence is background and while this is small in comparison to the signal (Supplementary Figure S3) we nevertheless wanted to remove it to better relate the measured fluorescence to nanoparticle numbers. Fortunately, we noted a very strong correlation between background fluorescence and cell area for cells not exposed to nanoparticles (Supplementary Figure S3), which allows us to predict the background fluorescence for a cell of a given area. By thus removing the background we were able to quantify the fluorescence stemming solely from the nanoparticles, something we then assumed is proportional to the number of nanoparticles, and hence the number of objects, that entered. Figure 4B shows the resulting distribution of nanoparticle fluorescence over cells, from which we observe a fairly well-defined distribution that appears roughly normally distributed, aside from a clear tail towards higher fluorescences.

Rees et al. developed a model to describe the distribution of number of nanoparticles per cell (Rees et al., 2019), and we decided it would be interesting to test their model also on our data. Their model is essentially based on two ingredients, namely, that the uptake of a particle is a Poisson process and that the probability of uptake is proportional to the area of a cell. Based on these two assumptions, and the empirical observation (Figure 3) that the cell area distribution is approximately a gamma distribution (Eq. 1), Rees et al. showed that the probability, p_N, that a cell has taken up N particles is given by

$$p_N(Ct) = \frac{\Gamma(k+N)}{N!\,\Gamma(k)} \frac{(\lambda\theta Ct)^N}{(1+\lambda\theta Ct)^{N+k}}. \tag{2}$$

Here k and θ are the two parameters of the cell area distribution (Eq. 1), and λ the rate of uptake per unit area and concentration. Furthermore, the probability of uptake depends on the two variables concentration, C, and time, t, which, however, in the model only enter together as their product, Ct.

One subtlety of the model that is important to note is that in principle it is formulated not in terms of the total number of *particles* within the cells, but the total number of nanoparticle *clusters* (single nanoparticles or nanoparticle agglomerates). Furthermore, what is important is the number of clusters *at the time of entrance*. In general this may be an issue, because at least the nanoparticles we use here cluster within organelles intracellularly (Sandin et al., 2012; Åberg et al., 2016). The number of clusters that we would count after some time of exposure (*e.g.*, 4 h in the case of Figure 4) therefore has no direct relation to the number of clusters at the time of entrance. Fortunately, the nanoparticles we use here are well-dispersed in medium and typically enter cells as single objects (Sandin et al., 2012; Åberg et al., 2016), so that the total number of nanoparticles is a good approximation to the number of objects that entered the cells. In general, though, using the model on nanoparticles that both agglomerate extracellularly and cluster within the cell would appear fraught with difficulties.

To test whether the model can describe our data we fitted the model with the normalised uptake rate, λ, as free parameter and the known cell area distribution parameters (k and θ) fixed from the experiment on cells not exposed to nanoparticles (Figure 3). Since the model is formulated in terms of number of objects, rather than fluorescence, we furthermore had to make an assumption on the fluorescence exhibited by a single nanoparticle. We used several different values, which, as expected, give different quantitative results, but give the same qualitative outcomes. We therefore focus the presentation here on one choice, but refer to the supplement for others (Supplementary Figures S4, S7). With this approach we observed that the model can describe the nanoparticle fluorescence distribution well, given that a fit of the model with only one free parameter shows good agreement (Figure 4B; inset), an outcome that is independent of the choice of the fluorescence of a single nanoparticle (Supplementary Figure S4) as well as whether we do the background subtraction or not (Supplementary Figure S5).

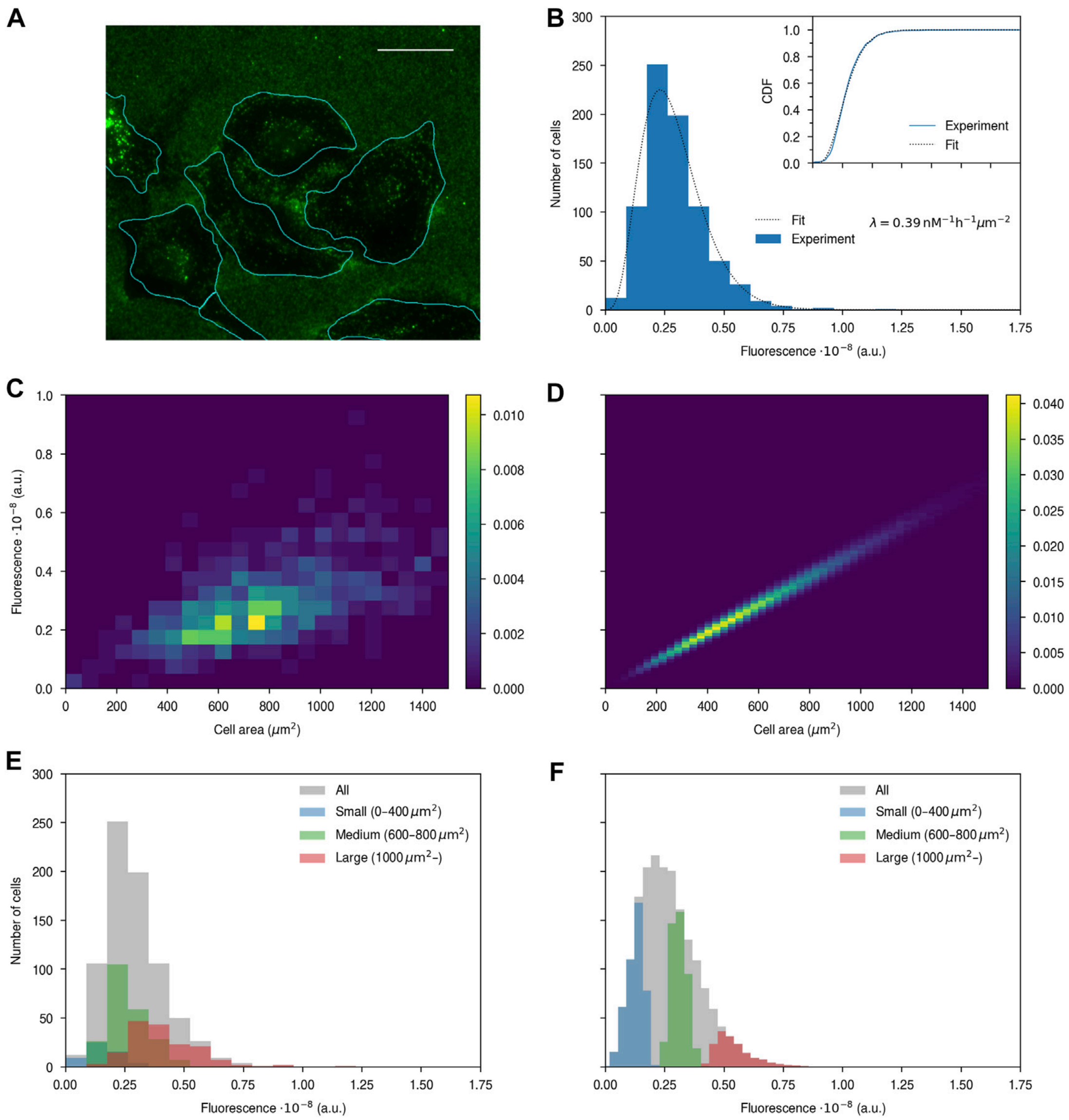

FIGURE 4
Nanoparticle uptake quantified by high-throughput fluorescence microscopy. HeLa cells were exposed to 100 μg/mL of the 100 nm nanoparticles for 4 h, stained with DAPI (cell nuclei) and WGA (cytoplasm), and observed using fluorescence microscopy. **(A)** Example image with nanoparticles in green and cell outlines (identified as exemplified in Figure 1C) in cyan. Note that there is a substantial number of nanoparticles stuck on the glass outside the cells. Scale bar 25 μm. **(B)** Fluorescence distribution over cells after background subtraction (Supplementary Figure S3). The histogram shows experimental data, while the dotted line is a fit of a model to the data, assuming a fluorescence per nanoparticle of 10^5 and using cell area parameters (*k* and θ) from control cells (Figure 3). λ is the resulting fitting parameter. Note that the fit was performed on the cumulative distribution function, so as to be independent of the bins chosen for the histogram. (Inset) Cumulative distribution function showing the goodness of fit. (Blue) Empirical cumulative distribution. (Dotted line) Fit. Same *x*-axis as the main figure. **(C–D)** Two-dimensional cell area-fluorescence distribution from **(C)** experiments and **(D)** simulations of the model. In both cases, the distribution has been normalised such that its integral is unity. **(E–F)** Fluorescence distributions of cells of a given size from **(E)** experiments and **(F)** simulations.

As a more detailed test of the model, we next investigated the interrelation between cell area and nanoparticle uptake (fluorescence) more directly. Thus we evaluated the two-dimensional distribution of fluorescence and cell area from the experimental data (Figure 4C), from which we observe a fairly wide distribution of fluorescence for a given cell area. To make this more explicit, we furthermore selected cells of a small (<400 μm^2), medium (600–800 μm^2) and large (>1,000 μm^2) size and considered the fluorescence distribution corresponding to these cells specifically (Figure 4E). Even though the sizes of these cell subpopulations were chosen not to overlap, we observe that the corresponding fluorescence distributions still overlap to a quite substantial degree.

To compare these results to what is predicted from the model, we performed simple numerical simulations (see Methods) based on the same assumptions that underlie the model, and evaluated the corresponding simulation data in the same way as the experimental data (Figures 4D, F). We observe that while the model describes the overall fluorescence distribution well (Figures 4B, F grey) it predicts a far too narrow distribution of fluorescence for a given cell size (Figure 4D). This conclusion is unaffected by using the cell area parameters evaluated from the cells exposed to nanoparticles (Supplementary Figure S6) rather than those we evaluated from cells not exposed to nanoparticles (Figure 3). Importantly, the conclusion remains the same also if we use a different assumed value for the fluorescence per nanoparticle (Supplementary Figure S4) as well as if we do not perform the background subtraction (Supplementary Figure S5). The only possibility for realising a wider variability within the model is to assume a much higher fluorescence per nanoparticle (Supplementary Figure S7). However, even then the agreement between model and experiments is rather poor and, furthermore, such high fluorescences would imply that a typical cell takes up only 13 nanoparticles under the conditions shown in Figure 4, contrary to previous observations from microscopy which suggest hundreds of nanoparticles after just a few minutes of nanoparticle exposure at similar concentrations [Supplementary Figure S7; (Åberg et al., 2016; Vtyurina et al., 2021)]. Finally, the corresponding fluorescence distributions of the subpopulations of small, medium and large cells are completely disjoint in the model (Figure 4F), while they strongly overlap experimentally (Figure 4E). All of these conclusions also remain valid at half the nanoparticle concentration (Supplementary Figure S8).

To test the model without assumptions on the fluorescence per particle, we next turned to flow cytometry. While flow cytometry reports on the nanoparticle fluorescence per cell, we were nevertheless able to use that fluorescence to explicitly measure, with high-throughput, the actual number of nanoparticles. To do so, we started from the literature observation that when micron-sized polystyrene particles are exposed to cells, under certain conditions one observes well-defined and well-separated peaks in the fluorescence distribution over cells (dos Santos et al., 2011), consistent with a distinction between cells that have taken up (or at least associate with) 0, 1, 2, *etc*., particles. We interpret such results as reflecting both a low extracellular particle concentration, and a consequent low probability of uptake, as well as the strong fluorescence of the micron-sized particles, which implies a favourable separation of the peaks from each other. We thus attempted to find conditions where a separation between individual peaks could also be observed for particles smaller than a few microns, which is more relevant for the present study. We succeeded in doing so using 500 nm polystyrene nanoparticles (as opposed to the 100 nm particles used for the results presented in Figure 4) by using a concentration of 150 μg/mL and exposing the cells between 0.5 and 4 h.

Figure 5A exemplifies the fluorescence distribution over cells for one such sample (black outline). We interpret these results to mean that some cells (zeroth peak) have no associated nanoparticles, while other cells have 1, 2, 3, *etc*., associated nanoparticles (first, second, and third peak, respectively). After the third peak, individual peaks become less well-defined (depending upon the concentration and exposure time). The measured cells are actually cells with associated particles, as opposed to just particles without the cells, as nothing is measured if we simply run the 500 nm particles by themselves through the flow cytometer (Supplementary Figure S9). By

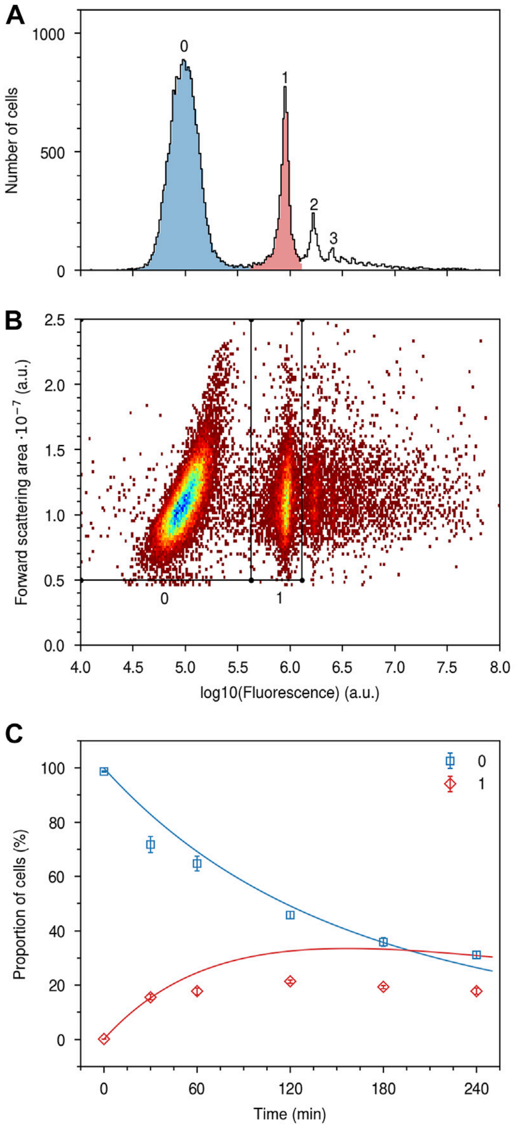

FIGURE 5
Nanoparticle uptake quantified in terms of numbers. HeLa cells were exposed to a 150 μg/mL concentration of the 500 nm particles for various times up to 4 h and then measured using flow cytometry. **(A)** Distribution of cell fluorescence for a sample exposed to nanoparticles for 1 h. (Black outline) All cells; (Blue) Cells within the zeroth, and (Red) first subpopulation indicated in panel **B**. The two subpopulations (blue and red) completely overlap with the full population (black outline) for the zeroth and first peaks, indicating that the two subpopulations have been well-identified. **(B)** Two-dimensional fluorescence-forward scattering distribution. Several subpopulations are easily identified and the first two are indicated by the polygons. The colour bar refers to the number of cells. **(C)** Proportion of cells with no nanoparticles and one nanoparticle, respectively, as a function of time. (Datapoints) Experimental data. Cells with no particles and cells with one particle were identified as illustrated by panels **A–B** and their proportion of the full population quantified. The data points represent the mean over 3 samples and the error bars the corresponding standard deviation. (Blue line) Fit of model (Eq. 3) to the experimentally determined proportion of cells with no nanoparticles, with $\theta\lambda C$ as fitting parameter and k fixed. (Red line) Subsequent parameter-free prediction of model (Eq. 4) for the proportion of cells with one nanoparticle. Repeat experiments are shown in Supplementary Figure S10.

considering also the forward scattering of the cells, one readily differentiates cells within the first two peaks from each other (Figure 5B). Indeed, by defining two subpopulations of cells based on their fluorescence intensity and forward scattering (polygons in Figure 5B) we find a good description of the two fluorescence peaks (Figure 5A, blue and red).

With the approach illustrated by Figures 5A, B, we were able to quantify the number of cells without any nanoparticles and the number of cells with one nanoparticle (this proved sufficient for our purposes but in principle we would be able to do the same also for higher nanoparticle numbers). This is something we can directly compare to the model (Eq. 2), which predicts that the proportion of cells with no nanoparticles is given by

$$p_0(Ct) = \frac{1}{(1+\theta\lambda Ct)^k} \tag{3}$$

while the proportion of cells with one nanoparticle is given by

$$p_1(Ct) = \frac{k(\theta\lambda Ct)}{(1+\theta\lambda Ct)^{k+1}}. \tag{4}$$

Here k and θ are the two parameters describing the cell area distribution (Figure 3), λ the normalised uptake rate, C the concentration and t the exposure time.

We thus exposed cells to nanoparticles for various times up to 4 h, thereby giving us experimental measures of the proportion of cells with, respectively, no nanoparticles and one nanoparticle as a function of time. Figure 5C (squares) shows how the proportion of cells without any nanoparticles starts at 100% before any nanoparticles have been supplied, and then decreases with time. While it may appear that there is a saturation of the proportion of cells that do not take up nanoparticles, a separate experiment, where we used the same nanoparticle concentration but exposed the cells for 18 h, showed that only 3.7% ± 0.2% (mean ± standard deviation of three samples) of the cells remained without particles. Turning to the cells with one nanoparticle, the proportion of such cells (diamonds) starts at 0% before nanoparticle exposure, then increases, and appears to plateau, before presumably decreasing again.

Since the cell area parameters (k and θ) are known and since we varied time t, we next fitted the model (Eq. 3) with $\theta\lambda C$ as free parameter to the experimentally determined proportion of cells with no nanoparticles. Note that λ, the normalised uptake rate, cannot be taken from our earlier results (Figure 4) because those were for the 100 nm nanoparticles and it seems reasonable to assume that the uptake rate is different for the 500 nm nanoparticles used here. Note, furthermore, that agreement between model and experiment for the first data point is a trivial outcome of the model, which, rightly, implies that no cells will have any nanoparticles before the nanoparticles have been supplied ($t = 0$ in Eq. 3). After performing the fit, we notice that the best fitted line (Figure 5C; blue line) describes the experimental data rather well. We subsequently used the model for a parameter-free prediction of the proportion of cells with one nanoparticle (Eq. 4), since all parameters of the model have now been independently specified (k and θ from the cell area distribution and $\theta\lambda C$ from the fit to the proportion of cells without nanoparticles). As may be observed, the prediction (Figure 5C; red line) does not describe the experimental data (diamonds) well. Again, note that agreement between model and experiment is trivial for the first data point, where the model implies that no cells will have one nanoparticle before the cells have been exposed to nanoparticles ($t = 0$ in Eq. 4). Repeat experiments show the same outcome (Supplementary Figure S10). Applying a similar procedure but leaving all parameters free (*i.e.*, using both k and $\theta\lambda C$ as fitting parameters) does give a better fit of the model to the data, but at the expense of giving a cell area distribution that is both unreasonable and different from what is experimentally observed (Supplementary Figure S11). Overall, it thus appears that the model cannot describe the experimental data well.

4 Conclusion

Fluorescence microscopy has several advantages over other techniques to quantify nanoparticle uptake, including that the cells can be viewed live and in their native state, and that cell parameters such as size and other visible phenotypic traits can be determined. In terms of image acquisition there are no major limitations on the number of cells that can be studied; however, the resulting image analysis has traditionally been a bottleneck preventing microscopy from becoming a true high-throughput technique.

Here we have demonstrated the use of the deep-learning based algorithm Cellpose (Stringer et al., 2021; Pachitariu and Stringer, 2022) on fluorescence microscopy images to quantify the uptake of nanoparticles by cells. The Cellpose cell identification worked very well on our microscopy images, but we nevertheless included manual review of cell identification as an additional quality control. We set up a systematic workflow, including the manual review step but that otherwise is fully automated, to ensure that all cells would be identified and that no cells would be double-counted.

While we here opted for a manual review step, we note that the cell identification was so good that the results are independent of whether we perform this manual review or not (Supplementary Figure S12). Future studies may thus consider using the results as-is and, potentially, instead add a filtering step to remove likely misidentifications. Such a filtering step is, for example, standard in flow cytometry, where one removes data that likely represent cell debris or cell doublets by only considering objects whose measured scattering values are within certain limits Salvati et al. (2018). One could do something similar with the cells identified from microscopy images: For example, identified cells with very small areas could be removed, as one may expect them to often represent debris or other non-cell objects. However, this has to be done with some care, as cells with an area substantially smaller than the average do exist, for example, when a cell divides. The nuclear signal may then give additional information, as dividing cells are expected to have a more intense nuclear signal. Similarly, identified cells with a very large area may be removed, as one would expect them to represent several cells that have been misidentified as a single cell. Again, cells with a substantially larger cell area than the average do exist, and the nuclear signal could be used to differentiate actual large cells (single nucleus) from multiple cells misidentified as one (several nuclei). Regardless of the specifics, it seems feasible to develop an approach to perform this filtering and with time and use have it become *de facto* standardised.

As a proof-of-concept we used our workflow to create a dataset of some thousands of cells, exposed or not exposed to nanoparticles.

We subsequently used this dataset to test a model which has been advanced to explain the observed variability in nanoparticle uptake between cells (Rees et al., 2019). This model is based on the assumptions that nanoparticle internalisation is a Poisson process and that nanoparticle uptake is proportional to cell area. While the model does indeed describe the distribution of nanoparticles over cells well, the model predicts a relationship between nanoparticle uptake and cell area which is quite different to that observed experimentally. Complementary flow cytometry measurements also show a discrepancy between model prediction and experiments. Overall, it thus appears that the model cannot describe the cell-to-cell variability in uptake of the polystyrene nanoparticles used in this study. A likely reason for this is that cell area is not the only relevant cell characteristic that matters, but that other factors also play a role. This is consistent with a recent study of ours, where multiple lines of evidence were presented suggest that, while nanoparticle uptake is certainly correlated with cell size, there are also other cellular characteristics at play (Åberg et al., 2021).

Overall, we have demonstrated the utility of deep-learning based cell identification, specifically the Cellpose algorithm (Stringer et al., 2021), to extract cell characteristics from fluorescence microscopy images. We set up a workflow which includes manual, but swift, human review of cell identification, that allowed us to measure nanoparticle uptake in thousands of cells with confidence. Thus, fluorescence microscopy can be routinely applied to measure nanoparticle uptake, at single-cell level and with high-throughput, and this technique also possesses some advantages compared to other high-throughput techniques.

Data availability statement

The original contributions presented in the study are included in the article/Supplementary Material, further inquiries can be directed to the corresponding author.

Author contributions

CÅ designed research; TG performed the high-throughput microscopy experiments; BY performed a preliminary analysis of the microscopy images using CellProfiler and analysed the corresponding data; CÅ and IA-Z set up the Cellpose analysis pipeline; CÅ performed the analysis of the microscopy images using Cellpose and analysed the corresponding data; BY and CÅ interpreted the microscopy data; CR performed the flow cytometry experiments, and the nanoparticle size characterisation; IdB and EN performed preliminary flow cytometry experiments; CÅ wrote the paper with comments and input from all. All authors listed have made a substantial, direct, and intellectual contribution to the work and approved it for publication.

Funding

CR was supported by a scholarship awarded under the Molecular Life and Health programme of the Faculty of Science and Engineering, University of Groningen.

Acknowledgments

The high-throughput microscopy experiments were carried out at the University Medical Center Groningen Imaging and Microscopy Center, which is sponsored by an NWO grant 40-00506-98–9021, while the flow cytometry measurements were carried out at the Flow Cytometry Unit of the University Medical Center Groningen. We thank the Department of Pharmaceutical Technology and Biopharmacy, Groningen Research Institute of Pharmacy, University of Groningen for providing access to the NanoSight LM14, and Henny C. van der Mei and Hans J. Kaper at the Department of Biomedical Engineering, University Medical Center Groningen for access to the Malvern ZetaSizer Nano ZS.

Conflict of interest

The authors declare that the research was conducted in the absence of any commercial or financial relationships that could be construed as a potential conflict of interest.

Publisher's note

Supplementary material

The Supplementary Material for this article can be found online at: https://www.frontiersin.org/articles/10.3389/fnano.2023.1181362/full#supplementary-material

References

Åberg, C., Kim, J. A., Salvati, A., and Dawson, K. A. (2017). Reply to "The interface of nanoparticles with proliferating mammalian cells. *Nat. Nanotechnol.* 12, 600–603. doi:10.1038/nnano.2017.139

Åberg, C. (2021). Kinetics of nanoparticle uptake into and distribution in human cells. *Nanoscale Adv.* 3, 2196–2212. doi:10.1039/D0NA00716A

Åberg, C., Piattelli, V., Montizaan, D., and Salvati, A. (2021). Sources of variability in nanoparticle uptake by cells. *Nanoscale* 13, 17530–17546. doi:10.1039/D1NR04690J

Åberg, C., Varela, J. A., Fitzpatrick, L. W., and Dawson, K. A. (2016). Spatial and structural metrics for living cells inspired by statistical mechanics. *Sci. Rep.* 6, 34457. doi:10.1038/srep34457

Akinc, A., Maier, M. A., Manoharan, M., Fitzgerald, K., Jayaraman, M., Barros, S., et al. (2019). The Onpattro story and the clinical translation of nanomedicines containing nucleic acid-based drugs. *Nat. Nanotechnol.* 14, 1084–1087. doi:10.1038/s41565-019-0591-y

Berg, S., Kutra, D., Kroeger, T., Straehle, C. N., Kausler, B. X., Haubold, C., et al. (2019). ilastik: Interactive machine learning for (bio)image analysis. *Nat. Methods* 16, 1226–1232. doi:10.1038/s41592-019-0582-9

Bhabra, G., Sood, A., Fisher, B., Cartwright, L., Saunders, M., Evans, W. H., et al. (2009). Nanoparticles can cause DNA damage across a cellular barrier. *Nat. Nanotechnol.* 4, 876–883. doi:10.1038/nnano.2009.313

Bogart, L. K., Pourroy, G., Murphy, C. J., Puntes, V., Pellegrino, T., Rosenblum, D., et al. (2014). Nanoparticles for imaging, sensing, and therapeutic intervention. *ACS Nano* 8, 3107–3122. doi:10.1021/nn500962q

Brayden, D. J., Cryan, S.-A., Dawson, K. A., O'Brien, P. J., and Simpson, J. C. (2015). High-content analysis for drug delivery and nanoparticle applications. *Drug Discov. Today* 20, 942–957. doi:10.1016/j.drudis.2015.04.001

Caicedo, J. C., Cooper, S., Heigwer, F., Warchal, S., Qiu, P., Molnar, C., et al. (2017). Data-analysis strategies for image-based cell profiling. *Nat. Methods* 14, 849–863. doi:10.1038/nmeth.4397

Carpenter, A. E., Jones, T. R., Lamprecht, M. R., Clarke, C., Kang, I. H., Friman, O., et al. (2006). CellProfiler: Image analysis software for identifying and quantifying cell phenotypes. *Genome Biol.* 7, R100. doi:10.1186/gb-2006-7-10-r100

Chakravarty, P., Qian, W., El-Sayed, M. A., and Prausnitz, M. R. (2010). Delivery of molecules into cells using carbon nanoparticles activated by femtosecond laser pulses. *Nat. Nanotechnol.* 5, 607–611. doi:10.1038/nnano.2010.126

Chen, H., and Murphy, R. F. (2022). Evaluation of cell segmentation methods without reference segmentations. *Mol. Biol. Cell* 2022, mbcE22080364. Published ahead of print. doi:10.1091/mbc.E22-08-0364

Chithrani, B. D., Ghazani, A. A., and Chan, W. C. W. (2006). Determining the size and shape dependence of gold nanoparticle uptake into mammalian cells. *Nano Lett.* 6, 662–668. doi:10.1021/nl052396o

Cho, E. C., Xie, J., Wurm, P. A., and Xia, Y. (2009). Understanding the role of surface charges in cellular adsorption versus internalization by selectively removing gold nanoparticles on the cell surface with a I_2/KI etchant. *Nano Lett.* 9, 1080–1084. doi:10.1021/nl803487r

Collinet, C., Stoter, M., Bradshaw, C. R., Samusik, N., Rink, J. C., Kenski, D., et al. (2010). Systems survey of endocytosis by multiparametric image analysis. *Nature* 464, 243–249. doi:10.1038/nature08779

Collins, A. R., Annangi, B., Rubio, L., Marcos, R., Dorn, M., Merker, C., et al. (2017). High throughput toxicity screening and intracellular detection of nanomaterials. *Wiley Interdiscip. Rev. Nanomed. Nanobiotechnol.* 9, e1413. doi:10.1002/wnan.1413

de Boer, I., Richards, C. J., and Åberg, C. (2022). Simultaneous exposure of different nanoparticles influences cell uptake. *Pharmaceutics* 14, 136. doi:10.3390/pharmaceutics14010136

dos Santos, T., Varela, J., Lynch, I., Salvati, A., and Dawson, K. A. (2011). Quantitative assessment of the comparative nanoparticle-uptake efficiency of a range of cell lines. *Small* 7, 3341–3349. doi:10.1002/smll.201101076

Dugershaw, B. B., Aengenheister, L., Hansen, S. S. K., Hougaard, K. S., and Buerki-Thurnherr, T. (2020). Recent insights on indirect mechanisms in developmental toxicity of nanomaterials. *Fibre Toxicol.* 17, 31. doi:10.1186/s12989-020-00359-x

Friedrichs, S., and Bowman, D. M. (2021). COVID-19 may become nanomedicine's finest hour yet. *Nat. Nanotechnol.* 16, 362–364. doi:10.1038/s41565-021-00901-8

Fries, C. N., Curvino, E. J., Chen, J.-L., Permar, S. R., Fouda, G. G., and Collier, J. H. (2021). Advances in nanomaterial vaccine strategies to address infectious diseases impacting global health. *Nat. Nanotechnol.* 16, 1–14. doi:10.1038/s41565-020-0739-9

Gibbs-Flournoy, E. A., Bromberg, P. A., Hofer, T. P., Samet, J. M., and Zucker, R. M. (2011). Darkfield-Confocal Microscopy detection of nanoscale particle internalization by human lung cells. *Fibre Toxicol.* 8, 2. doi:10.1186/1743-8977-8-2

Han, X., Xu, K., Taratula, O., and Farsad, K. (2019). Applications of nanoparticles in biomedical imaging. *Nanoscale* 11, 799–819. doi:10.1039/C8NR07769J

Jiang, X., Dausend, J., Hafner, M., Musyanovych, A., Röcker, C., Landfester, K., et al. (2010a). Specific effects of surface amines on polystyrene nanoparticles in their interactions with mesenchymal stem cells. *Biomacromolecules* 11, 748–753. doi:10.1021/bm901348z

Jiang, X., Röcker, C., Hafner, M., Brandholt, S., Dörlich, R. M., and Nienhaus, G. U. (2010b). Endo- and exocytosis of zwitterionic quantum dot nanoparticles by live HeLa cells. *ACS Nano* 4, 6787–6797. doi:10.1021/nn101277w

Kah, M., Johnston, L. J., Kookana, R. S., Bruce, W., Haase, A., Ritz, V., et al. (2021). Comprehensive framework for human health risk assessment of nanopesticides. *Nat. Nanotechnol.* 16, 955–964. doi:10.1038/s41565-021-00964-7

Kamentsky, L., Jones, T. R., Fraser, A., Bray, M.-A., Logan, D. J., Madden, K. L., et al. (2011). Improved structure, function and compatibility for CellProfiler: Modular high-throughput image analysis software. *Bioinformatics* 27, 1179–1180. doi:10.1093/bioinformatics/btr095

Kelly, S., Byrne, M. H., Quinn, S. J., and Simpson, J. C. (2021). Multiparametric nanoparticle-induced toxicity readouts with single cell resolution in HepG2 multicellular tumour spheroids. *Nanoscale* 13, 17615–17628. doi:10.1039/D1NR04460E

Kim, D., Kim, J., Park, Y. I., Lee, N., and Hyeon, T. (2018). Recent development of inorganic nanoparticles for biomedical imaging. *ACS Cent. Sci.* 4, 324–336. doi:10.1021/acscentsci.7b00574

Kim, J. A., Åberg, C., Salvati, A., and Dawson, K. A. (2012). Role of cell cycle on the cellular uptake and dilution of nanoparticles in a cell population. *Nat. Nanotechnol.* 7, 62–68. doi:10.1038/nnano.2011.191

Kisby, T., Yilmazer, A., and Kostarelos, K. (2021). Reasons for success and lessons learnt from nanoscale vaccines against COVID-19. *Nat. Nanotechnol.* 16, 843–850. doi:10.1038/s41565-021-00946-9

Kulkarni, J. A., Witzigmann, D., Thomson, S. B., Chen, S., Leavitt, B. R., Cullis, P. R., et al. (2021). The current landscape of nucleic acid therapeutics. *Nat. Nanotechnol.* 16, 630–643. doi:10.1038/s41565-021-00898-0

LeCun, Y., Bengio, Y., and Hinton, G. (2015). Deep learning. *Nature* 521, 436–444. doi:10.1038/nature14539

McQuin, C., Goodman, A., Chernyshev, V., Kamentsky, L., Cimini, B. A., Karhohs, K. W., et al. (2018). CellProfiler 3.0: Next-generation image processing for biology. *PLOS Biol.* 16, e2005970. doi:10.1371/journal.pbio.2005970

Mitchell, M. J., Billingsley, M. M., Haley, R. M., Wechsler, M. E., Peppas, N. A., and Langer, R. (2021). Engineering precision nanoparticles for drug delivery. *Nat. Rev. Drug Discov.* 20, 101–124. doi:10.1038/s41573-020-0090-8

Müller, T., Schumann, C., and Kraegeloh, A. (2012). STED microscopy and its applications: New insights into cellular processes on the nanoscale. *ChemPhysChem* 13, 1986–2000. doi:10.1002/cphc.201100986

Murschhauser, A., Röttgermann, P. J. F., Woschée, D., Ober, M. F., Yan, Y., Dawson, K. A., et al. (2019). A high-throughput microscopy method for single-cell analysis of event-time correlations in nanoparticle-induced cell death. *Commun. Biol.* 2, 35–11. doi:10.1038/s42003-019-0282-0

Oberdörster, G., Oberdörster, E., and Oberdörster, J. (2005). Nanotoxicology: An emerging discipline evolving from studies of ultrafine particles. *Environ. Health Perspect.* 113, 823–839. doi:10.1289/ehp.7339

Pachitariu, M., and Stringer, C. (2022). Cellpose 2.0: How to train your own model. *Nat. Methods* 19, 1634–1641. doi:10.1038/s41592-022-01663-4

Panarella, A., Bexiga, M. G., Galea, G., O' Neill, E. D., Salvati, A., Dawson, K. A., et al. (2016). A systematic high-content screening microscopy approach reveals key roles for Rab33b, OATL1 and Myo6 in nanoparticle trafficking in HeLa cells. *Sci. Rep.* 6, 28865. doi:10.1038/srep28865

Panet, E., Mashriki, T., Lahmi, R., Jacob, A., Ozer, E., Vecsler, M., et al. (2017). The interface of nanoparticles with proliferating mammalian cells. *Nat. Nanotechnol.* 12, 598–600. doi:10.1038/nnano.2017.140

Park, M. V. D. Z., Bleeker, E. A. J., Brand, W., Cassee, F. R., van Elk, M., Gosens, I., et al. (2017). Considerations for safe innovation: The case of graphene. *ACS Nano* 11, 9574–9593. doi:10.1021/acsnano.7b04120

Rees, P., Wills, J. W., Brown, M. R., Barnes, C. M., and Summers, H. D. (2019). The origin of heterogeneous nanoparticle uptake by cells. *Nat. Commun.* 10, 2341. doi:10.1038/s41467-019-10112-4

Rivera-Gil, P., Jimenez De Aberasturi, D., Wulf, V., Pelaz, B., Del Pino, P., Zhao, Y., et al. (2013). The challenge to relate the physicochemical properties of colloidal nanoparticles to their cytotoxicity. *Acc. Chem. Res.* 46, 743–749. doi:10.1021/ar300039j

Salvati, A., Nelissen, I., Haase, A., Åberg, C., Moya, S., Jacobs, A., et al. (2018). Quantitative measurement of nanoparticle uptake by flow cytometry illustrated by an interlaboratory comparison of the uptake of labelled polystyrene nanoparticles. *NanoImpact* 9, 42–50. doi:10.1016/j.impact.2017.10.004

Sandin, P., Fitzpatrick, L. W., Simpson, J. C., and Dawson, K. A. (2012). High-speed imaging of Rab family small GTPases reveals rare events in nanoparticle trafficking in living cells. *ACS Nano* 6, 1513–1521. doi:10.1021/nn204448x

Schermelleh, L., Ferrand, A., Huser, T., Eggeling, C., Sauer, M., Biehlmaier, O., et al. (2019). Super-resolution microscopy demystified. *Nat. Cell Biol.* 21, 72–84. doi:10.1038/s41556-018-0251-8

Schübbe, S., Cavelius, C., Schumann, C., Koch, M., and Kraegeloh, A. (2010). STED microscopy to monitor agglomeration of silica particles inside A549 cells. *Adv. Eng. Mat.* 12, 417–422. doi:10.1002/adem.201000093

Shapiro, H. M. (2003). "Chapter 7. Parameters and probes," in *Practical flow cytometry* (Hoboken, New Jersey: John Wiley and Sons, Inc.), 273–410.

Shi, J., Kantoff, P. W., Wooster, R., and Farokhzad, O. C. (2017). Cancer nanomedicine: Progress, challenges and opportunities. *Nat. Rev. Cancer* 17, 20–37. doi:10.1038/nrc.2016.108

Simpson, J. C., Joggerst, B., Laketa, V., Verissimo, F., Cetin, C., Erfle, H., et al. (2012). Genome-wide RNAi screening identifies human proteins with a regulatory function in the early secretory pathway. *Nat. Cell Biol.* 14, 764–774. doi:10.1038/ncb2510

Snijder, B., Sacher, R., Ramo, P., Damm, E.-M., Liberali, P., and Pelkmans, L. (2009). Population context determines cell-to-cell variability in endocytosis and virus infection. *Nature* 461, 520–523. doi:10.1038/nature08282

Sood, A., Salih, S., Roh, D., Lacharme-Lora, L., Parry, M., Hardiman, B., et al. (2011). Signalling of DNA damage and cytokines across cell barriers exposed to nanoparticles depends on barrier thickness. *Nat. Nanotechnol.* 6, 824–833. doi:10.1038/nnano.2011.188

Stewart, M. P., Sharei, A., Ding, X., Sahay, G., Langer, R., and Jensen, K. F. (2016). *In vitro* and *ex vivo* strategies for intracellular delivery. *Nature* 538, 183–192. doi:10.1038/nature19764

Stirling, D. R., Swain-Bowden, M. J., Lucas, A. M., Carpenter, A. E., Cimini, B. A., and Goodman, A. (2021). CellProfiler 4: Improvements in speed, utility and usability. *BMC Bioinforma.* 22, 433. doi:10.1186/s12859-021-04344-9

Stringer, C., Wang, T., Michaelos, M., and Pachitariu, M. (2021). Cellpose: A generalist algorithm for cellular segmentation. *Nat. Methods* 18, 100–106. doi:10.1038/s41592-020-01018-x

Summers, H. D., Rees, P., Holton, M. D., Brown, M. R., Chappell, S. C., Smith, P. J., et al. (2011). Statistical analysis of nanoparticle dosing in a dynamic cellular system. *Nat. Nanotechnol.* 6, 170–174. doi:10.1038/nnano.2010.277

Valsami-Jones, E., and Lynch, I. (2015). How safe are nanomaterials? *Science* 350, 388–389. doi:10.1126/science.aad0768

Varela, J. A., Åberg, C., Simpson, J. C., and Dawson, K. A. (2015). Trajectory-based co-localization measures for nanoparticle-cell interaction studies. *Small* 11, 2026–2031. doi:10.1002/smll.201401849

Varela, J. A., Bexiga, M., Åberg, C., Simpson, J. C., and Dawson, K. A. (2012). Quantifying size-dependent interactions between fluorescently labeled polystyrene nanoparticles and mammalian cells. *J. Nanobiotechnology* 10, 39. doi:10.1186/1477-3155-10-39

Vtyurina, N., Åberg, C., and Salvati, A. (2021). Imaging of nanoparticle uptake and kinetics of intracellular trafficking in individual cells. *Nanoscale* 13, 10436–10446. doi:10.1039/D1NR00901J

Wang, Z., Tiruppathi, C., Minshall, R. D., and Malik, A. B. (2009). Size and dynamics of caveolae studied using nanoparticles in living endothelial cells. *ACS Nano* 3, 4110–4116. doi:10.1021/nn9012274

Wilhelm, C., Gazeau, F., Roger, J., Pons, J. N., and Bacri, J.-C. (2002). Interaction of anionic superparamagnetic nanoparticles with cells: Kinetic analyses of membrane adsorption and subsequent internalization. *Langmuir* 18, 8148–8155. doi:10.1021/la0257337

Wolfram, J., and Ferrari, M. (2019). Clinical cancer nanomedicine. *Nano Today* 25, 85–98. doi:10.1016/j.nantod.2019.02.005

Xiong, R., Hua, D., Van Hoeck, J., Berdecka, D., Léger, L., De Munter, S., et al. (2021). Photothermal nanofibres enable safe engineering of therapeutic cells. *Nat. Nanotechnol.* 16, 1281–1291. doi:10.1038/s41565-021-00976-3

Yu, M., and Zheng, J. (2015). Clearance pathways and tumor targeting of imaging nanoparticles. *ACS Nano* 9, 6655–6674. doi:10.1021/acsnano.5b01320

Frontiers in Nanotechnology

TYPE Review
PUBLISHED 25 October 2023
DOI 10.3389/fnano.2023.1257240

OPEN ACCESS

EDITED BY
Jan M. Macak,
University of Pardubice, Czechia

REVIEWED BY
Xingyun Li,
Qingdao University, China
Amit Kumar,
Pohang University of Science and Technology, Republic of Korea

*CORRESPONDENCE
Mariana Molina-Torres,
✉ marian.mtt@hotmail.com
Ruben Mendoza-Cruz,
✉ rmendoza@materiales.unam.mx

RECEIVED 12 July 2023
ACCEPTED 19 September 2023
PUBLISHED 25 October 2023

CITATION
Molina-Torres M, Hernández-Cristóbal O and Mendoza-Cruz R (2023), Small but mighty: unlocking the catalytic power of individual iridium atoms on titanium oxide.
Front. Nanotechnol. 5:1257240.
doi: 10.3389/fnano.2023.1257240

Small but mighty: unlocking the catalytic power of individual iridium atoms on titanium oxide

Mariana Molina-Torres[1]*, Orlando Hernández-Cristóbal[2] and Ruben Mendoza-Cruz[1]*

[1]Materials Research Institute, National Autonomous University of Mexico, Mexico City, Mexico, [2]National School of Higher Studies, Morelia Unit, National Autonomous University of Mexico, Morelia, Mexico

Single atom catalysts (SACs) have emerged as a rapidly developing field of catalysis research, with great potential for improving the efficiency and selectivity of many chemical reactions. SACs consist of isolated metal atoms dispersed on a support material, providing a unique and well-defined atomic structure and composition, allowing for precise control over their properties. In particular, iridium SACs are applied in numerous reactions, from electrocatalytic to photocatalytic applications. By the other hand, titanium oxide is a semiconductor with important applications as a reducible support for different catalyst, widely used in different reactions because of its high activity and stability. This review covers recent developments and frontiers in the particular system of Ir – TiO_2 SACs. It discusses the importance, synthesis, characterization techniques such as XPS, STEM, Differential Reflectance Infrared Fourier Transform, and XAS, and the applications of Ir – TiO_2 SACs. The review also explores the stability and durability of single-atom catalysts and the importance of understanding their structure-activity relationships to optimize their performance. A key dimension emphasized in this review is the importance of investigating the iridium-titania system. Iridium exhibits superior properties compared to other metals, particularly in maintaining stability as a single atom, owing to its resistance to sintering. Gaining a comprehensive understanding of and optimizing these factors are instrumental in unlocking the full potential of Ir – TiO_2 SACs. This route offers a promising trajectory towards enhancing catalytic performance across a spectrum of applications and facilitating the discovery of novel chemical reactions.

KEYWORDS

single atom catalysts, iridium, TiO_2, SACs, metal dispersed, active sites, characterization, electron microscopy

1 Introduction

Catalysis plays a central role in shaping our lives, over 90% of all chemical products have at least one catalytic step in their manufacture (de Vries and Jackson, 2012). Supported metal nanostructures are the most used form of heterogeneous catalyst in the industrial processes. Considerable endeavors have been dedicated to enhancing the effectiveness of supported metal catalysts downsizing the metal particles (Yang et al., 2013). The size of metal particle is a critical factor in determining the effectiveness of the catalysts, new findings from both theoretical and experimental studies have shown that clusters with sizes smaller than a nanometer exhibit enhanced catalytic activity and/or selectivity compared to particles of nanometer-scale dimensions (Herzing et al., 2008; Turner et al., 2008). There have been reports indicating that active sites often correspond to low coordination sites, such as unsaturated atoms

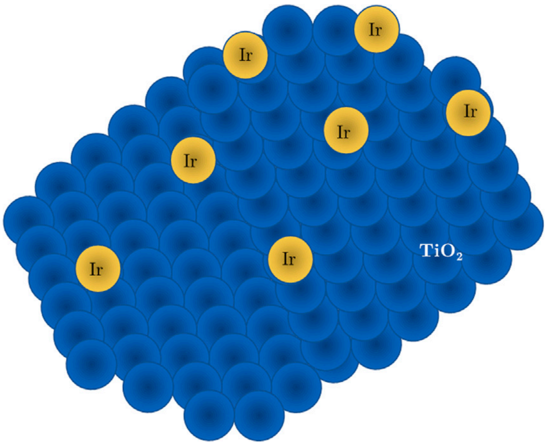

GRAPHICAL ABSTRACT
Ir catalyst supported by TiO_2.

(Remediakis et al., 2005). The size reduction also benefits the metal-support interactions, this phenomenon stems from the chemical bonding effect between the metal and the supports, as well as the associated interface, along with the charge transfer taking place between metal species and supports (Yang et al., 2013).

Late transition metals that are dispersed at the atomic level are often referred to as single atom catalysts (SACs). The SACs can be defined as a catalyst with isolated single atoms anchored onto its surface, capable of driving a catalytic reaction (Qiao et al., 2011). Generally, the single atoms are randomly and uncontrollably dispersed on the substrates. The interaction of these single-atoms with a metal oxide support can be different depending on its environment. The type of metal-support interactions regulates the electronic structure of catalysts, affecting the intrinsic activity of active sites (Samantaray et al., 2020). SACs can differentiate from other related single-site catalysts such as organometallic catalysts, in which in the latter case an organometallic complex are used to form the single-atom site, but keeping part of their ligands to achieve the catalytic reaction (Shan et al., 2022). SACs epitomize the utmost dispersion of a metal on a surface, with all the atoms being exposed. This holds paramount importance for the expensive and scarce noble metal catalysts, such as Ir, Pd, and Pt, which not only find the most applications but also attract significant interest for research purposes.

The significance of developing SACs becomes evident. Although the concept of having uniform active sites is highly appealing, the support structure in the vicinity of the single atom (SA) introduces heterogeneity to the active sites of the single atom catalyst (SAC, perhaps better conveys that the individual metal atoms are situated on the surface of another material) (Kottwitz et al., 2021). Consequently, the ideal uniform activity, which is characteristic of homogeneous catalysts, cannot be achieved. The combination of isolated single metals atoms with supports, gives rise to a distinct classification of catalysts. The synthesis of SAC presents a challenge, especially regarding the proper characterization of these materials, which is known to be inherently challenging owing to maximized atom utilization and precisely defining active centers, the direct observation of single atomic sites was not realized until the use of advanced characterization techniques such as atomic-resolution high-angle annular dark field scanning transmission electron microscopy (HAADF-STEM) which allowed imaging with atomic resolution (Li et al., 2019) that can directly measure the single atom to confirm the structure and conformation of the single metal atom, the chemical state of the metal center, and the conformation environment (Zonghua et al., 2020).

Supports play a critical role since they provide stability and enhance the efficiency of the catalysts. A common support is TiO_2 which has exhibited remarkable and intriguing properties. TiO_2 is a metal oxide with important applications in photocatalysis and oxidation reactions. Iridium, in turn, possesses excellent catalytic properties but its main limitation is its scarceness and high cost. Hence, iridium-based SAC improves the use of resources and, in combination with TiO_2 supports, represent excellent alternatives for the enhancement of catalytic activities towards different important reactions.

In this mini review, we centered in the recent developments and frontiers in the synthesis and characterization of SACs using TiO_2 as support, focusing on the stability and durability of SAC on TiO_2 and the importance of understanding their structure-activity relationships to optimize their performance. Despite the wide literature reviewing the field of SACs on different supports, this review gains importance in highlighting the contributions of TiO_2 supports forming SACs, in which much more limited information is available. First, a general view of the experimental finding about Ir as SACs is provided, reviewing its importance in catalytic reaction. Some common synthetic approaches to obtain SACs are summarized. Then, the experimental findings on $Ir - TiO_2$ SACs are introduced, discussing the common characterization techniques. Finally, applications and challenges of $Ir - TiO_2$ SACs and other metal oxide supports are reviewed.

2 Experimental findings about iridium as SACs

Fabrication of SACs is hard due to the tendency of single atoms to aggregate adds an additional layer of complexity, making it an even greater challenge. Elements with extremely low abundance on Earth are often the most active in catalytic reactions. This is precisely why optimizing the utilization efficiency of metal atoms and providing a greater number of exposed sites for reaction activation are crucial factors.

Iridium, the element with the 77th position on the periodic table, is classified among the 5 days transition metals. It crystallizes in a face-centered cubic (FCC) structure, but it stands as one of the most incompressible elements. Notably, iridium shares this distinction with other common metal centers that exhibit activity in numerous catalytic reactions. However, despite its potential, iridium has been limited in its exploration due to its scarcity in the Earth's crust and its high cost. As a result of their ability to undergo easy changes in oxidation state, iridium and its complexes find extensive use in catalysis for a wide range of industrial processes.

Single atom catalysts (SACs) offer a remarkable advantage in achieving 100% atomic utilization, serving as an exemplary strategy to significantly reduce noble-metal content without any compromise on catalytic efficiency. Hence, the study of metals, such as atomically dispersed iridium, does not impede the sustainable utilization of the metal. This exceptional property allows it to maintain its mechanical properties even at temperatures exceeding 2000°C and pressures up to 1.4 Mbar. Furthermore, iridium exhibits outstanding resistance to corrosion, making it highly suitable for a wide range of applications (Monteseguro et al., 2020).

TABLE 1 Summary of catalysts using iridium and different supports.

Single atom	Support	% Wt metal	Synthesis method	Application	Ref
Ir	ZIF-8	. . .	Impregnation Method	O.R.R.	Cao et al. (2019)
Ir	FeOx	0.01%	Co-Precipitation Method	Water-Gas Shift Reaction	Xiao et al. (2019)
Ir	MgAl2O4	0.20%	Wet-Impregnation	. . .	Bhirud et al. (2007)
Ir	ZrO2@C	0.60%	Pyrolysis	Hydrogenation of LA to GVL	Wang et al. (2022)
Ir	MgO	1%	Reported Method	Ethene Hydrogenation	Li et al. (2020)
Ir	TiO2 Rutile	1%	Impregnation Method	Catalytic Oxidation of ammonia	21
Ir	ZIF-8	1.20%	Pyrolysis	Formic Acid Oxidation	Shao et al. (2019a)
Ir	AP-POP	1.25%	Wet-Impregnation	Quasi-Homogeneous Hydrogenation Transformation of CO to Formate	Zhao et al. (2021)
Ir	H-Carbon ZIF-8	2.20%	Reported Method	O-H Carbenoid Insertion	Zhu et al. (2022a)
Ir	Co3O4	4.20%	Solid-State	Ammonia Production	Xiong et al. (2020)
Ir	C-N	4.40%	Pyrolysis	Epoxidation of Styrene	Shan et al. (2021)
Ir	Cobalt Oxide	4.93%	Surfactant-Mediated Method	O.E.R.	Wang et al. (2020)
Ir	NiO-CC	18%	Wet Immersion	O.E.R.	Xia et al. (2021)
Ir	N-C	40%	Pyrolysis	Electrochemical CO2 Reduction	Chen et al. (2018)

Noble metals of group VIII, such as Pd, Rh, Pt, and Ir, present outstanding catalytic activities, that together with transition metal oxide support catalyzes a wide number of reactions. In particular, iridium possesses a higher atomic mass compared to Pd and Rh, and it is the group with higher melting point. It possesses a versatile coordination chemistry, facilitating its dispersion in different metal oxide supports, such as MgO, FeOx, or MgAl$_2$O$_4$, with a strong interaction with the support (Lin et al., 2013; Pascarelli et al., 2019). For instance, Ir single-atom coordination with reduced Fe$_2$O$_3$, MgO, and TiO$_2$, corresponds to a substitutional configuration on the cation vacancies, with Ir coordinated with two oxygen atoms, which number could change after reaction (Xiao et al., 2019). A synergetic affect take place between the single atoms and their supports, lowering the reduction temperature of the support and generating a large amount of oxygen vacancies which contributes to their activity. The reducibility of the support also contributes to the stability of the single atoms, exhibiting high activity and selectivity.

Despite of this, few studies exist on Ir SACs in comparison with these other metals of the group, finding most applications in electrocatalysis. In this review, we aim to highlight the significance of studying this uncommon element when it is considered in its atomic form.

The pioneers in the field of catalysis utilizing iridium as an active center have posited that the success in fabricating single atom catalysts with iridium may be attributed to the remarkably low loading of the metal (Lu et al., 2019a). The probability of encountering short-range and long-range iridium-iridium interactions is estimated to be as minimal as 0.001 atoms nm^{-1}. Furthermore, upon increasing the iridium loading to 0.32%, a corresponding rise in observation frequency within the range of 0.5–1 nm was noted. Remarkably, no aggregation to sizes exceeding 1 nm was observed (Cao et al., 2019) therefore, it is advantageous to propose monodispersed iridium catalysts.

2.1 Summary of iridium as single atoms

In Table 1, examples of synthesis are presented where iridium has been used as a metal center on various supports, along with the synthesis routes employed and their applications.

Currently, there is ongoing research into synthesis methodologies aimed at creating Single Atom Catalysts, with wet impregnation being identified as the most promising approach. Although wet impregnation offers simplicity and scalability, it is important to acknowledge certain limitations. These include the challenge of achieving optimal metal loading and precise control over the anchoring position of isolated metal species on substrates, which can impact both catalytic efficiency and the feasibility of practical industrial applications.

2.2 Synthesis

The exploration and development of synthetic methodologies for single atom catalysts have become one of the most crucial research focuses. Fabricating single atom catalysts and maintaining the atomic dispersion of metal species under realistic synthesis and reaction conditions pose significant challenges. From a practical perspective,

TABLE 2 A comparison of different synthetic strategies, offering a comprehensive overview of their individual advantages and disadvantages.

Method	Advantages	Disadvantages	Ref
Wet chemical	Simple, low cost, easily scalable	Low metal loading, difficulty in managing metal atoms on substrates, strong dependence on synthesis factors	Haruta et al. (1987), Pham et al. (2023), Zanella et al. (2005)
Pyrolysis	Simple, large-scale production, inexpensive raw materials.	Uncontrollable metal sites on the selected substrates, instability of SA	Pham et al. (2023)
Electrochemical	Simple, controllable metal loading, relatively unexpensive	Uneven dispersion SA, limitation of thermodynamic control	Pham et al. (2023)
Photochemical reduction	Cost-effective, no extra treatment, controllable nucleation	sluggish nucleation growth rate, limited applicability	Pham et al. (2023)
Atomic Layer deposition	Controllable metal-loading, structure-performance exploration, Excellent uniformity and reproducibility. The loading of the SA could be adjusted through the number of cycles	High-cost equipment, slow synthetic process, high vacuum conditions, uncontrollable thickness and loading content, only materials with suitable ligands or functional groups could be chosen as support Not applicable for commercial preparation	Guo et al. (2022), Pham et al. (2023)
Atom trapping method	Simple, practical	High synthesis temperatures, requires a supply of mobile atoms and a support that can trap the mobile species	Guo et al. (2022)
Two-step doping method	Easy creation of vacancies on support and the high binding energies between the dopant and the vacancies, highly stable SACs	Limited to graphene	Guo et al. (2022)
Ball-milling method	Convert reactants into products during the reaction process, scale-up production, green	Not uniform sites, Requires high energy atom/ion generator,	Guo et al. (2022)
Photoreduction method	No special equipment, easy implementation	Catalytic active center not uniform	Guo et al. (2022)
In situ methods	Simple procedure, high dispersion, no metal loss	Limitation to specific systems, few references to a variety of metals	Liang et al. (2012), Cui et al. (2022)

an alternative and preferable approach is the development of wet-chemistry synthetic methods for single atom catalysts (SACs). This method offers easy operation and the potential for large-scale manufacturing. In wet-chemistry synthesis, mononuclear metal species are typically used as precursors. Therefore, implementing synthetic strategies to achieve atomically dispersed separation and isolation of the precursor, as well as preventing the migration and agglomeration of the formed single atoms, becomes crucial for successful SAC synthesis. These considerations are fundamental in ensuring the efficient and controlled production of SACs (Chen et al., 2018). Ir precursors are deposited onto the substrate surface using various wet-chemistry methods. This involves the metal precursors that are dispersed onto substrates through deposition-precipitation, coprecipitation, or wet-impregnation. Subsequently, reduction or activation procedures are carried out to form Ir-based catalysts with atomically dispersed Ir species. These steps are crucial in achieving the desired dispersion and isolation of individual Ir atoms on the substrate, enabling the synthesis of highly efficient catalysts with unique properties and reactivity (Pham et al., 2023).

2.2.1 Advantages and disadvantages of various synthetic approaches of SAC's

In Table 2, some advantages and disadvantages of various synthesis methods for obtaining SACs are presented (Pham et al., 2023).

The low metal content is mentioned as a disadvantage; however, for SACs, it is a notable advantage due to the reduced use of precious metals. Additionally, the possibility of industrial scalability is emphasized. Additionally, the potential for industrial-scale production is highlighted.

2.2.2 Deposition-precipitation with urea

Deposition-precipitation is a synthesis method commonly used in the preparation of catalysts. It involves the deposition of metal precursors onto a support material, followed by the precipitation of the metal species in the presence of a precipitating agent. This method allows for controlled and uniform distribution of the metal species on the support, resulting in catalysts with well-defined structures and properties. Deposition-precipitation offers advantages such as easy scalability, versatility, and the ability to tailor the catalyst composition by adjusting the deposition and precipitation conditions (Zanella et al., 2005; Qin et al., 2015).

The deposition-precipitation technique has been widely used to fabricate gold catalysts (Haruta et al., 1987; Haruta, 1997). In this method, the pH of an aqueous solution containing $HAuCl_4$ is carefully adjusted within the range of 6–10, taking into consideration the isoelectric points (IEP) of the metal oxide supports. This pH adjustment is crucial due to the amphoteric properties of $Au(OH)_3$, ensuring the formation of stable and well-dispersed gold species on the support material. The DP method offers ease of handling and provides control over the catalyst's composition and properties, making it a preferred choice in industrial catalyst production (Milone et al., 2010; Bokhimi et al., 2011; Qin et al., 2015).

2.2.3 Impregnation

The impregnation method is a technique used to deposit an active compound onto a porous surface or support. It involves immersing the support into a solution containing the active compound and allowing it to impregnate the porous surface through absorption. After impregnation, the support is subjected to drying or thermal treatment to remove the solvent and fix the active compound onto the support. This method offers great flexibility as it allows for control of the loading of the active compound and adjustment of the catalyst properties to specific application needs. It is widely employed in catalyst synthesis, particularly in the preparation of supported catalysts on porous solids (Van Dillen et al., 2003).

2.2.4 *In situ* techniques

Metal cations are chemically reduced to their metallic state by certain agents. In this state, they act directly as catalysts, facilitating chemical reactions involving the same agents. This process is straightforward and requires no additional purification. Consequently, it prevents potential catalyst loss or oxidation during the transfer process. By embracing this methodology, potential pitfalls associated with ligand presence, challenges stemming from uncontrollable variations in catalyst particle sizes, and concerns regarding mass loss or metal oxidation during purification and transfer procedures are all expertly sidestepped (Erdoğan et al., 2009; Liang et al., 2012; Cui et al., 2022; Zhang et al., 2022; Sun et al., 2023).

3 Experimental findings TiO_2 as support for Ir

Support materials play a crucial role in the stability and catalytic performance of single atom catalyst. These catalysts heavily rely on the support to provide a solid foundation for the deposition of active metal species. The choice of an appropriate support is of paramount importance as it directly influences the dispersion, accessibility, and reactivity of the active sites. Additionally, the support acts as a vital stabilizing agent, preventing the coalescence or aggregation of individual metal atoms and ensuring their sustained single-atom state during catalytic reactions. By offering a substantial surface area for the immobilization of metal atoms, the support facilitates efficient interactions with reactants, thereby enhancing catalytic reactions. Thus, meticulous selection and thoughtful design of suitable support materials are indispensable for the successful utilization of single atom catalysts in diverse catalytic applications.

Titanium is a metallic element that occupies the 22nd position in the periodic table. It is highly abundant in the Earth's crust and exists in three main crystal forms: anatase, rutile, and brookite. Titanium is known for its exceptional strength-to-weight ratio, corrosion resistance, biocompatibility, affordability, and eco-friendliness (Ramos-Delgado et al., 2016). These properties make it a valuable material in various industries, as it offers a cost-effective and environmentally friendly solution. Titanium also serves a significant role in catalysis. TiO_2 are employed both as supports for catalysts and as catalysts themselves. These catalysts, including metal/TiO_2 and metal oxide/TiO_2 composites, play a significant role in diverse reactions such as hydrogenations, hydrodesulfurizations, selective oxidations, reductions, and Fischer-Tropsch processes. An additional notable feature lies in its capacity as a photocatalyst, which stems from its inherent semiconducting properties (Kominami et al., 1997; Scirè et al., 2021).

The proper selection of a catalyst support is crucial for enhancing the dispersion of active components and modulating the catalytic functionalities through metal-support interactions. The catalyst support significantly influences the overall performance and stability of the catalyst system, allowing for improved control over reaction rates and selectivity. It acts as a substrate that facilitates the anchoring and distribution of active species, providing a stable environment for catalytic reactions (Palcheva et al., 2013). The interaction between metal/TiO_2 has been studied as SMSI effect. The finding of heteroatomic metal-metal bonding suggested that titanium cations at surfaces might be capable of bonding to metal cations or metal atoms in a supported phase due to of the possibility of an interaction between the d orbital electrons of the surface cations and those of the supported metal atoms (Tauster et al., 1981).

As mentioned previously, other supports such as MgO, ZIF-8, and Al_2O_3 have been extensively explored in the literature for supporting iridium catalysts. However, titanium dioxide (TiO_2) has not been the preferred choice as a support material, which presents an area of opportunity for further investigation. TiO_2 offers distinct advantages, including its large surface area and high stability. Moreover, the use of the rutile phase of TiO_2 has been found to enhance the dispersion of the metal compared to other phases. The rutile phase provides a favorable environment for the dispersion of iridium species (Kim et al., 2018) promoting their accessibility and reactivity in catalytic reactions. This unique characteristic of the rutile phase, combined with the advantageous properties of TiO_2 as a support, makes it a promising candidate for supporting iridium catalysts. Exploring the potential of TiO_2, particularly its rutile phase, as a support material for iridium catalysts holds great promise in the development of highly efficient and selective catalytic systems.

4 Comprehending the nature of catalytic sites on the surface

X-ray photoelectron spectroscopy (XPS), transmission electron microscopy (TEM), including aberration-corrected high-angle annular dark-field scanning transmission electron microscopy (HAADF-STEM), diffuse reflectance infrared Fourier-transform spectroscopy (DRIFT), and X-ray absorption spectroscopies (XAS) are the key techniques employed for the analysis and authentication of iridium single atom catalysts (SACs). XPS allows for the investigation of surface composition and chemical states. HAADF-STEM provide atomic-scale resolution to directly examine the structure and coordination environments of isolated iridium atoms. DRIFT enables the study of molecular adsorption and surface species reactivity. With XAS it is possible to investigate a broad spectrum of surface structures. These techniques collectively play a pivotal role in the comprehensive characterization and understanding of iridium-based catalysts.

4.1 X-ray photoelectron spectroscopy

X-ray photoelectron spectroscopy (XPS) is a highly valuable technique employed in catalysis research for the analysis of catalyst surfaces. It serves the purpose of examining the surface composition and chemical states of catalyst materials. By utilizing X-ray photons to stimulate the ejection of inner-shell electrons from atoms within the catalyst, XPS enables the measurement of electron kinetic energy and intensity. This data provides crucial insights into the elemental composition, oxidation states, and bonding environments present on the catalyst surface (Greczynski and Hultman, 2020).

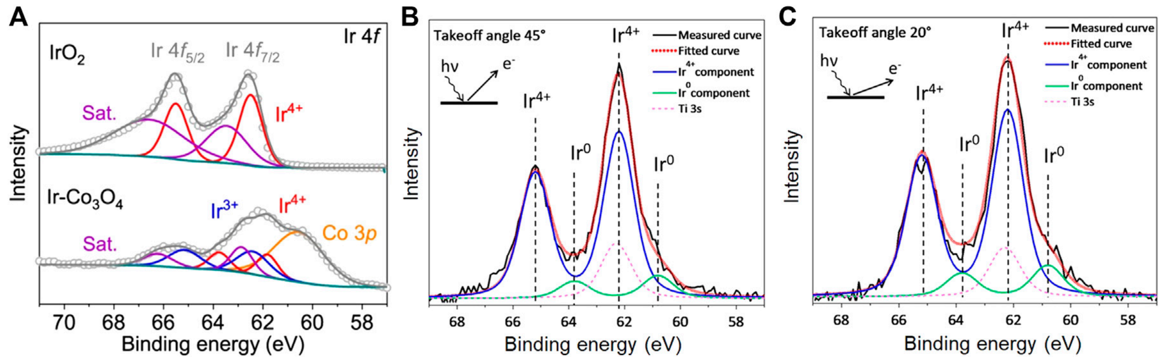

FIGURE 1
(A) XPS spectrum of characteristic Ir^{4+}. Adapted from Zhu et al. (2022b), licensed under CC BY 4.0. **(B,C)** Spectra of Ir^0, Ir^{4+}, and the overlap of Ti 3s. Adapted from Lee et al. (2018), licensed under CC BY 4.0.

In the realm of catalysis, XPS plays a pivotal role in elucidating surface chemistry and catalytic reactivity. It facilitates the investigation of active sites and their electronic structures, which are fundamental to catalytic processes. By employing XPS, researchers can explore changes in oxidation states of catalytic metals under reaction conditions, observe adsorbed species or reaction intermediates, and analyze the effects of environmental factors such as temperature and pressure on the catalyst surface (Oswald et al., 2013).

Moreover, XPS proves to be a valuable tool for pre- and post-reaction analysis of catalysts, allowing the detection of surface modifications, elucidation of catalyst deactivation mechanisms, and determination of catalyst stability. The technique can also be utilized for *in situ* characterization, enabling real-time monitoring of catalyst performance during catalytic reactions.

In summary, X-ray photoelectron spectroscopy is an indispensable technique in catalysis research, offering valuable insights into the surface chemistry and reactivity of catalysts. Its ability to probe the atomic-scale properties of catalyst surfaces provides crucial information for understanding catalytic mechanisms, optimizing catalyst design, and advancing the development of more efficient and selective catalytic processes. XPS enables the determination of the oxidation state of iridium, providing valuable insights into its chemical state.

In Figure 1A, Yiming Zhu et al. shows the XPS spectrum of IrO_2 displays a characteristic doublet at 62.5 and 65.4 eV, corresponding to the presence of Ir^{4+} species. On the other hand, for Ir-Co_3O_4, the Ir 4f spectrum exhibits two sets of doublets centered at 61.8/63.7 eV and 62.4/65.3 eV. These doublets can be attributed to the coexistence of Ir^{4+} and Ir^{3+} species, respectively.

In Figures 1B, C Lee et al. (2018) shows the spectra of the Ir $4f_{5/2}$ and $4f_{7/2}$ core level peaks are presented in Figures 1B, C. The deconvolution of the peak profile revealed the presence of both Ir^{4+} and Ir^0 components in the Ir:$SrTiO_3$ film. By measuring spectra at different takeoff angles, the depth distribution of the Ir^{4+} and Ir^0 components can be estimated due to the limited inelastic mean free path of photoelectrons in XPS measurements. Measurements performed at higher takeoff angles, which are more surface-sensitive, demonstrated a higher Ir^0 ratio (~13%) compared to measurements taken at a 45° angle (~10%). Interestingly, while tetravalent Ir^{4+} is expected based on DFT calculations for iridium atoms substituting Ti, the presence of metallic Ir^0 was observed.

X-ray photoelectron spectroscopy (XPS) analysis reveals the presence of metallic iridium supported on TiO_2, which holds significant importance as it signifies the catalytically active state of the material. The observation of metallic iridium on the surface of TiO_2 confirms its availability as an active species for catalytic reactions. Furthermore, the ability to deposit isolated iridium atoms at low metal loadings underscores the potential for achieving single-atom dispersion. This discovery unveils promising avenues for leveraging the distinctive reactivity and selectivity of single atom catalysts supported on TiO_2, thereby offering compelling prospects for catalytic applications.

4.2 Aberration-corrected scanning transmission electron microscopy

Transmission electron microscopy (TEM) is an advanced scientific instrument that employs a focused and accelerated beam of electrons to obtain detailed and high-resolution images of samples at the micro and nanoscale. By passing the electron beam through the sample, TEM can generate valuable information about the sample's internal structure, composition, and morphology. This technique relies on the interaction between the electrons and the atoms in the sample, producing signals that are captured by detectors and transformed into visual representations. With its exceptional resolving power, TEM enables researchers to explore the intricate details of materials, including the arrangement of atoms and the presence of defects or nanoscale features. There are two main transmission modes in TEM: the conventional TEM and the scanning transmission electron microscopy (STEM).

In conventional TEM, electrons coming from the electron source are focused on the sample in a wide and quasi-parallel beam, formed by the illumination system composed by electromagnetic condenser lenses, Figure 2A. These lenses are the responsible of forming the incoming beam and the manner of how it hits on the sample. Once the electron beam passes through the sample, the transmitted beam is collected by the objective lens and

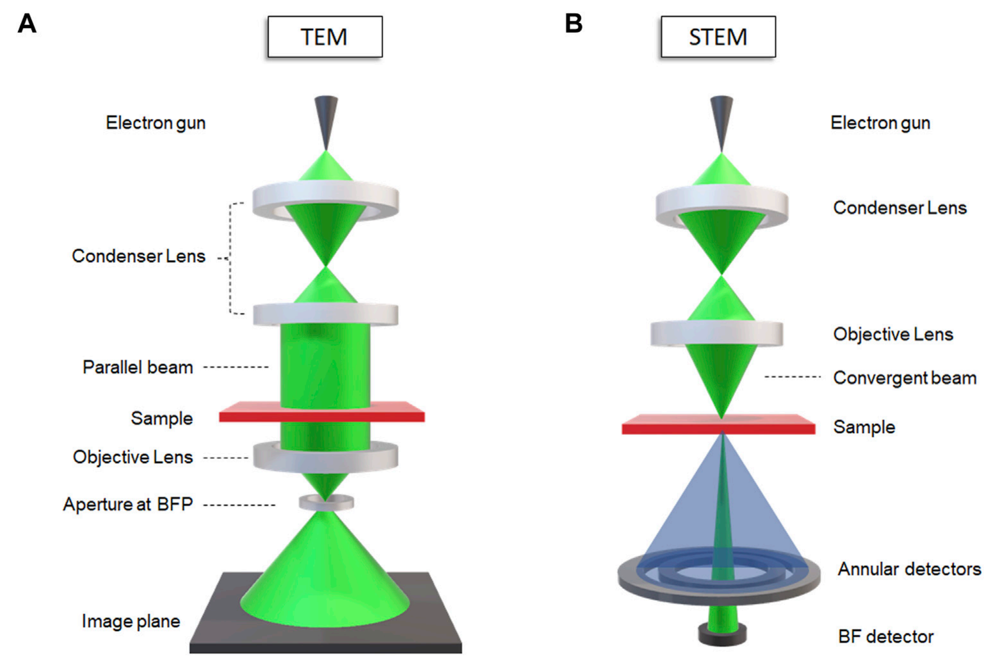

FIGURE 2
Sketch of the two main modes in TEM: conventional TEM **(A)** and STEM **(B)**.

projected to the screen. An image of the sample is instantaneously produced of all the illuminated area.

The incident electrons are described as a plane electron wave $\psi(r)$, which interacts with the sample and undergoes different dispersion phenomena. The exit electron wave at the end of the specimen plane, described as $\psi_{exit}(r)$, is formed by interference of the waves scattered by the atoms of the sample. These scattered waves are collected by the objective lens and focused at its back focal plane (BFP). If the lens is ideal and in focus, the recovered wave at the image plane, $\psi_{im}(r)$, should be:

$$\psi_{im}(r) = \psi_{exit}(r)$$

And the intensity distribution will be

$$I_{im}(r) = \psi_{im}(r)\cdot\psi_{im}^{*}(r) = 1$$

However, there is no perfect lenses, so the wave at the image plane will be:

$$\psi_{im}(r) = \psi_{exit}(r) \otimes OL(r)$$

where *OL(r)* is a function describing the behavior of the objective lens (Pennycook and Nellist, 2011; Deepak et al., 2015).

The phase shift produced by the lens can be described as (Carter, 2009):

$$\chi(u) = \pi\Delta f\,\lambda\,u^2 + \frac{1}{2}\pi C_s\lambda^3 u^4$$

Therefore, it is observed that the final image will depend on how the electron beam interacted with the sample and the phase shift produced by the objective lens, which in turn depends directly on the defocus Δf, the wavelength of the incoming electrons λ, and the spherical aberration constant, *Cs*. The interpretation of high-resolution TEM images is not straightforward because the image contrast will depend on our optical system, defocus conditions, sample thickness, and aberrations.

In STEM, instead of a wide and parallel beam, a highly focused convergent beam of electrons is scanned over the sample, Figure 2B. The electron probe is formed by the interference of an infinite number of plane waves at all the different convergence angles forming the illumination cone. No lenses are present below the sample, so the electrons that have interacted with the sample are collected directly by different detectors placed below the sample plane. The coherent beam is focused on each point of the sample, so the diffracted beams form discs that interfere to each other and provides the contrast interpreted as images, Figure 3A.

The amplitude of the waves is moderated by the partial coherence of the electron beam, which depend on the convergence angle and aperture size which limits the space from $-\mathbf{k}_{\max}$ to $\mathbf{k}_{\max}$ ($\mathbf{k}_{\max} = \lambda/\alpha$), Figure 3B. In real space, the amplitude of the electron probe $P(r)$ can be described as:

$$P(r) = \int A(k)\exp[i2\pi kr]\,dk$$

where $A(\mathbf{k})$ corresponds to a function of the circular aperture defining the convergence angle. In STEM, the upper objective lens is the one responsible of forming the electron probe, and will be affected by aberrations. The aberration coefficients have dimensions of length and can be expressed in power series of scattering angle θ as (Carter and Williams, 2016):

$$\gamma(\theta) = \frac{1}{2}\Delta f\theta^2 + \frac{1}{4}C_3\theta^4 + \frac{1}{6}C_5\theta^6 + \frac{1}{8}C_7\theta^8 + \cdots$$

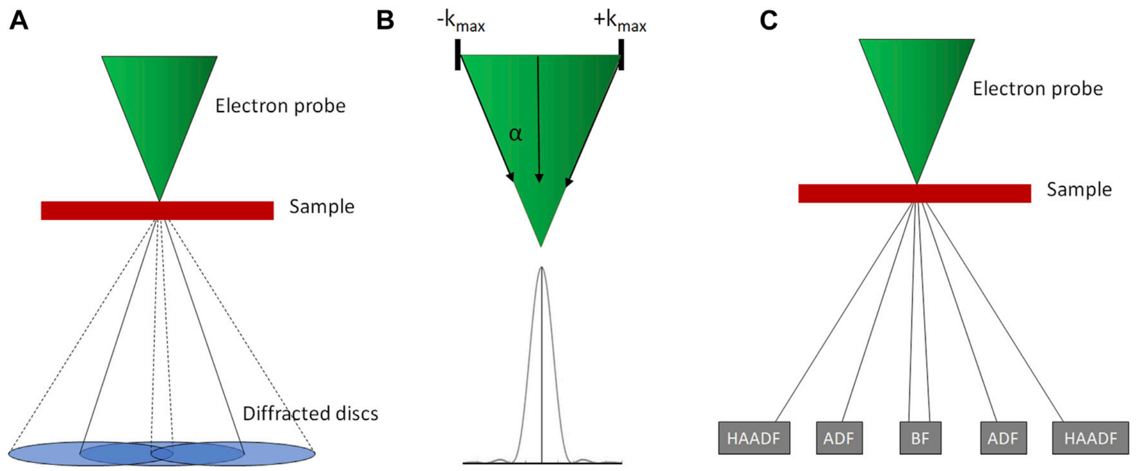

FIGURE 3
(A) The convergent electron probe form diffracted discs. **(B)** Schematics of the reciprocal and real space of the electron probe formed by coherent plane waves passing through an aperture defining a semi angle α. **(C)** Diffracted electrons from the sample are collected by detectors placed at different angles.

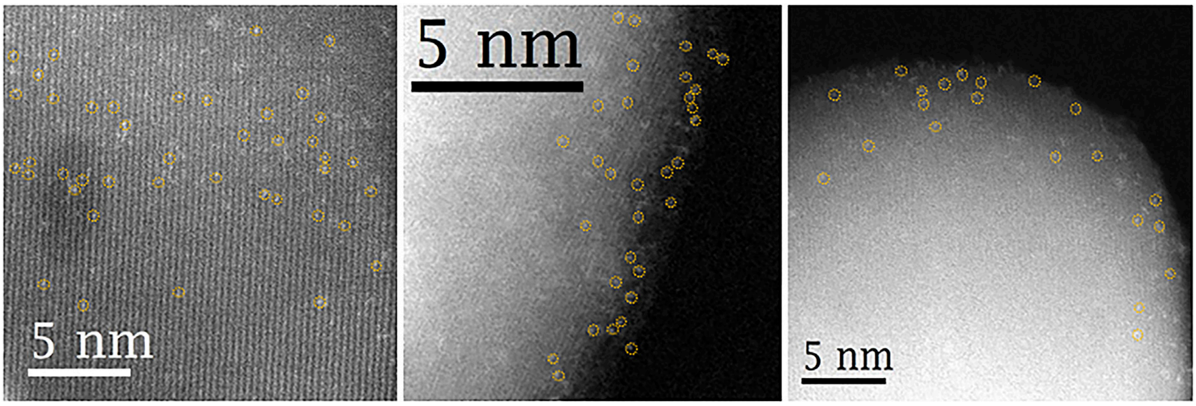

FIGURE 4
AC-HAADF-STEM measurements were employed to visually inspect the distribution of Ir in the 0.25% Ir/TiO$_2$ catalyst. Notably, no Ir nanoclusters were observed, and individual Ir atoms were identified as bright dots highlighted in yellow.

With $\chi = 2\pi\gamma$. The C_s coefficients are positive values. The amplitude of the STEM probe can be described as:

$$P(r) = \int A(k) \exp[i2\pi kr] \exp[-i\chi(k)]\, dk$$

And the probe intensity is its square $|P(r)|^2$.

In an uncorrected probe, the third order spherical aberration (C_3) can be compensated by negative defocus. In a spherical-aberration corrected probe, the next higher order aberration C_5 can be compensated by a slight negative C_3 (Carter and Williams, 2016). The optimal resolution for an uncorrected system can be expressed as:

$$d_{opt} = 0.43\lambda^{3/4} C_3^{1/4}$$

and for a *Cs* corrected system, the limiting resolution due to the *n*th order aberration:

$$d_{opt} = 0.45\lambda^{5/6} C_3^{1/6}$$

In a 200 keV aberration-corrected microscope, C_3 can be set to positive or negative values close to cero, while for an uncorrected high-resolution microscope C_3 is close to 0.5 mm. The electron probe diameter in STEM can be reduced through the aberration-corrected system, which consists of a hexapole-corrector with two multipole stages and it compensates all aberrations up to third order (CESCOR, 2023). Then, this small probe is scanned through the sample and interact with its atoms, which can be seen as an arrangement of individual scatters. Now the highly-convergent electron beam interacts individually with each scatter (instead of a wide parallel beam interacting with a large number of scatters in TEM). Each atom (a spike of potential) will scatter in proportion to the local probe intensity. Therefore, the intensity of the image can be written as:

$$I(r) = O(r) \otimes |P(r)|^2$$

i.e., the intensity at the image is the convolution of the object *O(r)* (array of scatters) and the probe intensity profile *P(r)*. The sharper the probe, the clearer the atoms are seen.

In STEM, when the beam is scanned over the sample, the collection of scattered electrons is done by the detectors placed below the sample, Figure 3C. The angle of scattering will depend on the atomic number Z of its constituent elements. Hence, detectors are placed to collect the scattered electrons at different angles, thus collecting different information of the sample. A bright-field detector (BF) collects those electrons scattered at low angles (~<10 mrad), and the images are similar to conventional TEM. An annular dark-field detector (ADF) can be placed to collect electrons scattered at higher angles (~10–50 mrad), which contain information of the chemical composition of the sample. A high-angle annular dark-field detector (HAADF) collects those electrons passing close to the atoms nucleus electrons, being scattered at much high angles (>50 mrad). These high-angle scattered electrons contain pure Z-contrast information from the sample and possess incoherent characteristics (Carter and Williams, 2016; Plascencia-Villa et al., 2020; Plascencia-Villa and Mendoza-Cruz, 2022).

STEM and TEM are powerful techniques widely used in catalysis research. One of the key features of these techniques is their ability to correct spherical aberration, allowing for high-resolution imaging at the atomic scale. With the advent of advanced electron microscopy instruments, aberration-corrected STEM offers the capability to visualize individual atoms and atomic structures in catalyst materials. This level of resolution is particularly valuable in the study of single atom catalysts (SACs), where the dispersion and arrangement of individual metal atoms play a critical role in their catalytic activity.

The aberration-corrected STEM/TEM imaging allows researchers to directly observe the presence and distribution of single atoms on the catalyst surface, and with the advantage of Z-contrast, atomic-resolution structural and chemical information can be obtained in a single image, Figure 4. This information is essential for understanding the relationship between atomic structure and catalytic properties, as well as for investigating the dynamics and behavior of single atoms during catalytic reactions.

Advanced AC-HAADF-STEM measurements were employed to visually inspect the distribution of Ir in the 0.25% Ir/TiO_2 catalyst. Notably, no Ir nanoclusters were observed, and individual Ir atoms were identified as bright dots highlighted in yellow. These Ir atoms were consistently located on the Ti sites of the TiO_2 support.

Individual Ir atoms were observed by AC-HAADF-STEM. The Ir sacs were resolved using an intensity profile since the observation was complicated due to the thickness of TiO_2 crystal. Nevertheless, it is possible to analyze the intensity profile and distinguish the presence of iridium atoms, Figure 5. These Ir atoms were consistently located on the Ti sites of the TiO_2 support.

4.3 IR/DRIFT

Diffuse Reflectance Infrared Fourier Transform Spectroscopy (DRIFTS) is a powerful analytical technique used in catalysis research for the characterization of catalysts and the investigation of surface species and adsorbed molecules. It utilizes infrared radiation to probe the vibrational modes of molecules on the catalyst surface. By measuring the changes in infrared absorption and reflection, DRIFTS provides valuable information about the surface chemistry, adsorption properties, and catalytic reactions occurring on the catalyst surface. This technique offers insights into the nature of active sites, the interaction between the catalyst and reactants, and the mechanism of catalytic reactions. It is a versatile tool for understanding the structure-function relationships of catalysts and designing more efficient catalytic systems.

DRIFTS works by irradiating the catalyst sample with infrared radiation and analyzing the resulting diffusely reflected light. The infrared radiation consists of a range of wavelengths that corresponds to the vibrational frequencies of chemical bonds in molecules. When the infrared light interacts with the catalyst surface, it is absorbed by the molecules present, causing them to vibrate and undergo changes in their dipole moment. These changes in dipole moment result in the scattering and reflection of the infrared light (Mitchell, 1993).

The diffusely reflected light is collected by a detector, such as a Fourier Transform Infrared (FT-IR) spectrometer, which measures the intensity of the reflected light as a function of wavelength. This spectrum provides information about the vibrational modes of the molecules on the catalyst surface, allowing for the identification of specific functional groups and the determination of surface species (Díaz et al., 2011).

By comparing the DRIFTS spectra of the catalyst before and after exposure to reactants or under different reaction conditions, researchers can gain insights into the adsorption and desorption processes, the formation of reaction intermediates, and the overall catalytic activity. The conducted studies have revealed the absorption band of iridium between 2075 and 2068 cm^{-1} (Díaz et al., 2011).

In Figure 6, the DRIFT spectra presented in this study demonstrate the adsorption of CO on catalysts that were reduced *in situ* in a hydrogen flow at 300°C. The iridium-based catalysts, namely, Ir/TiO_2 and Au-Ir/TiO_2-S, exhibited strong absorption bands in the range around 2100 cm^{-1}. These bands are characteristic of CO molecules adsorbed on iridium metal. The monometallic Ir catalyst showed a particularly intense absorption band centered at approximately 2068 cm^{-1}, accompanied by a broad contribution in the low-frequency side. These absorption bands in the region can be attributed to CO linearly adsorbed on various Ir^0 sites. Additionally, bands characterizing cationic iridium species were also observed in the spectral region between 2000 and 2107 cm^{-1} (Gómez-Cortés et al., 2009).

Rojas et al. (2015) showed that the Ir/TiO_2 catalyst exhibited a prominent absorption band with a pronounced peak at 2073 cm^{-1}, indicating the adsorption of CO on Ir^0 sites. Furthermore, it has been demonstrated that it is possible to deposit isolated atoms on TiO_2.

DRIFT is a valuable technique that plays a crucial role in the comprehensive characterization of the support surface. In the specific case of iridium catalysts supported on TiO_2, DRIFT analysis enables the direct observation of CO absorption bands, providing valuable insights into the presence and reactivity of iridium sites on the catalyst surface. The detection of CO absorption bands signifies that the iridium species maintain their reactivity and availability for catalytic reactions, despite the strong interaction and bonding with the TiO_2 support. This finding highlights the remarkable reactivity of iridium, which positions it as a highly promising catalyst for various catalytic applications. The ability to maintain its reactivity and accessibility on

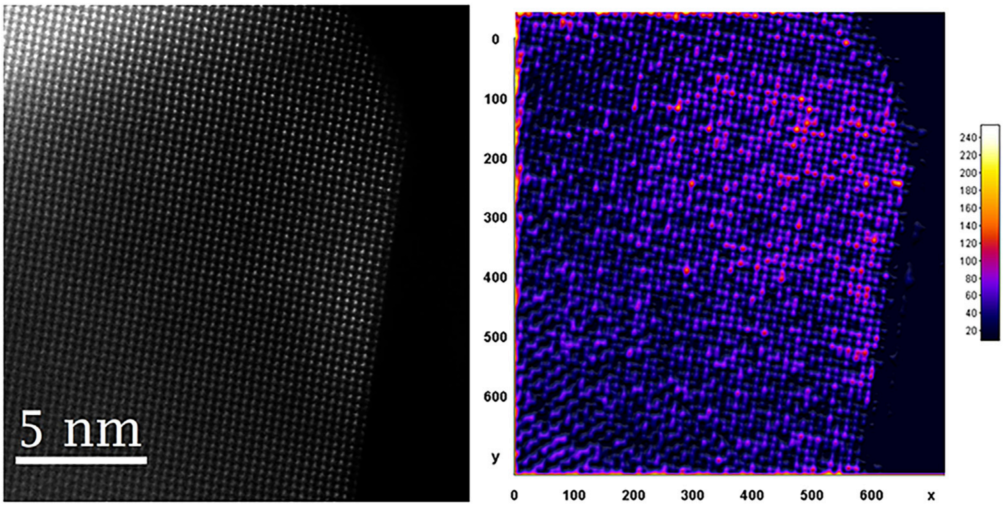

FIGURE 5
AC-HAADF-STEM of Ir in the 0.25% Ir/TiO_2 catalyst and its intensity profile.

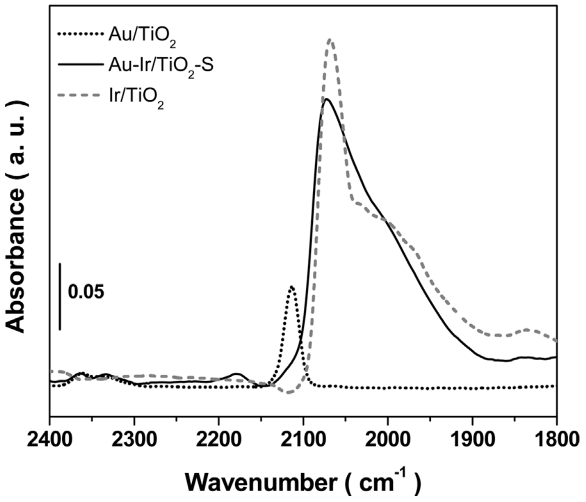

FIGURE 6
DRIFT spectra of Ir/TiO_2 3.7 %wt (Adapted from Gómez-Cortés et al. (2009), with permission from Copyright © 2009 American Chemical Society).

the support surface makes iridium an attractive choice for catalytic transformations, offering opportunities for enhanced catalytic performance and selectivity in various chemical processes.

4.4 X-ray absorption spectroscopies

X-ray absorption spectroscopy (XAS) is currently being utilized to investigate a broad spectrum of surface structures. In the extended X-ray absorption fine structure (EXAFS) regime, single scattering is typically employed, enabling the straightforward determination of near-neighbor distances (R) and coordination numbers (A).

XANES is commonly affected by intra-molecular scattering, potentially providing straightforward insights into molecular orientation, intramolecular distances, and, consequently, the specifics of bonding with the surface. Moreover, it can reveal the atom's oxidation state, the chemical environment, and electronic transitions occurring near the central atom (Norman, 1986). XAS will only be shown in this review to observe the possibility of iridium binding in TiO_2.

EXAFS specializes in the examination of atomic arrangements around a central atom within a material, offering a meticulous investigation of its local atomic structure. This analytical method delves into the energy region situated beyond the critical point of X-ray absorption. EXAFS has a unique advantage over more standard methods like X-ray diffraction because one can directly determine the location of atoms surrounding each constituent separately (Sayers et al., 1970). In contrast, XANES concentrates on furnishing insights into the valency of atoms and their chemical environment, closely exploring the region proximate to the X-ray absorption edge. It is widely acknowledged that XANES exhibits sensitivity to the adsorption of various substances. Initially, we isolate changes in the metal's XANES data due to the presence of the adsorbate. This involves obtaining two separate XANES spectra: one for the metal with the adsorbate and another for the metal under different conditions, such as altered potential, current, or in a vacuum. The latter serves as the reference baseline. This technique can be viewed as a subtractive approach, aimed at isolating the influence of the adsorbate. Consequently, the resulting spectral shape provides insights into the chemistry, site symmetry, and quantity of adsorbed species on the surface (Ramaker and Koningsberger, 2010).

These two techniques synergistically complement each other and are jointly employed to achieve a comprehensive understanding of a material's structure and chemistry (Koningsberger and Prins, 1987).

X-radiation, when passing through matter, is absorbed through various mechanisms, including the photoelectric process, which involves the direct excitation of occupied core electrons to unoccupied levels see Figure 7 (Norman, 1986). The origins of EXAFS stem from fluctuations in the photoelectric cross-section

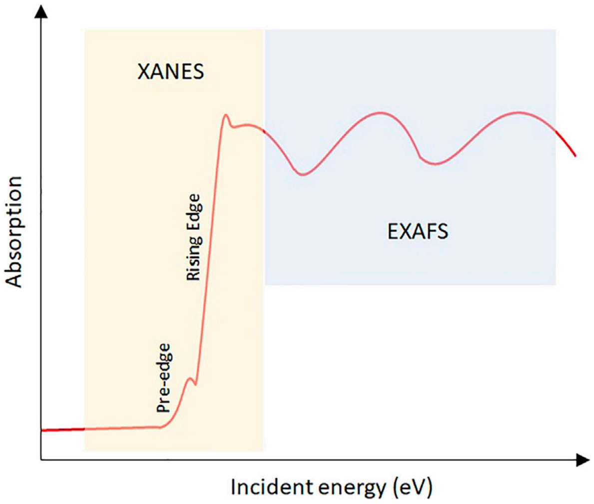

FIGURE 7
Schematic of the X-ray absorption spectrum, highlighting the different regions in which is divided.

resulting from the scattering of the emitted photoelectron by neighboring atoms encircling the absorbing atom (Sayers et al., 1971).

XANES is commonly affected by intra-molecular scattering, potentially providing straightforward insights into molecular orientation, intramolecular distances, and, consequently, the specifics of bonding with the surface. XANES directly examines the angular momentum of unoccupied electronic states, which can encompass bound or unbound, discrete or broad, atomic or molecular characteristics (Vaithianathan et al., 2006). Moreover, it can reveal the atom's oxidation state, the chemical environment, and electronic transitions occurring near the central atom (Norman, 1986). XAS will only be shown in this review to observe the possibility of iridium binding in TiO_2.

The chemical coordination environments of the Ir single atom species were investigated by acquiring extended X-ray absorption fine structure (EXAFS) data at the L_3-edge of the Ir species, using the Ir/AC nano catalyst for comparison with other standard Ir compounds.

Porous organic polymers based on aminopyridine show that Ir's closest neighbors are Ir-Ir and Ir-O. This result can explain the presence of Ir metal on the surface. The fitted EXAFS data indicate the presence of Ir-Cl, suggesting that the Ir species existed as isolated metal atoms and possibly maintained their high coordination number as a result of ligand exchange with the support. In summary, EXAFS data show that mononuclear Ir is situated on the framework using $-Cl_2$, $-O_2$, or -OH groups as ligands. The Ir single atom species was evidently coordinated by two neighboring oxygen nuclei associated with the support (Shao et al., 2019b).

In atomically-dispersed iridium on tin oxide, they performed *ex situ* and *in situ* X-ray absorption spectroscopy and have shown data in R-space that correspond to Ir-O, with a lack of strong contributions from Ir-Ir or Ir-O-Ir interactions. They conducted this study to investigate the oxygen evolution reaction (OER) mechanism, for which they computed the mechanisms using the structures of $Ir\text{-}_{SAC}$-ITO. In these structures, they've demonstrated the binding of Ir sites with oxygen. In this study, they observed IrO_2 (Ir_{IV}). The oxidation states of Ir were assigned as Ir_{III}, Ir_{IV}, and Ir_V (Lebedev et al., 2020).

In Figure 8, the researchers constructed computational models based on Ir-SAC, and these models illustrated the coordination of Ir atoms with oxygen sites present on the support material. Within the proposed mechanism, the researchers further elucidated the bonding interactions by showcasing how the Ir sites form bonds with hydroxyl (OH) groups. This detailed analysis provides valuable insights into the intricate chemical processes occurring at the atomic level, shedding light on the catalytic behavior of $Ir\text{-}_{SAC}$ in various reactions, including the oxygen evolution reaction. Computed studies of iridium nanoparticles using density functional theory calculations have shown that the planar configurations are more stable than the three-dimensional ones, with each arranged in decreasing order of stability (Pawluk et al., 2005).

In the analysis of Ir/TiO_2 for CO oxidation, both EXAFS and XANES techniques were used to understand the rate-controlling steps for CO oxidation. Ir single-atom sites within the catalyst were found to be uniformly distributed.

DRIFT spectrum of the Ir_1/TiO_2 catalyst in Figure Xb shows two CO bands at 2077 and 1995 cm^{-1}, attributed to Ir gem-dicarbonyl ($Ir(CO)_{2\text{-support}}$).

In Figure 9 (Xanes region), the EXAFS spectra reveal a dicarbonyl state (two Ir-CO). Besides, the model fit indicates two Ir-O bonds from the support and one Ir-Ti bond. XAS results indicate Ir initially exists as $Ir(CO_2(O)_2$ after reduction and gets oxidized to Ir(CO) $(O)_3$ during/after reaction. For the Density Functional Theory (DFT) calculations (Figure 9), we opted for adsorbed Ir single atoms to represent the experimental structure. This choice was made because these Ir single atoms can potentially form a dicarbonyl in the CO-reducing environment. It is important to note that Ir single atoms embedded within the TiO_2 lattice could not maintain a stable dicarbonyl structure.

It is imperative to underscore that this investigation was undertaken using TiO_2 in the anatase phase. Consequently, it is strongly advised to contemplate a parallel inquiry employing rutile TiO_2, as the variations in the crystalline phase can yield distinctive outcomes.

5 Exploring the catalytic capabilities of iridium: applications

$Ir\text{-}_{SACs}$ have been applied widely in numerous applications, in particular, in electrocatalytic reactions, such as ORR, water splitting, CO_2 reduction, HER, epoxidation of ethylene (Yang et al., 2023). Ir on TiO_2 as a SAC, is a more specific system that has been applied in oxidation and reduction reactions, photocatalysis, electrocatalysis. Here, we review some application of Ir SACs supported on metal oxides.

5.1 Oxidation reactions

Carbon monoxide (CO) and ammonia oxidation are important reactions, since they are harmful residual gases from the incomplete combustion of industrial compounds. By the other hand, CO oxidation is a model reaction for the fundamental understanding

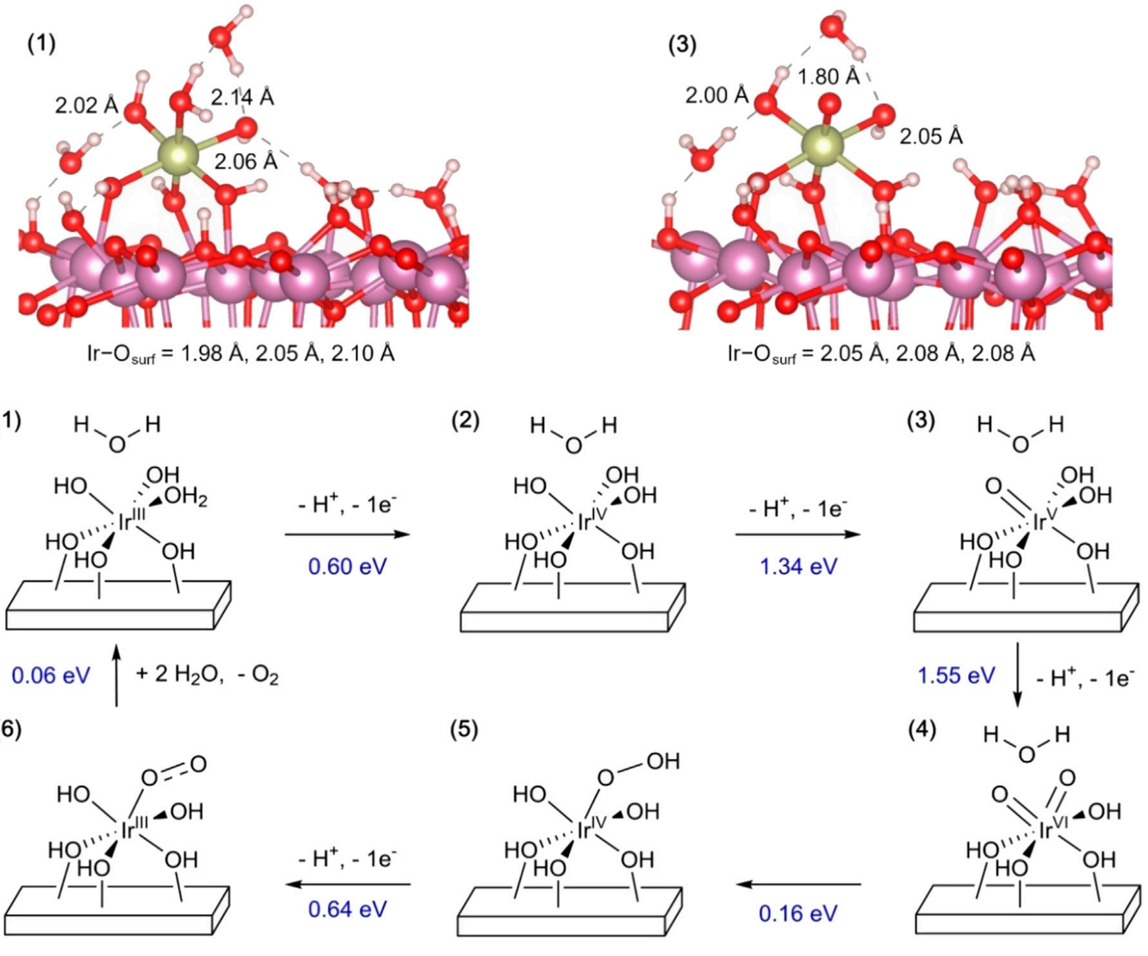

FIGURE 8
Computed OER with the structures of Ir-$_{SAC}$-ITO. Reproduced from Lebedev et al. (2020), with permission from Copyright © 2023 American Chemical Society, licensed under CC BY 4.0.

of catalytic processes which can be applied to generate products of industrial relevance. Hence, efforts to improve this reaction in which Ir-based SACs play an important role have been done.

Jian Lin and coworkers designing an Ir-Fe(OH)x catalyst which stabilized Ir single atoms for the oxidation of CO. HAADF imaging showed that Ir single atoms distributed uniformly over the support, with small clusters below 1 nm. The adsorption and activation of O_2 was promoted by the support, reflecting its erole in the activity of Ir-based catalysts for the CO oxidation (Lin et al., 2012). Lu Dai and collaborators, reported the promotion of CO oxidation of Ir-TiO_2 catalysts. The promotion was achieved by the tuning of the metal-support interaction, induced by the incorporation of small amounts of CeO_2 into the TiO_2 structure. The presence of a small amount of CeO_2 promoted the CO oxidation significantly, and the activities enhanced with the increase of CeO_2 amount, being Ir/$Ce_{0.2}$Ti the sample with the highest activity (Lu et al., 2023).

Ir-TiO_2 single-atom catalyst were prepared by Y Wang et al. The catalyst showed excellent low-temperature selective catalytic oxidation of ammonia. They found that rutile phase performed better than it counterpart anatase. Ir atoms had a better dispersion on rutile. The activity was related to the stronger electronic metal-support interaction with rutile than other phases 15 (Li et al., 2020).

C.B. Thompson studied the rate-controlled elementary steps for CO oxidation of the Ir-TiO_2 system. They showed that the supported Ir SACs were catalytically active for CO oxidation at atmospheric pressure and temperature ranges from 150°C to 200°C in 0.1%–10% CO and 1%–17% kPa O_2, providing insight into the reaction mechanism (Coogan et al., 2023).

Y. Lu studied SAC of Ir on $MgAl_2O_4$ for the CO oxidation reaction. They applied operando infrared and X-ray absorption spectroscopies and quantum chemical calculations to identify the Ir single-atom complex formed during CO oxidation. They found that Ir(CO) is the active complex, and the formation of Ir single-atom complex promotes the CO oxidation via an Eley–Rideal mechanism where Ir(CO) (O) is the resting state of the catalyst. Their results showed that strong adsorption by a ligand does not necessarily lead to catalyst poisoning due to the ability of single-atoms to bind to more than one ligand. DFT results indicated that Ir single atoms had a critical role in facilitating O_2 activation, while the CO ligand lowers the barrier for the Eley–Rideal rate-limiting step (Lu et al., 2019b).

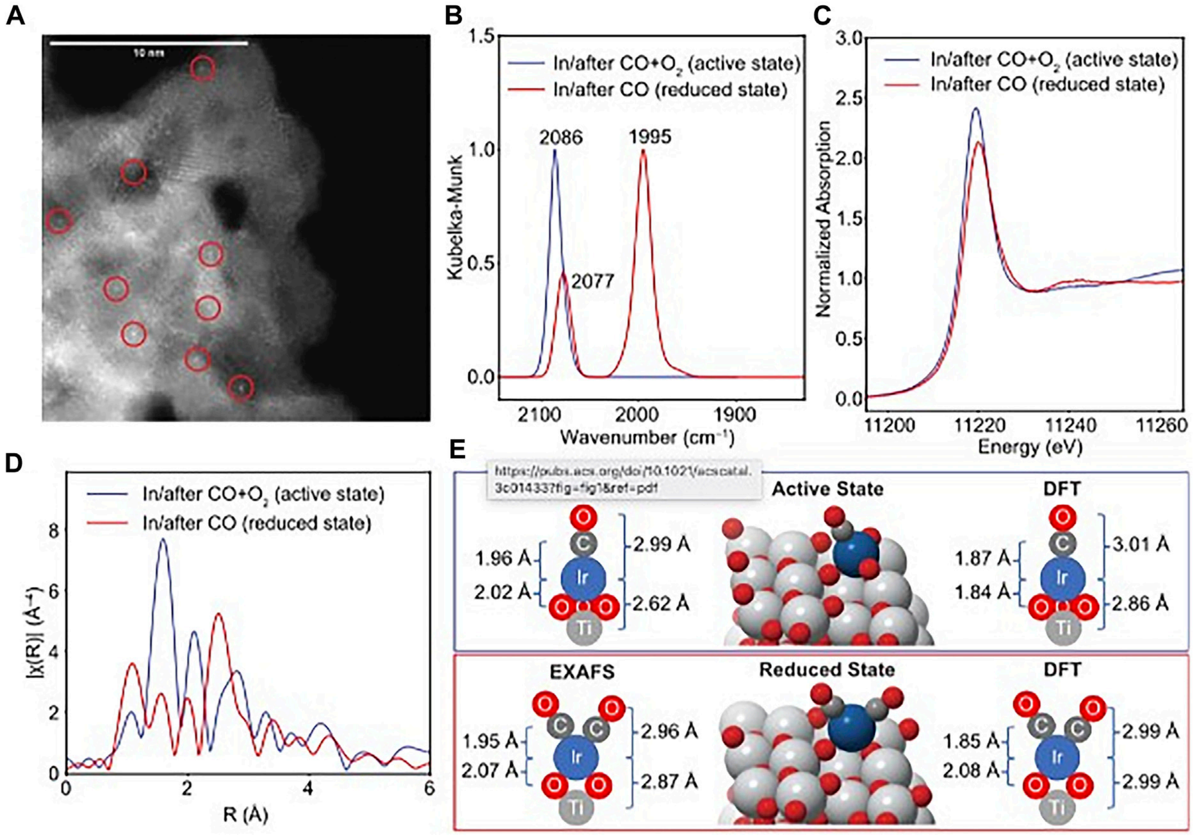

FIGURE 9
Ir/TiO_2 Characterization. **(A)** Scanning Transmission Electron Microscopy (STEM) image of the 0.1 wt% Ir/TiO_2 catalyst post-CO oxidation kinetic measurements at 170°C followed by CO reduction. **(B)** Differential Reflectance Infrared Fourier Transform (DRIFT) spectra recorded after CO oxidation at 170°C (blue) and post-reduction in CO at 170°C (red). **(C)** Ir-L_3 X-ray Absorption Near Edge Structure (XANES) spectra of the catalyst, showcasing the active state (blue) and the reduced state (red). **(D)** Magnitude component of the Fourier-transformed k3-weighted χ(k) data (Δk = 2.5–12 Å–1). For XANES/EXAFS, the reduced-state spectra were acquired in CO at 180°C, whereas the active-state spectra were recorded in CO and O_2 at 35°C, following CO oxidation at 195°C. **(E)** Representation of the local structures of Ir_1/TiO_2, combining experimental and theoretical insights. Color coding: O, red; Ti, silver; Ir, blue; C, gray. Reproduced from Coogan et al. (2023), with permission from Copyright © 2023 American Chemical Society.

5.2 Hydrogenation reactions

One of the first reports on single atom catalyst was done by Gates (Uzun et al., 2010). They reported the ethene hydrogenation by isolated atoms of Ir supported on MgO at room temperature and atmospheric pressure.

A dual single atom catalysts made of $IrMo/TiO_2$ was reported by J Fu and collaborators. The dual catalyst was consisted in discrete Ir single atoms and Mo single atoms anchored on TiO_2, showing great catalytic activity and chemoselectrivity in the hydrogenation of 4-nitrostyrene nad 4-vinylaniline that their monometallic counterparts. According to their density funcional theory calculations, they demonstrate that Ir sites were responsible for H_2 activation, while Mo sites were active site for the adsorption of 4-nitrostyrene via the nitro group (Fu et al., 2021).

A. Jia et al. (2023) reported the selective hydrogenation of crotonaldehyde (CROL) over Ir/TiO_2 catalyst. They studied the effect of metal size, from single atoms to nanoclusters (NC) to nanoparticles (NP), on the selective hydrogenation of this compound. Ir single atoms, clusters and nanoparticles were prepared on anatse TiO2. The reaction rates and TOFs of the different Ir/TiO_2 catalysts followed the order Ir(NP) > Ir(NC) > Ir(SA), while the selectivity was higher than 80% for Ir(SA) supported on TiO_2(101).

5.3 H_2 production

X Zhou and coworkers reported an approach to trap and stabilize Ir SACs on TiO_2 nanotubes, using the high density of Ti^{3+} - oxygen vacancies surface defect which served as highly effective SA iridium traps. The stably trapped SACs showed turnover frequencies of 4×10^6 h^{-1} in the photocatalytic H_2 production (Zhou et al., 2021).

5.4 Water gas shift

Ir_1/FeOx Single atom catalyst had a remarkable performance for water gas shift reaction, being superior to its Pt-based counterpart. Ir single atoms enhanced the reducibility of FeOx and generation of oxygen species (Luet al., 2019a).

5.5 Oxygen evolution reaction

MQ Yang et al. (2022) reported an strategy to improve the activity of Ir SACS by anchoring atomic Ir on oxygen vacancies of a $CoNiO_2$ support. The prepared SACs presented an overpotential of 183 mV at the current density was of 10 mA cm^{-2}, which was lower than a catalyst using Ir clusters.

The oxygen vacancies provided abundant active sites for the adsorption of OH* for OER. Based on Density Functional Theory (DFT) calculations, the enhanced activity of iridium (Ir) could be attributed to the Ir-S moiety in Ir_1/NFS, which is evident in the favorable formation of the *OOH intermediate during the Oxygen Evolution Reaction (OER) process (Lei et al., 2022).

L. Suhadolnik and collaborators prepared nanotubular TiOxNy-supported Ir single atoms, combined with clusters, as thin-film electrocatalysts. The nanomaterials consisted of a porous morphology. The catalyst exhibited very high oxygen evolution reaction activity in 0.1 M $HClO_4$, reaching 1,460 $Ag\text{-}_1Ir$ at 1.6 V *versus* a referente hydrogen electrode (Suhadolnik et al., 2023).

Yin et al. (2020) reported a strategy for the preparation of Ir single atoms supported on ultrathin $NiCo_2O_4$ porous nanosheets. The samples were produced by a co-elecgtrodeposition method. The catalysts showed higher OER activity and stability in acidic media due to the coupling of Ir single atoms with oxygen vacancies. An ultralow overpotencial of 240 mV a j = 10 $mAcm^{-2}$ was reported, with a long-term stabilty of 70 h. The surface electronic exchange-and-transfer activities of Ir atoms incorporated on the intrinsic oxygen vacancies of the metal support is the responsible to the high OER performance.

An influential work was done by Q. Wang and collaborators, who developed a catalyst consisted of a nickel oxide matrix, loaded with ultra-high content of Ir single atoms, up to 18 wt%. The catalyst showed enhanced OER in alkaline electrolyte, with an overpotential of 215 mV at 10 $mAcm^{-2}$, surprasing the activities of pure NiO and IrO2 catalysts. XPS and XANES results on the chemical state of Ir single atoms indicated that Ir was highly oxidized, with an oxidation state close to 4^+. After Ir doping, the oxidation state of Ni also modified, being higher than NiO. Ir atoms were well dispersed on the metal oxide surface with chemical bonding with the NiO substrate in a six-coordinated Ir − O (Wang et al., 2020).

5.6 Theoretical research

Undeniably, theoretical work on the interaction between metal atoms and molecules, as well as supports, have broaden the understanding of the behavior and stability of SACs. The calculations of their coordination environment and interactions have delivered important information on the single atom's contribution to the catalytic activity for different reactions.

For instance, Lin et al. (2020) studied the molecular adsorption properties of CH_4 on single atoms supported on anatase TiO_2(101) using the first-principles method based on density functional theory (DFT). The calculated formation energy of Ir-TiO_2 was de lowest, compare to other noble metal systems. Their results showed that Ir was the most stable system.

In their theoretical work, V. Fung and collaborators reported that single atoms dispersed on TiO_2 acomplish strong methane chemisorption and facle C-H activations. The calculations for chemisorption of methane were done by replacing a surface Ti atom (110) with the single metallic atom, coordinated to four surface oxygens and one subsurface oxygen. The coordination to the rutile TiO_2 surface modified the electronic structure of the single atoms site for chemisorption. They showed that Ir single atoms and other SACs on rutile TiO_2(119) can active C-H of methane at low temperature. Methane adsorption was found to be stronger on the single atom site on the rutile (110) surface than on the anatase (101) surface, with Ir and Pt single atoms being the metals with stronger CH_4 adsorption (Fung et al., 2018).

6 Future challenges

Several challenges exist for the practical implementation of Ir SACs, with a primary concern being the enhancement of the metal-support interaction. Potential strategies include investigating the DPU synthesis method, employing the impregnation method, and exploring in situ-synthesis techniques with low metal loading. Furthermore, a comprehensive characterization of the Ir-$TiO_{2\text{-rutile}}$ surface through XAS, XPS, HR-STEM, and DRIFT studies is essential to improve the catalyst's performance. Additionally, an evaluation of its activity, such as CO conversion, for comparative analysis with existing Ir/TiO_2 systems is crucial. Finally, the application of DFT studies to examine Iridium-SACs in various facets of TiO_2 may yield valuable insights into their catalytic behavior. It is imperative to continue studying the mechanisms involved during the catalytic processes to gain a better understanding of the contributions of Ir SACs. There are still few reports on this area and further research is of great importance.

7 Conclusion

In conclusion, despite the challenges involved in the synthesis and characterization of single atom catalysts (SACs), this study demonstrates the successful deposition of iridium as isolated atoms on TiO_2. The presence of these iridium atoms on the catalyst surface has been confirmed, highlighting the potential of TiO_2 as a suitable support for SACs. Furthermore, the reactivity of these isolated iridium atoms in catalytic reactions has been observed, emphasizing their functional role in driving catalytic processes.

The ability to deposit and retain iridium atoms as isolated entities on the TiO_2 support opens up new possibilities for the design and development of highly efficient catalysts. The presence of these reactive iridium species on the catalyst surface offers enhanced catalytic performance and selectivity. Despite the challenges associated with the synthesis and characterization of SACs, the findings from this study demonstrate the feasibility of achieving and maintaining isolated iridium atoms on the TiO_2 support, providing valuable insights for future catalyst design and optimization.

Overall, the successful deposition of isolated iridium atoms on TiO_2, their retention on the support surface, and their reactivity in catalysis highlight the promising potential of SACs in various catalytic applications. Further research and development efforts are warranted to fully explore and harness the capabilities of SACs supported on TiO_2, with the aim of advancing catalytic technologies and addressing current environmental and energy challenges.

Author contributions

MM-T: Conceptualization, Investigation, Writing–original draft. OH-C: Supervision, Validation, Writing–review and editing. RM-C: Conceptualization, Funding acquisition, Supervision, Validation, Writing–review and editing.

Funding

The authors declare financial support was received for the research, authorship, and/or publication of this article. The research was founded by Dirección General de Asuntos del Personal Académico (DGAPA) through grant PAPIIT IA-106623.

Acknowledgments

Acknowledgments to Dr. Gabriela Díaz-Guerrero, Dr. Rodolfo Zanella Specia, Dr. Raúl Herrera, Dr. Antonio Gómez-Cortés, Phys. Josué Romero, Dr. Lourdes Bazán, Dr. Omar Novelo, M.S Ana Karla Bobadilla, Phys. Lázaro Huerta Arcos, M.S. Adriana Tejeda, M.S. Viridiana Maturano Rojas, M.S. Alejandro Pompa-García, Dr. Samuel Tehuacanero-Cuapa, and Eng. Cristina Zorrilla for all the scientific and technical support provided.

Conflict of interest

Publisher's note

References

Bhirud, V. A., Uzun, A., Kletnieks, P. W., Craciun, R., Haw, J. F., Dixon, D. A., et al. (2007). Synthesis and crystal structure of Ir(C2H4)2(C5H7O2). *J. Organomet. Chem.* 692 (10), 2107–2113. doi:10.1016/j.jorganchem.2007.01.008

Bokhimi, X., Zanella, R., Morales, A., Maturano, V., and Ángeles-Chávez, C. (2011). Au/rutile catalysts: effect of the activation atmosphere on the gold-support interaction. *J. Phys. Chem. C* 115 (13), 5856–5862. doi:10.1021/jp111483v

Cao, W., Lu, L., Qi, H., Qian, He, Wu, Z., Wang, A., et al. (2019), *In-situ* synthesis of single-atom Ir by utilizing metal-organic frameworks: an acid-resistant catalyst for hydrogenation of levulinic acid to γ-valerolactone. *J. Catal.* 373, 161–172. doi:10.1016/j.jcat.2019.03.035

Carter, C. B., and Williams, D. B. (2016). *Transmission electron microscopy: Diffraction, imaging, and spectrometry*. Berlin, Germany: Springer.

Carter, D. B. W. C. B. (2009). *Transmission electron microscopy A textbook for materials science*. Berlin, Germany: Springer publication.

Cescor, (2023). Cescor - Cs-corrector for stem. https://www.ceos-gmbh.de/en/produkte/stemkorrektoren/cescor.

Chen, Y., Ji, S., Chen, C., Peng, Q., Wang, D., and Li, Y. (2018). Single-atom catalysts: synthetic strategies and electrochemical applications. *Joule* 2 (7), 1242–1264. doi:10.1016/j.joule.2018.06.019

Coogan, B., Liping, L., Leshchev, D. S., Hoffman, A. S., Hong, J., Bare, S. R., et al. (2023). CO oxidation on Ir1/TiO2: resolving ligand dynamics and elementary reaction steps. *ACS Catal.* 13 (12), 7802–7811. doi:10.1021/acscatal.3c01433

Cui, T., Li, L., Ye, C., Li, X., Liu, C., Zhu, S., et al. (2022). Heterogeneous single atom environmental catalysis: fundamentals, applications, and opportunities. *Adv. Funct. Mater.* 32 (9), 2108381. doi:10.1002/adfm.202108381

de Vries, J., and Jackson, S. (2012). Homogeneous and heterogeneous catalysis in industry. *Catal. Sci. Technol.* 2, 2009. doi:10.1039/C2CY90039D

Deepak, F. L., Mayoral, A., and Arenal, R. (2015). *Advanced transmission electron microscopy: Applications to nanomaterials*. Berlin, Germany: Springer.

Díaz, G., Gómez-Cortés, A., Hernández-Cristobal, O., Murcia, J. J., Borda, G., and Rojas, H. (2011). Hydrogenation of citral over IrAu/TiO2 catalysts. Effect of the preparation method. *Top. Catal.* 54, 467–473. doi:10.1007/s11244-011-9609-x

Erdoğan, H., Metin, Ö., and Özkar, S. (2009). *In situ*-generated PVP-stabilized palladium(0) nanocluster catalyst in hydrogen generation from the methanolysis of ammonia–borane. *Phys. Chem. Chem. Phys.* 11 (44), 10519. doi:10.1039/b916459f

Fu, J., Dong, J., Si, R., Sun, K., Zhang, J., Li, M., et al. (2021). Synergistic effects for enhanced catalysis in a dual single-atom catalyst. *ACS Catal.* 11 (4), 1952–1961. doi:10.1021/acscatal.0c05599

Fung, V., Tao, F., Feng), and Jiang, D. (2018). Low-temperature activation of methane on doped single atoms: descriptor and prediction. *Phys. Chem. Chem. Phys.* 20 (35), 22909–22914. doi:10.1039/C8CP03191F

Gómez-Cortés, A., Díaz, G., Zanella, R., Ramírez, H., Santiago, P., and JoséSaniger, M. (2009). Au–Ir/TiO$_2$ prepared by deposition precipitation with urea: improved activity and stability in CO oxidation. *J. Phys. Chem. C* 113 (22), 9710–9720. doi:10.1021/jp810905n

Greczynski, G., and Hultman, L. (2020). X-Ray photoelectron spectroscopy: towards reliable binding energy referencing. *Prog. Mater. Sci.* 107, 100591. doi:10.1016/j.pmatsci.2019.100591

Guo, J., Liu, H., Li, D., Wang, J., Djitcheu, X., He, D., et al. (2022). A minireview on the synthesis of single atom catalysts. *RSC Adv.* 12 (15), 9373–9394. doi:10.1039/D2RA00657J

Haruta, M., Kobayashi, T., Sano, H., and Yamada, N. (1987). Novel gold catalysts for the oxidation of carbon monoxide at a temperature far below 0 C. *Chem. Lett.* 16 (2), 405–408. doi:10.1246/cl.1987.405

Haruta, M. (1997). Novel catalysis of gold deposited on metal oxides. *Catal. Surv. Asia* 1 (1), 61–73. doi:10.1023/A:1019068728295

Herzing, A. A., Kiely, C. J., Carley, A. F., Landon, P., and Hutchings, G. J. (2008). Identification of active gold nanoclusters on iron oxide supports for CO oxidation. *Science* 321 (5894), 1331–1335. doi:10.1126/science.1159639

Jia, A., Zhang, W., Peng, H., Zhang, Y., Song, T., Li, L., et al. (2023). Selective hydrogenation of crotonaldehyde over Ir/TiO2 catalysts: unraveling the metal-support interface related reaction mechanism. *J. Catal.* 425, 57–69. doi:10.1016/j.jcat.2023.05.029

Kim, A., Debecker, D. P., Devred, F., Dubois, V., Sanchez, C., and Sassoye, C. (2018). CO2 methanation on Ru/TiO2 catalysts: on the effect of mixing anatase and rutile TiO2 supports. *Appl. Catal. B Environ.* 220, 615–625. doi:10.1016/j.apcatb.2017.08.058

Kominami, H., Kato, J. I., Takada, Y., Doushi, Y., Ohtani, B., Nishimoto, S. I., et al. (1997). Novel synthesis of microcrystalline titanium (IV) oxide having high thermal stability and ultra-high photocatalytic activity: thermal decomposition of titanium (IV) alkoxide in organic solvents. *Catal. Lett.* 46 (3-4), 235–240. doi:10.1023/A:1019022719479

Koningsberger, D. C., and Prins, (1987). *R. X-ray absorption: Principles, applications, techniques of EXAFS, SEXAFS and XANES*. Hoboken, New Jersey, United States: Wiley.

Kottwitz, M., Li, Y., Wang, H., Frenkel, A. I., and Nuzzo, R. G. (2021). Single atom catalysts: A review of characterization methods. *Chem. - Methods* 1, 278–294. doi:10.1002/cmtd.202100020

Lebedev, D., Ezhov, R., Heras-Domingo, J., Comas-Vives, A., Kaeffer, N., Willinger, M., et al. (2020). Atomically dispersed iridium on indium tin oxide efficiently catalyzes water oxidation. *ACS Central Sci.* 6 (7), 1189–1198. doi:10.1021/acscentsci.0c00604

Lee, M., Arras, R., Takahashi, R., Warot-Fonrose, B., Daimon, H., Marie-José, C., et al. (2018). Noble metal nanocluster formation in epitaxial perovskite thin films. *ACS Omega* 3 (2), 2169–2173. doi:10.1021/acsomega.7b02071

Lei, Z., Cai, W., Rao, Y., Wang, K., Jiang, Y., Liu, Y., et al. (2022). Coordination modulation of iridium single-atom catalyst maximizing water oxidation activity. *Nat. Commun.* 13, 24. doi:10.1038/s41467-021-27664-z

Li, Z., Chen, Y., Ji, S., Tang, Y., Chen, W., Li, A., et al. (2020). Iridium single-atom catalyst on nitrogen-doped carbon for formic acid oxidation synthesized using a general host–guest strategy. *Nat. Chem.* 12, 764–772. doi:10.1038/s41557-020-0473-9

Li, Z., Ji, S., Liu, Y., Cao, X., Tian, S., Chen, Y., et al. (2019). Well-defined materials for heterogeneous catalysis: from nanoparticles to isolated single-atom sites. *Chem. Rev.* 120, 623–682. doi:10.1021/acs.chemrev.9b00311

Liang, H., Chen, G., Desinan, S., Rosei, R., Rosei, F., and Ma, D. (2012). *In situ* facile synthesis of ruthenium nanocluster catalyst supported on carbon black for hydrogen generation from the hydrolysis of ammonia-borane. *Int. J. Hydrogen Energy* 37 (23), 17921–17927. doi:10.1016/j.ijhydene.2012.09.026

Lin, J., Wang, A., Qiao, B., Liu, X., Yang, X., Wang, X., et al. (2013). Remarkable performance of Ir$_1$/FeO$_x$ single-atom catalyst in water gas shift reaction. *J. Am. Chem. Soc.* 135 (41), 15314–15317. doi:10.1021/ja408574m

Lin, J., Qiao, B., Liu, J., Huang, Y., Wang, A., Li, L., et al. (2012). Design of a highly active Ir/Fe(OH)$_x$Catalyst: versatile application of Pt-group metals for the preferential oxidation of carbon monoxide. *Angew. Chem. Int. Ed.* 51 (12), 2920–2924. doi:10.1002/anie.201106702

Lin, L., Shi, Z., Huang, J., Wang, P., Yu, W., He, C., et al. (2020). Molecular adsorption properties of CH4 with noble metals doped onto oxygen vacancy defect of anatase TiO2 (101) surface: first-principles calculations. *Appl. Surf. Sci.* 514, 145900. doi:10.1016/j.apsusc.2020.145900

Lu, D., Li, B., Peng, Y., Hao, X., Xuan, R., Huang, H., et al. (2023). Tuning interaction strength between CeO2 and iridium to promote CO oxidation over Ir/TiO2. *J. Rare Earths*, 1002–0721. doi:10.1016/j.jre.2023.05.006

Lu, Y., Kuo, C.-Te, Kovarik, L., Hoffman, A. S., Boubnov, A., Driscoll, D. M., et al. (2019a). A versatile approach for quantification of surface site fractions using reaction kinetics: the case of CO oxidation on supported Ir single atoms and nanoparticles. *J. Catal.* 378, 121–130. doi:10.1016/j.jcat.2019.08.023

Lu, Y., Wang, J., Yu, L., Kovarik, L., Zhang, X., Hoffman, A. S., et al. (2019b). Identification of the active complex for CO oxidation over single-atom Ir-on-MgAl$_2$O$_4$ catalysts. *Nat. Catal.* 2, 149–156. doi:10.1038/s41929-018-0192-4

Milone, C., Trapani, M., Zanella, R., Piperopolulos, E., and Galvagno, S. (2010). Deposition-precipitation with urea to prepare Au/Mg(OH)2 catalysts: influence of the preparation conditions on metal size and load. *Mater. Res. Bull.* 45 (12), 1925–1933. doi:10.1016/j.materresbull.2010.08.014

Mitchell, M. B. (1993). *Fundamentals and applications of diffuse reflectance infrared fourier transform (DRIFT) spectroscopy*. Washington, D.C. USA: ACS Publications, 351–375. doi:10.1021/ba-1993-0236.ch013

Monteseguro, V., Sans, J. A., Cuartero, V., Cova, F., Abrikosov, I. A., Olovsson, W., et al. (2020). Single-atom catalysts across the periodic table. *Chem. Rev.* 120, 11703–11809. doi:10.1021/acs.chemrev.0c00576

Norman, D. (1986). X-ray absorption spectroscopy (EXAFS and XANES) at surfaces. *J. Phys. C Solid State Phys.* 19 (18), 3273–3311. doi:10.1088/0022-3719/19/18/006

Oswald, S. (2013). “X-ray photoelectron spectroscopy in analysis of surfaces update based on the original article by steffen oswald, encyclopedia of analytical chemistry,” in *Encyclopedia of analytical chemistry*. Editors R. A. Meyers and R. A. Meyers (Hoboken, New Jersey, United States: John Wiley & Sons, Ltd). doi:10.1002/9780470027318.a2517.pub2

Palcheva, R., Dimitrov, L., Tyuliev, G., Spojakina, A., and Jiratova, K. (2013). TiO2 nanotubes supported NiW hydrodesulphurization catalysts: characterization and activity. *Appl. Surf. Sci.* 265, 309–316. doi:10.1016/j.apsusc.2012.11.001

Pascarelli, S., Garbarino, G., Jönsson, H. J. M., Irifune, T., Errandonea, D., Olovsson, W., et al. (2019). Phase stability and electronic structure of iridium metal at the megabar range. *Sci. Rep.* 9 (1), 8940. doi:10.1038/s41598-019-45401-x

Pawluk, T., Hirata, Y., and Wang, L. (2005). Studies of iridium nanoparticles using density functional theory calculations. *J. Phys. Chem. B* 109 (44), 20817–20823. doi:10.1021/jp053563b

Pennycook, S. J., and Nellist, P. D. (2011). *Scanning transmission electron microscopy: Imaging and analysis*. Berlin, Germany: Springer Science & Business Media.

Pham, H. Q., Pham, H. T. Q., Huynh, Q., and Huynh, T. T. (2023). Single-atom iridium-based catalysts: synthesis strategies and electro(photo)-catalytic applications for renewable energy conversion and storage. *Coord. Chem. Rev.* 486, 215143. doi:10.1016/j.ccr.2023.215143

Plascencia-Villa, G., Mendoza-Cruz, R., Bazán-Díaz, L., and José-Yacamán, M. (2020). Gold nanoclusters, gold nanoparticles, and analytical techniques for their characterization. *Nanoparticles Biol. Med. Methods Protoc.* 2118, 351–382. doi:10.1007/978-1-0716-0319-2_26

Plascencia-Villa, G., and Mendoza-Cruz, R. (2022). “Gold nanoparticles for biocatalysis,” in *Nanomaterials for biocatalysis* (Amsterdam, Netherlands: Elsevier), 377–434.

Qiao, B., Wang, A., Yang, X., Allard, L. F., Jiang, Z., Cui, Y., et al. (2011). Single-atom catalysis of CO oxidation using Pt1/FeOx. *Nat. Chem.* 3, 634–641. doi:10.1038/nchem.1095

Qin, H., Tan, X., Huang, W., Jiang, J., and Jiang, H. (2015). Application of urea precipitation method in preparation of advanced ceramic powders. *Ceram. Int.* 41 (9), 11598–11604. doi:10.1016/j.ceramint.2015.06.032

Ramaker, D. E., and Koningsberger, D. C. (2010). The atomic AXAFS and Δμ XANES techniques as applied to heterogeneous catalysis and electrocatalysis. *Phys. Chem. Chem. Phys.* 12 (21), 5514. doi:10.1039/b927120c

Ramos-Delgado, N. A., Gracia-Pinilla, M. Á., Mangalaraja, R. V., O’Shea, K., and Dionysiou, D. D. (2016). Industrial synthesis and characterization of nanophotocatalysts materials: titania. *Nanotechnol. Rev.* 5 (5), 467–479. doi:10.1515/ntrev-2016-0007

Remediakis, I. N., Lopez, N., and Nørskov, J. K. (2005). CO oxidation on rutile-supported Au nanoparticles. *Angew. Chem. Int. Ed.* 44, 1824–1826. doi:10.1002/anie.200461699

Rojas, H. A., Martínez, J. J., Díaz, G., and Gómez-Cortés, A. (2015). The effect of metal composition on the performance of Ir–Au/TiO2 catalysts for citral hydrogenation. *Appl. Catal. A General* 503, 196–202. doi:10.1016/j.apcata.2015.07.023

Samantaray, M. K., D’Elia, V., Pump, E., Falivene, L., Harb, M., Ould Chikh, S., et al. (2020). The comparison between single atom catalysis and surface organometallic catalysis. *Chem. Rev.* 120 (2), 734–813. doi:10.1021/acs.chemrev.9b00238

Sayers, D. E., Lytle, F. W., and Stern, E. A. (1970). *Advances in X-ray analysis*. New York, NY, USA: Plenum.

Sayers, D. E., Stern, E. A., and Lytle, F. W. (1971). New technique for investigating noncrystalline structures: fourier analysis of the extended X-ray—absorption fine structure. *Phys. Rev. Lett.* 27 (18), 1204–1207. doi:10.1103/physrevlett.27.1204

Scirè, S., Fiorenza, R., Bellardita, M., and Palmisano, L. (2021). “Catalytic applications of TiO2,” in *Titanium dioxide (TiO) and its applications* (Amsterdam, Netherlands: Elsevier), 637–679. doi:10.1016/B978-0-12-819960-2.00006-7

Shan, J., Ye, C., Jiang, Y., Jaroniec, M., Zheng, Y., and Qiao, S. Z. (2022). Metal-metal interactions in correlated single-atom catalysts. *Sci. Adv.* 8 (17), eabo0762. doi:10.1126/sciadv.abo0762

Shan, J., Ye, C., Chen, S., Sun, T., Jiao, Y., Liu, L., et al. (2021). Short-range ordered iridium single atoms integrated into cobalt oxide spinel structure for highly efficient electrocatalytic water oxidation. *J. Am. Chem. Soc.* 143 (13), 5201–5211. doi:10.1021/jacs.1c01525

Shao, X., Yang, X., Xu, J., Liu, S., Miao, S., Liu, X., et al. (2019a). Iridium single-atom catalyst performing a quasi-homogeneous hydrogenation transformation of CO2 to formate. *Chem* 5, 693–705. doi:10.1016/j.chempr.2018.12.014

Shao, X., Yang, X., Xu, J., Liu, S., Miao, S., Liu, X., et al. (2019b). Iridium single-atom catalyst performing a quasi-homogeneous hydrogenation transformation of CO2 to formate. *Chem* 5, 693–705. doi:10.1016/j.chempr.2018.12.014

Suhadolnik, L., Bele, M., Čekada, M., Jovanovič, P., Maselj, N., Lončar, A., et al. (2023). Nanotubular TiO$_x$N$_y$-supported Ir single atoms and clusters as thin-film electrocatalysts for oxygen evolution in acid media. *Chem. Mater.* 35 (6), 2612–2623. doi:10.1021/acs.chemmater.3c00125

Sun, L., Liang, X., Liu, H., Cao, H., Liu, X., Jin, Y., et al. (2023). Activation of Co-O bond in (110) facet exposed Co3O4 by Cu doping for the boost of propane catalytic oxidation. *J. Hazard. Mater.* 452, 131319. doi:10.1016/j.jhazmat.2023.131319

Tauster, S. J., Fung, S. C., Baker, R. T. K., and Horsley, J. A. (1981). Strong interactions in supported-metal catalysts. *Science* 211 (4487), 1121–1125. doi:10.1126/science.211.4487.1121

Turner, M., Golovko, V., Vaughan, O., Abdulkin, P., Berenguer-Murcia, A., Tikhov, M., et al. (2008). Selective oxidation with dioxygen by gold nanoparticle catalysts derived from 55-atom clusters. *Nature* 454, 981–983. doi:10.1038/nature07194

Uzun, A., Ortalan, V., Browing, N. D., and Gates, B. C. (2010). A site-isolated mononuclear iridium complex catalyst supported on MgO: characterization by spectroscopy and aberration-corrected scanning transmission electron microscopy. *J. Catal.* 269 (2), 318–328. doi:10.1016/j.jcat.2009.11.017

Vaithianathan, V., Lee, B.-T., Chang, C.-H., Asokan, K., and Kim, S. S. (2006). Characterization of As-doped, p-type ZnO by x-ray absorption near-edge structure spectroscopy. *Appl. Phys. Lett.* 88 (11), 112103. doi:10.1063/1.2186383

Van Dillen, A. J., Terörde, R. J. A. M., Lensveld, D. J., Geus, J. W., and de Jong, K. P. (2003). Synthesis of supported catalysts by impregnation and drying using aqueous chelated metal complexes. *J. Catal.* 216 (1–2), 257–264. doi:10.1016/S0021-9517(02)00130-6

Wang, Q., Huang, X., Zhao, Z. L., Wang, M., Xiang, B., Li, J., et al. (2020). Ultrahigh-loading of Ir single atoms on NiO matrix to dramatically enhance oxygen evolution reaction. *J. Am. Chem. Soc.* 142, 7425–7433. doi:10.1021/jacs.9b12642

Wang, Y., Xu, W., Chen, X., Li, C., Xie, J., Yang, Y., et al. (2022). Single–atom Ir1 supported on rutile TiO2 for excellent selective catalytic oxidation of ammonia. *J. Hazard. Mater.* 432 (128670), 128670. doi:10.1016/j.jhazmat.2022.128670

Xia, C., Qiu, Y., Xia, Y., Zhu, P., King, G., Zhang, X., et al. (2021). General synthesis of single-atom catalysts with high metal loading using graphene quantum dots. *Nat. Chem.* 13, 887–894. doi:10.1038/s41557-021-00734-x

Xiao, M., Zhu, J., Li, G., Li, N., Li, S., Cano, Z. P., et al. (2019). A single-atom iridium heterogeneous catalyst in oxygen reduction reaction. *Angew. Chem. Int. Ed.* 58, 9640–9645. doi:10.1002/anie.201905241

Xiong, Y., Sun, W., Xin, P., Chen, W., Zheng, X., Yan, W., et al. (2020). Gram-scale synthesis of high-loading single-atomic-site fe catalysts for effective epoxidation of styrene. *Adv. Mater.* 32, 2000896. doi:10.1002/adma.202000896

Yang, H., Wang, X., Liu, Q., Huang, A., Zhang, X., Yi, Yu, et al. (2023). Heterogeneous iridium single-atom molecular-like catalysis for epoxidation of ethylene. *J. Am. Chem. Soc.* 145 (12), 6658–6670. doi:10.1021/jacs.2c11380

Yang, M.-Q., Zhou, K.-L., Wang, C., Zhang, M.-C., Wang, C.-H., Ke, X., et al. (2022). Iridium single-atom catalyst coupled with lattice oxygen activated CoNiO2 for accelerating the oxygen evolution reaction. *J. Mater. Chem. A* 10 (48), 25692–25700. doi:10.1039/D2TA07292K

Yang, X.-F., Wang, A., Qiao, B., Li, J., Liu, J., and Zhang, T. (2013). Single-atom catalysts: A new frontier in heterogeneous catalysis. *Accounts Chem. Res.* 46 (8), 1740–1748. doi:10.1021/ar300361m

Yin, J., Jin, J., Lu, M., Huang, B., Zhang, H., Peng, Y., et al. (2020). Iridium single atoms coupling with oxygen vacancies boosts oxygen evolution reaction in acid media. *J. Am. Chem. Soc.* 142 (43), 18378–18386. doi:10.1021/jacs.0c05050

Zanella, R., Delannoy, L., and Louis, C. (2005). Mechanism of deposition of gold precursors onto TiO2 during the preparation by cation adsorption and deposition-precipitation with NaOH and urea. *Appl. Catal. A General* 291 (1–2), 62–72. doi:10.1016/j.apcata.2005.02.045

Zhang, M., Sui, X., Zhang, X., Niu, M., Li, C., Wan, H., et al. (2022). Multi-defects engineering of NiCo2O4 for catalytic propane oxidation. *Appl. Surf. Sci.* 600, 154040. doi:10.1016/j.apsusc.2022.154040

Zhang, N., Wang, W., Zhou, T., Tian, Y., and Chu, W. (2021). Exploring structure-function relationship of two-dimensional electrocatalysts with synchrotron radiation X-ray absorption spectrum. *Curr. Chin. Sci.* 1 (1), 22–42. doi:10.2174/2210298101999201008142619

Zhao, J., Ji, S., Guo, C., Li, H., Dong, J., Guo, P., et al. (2021). A heterogeneous iridium single-atom-site catalyst for highly regioselective carbenoid O–H bond insertion. *Nat. Catal.* 4, 523–531. doi:10.1038/s41929-021-00637-7

Zhou, X., Hwang, I., Tomanec, O., Fehn, D., Mazare, A., Zboril, R., et al. (2021). Advanced photocatalysts: pinning single atom co-catalysts on titania nanotubes. *Adv. Funct. Mater.* 31 (30), 2102843. doi:10.1002/adfm.202102843

Zhu, Y., Wang, J., Koketsu, T., Kroschel, M., Chen, J. M., Hsu, S. Y., et al. (2022b). Iridium single atoms incorporated in Co3O4 efficiently catalyze the oxygen evolution in acidic conditions. *Nat. Commun.* 13, 7754. doi:10.1038/s41467-022-35426-8

Zhu, Y., Wang, J., Koketsu, T., Kroschel, M., Chen, J. M., Hsu, S. Y., et al. (2022a). Iridium single atoms incorporated in Co3O4 efficiently catalyze the oxygen evolution in acidic conditions. *Nat. Commun.* 13 (1), 7754. doi:10.1038/s41467-022-35426-8

Zonghua, pu, Ibrahim, A., Cheng, R., Wang, P., Zhang, C., Mu, S., et al. (2020). Single-atom catalysts for electrochemical hydrogen evolution reaction: recent advances and future perspectives. *Nano-Micro Lett.* 12, 21. doi:10.1007/s40820-019-0349-y

Frontiers in Nanotechnology

TYPE Review
PUBLISHED 16 November 2023
DOI 10.3389/fnano.2023.1291338

OPEN ACCESS

EDITED BY
Wee-Jun Ong,
Xiamen University, Malaysia

REVIEWED BY
Dexian Ye,
Virginia Commonwealth University,
United States
Rajan Saini,
Akal University, India
Fengxian Ma,
Hebei Normal University, China

*CORRESPONDENCE
Addis S. Fuhr,
fuhras@ornl.gov

RECEIVED 09 September 2023
ACCEPTED 06 November 2023
PUBLISHED 16 November 2023

CITATION
Fuhr AS, Sumpter BG and Ganesh P (2023), Defects go green: using defects in nanomaterials for renewable energy and environmental sustainability.
Front. Nanotechnol. 5:1291338.
doi: 10.3389/fnano.2023.1291338

Defects go green: using defects in nanomaterials for renewable energy and environmental sustainability

Addis S. Fuhr*, Bobby G. Sumpter and Panchapakesan Ganesh

Center for Nanophase Materials Sciences, Oak Ridge National Laboratory, Oak Ridge, TN, United States

Induction of point defects in nanomaterials can bestow upon them entirely new physics or augment their pre-existing physical properties, thereby expanding their potential use in green energy technology. Predicting structure-property relationships for defects *a priori* is challenging, and developing methods for precise control of defect type, density, or structural distribution during synthesis is an even more formidable task. Hence, tuning the defect structure to tailor nanomaterials for enhanced device performance remains an underutilized tool in materials design. We review here the state of nanomaterial design through the lens of computational prediction of defect properties for green energy technology, and synthesis methods to control defect formation for optimal performance. We illustrate the efficacy of defect-focused approaches for refining nanomaterial physics by describing several specific applications where these techniques hold potential. Most notably, we focus on quantum dots for reabsorption-free solar windows and net-zero emission buildings, oxide cathodes for high energy density lithium-ion batteries and electric vehicles, and transition metal dichalcogenides for electrocatalytic green hydrogen production and carbon-free fuels.

KEYWORDS

point defects, nanomaterial synthesis, solar energy, batteries, catalysis, green hydrogen, density functional theory

1 Introduction

The industrial revolution—largely propelled by burning hydrocarbon-containing materials to provide electricity, heating, and power engines (e.g., in motor vehicles)—facilitated over 200 years of sustained human development (Chu and Majumdar, 2012). However, an unfortunate byproduct of burning fossil fuels are large-scale greenhouse gas emissions, which contribute to climate change and ecological deterioration (Chu and Majumdar, 2012; Alstone et al., 2015; Clark et al., 2016; Hallegatte et al., 2016; Schleussner et al., 2016). To ameliorate environmental damage associated with climate change, public policy endeavors must focus on curbing greenhouse gas emissions, while also supporting sustained global development through the expansion of access to inexpensive and reliable energy. Technological innovation will therefore play a pivotal role in achieving a sustainable future. Nanomaterials in particular are poised to contribute to the development of renewable energy production and storage (Chen et al., 2012).

Point defects are single or multiple atom disruptions in the long-range periodicity of crystallographic materials. These atomic impurities often form in nanomaterials,

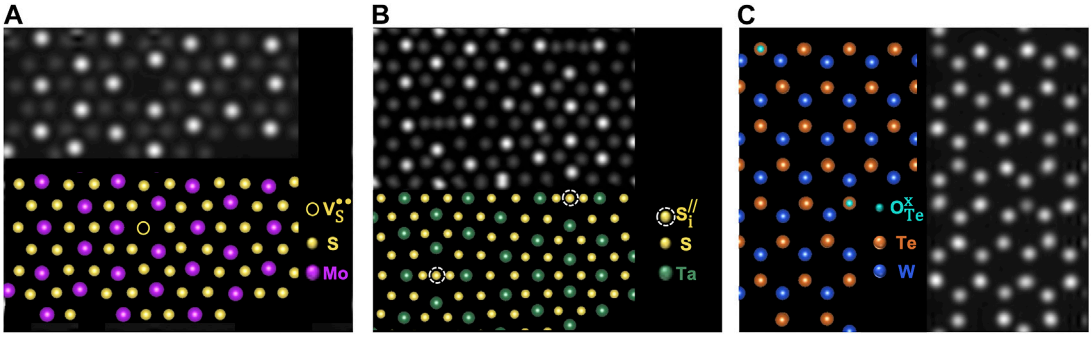

FIGURE 1
(A–C) DFT generated STEM digital twins for defects in monolayer TMDs. Reproduced with permission from Fuhr et al. (2023).

dramatically alter their physical properties (e.g., induce magnetism or metal-insulator transitions) (Lopez-Bezanilla et al., 2015a; Lopez-Bezanilla et al., 2015b; Ganesh et al., 2020; Bennett et al., 2022), and offer a potentially rewarding route for tuning their functionality for enhanced device performance in a broad array of applications. However, predicting the relationship between crystal growth conditions, defect formation, and their corresponding physics is challenging, and has served as a bottleneck to the commercialization of many ubiquitous technologies such as $In_xGa_{1-x}N$ heterostructure blue light-emitting diodes (LEDs) (Nakamura, 1998). Hence, defect engineering represents an encouraging, but underexplored paradigm to tailor nanostructures for a diverse array of green technology such as solar energy (Giustino and Snaith, 2016) or batteries (Zhao et al., 2020).

Defect engineering efforts will require innovations that link theoretical predictions of defect properties with experimental methods for controlling defect formation in nanomaterials. First principles calculation methods such as density functional theory (DFT) have become a powerful tool in predicting defect physical properties, and guiding experimental efforts to detect and control defect formation during synthesis or post-processing (Freysoldt et al., 2014; Dreyer et al., 2018). Recent advances in scanning transmission electron microscopy (STEM) enable direct measurement and quantification of defects in nanomaterials (Ziatdinov et al., 2017; Madsen et al., 2018; Zhao et al., 2018; Maksov et al., 2019; Ziatdinov et al., 2019; Lee et al., 2020; Guo et al., 2021; Trentino et al., 2021; Yang et al., 2021; Lee et al., 2022; Wu et al., 2022). These *ab initio* and experimental approaches can be combined with other supplemental experimental techniques such as spectroscopy and scanning tunneling microscopy (STM) to directly resolve nanomaterial defect physics (Ziatdinov et al., 2019). In this context, we review computational and experimental approaches for elucidating defect synthesis-structure-property relationships with the specific aim of unleashing the full potential of defects for green technology. Additionally, we delve into several examples of green technologies where defect engineering has shown promise. These systems of interest include optical defects in quantum dots for Stokes-shift engineered luminescent solar concentrators and net zero-energy buildings, cation-disordered oxides for lithium-ion battery cathodes with improved energy storage capabilities, and defects in transition metal dichalcogenide electrocatalysts for green hydrogen production.

2 Defect formation in nanomaterials: theory and chemistry

2.1 Types of defects

Crystallographic materials exhibit periodicity wherein atoms are arranged in a consistent repeating pattern. The term point defect is generally used to indicate a single or few atom "break" in periodicity such as a missing or misplaced native lattice atom (intrinsic defect), or a foreign atom not normally present in the lattice (extrinsic defect, Figure 1) (Tuller and Bishop, 2011; Freysoldt et al., 2014; Dreyer et al., 2018; Fuhr et al., 2023). Intrinsic defects are generally classified as either vacancies (missing anion or cation), anti-site defects (atomic species in the lattice swap positions such as a cation occupying a lattice site expected to be an anion), or interstitials (cation or anion occupies an interstitial space in the lattice). Extrinsic defects can occupy substitutional or interstitial lattice sites as dopants, or form as adatoms on the surface. The specific lattice site and charge of point defects are commonly described using Kroger-Vink notation (Kröger et al., 1956). Defect atomic identity is indicated by the first letter, and for most defect types (intrinsic or extrinsic), the subscript designates the lattice site where the defect occurs. The exceptions to this rule are vacancies and interstitials for which "V" is used to indicate a vacancy and the subscript "i" is used to indicate interstitial. The superscript indicates the electronic charge at the defect lattice point: "x" signifies no charge, "/" denotes a negative charge, and "•" represents a positive charge. For example, a sulfur anion vacancy with a +2 charge in MoS_2 would be denoted as $V_S^{\bullet\bullet}$ (a sulfur atom is missing from a sulfur lattice site leaving a +2 charge, Figure 1A), a sulfur interstitial in MoS_2 with a −2 charge would be indicated as $S_i^{//}$ (Figure 1B) and a O^{2-} dopant on a Te^{2-} site in WTe_2 (net charge of 0) as O_{Te}^x (Figure 1C) (Kröger et al., 1956).

Kroger-Vink theory—in its original conception—describes defect formation under thermodynamic equilibrium by charge-compensated formal reaction pathways. If we consider a simple binary ionic material (MA where M is a 2+ metal cation and A is a chalcogen or oxygen 2− anion), these reaction pathways could include Schottky defects ($V_A^{\bullet\bullet} + V_M^{//}$), Frenkel pairs ($V_A^{\bullet\bullet} + M_i^{//}$, or $V_M^{\bullet\bullet} + M_i^{//}$), antisite defect pairs ($M_A^{\bullet\bullet\bullet\bullet} + A_M^{////}$), or non-stoichiometric defects wherein a charged defect is compensated by the oxidation or reduction of another atom (e.g., $V_A^{\bullet\bullet} + 2M_M^{/}$). Regions of lattice disorder, (Cen et al., 2023), distortion (Ding et al., 2018), or non-stoichiometry (Fuhr et al., 2020a) are not always well described by Kroger-Vink reaction pathways, but the notation is still commonly used. Using the notation we described earlier for ionic material MA, metal or anion deficient synthesis conditions could yield $M_{1-x}A$ or MA_{1-x} structures with ordered metal vacancies. For this illustrative example the material would not have defects in the traditional sense. Yet, the Kroger-Vink metal vacancy notation is still often used (e.g., as observed with iron sulfides, ceria, or strontium titanate) (Zhuang et al., 2014; Li et al., 2017a; Luo et al., 2021).

2.2 Predicting defect stability

Despite its clarity, consistent bookkeeping of all charge-compensating Kroger-Vink reactions is unrealistic for nanomaterials at-scale (Freysoldt et al., 2014). This problem is even further exacerbated in off-equilibrium processes such as ion implantation. However, the creation of defects alters local chemical bonding (e.g., breaking bonds to form vacancies) in nanomaterials and generally invokes an enthalpic energy penalty. Density functional theory (DFT) or similar electronic structure approaches can therefore be used to calculate formation enthalpies and predict the type and relative concentrations of defects (Freysoldt et al., 2014; Dreyer et al., 2018). This approach assumes a grand canonical material system wherein individual defects interact with an electron reservoir (described by the Fermi level), and their energy can be calculated as a function of the energy of the electron reservoir and relative concentration of each atomic species. The DFT route can shed light onto the likelihood of various defects to form under thermal equilibrium conditions, their relative concentration, local geometry, and corresponding structure-property relationships.

The usual approach for calculating defect formation energy via DFT or related methods is to separately optimize the geometry of a pristine supercell or surface, and compare its energy to the same structure with defect “X” at charge state “q” using Eq. 1:

$$E_f[X^q] = E_{tot}[X^q] - E_{tot}[\text{pristine}] - \sum_i n_i \mu_i + qE_F + E_{corr} \quad (1)$$

where $E_{tot}[X^q]$ is the total energy of a supercell or surface with the specified defect in charge state q, $E_{tot}[\text{pristine}]$ is the total energy of the defect-free supercell or surface, μ_i represents the chemical potential for atomic species i either added (positive n_i where n notes the number of atoms added by exchange *from* a chemical reservoir) or subtracted (negative n_i where n notes the number of atoms removed by exchange *to* a chemical reservoir). The Fermi-level (E_F) describes the energy of the electron reservoir that exchanges electrons with the lattice resulting in a positive or negative charge (q) for electrons removed or gained by the material, respectively. E_F is conventionally described in relation to the valence-band (VB) where $E_F = 0$ reflects a Fermi-level exactly at the valence band maximum, and the upper bound for E_F is the conduction band (CB) of the material. A correction term E_{corr} is often added to account for the finite-size of the supercells and k-point meshes on elastic or electrostatic interactions and are described in greater detail elsewhere (Makov and Payne, 1995; Lany and Zunger, 2008; Freysoldt et al., 2009; Komsa et al., 2012; Freysoldt et al., 2014; Dreyer et al., 2018).

The low concentration of defects in materials requires that DFT approaches use large supercells (e.g., 50–200 atoms). Computational expense for DFT based approaches scale with size and the number of electrons in the material, which makes predicting defect stability and structure-property relationships challenging. For example, it is well-known that pure DFT functionals such as the Perdew Burke Ernzerhof (PBE) do not accurately predict semiconductor band gaps (Le Bahers et al., 2014). One route to improve the accuracy of DFT is to include some degree of Hartree Fock direct exchange using a hybrid functional (e.g., HSE06), but this comes at significantly greater computational expense. Hence, predicting optical transitions for defects is much more complicated than for defect-free materials due to the simultaneous requirement of computationally expensive functionals and large supercells. In addition, DFT treatment of surfaces (with or without defects) is often required to predict structure-property relationships at the nanoscale, and similarly scales poorly with hybrid functional or other beyond pure DFT methods. While we do not focus here on specific electronic structure approaches for dealing with large supercells, these are important considerations for predicting defect formation and corresponding physics and are reviewed elsewhere (Makkar and Ghosh, 2021; Broberg et al., 2023).

DFT-calculated formation enthalpy is typically determined at 0 K, and the usually positive value is often interpreted to indicate that entropy and temperature are needed to overcome the enthalpic energy barrier—resulting in a negative Gibbs free energy and enabling defects to spontaneously form. Among the various types of entropy, configurational and vibrational are the most frequently discussed. In the context of understanding defects, configurational entropy pertains to atomic rearrangements resulting from local disruptions of periodicity, while vibrational entropy encompasses modified phonon interactions and changes in chemical bonding. Configurational entropy can be calculated by combining cluster expansion approaches with Monte Carlo, while packages such as Phonopy can be used to determine vibrational entropy using either the Hessian matrix from density functional perturbation theory (DFPT) calculations or the finite displacement method (Freysoldt et al., 2014; Sutton and Levchenko, 2020; Kaczkowski et al., 2021). These additional contributions are typically ignored in most studies due to the high computational cost of performing both enthalpic and entropic calculations. DFT-calculated formation enthalpy is generally considered sufficient to predict structure-property relationships and general trends in the type and relative concentration of defects that will form in nanomaterials under different oxidizing/reductive environments and relative precursor concentration (e.g., metal deficient synthesis vs. chalcogen deficient synthesis). However, interest in high-throughput DFT and beyond 0 K approaches is growing, and are essential to predict more precise relationships between synthesis conditions and defect creation (Balachandran et al., 2017; Choudhary et al., 2023; Mosquera-Lois et al., 2023).

2.3 Synthesis and control of defect formation

The theoretical principles underpinning defect formation predictions have several general implications for nanomaterial synthesis. The type and concentration of defects that form in

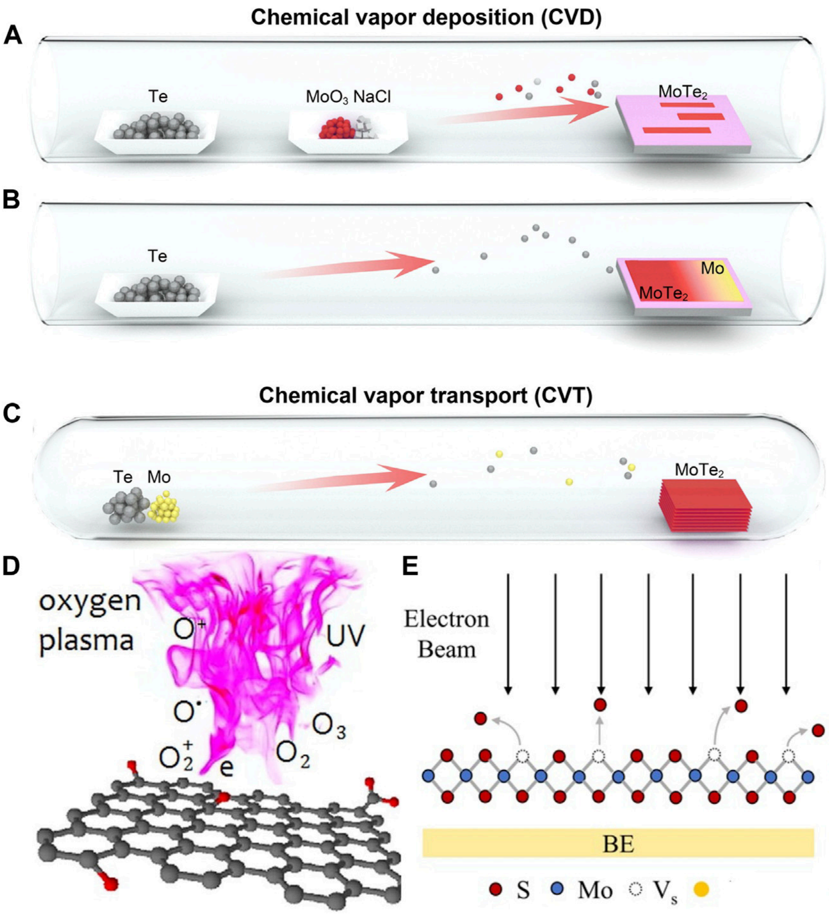

FIGURE 2
Schematic depiction of CVD vs. CVT process for creating defects in TMDs **(A–C)**, light and plasma induced defects in graphene oxide **(D)**, and electron beam induced defects on TMDs **(E)**. Figures reproduced with permission from Deng et al. (2021) for **(A–C)**, Kondratowicz et al. (2018) for **(D)**, and Wu et al. (2022) for **(E)**.

nanomaterials is strongly influenced by the relative concentration of each atomic species during synthesis or post-processing, as well as whether the experiments are conducted in a more reductive (high E_F) or oxidative (low E_F) environment (Liu et al., 2014a; Du et al., 2021). The set of defects with the lowest formation energies under the specific experimental conditions will prevail. For instance, ignoring kinetic considerations, cation-poor and oxidative growth conditions could favor the creation of negatively charged metal vacancies. Furthermore, the repercussions of local geometric and electrostatic distortions vary by chemical bonding motif. Although the first principles assessment of chemical bonding in the material is not flawless, it remains instructive. For example, closed packed structures less frequently exhibit Frenkel defects due to the additional energy required to squeeze an interstitial ion into the lattice (geometric penalty). On the other hand, materials with metallic or covalent bonds tend to form antisite defects or partial cation disorder due to the lower electrostatic penalty compared to ionically bonded materials (YOO and TULLER, 1987; Tuller and Bishop, 2010; Tuller and Bishop, 2011; Hu et al., 2017).

As discussed earlier, the formation enthalpy of defects is generally positive (unfavorable). Entropic stabilization or external energy is therefore required to overcome the enthalpic penalty to create defects in most materials. These observations are suggestive that growth/post-processing temperature—or the inclusion of external energy sources such as plasmas or light—can be used to control defect formation. Hence, most defect engineering strategies revolve around managing the relative concentrations of each species, establishing an oxidative or reductive environment, and/or controlling external energy factors such as temperature during nanomaterial synthesis or post-processing. For extrinsic defects such as dopants, solubility (maximum concentration attainable by a dopant) and diffusivity (rate at which atomic species spreads across the material at a finite temperature) also need to be taken in consideration (Freysoldt et al., 2014).

The predominant method for managing defect distribution *in-situ* during nanomaterial synthesis typically entails regulating temperature and atomic species concentration. The synthesis of V_O-rich SnO_{2-x} nanosheets, achieved through a hot-injection reaction between SnSe nanosheets and organic residue, serves as an illustrative method for creating anion vacancies via temperature control (Zhong et al., 2019). Multinary nanomaterials—such as $Cu_xIn_{2-x}Se_yS_{2-y}$ (CISeS) nanocrystals—frequently have their defect distribution tuned by adjusting precursor ratios. In this case, Cu-deficient nanocrystals tend to form V_{Cu}' whereas Cu_{In}'' are more commonly observed in near-stoichiometric or Cu-rich nanocrystals (Ueng and Hwang, 1989; Ueng and Hwang, 1990; Kim et al., 2012; Jara et al., 2016; Fuhr et al., 2017; Yun et al., 2018; Houck et al., 2019; Fuhr et al., 2020a; Fuhr et al., 2020b; Du et al., 2020; Frick et al., 2020; Liang et al., 2023). Adjusting synthesis temperature and precursor ratios has been shown to enhance the density of vacancies during chemical vapor deposition (CVD) or chemical vapor transport (CVT) synthesis of transition metal dichalcogenides (TMDs, Figure 2) (Enyashin et al., 2013; Lin et al., 2016; Li et al., 2017b; Liang et al., 2021). CVD synthesis occurs at a lower temperature than CVT, and uses more volatile precursors and shorter growth times (Shi et al., 2015). The density of sulfur vacancies can be controlled by the sulfur rate (rate at which sulfur-containing compounds are introduced to the reaction environment) (Gutiérrez et al., 2013; Peimyoo et al., 2013; van der Zande et al., 2013). Both CVD and CVT have also been used to dope nanostructures (Chen et al., 2013; Dumcenco et al., 2013; Zhang et al., 2014a; Feng et al., 2014; Suh et al., 2014; Tongay et al., 2014; Li et al., 2015; Gao et al., 2016; Lin et al., 2016; Deng et al., 2021; Liang et al., 2021). However, the high temperature and long growth times generally leads to greater control of the spatial distribution and density of defects with CVT, which has been demonstrated with $Mo_xW_{1-x}S_y$, $Mo_xW_{1-x}S_ySe_{2-y}$, and MoS_xSe_{2-x} monolayers. Enhanced control of dopant distribution has also been observed in colloidal quantum dots by using hot-injection and diffusion methods to dope Mn in CdSe, ZnSe, and PbSe quantum dots (Mikulec et al., 2000; Norris et al., 2001; Ji et al., 2003; Jian et al., 2003; Vlaskin et al., 2013; Rice et al., 2016; Singh et al., 2019). The high energy of interstitial defects typically precludes their formation in QDs, and dopants are usually assumed to be substitutional unlike nanostructured oxides where both substitutional and interstitial defects are well-known to form (Norris et al., 2001; Robertson et al., 2011; Zhang et al., 2014b).

Despite the major advances, controlling the density and distribution of defects in nanomaterials *in-situ* remains difficult and post-processing methods are often required. Post-synthesis annealing and altering the cooling rate after calcination have been used to create antisite defects and cation site disorder in $LiNi_xMn_{2-x}O_4$ and $LiNi_{0.45}Mn_{1.45}Cr_{0.1}O_4$ phases (Liu et al., 2012; Zheng et al., 2012; Liu et al., 2014b). High-temperature annealing of oxide films in an oxygen deficient environment has been well established to induce oxygen loss and create V_O even in inert environments (Kell et al., 2022). This effect can be further enhanced by inclusion of a reductant such as hydrogen (Merdrignac et al., 1992; Jeong et al., 2003; Chen et al., 2011; Shi et al., 2014; Bonu et al., 2015; Chen et al., 2015; Xiong et al., 2018; Kim et al., 2020; Xiong et al., 2022). Thermal annealing in a pre-determined atmosphere has been extended to non-oxide systems to control the distribution of other anion vacancies such as V_N in C_3N_4 (Niu et al., 2014), or chalcogenide vacancies in $MoTe_2$, VSe_2, or $PdSe_2$ (Zhu et al., 2017; Chen et al., 2019; Chua et al., 2020; Zhang et al., 2020). Similar to *in-situ* methods, control of the heating rate and duration is central to controlling defect density and distribution. This approach can also be extended to nanomaterial doping as exemplified by $PdSe_2$ wherein the use of an oxidative ozone environment was used to generate oxygen dopants (Liang et al., 2020a). High temperature annealing is not always required to create an oxidative or reductive environment, and solution phase routes can be advantageous for large-scale manufacturing due to their lower energy input requirements, decreased use of harmful chemicals, and overall improved safety. $NaBH_4$ is a frequently employed solution-phase reducing agent capable of extracting lattice oxygen atoms in materials (e.g., $K_4Nb_6O_{17}$ ultrathin nanosheets or TiO_2 nanoparticles) to create V_O (Bi et al., 2014; Fang et al., 2014; Mao et al., 2014). Chemical reduction with $NaBH_4$ can create V_O in ZnO nanorods or SnO_2 nanoparticles at temperatures as low as 30°C–190°C, which is far lower than that required for vacuum annealing (500°C–800°C) (Ansari et al., 2013; Lv et al., 2013; Bonu et al., 2014; Wang et al., 2015a; Wang et al., 2018a; Sahu et al., 2019; Zeng et al., 2020; Xiong et al., 2022). Similar success in controlling the density of V_O has been demonstrated using other solution-phase reductants, including ethylene glycol or glycerol for oxygen vacancy formation in BiOCl or Bi_2WO_6 (Jiang et al., 2013; Ye et al., 2015; Chen et al., 2023).

Temperature and oxidative/reductive environments are not the only post-growth methods capable of generating ample external energy to surmount enthalpic barriers for defect generation. Bi-O bonds in BiOCl nanosheets are long and have a low bond energy, which can be broken with UV photons to create surface oxygen vacancies (Ye et al., 2011; Ye et al., 2012; Jiang et al., 2013; Wu et al., 2018). Photons can also employed to convert chalcogen vacancies to oxygen dopants, as demonstrated in the case of WSe_2 (Lu et al., 2015). Ion-beam bombardment is a common route for substitutional dopant creation—such as Sb-implantation of SnO_2 nanowires (Zhu et al., 2005; Kim et al., 2020). Perhaps counterintuitively, they can also be used to expel lattice atoms and cause atomic rearrangement on the surface without any substitutional doping, as demonstrated with the creation of $O_i^{//}$ and $Sn_i^{\bullet\bullet\bullet\bullet}$ in SnO_2 nanostructures by high-energy (45–75 MeV) bombardment of Ni^+ and He^{2+} ions, or vacancy formation in $MoSe_2$ monolayers via He^+ ion beam nanoforging (Jeong et al., 2003; Rani et al., 2008; Shi et al., 2014; Iberi et al., 2016; Kwon et al., 2016). Electron beams can create electrons with sufficient kinetic energy to cause knock-on effects. This phenomena can be understood as high-energy electrons from the electron beam transferring enough energy to dislodge atoms from the nanomaterial and create atomic defects (Lingerfelt et al., 2019; Lingerfelt et al., 2020; Lingerfelt et al., 2021). This effect has been demonstrated with nanomaterials such as graphene and TMDs (e.g., $MoTe_2$, MoS_2, WS_2, and WSE_2) (Algara-Siller et al., 2013; Komsa et al., 2013; Zan et al., 2013; Ziatdinov et al., 2017; Wang et al., 2018b; Elibol et al., 2018; Moody et al., 2018; Nguyen et al., 2018; Maksov et al., 2019; Dyck et al., 2020; Roccapriore et al., 2022). The latter case is particularly well-known due to the high mobility of chalcogen atoms and their relative ease of diffusion out of the structure due to beam-matter interactions. However, these effects are not limited to carbon or chalcogen materials and have been demonstrated in oxides as well (Egdell et al., 1987; Belloni, 2006; Komuro and Matsumoto, 2011). Plasma etching is also a powerful method to create anion vacancies in TMDs, and chalcogen vacancy creation has been demonstrated using Ar plasmas in $MoS_{2,}$ WSe_2, $PdSe_2$, and $PtSe_2$ (Wu et al., 2017; Oyedele et al., 2019; Shawkat et al., 2020; Tsai et al., 2022). Exposure to plasmas can create vacancies in these and other structures, and the defect type and concentration can be controlled by adjusting the plasma gas type (Kondratowicz et al., 2018), irradiation time, or intensity (e.g., generating

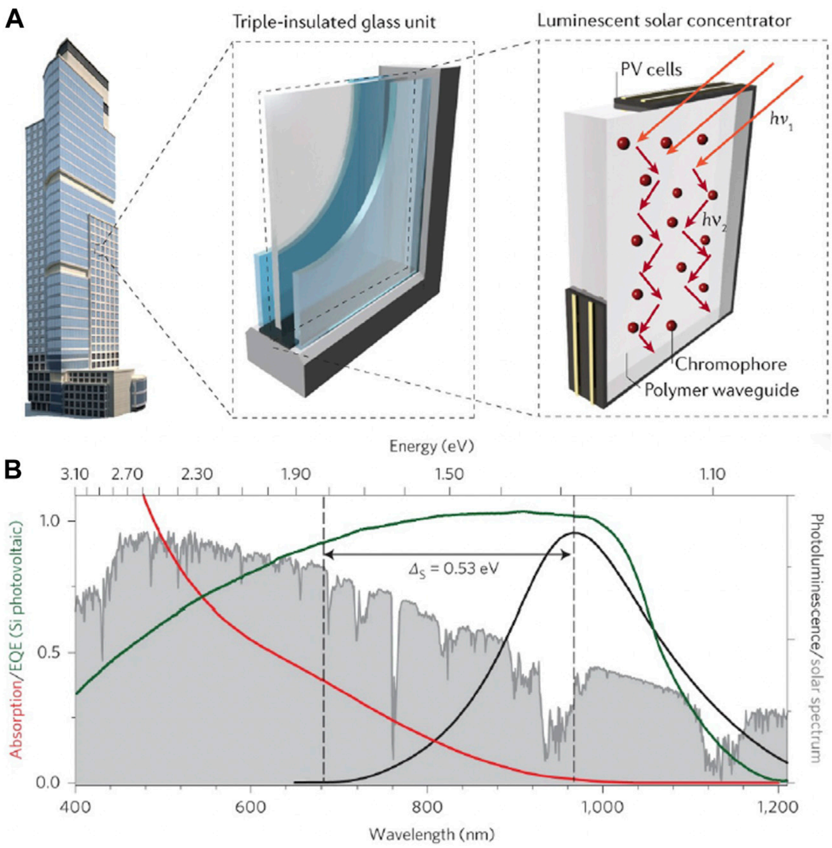

FIGURE 3
(A) Schematic depiction of LSCs, and their potential usage as building-integrated photovoltaic units. Reproduced with permission from Meinardi et al. (2017). **(B)** CISeS absorption and emission spectra (red and black lines) compared with the solar spectrum (grey shading) and Si solar cell peak EQE (green line). Reproduced with permission from Meinardi et al. (2015).

O-Mo bonds using oxygen plasma) (Islam et al., 2014; Kang et al., 2014; Nan et al., 2014).

3 Energy harvesting: luminescent solar concentrators and net-zero emission buildings

The juxtaposition of global urbanization and the need to lower greenhouse gas emissions require net zero emission buildings wherein annual power consumption is fully counterbalanced by on-site renewable generated energy. Installing conventional photovoltaic (PV) units on a large scale is challenging within dense urban layouts. Energy demands for large buildings frequently exceed those of individual housing units, and PV cells are constrained to rooftop space that is inadequate to meet energy demands (Meinardi et al., 2017). To address these issues, interest has grown in using luminescent solar concentrators (LSCs) as potential building-integrated semi-transparent PV windows (Debije and Verbunt, 2012; Meinardi et al., 2017; Papakonstantinou et al., 2021). LSCs are constructed by doping or coating a glassy or polymeric waveguide with chromophores (Figure 3A) (Debije and Verbunt, 2012; Meinardi et al., 2017). The chromophores absorb broadband solar radiation and re-emit at a specific wavelength, which is guided by internal reflection within the waveguide to the edges or window frame where it is converted into electricity by PV cells (Yablonovitch, 1980; Currie et al., 2008; Sark et al., 2008; Banal et al., 2014). The specific wavelength of re-emission varies by the chromophore material, but near-infrared emission is generally targeted because it is semi-transparent, aesthetically pleasing, and more likely to attain public acceptance (Saifullah et al., 2016).

An ideal LSC chromophore should hold three major optical properties: a large absorption cross-section for capturing sunlight, a high emission efficiency (defined by quantum yield, or $\mathbf{\Phi} = \frac{\mathbf{N}_{\text{photons emitted}}}{\mathbf{N}_{\text{photons absorbed}}}$) particularly in the near-infrared region, and a large Stokes shift (Klimov et al., 2016; Gungor et al., 2022). While this review centers on chromophore materials design, other device aspects are important to consider and are discussed elsewhere (Yablonovitch, 1980; Currie et al., 2008; Sark et al., 2008; Banal et al., 2014; Saifullah et al., 2016). Regarding the first two properties, exemplary chromophores should absorb sunlight in both the visible and near-infrared (near-IR) spectral ranges, and re-emit at near 100% quantum yield (QY) allowing for collection by the PV edges. The emitted photons would preferably fall within the near-IR range to achieve both a semi-transparent aesthetic, and also to boost device performance by matching the peak external quantum efficiency (EQE) of the PV device (Figure 3B) (Sark et al., 2008;

Meinardi et al., 2015). The chromophore should also have a large Stokes shift, or exhibit peak emission markedly red-shifted from the absorption onset energy. The large Stokes shift is crucial to mitigate reabsorption losses, which are caused by substantial spectral overlap between absorption and emission. Reabsorption losses scale with device dimensions, and chromophores with small Stokes shifts will have poor performance if manufactured at conventional window sizes (Klimov et al., 2016; Gungor et al., 2022).

Several dyes such as 4-dicyanomethyl-6-dimethylaminostiryl-4H-pyran (DCM), CRS040 Yellow, or Lumogen Red have been explored as potential chromophores for LSCs (Batchelder et al., 1979; Sark et al., 2008; Desmet et al., 2012). Though well-studied, molecular dyes struggle to combine all three LSC chromophore optical requirements in the same material: strong broadband optical absorption, high QY, and large Stokes shift with near-IR emission. Quantum dots (QDs) have been proposed as alternative chromophores because of their well-known size-tunable broadband absorption, and the ability to achieve high QY in the near-IR spectral ranges (Pietryga et al., 2016). However, most conventional QDs such as CdSe have a small Stokes shift (tens of meV), which make them unsuitable for LSCs due to prominent reabsorption losses (Pietryga et al., 2016). Several routes have been explored to induce large Stokes shifts in QDs without losing their other potential advantages as LSC chromophores. Most of these approaches involve either doping the QDs with substitutional defects, or designing multinary QD alloys (e.g., ternary or quaternary) that typically form intrinsic defects.

Binary QDs (e.g., CdSe) can be doped directly during crystal growth, or via cation exchange (Mikulec et al., 2000; Norris et al., 2001; Ji et al., 2003; Jian et al., 2003; Meulenberg et al., 2004; Stouwdam and Janssen, 2009; Corrado et al., 2010; Gul et al., 2011; Srivastava et al., 2011; Viswanatha et al., 2011; Vlaskin et al., 2013; Rice et al., 2016; Pinchetti et al., 2018; Singh et al., 2019; Najafi et al., 2021). In the first case, QDs are grown by a conventional strategy such as hot injection wherein precursors are injected into a solvent at high temperature to induce rapid nucleation and growth for size control. During the conventional synthesis route, a dopant is introduced and kinetically competes with host cations during crystal growth. A challenge with this route is that impurity atom binding is unfavorable due to physical attribute mismatching (e.g., differences in charge or ionicity). Cation exchange, on the other hand, involves first synthesizing the QD with conventional methods, and then immersing them in a cation exchange solution with potential dopants. An advantage of such an approach is that the anion sublattice is retained, and crystal composition can be altered without dramatic changes in QD size or shape. This physical process is governed by rapid diffusion driven by the differences in the chemical potential of the QD and impurity solution. While cation exchange often provides for better compositional control than kinetic doping, cation combinations are more limited.

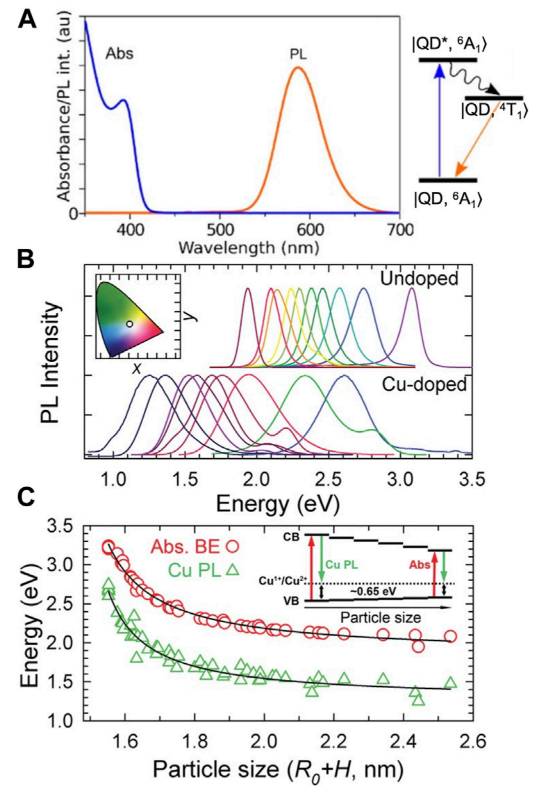

FIGURE 4
Absorption and emission spectra for Mn-doped QDs **(A)**, and a comparison between Cu-doped and undoped QDs in **(B,C)**. Reproduced with permission from Erickson et al. (2014) for **(A)** and Viswanatha et al. (2011) for **(B,C)**. For Mn-doped QDs the absorption and emission mechanism is depicted schematically in an additional panel to the right of **(A)**, and for Cu-doped QDs it is depicted in the inset of **(C)**.

Substitutional transition metal impurities induce red-shifted emission without significantly altering the absorption onset, concurrently increasing the Stokes shift to mitigate reabsorption losses in LSCs. Substitutional Mn^{2+} dopants are the most extensively studied in II-VI QDs—emitting photons via an internal $^4T_1 \rightarrow {}^6A_1$ d-d transition following excitation by energy transfer from the QD host. The energy of photon emission is fixed at approximately ~590 nm or 2.1 eV (Figure 4A) (Norris et al., 2001; Erwin et al., 2005; Beaulac et al., 2009), while QD absorption is tunable by nanocrystal size. The absorption onset can therefore be shifted to bluer spectral energies until there is virtually zero overlap between absorption and emission, which results in reabsorption-free LSCs (Erickson et al., 2014). However, the fixed wavelength resulting from the internal emission process for Mn^{2+} dopants yields two key drawbacks. Solar absorption is confined to a narrow spectral region due to the potential of reabsorption when the QD band gap is smaller than 2.2 eV (~560 nm). Furthermore, the emission exhibits a pronounced yellow-orange hue instead of the preferred semi-transparent shading (Pietryga et al., 2016).

The emission mechanism for Ag^+ and Cu^{2+} dopants is markedly different from Mn^{2+} dopants. Radiative recombination occurs via relaxation of a conduction band (CB) electron from the QD host and a hole localized at the dopant energy level (Figures 4B, C) (Lingerfelt et al., 2019, Lingerfelt et al., 2020, Lingerfelt et al., 2021, Wang et al., 2018a, Elibol et al., 2018, Komsa et al., 2013, Algara-Siller et al., 2013, Roccapriore et al., 2022). While the emission transition for both Ag^+ and Cu^+ dopants appears to be similar, the hole localization process differs for each structure due to their distinct electron configurations. Cu^{2+} dopants have a $3d^9$ electron configuration, which results in a pre-existing hole in its ground state that can

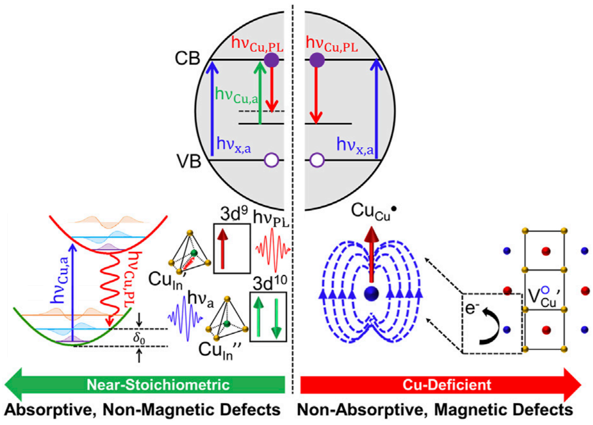

FIGURE 5
Antisite defects in CIS QDs have been predicted to form in near-stoichiometric structures (left panel) and copper vacancies charge compensated by lattice copper oxidation in Cu-deficient structures (right panel). CIS has two absorption pathways if antisite defects are present ($h\upsilon_x$ and $h\upsilon_{Cu,\alpha}$ for band-edge absorption and Cu^{1+} absorption, respectively). CIS with V_{Cu} + $Cu_{Cu}^{\bullet}$ only exhibit the $h\upsilon_x$ pathway. Antisite defects undergo excited state reorganization, which further red-shifts emission due to the Cu_{In}'' → Cu_{In}' Jahn-Teller distorted photoconversion process (similar to the singlet-triplet splitting model). "Near-stoichiometric" CIS therefore has absorption/emission dominated by the antisite defect pathway (similar to Ag^+-doped QDs), and Cu-deficient CIS by the V_{Cu} induced $Cu_{Cu}^{\bullet}$ pathway (similar to Cu^{2+}-doped QDs). Reproduced with permission from Fuhr et al. (2020a).

directly recombine with the excited-state CB electron from the host QD (Viswanatha et al., 2011; Knowles et al., 2015; Nelson and Gamelin, 2018; Fuhr et al., 2019; Hughes et al., 2019; Harchol et al., 2022). On the other hand, Ag^+ has a $3d^{10}$ electron configuration, which must capture a photogenerated hole from the VB (Pinchetti et al., 2018; Najafi et al., 2021). For both cases, the emission wavelength is consequently governed by the energy difference between the hole localized at the Ag^+ or Cu^{2+} dopant and the CB electron. The Stokes shift is determined by the energy difference between the hole localized at the dopant site and the valence band (VB). The CB electron energy is size-tunable, which allows for larger QDs with redder absorption and near-IR emission to be synthesized without dramatically increasing reabsorption.

The band gap for copper and silver doped QDs is still somewhat large, which limits spectral absorption coverage for LSCs and has driven research interest in $Cu_xIn_{2-x}Se_{2-y}S_y$ (CISeS) QDs. CISeS QDs have size tunable absorption all the way to the near-IR range, a large Stokes shift (300–500 meV), a near colorless emission wavelength that well-matches the peak EQE of the LSC PV cells (Figure 3B), and have recently achieved greater than 95% QY (Ueng and Hwang, 1989; Ueng and Hwang, 1990; Kim et al., 2012; Knowles et al., 2015; Jara et al., 2016; Fuhr et al., 2017; Xia et al., 2017; Bergren et al., 2018; Nelson and Gamelin, 2018; Yun et al., 2018; Houck et al., 2019; Hughes et al., 2019; Makarov et al., 2019; Fuhr et al., 2020a; Fuhr et al., 2020b; Du et al., 2020; Frick et al., 2020; Velarde et al., 2020; Hinterding et al., 2021; Xia et al., 2021; Harchol et al., 2022; Liang et al., 2023). The origin of CISeS Stokes shifted emission has commonly been ascribed to defects, but with several other proposed mechanisms depending on the type of defect that forms, and the band-edge transition itself (described later in the review). It has been suggested that near-stoichiometric (and especially Cu-rich) CISeS QDs have antisite (Cu_{In}'') defects, and that Cu-deficient QDs have V_{Cu}' charge compensated by oxidation of a lattice Cu^+ atom to Cu^{2+} ($Cu_{Cu}^{\bullet}$) (Fuhr et al., 2020a; Fuhr et al., 2020b). Considering that Cu_{In}'' defects are in the +1 oxidation state ($3d^{10}$ configuration) and Cu^{2+} defects in the $3d^9$ configuration, hole localization is thought to occur via a similar process as Ag^+ dopants for Cu_{In}'' (near-stoichiometric or Cu-rich QDs) and Cu^{2+} dopants for $Cu_{Cu}^{\bullet}$ (Cu-deficient QDs).

Both defects involve recombination from a delocalized CB electron, sharing many of the same advantages as Ag^+ and Cu^{2+}-doped structures. However, precise control of synthesis conditions becomes crucial due to variations in emission channels between each defect type. Specifically, the hole localization process for Cu_{In}'' defects involves intragap absorption, which is absent for $Cu_{Cu}^{\bullet}$ defects (Figure 5). A potential conclusion from this observation would be that the sharper absorption edge for Cu-deficient structures arising from the removal of Cu_{In}'' defects should lead to superior LSC performance via reduced spectral overlap between absorption and emission, and correspondingly improved reabsorption losses. This prediction is partially correct, but misses quantum yield considerations. Moderately Cu-deficient structures exhibit sharper absorption, reduced spectral overlap, and even higher QY due to deactivation of hole trapping pathways (Jara et al., 2016; Fuhr et al., 2020a; Fuhr et al., 2020b). However, if QDs become too Cu-deficient eventually other defects (e.g., $In_{Cu}^{\bullet\bullet}$) can form in larger densities and reduce QY via electron trapping (Jara et al., 2016; Fuhr et al., 2020a; Fuhr et al., 2020b). These findings are suggestive that the defect chemistry of CISeS QDs is highly sensitive to synthesis conditions, and that likely the complex distribution of defects and LSC performance will strongly vary with other experimental parameters such as temperature or pH.

The precise emission mechanism is still under debate for CISeS QDs, and other models that do not require defects such as the self-trapped exciton or inverted band-edge hole model have been discussed (Knowles et al., 2015; Shabaev et al., 2015; Nagamine et al., 2018; Nelson and Gamelin, 2018; Hughes et al., 2019; Anand et al., 2020; Harchol et al., 2022). For the purposes of this general review on defects in nanomaterials we do not attempt to determine the model that most accurately depicts the exact CISeS emission mechanism. We instead focus on two key points: 1) many of these proposed models are not mutually exclusive, and 2) defects likely affect the emission process, LSC performance, and their formation is sensitive to chemical processing conditions. The predicted Stokes shift for the band-edge hole inversion model is expected to be smaller than the defect-induced emission, and are difficult to resolve experimentally due to partial overlap with strong Cu-defect emission unless defect-free QDs can be synthesized (Batchelder et al., 1979, Desmet et al., 2012, Meinardi et al., 2015). The self-trapped exciton model involves the same hole localization and excited-state reorganization mechanism described for antisite defects and Ag^+ dopants, but is argued to instead occur via band-edge states to cause the large Stokes shift without the need for defects (Batchelder et al., 1979, Desmet et al., 2012, Meinardi et al., 2015).

These distinctions may prove valuable in future LSC efforts, particularly in resolving routes to reduce spectral linewidths to further diminish reabsorpiton losses. However, it is important to note that regardless of the precise emission mechanism, defects likely strongly impact spectral properties for CISeS QDs and are important to control for LSC performance. There is extensive evidence that the spectral properties of CISeS QDs are *highly* sensitive to chemical processing in ways that binary QDs are not. Single particle spectroscopy studies have shown radiative lifetimes and photoluminescence (PL) linewidths that can vary by several hundreds of ns or several hundreds of meV, respectively (Zang et al., 2017; Hinterding et al., 2021; Xia et al., 2021). Ensemble absorption and emission spectroscopy has resolved both two channel absorption and two channel emssion (Jara et al., 2016; Fuhr et al., 2020a; Fuhr et al., 2020b; Xia et al., 2021), and the magneto-optical charateristics vary significantly across studies with different QD batches. (Rice et al., 2014; Knowles et al., 2015; Fuhr et al., 2020a; Anand et al., 2020; Fuhr et al., 2020b). These large variations are atypical for QDs, and defect-free structures are atypical for covalently bonded multinary structures—especially those with large variations in stoichiometry (Alvarez-Garcia et al., 2000; Hahn et al., 2001; Paier et al., 2009; Ye et al., 2019; Vijay et al., 2021; Han et al., 2022; Quadir et al., 2022). Given these characteristics and the well-known tendency to form defects in the bulk CISeS phase (Ueng and Hwang, 1989; Ueng and Hwang, 1990; Alvarez-Garcia et al., 2000; Hahn et al., 2001), it is highly likely that defects are impacting the spectral properties in *some* way, and that regardless of the precise emission mechanism understanding synthesis-defect formation relationships for CISeS QDs could improve LSC performance.

4 Energy storage: batteries and electric vehicles

Fossil fuel powered vehicles are a major contributor to CO_2 emissions and climate change. As such, electric vehicles (EVs) have attracted widespread interest, and their proliferation persists. In this context, lithium-ion batteries (LIBs) power a diverse array of consumer electronics that have become indispensable to modern-society, and their integration into commercial EVs has enabled an alternative to the combustion engine. In conjunction with a greener grid (e.g., utilizing recent innovations in solar and wind technology) EVs powered by LIBs will be critical in lowering CO_2 emissions and reducing the deleterious impacts of climate change (Chu and Majumdar, 2012; Clark et al., 2016). A typical LIB has a solid-state anode and cathode separated by a liquid or gel electrolyte that shuttles ions between the two electrodes during charging and discharging (Manthiram, 2020). For EVs, ideal electrode materials should yield a high energy density, superior rate capability, and long cycle life for consumer acceptability—allowing for extended driving ranges, fast charging, and low maintenance costs.

The achievable energy density of an electrode material is proportional to its capacitance and voltage. Capacitance represents the amount of charge each electrode material can store, and the voltage represents the energy difference between the anode and cathode redox potentials. Hence, an optimal anode would exhibit stable, redox-inactive lower energy levels and a high lying energy band—relative to vacuum or the standard Hydrogen electrode—where redox reactions occur. The opposite is true for the cathode, which should have its highest redox active energy band at the lowest feasible energy (within the limitations of electrolyte stability). Stanley Whittingham demonstrated the first rechargeable LIB at Exxon Corporation using a TiS_2 cathode, which could not be commercialized due to the safety hazards of using Li metal as an anode, and the limited energy density arising from the 2.5 V discharge voltage (Whittingham, 1976). Oxide p-bands lie at lower energies than sulfides (2p vs. 3p electrons), and allow the access of lower lying redox energy states such as the $Co^{3+/4+}$ redox couple in $LiCoO_2$ (Goodenough, 1971; Mizushima et al., 1981). Oxide cathodes, specifically $LiCoO_2$, extended the voltage range of LIBs to 4V and allowed for the usage of graphite as an anode material by incorporating Li into its as-synthesized lattice structure. These advancements improved the energy density and safety of LIBs, were central to the eventual commercial success of LIBs, and awarded the Nobel prize in chemistry.

The success of $LiCoO_2$ in commercializing LIBs is laudable, but many challenges persist. $LiCoO_2$ has a layered cathode structure with a cubic close-packed oxide sublattice and Li^+ and Co^{3+} ions ordered on alternate (111) planes (Mizushima et al., 1981). The good cation ordering stems from the significant size difference between Li^+ and Co^{3+} and aids electronic and ionic conduction. Li^+ ionic conduction occurs via low energy barrier face-sharing tetrahedral voids between octahedra (o-t-o pathway). Shared octahedra along the cobalt plane enable Co-Co interactions for enhanced electronic conductivity. Specifically, Co^{3+} is oxidized to low-spin Co^{4+} during LIB charging, leading to the inclusion of holes in the cobalt t_2g^{6-x} band, and causing $Li_{1-x}CoO_2$ to become metallic during charging (Nishizawa and Yamamura, 1998; Chebiam et al., 2001a). However, the overlap between the top of the O^{2-}:2p and $Co^{3+/4+}$ bands leads to the release of oxygen if charged more than 50% (Chebiam et al., 2001b; Venkatraman et al., 2003). This limits the *practical* capacity (~140 mA h g^{-1}), and in conjunction with the high cost of cobalt has driven the search for new rock salt $LiMO_2$ (where M = a transition metal) alloys.

Cation-ordered $LiMO_2$ structures crystallize in several common motifs such as the γ-$LiFeO_2$ (tetragonal structure where Li^+ and Fe^{3+} ions are well-ordered on octahedral sites, Figure 6A), low-temperature spinel-like $LiCoO_2$ structure (all Li^+ ions are ordered on the 16c octahedral sites, Figure 6B), or **α**-$NaFeO_2$ (Li and M are ordered along alternating (111) planes, Figure 6C). Cation-disordered structures can also form, as exemplified by **α**-$LiFeO_2$ for which Li and M are randomly distributed (Figure 6D). Li^+ ions are located on octahedral O_h sites in both ordered and disordered structures, but cation disorder prevents the earlier described o-t-o Li-migration mechanism (Figure 6E) (Sebastian and Gopalakrishnan, 2003; Manthiram, 2020; Wang et al., 2022a) Specifically, the randomness of cation distribution on the octahedral sites means that the intermediate tetrahedral site in the o-t-o diffusion mechanism could now be connected to *either* Li or M octahedra. The electrostatic interactions between the four cations of the face-sharing octahedra and the size of the tetrahedral diffusion site (T_d) determine the barrier to diffusion. If surrounded only by Li cations (0-TM channel, Figure 6F), Li^+ ions will have smaller required distances to diffuse through, combined with weaker electrostatic repulsion due to the low valency of lithium. This

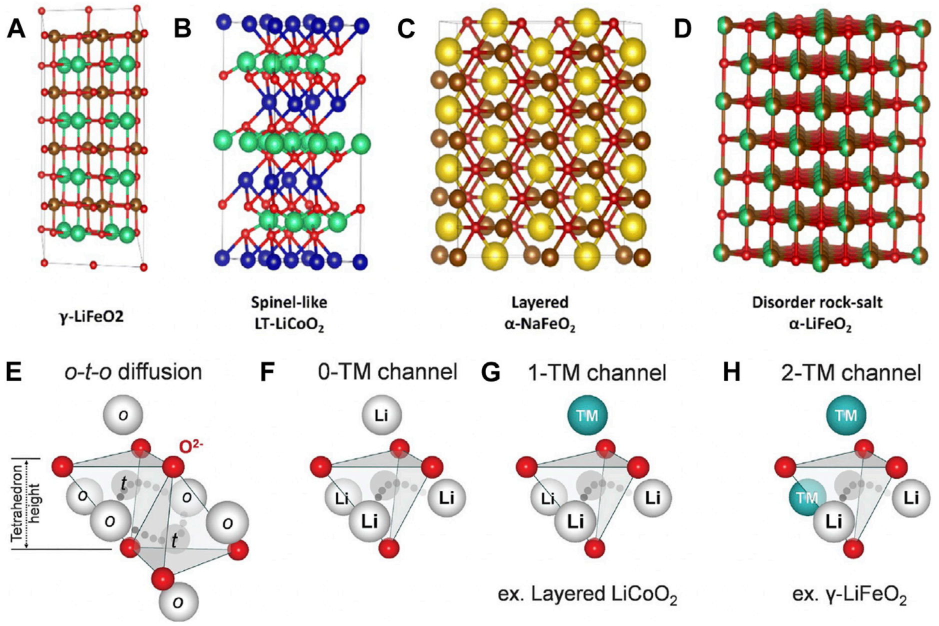

FIGURE 6
(A–D) Types of rock salt cathode structures. The cation ordered structures are shown in **(A–C)**, and an example of cation disorder is shown in **(D)**. Reproduced with permission from Zhang et al. (2023). **(E,F)** Diffusion models for ordered **(E)** structures versus disordered structures **(F–H)**. The disordered 0-TM channel (transition metal-free) is shown in **(F)**, while the channels with higher barriers due to transition metals are shown in **(G)** and **(H)**, for 1 transition metal and 2 transition metals, respectively. Reproduced with permission from Lee et al. (2014).

pathway therefore exhibits facile lithium migration. However, if one or more of the cations are transition metals (1-TM or 2-TM channels, Figures 6G, H) the increase in both migration distances and electrostatic repulsion will lead to a higher energy barrier, which reduces Li$^+$ conductivity by disabling the formation of a percolation network for long-distance diffusion (Wang et al., 2022a; Zhang et al., 2023). Inability to efficiently transport Li$^+$ through the o-t-o pathway initially led to little interest in cation disordered rock salt structures.

Monte Carlo simulations have since shown that 0-TM percolation networks can be created if excess lithium (e.g., 10%) in $Li_{1+x}M_{1-x}O_2$ is incorporated into the structure (Lee et al., 2014), giving high conductivity as well as capacity, which has led to renewed interest in these materials (Dixit et al., 2014; Chen et al., 2021a; Szymanski et al., 2022; Patil et al., 2023; Szymanski et al., 2023). Equivalently, when partial Li-occupancies are present, high Li-ion conductivity is expected (Dathar et al., 2017). Lithium-excess cation disordered rock salt structures can be synthesized in any of the structure-types described earlier: γ-LiFeO$_2$, layered, spinel-like LiCoO$_2$, and the layered **α**-NaFeO$_2$ structure-type. Several of these structures have demonstrated capacities beyond currently commercialized LIB cathode materials (Lee et al., 2014; Urban et al., 2014; Wang et al., 2022a; Zhang et al., 2023). Disordered structures that use nickel or manganese for the redox transition metal are the most well-studied. Many nickel alloy (e.g., with Ti, Nb, or Mo) cathodes have been synthesized with high average voltage and tilt slope (Pralong et al., 2012; Lee et al., 2015; Lee et al., 2017a; Källquist et al., 2019; Ouyang et al., 2020). If charged up to 4.6 V, overlap between e_g orbitals in Ni with hybridized Li-O-Li orbitals prevents the complete oxidation/reduction of Ni due to competition with O oxidation (Pralong et al., 2012; Lee et al., 2015; Lee et al., 2017a; Källquist et al., 2019; Ouyang et al., 2020; Zhang et al., 2023). While there are challenges related to the corresponding release of CO$_2$ and O$_2$ during the cycling process (surface densification), these materials have exhibited capacities greater than 220 mAh/g (Lee et al., 2015; Yu et al., 2019; Wang et al., 2022a). Manganese structures are also well studied, and $Li_4Mn_2O_5$ has been shown to exhibit discharge capacities as high as 287 mAh/g (Pralong et al., 2012). Alloying with other metals such as Ti or Nb in $Li_{1.2}Mn_{0.4}Ti_{0.4}O_4$ or $Li_{1.3}Nb_{0.3}Mn_{0.4}{}^{3+}O_2$ can further increase the discharge capacity to 300 mAh/g (Yabuuchi et al., 2016a; Lee et al., 2017a). However, irreversible O redox reactions contribute to a large initial discharge capacity, which eventually fades and limits cycle life (Wang et al., 2015b; Lun et al., 2019). Iron and vanadium systems such as Li-Ti-Fe-O and Li-Nb-V-O also show promise. For example, LIBs with discharge capacities equal to or greater than 200 mAh/g have been demonstrated with $Li_{1.2}Ti_{0.4}Fe_{0.4}O_2$ and $Li_{1.25}Nb_{0.25}V_{0.5}O_2$ (Yabuuchi et al., 2016b; Nakajima and Yabuuchi, 2017; Wandt et al., 2018; Wang et al., 2019).

Rock salts are not the only class of disordered cathode materials with the potential to improve LIB performance. Spinel $LiMn_2O_4$ structures have a cubic-closed pack oxygen sublattice where ordered structures consist of Mn^{3+} and Mn^{4+} ions occupying octahedral centers (16d) and Li$^+$ tetrahedral (8a) sites (Thackeray et al., 1983; Manthiram, 2020). $LiMn_2O_4$ has a three-dimensional Li$^+$ diffusion pathway that enables fast Li conduction; Li$^+$ ions migrate between 8a tetrahedral sites via transitioning through low migration barrier empty 16c octahedral sites. Dissimilar to the $Li_{1-x}CoO_2$ metallic transition during the charge-discharge process, $LiMn_2O_4$ remains a small polaron semiconductor. Regardless, Mn-Mn interactions from mixed valence t_{2g} and e_g states in Mn$^{3+/4+}$ facilitates electron hopping

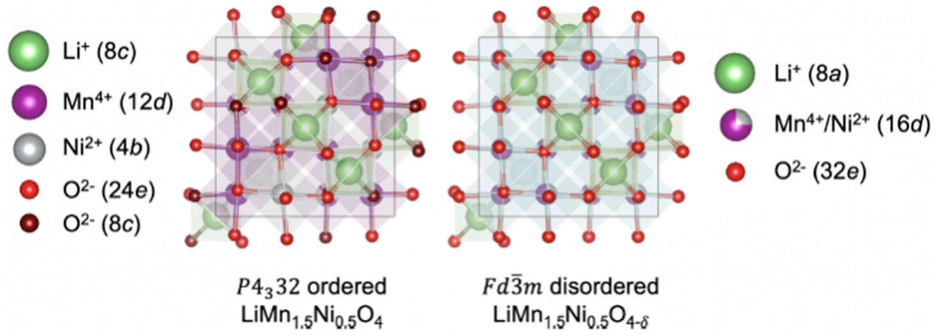

FIGURE 7
Comparing cation ordered and disordered LMNO structures based on their Wyckoff positions. Reproduced with permission from Cen et al. (2023).

and yields good electronic conductivity and high operating voltages (Gul et al., 2011). Jahn-Teller distortions in Mn^{3+}:$t_{2g}^{3}e_{g}^{1}$ contributes to a cubic to tetragonal phase transition, which presents a challenge for LIB performance because of the large volume change induced by the $2Mn^{3+} \rightarrow Mn^{2+} + Mn^{4+}$ disproportionation reaction (Manthiram, 2020). This leads to dissolution of Mn in the electrolyte and poor cycle life. One route to somewhat circumvent this issue is to alloy $LiMn_2O_4$ with Ni to form cation disordered $LiMn_{1.5}Ni_{0.5}O_4$ (LMNO). The Ni dopants partially occupy Mn sites, reduce the Mn^{3+} site prevalence, and contribute to a high 4.7 V Ni^{2+}/Ni^{4+} redox couple (Kan et al., 2017; Liang et al., 2020b; Cen et al., 2023).

LMNO can be synthesized with or without site disorder depending on the temperature (e.g., post synthesis calcination in air above 700°C leads to the formation of the disordered phase and temperatures at or below 700°C the ordered phase, Figure 7) (Kim et al., 2004). Mn atoms are in the +4 oxidation state in the ordered ($P4_332$) phase with Ni and Mn located on the 4b and 12d Wyckoff sites, respectively (Kunduraci and Amatucci, 2006; Lee et al., 2017b; Liu et al., 2017). If synthesized at higher temperatures (e.g., greater than 700°C) LMNO forms in the $Fd\bar{3}m$ space group. The partial reduction of Mn^{4+} to Mn^{3+} occurs alongside oxygen vacancy formation, Mn/Ni site disorder, and varied additional impurity phases (e.g., $Li_xNi_{1-x}O$) (Chebiam et al., 2001a; Venkatraman et al., 2003; Kunduraci and Amatucci, 2006; Shin et al., 2012; Casas-Cabanas et al., 2016; Aktekin et al., 2019; Haruna et al., 2021; Cen et al., 2023). The partial reduction of Mn^{4+} to Mn^{3+} in the cation disordered phase increases the electronic conductivity (>2.5 orders of magnitude) relative to the ordered phase (Kunduraci and Amatucci, 2006). Charging/discharging disordered LMNO as a LIB cathode results in a two-phase reaction when x in $Li_xNi_{0.5}Mn_{1.5}O_4$ is below 0.5 (between $Li_{0.5}Ni_{0.5}Mn_{1.5}O_4$ and $Ni_{0.25}Mn_{0.74}O_4$), and a solid-solution reaction when x is between 0.5 and 1 due to the $Ni^{2+/3+}$ redox couples (Liang et al., 2020b). The solid-solution reaction involves size changes in the parental lattice during charging/discharging, or insertion/extraction of lithium. On the other hand, the two-phase reaction involves interconversion and destruction of the parent cathode structure, which limits lithiation and delithiation kinetics. Notably, the two-phase reaction occurs across the *entire* x charging range for the ordered LMNO phase (between $LiNi_{0.5}Mn_{1.5}O_4/Li_{0.5}Ni_{0.5}Mn_{1.5}O_4$ and $Li_{0.5}Ni_{0.5}Mn_{1.5}O_4/Ni_{0.5}Mn_{1.5}O_4$), leads to poorer electrochemical stability, reduced rate capability, and lower cycling stability than the disordered structure (Ariyoshi et al., 2004; Liang et al., 2020c).

Doping LMNO with other metals can further improve the cycling stability and rate capability. Sodium dopants have been shown to enhance cation disorder, decrease particle size, and improve charge transfer by providing extra pathways for electron hopping (Wang et al., 2014). The 5% Na-doped LMNO structure achieved superior rate performance arising from the reduced voltage polarization. Al can be incorporated into LMNO as either substitutional dopants at the Ni/Mn sites via a thermopolymerization method, or in empty surface 16c octahedral sites using atomic layer deposition (ALD), and can prevent transition metal dissolution (Zhong et al., 2011; Piao et al., 2018). This process improves the rate capability and cycling stability by mitigating electrolyte/electrode side-reactions and enabling fast Li^+ diffusion. The concentration of Mn^{3+} can be increased with iron dopants, which enhances electronic conductivity, reduces voltage polarization, and correspondingly improves cycling performance and rate capability (Liu and Manthiram, 2009). Cr-doped LMNO structures (e.g., $LiNi_{0.45}Cr_{0.1}Mn_{1.45}O_4$) have also exhibited improved electronic/ionic conductivity with a wide voltage plateau, and cycle-stable structure (Wang et al., 2018c).

5 Energy conversion: electrocatalytic green hydrogen production

Hydrogen has a high energy density (142 MJ/kg), is abundant, and can potentially be used as a clean CO_2 emission-free fuel (Dincer, 2012; Abdin et al., 2020). However, despite these potential advantages over conventional greenhouse gas emitting fuels, H_2 is not readily available in its free form in nature. The predominant industrial routes for hydrogen production rely on thermochemical fossil fuel-related processes such as steam-methane or hydrocarbon reforming, pyrolysis, or coal gasification (Nikolaidis and Poullikkas, 2017; Abdin et al., 2020; Megía et al., 2021). Each of these industrial-scale processes emit greenhouse gases, which has motivated interest in “green hydrogen” production wherein hydrogen is produced via carbon neutral routes. Water electrolysis offers a potentially viable route to produce hydrogen without carbon emissions (Lu et al., 2021; Tan et al., 2023). Catalyst design represents a pertinent challenge for water electrolysis at industrial scales though. To date, the catalysts with the best performance utilize rare metals such as platinum, palladium, iridium, or rhodium (Chen et al., 2021b). These rare earth metals catalysts are known to be commercially expensive and to have negative mining impacts that limit their utility for economically viable and environmentally sustainable hydrogen production at-scale (Glaister and Mudd, 2010; Lu et al., 2021; Tan et al., 2023).

MX_2 phases (where M is a transition metal and X is an oxygen or chalcogenide) are of great interest for many electronic and optical applications (Manzeli et al., 2017). Transition metal dichalcogenides (TMDs) are the most well-studied branch of these materials, and several phases such as MoS_2 and WS_2 are under consideration for replacing platinum group metals catalysts for the hydrogen evolution reaction (HER) (Hinnemann et al., 2005). These two dimensional structures are similar to graphene except that instead of stacked carbon layers separated by weak van der Waals forces (graphite) the bulk structure has stacked metal chalcogen or oxide layers, which similarly can be exfoliated as either a few-layer stacked structure, or as monolayers (Chhowalla et al., 2013). The basal plane of defect-free 2D TMDs is unfortunately catalytically inert, which impedes their electrocatalytic HER performance (Xu et al., 2015). The basal planes can be activated by either inducing defect formation or altering the TMD phase. The latter of these two approaches is often difficult (Kibs et al., 2012; Kong et al., 2013; Voiry et al., 2013; Jiao et al., 2018; Wei et al., 2019; Li et al., 2021; Tan et al., 2023). Using MoS_2 as an example, the 2H phase is a semiconductor and therefore has a lower electron mobility than the metallic 1T phase—yielding reduced HER performance. While converting the 2H phase to 1T could potentially improve charge transfer kinetics, it also involves harsh chemicals and produces only a metastable phase that eventually converts back to the thermodynamically more stable 2H phase (Lukowski et al., 2013). Routes for exposing more catalytically active edge sites on the 2H MoS_2 phase can improve performance, but these do not alter the electronic conductivity significantly.

Alternatively, controlling the density and distribution of defects in TMDs can increase the density of active sites, while simultaneously improving electron mobility by altering the electronic structure. This route is particularly viable with TMDs, which as discussed in the "Synthesis and Control of Defect Formation" section are well-known to form defects *in-situ* and have many post-processing routes to further control their distribution and density. The Sabatier principle guides HER catalysis design, and states that heterogeneous catalysts that have intermediate binding strengths with reaction intermediates will yield the best performance. Specifically, a catalyst that binds too strongly with the reaction products will not allow for product dissociation, and the active sites of the catalyst will be permanently blocked. On the other hand, a catalyst that binds too weakly to the reactants will not be able to weaken chemical bonds and lower the reaction barrier to improve product yield or selectivity. The most common tool used to illustrate this Goldilocks principle is the volcano plot, which for HER describes ΔG_{H^*} (binding strength) versus j (exchange current density, Figure 8) (Parsons, 1958).

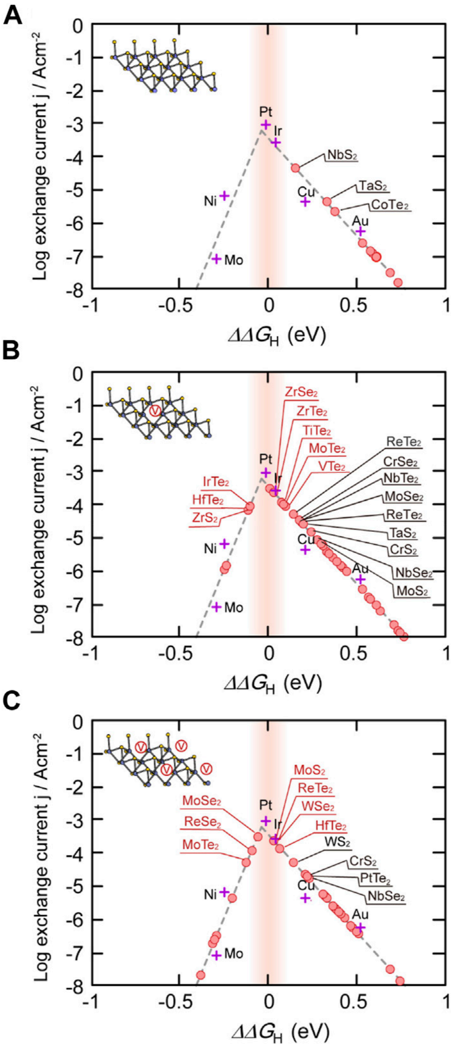

FIGURE 8
(A–C) Volcano plots comparing hydrogen adsorption free energies to Pt for defect-free TMDs (a, depicted by a vacancy-free representative structure in the figure inset), low density anion vacancy concentration (6.25%, b, depicted by a representative structure with a single vacancy), and higher density anion vacancy concentration (25%, c, depicted by a representative structure with four vacancies). Reproduced with permission from Lee et al. (2018).

Among the many defect engineering techniques outlined earlier, the management of vacancy formation in TMDs through a combination of *in-situ* and *ex-situ* approaches are the most well-developed, and consequently, the most widely employed for enhancement of ΔG_{H^*} in TMD-catalyzed HER. First principles calculations have shown that there is an inverse relationship between vacancy formation energy and ΔG_{H^*} (Lee et al., 2018; Wang et al., 2022b). Localized electronic states resulting from vacancy creation interact with hydrogen electronic states during chemical bonding to reduce the energy cost of bond-breaking from vacancy formation. This process results in stronger hydrogen adsorption for vacancies with larger formation energies. Smaller HOMO-LUMO gaps (highest occupied molecular orbital and lowest unoccupied molecular orbital, respectively), which may encompass localized defect states in addition to band-edges, are also favored. To

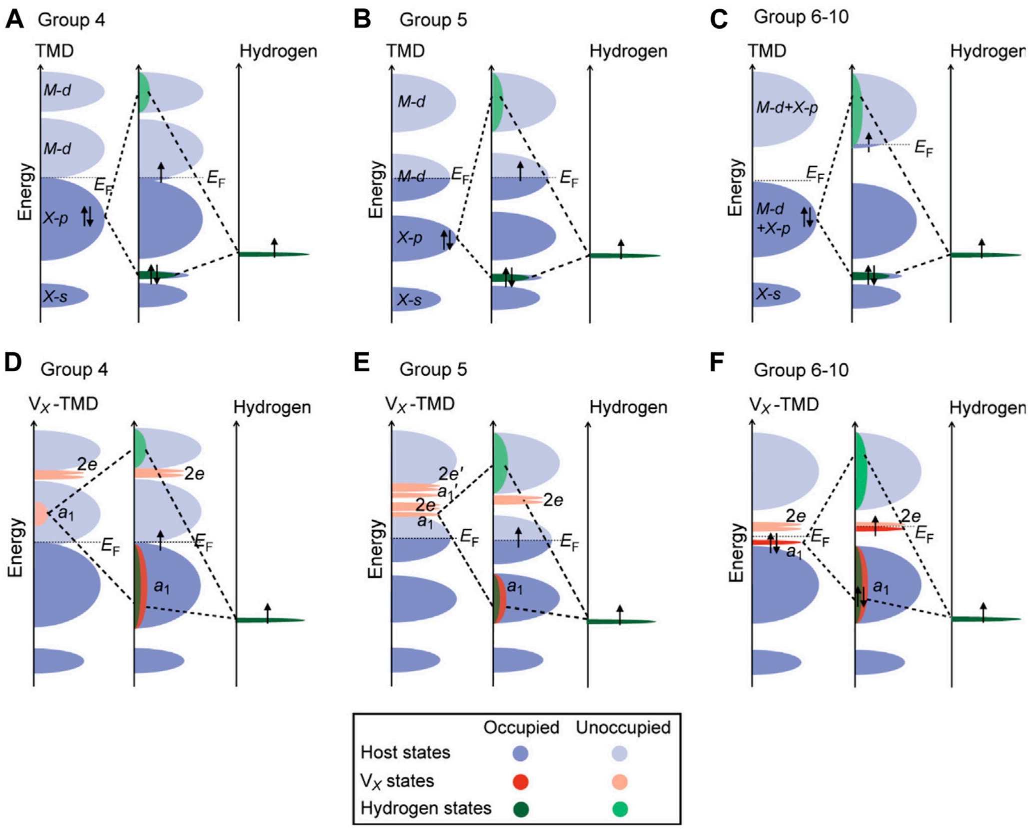

FIGURE 9
Schematic depiction of TMD/hydrogen band diagrams where **(A–C)** represents defect-free TMDs with group 4, 5, and 6–10 transition metals, and **(D–F)** represents the same structures with anion vacancies. Reproduced with permission from Lee et al. (2018).

illustrate the desirability of a small HOMO-LUMO gap, let's consider group 5 transition metals. As previously described, the hybridization process requires the transfer of two electrons from the HOMO to the bonding state, which necessitates "left-over" electrons occupy the LUMO (Figure 9). This process helps explain the superior performance of $ZrSe_2$, $ZrTe_2$, and $TiTe_2$, which have ΔG_{H^*} closer to Pt than other TMDs in the volcano plot in Figure 9. An inherent challenge in establishing defect relationships with TMDs lies in the fact that the identical defect types (e.g., vacancies) can elicit distinct effects within the same class of TMDs in different phases. One such example is VS_2 wherein vacancies improve hydrogen adsorption in the 2H phase, but hamper performance in the 1T phase (Zhang et al., 2017). While the general relationships explored so far between vacancy formation and HER performance are informative, each TMD system still requires careful examination.

HER performance enhancement via vacancy creation is sensitive to the concentration of defects, and the relationship between vacancy density and performance varies by specific TMD system (Lee et al., 2018). *Ab initio* computational screening studies have categorized the effects of vacancy density on TMD HER performance into four types. Type-I TMDs exhibit low ΔG_{H^*} without vacancies. As the vacancy concentration increases the HER performance will improve until it eventually approaches Pt HER performance (e.g., MoS_2, WSe_2, or $ReSe_2$). Hence, type-I TMDs are initially poor choices for HER catalysts but can be dramatically improved by increasing the vacancy concentration. Type-II TMDs (e.g., $MoSe_2$ and $MoTe_2$) have an intermediate ΔG_{H^*}, or moderately positive $\Delta\Delta G_{H^*}$ (defined as ΔG_{H^*} relative to Pt) without vacancies. As the vacancy formation is induced in these structures, there is an initial improvement from their already relatively strong HER performance (eventually matching Pt). However, if the vacancy concentration becomes too large $\Delta\Delta G_{H^*}$ will become negative and there will be a performance drop. Type-III TMDs (e.g., $ZrSe_2$ and $ZrTe_2$) exhibit similar properties as type-II, but with ΔG_{H^*} already near that of Pt, which indicates that while similar trends hold as described for type-II, the tolerance for including more vacancies is much smaller. The ΔG_{H^*} for type-I through type-III can therefore be thought of as: TMDs where large vacancy concentrations (type-I), intermediate vacancy concentrations (type-II), and small vacancy concentrations (type-III) are desirable. Type-IV TMDs differ from the other three by exhibiting the *opposite* ΔG_{H^*} relationship. For these TMD structures, ΔG_{H^*} is already larger than Pt, and vacancies will yield a HER performance reduction.

An alternative scheme of modifying TMDs for optimal HER performance is via edge-engineering (Peng et al., 2016; Cui et al., 2017; Hu et al., 2019). As described earlier, the basal plane of non-defective TMDs are catalytically inert. However, stacking 2D TMDs along the edges can increase the exposure of catalytically active edges, and lead to a larger effective surface-area of very active catalytic sites. Recently it was demonstrated using first principles calculations that different types of non-stoichiometric edges in $MoSe_2$, many of whom have been recently synthesized under a scanning transmission electron microscope (STEM) (Sang et al., 2018), can have near optimal HER activity over conventional stoichiometric edges. They found a strong linear correlation between Bader charges on H and the Gibbs free energy of hydrogen adsorption (ΔG^{*}_{H}) at these edges, providing a design principle for discovering better HER catalytic edges. HER activity was found to be not only influenced by the formation of H–Se/Mo chemical bonds as previously thought, but also by geometric reconstructions and charge redistribution. The same group subsequently discovered via high-throughput computational screening about nine thermodynamically stable multi-functional edges in MoS_2, many showing optimal HER performance (Hu et al., 2020). STEM was subsequently used as an atomic drill bit for targeted synthesis of specific edge-patterns in 2D TMDs. (Boebinger et al., 2023). Nevertheless, a scalable approach to engineer edges in 2D materials is still lacking, but has significant potential in achieving high HER in TMDs with earth-abundant elements and without involving any critical materials.

These classifications explain many experimental trends, but as observed through other defect systems, *a priori* prediction of structure-property relationships for defects is complex and difficult. DFT studies on MoS_2 electrocatalysts indicate that high concentrations of sulfur vacancies preferentially agglomerate instead of randomly dispersing throughout the lattice, which partially negates its classification as a type-I defect system (Zhou et al., 2021). However, experimental studies *have* shown improved performance at high vacancy concentrations because of the unusual interplay between sulfur vacancy formation and exposure of under-coordinated Mo atoms, which become synergistically active as catalytic sites (Li et al., 2019). This is just one of many demonstrations that vacancy formation in TMDs should not only be considered in isolation to other effects in the atomic or electronic structure. Excess vacancy formation can damage the structural integrity of TMDs such as inducing cracks or holes, and the existence of dangling bonds can adsorb other non-hydrogen species (particularly in air) (He et al., 2018; Yang et al., 2019). At low concentrations the co-creation of other defects (e.g., Frenkel pairs) can improve performance by providing additional adsorption sites, or possibly even alternative adsorption mechanisms such as in MoS_2 where the preferred hydrogen adsorption site shifts to a region between the vacancy and interstitial in the Frenkel pair (Xu et al., 2022). This process improved the performance even relative to Pt-doped MoS_2. It is also well-known that defect creation semiconductors leads to localized intragap states, which can contribute to improved electrical conductivity and enhance hydrogen adsorption, but in ways that will wildly vary by which defects form (Li et al., 2016).

6 Challenges and future prospects

Understanding defect formation mechanisms and elucidating their structure-property relationships in nanomaterials is a highly prospective route to commercialize new green energy device architectures, or improve existing ones. A key challenge to address for the future of defect engineering is the development of better integrated theory-experiment workflows wherein the physical properties of a specific defect can be predicted *a priori* to experiment and the synthesis (or post-synthesis) methods to control the type, concentration, and distribution of defects are known. While partial implementation of such workflows are feasible today, unlocking their full potential requires significant advances in theory and experimental methods. DFT methods for predicting synthesis-structure-property relationships are ever-improving, but the time-scale for calculations is often only marginally faster than running experiments. Avenues for defective material design are continually expanding with the advent of beyond 0 K computational chemistry methods for predicting defect phase stability and advanced electronic structure calculation methods compatible with large supercells for predicting electronic and optical properties of defects. However, each of these routes is computationally expensive and are generally used to explain experimental results *posteriori*. This problem is further exacerbated if excited-state modeling is considered for gaining mechanistic understanding of QD optical emission processes for optimizing LSCs, or electrochemical-interface modeling is required to improve cation disordered oxides for LIB cathodes or TMDs as catalysts for HER. Hence, further advances in high-throughput calculation methods are required for electronic structure calculations and computational chemistry to be effectively integrated in theory-experiment workflows.

From an experimental perspective, determining synthesis conditions for controlling defect formation in nanomaterials has traditionally relied on an Edisonian trial-and-error methodology. This approach entails selection of initial synthesis conditions, measurement of basic material structure without accounting for defects (e.g., XRD for crystal structure and/or mass spectroscopy for composition), measurement of nanomaterial physical properties (e.g., emission energy), and potentially device performance. The influence of defects on these properties is oftentimes only considered if anomalous characteristics arise. Synthesis methods are then iteratively adjusted to enhance, modify, or eliminate these characteristics. True experimental control of defect chemistry will likely only be achieved if routes for measuring defect structure are regularly integrated in the initial measurement of structure, and the direct impact of synthesis conditions and post-processing on defect distribution are consistently considered. Further advances in *in-situ* and operando microscopy and spectroscopy techniques, aimed at achieving atomic-level control over defect formation during synthesis (*in-situ*) or observing their effects on device performance (operando), is equally crucial.

An additional but related challenge is that state-of-the-art techniques for measuring defect structure, such as STEM are also used to create defects. This challenge is particularly pronounced in materials such as TMDs where it is well-known that STEM serves a dual purpose—evaluating the defect distribution in as-synthesized flakes and using the electron beam directly to create defects. Regardless, the prospects for such workflows has been significantly heightened by a recent surge of computational power improving the efficiency of first principles calculations, the synthesis methods outlined here, and advances in material imaging capabilities. The integration of these ever-evolving methods for modeling, synthesis, and imaging into workflows is likely key for defect engineering to reach its full potential. The resulting improvements in nanomaterial design could enable the development of Stokes shift engineered QDs for building integrated photovoltaic units, high-voltage lithium-ion batteries utilizing cation disordered oxides in electric vehicles, and TMD electrocatalysts for green hydrogen production. If the described technologies are then integrated into contemporary cities, a future marked by net-zero emission buildings, fossil fuel-free transportation, and carbon neutral hydrogen production would mark a major step forward in achieving a sustainable future.

Author contributions

AF: Conceptualization, Investigation, Writing–original draft. BS: Conceptualization, Investigation, Writing–review and editing. PG: Conceptualization, Investigation, Writing–review and editing.

Funding

The authors declare financial support was received for the research, authorship, and/or publication of this article. This work was supported by the Center for Nanophase Materials Science (CNMS) and the Alvin M. Weinberg Fellowship at Oak Ridge National Laboratory.

The authors declare that this study received funding from Oak Ridge National Laboratory. The funder was not involved in the study design, collection, analysis, interpretation of data, the writing of this article, or the decision to submit it for publication.

Acknowledgments

AF acknowledges support from the Alvin M. Weinberg Fellowship at Oak Ridge National Laboratory. This work was carried out at Oak Ridge National Laboratory's Center for Nanophase Materials Sciences, a US Department of Energy Office of Science User Facility.

Licenses and permissions

Conflict of interest

All authors are employees of Oak Ridge National Laboratory, managed by UT-Battelle LLC, an M&O contractor for the U.S. Department of Energy.

Publisher's note

References

Abdin, Z., Zafaranloo, A., Rafiee, A., Mérida, W., Lipiński, W., and Khalilpour, K. R. (2020). Hydrogen as an energy vector. *Renew. Sustain. Energy Rev.* 120, 109620. doi:10.1016/j.rser.2019.109620

Aktekin, B., Valvo, M., Smith, R. I., Sørby, M. H., Lodi Marzano, F., Zipprich, W., et al. (2019). Cation ordering and oxygen release in LiNi0.5−xMn1.5+xO4−y (LNMO): *in situ* neutron diffraction and performance in Li ion full cells. *ACS Appl. Energy Mater.* 2 (5), 3323–3335. doi:10.1021/acsaem.8b02217

Algara-Siller, G., Kurasch, S., Sedighi, M., Lehtinen, O., and Kaiser, U. (2013). The pristine atomic structure of MoS2 monolayer protected from electron radiation damage by graphene. *Appl. Phys. Lett.* 103 (20). doi:10.1063/1.4830036

Alstone, P., Gershenson, D., and Kammen, D. M. (2015). Decentralized energy systems for clean electricity access. *Nat. Clim. Change* 5 (4), 305–314. doi:10.1038/nclimate2512

Alvarez-Garcia, J., Marcos-Ruzafa, J., Pérez-Rodriguez, A., Romano-Rodriguez, A., Morante, J. R., and Scheer, R. (2000). MicroRaman scattering from polycrystalline CuInS2 films: structural analysis. *Thin Solid Films* 361-362, 208–212. doi:10.1016/s0040-6090(99)00847-0

Anand, A., Zaffalon, M. L., Gariano, G., Camellini, A., Gandini, M., Brescia, R., et al. (2020). Evidence for the band-edge exciton of CuInS2 nanocrystals enables record efficient large-area luminescent solar concentrators. *Adv. Funct. Mater.* 30 (4), 1906629. doi:10.1002/adfm.201906629

Ansari, S. A., Khan, M. M., Kalathil, S., Nisar, A., Lee, J., and Cho, M. H. (2013). Oxygen vacancy induced band gap narrowing of ZnO nanostructures by an electrochemically active biofilm. *Nanoscale* 5 (19), 9238–9246. doi:10.1039/c3nr02678g

Ariyoshi, K., Iwakoshi, Y., Nakayama, N., and Ohzuku, T. (2004). Topotactic two-phase reactions of Li [Ni1/2Mn3/2] O 4 (P4332) in nonaqueous lithium cells. *J. Electrochem. Soc.* 151 (2), A296. doi:10.1149/1.1639162

Balachandran, J., Lin, L., Anchell, J. S., Bridges, C. A., and Ganesh, P. (2017). Defect genome of cubic perovskites for fuel cell applications. *J. Phys. Chem. C* 121 (48), 26637–26647. doi:10.1021/acs.jpcc.7b08716

Banal, J. L., Ghiggino, K. P., and Wong, W. W. H. (2014). Efficient light harvesting of a luminescent solar concentrator using excitation energy transfer from an aggregation-induced emitter. *Phys. Chem. Chem. Phys.* 16 (46), 25358–25363. doi:10.1039/c4cp03807j

Batchelder, J. S., Zewai, A. H., and Cole, T. (1979). Luminescent solar concentrators. 1: theory of operation and techniques for performance evaluation. *Appl. Opt.* 18 (18), 3090–3110. doi:10.1364/ao.18.003090

Beaulac, R., Schneider, L., Archer, P. I., Bacher, G., and Gamelin, D. R. (2009). Light-induced spontaneous magnetization in doped colloidal quantum dots. *Science* 325 (5943), 973–976. doi:10.1126/science.1174419

Belloni, J. (2006). Nucleation, growth and properties of nanoclusters studied by radiation chemistry: application to catalysis. *Catal. Today* 113 (3), 141–156. doi:10.1016/j.cattod.2005.11.082

Bennett, M. C., Hu, G., Wang, G., Heinonen, O., Kent, P. R. C., Krogel, J. T., et al. (2022). Origin of metal-insulator transitions in correlated perovskite metals. *Phys. Rev. Res.* 4 (2), L022005. doi:10.1103/physrevresearch.4.l022005

Bergren, M. R., Makarov, N. S., Ramasamy, K., Jackson, A., Guglielmetti, R., and McDaniel, H. (2018). High-performance CuInS2 quantum dot laminated glass luminescent solar concentrators for windows. *ACS Energy Lett.* 3 (3), 520–525. doi:10.1021/acsenergylett.7b01346

Bi, W., Ye, C., Xiao, C., Tong, W., Zhang, X., Shao, W., et al. (2014). Spatial location engineering of oxygen vacancies for optimized photocatalytic H2 evolution activity. *Small* 10 (14), 2820–2825. doi:10.1002/smll.201303548

Boebinger, M. G., Brea, C., Ding, L.-P., Misra, S., Olunloyo, O., Yu, Y., et al. (2023). The atomic drill bit: precision controlled atomic fabrication of 2D materials. *Adv. Mater.* 35 (14), 2210116. doi:10.1002/adma.202210116

Bonu, V., Das, A., Amirthapandian, S., Dhara, S., and Tyagi, A. K. (2015). Photoluminescence of oxygen vacancies and hydroxyl group surface functionalized SnO2 nanoparticles. *Phys. Chem. Chem. Phys.* 17 (15), 9794–9801. doi:10.1039/c5cp00060b

Bonu, V., Das, A., Prasad, A. K., Krishna, N. G., Dhara, S., and Tyagi, A. K. (2014). Influence of in-plane and bridging oxygen vacancies of SnO2 nanostructures on CH4 sensing at low operating temperatures. *Appl. Phys. Lett.* 105 (24). doi:10.1063/1.4904457

Broberg, D., Bystrom, K., Srivastava, S., Dahliah, D., Williamson, B. A. D., Weston, L., et al. (2023). High-throughput calculations of charged point defect properties with semi-local density functional theory—performance benchmarks for materials screening applications. *npj Comput. Mater.* 9 (1), 72. doi:10.1038/s41524-023-01015-6

Casas-Cabanas, M., Kim, C., Rodríguez-Carvajal, J., and Cabana, J. (2016). Atomic defects during ordering transitions in LiNi0.5Mn1.5O4 and their relationship with electrochemical properties. *J. Mater. Chem. A* 4 (21), 8255–8262. doi:10.1039/c6ta00424e

Cen, J., Zhu, B., Kavanagh, S. R., Squires, A. G., and Scanlon, D. O. (2023). Cation disorder dominates the defect chemistry of high-voltage LiMn1.5Ni0.5O4 (LMNO) spinel cathodes. *J. Mater. Chem. A* 11 (25), 13353–13370. doi:10.1039/d3ta00532a

Chebiam, R. V., Kannan, A. M., Prado, F., and Manthiram, A. (2001b). Comparison of the chemical stability of the high energy density cathodes of lithium-ion batteries. *Electrochem. Commun.* 3 (11), 624–627. doi:10.1016/s1388-2481(01)00232-6

Chebiam, R. V., Prado, F., and Manthiram, A. (2001a). Soft chemistry synthesis and characterization of layered Li1-xNi1-yCoyO2-δ (0 ≤ x ≤ 1 and 0 ≤ y ≤ 1). *Chem. Mater.* 13 (9), 2951–2957. doi:10.1021/cm0102537

Chen, D., Ahn, J., Self, E., Nanda, J., and Chen, G. (2021a). Understanding cation-disordered rocksalt oxyfluoride cathodes. *J. Mater. Chem. A* 9 (12), 7826–7837. doi:10.1039/d0ta12179g

Chen, J., Ryu, G. H., Sinha, S., and Warner, J. H. (2019). Atomic structure and dynamics of defects and grain boundaries in 2D Pd2Se3 monolayers. *ACS Nano* 13 (7), 8256–8264. doi:10.1021/acsnano.9b03645

Chen, L., Xu, B., Jin, M., Chen, L., Yi, G., Xing, B., et al. (2023). Excellent photocatalysis of Bi2WO6 structured with oxygen vacancies in degradation of tetracycline. *J. Mol. Struct.* 1278, 134911. doi:10.1016/j.molstruc.2023.134911

Chen, X., Li, C., Grätzel, M., Kostecki, R., and Mao, S. S. (2012). Nanomaterials for renewable energy production and storage. *Chem. Soc. Rev.* 41 (23), 7909–7937. doi:10.1039/c2cs35230c

Chen, X., Liu, L., and Huang, F. (2015). Black titanium dioxide (TiO2) nanomaterials. *Chem. Soc. Rev.* 44 (7), 1861–1885. doi:10.1039/c4cs00330f

Chen, X., Liu, L., Yu, P. Y., and Mao, S. S. (2011). Increasing solar absorption for photocatalysis with black hydrogenated titanium dioxide nanocrystals. *Science* 331 (6018), 746–750. doi:10.1126/science.1200448

Chen, Y., Qiao, Q., Cao, J., Li, H., and Bian, Z. (2021b). Precious metal recovery. *Joule* 5 (12), 3097–3115. doi:10.1016/j.joule.2021.11.002

Chen, Y., Xi, J., Dumcenco, D. O., Liu, Z., Suenaga, K., Wang, D., et al. (2013). Tunable band gap photoluminescence from atomically thin transition-metal dichalcogenide alloys. *ACS Nano* 7 (5), 4610–4616. doi:10.1021/nn401420h

Chhowalla, M., Shin, H. S., Eda, G., Li, L.-J., Loh, K. P., and Zhang, H. (2013). The chemistry of two-dimensional layered transition metal dichalcogenide nanosheets. *Nat. Chem.* 5 (4), 263–275. doi:10.1038/nchem.1589

Choudhary, K., and Sumpter, B. G. (2023). Can a deep-learning model make fast predictions of vacancy formation in diverse materials? *AIP Adv.* 13 (9). doi:10.1063/5.0135382

Chu, S., and Majumdar, A. (2012). Opportunities and challenges for a sustainable energy future. *Nature* 488 (7411), 294–303. doi:10.1038/nature11475

Chua, R., Yang, J., He, X., Yu, X., Yu, W., Bussolotti, F., et al. (2020). Can reconstructed Se-deficient line defects in monolayer VSe2 induce magnetism? *Adv. Mater.* 32 (24), 2000693. doi:10.1002/adma.202000693

Clark, P. U., Shakun, J. D., Marcott, S. A., Mix, A. C., Eby, M., Kulp, S., et al. (2016). Consequences of twenty-first-century policy for multi-millennial climate and sea-level change. *Nat. Clim. Change* 6 (4), 360–369. doi:10.1038/nclimate2923

Corrado, C., Hawker, M., Livingston, G., Medling, S., Bridges, F., and Zhang, J. Z. (2010). Enhanced Cu emission in ZnS: Cu,Cl/ZnS core–shell nanocrystals. *Nanoscale* 2 (7), 1213–1221. doi:10.1039/c0nr00056f

Cui, W., Xu, S., Yan, B., Guo, Z., Xu, Q., Sumpter, B. G., et al. (2017). Triphasic 2D materials by vertically stacking laterally heterostructured 2H-/1T′-MoS2 on graphene for enhanced photoresponse. *Adv. Electron. Mater.* 3 (7), 1700024. doi:10.1002/aelm.201700024

Currie, M. J., Mapel, J. K., Heidel, T. D., Goffri, S., and Baldo, M. A. (2008). High-efficiency organic solar concentrators for photovoltaics. *Science* 321 (5886), 226–228. doi:10.1126/science.1158342

Dathar, G. K. P., Balachandran, J., Kent, P. R. C., Rondinone, A. J., and Ganesh, P. (2017). Li-ion site disorder driven superionic conductivity in solid electrolytes: a first-principles investigation of β-Li3PS4. *J. Mater. Chem. A* 5 (3), 1153–1159. doi:10.1039/c6ta07713g

Debije, M. G., and Verbunt, P. P. C. (2012). Thirty years of luminescent solar concentrator research: solar energy for the built environment. *Adv. Energy Mater.* 2 (1), 12–35. doi:10.1002/aenm.201100554

Deng, Y., Zhao, X., Zhu, C., Li, P., Duan, R., Liu, G., et al. (2021). MoTe2: semiconductor or semimetal? *ACS Nano* 15 (8), 12465–12474. doi:10.1021/acsnano.1c01816

Desmet, L., Ras, A. J. M., de Boer, D. K. G., and Debije, M. G. (2012). Monocrystalline silicon photovoltaic luminescent solar concentrator with 4.2% power conversion efficiency. *Opt. Lett.* 37 (15), 3087–3089. doi:10.1364/ol.37.003087

Dincer, I. (2012). Green methods for hydrogen production. *Int. J. Hydrogen Energy* 37 (2), 1954–1971. doi:10.1016/j.ijhydene.2011.03.173

Ding, J., Balachandran, J., Sang, X., Guo, W., Anchell, J. S., Veith, G. M., et al. (2018). The influence of local distortions on proton mobility in acceptor doped perovskites. *Chem. Mater.* 30 (15), 4919–4925. doi:10.1021/acs.chemmater.8b00502

Dixit, H., Zhou, W., Idrobo, J.-C., Nanda, J., and Cooper, V. R. (2014). Facet-Dependent disorder in pristine high-voltage lithium–manganese-rich cathode material. *ACS Nano* 8 (12), 12710–12716. doi:10.1021/nn505740v

Dreyer, C. E., Alkauskas, A., Lyons, J. L., Janotti, A., and Walle, C. G. V. d. (2018). First-principles calculations of point defects for quantum technologies. *Annu. Rev. Mater. Res.* 48 (1), 1–26. doi:10.1146/annurev-matsci-070317-124453

Du, J., Singh, R., Fedin, I., Fuhr, A. S., and Klimov, V. I. (2020). Spectroscopic insights into high defect tolerance of Zn:CuInSe2 quantum-dot-sensitized solar cells. *Nat. Energy* 5 (5), 409–417. doi:10.1038/s41560-020-0617-6

Du, M.-H., Yan, J., Cooper, V. R., and Eisenbach, M. (2021). Tuning Fermi levels in intrinsic antiferromagnetic topological insulators MnBi2Te4 and MnBi4Te7 by defect engineering and chemical doping. *Adv. Funct. Mater.* 31 (3), 2006516. doi:10.1002/adfm.202006516

Dumcenco, D. O., Kobayashi, H., Liu, Z., Huang, Y.-S., and Suenaga, K. (2013). Visualization and quantification of transition metal atomic mixing in Mo1−xWxS2 single layers. *Nat. Commun.* 4 (1), 1351. doi:10.1038/ncomms2351

Dyck, O., Zhang, C., Rack, P. D., Fowlkes, J. D., Sumpter, B., Lupini, A. R., et al. (2020). Electron-beam introduction of heteroatomic Pt–Si structures in graphene. *Carbon* 161, 750–757. doi:10.1016/j.carbon.2020.01.042

Egdell, R. G., Eriksen, S., and Flavell, W. R. (1987). A spectroscopic study of electron and ion beam reduction of SnO2(110). *Surf. Sci.* 192 (1), 265–274. doi:10.1016/s0039-6028(87)81175-5

Elibol, K., Susi, T., Argentero, G., Reza Ahmadpour Monazam, M., Pennycook, T. J., Meyer, J. C., et al. (2018). Atomic structure of intrinsic and electron-irradiation-induced defects in MoTe2. *Chem. Mater.* 30 (4), 1230–1238. doi:10.1021/acs.chemmater.7b03760

Enyashin, A. N., Bar-Sadan, M., Houben, L., and Seifert, G. (2013). Line defects in molybdenum disulfide layers. *J. Phys. Chem. C* 117 (20), 10842–10848. doi:10.1021/jp403976d

Erickson, C. S., Bradshaw, L. R., McDowall, S., Gilbertson, J. D., Gamelin, D. R., and Patrick, D. L. (2014). Zero-reabsorption doped-nanocrystal luminescent solar concentrators. *ACS Nano* 8 (4), 3461–3467. doi:10.1021/nn406360w

Erwin, S. C., Zu, L., Haftel, M. I., Efros, A. L., Kennedy, T. A., and Norris, D. J. (2005). Doping semiconductor nanocrystals. *Nature* 436 (7047), 91–94. doi:10.1038/nature03832

Fang, W., Xing, M., and Zhang, J. (2014). A new approach to prepare Ti3+ self-doped TiO2 via NaBH4 reduction and hydrochloric acid treatment. *Appl. Catal. B Environ.* 160-161, 240–246. doi:10.1016/j.apcatb.2014.05.031

Feng, Q., Zhu, Y., Hong, J., Zhang, M., Duan, W., Mao, N., et al. (2014). Growth of large-area 2D MoS2(1-x)Se2x semiconductor alloys. *Adv. Mater.* 26 (17), 2648–2653. doi:10.1002/adma.201306095

Freysoldt, C., Grabowski, B., Hickel, T., Neugebauer, J., Kresse, G., Janotti, A., et al. (2014). First-principles calculations for point defects in solids. *Rev. Mod. Phys.* 86 (1), 253–305. doi:10.1103/revmodphys.86.253

Freysoldt, C., Neugebauer, J., and Van de Walle, C. G. (2009). Fully *ab initio* finite-size corrections for charged-defect supercell calculations. *Phys. Rev. Lett.* 102 (1), 016402. doi:10.1103/physrevlett.102.016402

Frick, J. J., Cheng, G., Kushwaha, S., Yao, N., Wagner, S., Bocarsly, A. B., et al. (2020). Observation of [VCu1−ini2+VCu1−] defect triplets in Cu-deficient CuInS2. *J. Phys. Chem. C* 124 (48), 26415–26427. doi:10.1021/acs.jpcc.0c08872

Fuhr, A., Yun, H. J., Crooker, S. A., and Klimov, V. I. (2020b). Spectroscopic and magneto-optical signatures of Cu1+ and Cu2+ defects in copper indium sulfide quantum dots. *ACS Nano* 14 (2), 2212–2223. doi:10.1021/acsnano.9b09181

Fuhr, A. S., Alexandrova, A. N., and Sautet, P. (2020a). Stoichiometry-controllable optical defects in CuxIn2−xSy quantum dots for energy harvesting. *J. Mater. Chem. A* 8 (25), 12556–12565. doi:10.1039/d0ta03954c

Fuhr, A. S., Ganesh, P., Vasudevan, R. K., and Sumpter, B. G. (2023). *Bridging theory with experiment: digital twins and deep learning segmentation of defects in monolayer MX2 phases*. arXiv:2305.02917. doi:10.48550/arXiv.2305.02917

Fuhr, A. S., Sautet, P., and Alexandrova, A. N. (2019). Heterogeneity in local chemical bonding explains spectral broadening in quantum dots with Cu impurities. *J. Phys. Chem. C* 123 (9), 5705–5713. doi:10.1021/acs.jpcc.8b12023

Fuhr, A. S., Yun, H. J., Makarov, N. S., Li, H., McDaniel, H., and Klimov, V. I. (2017). Light emission mechanisms in CuInS2 quantum dots evaluated by spectral electrochemistry. *ACS Photonics* 4 (10), 2425–2435. doi:10.1021/acsphotonics.7b00560

Ganesh, P., Lechermann, F., Kylänpää, I., Krogel, J. T., Kent, P. R. C., and Heinonen, O. (2020). Doping a bad metal: origin of suppression of the metal-insulator transition in nonstoichiometric VO_{2}. *Phys. Rev. B* 101 (15), 155129. doi:10.1103/physrevb.101.155129

Gao, J., Kim, Y. D., Liang, L., Idrobo, J. C., Chow, P., Tan, J., et al. (2016). Transition-metal substitution doping in synthetic atomically thin semiconductors. *Adv. Mater.* 28 (44), 9735–9743. doi:10.1002/adma.201601104

Giustino, F., and Snaith, H. J. (2016). Toward lead-free perovskite solar cells. *ACS Energy Lett.* 1 (6), 1233–1240. doi:10.1021/acsenergylett.6b00499

Glaister, B. J., and Mudd, G. M. (2010). The environmental costs of platinum–PGM mining and sustainability: is the glass half-full or half-empty? *Miner. Eng.* 23 (5), 438–450. doi:10.1016/j.mineng.2009.12.007

Goodenough, J. B. (1971). Metallic oxides. *Prog. Solid State Chem.* 5, 145–399. doi:10.1016/0079-6786(71)90018-5

Gul, S., Cooper, J. K., Corrado, C., Vollbrecht, B., Bridges, F., Guo, J., et al. (2011). Synthesis, optical and structural properties, and charge carrier dynamics of Cu-doped ZnSe nanocrystals. *J. Phys. Chem. C* 115 (43), 20864–20875. doi:10.1021/jp2047272

Gungor, K., Du, J., and Klimov, V. I. (2022). General Trends in the Performance of quantum dot luminescent solar concentrators (LSCs) revealed Using the “effective LSC quality factor”. *ACS Energy Lett.* 7 (5), 1741–1749. doi:10.1021/acsenergylett.2c00781

Guo, Y., Kalinin, S. V., Cai, H., Xiao, K., Krylyuk, S., Davydov, A. V., et al. (2021). Defect detection in atomic-resolution images via unsupervised learning with translational invariance. *npj Comput. Mater.* 7 (1), 180. doi:10.1038/s41524-021-00642-1

Gutiérrez, H. R., Perea-López, N., Elías, A. L., Berkdemir, A., Wang, B., Lv, R., et al. (2013). Extraordinary room-temperature photoluminescence in triangular WS2 monolayers. *Nano Lett.* 13 (8), 3447–3454. doi:10.1021/nl3026357

Hahn, T., Metzner, H., Plikat, B., and Seibt, M. (2001). Order and disorder in epitaxially grown CuInS2. *Thin Solid Films* 387 (1), 83–85. doi:10.1016/s0040-6090(01)00790-8

Hallegatte, S., Rogelj, J., Allen, M., Clarke, L., Edenhofer, O., Field, C. B., et al. (2016). Mapping the climate change challenge. *Nat. Clim. Change* 6 (7), 663–668. doi:10.1038/nclimate3057

Han, D., Rudel, S. S., Schnick, W., and Ebert, H. (2022). Self-doping behavior and cation disorder in $MgSnN_2$. *Phys. Rev. B* 105 (12), 125202. doi:10.1103/physrevb.105.125202

Harchol, A., Barak, Y., Hughes, K. E., Hartstein, K. H., Jöbsis, H. j., Prins, P. T., et al. (2022). Optically detected magnetic resonance spectroscopy of Cu-doped CdSe/CdS and CuInS2 colloidal quantum dots. *ACS Nano* 16 (8), 12866–12877. doi:10.1021/acsnano.2c05130

Haruna, A. B., Mwonga, P., Barrett, D., Rodella, C. B., Forbes, R. P., Venter, A., et al. (2021). Defect-engineered β-MnO2−δ precursors control the structure–property relationships in high-voltage spinel LiMn1.5Ni0.5O4−δ. *ACS Omega* 6 (39), 25562–25573. doi:10.1021/acsomega.1c03656

He, Z., Zhao, R., Chen, X., Chen, H., Zhu, Y., Su, H., et al. (2018). Defect engineering in single-layer MoS2 using heavy ion irradiation. *ACS Appl. Mater. Interfaces* 10 (49), 42524–42533. doi:10.1021/acsami.8b17145

Hinnemann, B., Moses, P. G., Bonde, J., Jørgensen, K. P., Nielsen, J. H., Horch, S., et al. (2005). Biomimetic hydrogen evolution: MoS2 nanoparticles as catalyst for hydrogen evolution. *J. Am. Chem. Soc.* 127 (15), 5308–5309. doi:10.1021/ja0504690

Hinterding, S. O. M., Mangnus, M. J. J., Prins, P. T., Jöbsis, H. J., Busatto, S., Vanmaekelbergh, D., et al. (2021). Unusual spectral diffusion of single CuInS2 quantum dots sheds light on the mechanism of radiative decay. *Nano Lett.* 21 (1), 658–665. doi:10.1021/acs.nanolett.0c04239

Houck, D. W., Assaf, E. I., Shin, H., Greene, R. M., Pernik, D. R., and Korgel, B. A. (2019). Pervasive cation vacancies and antisite defects in copper indium diselenide (CuInSe2) nanocrystals. *J. Phys. Chem. C* 123 (14), 9544–9551. doi:10.1021/acs.jpcc.9b00558

Hu, C., Zeng, X., Liu, Y., Zhou, M., Zhao, H., Tritt, T. M., et al. (2017). Effects of partial La filling and Sb vacancy defects on CoS b_3 skutterudites. *Phys. Rev. B* 95 (16), 165204. doi:10.1103/physrevb.95.165204

Hu, G., Fung, V., Sang, X., Unocic, R. R., and Ganesh, P. (2019). Superior electrocatalytic hydrogen evolution at engineered non-stoichiometric two-dimensional transition metal dichalcogenide edges. *J. Mater. Chem. A* 7 (31), 18357–18364. doi:10.1039/c9ta05546k

Hu, G., Fung, V., Sang, X., Unocic, R. R., and Ganesh, P. (2020). Predicting synthesizable multi-functional edge reconstructions in two-dimensional transition metal dichalcogenides. *npj Comput. Mater.* 6 (1), 44. doi:10.1038/s41524-020-0327-4

Hughes, K. E., Ostheller, S. R., Nelson, H. D., and Gamelin, D. R. (2019). Copper's role in the photoluminescence of Ag1−xCuxInS2 nanocrystals, from copper-doped AgInS2 (x ∼ 0) to CuInS2 (x = 1). *Nano Lett.* 19 (2), 1318–1325. doi:10.1021/acs.nanolett.8b04905

Iberi, V., Liang, L., Ievlev, A. V., Stanford, M. G., Lin, M.-W., Li, X., et al. (2016). Nanoforging single layer MoSe2 through defect engineering with focused helium ion beams. *Sci. Rep.* 6 (1), 30481. doi:10.1038/srep30481

Islam, M. R., Kang, N., Bhanu, U., Paudel, H. P., Erementchouk, M., Tetard, L., et al. (2014). Tuning the electrical property via defect engineering of single layer MoS2 by oxygen plasma. *Nanoscale* 6 (17), 10033–10039. doi:10.1039/c4nr02142h

Jara, D. H., Stamplecoskie, K. G., and Kamat, P. V. (2016). Two distinct transitions in CuxInS2 quantum dots. Bandgap versus sub-bandgap excitations in copper-deficient structures. *J. Phys. Chem. Lett.* 7 (8), 1452–1459. doi:10.1021/acs.jpclett.6b00571

Jeong, J., Choi, S.-P., Chang, C. I., Shin, D. C., Park, J. S., Lee, B. T., et al. (2003). Photoluminescence properties of SnO2 thin films grown by thermal CVD. *Solid State Commun.* 127 (9), 595–597. doi:10.1016/s0038-1098(03)00614-8

Ji, T., Jian, W.-B., and Fang, J. (2003). The first synthesis of Pb1-xMnxSe nanocrystals. *J. Am. Chem. Soc.* 125 (28), 8448–8449. doi:10.1021/ja0351746

Jian, W. B., Fang, J., Ji, T., and He, J. (2003). Quantum-size-effect-enhanced dynamic magnetic interactions among doped spins in Cd1−xMnxSe nanocrystals. *Appl. Phys. Lett.* 83 (16), 3377–3379. doi:10.1063/1.1619564

Jiang, J., Zhang, L., Li, H., He, W., and Yin, J. J. (2013). Self-doping and surface plasmon modification induced visible light photocatalysis of BiOCl. *Nanoscale* 5 (21), 10573–10581. doi:10.1039/c3nr03597b

Jiao, Y., Hafez, A. M., Cao, D., Mukhopadhyay, A., Ma, Y., and Zhu, H. (2018). Metallic MoS2 for high performance energy storage and energy conversion. *Small* 14 (36), 1800640. doi:10.1002/smll.201800640

Kaczkowski, J., and Płowaś-Korus, I. (2021). The vibrational and thermodynamic properties of CsPbI3 polymorphs: an improved description based on the SCAN meta-GGA functional. *J. Phys. Chem. Lett.* 12 (28), 6613–6621. doi:10.1021/acs.jpclett.1c01798

Källquist, I., Naylor, A. J., Baur, C., Chable, J., Kullgren, J., Fichtner, M., et al. (2019). Degradation mechanisms in Li2VO2F Li-rich disordered rock-salt cathodes. *Chem. Mater.* 31 (16), 6084–6096. doi:10.1021/acs.chemmater.9b00829

Kan, W. H., Kuppan, S., Cheng, L., Doeff, M., Nanda, J., Huq, A., et al. (2017). Crystal chemistry and electrochemistry of LixMn1.5Ni0.5O4 solid solution cathode materials. *Chem. Mater.* 29 (16), 6818–6828. doi:10.1021/acs.chemmater.7b01898

Kang, N., Paudel, H. P., Leuenberger, M. N., Tetard, L., and Khondaker, S. I. (2014). Photoluminescence quenching in single-layer MoS2 via oxygen plasma treatment. *J. Phys. Chem. C* 118 (36), 21258–21263. doi:10.1021/jp506964m

Kelley, K. P., Morozovska, A. N., Eliseev, E. A., Sharma, V., Yilmaz, D. E., van Duin, A. C. T., et al. (2022). Oxygen vacancy injection as a pathway to enhancing electromechanical response in ferroelectrics. *Adv. Mater.* 34 (2), 2106426. doi:10.1002/adma.202106426

Kibsgaard, J., Chen, Z., Reinecke, B. N., and Jaramillo, T. F. (2012). Engineering the surface structure of MoS2 to preferentially expose active edge sites for electrocatalysis. *Nat. Mater.* 11 (11), 963–969. doi:10.1038/nmat3439

Kim, J.-H., Mirzaei, A., Kim, J.-Y., Lee, J.-H., Kim, H. W., Hishita, S., et al. (2020). Enhancement of gas sensing by implantation of Sb-ions in SnO2 nanowires. *Sensors Actuators B Chem.* 304, 127307. doi:10.1016/j.snb.2019.127307

Kim, J. H., Myung, S. T., Yoon, C. S., Kang, S. G., and Sun, Y. K. (2004). Comparative study of LiNi0.5Mn1.5O4-δ and LiNi0.5Mn1.5O4 cathodes having two crystallographic structures: Fd3m and P4332. *Chem. Mater.* 16 (5), 906–914. doi:10.1021/cm035050s

Kim, Y.-K., Ahn, S.-H., Chung, K., Cho, Y.-S., and Choi, C.-J. (2012). The photoluminescence of CuInS2 nanocrystals: effect of non-stoichiometry and surface modification. *J. Mater. Chem.* 22 (4), 1516–1520. doi:10.1039/c1jm13170b

Klimov, V. I., Baker, T. A., Lim, J., Velizhanin, K. A., and McDaniel, H. (2016). Quality factor of luminescent solar concentrators and practical concentration limits attainable with semiconductor quantum dots. *ACS Photonics* 3 (6), 1138–1148. doi:10.1021/acsphotonics.6b00307

Knowles, K. E., Nelson, H. D., Kilburn, T. B., and Gamelin, D. R. (2015). Singlet–triplet splittings in the luminescent excited states of colloidal Cu+:CdSe, Cu+:InP, and CuInS2 nanocrystals: charge-transfer configurations and self-trapped excitons. *J. Am. Chem. Soc.* 137 (40), 13138–13147. doi:10.1021/jacs.5b08547

Komsa, H.-P., Kurasch, S., Lehtinen, O., Kaiser, U., and Krasheninnikov, A. V. (2013). From point to extended defects in two-dimensional MoS_2: evolution of atomic structure under electron irradiation. *Phys. Rev. B* 88 (3), 035301. doi:10.1103/physrevb.88.035301

Komsa, H.-P., Rantala, T. T., and Pasquarello, A. (2012). Finite-size supercell correction schemes for charged defect calculations. *Phys. Rev. B* 86 (4), 045112. doi:10.1103/physrevb.86.045112

Komuro, Y., and Matsumoto, Y. (2011). Electron beam irradiation-induced reduction of SnO2 deposited on TiO2(110) surfaces. *J. Phys. Chem. C* 115 (14), 6618–6621. doi:10.1021/jp111703p

Kondratowicz, I., Nadolska, M., Şahin, S., Łapiński, M., Prześniak-Welenc, M., Sawczak, M., et al. (2018). Tailoring properties of reduced graphene oxide by oxygen plasma treatment. *Appl. Surf. Sci.* 440, 651–659. doi:10.1016/j.apsusc.2018.01.168

Kong, D., Wang, H., Cha, J. J., Pasta, M., Koski, K. J., Yao, J., et al. (2013). Synthesis of MoS2 and MoSe2 Films with Vertically Aligned Layers. *Nano Lett.* 13 (3), 1341–1347. doi:10.1021/nl400258t

Kröger, F. A., and Vink, H. J. (1956). “Relations between the concentrations of imperfections in crystalline solids,” in *Solid state physics*. Editors F. Seitz and D. Turnbull (Academic Press), 307–435.

Kunduraci, M., and Amatucci, G. G. (2006). Synthesis and characterization of nanostructured 4.7 V lix Mn1.5Ni0.5O4 spinels for high-power lithium-ion batteries. *J. Electrochem. Soc.* 153 (7), A1345. doi:10.1149/1.2198110

Kwon, Y. J., Kang, S. Y., Wu, P., Peng, Y., Kim, S. S., and Kim, H. W. (2016). Selective improvement of NO2 gas sensing behavior in SnO2 nanowires by ion-beam irradiation. *ACS Appl. Mater. Interfaces* 8 (21), 13646–13658. doi:10.1021/acsami.6b01619

Lany, S., and Zunger, A. (2008). Assessment of correction methods for the band-gap problem and for finite-size effects in supercell defect calculations: case studies for ZnO and GaAs. *Phys. Rev. B* 78 (23), 235104. doi:10.1103/physrevb.78.235104

Le Bahers, T., Rérat, M., and Sautet, P. (2014). Semiconductors used in photovoltaic and photocatalytic devices: assessing fundamental properties from DFT. *J. Phys. Chem. C* 118 (12), 5997–6008. doi:10.1021/jp409724c

Lee, C.-H., Khan, A., Luo, D., Santos, T. P., Shi, C., Janicek, B. E., et al. (2020). Deep learning enabled strain mapping of single-atom defects in two-dimensional transition metal dichalcogenides with sub-picometer precision. *Nano Lett.* 20 (5), 3369–3377. doi:10.1021/acs.nanolett.0c00269

Lee, J., Kang, S., Yim, K., Kim, K. Y., Jang, H. W., Kang, Y., et al. (2018). Hydrogen evolution reaction at anion vacancy of two-dimensional transition-metal dichalcogenides: *ab initio* computational screening. *J. Phys. Chem. Lett.* 9 (8), 2049–2055. doi:10.1021/acs.jpclett.8b00712

Lee, J., Papp, J. K., Clément, R. J., Sallis, S., Kwon, D.-H., Shi, T., et al. (2017a). Mitigating oxygen loss to improve the cycling performance of high capacity cation-disordered cathode materials. *Nat. Commun.* 8 (1), 981. doi:10.1038/s41467-017-01115-0

Lee, J., Seo, D.-H., Balasubramanian, M., Twu, N., Li, X., and Ceder, G. (2015). A new class of high capacity cation-disordered oxides for rechargeable lithium batteries: Li–Ni–Ti–Mo oxides. *Energy & Environ. Sci.* 8 (11), 3255–3265. doi:10.1039/c5ee02329g

Lee, J., Urban, A., Li, X., Su, D., Hautier, G., and Ceder, G. (2014). Unlocking the potential of cation-disordered oxides for rechargeable lithium batteries. *Science* 343 (6170), 519–522. doi:10.1126/science.1246432

Lee, K., Park, J., Choi, S., Lee, Y., Lee, S., Jung, J., et al. (2022). STEM image analysis based on deep learning: identification of vacancy defects and polymorphs of MoS2. *Nano Lett.* 22 (12), 4677–4685. doi:10.1021/acs.nanolett.2c00550

Lee, K., Yang, G. J., and Kim, Y. (2017b). Improvement of the electrochemical properties of LiNi0.5Mn1.5O4 by controlling the heating atmosphere during synthesis. *Ceram. Int.* 43 (17), 15510–15518. doi:10.1016/j.ceramint.2017.08.100

Li, B., Huang, L., Zhong, M., Huo, N., Li, Y., Yang, S., et al. (2015). Synthesis and transport properties of large-scale alloy Co0.16Mo0.84S2 bilayer nanosheets. *ACS Nano* 9 (2), 1257–1262. doi:10.1021/nn505048y

Li, G., Blake, G. R., and Palstra, T. T. M. (2017a). Vacancies in functional materials for clean energy storage and harvesting: the perfect imperfection. *Chem. Soc. Rev.* 46 (6), 1693–1706. doi:10.1039/c6cs00571c

Li, H., Tsai, C., Koh, A. L., Cai, L., Contryman, A. W., Fragapane, A. H., et al. (2016). Activating and optimizing MoS2 basal planes for hydrogen evolution through the formation of strained sulphur vacancies. *Nat. Mater.* 15 (1), 48–53. doi:10.1038/nmat4465

Li, L., Qin, Z., Ries, L., Hong, S., Michel, T., Yang, J., et al. (2019). Role of sulfur vacancies and undercoordinated Mo regions in MoS2 nanosheets toward the evolution of hydrogen. *ACS Nano* 13 (6), 6824–6834. doi:10.1021/acsnano.9b01583

Li, X., Puretzky, A. A., Sang, X., Kc, S., Tian, M., Ceballos, F., et al. (2017b). Suppression of defects and deep levels using isoelectronic tungsten substitution in monolayer MoSe2. *Adv. Funct. Mater.* 27 (19), 1603850. doi:10.1002/adfm.201603850

Li, Y., Zuo, S., Li, Q.-H., Wu, X., Zhang, J., Zhang, H., et al. (2021). Vertically aligned MoS2 with in-plane selectively cleaved Mo–S bond for hydrogen production. *Nano Lett.* 21 (4), 1848–1855. doi:10.1021/acs.nanolett.0c04978

Liang, G., Didier, C., Guo, Z., Pang, W. K., and Peterson, V. K. (2020c). Understanding rechargeable battery function using in operando neutron powder diffraction. *Adv. Mater.* 32 (18), 1904528. doi:10.1002/adma.201904528

Liang, G., Peterson, V. K., See, K. W., Guo, Z., and Pang, W. K. (2020b). Developing high-voltage spinel LiNi0.5Mn1.5O4 cathodes for high-energy-density lithium-ion batteries: current achievements and future prospects. *J. Mater. Chem. A* 8 (31), 15373–15398. doi:10.1039/d0ta02812f

Liang, Q., Zhang, Q., Gou, J., Song, T., Arramel, H., Chen, H., et al. (2020a). Performance improvement by ozone treatment of 2D PdSe2. *ACS Nano* 14 (5), 5668–5677. doi:10.1021/acsnano.0c00180

Liang, Q., Zhang, Q., Zhao, X., Liu, M., and Wee, A. T. S. (2021). Defect engineering of two-dimensional transition-metal dichalcogenides: applications, challenges, and opportunities. *ACS Nano* 15 (2), 2165–2181. doi:10.1021/acsnano.0c09666

Liang, W., Nie, C., Du, J., Han, Y., Zhao, G., Yang, F., et al. (2023). Near-infrared photon upconversion and solar synthesis using lead-free nanocrystals. *Nat. Photonics* 17 (4), 346–353. doi:10.1038/s41566-023-01156-6

Lin, Z., Carvalho, B. R., Kahn, E., Lv, R., Rao, R., Terrones, H., et al. (2016). Defect engineering of two-dimensional transition metal dichalcogenides. *2D Mater.* 3 (2), 022002. doi:10.1088/2053-1583/3/2/022002

Lingerfelt, D. B., Ganesh, P., Jakowski, J., and Sumpter, B. G. (2019). Electronically nonadiabatic structural transformations promoted by electron beams. *Adv. Funct. Mater.* 29 (52), 1901901. doi:10.1002/adfm.201901901

Lingerfelt, D. B., Ganesh, P., Jakowski, J., and Sumpter, B. G. (2020). Understanding beam-induced electronic excitations in materials. *J. Chem. Theory Comput.* 16 (2), 1200–1214. doi:10.1021/acs.jctc.9b00792

Lingerfelt, D. B., Yu, T., Yoshimura, A., Ganesh, P., Jakowski, J., and Sumpter, B. G. (2021). Nonadiabatic effects on defect diffusion in silicon-doped nanographenes. *Nano Lett.* 21 (1), 236–242. doi:10.1021/acs.nanolett.0c03587

Liu, B., Cooper, V. R., Xu, H., Xiao, H., Zhang, Y., and Weber, W. J. (2014a). Composition dependent intrinsic defect structures in SrTiO3. *Phys. Chem. Chem. Phys.* 16 (29), 15590–15596. doi:10.1039/c4cp01510j

Liu, D., Hamel-Paquet, J., Trottier, J., Barray, F., Gariépy, V., Hovington, P., et al. (2012). Synthesis of pure phase disordered LiMn1.45Cr0.1Ni0.45O4 by a post-annealing method. *J. Power Sources* 217, 400–406. doi:10.1016/j.jpowsour.2012.06.063

Liu, D., Zhu, W., Trottier, J., Gagnon, C., Barray, F., Guerfi, A., et al. (2014b). Spinel materials for high-voltage cathodes in Li-ion batteries. *RSC Adv.* 4 (1), 154–167. doi:10.1039/c3ra45706k

Liu, G., Zhang, J., Zhang, X., Du, Y., Zhang, K., Li, G., et al. (2017). Study on oxygen deficiency in spinel LiNi0.5Mn1.5O4 and its Fe and Cr-doped compounds. *J. Alloys Compd.* 725, 580–586. doi:10.1016/j.jallcom.2017.07.202

Liu, J., and Manthiram, A. (2009). Understanding the improved electrochemical performances of Fe-substituted 5 V spinel cathode LiMn1.5Ni0.5O4. *J. Phys. Chem. C* 113 (33), 15073–15079. doi:10.1021/jp904276t

Lopez-Bezanilla, A., Ganesh, P., and Littlewood, P. B. (2015a). Magnetism and metal-insulator transition in oxygen-deficient SrTiO3. *Phys. Rev. B* 92 (11), 115112. doi:10.1103/physrevb.92.115112

Lopez-Bezanilla, A., Ganesh, P., and Littlewood, P. B. (2015b). Research Update: plentiful magnetic moments in oxygen deficient SrTiO3. *Apl. Mater.* 3 (10). doi:10.1063/1.4932347

Lu, J., Carvalho, A., Chan, X. K., Liu, H., Liu, B., Tok, E. S., et al. (2015). Atomic healing of defects in transition metal dichalcogenides. *Nano Lett.* 15 (5), 3524–3532. doi:10.1021/acs.nanolett.5b00952

Lu, X. F., Zhang, S. L., Sim, W. L., Gao, S., and Lou, X. W. (2021). Phosphorized CoNi2S4 yolk-shell spheres for highly efficient hydrogen production via water and urea electrolysis. *Angew. Chem. Int. Ed.* 60 (42), 22885–22891. doi:10.1002/anie.202108563

Lukowski, M. A., Daniel, A. S., Meng, F., Forticaux, A., Li, L., and Jin, S. (2013). Enhanced hydrogen evolution catalysis from chemically exfoliated metallic MoS2 nanosheets. *J. Am. Chem. Soc.* 135 (28), 10274–10277. doi:10.1021/ja404523s

Lun, Z., Ouyang, B., Kitchaev, D. A., Clément, R. J., Papp, J. K., Balasubramanian, M., et al. (2019). Improved cycling performance of Li-excess cation-disordered cathode materials upon fluorine substitution. *Adv. Energy Mater.* 9 (2), 1802959. doi:10.1002/aenm.201802959

Luo, S., Li, M., Fung, V., Sumpter, B. G., Liu, J., Wu, Z., et al. (2021). New insights into the bulk and surface defect structures of ceria nanocrystals from neutron scattering study. *Chem. Mater.* 33 (11), 3959–3970. doi:10.1021/acs.chemmater.1c00156

Lv, Y., Pan, C., Ma, X., Zong, R., Bai, X., and Zhu, Y. (2013). Production of visible activity and UV performance enhancement of ZnO photocatalyst via vacuum deoxidation. *Appl. Catal. B Environ.* 138-139, 26–32. doi:10.1016/j.apcatb.2013.02.011

Madsen, J., Liu, P., Kling, J., Wagner, J. B., Hansen, T. W., Winther, O., et al. (2018). A deep learning approach to identify local structures in atomic-resolution transmission electron microscopy images. *Adv. Theory Simulations* 1 (8), 1800037. doi:10.1002/adts.201800037

Makarov, N. S., Ramasamy, K., Jackson, A., Velarde, A., Castaneda, C., Archuleta, N., et al. (2019). Fiber-coupled luminescent concentrators for medical diagnostics, agriculture, and telecommunications. *ACS Nano* 13 (8), 9112–9121. doi:10.1021/acsnano.9b03335

Makkar, P., and Ghosh, N. N. (2021). A review on the use of DFT for the prediction of the properties of nanomaterials. *RSC Adv.* 11 (45), 27897–27924. doi:10.1039/d1ra04876g

Makov, G., and Payne, M. C. (1995). Periodic boundary conditions in *ab initio* calculations. *Phys. Rev. B* 51 (7), 4014–4022. doi:10.1103/physrevb.51.4014

Maksov, A., Dyck, O., Wang, K., Xiao, K., Geohegan, D. B., Sumpter, B. G., et al. (2019). Deep learning analysis of defect and phase evolution during electron beam-induced transformations in WS2. *npj Comput. Mater.* 5 (1), 12. doi:10.1038/s41524-019-0152-9

Manthiram, A. (2020). A reflection on lithium-ion battery cathode chemistry. *Nat. Commun.* 11 (1), 1550. doi:10.1038/s41467-020-15355-0

Manzeli, S., Ovchinnikov, D., Pasquier, D., Yazyev, O. V., and Kis, A. (2017). 2D transition metal dichalcogenides. *Nat. Rev. Mater.* 2 (8), 17033. doi:10.1038/natrevmats.2017.33

Mao, C., Zuo, F., Hou, Y., Bu, X., and Feng, P. (2014). *In situ* preparation of a Ti3+ self-doped TiO2 film with enhanced activity as photoanode by N2H4 reduction. *Angew. Chem. Int. Ed.* 53 (39), 10485–10489. doi:10.1002/anie.201406017

Megía, P. J., Vizcaíno, A. J., Calles, J. A., and Carrero, A. (2021). Hydrogen production technologies: from fossil fuels toward renewable sources. A mini review. *Energy & Fuels* 35 (20), 16403–16415. doi:10.1021/acs.energyfuels.1c02501

Meinardi, F., Bruni, F., and Brovelli, S. (2017). Luminescent solar concentrators for building-integrated photovoltaics. *Nat. Rev. Mater.* 2 (12), 17072. doi:10.1038/natrevmats.2017.72

Meinardi, F., McDaniel, H., Carulli, F., Colombo, A., Velizhanin, K. A., Makarov, N. S., et al. (2015). Highly efficient large-area colourless luminescent solar concentrators using heavy-metal-free colloidal quantum dots. *Nat. Nanotechnol.* 10 (10), 878–885. doi:10.1038/nnano.2015.178

Merdrignac, O. M., Moseley, P. T., Peat, R., Sofield, C. J., and Sugden, S. (1992). The modification of gas-sensing properties of semiconducting oxides by treatment with ionizing radiation. *Sensors Actuators B Chem.* 7 (1), 651–655. doi:10.1016/0925-4005(92)80380-g

Meulenberg, R. W., van Buuren, T., Hanif, K. M., Willey, T. M., Strouse, G. F., and Terminello, L. J. (2004). Structure and composition of Cu-doped CdSe nanocrystals using soft X-ray absorption spectroscopy. *Nano Lett.* 4 (11), 2277–2285. doi:10.1021/nl048738s

Mikulec, F. V., Kuno, M., Bennati, M., Hall, D. A., Griffin, R. G., and Bawendi, M. G. (2000). Organometallic synthesis and spectroscopic characterization of manganese-doped CdSe nanocrystals. *J. Am. Chem. Soc.* 122 (11), 2532–2540. doi:10.1021/ja991249n

Mizushima, K., Jones, P. C., Wiseman, P. J., and Goodenough, J. (1981). LixCoO2 (0<x≤1): a new cathode material for batteries of high energy density. *Solid State Ionics* 3-4, 171–174. doi:10.1016/0167-2738(81)90077-1

Moody, G., Tran, K., Lu, X., Autry, T., Fraser, J. M., Mirin, R. P., et al. (2018). Microsecond Valley lifetime of defect-bound excitons in monolayer WSe2. *Phys. Rev. Lett.* 121 (5), 057403. doi:10.1103/physrevlett.121.057403

Mosquera-Lois, I., Kavanagh, S. R., Klarbring, J., Tolborg, K., and Walsh, A. (2023). Imperfections are not 0 K: free energy of point defects in crystals. *Chem. Soc. Rev.* 52 (17), 5812–5826. doi:10.1039/d3cs00432e

Nagamine, G., Nunciaroni, H. B., McDaniel, H., Efros, A. L., de Brito Cruz, C. H., and Padilha, L. A. (2018). Evidence of band-edge hole levels inversion in spherical CuInS2 quantum dots. *Nano Lett.* 18 (10), 6353–6359. doi:10.1021/acs.nanolett.8b02707

Najafi, A., Sharma, M., Delikanli, S., Bhattacharya, A., Murphy, J. R., Pientka, J., et al. (2021). Light-induced paramagnetism in colloidal Ag+-Doped CdSe nanoplatelets. *J. Phys. Chem. Lett.* 12 (11), 2892–2899. doi:10.1021/acs.jpclett.1c00398

Nakajima, M., and Yabuuchi, N. (2017). Lithium-excess cation-disordered rocksalt-type oxide with nanoscale phase segregation: Li1.25Nb0.25V0.5O2. *Chem. Mater.* 29 (16), 6927–6935. doi:10.1021/acs.chemmater.7b02343

Nakamura, S. (1998). The roles of structural imperfections in InGaN-based blue light-emitting diodes and laser diodes. *Science* 281 (5379), 956–961. doi:10.1126/science.281.5379.956

Nan, H., Wang, Z., Wang, W., Liang, Z., Lu, Y., Chen, Q., et al. (2014). Strong photoluminescence enhancement of MoS2 through defect engineering and oxygen bonding. *ACS Nano* 8 (6), 5738–5745. doi:10.1021/nn500532f

Nelson, H. D., and Gamelin, D. R. (2018). Valence-band electronic structures of Cu+-Doped ZnS, alloyed Cu–in–Zn–S, and ternary CuInS2 nanocrystals: a unified description of photoluminescence across compositions. *J. Phys. Chem. C* 122 (31), 18124–18133. doi:10.1021/acs.jpcc.8b05286

Nguyen, G. D., Liang, L., Zou, Q., Fu, M., Oyedele, A. D., Sumpter, B. G., et al. (2018). 3D imaging and manipulation of subsurface selenium vacancies in PdSe2. *Phys. Rev. Lett.* 121 (8), 086101. doi:10.1103/physrevlett.121.086101

Nikolaidis, P., and Poullikkas, A. (2017). A comparative overview of hydrogen production processes. *Renew. Sustain. Energy Rev.* 67, 597–611. doi:10.1016/j.rser.2016.09.044

Nishizawa, M., and Yamamura, S. (1998). Irreversible conductivity change of Li1–CoO2 on electrochemical lithium insertion/extraction, desirable for battery applications. *Chem. Commun.* (16), 1631–1632. doi:10.1039/a802962h

Niu, P., Yin, L.-C., Yang, Y.-Q., Liu, G., and Cheng, H.-M. (2014). Increasing the visible light absorption of graphitic carbon nitride (melon) photocatalysts by homogeneous self-modification with nitrogen vacancies. *Adv. Mater.* 26 (47), 8046–8052. doi:10.1002/adma.201404057

Norris, D. J., Yao, N., Charnock, F. T., and Kennedy, T. A. (2001). High-quality manganese-doped ZnSe nanocrystals. *Nano Lett.* 1 (1), 3–7. doi:10.1021/nl005503h

Ouyang, B., Artrith, N., Lun, Z., Jadidi, Z., Kitchaev, D. A., Ji, H., et al. (2020). Effect of fluorination on lithium transport and short-range order in disordered-rocksalt-type lithium-ion battery cathodes. *Adv. Energy Mater.* 10 (10), 1903240. doi:10.1002/aenm.201903240

Oyedele, A. D., Yang, S., Feng, T., Haglund, A. V., Gu, Y., Puretzky, A. A., et al. (2019). Defect-mediated phase transformation in anisotropic two-dimensional PdSe2 crystals for seamless electrical contacts. *J. Am. Chem. Soc.* 141 (22), 8928–8936. doi:10.1021/jacs.9b02593

Paier, J., Asahi, R., Nagoya, A., and Kresse, G. (2009). Cu_2ZnSnS_4 as a potential photovoltaic material: a hybrid Hartree-Fock density functional theory study. *Phys. Rev. B* 79 (11), 115126. doi:10.1103/physrevb.79.115126

Papakonstantinou, I., Portnoi, M., and Debije, M. G. (2021). The hidden potential of luminescent solar concentrators. *Adv. Energy Mater.* 11 (3), 2002883. doi:10.1002/aenm.202002883

Parsons, R. (1958). The rate of electrolytic hydrogen evolution and the heat of adsorption of hydrogen. *Trans. Faraday Soc.* 54 (0), 1053–1063. doi:10.1039/tf9585401053

Patil, S., Darbar, D., Self, E. C., Malkowski, T., Wu, V. C., Giovine, R., et al. (2023). Alternate synthesis method for high-performance manganese rich cation disordered rocksalt cathodes. *Adv. Energy Mater.* 13 (4), 2203207. doi:10.1002/aenm.202203207

Peimyoo, N., Shang, J., Cong, C., Shen, X., Wu, X., Yeow, E. K. L., et al. (2013). Nonblinking, intense two-dimensional light emitter: monolayer WS2 triangles. *ACS Nano* 7 (12), 10985–10994. doi:10.1021/nn4046002

Peng, R., Liang, L., Hood, Z. D., Boulesbaa, A., Puretzky, A., Ievlev, A. V., et al. (2016). In-plane heterojunctions enable multiphasic two-dimensional (2D) MoS2 nanosheets as efficient photocatalysts for hydrogen evolution from water reduction. *ACS Catal.* 6 (10), 6723–6729. doi:10.1021/acscatal.6b02076

Piao, J.-Y., Sun, Y.-G., Duan, S.-Y., Cao, A.-M., Wang, X.-L., Xiao, R.-J., et al. (2018). Stabilizing cathode materials of lithium-ion batteries by controlling interstitial sites on the surface. *Chem* 4 (7), 1685–1695. doi:10.1016/j.chempr.2018.04.020

Pietryga, J. M., Park, Y.-S., Lim, J., Fidler, A. F., Bae, W. K., Brovelli, S., et al. (2016). Spectroscopic and device aspects of nanocrystal quantum dots. *Chem. Rev.* 116 (18), 10513–10622. doi:10.1021/acs.chemrev.6b00169

Pinchetti, V., Di, Q., Lorenzon, M., Camellini, A., Fasoli, M., Zavelani-Rossi, M., et al. (2018). Excitonic pathway to photoinduced magnetism in colloidal nanocrystals with nonmagnetic dopants. *Nat. Nanotechnol.* 13 (2), 145–151. doi:10.1038/s41565-017-0024-8

Pralong, V., Gopal, V., Caignaert, V., Duffort, V., and Raveau, B. (2012). Lithium-rich rock-salt-type vanadate as energy storage cathode: Li2–xVO3. *Chem. Mater.* 24 (1), 12–14. doi:10.1021/cm203281q

Quadir, S., Qorbani, M., Sabbah, A., Wu, T.-S., Anbalagan, A. k., Chen, W.-T., et al. (2022). Short- and long-range cation disorder in (AgxCu1−x)2ZnSnSe4 kesterites. *Chem. Mater.* 34 (15), 7058–7068. doi:10.1021/acs.chemmater.2c01489

Rani, S., Bhatnagar, M. C., Roy, S. C., Puri, N. K., and Kanjilal, D. (2008). p-Type gas-sensing behaviour of undoped SnO2 thin films irradiated with a high-energy ion beam. *Sensors Actuators B Chem.* 135 (1), 35–39. doi:10.1016/j.snb.2008.07.014

Rice, W. D., Liu, W., Baker, T. A., Sinitsyn, N. A., Klimov, V. I., and Crooker, S. A. (2016). Revealing giant internal magnetic fields due to spin fluctuations in magnetically doped colloidal nanocrystals. *Nat. Nanotechnol.* 11 (2), 137–142. doi:10.1038/nnano.2015.258

Rice, W. D., McDaniel, H., Klimov, V. I., and Crooker, S. A. (2014). Magneto-optical properties of CuInS2 nanocrystals. *J. Phys. Chem. Lett.* 5 (23), 4105–4109. doi:10.1021/jz502154m

Robertson, J., and Falabretti, B. (2011). "Electronic structure of transparent conducting oxides," in *Handbook of transparent conductors*. Editor D. S. Ginley (Boston, MA: Springer US), 27–50.

Roccapriore, K. M., Boebinger, M. G., Dyck, O., Ghosh, A., Unocic, R. R., Kalinin, S. V., et al. (2022). Probing electron beam induced transformations on a single-defect level via automated scanning transmission electron microscopy. *ACS Nano* 16 (10), 17116–17127. doi:10.1021/acsnano.2c07451

Sahu, B. K., Das, A., Prasad, A. K., and Mangamma, G. (2019). The role of in-plane oxygen vacancy defects in SnO2 nanoparticles for CH4 sensing. *J. Nanosci. Nanotechnol.* 19 (12), 7764–7770. doi:10.1166/jnn.2019.16736

Saifullah, M., Gwak, J., and Yun, J. H. (2016). Comprehensive review on material requirements, present status, and future prospects for building-integrated semitransparent photovoltaics (BISTPV). *J. Mater. Chem. A* 4 (22), 8512–8540. doi:10.1039/c6ta01016d

Sang, X., Li, X., Zhao, W., Dong, J., Rouleau, C. M., Geohegan, D. B., et al. (2018). *In situ* edge engineering in two-dimensional transition metal dichalcogenides. *Nat. Commun.* 9 (1), 2051. doi:10.1038/s41467-018-04435-x

Sark, W. G. v., Barnham, K. W. J., Slooff, L. H., Chatten, A. J., Büchtemann, A., Meyer, A., et al. (2008). Luminescent Solar Concentrators - a review of recent results. *Opt. Express* 16 (26), 21773–21792. doi:10.1364/oe.16.021773

Schleussner, C.-F., Rogelj, J., Schaeffer, M., Lissner, T., Licker, R., Fischer, E. M., et al. (2016). Science and policy characteristics of the Paris Agreement temperature goal. *Nat. Clim. Change* 6 (9), 827–835. doi:10.1038/nclimate3096

Sebastian, L., and Gopalakrishnan, J. (2003). Li2MTiO4 (M=Mn, Fe, Co, Ni): new cation-disordered rocksalt oxides exhibiting oxidative deintercalation of lithium. Synthesis of an ordered Li2NiTiO4. *J. Solid State Chem.* 172 (1), 171–177. doi:10.1016/s0022-4596(03)00010-0

Shabaev, A., Mehl, M. J., and Efros, A. L. (2015). Energy band structure of CuInS2 and optical spectra of CuInS2 nanocrystals. *Phys. Rev. B* 92 (3), 035431. doi:10.1103/physrevb.92.035431

Shawkat, M. S., Gil, J., Han, S. S., Ko, T.-J., Wang, M., Dev, D., et al. (2020). Thickness-independent semiconducting-to-metallic conversion in wafer-scale two-dimensional

PtSe2 layers by plasma-driven chalcogen defect engineering. *ACS Appl. Mater. Interfaces* 12 (12), 14341–14351. doi:10.1021/acsami.0c00116

Shi, S., Gao, D., Xu, Q., Yang, Z., and Xue, D. (2014). Singly-charged oxygen vacancy-induced ferromagnetism in mechanically milled SnO2powders. *RSC Adv.* 4 (85), 45467–45472. doi:10.1039/c4ra05475j

Shi, Y., Li, H., and Li, L.-J. (2015). Recent advances in controlled synthesis of two-dimensional transition metal dichalcogenides via vapour deposition techniques. *Chem. Soc. Rev.* 44 (9), 2744–2756. doi:10.1039/c4cs00256c

Shin, D. W., Bridges, C. A., Huq, A., Paranthaman, M. P., and Manthiram, A. (2012). Role of cation ordering and surface segregation in high-voltage spinel LiMn1.5Ni0.5–xMxO4 (M = Cr, Fe, and Ga) cathodes for lithium-ion batteries. *Chem. Mater.* 24 (19), 3720–3731. doi:10.1021/cm301844w

Singh, R., Liu, W., Lim, J., Robel, I., and Klimov, V. I. (2019). Hot-electron dynamics in quantum dots manipulated by spin-exchange Auger interactions. *Nat. Nanotechnol.* 14 (11), 1035–1041. doi:10.1038/s41565-019-0548-1

Srivastava, B. B., Jana, S., and Pradhan, N. (2011). Doping Cu in semiconductor nanocrystals: some old and some new physical insights. *J. Am. Chem. Soc.* 133 (4), 1007–1015. doi:10.1021/ja1089809

Stouwdam, J. W., and Janssen, R. A. J. (2009). Electroluminescent Cu-doped CdS quantum dots. *Adv. Mater.* 21 (28), 2916–2920. doi:10.1002/adma.200803223

Suh, J., Park, T.-E., Lin, D.-Y., Fu, D., Park, J., Jung, H. J., et al. (2014). Doping against the native propensity of MoS2: degenerate hole doping by cation substitution. *Nano Lett.* 14 (12), 6976–6982. doi:10.1021/nl503251h

Sutton, C., and Levchenko, S. V. (2020). First-principles atomistic thermodynamics and configurational entropy. *Front. Chem.* 8, 757. doi:10.3389/fchem.2020.00757

Szymanski, N. J., Lun, Z., Liu, J., Self, E. C., Bartel, C. J., Nanda, J., et al. (2023). Modeling short-range order in disordered rocksalt cathodes by pair distribution function analysis. *Chem. Mater.* 35 (13), 4922–4934. doi:10.1021/acs.chemmater.2c03827

Szymanski, N. J., Zeng, Y., Bennett, T., Patil, S., Keum, J. K., Self, E. C., et al. (2022). Understanding the fluorination of disordered rocksalt cathodes through rational exploration of synthesis pathways. *Chem. Mater.* 34 (15), 7015–7028. doi:10.1021/acs.chemmater.2c01474

Tan, Z. H., Kong, X. Y., Ng, B.-J., Soo, H. S., Mohamed, A. R., and Chai, S.-P. (2023). Recent advances in defect-engineered transition metal dichalcogenides for enhanced electrocatalytic hydrogen evolution: perfecting imperfections. *ACS Omega* 8 (2), 1851–1863. doi:10.1021/acsomega.2c06524

Thackeray, M. M., David, W. I. F., Bruce, P. G., and Goodenough, J. B. (1983). Lithium insertion into manganese spinels. *Mater. Res. Bull.* 18 (4), 461–472. doi:10.1016/0025-5408(83)90138-1

Tongay, S., Narang, D. S., Kang, J., Fan, W., Ko, C., Luce, A. V., et al. (2014). Two-dimensional semiconductor alloys: monolayer Mo1−xWxSe2. *Appl. Phys. Lett.* 104 (1). doi:10.1063/1.4834358

Trentino, A., Madsen, J., Mittelberger, A., Mangler, C., Susi, T., Mustonen, K., et al. (2021). Atomic-level structural engineering of graphene on a mesoscopic scale. *Nano Lett.* 21 (12), 5179–5185. doi:10.1021/acs.nanolett.1c01214

Tsai, J.-Y., Pan, J., Lin, H., Bansil, A., and Yan, Q. (2022). Antisite defect qubits in monolayer transition metal dichalcogenides. *Nat. Commun.* 13 (1), 492. doi:10.1038/s41467-022-28133-x

Tuller, H. L., and Bishop, S. R. (2010). Tailoring material properties through defect engineering. *Chem. Lett.* 39 (12), 1226–1231. doi:10.1246/cl.2010.1226

Tuller, H. L., and Bishop, S. R. (2011). Point defects in oxides: tailoring materials through defect engineering. *Annu. Rev. Mater. Res.* 41 (1), 369–398. doi:10.1146/annurev-matsci-062910-100442

Ueng, H. Y., and Hwang, H. L. (1989). The defect structure of CuInS2. part I: intrinsic defects. *J. Phys. Chem. Solids* 50 (12), 1297–1305. doi:10.1016/0022-3697(89)90403-4

Ueng, H. Y., and Hwang, H. L. (1990). The defect structure of CuInS2. part II: thermal annealing defects. *J. Phys. Chem. Solids* 51 (1), 1–10. doi:10.1016/0022-3697(90)90125-y

Urban, A., Lee, J., and Ceder, G. (2014). The configurational space of rocksalt-type oxides for high-capacity lithium battery electrodes. *Adv. Energy Mater.* 4 (13), 1400478. doi:10.1002/aenm.201400478

van der Zande, A. M., Huang, P. Y., Chenet, D. A., Berkelbach, T. C., You, Y., Lee, G.-H., et al. (2013). Grains and grain boundaries in highly crystalline monolayer molybdenum disulphide. *Nat. Mater.* 12 (6), 554–561. doi:10.1038/nmat3633

Velarde, A. R. M., Bartlett, E. R., Makarov, N. S., Castañeda, C., Jackson, A., Ramasamy, K., et al. (2020). Optimizing the aesthetics of high-performance CuInS2/ZnS quantum dot luminescent solar concentrator windows. *ACS Appl. Energy Mater.* 3 (9), 8159–8163. doi:10.1021/acsaem.0c01288

Venkatraman, S., Shin, Y., and Manthiram, A. (2003). Phase relationships and structural and chemical stabilities of charged Li1 − x CoO2 − δ and Li1 − x Ni0.85Co0.15 O 2 − δ cathodes. *Electrochem. Solid State Lett.* 6, A9. doi:10.1149/1.1525430

Vijay, V., Harish, S., Archana, J., and Navaneethan, M. (2021). Cation disorder and bond anharmonicity synergistically boosts the thermoelectric performance of p-type AgSbSe2. *CrystEngComm* 23 (32), 5522–5530. doi:10.1039/d1ce00599e

Viswanatha, R., Brovelli, S., Pandey, A., Crooker, S. A., and Klimov, V. I. (2011). Copper-doped inverted core/shell Nanocrystals with “permanent” optically active holes. *Nano Lett.* 11 (11), 4753–4758. doi:10.1021/nl202572c

Vlaskin, V. A., Barrows, C. J., Erickson, C. S., and Gamelin, D. R. (2013). Nanocrystal diffusion doping. *J. Am. Chem. Soc.* 135 (38), 14380–14389. doi:10.1021/ja4072207

Voiry, D., Salehi, M., Silva, R., Fujita, T., Chen, M., Asefa, T., et al. (2013). Conducting MoS2 nanosheets as catalysts for hydrogen evolution reaction. *Nano Lett.* 13 (12), 6222–6227. doi:10.1021/nl403661s

Wandt, J., Freiberg, A. T. S., Ogrodnik, A., and Gasteiger, H. A. (2018). Singlet oxygen evolution from layered transition metal oxide cathode materials and its implications for lithium-ion batteries. *Mater. Today* 21 (8), 825–833. doi:10.1016/j.mattod.2018.03.037

Wang, C., Wu, D., Wang, P., Ao, Y., Hou, J., and Qian, J. (2015a). Effect of oxygen vacancy on enhanced photocatalytic activity of reduced ZnO nanorod arrays. *Appl. Surf. Sci.* 325, 112–116. doi:10.1016/j.apsusc.2014.11.003

Wang, J., Chen, R., Xiang, L., and Komarneni, S. (2018a). Synthesis, properties and applications of ZnO nanomaterials with oxygen vacancies: a review. *Ceram. Int.* 44 (7), 7357–7377. doi:10.1016/j.ceramint.2018.02.013

Wang, J., Lin, W., Wu, B., and Zhao, J. (2014). Syntheses and electrochemical properties of the Na-doped LiNi0.5Mn1.5O4 cathode materials for lithium-ion batteries. *Electrochimica Acta* 145, 245–253. doi:10.1016/j.electacta.2014.07.140

Wang, J., Nie, P., Xu, G., Jiang, J., Wu, Y., Fu, R., et al. (2018c). High-voltage LiNi0.45Cr0.1Mn1.45O4 cathode with superlong cycle performance for wide temperature lithium-ion batteries. *Adv. Funct. Mater.* 28 (4), 1704808. doi:10.1002/adfm.201704808

Wang, M., Chen, X., Yao, H., Lin, G., Lee, J., Chen, Y., et al. (2022a). Research progress in lithium-excess disordered rock-salt oxides cathode. *ENERGY & Environ. Mater.* 5 (4), 1139–1154. doi:10.1002/eem2.12413

Wang, R., Huang, B., Qu, Z., Gong, Y., He, B., and Wang, H. (2019). Research on the kinetic properties of the cation disordered rock-salt Li-excess Li1.25Nb0.25Mn0.5O2 material. *Solid State Ionics* 339, 114999. doi:10.1016/j.ssi.2019.06.007

Wang, R., Li, X., Liu, L., Lee, J., Seo, D.-H., Bo, S.-H., et al. (2015b). A disordered rock-salt Li-excess cathode material with high capacity and substantial oxygen redox activity: Li1.25Nb0.25Mn0.5O2. *Electrochem. Commun.* 60, 70–73. doi:10.1016/j.elecom.2015.08.003

Wang, S., Robertson, A., and Warner, J. H. (2018b). Atomic structure of defects and dopants in 2D layered transition metal dichalcogenides. *Chem. Soc. Rev.* 47 (17), 6764–6794. doi:10.1039/c8cs00236c

Wang, X., Wu, J., Zhang, Y., Sun, Y., Ma, K., Xie, Y., et al. (2022b). Vacancy defects in 2D transition metal dichalcogenide electrocatalysts: from aggregated to atomic configuration. *Adv. Mater.*, 2206576. doi:10.1002/adma.202206576

Wei, C., Rao, R. R., Peng, J., Huang, B., Stephens, I. E. L., Risch, M., et al. (2019). Recommended practices and benchmark activity for hydrogen and oxygen electrocatalysis in water splitting and fuel cells. *Adv. Mater.* 31 (31), 1806296. doi:10.1002/adma.201806296

Whittingham, M. S. (1976). Electrical energy storage and intercalation chemistry. *Science* 192 (4244), 1126–1127. doi:10.1126/science.192.4244.1126

Wu, S., Sun, W., Sun, J., Hood, Z. D., Yang, S.-Z., Sun, L., et al. (2018). Surface reorganization leads to enhanced photocatalytic activity in defective BiOCl. *Chem. Mater.* 30 (15), 5128–5136. doi:10.1021/acs.chemmater.8b01629

Wu, X., Gu, Y., Ge, R., Serna, M. I., Huang, Y., Lee, J. C., et al. (2022). Electron irradiation-induced defects for reliability improvement in monolayer MoS2-based conductive-point memory devices. *npj 2D Mater. Appl.* 6 (1), 31. doi:10.1038/s41699-022-00306-8

Wu, Z., Zhao, W., Jiang, J., Zheng, T., You, Y., Lu, J., et al. (2017). Defect activated photoluminescence in WSe2 monolayer. *J. Phys. Chem. C* 121 (22), 12294–12299. doi:10.1021/acs.jpcc.7b03585

Xia, C., Meeldijk, J. D., Gerritsen, H. C., and de Mello Donega, C. (2017). Highly luminescent water-dispersible NIR-emitting wurtzite CuInS2/ZnS core/shell colloidal quantum dots. *Chem. Mater.* 29 (11), 4940–4951. doi:10.1021/acs.chemmater.7b01258

Xia, C., Tamarat, P., Hou, L., Busatto, S., Meeldijk, J. D., de Mello Donega, C., et al. (2021). Unraveling the emission pathways in copper indium sulfide quantum dots. *ACS Nano* 15 (11), 17573–17581. doi:10.1021/acsnano.1c04909

Xiong, J., Di, J., Xia, J., Zhu, W., and Li, H. (2018). Surface defect engineering in 2D nanomaterials for photocatalysis. *Adv. Funct. Mater.* 28 (39), 1801983. doi:10.1002/adfm.201801983

Xiong, Y., Lin, Y., Wang, X., Zhao, Y., and Tian, J. (2022). Defect engineering on SnO2 nanomaterials for enhanced gas sensing performances. *Adv. Powder Mater.* 1 (3), 100033. doi:10.1016/j.apmate.2022.02.001

Xu, J., Shao, G., Tang, X., Lv, F., Xiang, H., Jing, C., et al. (2022). Frenkel-defected monolayer MoS2 catalysts for efficient hydrogen evolution. *Nat. Commun.* 13 (1), 2193. doi:10.1038/s41467-022-29929-7

Xu, Y., Zheng, C., Wang, S., and Hou, Y. (2015). 3D arrays of molybdenum sulphide nanosheets on Mo meshes: efficient electrocatalysts for hydrogen evolution reaction. *Electrochimica Acta* 174, 653–659. doi:10.1016/j.electacta.2015.06.040

Yablonovitch, E. (1980). Thermodynamics of the fluorescent planar concentrator. *J. Opt. Soc. Am.* 70 (11), 1362–1363. doi:10.1364/josa.70.001362

Yabuuchi, N., Nakayama, M., Takeuchi, M., Komaba, S., Hashimoto, Y., Mukai, T., et al. (2016a). Origin of stabilization and destabilization in solid-state redox reaction of oxide ions for lithium-ion batteries. *Nat. Commun.* 7 (1), 13814. doi:10.1038/ncomms13814

Yabuuchi, N., Takeuchi, M., Komaba, S., Ichikawa, S., Ozaki, T., and Inamasu, T. (2016b). Synthesis and electrochemical properties of Li1.3Nb0.3V0.4O2 as a positive electrode material for rechargeable lithium batteries. *Chem. Commun.* 52 (10), 2051–2054. doi:10.1039/c5cc08034g

Yang, J., Wang, Y., Lagos, M. J., Manichev, V., Fullon, R., Song, X., et al. (2019). Single atomic vacancy catalysis. *ACS Nano* 13 (9), 9958–9964. doi:10.1021/acsnano.9b05226

Yang, S.-H., Choi, W., Cho, B. W., Agyapong-Fordjour, F.O.-T., Park, S., Yun, S. J., et al. (2021). Deep learning-assisted quantification of atomic dopants and defects in 2D materials. *Adv. Sci.* 8 (16), 2101099. doi:10.1002/advs.202101099

Ye, K., Siah, S. C., Erslev, P. T., Akey, A., Settens, C., Hoque, M. S. B., et al. (2019). Tuning electrical, optical, and thermal properties through cation disorder in Cu2ZnSnS4. *Chem. Mater.* 31 (20), 8402–8412. doi:10.1021/acs.chemmater.9b02287

Ye, L., Deng, K., Xu, F., Tian, L., Peng, T., and Zan, L. (2012). Increasing visible-light absorption for photocatalysis with black BiOCl. *Phys. Chem. Chem. Phys.* 14 (1), 82–85. doi:10.1039/c1cp22876e

Ye, L., Jin, X., Leng, Y., Su, Y., Xie, H., and Liu, C. (2015). Synthesis of black ultrathin BiOCl nanosheets for efficient photocatalytic H2 production under visible light irradiation. *J. Power Sources* 293, 409–415. doi:10.1016/j.jpowsour.2015.05.101

Ye, L., Zan, L., Tian, L., Peng, T., and Zhang, J. (2011). The {001} facets-dependent high photoactivity of BiOCl nanosheets. *Chem. Commun.* 47 (24), 6951–6953. doi:10.1039/c1cc11015b

Yoo, H.-I., and Tuller, H. L. (1987). Iron-excess manganese ferrite: electrical conductivity and cation distributions. *J. Am. Ceram. Soc.* 70 (6), 388–392. doi:10.1111/j.1151-2916.1987.tb05656.x

Yu, Z., Qu, X., Dou, A., Su, M., Liu, Y., and Wu, F. (2019). Synthesis and redox mechanism of cation-disordered, rock-salt cathode-material Li–Ni–Ti–Nb–O compounds for a Li-ion battery. *ACS Appl. Mater. Interfaces* 11 (39), 35777–35787. doi:10.1021/acsami.9b12822

Yun, H. J., Lim, J., Fuhr, A. S., Makarov, N. S., Keene, S., Law, M., et al. (2018). Charge-transport mechanisms in CuInSexS2−x quantum-dot films. *ACS Nano* 12 (12), 12587–12596. doi:10.1021/acsnano.8b07179

Zan, R., Ramasse, Q. M., Jalil, R., Georgiou, T., Bangert, U., and Novoselov, K. S. (2013). Control of radiation damage in MoS2 by graphene encapsulation. *ACS Nano* 7 (11), 10167–10174. doi:10.1021/nn4044035

Zang, H., Li, H., Makarov, N. S., Velizhanin, K. A., Wu, K., Park, Y.-S., et al. (2017). Thick-Shell CuInS2/ZnS quantum Dots with suppressed "blinking" and narrow single-particle emission line widths. *Nano Lett.* 17 (3), 1787–1795. doi:10.1021/acs.nanolett.6b05118

Zeng, Q., Cui, Y., Zhu, L., and Yao, Y. (2020). Increasing oxygen vacancies at room temperature in SnO2 for enhancing ethanol gas sensing. *Mater. Sci. Semicond. Process.* 111, 104962. doi:10.1016/j.mssp.2020.104962

Zhang, G., Xie, C., Zhang, S., Zhang, S., and Xiong, Y. (2014b). Defect chemistry of the metal cation defects in the p- and n-doped SnO2 nanocrystalline films. *J. Phys. Chem. C* 118 (31), 18097–18109. doi:10.1021/jp503059e

Zhang, H., Gao, X., Cai, Q., Zhang, X., Tian, Y., Jia, M., et al. (2023). Recent progress and perspectives on cation disordered rock-salt material for advanced Li-ion batteries. *J. Mater. Chem. A* 11 (16), 8426–8452. doi:10.1039/d3ta00852e

Zhang, L., Yang, T., He, X., Zhang, W., Vinai, G., Tang, C. S., et al. (2020). Molecular beam epitaxy of two-dimensional vanadium-molybdenum diselenide alloys. *ACS Nano* 14 (9), 11140–11149. doi:10.1021/acsnano.0c02124

Zhang, M., Wu, J., Zhu, Y., Dumcenco, D. O., Hong, J., Mao, N., et al. (2014a). Two-dimensional molybdenum tungsten diselenide alloys: photoluminescence, Raman scattering, and electrical transport. *ACS Nano* 8 (7), 7130–7137. doi:10.1021/nn5020566

Zhang, Y., Chen, X., Huang, Y., Zhang, C., Li, F., and Shu, H. (2017). The role of intrinsic defects in electrocatalytic activity of monolayer VS2 basal planes for the hydrogen evolution reaction. *J. Phys. Chem. C* 121 (3), 1530–1536. doi:10.1021/acs.jpcc.6b11987

Zhao, Q., Stalin, S., Zhao, C.-Z., and Archer, L. A. (2020). Designing solid-state electrolytes for safe, energy-dense batteries. *Nat. Rev. Mater.* 5 (3), 229–252. doi:10.1038/s41578-019-0165-5

Zhao, X., Dan, J., Chen, J., Ding, Z., Zhou, W., Loh, K. P., et al. (2018). Atom-by-Atom fabrication of monolayer molybdenum membranes. *Adv. Mater.* 30 (23), 1707281. doi:10.1002/adma.201707281

Zheng, J., Xiao, J., Yu, X., Kovarik, L., Gu, M., Omenya, F., et al. (2012). Enhanced Li+ ion transport in LiNi0.5Mn1.5O4 through control of site disorder. *Phys. Chem. Chem. Phys.* 14 (39), 13515–13521. doi:10.1039/c2cp43007j

Zhong, G. B., Wang, Y. Y., Zhang, Z. C., and Chen, C. H. (2011). Effects of Al substitution for Ni and Mn on the electrochemical properties of LiNi0.5Mn1.5O4. *Electrochimica Acta* 56 (18), 6554–6561. doi:10.1016/j.electacta.2011.03.093

Zhong, Y., Li, W., Zhao, X., Jiang, X., Lin, S., Zhen, Z., et al. (2019). High-response room-temperature NO2 sensor and ultrafast humidity sensor based on SnO2 with rich oxygen vacancy. *ACS Appl. Mater. Interfaces* 11 (14), 13441–13449. doi:10.1021/acsami.9b01737

Zhou, W., Dong, L., Tan, L., and Tang, Q. (2021). First-principles study of sulfur vacancy concentration effect on the electronic structures and hydrogen evolution reaction of MoS2. *Nanotechnology* 32 (14), 145718. doi:10.1088/1361-6528/abd49f

Zhu, B. L., Xie, C. S., Zeng, D. W., Song, W. L., and Wang, A. H. (2005). Investigation of gas sensitivity of Sb-doped ZnO nanoparticles. *Mater. Chem. Phys.* 89 (1), 148–153. doi:10.1016/j.matchemphys.2004.08.028

Zhu, H., Wang, Q., Cheng, L., Addou, R., Kim, J., Kim, M. J., et al. (2017). Defects and surface structural stability of MoTe2 under vacuum annealing. *ACS Nano* 11 (11), 11005–11014. doi:10.1021/acsnano.7b04984

Zhuang, H. L., Ganesh, P., Cooper, V. R., Xu, H., and Kent, P. R. C. (2014). Understanding the interactions between oxygen vacancies at $SrTiO_3$ (001) surfaces. *Phys. Rev. B* 90 (6), 064106. doi:10.1103/physrevb.90.064106

Ziatdinov, M., Dyck, O., Li, X., Sumpter, B. G., Jesse, S., Vasudevan, R. K., et al. (2019). Building and exploring libraries of atomic defects in graphene: scanning transmission electron and scanning tunneling microscopy study. *Sci. Adv.* 5 (9), eaaw8989. doi:10.1126/sciadv.aaw8989

Ziatdinov, M., Dyck, O., Maksov, A., Li, X., Sang, X., Xiao, K., et al. (2017). Deep learning of atomically resolved scanning transmission electron microscopy images: chemical identification and tracking local transformations. *ACS Nano* 11 (12), 12742–12752. doi:10.1021/acsnano.7b07504

frontiers | Frontiers in Nanotechnology

TYPE Brief Research Report
PUBLISHED 21 February 2024
DOI 10.3389/fnano.2024.1291328

OPEN ACCESS

EDITED BY
John Fourkas,
University of Maryland, United States

REVIEWED BY
Mohammad K. Anvarifard,
University of Guilan, Iran
Yaping Dan,
Shanghai Jiao Tong University, China

*CORRESPONDENCE
Feng Xiong,
✉ f.xiong@pitt.edu
Haitao Liu,
✉ hliu@pitt.edu

†These authors have contributed equally to this work

RECEIVED 09 September 2023
ACCEPTED 08 February 2024
PUBLISHED 21 February 2024

CITATION
Bai R, Liu Y, Zhang B, Chen B, Xiong F and Liu H (2024), DNA-based doping and fabrication of PN diodes.
Front. Nanotechnol. 6:1291328.
doi: 10.3389/fnano.2024.1291328

DNA-based doping and fabrication of PN diodes

Ruobing Bai[1†], Yihan Liu[2†], Bomin Zhang[2], Beishan Chen[3], Feng Xiong[2*] and Haitao Liu[1*]

[1]Department of Chemistry, University of Pittsburgh, Pittsburgh, PA, United States, [2]Department of Electrical and Computer Engineering, University of Pittsburgh, Pittsburgh, PA, United States, [3]Department of Biological Sciences, University of Pittsburgh, Pittsburgh, PA, United States

This paper reports the fabrication of silicon PN diode by using DNA nanostructure as the etching template for SiO_2 and also as the n-dopant of Si. DNA nanotubes were deposited onto p-type silicon wafer that has a thermal SiO_2 layer. The DNA nanotubes catalyze the etching of SiO_2 by HF vapor to expose the underlying Si. The phosphate groups in the DNA nanotube were used as the doping source to locally n-dope the Si wafer to form vertical P-N junctions. Prototype PN diodes were fabricated and exhibited expected blockage behavior with a knee voltage of *ca.* 0.7 V. Our work highlights the potential of DNA nanotechnology in future fabrication of nanoelectronics.

KEYWORDS

DNA nanotechnology, lithography, semiconductor, nanofabrication, doping

Introduction

As the demand for high performance of electronic devices in terms of power, speed and density continues to grow, there is an increasing need for new technologies to produce nanoelectronic devices (Ito and Okazaki, 2000; Thompson and Parthasarathy, 2006). A major driving force of the semiconductor industry has been the continuous reduction of the feature size and the overall manufacturing cost (Peercy, 2000; Charles, 2005). As a result, there has been persistent interests in developing technologies for high-resolution, low-cost, and large-scale fabrication of semiconductor materials.

Photolithography is the dominate patterning method for high-volume fabrication of electronic devices (Seisyan, 2011). Although this method is very successful and widely used in industry and research, photolithography requires a clean environment, expensive masks and equipment, all of which increase the overall manufacturing costs, especially at small scale (Wu et al., 2002). In addition, Si-based nanoelectronics typically require multiple doping types and doping concentrations in different regions of the wafer. Each doping step requires a separate cycle of lithography to define the doped region, which further increases the manufacturing cost and complexity (Costner et al., 2009; Škereň et al., 2018).

In recent years, DNA-based nanofabrication has drawn increasing attention due to its potential in realizing high-resolution low-cost patterning. We and others have reported various approaches to achieve high-resolution pattern transfer from DNA nanostructure templates to many substrates, such as SiO_2, Si, polymers, graphite, and self-assembled monolayers (Surwade et al., 2011; Surwade et al., 2013; Zhou et al., 2015; Surwade et al., 2016; Ricardo et al., 2017; Tian et al., 2017). A major motivation of these studies is for the future application and integration of DNA nanotechnology in the nanoelectronics industry. In this context, DNA-based nanofabrication has unique advantages when compared to the traditional, photolithography-based approaches. First, DNA-based nanofabrication combines the best features of top-down and bottom-up fabrication methods, in the sense that it is based on self-assembly (a unique feature of bottom-up methods) but can also produce almost any arbitrary patterns (used to be a unique feature of top down methods) (Biswas et al., 2012; Arole and Munde, 2014). Second, the cost of the DNA template for 2D patterning is extremely low (on the order of *ca*. \$1/m^2), which may enable low-cost, high-resolution patterning in very large scales. (Zhang et al., 2013).

DNA nanostructures are not only useful as templates for nanofabrication, they can also be used as dopant. Inspired by monolayer doping (Ho et al., 2009; Gao et al., 2018), we recently reported the use of DNA nanostructures to achieve site-specific doping of Si. In this approach, a DNA nanostructure was deposited onto a Si wafer and the phosphorous atoms (an *n*-type dopant) naturally present in the DNA were thermally diffused into the Si wafer to form *n*-doped regions. Unlike the traditional doping process, where the doped regions are defined by photolithography, the doped regions in this approach are defined by the shape of the DNA nanostructure. By using self-assembled monolayer as an intermediate, we also demonstrated *p*-doping of Si. This approach makes it possible to tune the doping level by adjusting the density of DNA molecules (e.g., one layer vs. two layers) or even introducing new types of dopants via chemically functionalization. Therefore, this DNA-based doping strategy has great potential to reduce the overall complexity of the fabrication of Si nanoelectronics. (Bai et al., 2020).

With various forms of DNA-enabled patterning and doping methods at hand, it is now possible to integrate DNA nanotechnology into the fabrication of nanoelectronics devices, potentially reducing or even eliminating photolithography and the associated etching, deposition, and doping steps. Such a goal, if realized, could lead to a drastic reduction of the manufacturing cost of nanoelectronic devices. In our previous work, we demonstrated the fabrication of prototype filed effect devices from a native Si substrate that has been site-specifically doped by DNA nanostructure templates. In this work, we describe the fabrication of vertical PN diodes by using DNA nanostructures to pattern and dope a *p*-type Si substrate.

Methods

Materials

p-type silicon wafers [100] with native oxide layers (Boron doped, 1–10 Ω·cm, double side polished) were purchased from University Wafer. DNA strands for the synthesis were purchased from IDT. Sulfuric acid, 2-Amino-2-(hydroxymethyl)-1,3-propanediol (Trizma base or Tris, ≥99.9%), ethylenediaminetetraacetic acid (EDTA, ≥99%), acetic acid (≥99.7%), magnesium acetate tetrahydrate (≥99%), hydrogen peroxide solution (30% wt. % in water), sodium chloride, methanol and ethanol were purchased from Sigma-Aldrich (St. Louis, MO). Nanopure water (18.3 MΩ) was obtained using a water purification system (Barnstead MicroPure Standard, Thermo Scientific, Waltham, MA) and used throughout the entire experiment to prepare chemical solutions and clean experimental samples.

Atomic force microscopy (AFM) and scanning electron microscopy (SEM) characterization

Throughout the study, AFM topography images were acquired in tapping mode in air using an Asylum MFP-3D Atomic Force Microscope with HQ:NSC15/Al BS AFM probes (325 kHz, 40 N/m) purchased from MikroMasch (NanoAndMore United States). SEM images were obtained by a ZEISS Sigma 500 VP microscope.

Synthesis and deposition of DNA nanotubes onto silicon wafer

The synthesis of DNA nanotubes here were based on previously published procedures. (Liu et al., 2006; Tian et al., 2017). The nanotube was prepared by self-polymerization of a single stranded DNA of the following sequence: 5′- CCAAGCTTGGAC TTCAGGCCTGAAGTGGTCATTCGAATGACCTGAGCGCTC A-3′. We diluted the DNA strand in 10 × TAE-Mg^{2+} buffer (400 mM tris-acetic acid, 10 mM EDTA, 125 mM Mg^{2+}, pH = 8.0) to a final concentration of 2 μM. The DNA single strand solution was then slowly cooled down from 95°C to 23°C in 2 days and stored at 4°C overnight for the subsequent deposition step.

The *p*-type Si substrate was cleaned by piranha solution [3/7 (v/v) hydrogen peroxide/sulfuric acid solution] for 30 min (*Warning: piranha solution reacts violently with organic compounds, please handle in a fume hood and use proper personal protection equipment*). The clean substrate was placed in a furnace at 900°C for 3 h to grow SiO_2, and the surface of the substrate was cleaned again by piranha solution. The prepared DNA sample (10 μL) was then pipetted onto the cleaned wafer and placed in a plastic petri dish. We then inserted a wet Kimwipe between the lid and the bottom to maintain high humidity inside the petri dish and reduce the evaporation. After 40 min of undisturbed incubation, we dried the Si substrate with a stream of N_2 gas, then immersed it into an 8/2 (v/v) ethanol/water solution for 20 s to remove salt residues on the surface and then dried the substrate with N_2 gas again. This washing and drying process was repeated 3 times.

Selective etching of SiO_2 under the DNA nanostructure template

The selective etching of SiO_2 is based on the DNA-enhanced HF-etching of SiO_2, reported in our previous work. (Zhou et al., 2015). Briefly, we exposed the Si/SiO_2 substrate with deposited DNA nanotubes to HF vapor. The etching of SiO_2 is much faster in the presence of DNA nanostructure than in its absence. We control the etching time to remove all SiO_2 under the DNA nanotubes to produce trenches while leaving a thin SiO_2 layer everywhere else. The thickness of the remaining SiO_2 was measured by ellipsometry, and the depth of the etched trench was measured by AFM. From these two measurements, we can determine if the SiO_2 under the DNA nanotube was completely removed.

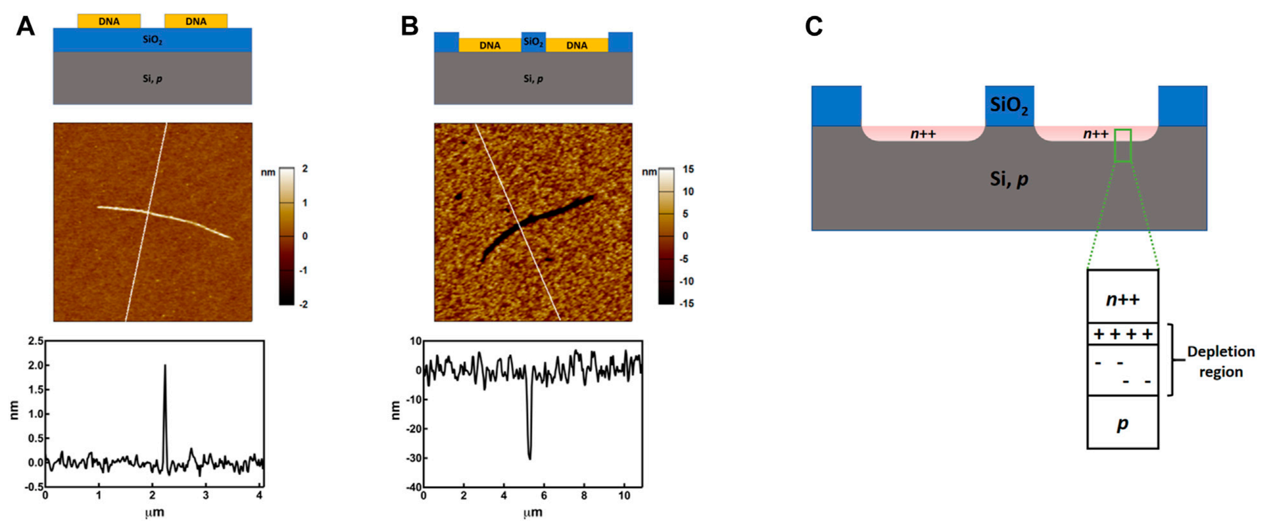

FIGURE 1
Schematic diagrams, AFM images and cross sections (the vertical lines in the AFM images indicate the locations of the cross section) of the silicon wafer during the patterning and doping process. **(A)**, DNA nanotubes deposited onto a Si/SiO_2 substrate. **(B)**, Trench formed as a result of the selective removal of the SiO_2 underneath the DNA through DNA-enhanced etching of SiO_2. **(C)**, Schematic diagram of the sample after the DNA-based doping. Multiple doped regions were shown but devices were fabricated on an individual doped region.

Site-specific doping of Si by DNA

The procedure was adopted from our previous work (Bai et al., 2020). Briefly, after DNA-mediated etching, the Si substrate was subjected to a UV/O_3 treatment (Novascan UV/ozone cleaner) for 3 h to oxidize the DNA nanotube. Our previous work showed that the oxidation leaves a residue, presumably phosphates. Then the sample was coated by a 20 nm of Al_2O_3 grown by atomic layer deposition (ALD) using a Cambridge Nanotech Fiji ALD instrument. The role of the Al_2O_3 layer is to minimize the loss and the lateral diffusion of the phosphate dopants. After depositing the Al_2O_3 capping layer, the samples were subjected to a rapid thermal annealing (RTA) process using a Surface Science Integration RTA Solaris 75 instrument. During this process, the temperature of the wafer rose to 1,000°C within 20 s and kept at this temperature for 10 s. Then the temperature was cooled down to 150°C within 3 min. After the RTA treatment, we used H_3PO_4 solution (2 M) to remove the Al_2O_3 capping layer and used a hot piranha solution to wash away (60 min) any residues on the surface. Finally, the sample was washed with deionized water and dried with N_2 gas.

Device fabrication and electrical measurements

The dielectric layer and metal contacts were patterned by electron beam lithography using a Raith e-Line system. In order to reduce leakage current, we deposited a 20 nm of HfO_2 layer by ALD (Cambridge Nanotech Fiji ALD) to cover all the surface where the metal contact would be later deposited except for the small area near the DNA-doped region. The metal contacts consist of 2 nm of Ti and 60 nm of Au evaporated using a Plassys electron beam evaporator. Finally, the metal contacts were wire-bonded to a chip carrier using aluminum wires. Electrical characteristics were measured using a Keithley 4200A-SCS Parameter Analyzer in air at room temperature.

Results and discussion

Fabrication of P-N junction using DNA-based doping

We used DNA nanotubes to form *n*-type site-specific doped regions on a *p*-type silicon wafer, thereby forming a vertical PN junction. The method for forming *n*-type site-specific doping here follows our previous work where we use the phosphates in DNA as the doping source. First, we prepared DNA nanotubes by self-assembly of one short single-strand DNA containing four palindromic segments, which allows the strands to self-polymerize into nanotubes. We then deposited the DNA nanotubes onto a *p*-type wafer that has a 40 nm thick of SiO_2 (Figure 1A). (Bai et al., 2021) Once deposited, these DNA nanotubes have a width of *ca.* 70 nm and a height of *ca.* 2.0 nm. The small thickness is consistent with the expected drying-induced collapse of the tube structure after deposition onto the Si substrate.

To dope Si, we first exposed the wafer to HF vapor to remove all the SiO_2 under the DNA nanotubes, while leaving about 30 nm of SiO_2 everywhere else to eliminate undesirable doping of the background region during the RTA (Figure 1B). The SiO_2 underneath the DNA nanotube was etched faster because DNA absorbs water, which is a catalyst for HF etching of SiO_2. After the etching, the DNA nanotubes left narrow trenches on the wafer. We used ellipsometry and AFM to measure the average thickness of the SiO_2 on the wafer and the depth of the trench formed by the DNA nanotube, respectively. The two measurement gave very similar

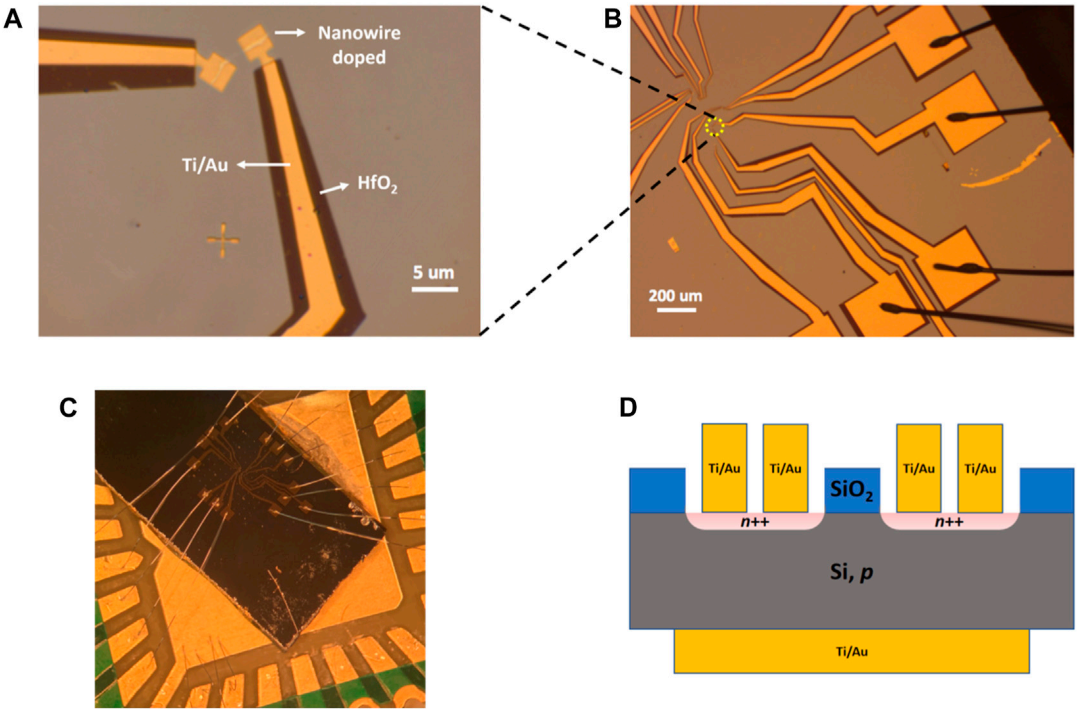

FIGURE 2
Fabrication of PN diodes from a single "nanowire"-shaped doped region. **(A,B)**, Optical image of the patterned electrodes. **(C)**, Photograph of the device after wire bonding. **(D)**, Schematic diagram of the PN diode.

values, *ca.* 30 nm, indicating that the SiO_2 under the DNA nanotubes has been completely removed to expose the underlying Si.

The sample was then treated with UV/O_3 to remove the organic components of the DNA. During this process, carbon and nitrogen atoms within the DNA and the buffer residue, if any, are removed by O_3 oxidation, leaving a phosphate residue that will serve as the doping source. While not investigated in this study, it will be important to maintain an ultraclean environment to minimize undesired deactivation of dopants due to contamination from the DNA solution and ambient. The wafer was then covered with 20 nm of Al_2O_3 to limit the lateral diffusion and desorption of the dopants. To initiate the doping, the wafer was treated with RTA for 10 s at 1,000°C. After cooling to r.t., it was washed with H_3PO_4 to remove the Al_2O_3 capping layer and washed with piranha solution to remove any inorganic residue on the surface. We previously showed that this process resulted in high level *n*-doping of native Si wafer, achieving dopant concentration of 6.4×10^{18} cm^{-3}. The *p*-type wafer used in this study was doped by boron and has a resistivity of 1–10 Ω·cm, from which we estimated a *p*-dopant concentration of *ca.* 10^{16} cm^{-3}. Therefore, after the heavy *n*-doping by DNA nanotube, nanowire-shaped vertical P-N junctions will be formed on the Si wafer (Figure 1C).

Fabrication of PN diodes

We used electron beam lithography to pattern electrodes on a single nanowire-shaped PN junction region (Figures 2A, B) to form a vertical PN diode. Before patterning metal electrodes, we deposited a thin layer of HfO_2 (20 nm) to cover the whole wafer except the targeted area containing the nanowire-shaped PN junction. After patterning electrodes, we used wire bonding to connect the electrodes to a chip carrier to avoid mechanical damage of the HfO_2 layer during electrical measurement. Figure 2C is a photograph of the device after wire bonding. A schematic diagram of the sample ready for testing is also shown in Figure 2D, where two identical devices were shown. Control devices were also fabricated on the same wafer in areas without DNA nanotubes; in the absence of DNA nanotubes, the SiO_2 layer was not completely etched away to expose Si and therefore such region was not doped by DNA and also covered by the HfO_2. Current measured from the control device are due to leakage through the HfO_2 layer.

Characterization of PN diode

To evaluate the electrical characteristics of the PN diode, we wired the device according to Figure 3A. The current-voltage (I-V) characteristic of the device is shown in Figures 3B, C. It can be seen that the device fabricated from the DNA-doped region exhibits the characteristic blockage behavior of the PN diode, while the control device fabricated on non-doped region does not. The small current measured from the control device also confirms that the leakage current through the HfO_2 coating is negligible. Further analysis shows that the knee voltage of the PN diode is *ca.* 0.7 V, which is consistent with the theoretical value of Si (Sawant and Baliga, 2000; Ghazi et al., 2009). The result

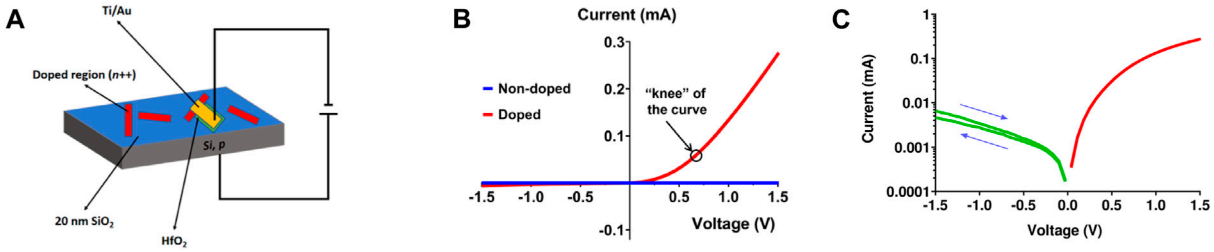

FIGURE 3
Characterization of the PN diode. **(A)**, Schematic diagram for the test of the device. **(B)**, I-V curves for the "nanowire" doped region and non-doped region. **(C)**, semilog plot of I-V curve. Arrows indicate I-V scan direction.

confirms the successful site-specific SiO$_2$ etching, *n*-doping by DNA, formation of PN junction, and fabrication of vertical PN diodes. However, the I-V curve also gives an ideality factor (*ca.* 6.5, within 0.2–0.5 V of forward bias) that is significantly larger than 1, suggesting that the device characteristics are far from that of ideal silicon behavior and possibility involve trap-assisted tunneling, carrier leakage, and large serial resistance. (Martil and Diaz, 1991; Zhu et al., 2009).

Conclusion

In summary, we have successfully formed vertical PN junctions by using DNA nanotube to dope a *p*-type Si substrate. PN diodes were fabricated from these junctions and their electrical characteristics are consistent with those of their conventional counterparts. The successful fabrication of PN diodes highlights the potential of using DNA nanostructure to pattern and dope Si and based on which, to manufacture functional nanoelectronic devices. That being said, we recognize that there are still many challenges that need to be addressed before this technology can make a real impact on semiconductor manufacturing. In this regard, we are investigating ways to combine conventional lithography with DNA nanotechnology for large scale fabrication of devices. For example, use existing lithography techniques to define a micrometer-sized area, within which self-assembled DNA nanostructures, such as DNA 2D lattice, defines multiple doping areas and devices. We hope that this work will catalyze further research on DNA-based nanofabrication and ultimately a simpler, lower-cost manufacturing approach based on biomolecular templates.

Data availability statement

The raw data supporting the conclusion of this article will be made available by the authors, without undue reservation.

Author contributions

RB: Data curation, Investigation, Writing–original draft, Writing–review and editing. YL: Data curation, Investigation, Writing–review and editing. BZ: Data curation, Investigation, Writing–review and editing. BC: Data curation, Investigation, Writing–review and editing. FX: Conceptualization, Funding acquisition, Writing–review and editing. HL: Conceptualization, Funding acquisition, Project administration, Resources, Supervision, Writing–review and editing.

Funding

The author(s) declare financial support was received for the research, authorship, and/or publication of this article. HL and FX acknowledge partial support from NSF CMMI-2229131 and ECCS-2235294; YL and FX acknowledge support from NSF ECCS-1943683.

Conflict of interest

The authors declare that the research was conducted in the absence of any commercial or financial relationships that could be construed as a potential conflict of interest.

The author(s) declared that they were an editorial board member of Frontiers, at the time of submission. This had no impact on the peer review process and the final decision.

Publisher's note

References

Arole, V., and Munde, S. (2014). Fabrication of nanomaterials by top-down and bottom-up approaches-an overview. *JAAST:Material Science (Special Issue)*, 1, 89–93.

Bai, R., Du, Y., Xu, A., Hu, Y., Erickson, J. R., Hui, L., et al. (2020). DNA-Based strategies for site-specific doping. *Adv. Funct. Mater.* 31, 2005940. doi:10.1002/adfm.202005940

Bai, R., Du, Y., Xu, A., Hu, Y., Erickson, J. R., Hui, L., et al. (2021). DNA-Based strategies for site-specific doping. *Adv. Funct. Mater.* 31 (1), 2005940. doi:10.1002/adfm.202005940

Biswas, A., Bayer, I. S., Biris, A. S., Wang, T., Dervishi, E., and Faupel, F. (2012). Advances in top–down and bottom–up surface nanofabrication: techniques, applications and future prospects. *Adv. Colloid Interface Sci.* 170 (1-2), 2–27. doi:10.1016/j.cis.2011.11.001

Charles, H. K., Jr (2005). Miniaturized electronics. *Johns Hopkins Apl. Tech. Dig.* 26 (4), 402–413.

Costner, E. A., Lin, M. W., Jen, W.-L., and Willson, C. G. (2009). Nanoimprint lithography materials development for semiconductor device fabrication. *Annu. Rev. Mater. Res.* 39, 155–180. doi:10.1146/annurev-matsci-082908-145336

Gao, X., Guan, B., Mesli, A., Chen, K., and Dan, Y. (2018). Deep level transient spectroscopic investigation of phosphorus-doped silicon by self-assembled molecular monolayers. *Nat. Commun.* 9 (1), 118. doi:10.1038/s41467-017-02564-3

Ghazi, H. E., Jorio, A., and Zorkani, I. (2009). Analysis of temperature effect on IV characteristics of silicon (npn) emitter-base. *Moroc. J. Condens. Matter* 11 (2), 30–34.

Ho, J. C., Yerushalmi, R., Smith, G., Majhi, P., Bennett, J., Halim, J., et al. (2009). Wafer-scale, sub-5 nm junction formation by monolayer doping and conventional spike annealing. *Nano Lett.* 9 (2), 725–730. doi:10.1021/nl8032526

Ito, T., and Okazaki, S. (2000). Pushing the limits of lithography. *Nature* 406 (6799), 1027–1031. doi:10.1038/35023233

Liu, H., Chen, Y., He, Y., Ribbe, A. E., and Mao, C. (2006). Approaching the limit: can one DNA oligonucleotide assemble into large nanostructures? *Angew. Chem. Int. Ed.* 45 (12), 1942–1945. doi:10.1002/anie.200504022

Martil, I., and Diaz, G. G. (1991). A laboratory experiment for DC characterization of p-n devices. *Eur. J. Phys.* 12 (3), 149–152. doi:10.1088/0143-0807/12/3/010

Peercy, P. S. (2000). The drive to miniaturization. *Nature* 406 (6799), 1023–1026. doi:10.1038/35023223

Ricardo, K. B., Xu, A., Salim, M., Zhou, F., and Liu, H. (2017). Deposition of DNA nanostructures on highly oriented pyrolytic graphite. *Langmuir* 33 (16), 3991–3997. doi:10.1021/acs.langmuir.6b03836

Sawant, S., and Baliga, B. J. (2000). Current saturation control in silicon emitter switched thyristors. *Solid-State Electron.* 44 (1), 133–142. doi:10.1016/s0038-1101(99)00217-8

Seisyan, R. (2011). Nanolithography in microelectronics: a review. *Tech. Phys.* 56 (8), 1061–1073. doi:10.1134/s1063784211080214

Škereň, T., Pascher, N., Garnier, A., Reynaud, P., Rolland, E., Thuaire, A., et al. (2018). CMOS platform for atomic-scale device fabrication. *Nanotechnology* 29 (43), 435302. doi:10.1088/1361-6528/aad7ab

Surwade, S., Zhou, F., Li, Z., Powell, A., O'Donnell, C., and Liu, H. (2016). Nanoscale patterning of self-assembled monolayers using DNA nanostructure templates. *Chem. Commun.* 52 (8), 1677–1680. doi:10.1039/c5cc08183a

Surwade, S. P., Zhao, S., and Liu, H. (2011). Molecular lithography through DNA-mediated etching and masking of SiO2. *J. Am. Chem. Soc.* 133 (31), 11868–11871. doi:10.1021/ja2038886

Surwade, S. P., Zhou, F., Wei, B., Sun, W., Powell, A., O'Donnell, C., et al. (2013). Nanoscale growth and patterning of inorganic oxides using DNA nanostructure templates. *J. Am. Chem. Soc.* 135 (18), 6778–6781. doi:10.1021/ja401785h

Thompson, S. E., and Parthasarathy, S. (2006). Moore's law: the future of Si microelectronics. *Mater. Today* 9 (6), 20–25. doi:10.1016/s1369-7021(06)71539-5

Tian, C., Kim, H., Sun, W., Kim, Y., Yin, P., and Liu, H. (2017). DNA nanostructures-mediated molecular imprinting lithography. *ACS Nano* 11 (1), 227–238. doi:10.1021/acsnano.6b04777

Wu, M.-H., Park, C., and Whitesides, G. M. (2002). Fabrication of arrays of microlenses with controlled profiles using gray-scale microlens projection photolithography. *Langmuir* 18 (24), 9312–9318. doi:10.1021/la015735b

Zhang, G., Surwade, S. P., Zhou, F., and Liu, H. (2013). DNA nanostructure meets nanofabrication. *Chem. Soc. Rev.* 42 (7), 2488–2496. doi:10.1039/c2cs35302d

Zhou, F., Michael, B., Surwade, S. P., Ricardo, K. B., Zhao, S., and Liu, H. (2015). Mechanistic study of the nanoscale negative-tone pattern transfer from DNA nanostructures to SiO2. *Chem. Mater.* 27 (5), 1692–1698. doi:10.1021/cm5044914

Zhu, D., Xu, J., Noemaun, A. N., Kim, J. K., Schubert, E. F., Crawford, M. H., et al. (2009). The origin of the high diode-ideality factors in GaInN/GaN multiple quantum well light-emitting diodes. *Appl. Phys. Lett.* 94 (8), 081113. doi:10.1063/1.3089687

Frontiers in
Nanotechnology

Explores nanoscale science and engineering of materials, devices and tools

An interdisciplinary journal across nanoscience and nanotechnology, at the interface of chemistry, physics, materials science and engineering. It focuses on new nanofabrication methods and their applications.

Discover the latest Research Topics

See more →

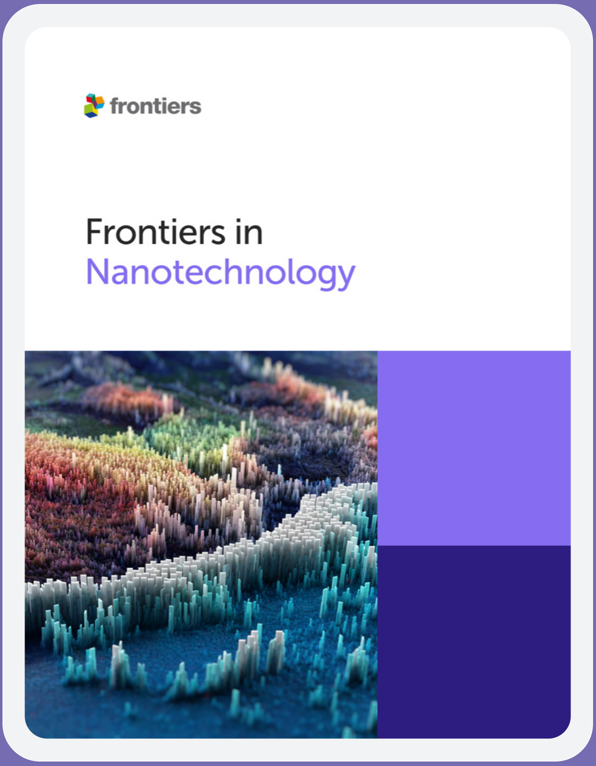
frontiers

Frontiers in
Nanotechnology

Frontiers

Avenue du Tribunal-Fédéral 34
1005 Lausanne, Switzerland
frontiersin.org

Contact us

+41 (0)21 510 17 00
frontiersin.org/about/contact